



Crystal Engineering of γ -Amino Butanoic Acid and its Pharmaceutically Active Derivatives

Dissertation

zur Erlangung des Doktorgrades

der Mathematisch-Naturwissenschaftlichen Fakultät

der Heinrich-Heine-Universität Düsseldorf

vorgelegt von

Daniel Komisarek

aus Bochum

Düsseldorf, Februar 2023

Aus dem Institut für Anorganische Chemie und Strukturchemie I
Der Heinrich-Heine-Universität Düsseldorf

Gedruckt mit der Genehmigung der
Mathematisch-Naturwissenschaftlichen Fakultät der
Heinrich-Heine-Universität Düsseldorf

1. Gutachter: Univ. Prof. Dr. Christoph Janiak
2. Gutachter: Univ. Prof. Dr. Christian Ganter

Tag der mündlichen Prüfung:

28.03.2023

Eidesstattliche Versicherung

Ich, Herr Daniel Komisarek, versichere an Eides statt, dass die vorliegende Dissertation von mir selbstständig und ohne unzulässige fremde Hilfe unter Beachtung der „Grundsätze zur Sicherung guter wissenschaftlicher Praxis an der Heinrich-Heine-Universität Düsseldorf“ erstellt worden ist. Diese Arbeit wurde bisher keiner anderen Fakultät vorgelegt und keine vorherigen erfolglosen Promotionsversuche unternommen.

Ort, Datum

Unterschrift

Danksagung

Ich möchte diese Stelle nutzen, um meinen Dank an Personen auszusprechen, die meine Promotion ermöglicht und unterstützt haben.

Zunächst möchte ich meiner Betreuerin Vera Vasylyeva-Shor danken. Du warst immer ansprechbar, hast mit Rat und Tat zur Seite gestanden und mir sehr viel Freiheit bei meiner Arbeit gelassen. Ich hoffe, dass ich diese Freiheit gut genutzt habe und du mit den Ergebnissen genauso zufrieden bist, wie ich am Ende auch. Danke, dass du so eine großartige Betreuerin warst.

Weiterhin möchte ich Prof. Dr. Christoph Janiak und Prof. Dr. Christian Ganter dafür danken, dass sie die offiziellen Gutachterpositionen der Promotion übernommen haben. Insbesondere Herrn Janiak möchte ich auch dafür danken, dass er mir einen Arbeits- und Laborplatz zur Verfügung gestellt und mich an seinem Lehrstuhl aufgenommen hat.

Auch möchte ich den Festangestellten des Lehrstuhls Birgit Tommes, Marcell Demandt, Annette Ricken und Linda Kronenbarg danken. Danke dafür, dass ihr den Laden am Laufen haltet und bei technischen Fragen immer für mich ansprechbar wart. Birgit, es war immer schön mit dir das Biochemiker Praktikum zu betreuen. Ich hoffe du wirst da zukünftig weiter nette Leute haben.

Ich möchte auch allen weiteren Postdocs, Doktoranden, Master- und Bachelorstudenten danken, die während meiner Promotion dabei waren. Es war angenehm für mich, mit euch zusammenzuarbeiten und ich bin immer gerne zur Arbeit gekommen. Insbesondere möchte ich meine beiden *Co-Crystal-Engineers* Tobias Heinen und Takin Haj Hassani Sohi hervorheben. Tobi, bei dir ist es bald auch so weit und ich wünsche dir viel Erfolg, freue mich auf deine Promotion. Takin, denk dran: *Komisarek & Sohi Partnerschaftsgesellschaft mbH*. Haha.

Zuletzt möchte ich Familie und Freunden danken. Mama, Papa, Kira, Onkel Anton, Tante Liliane, Vanessa, danke dass ihr für mich da seid. Alex, Daniel, Fabian, Julian, Kevin, Marvin, Philipp, Simon, Sören, danke euch, dass ihr so gute Freunde seid. Ich sollte mich wieder öfter melden. Anni ich liebe dich und du bist auch sehr bald fertig mit deiner Promotion. Auf ein gemeinsames Leben und eine gemeinsame Zukunft. Du bist der wichtigste Mensch für mich, dir widme ich meine Arbeit.

Table of Contents

I Publications	1
II Kurzzusammenfassung	2
III Short Summary	3
IV List of Abbreviations	4
1 Introduction	5
1.1 Basics of (pharmaceutical) crystal engineering	5
1.1.1 Crystal Engineering: A brief introduction on history and challenges in a developing field.....	5
1.1.2 The crystallization process	8
1.1.3 Classification and properties of (crystalline) solids	12
1.1.4 Intermolecular interactions: ionic bond and hydrogen bond, π - interactions and dispersive forces.....	16
1.1.5 Interim Summary I	20
1.2 Experimental, analytical, and computational approaches.....	21
1.2.1 Experimental approaches to (pharmaceutical) crystal engineering ...	21
1.2.2 Analytical approaches to (pharmaceutical) crystal engineering	23
1.2.3 Computational approaches to (pharmaceutical) crystal engineering .	27
1.2.4 Interim Summary II	30
1.3 γ -amino butanoic acid and its pharmaceutically active derivatives.....	31
1.3.1 γ -amino butanoic acid (GABA)	31
1.3.2 2-(1-(aminomethyl)-cyclohexyl)acetic acid (Gabapentin).....	31
1.3.3 3-(aminomethyl)-5-methylhexanoic acid (Pregabalin).....	32
1.3.4 γ -Amino-3-phenylbutanoic acid (Phenibut)	33
1.3.5 γ -Amino-3-(4-chlorophenyl)butanoic acid (Baclofen).....	33
1.3.6 Co-formers.....	34
1.3.7 Interim Summary III	34
2 Motivation	36

3 Published works	38
3.1 Crystal Structure and Thermal Properties of Phenibut, Phenibut H ₂ O and Phenibut HCl: a Case for Phase Stability Based on Structural Considerations .	39
3.2 A Lesson in Humbleness: Crystallization of Chiral and Zwitterionic APIs Baclofen and Phenibut	62
3.3 Co-crystals of zwitterionic GABA API's pregabalin and phenibut: properties and application	112
3.4 Maleic Acid as a Co-former for Pharmaceutically Active GABA Derivatives: Mechanochemistry or Solvent Crystallization?	182
3.5 Understanding Polymorphism and Multicomponent Crystal Formation of GABA and Gabapentin	229
4 Summary and Outlook	314
5 References	318

I Publications

First-Author Publications:

Komisarek, D.; Pallaske, M.; Vasylyeva, V. Crystal Structure and Thermal Properties of Phenibut, Phenibut H₂O and Phenibut HCl: a Case for Phase Stability Based on Structural Considerations, *Z. Anorg. Allg. Chem.*, **2021**, 647, 984–991.

Herbst, M. & Komisarek, D.; Strothmann, T.; Vasylyeva, V. A Lesson in Humbleness: Crystallization of Chiral and Zwitterionic APIs Baclofen and Phenibut, *Crystals*, **2022**, 12, 1393.

Komisarek, D.; Haj Hassani Sohi, T.; Vasylyeva, V. Co-crystals of zwitterionic GABA API's pregabalin and phenibut: properties and application, *CrystEngComm*, **2022**, 24, 8390-8398.

Komisarek, D.; Taskiran, E.; Vasylyeva, V. Maleic Acid as a Co-former for Pharmaceutically Active GABA Derivatives: Mechanochemistry or Solvent Crystallization?, Submitted to *Materials*, **Jan. 2023**

Komisarek, D.; Demirbas, F.; Merz, K.; Schauerte, C.; Vasylyeva, V. Understanding Polymorphism and Multicomponent Crystal Formation of GABA and Gabapentin, Submitted to *Cryst. Growth Des.*, **Feb. 2023**

Co-Author Publications:

Nieland, E.; Komisarek, D.; Hohloch, S.; Wurst, K.; Vasylyeva, V.; Weingart, O.; Schmidt, B. M. Supramolecular networks by imine halogen bonding, *ChemComm*, **2022**, 58, 5233-5236

Lamkwoski, L.; Komisarek, D.; Merz, K. GABA-Controlled Synthesis of the Metastable Polymorphic Form and Crystallization Behavior with a Chiral Malic Acid, *Cryst. Growth Des.*, **2022**, 22, 356–362.

II Kurzzusammenfassung

Crystal Engineering hat sich spätestens seit den neunziger Jahren des vergangenen Jahrhunderts als eigenständige Subdisziplin der supramolekularen Chemie etabliert. Allerdings sind viele Vorgänge, die das supramolekulare Aggregationsverhalten betreffen, auch über dreißig Jahre später noch nicht vollkommen aufgeklärt. Daraus ergeben sich zahlreiche Probleme für das Feld, welche vor Allem die Vorhersagbarkeit von Struktur und Eigenschaften kristalliner Festkörper betreffen. In der Pharmazie gipfelt diese geminderte Kontrollfähigkeit über die Festphase im Phänomen der sogenannten *Disappearing Polymorphs*. In so bezeichneten Fällen ist es im industriellen Maßstab plötzlich nicht mehr möglich ein zuvor über lange Zeit wohldefiniertes Produkt unter den scheinbar gleichen Bedingungen wie in der Vergangenheit zu erhalten. Ein unerkannter Einfluss begünstigt dabei einen unerwarteten Phasenwechsel des Zielproduktes zu einer anderen polymorphen Modifikation. Dieses Problem ist beispielhaft für die Herausforderungen des modernen Crystal Engineerings: der Komplexität des Kristallisationsvorgangs mit Mitteln Herr zu werden, die kaum die Vielzahl an möglichen Einflüssen auf diesen Prozess erfassen können. In den vorliegenden Arbeiten wurde die Kristallisation der γ -Aminobuttersäure (GABA) und ihren Derivaten Gabapentin, Pregabalin, Phenibut und Baclofen im Vergleich miteinander untersucht. Dabei wurden zahlreiche Kristallstrukturen sowohl von Einzel- als auch Multikomponentenphasen wie Salzen und Co-Kristallen dieser Stoffe mit einer Auswahl an Carbonsäuren aufgeklärt und ihre physikochemischen Eigenschaften bestimmt. Dazu wurden sowohl analytische Methoden wie auch Computer basierte Rechnungsmodelle verwendet. Es konnte gezeigt werden, dass in vielerlei Hinsicht ein ähnliches Verhalten in den Bindungsmodi der supramolekularen Aggregation der untersuchten Substanzen besteht. Solche Gemeinsamkeiten bleiben jedoch oberflächlich. So wurde beispielsweise festgestellt, dass die Bildung von Multikomponentensystemen mit der selben Carbonsäure oftmals mit mehr als einem GABA-Derivat möglich ist. Allerdings unterscheiden sich die erhaltenen Produkte in vielerlei Fällen sowohl strukturell als auch in ihren Eigenschaften. Ein kristallisationsbasiertes Verfahren zur Deracemisierung von Pregabalin ist nicht in gleicher Weise auf Phenibut übertragbar. Die Arbeit zeigt auf, dass sogar zwischen molekular nah verwandten Spezies gravierende Unterschiede im Kristallisationsverhalten bestehen können, denen nicht einfach Herr zu werden ist.

III Short Summary

Crystal engineering has been established as an independent subdiscipline of supramolecular chemistry since the 1990s of the previous century at the latest. However, many processes affecting supramolecular aggregation behaviour have not been fully elucidated even more than thirty years later. This poses numerous problems for the field, mainly concerning the predictability of structure and properties of crystalline solids. In pharmaceuticals, this diminished ability to control the solid phase culminates in the phenomenon known as *disappearing polymorphs*. In such cases, it is suddenly no longer possible on an industrial scale to obtain a product that has previously been well-defined over a long period of time under what appear to be the same synthesis conditions as in the past. In this case, an unrecognized influence favours an unexpected phase change of the target product to a different polymorphic modification. This problem is exemplary for the challenges of modern crystal engineering: to cope with the complexity of the crystallization process by means that can hardly capture the multitude of possible influences on this process. In the present work, the crystallization of γ -amino butanoic acid (GABA) and its derivatives Gabapentin, Pregabalin, Phenibut, and Baclofen were studied in comparison with each other. Numerous crystal structures of both single and multicomponent phases such as salts and co-crystals of these substances with a selection of carboxylic acids were elucidated and their physicochemical properties were determined. Both analytical and computational models were used for this purpose. It was shown that in many respects there is similar behaviour in the binding modes of supramolecular aggregation of the studied substances. However, such similarities remain superficial. For example, it was found that the formation of multicomponent systems with the same carboxylic acid is often possible with more than one GABA-derivative. However, in many cases the products obtained differ both structurally and in their properties. A crystallization-based procedure for the deracemization of Pregabalin is not equally applicable to Phenibut. The work demonstrates that even between molecularly closely related species there can be serious differences in crystallization behaviour that are not easy to master.

IV List of Abbreviations

HB	– hydrogen bond
GABA	– γ -amino butanoic acid
CSD	– Cambridge Structural Database
API	– active pharmaceutical ingredient
GRAS	– generally recognized as safe
FDA	– Food and Drug Administration
PXRD	– powder X-ray diffraction
SCXRD	– single crystal X-ray diffraction
IR	– infra red
ATR	– attenuated total reflection
¹H-NMR	– proton nuclear magnetic resonance
DSC	– differential scanning calorimetry
TGA	– thermogravimetric analysis
DFT	– density functional theory

1 Introduction

1.1 Basics of (pharmaceutical) crystal engineering

1.1.1 Crystal Engineering: A brief introduction on history and challenges in a developing field

Crystal Engineering is a comparatively new research field that has developed from a concept regarding solid state matrices of specific purposes to a strongly diversified topic over several decades. In 1955 Raymond Pepinsky was the first to introduce the term crystal engineering in his Physical Review contribution *Crystal Engineering – New Concept in Crystallography*.^[1] However, filling this term with meaning is most commonly attributed to Gerhard Schmidt's *Photodimerization in the solid state* published in 1971.^[2] Schmidt viewed crystal engineering as the use of a crystalline matrix to influence the outcome of photochemical reactions. His particular interest was the targeted formation of a photo reaction product without impurities. By using a solid crystalline template to limit unwanted molecular configurations, he was able to reduce by-products that occur in solvent-based reactions. Many published works from the 1970s and 1980s refer to this early established relation to photochemistry.^[3–8] Parallel to this a more general view on the topic has developed that focuses on the crystalline solid state as a whole rather than just its applicability in photochemistry.^[9–11] This process has been remarkably impacted by Gautam Desiraju who published many of the early works on crystal engineering and established concepts such as noncovalent attractive interactions without the involvement of hydrogen.^[12–23]

In the 1990s, crystal engineering research topics continued to diversify, and pharmaceutical crystal engineering emerged as one of the most commonly addressed subject matters, which remains important to this day.^[24–36] In 1992, Peter York was the first to review crystal engineering in a pharmaceutical context and used the term crystal engineering, even though earlier works had already established connections between crystal structure and pharmaceutical properties.^[37] Just three years later in 1995 Bernstein and Dunitz described an interesting phenomenon that highlighted what would prove to be a major challenge to overcome for crystal engineering in general and pharmaceutical crystal engineering in particular. Their contribution *Disappearing Polymorphs* showcases the unpredictability and unreliability of the crystal phase.^[38]

The article described how previously obtainable crystalline modifications of pharmaceutical substances become unavailable in industrial production settings for seemingly no discernible reason. Over the years this topic has been brought up time and again in differing contexts,^[39–50] and sometimes ways have been found to make a disappeared polymorph reappear. In 2015, Bernstein, Bučar, and Lancaster revisited the issue 20 years after the first publication, but their contribution did not end on a positive note. They essentially concluded that while methods have improved, a definitive solution cannot be proposed.^[51]

In the 1980s and 1990s, research interests began to focus on developing ways to control crystallization outcomes, and this led to the generation of numerous perspectives that address this problem.^[52–58] Maybe one of the most accessible solutions regarding the question of crystal phase predictability was proposed by Desiraju. His concept of the supramolecular synthon explains how subunits in organic molecules can serve as building blocks for supramolecular assembly, for example, by enabling hydrogen bonds (HBs) (**Figure 1**).^[59–62]

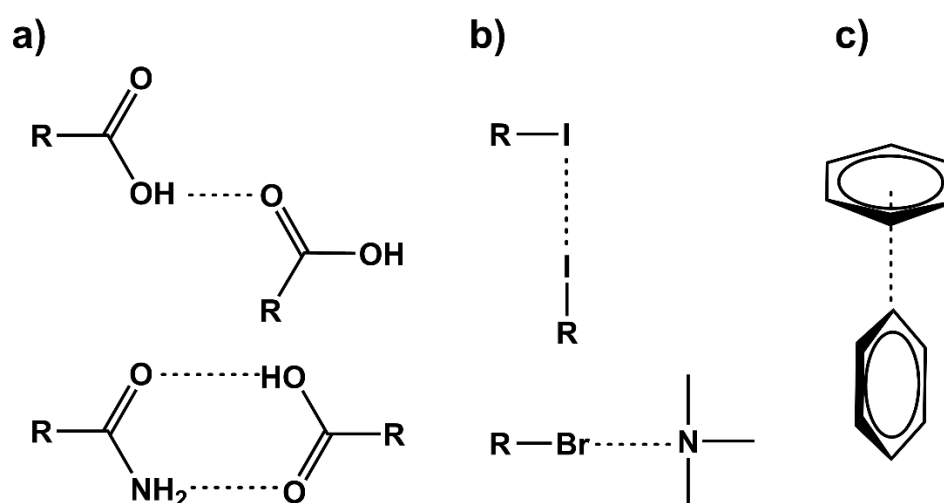


Figure 1. Examples for supramolecular synthons. Single hydrogen bond between two carboxylic acid subunits and a heterodimer between an amide and a carboxylic acid synthon **a**), halogen bond between two iodine residues as well as a bromine residue and trimethylamine **b**), and an edge-to-face π -interaction with benzene rings **c**).

The supramolecular synthon might be deemed as a first attempt to identify obvious regularities in crystallization, and to generate an accessible, visible understanding of crystallization behaviour. Despite being a staple in the field for close to thirty years after its introduction,^[63–67] it has been subject to critique. Predicting whether a desired supramolecular synthon will form upon crystallization is not always easy, as expected interaction motifs based on the strongest synthon do not always occur reliably.^[68,69] This model simply overlooks too many other factors that play a role in the crystallization

process, such as the crystallization medium or method, temperature, saturation level, pH-value, additives, choice of antisolvent, and their manifold influences on modes of prenucleation, nucleation and crystal growth.^[70–73] Thus, the effectiveness of identifying a supramolecular synthon for crystal structure prediction should not be overestimated.

Although the supramolecular synthon offers a simple method to predict possible interaction motifs, more quantifiable methods have become prevalent in crystal engineering around the same time as well. Computational approaches, initially used as a tool for crystal structure solutions, were enhanced during this time. Applications to analyse connections between structure and physical properties, find ways to quantify intermolecular interactions, attempt crystal structure predictions or understand the steps of the crystallization process were developed.^[74–83] These methods were continuously advanced during the following years.^[73,84–102] Concomitant to the increasing computerization was and is the emergence and growing importance of databases for recorded crystal data, such as the Cambridge Structural Database (CSD).^[103] Established in 1965, the CSD is one of the most important collections of single crystal data of organic and metal-organic compounds, enabling analysis of large file sets. As more dedicated artificial intelligence-based tools become available, their capability to connect non-obvious and complex correlations in huge datasets could solve the problem of making crystallization actually predictable.^[104–107]

This short introduction highlights how crystal engineering has developed from a very specified niche to a diversified and broad field over the years of its existence (**Figure 2**). Crystal engineering still faces key problems that already occurred during its infancy. The unpredictability of crystal structures and the complex interplay of factors that influence their formation continue to pose challenges for researchers. This is especially problematic for pharmaceutical crystal engineering, where high standards of phase purity and product effectiveness are applied that all depend on reliable production processes. Experimental trial and error approaches, computational modelling to various degrees, or mixtures of both remain the methodology of choice to overcome these challenges. While artificial intelligence may be able to find order in the complexity of the supramolecular field in the future, at this point each system of interest must be investigated thoroughly and understood on its own, with only limited applicability of generalizations concerning other systems. The crystallization process, solid-phase classification, intermolecular interactions, experimental crystallization

approaches, analytical methods in characterization, computational models to identify phase properties and a specific set of herein investigated compounds shall be discussed to understand the framework upon which the published works concerning this thesis were prepared.

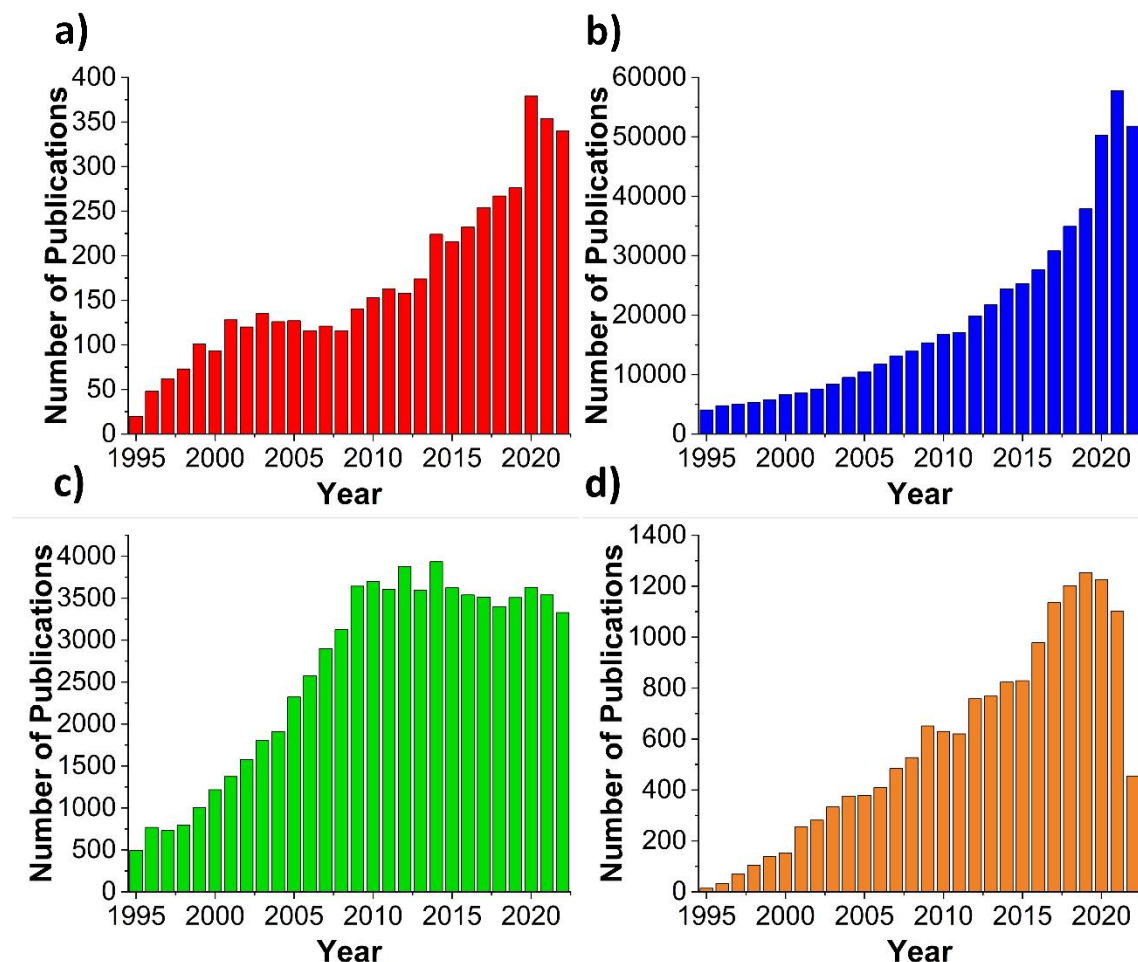


Figure 2. Scifinder-n searches conducted in Jan. 2023 using the terms: a) Crystal Engineering, b) Pharmaceutical Crystal Engineering, c) Supramolecular Synthon, and d) Computational Crystal Engineering. The search results highlight how interest in the presented topics has developed over the last years.

1.1.2 The crystallization process

More than 125 years ago, Wilhelm Ostwald proposed that during crystallization, the most stable product is not always formed first. Instead, multiple stages must be passed before the thermodynamically most beneficial entity is reached.^[108,109] In modern times, crystallization is categorized into three possible steps, two of which must necessarily occur: nucleation (classical or non-classical nucleation theory), crystal growth, and potential solid phase transformations.^[71,110–112] Each system must undergo some form of nucleation and crystal growth steps to form a visible crystalline entity. Various mechanisms for the formation of early-stage clusters, nuclei, or seeds have been

proposed, the mechanism that takes action depends on the system being crystallized.^[113]

In the classical sense, nucleation can be summarized as the one-step formation of larger molecular or ion clusters from smaller particles in the crystallization environment. If the energy barrier for coagulation is breached, cluster formation is induced, depending on various thermodynamic factors such as temperature, saturation level, pressure, mechanical stress, or the presence of impurities (heterogeneous nucleation). These formed clusters or seeds either dissolve again or start to undergo crystal growth.^[73,114–122] This level of understanding for the nucleation process is sufficient in many cases, but recent research results concerning nano structures contradict this simple model. Classically, a spherical form for early-stage clusters is assumed, which is not always the case.^[73] Non-classical nucleation theory offers various possible mechanisms for the nucleation stage, taking into consideration non-spherical cluster formations as well. For example, the spontaneous separation of phases from solution without actual nucleation occurs for metals in the so-called spinodal region and leads to a crystalline product if the phases are sufficiently separated.^[119,121] Other described mechanisms include the formation of phase intermediates prior to nucleation. These intermediates can be seen as dense solution droplets or surface ordered droplets and be of crystalline, amorphous, or mixed nature.^[119] Phase intermediates do not necessarily nucleate in one step, and multistep nucleation can undergo all various intermediate stages before forming a seed. An interesting specific mechanism that was discovered for protein crystal growth on a MoS₂ surface is called direct nucleation. This nucleation mode occurs for systems that can crystallize one array at a time, forming monolayers on a given surface. As such the energy barrier necessary to form three dimensional clusters is circumvented, thus contradicting classical nucleation theory.^[123]

The complexity of the crystal growth stage is not reduced compared to nucleation. Again, there is a classical and a non-classical understanding of the growth mechanisms. In the classical understanding, monomers from the crystallization environment are adsorbed onto the surface of a formed nucleus that is of a sufficient size to remain stable. Subsequently, these monomers diffuse over to the thermodynamically most favourable surface and cause its growth, layer by layer.^[117,119,122,124,125] However, observations contrary to the classical understanding have been conducted in the past. For example, nuclei of varying sizes can be present

that are converted into either larger or smaller sizes, the nuclei morphology can undergo drastic changes, and nuclei of different sizes can aggregate. Modes of growth can also depend on a previously present substrate. Ostwald ripening and digestive ripening are examples for the first mentioned category.^[126,127] In the former, smaller nuclei dissolve in favour of larger ones, minimizing surface energy and thus facilitating the crystal growth. In the latter the reverse takes place, which occurs in cases of charged colloidal solutions. The contribution of the chemical potential to the modified Gibbs-Thomson equation proposed by Park et al. leads to an equilibrium state for smaller sized particles as opposed to bulk material. Intraparticle growth, which is an example for morphology changing nuclei, is dependent on shifts in diffusion dynamics near the crystallite.^[128] If the growth facet's surface energy becomes approximately equal to that of the bulk solution, previously unfavourable surface facets turn energetically beneficial.^[117,119] In coalescence and oriented attachment already formed larger crystallites fuse.^[129–132] Both modes are distinctive for how that occurs: in a coalescence lattice orientation does not influence the aggregation of the crystallites impactfully, while in an oriented attachment a crystallographic alignment of the particles takes place. Lastly, crystal growth can be affected by a substrate or template on which a new phase is deployed. Li et al. have shown that gold deposited on MgO shows different growth properties from gold deposited on amorphous carbon.^[133]

Even if nucleation and growth processes lead to a desired crystalline entity in the first place, solid phase transitions can occur long after the initial crystallization. In many cases such transitions require some form of energetic input, for example in form of high temperatures,^[134] high pressures,^[135] mechanical stress,^[136] or environmental changes that benefit recrystallization.^[137] Especially the last-mentioned example can become problematic when the energetic barrier for phase transitions happens to be low. The literature mentions various cases where a target product undergoes a polymorphic phase transition or formation of a hydrate even from the solid-state during storage or processing. Krishnan et al. have reported a case of single crystal to single crystal transition which is apparently temperature controlled but can also occur at ambient temperature given enough time.^[138] Much more common are phase transitions induced through atmospheric humidity. These can include transitions between anhydrous forms as well as the formation of a hydrate.^[139–142] Maybe the most inconvenient cases of phase transitions concern processing induced changes, for

example by tableting.^[143] Inability to bring a pharmaceutical product into a marketable form can turn into a costly endeavour.

The stated insights regarding the crystallization process highlight its complexity as well as how vulnerable for disturbance each stage of this event might be (**Figure 3**).

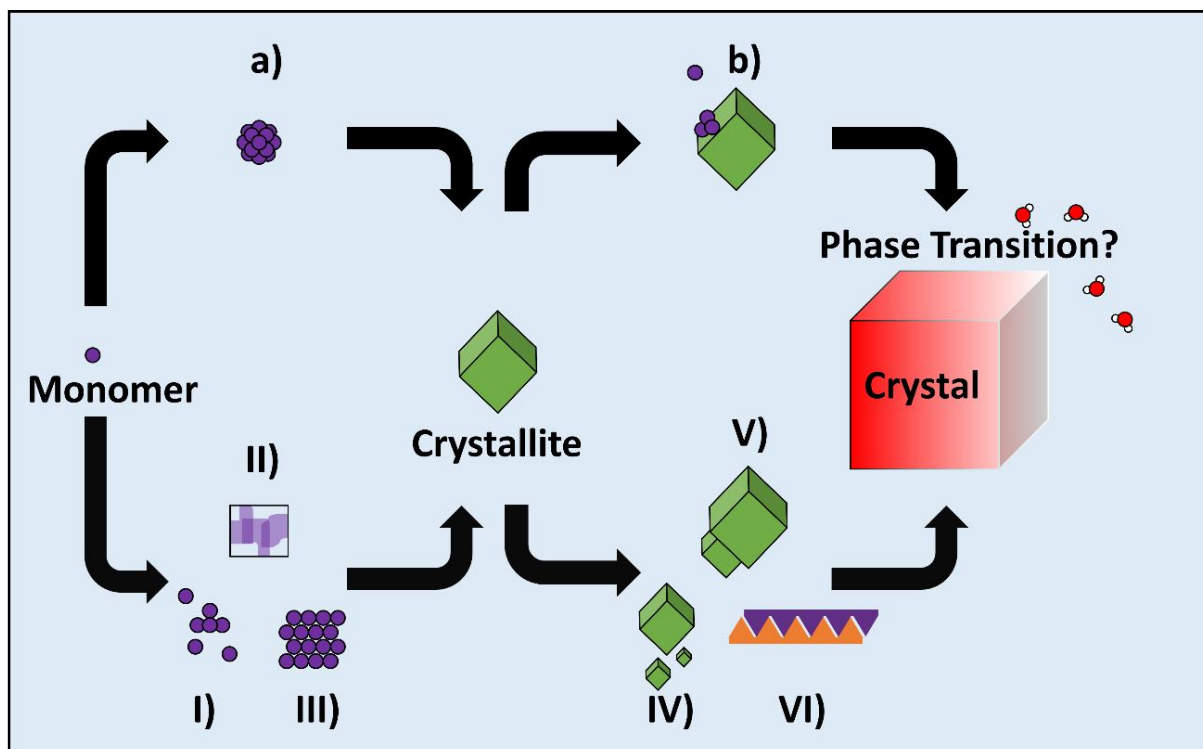


Figure 3. Visual representation of the different crystallization stages with classical and non-classical routes including a choice of examples. The classical nucleation is depicted in **a**), classical monomer layer growth in **b**). The non-classical route is highlighted with roman numerals. A schematic depiction of a phase intermediate is shown in **I**), spinodal decomposition in **II**), direct nucleation in **III**). Non-classical growth routes are presented in **IV**) for Ostwald ripening, **V**) for coalescence, and **VI**) for substrate growth. The influence of atmospheric humidity on possible phase transitions is illustrated by a portrayal of loose water molecules. This figure is based on similar representations in recent literature.^[73,110,117,119–122]

Numerous factors can potentially influence crystallization at every stage. In 2009, Kitamura proposed a categorization of such influences regarding the control of polymorphism into primary and secondary factors.^[71] Primary factors include items that directly concern the crystallization reactants, such as saturation, temperature, stirring rate, mixing rate of reactants or solution, antisolvent, and seed crystals. Secondary factors include items that are connected to the crystallization environment, such as the solvent, presence of additives, a crystallization interface, the pH-value, or host-guest composition. While this list may not be complete, there are various examples in recent literature that show how control on one or more of the proposed factors lead to a desired crystallization product.^[73,114,144–151]

Understanding the complexity of the crystallization process and the different factors which can change its outcome is a key to comprehend how the historically established challenges in crystal engineering are not yet overcome. The next section shall elucidate on possible product outcomes, and how their complicated interrelationships further impede simple solutions in generalization of the crystallization process.

1.1.3 Classification and properties of (crystalline) solids

The structure of a crystalline solid is linked to its thermodynamic properties such as solubility and thermal stability, but also mechanical properties such as the tableability or pharmaceutical properties such as the bioavailability upon consumption.^[152–158] Categorization of phases is thus an attempt to understand links between structure and these properties but also to form a legal basis for potential marketability.^[159–163] Different disciplines may have different interpretations of what constitutes a specific solid-phase, and even within a given field, there may be differences in the use of terminology. For example, a pharmaceutical crystal engineer might deem a crystalline system composed of two different molecular species that is devoid of long-range order a solid solution, or a mixed crystal.^[164–166] A metallurgist on the other hand might rather view a similar entity composed of distinctive metals as an alloy.^[167–169] However, this does not necessarily mean that these terms are not interchangeable,^[170–172] or that they are not also used in entirely different contexts altogether,^[173,174] at least historically. Henceforth the pharmaceutical crystal engineering point of view will be used as the focus for further explanations, to keep the scope of this discussion in a reasonable range.

In pharmaceutical crystal engineering, the classification of the crystalline solid depends on several factors, including the charge status of the crystallized molecules, whether one of the crystallized species could be deemed a solvent or water, whether all species are organic, inorganic, or a mix of both, and whether a crystalline system is composed stoichiometrically or statistically. It furthermore plays a role whether the crystal structure is formed by a single or multiple molecular species (**Figure 4**).^[159–163,175–177] The figure illustrates the complexity of crystalline systems: they may involve iterations of multiple chemical entities that could be organic, inorganic, a metal, or a solvent and each system has the potential to form polymorphs. Polymorphism refers to the ability of a substance to crystallize in more than one lattice modification.

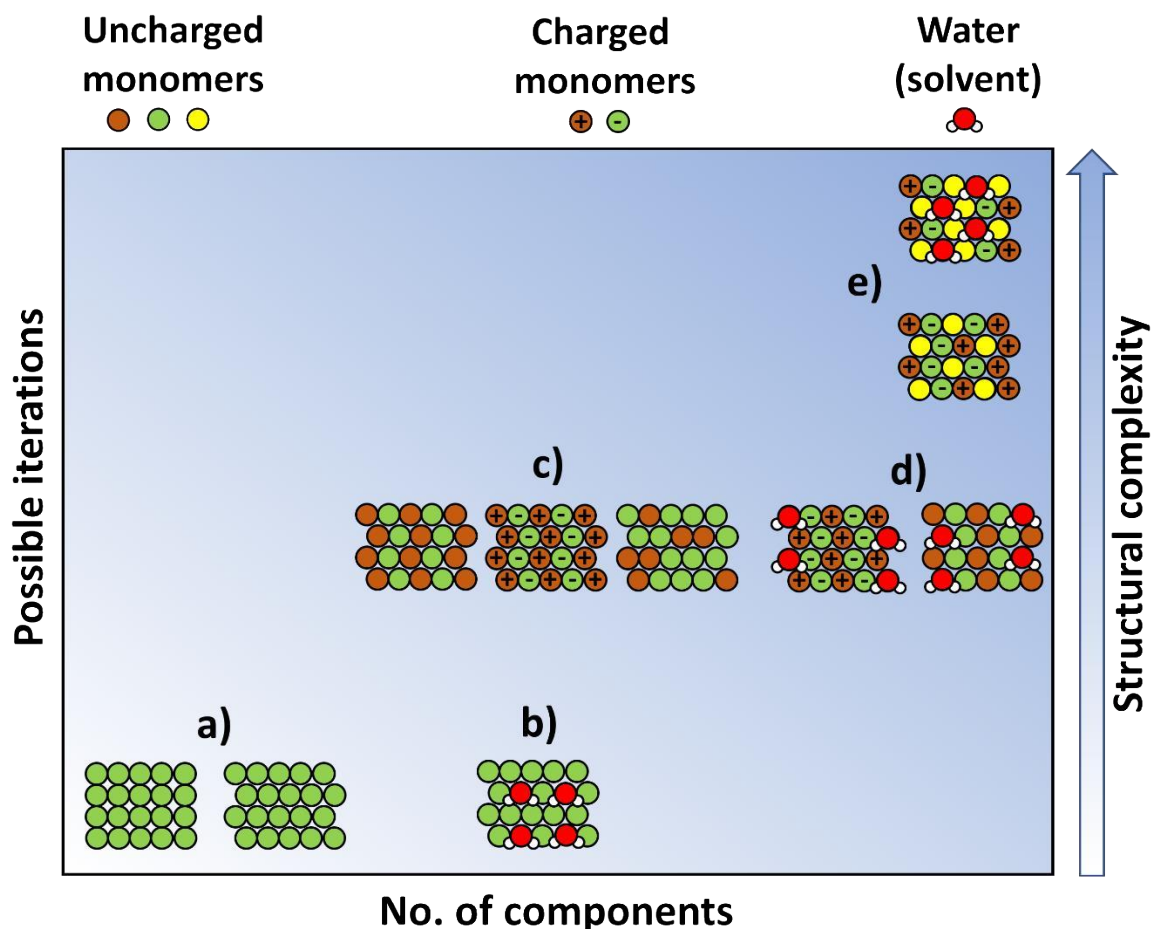


Figure 4. Depiction of choice crystalline solids, ordered by the number of singular compounds that participate in a lattice and how many possible iterations of organic, inorganic or metallic species could be present. Polymorphs of single species crystallized in two different lattices **a)**, hydrate of a single species **b)**, from left to right: co-crystal composed of neutral species, salt composed of charged species, mixed crystal composed of neutral species but distributed stochastically **c)**, from left to right: hydrate of salt and hydrate of co-crystal **d)**, and from bottom to top: ionic co-crystal or co-crystal salt composed of charged as well as neutral species, and ionic co-crystal hydrate **e)**. This figure is based on similar representations in recent literature.^[159–161,163,175]

This is shown in **a)** of **Figure 4** for a single-component crystal. The incorporation of water or a solvent into a crystal lattice is called a hydrate (**b)**) or solvate (**d)**), sometimes pseudopolymorph,^[178–180] although the use of this term was discouraged in the past.^[181] The distinction between hydrates and solvates especially in comparison to co-crystals may seem arbitrary, but it is historically grown and widely accepted. Multicomponent entities of stoichiometric composition formed by uncharged species are called co-crystals, and the different singular compounds co-formers. For charged forms, such entities are deemed salts, with the positively charged part referred to as a cation and the negatively charged part as an anion. A multicomponent system with stochastically distributed co-formers is the previously mentioned solid solution. These bi-component forms are shown in **c)**. Ionic co-crystals or co-crystal salts form a crystal lattice composed of anions, cations, and a further co-former, depiction in **e)**. Polymorphs,

hydrates and solvates, as well as co-crystals, salts and ionic co-crystals will be discussed in more detail in the upcoming paragraphs.

The formation of an undesired polymorphic phase after prior crystallization of the desired one is the original crystallographic problem for pharmaceutical crystal engineering described by Dunitz and Bernstein.^[38,51] Similarly, pseudopolymorphs can be unreliable because they can either decompose to an undesired anhydrous form or form from a different desired species during storage or processing.^[182–188] Transition events like these can cause severe changes in targeted properties of an active pharmaceutical ingredient (API). In case of true polymorphs, past studies have shown that energetic relations between polymorphs are often closely related, facilitating phase transitioning.^[189–191] For hydrates or solvates, on the other hand, formation is linked to molecular structure, especially molecular size, and the ability to form solvent accessible voids, as well as capability to form a strong intermolecular interaction with a solvent molecule that exceeds solvent-solvent interaction energies.^[192–194] The possible fragility of these examples of relative crystallographic simplicity has given rise to more complex formulations to circumvent their propensity to change phases.

The production of multicomponent crystalline entities, such as salts and co-crystals, is a long established process.^[195,196] While they still have the potential to undergo unwanted transitions,^[180,188] they can be the solution to phase changes of unreliable single phase compounds, or enable targeted properties on their own.^[50,197–200] The first question that might arise in context of these crystallographically more complex multicomponent entities is how the co-former or counterion should be chosen. Chemically, this question is answered for example through Desiraju's supramolecular synthon concept.^[60] This involves identifying supramolecular synthons that enable intermolecular interactions between target molecule and co-former or counterion. These could for example involve HB sites or π -systems. For salt formations it might be the potential to be ionized on the target API and chosen counterion. When considering potential co-formers or counterions, it is important to ensure that they are harmless upon human consumption. The generally recognized as safe (GRAS) list, evaluated and updated by the US-based food and drug administration (FDA), is a useful resource for identifying such compounds.^[201–203] The second emerging question on the background of the discussed relationships between structure and properties may be how valid the classification of crystallographically complex solids actually is, and whether there are specific properties that are inherent to one or the other category. To

answer this question, ionic co-crystals should be considered. In 2010 Braga et al. published their work on new crystalline forms of barbituric acid with inorganic acid/base pairs of alkali halogenides coining the term ionic co-crystal.^[176] Ever since these compounds were established, numerous other examples of similar nature were described, also involving completely organic formulations.^[203–209] The mere existence of these species might be deemed as emphasizing of an understanding about crystalline solids first established by Childs et al. in 2007: crystal species are best recognized on a spectrum, on the *salt-cocrystal continuum*.^[210] In their early work they link crystallization environment as well as pKa-values inherent to the single component species and specifically the deviation of pKa-values in two or more co-formers to rather form charged salts or neutral co-crystals upon multicomponent crystallization. Empirically recorded, the *salt-cocrystal continuum* predicts salt formation to rather occur if $\Delta pK_a \geq 3$ or co-crystal formation if $\Delta pK_a \leq 0$. Especially in between those ranges, multicomponent entity formation can become hardly reliable. Subsequently, various techniques for the identification of the proton position were established over the years,^[211–213] and examples of molecularly related species crystallizing under similar conditions in different crystal phase categories presented.^[214–218] This shows how close the call of forming one class of solid over the other can be. There are some choice connections between (structural) properties that could be identified: choosing a well-soluble co-former in a co-crystallization with a worse soluble target compound leads to solubility increases in the multicomponent entity.^[219] Furthermore, properties such as solubility and melting point appear to show an inverse correlation.^[220–223] However, there is no clear distinction of a co-crystal, salt, or ionic co-crystal regarding their possible respective physicochemical behaviours. The described connections can occur independent of how the compound of interest would be classified. Thus, crystal-phase classification should be deemed as a tool to understand structural features rather than compound properties.^[224] The potential complexity of crystalline systems and the difficult interrelationship of structure and properties is not yet understood sufficiently enough to propose a property-based categorization system.

The key to understand the structural features of the different crystalline embodiments lies in a comprehension of how the participating molecular entities aggregate. Therefore, intermolecular interactions relevant for the formation of crystal systems received in this work will be discussed next.

1.1.4 Intermolecular interactions: ionic bond and hydrogen bond, π -interactions and dispersive forces

Crystalline solids are formed through interactions between atoms, ions, or molecules. Supramolecular bonding is a type of attractive interaction that does not lead to the formation of a new chemical compound but binds particles in a specific way to a defined position in relation to other aggregated co-formers or ions. In contrast to that the formation of a covalent bond leads to a new chemical entity. The key distinction between these two examples is whether electrons are shared or whether these interactions occur with a closed electron shell. Examples for the former include the covalent or metallic bond. Examples for the latter are the ionic bond, HBs, π -interactions or van-der-Waals forces. However, similar to solid compound categories these should not be viewed as rigid classes that stand for themselves. Rather than that, there are usually different contributions of factors such as electron induction, electrostatic forces, or dispersive forces, and covalent bonds can be characterized by ionic contributions and vice versa.^[225–229] As bonds of closed shell type are the relevant type in pharmaceutical crystal engineering, or supramolecular chemistry in general, some chosen examples shall be discussed in further detail (**Figure 5**). The depicted structures are ordered by interaction or bond strength and directionality. The interaction strength is quantified by modelled energy values for the respective interactions as well as observable variables such as binding sites distances and angles. Directionality in the discussed context means how dominant the depicted interactions usually are in a given supramolecular system. For example, a chloride anion is very likely to be in the vicinity of a cationic subgroup in a crystal structure. HB binding sites are more likely to interact the stronger they are. On the other hand, if ionic sites or HB sites suitable for strong HBs are present, π -interactions might occur between relevant aryl residues, but not necessarily. The formation of the crystal compound will rather be directed via the stronger binding moieties and the weaker ones will take place if possible. The overall makeup of a crystalline solid is rather determined by stronger interactions than by weaker forces, and thus they are deemed more directional.

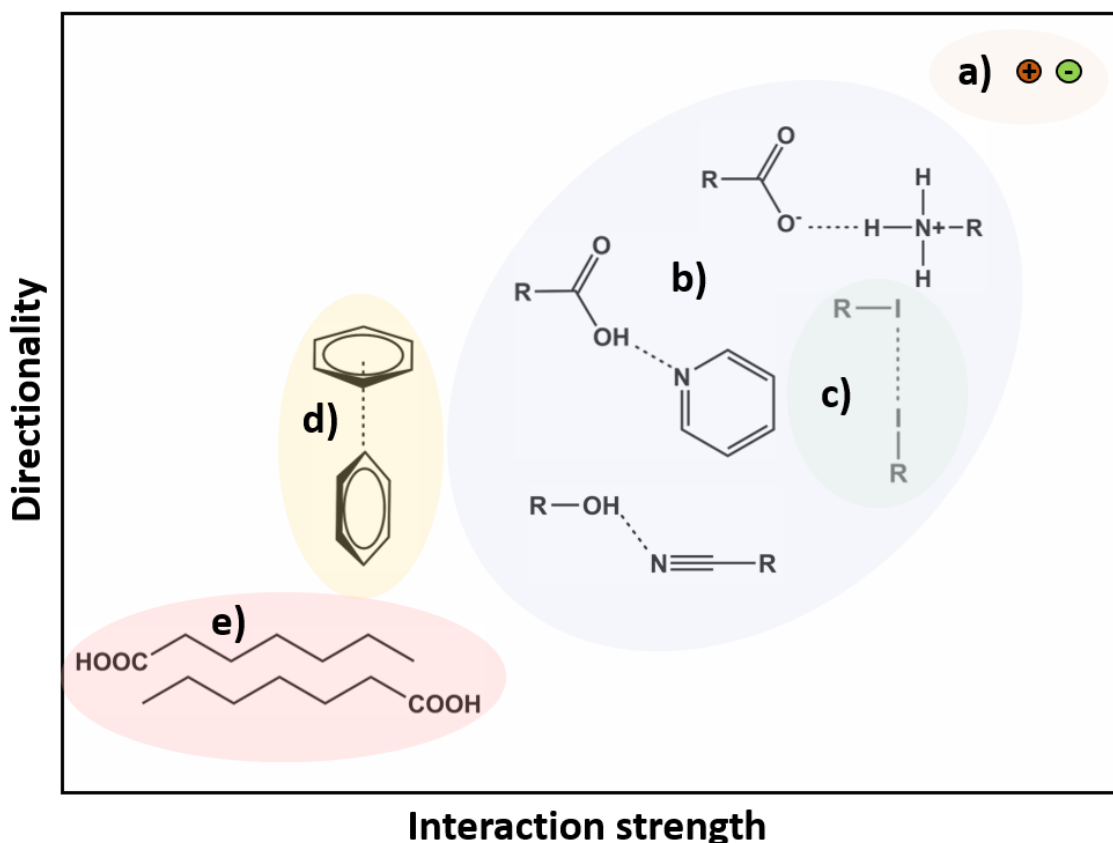


Figure 5. Chosen attractive interaction types roughly sorted by interaction strength and directionality. Ionic attraction of an anion and cation **a)**; strong, charge assisted hydrogen bond, mid-strength neutral hydrogen bond, and weak neutral hydrogen bond **b)**; halogen bond between two halogens **c)**; π -interaction of T-shaped type between aryls **d)**; and dispersive van-der-Waals forces between alkyl chains **e)**. Contents are based on recent literature.^[225,228]

The defining feature of a salt is the presence of ionicity, whether it is composed of completely inorganic ions or ionized molecules.^[230,231] For inorganic salts, in particular exceedingly high bond energies are reported, reaching values up to about -920 kJmol^{-1} .^[232–235] Even though such high binding energies via the ionic bond are possible, the presence of large organic residues on anions or cations enables the formation of liquid crystalline phases composed of salts.^[236–238] This illustrates how the repulsive forces between such residues, even though weak by nature, can cancel out the strong ionic bond. These ionic liquid crystals demonstrate how competing influences on the level of intermolecular interactions shape and influence the nature of a crystalline product. Similarly, molecular ionicity potentially influences the nature of the HB and thereby makeup and classification of a crystal.

HBs can be seen as the most important non-covalent interaction type. They should be considered in congruence with the ionic bond, as both interaction types pose some similarities in many cases. The HB was referred to a proton transfer *frozen* before completion in Steiner's important 2002 publication *The Hydrogen Bond in the Solid*

State.^[239] In its simplest description, the HB can be understood as an interaction between an electronegative atom with a covalently bound hydrogen, the donor, forming an attractive interaction towards another electronegative atom, the acceptor, via said hydrogen. This can be written in the form X-H...Y-Z, where X is the electronegative donor atom, H is the respective hydrogen, Y the electronegative acceptor atom, and Z a residue atom, often a carbon. The covalent bond between X and H is not broken but elongated.^[239–242] The energetic range for this type of interaction is approximately between -1 kJmol⁻¹ and -170 kJmol⁻¹.^[239,240,243] Furthermore, there are visual indicators that can demonstrate the strength of HBs. For example, stronger interactions show the shortest H...Y and X...Y distances between 1.2 – 1.5 Å and 2.2 – 2.5 Å respectively, as well as bond angles close to 180°. Moderately strong HBs pose H...Y and X...Y distances between 1.5 – 2.2 Å and 2.5 – 3.2 Å, and bond angles larger than 130°. Lastly, weak HBs show H...Y and X...Y distances larger than 2.2 Å and 3.2 Å, and bond angles which are at least larger than 90°. ^[239] Similar to the pKa influences on the *salt-cocystal continuum*, differences in acidity play an important role the strength of the HB, at least for heterogenic interactions between different molecular synthons. Here, the proton transfer is driven by a Brønsted understanding of acidity. If the difference in pKa-values is too large, complete deprotonation will occur. In case of homogenic interaction, between for example two carboxylic acid subunits of the same molecular entity, the HB character is more covalent. In these systems, the bond can be understood as half covalently bound to X and to Y.^[239,243,244] To better categorize HBs, it has become common to identify and quantify the different force contributions. As such electrostatic, inductive, and dispersive forces have been mentioned as the most important contributions to the attractive nature of the HB, furthermore resonance effects of multiple HBs in close vicinity enhance their strength.^[239,242,245] On the strong side, inductive effects that locally change electron density, in combination with electrostatic forces are the dominant factors for the HB formation. Moderate HBs are mainly of an electrostatic nature, while weaker HBs take on a dispersive character, similar to van-der-Waals or other dispersive attractions.

Next to the stronger ionic bond or HBs there are π -interactions and dispersive forces. The former depend on the presence of π -systems on the molecular entities, mostly aryl residues and various related derivatives. Furthermore, π -interactions are subdivided into cofacial or face-to-face interactions, parallelly displaced or offset stacking interactions, and T-shaped or edge-to-face interactions (**Figure 6**).^[246–249] The

typical interaction distance between ring centres or between a ring centre and edge is about 3 – 4 Å and the energy range is between -1 kJmol⁻¹ and -50 kJmol⁻¹, but it can be higher when a π-system interacts with an anion or cation.^[249,250] The type of π-interaction that occurs depends on the substituents of the aryl subunit.

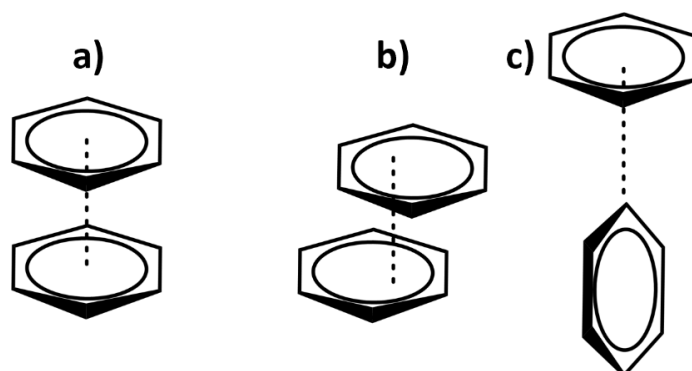


Figure 6. Different geometries of π-interactions. Cofacial stacking **a)**, parallel displacement **b)**, and edge-to-face stacking **c)**.

Cofacial stacking is uncommon and mostly occurs between substituted phenyl rings. Here, the substitution influences the charge distribution on the π-system in such a way that face-to-face stacking becomes the most beneficial geometry. However, parallel displacement is still the more common stacking mode for substituted or large aryl species. In unsubstituted aryl systems, the charge distribution on the ring system is equal between the different molecular entities. Thus, they align in such a way that opposite charges face, which is usually the edge-to-face geometry.^[247,251] In some cases, there is potential for overlap of intermolecular interaction, for example through the aforementioned π/ionic interactions.^[250,252,253] Excluding these cases where inductive forces can play an important role, it is mostly electrostatic and dispersive forces that influence the π-interaction.^[246,250,252] Solely dependent on dispersive forces are van-der-Waals interactions. Fluctuations of molecular electron density, so-called dipole waves, offer both attractive and repulsive contributions of these interactions.²⁵⁴ Interactions of the van-der-Waals type are binding in a low energy range and are mostly important for macrostructures lacking any potential for stronger interactions, such as graphene.^[227,255]

Further types of intermolecular interactions exist, such as the halogen bond, pnictogen bond or chalcogen bond.^[256–261] The presented examples illustrate the overlap of attractive forces and how the attractive interactions in these systems are interrelated, much like the overlapping categories of crystalline solids. This fluid nature of both

intermolecular interactions and crystal structure types serves as an indication on why reliable crystal synthesis and property prediction is so difficult to achieve.

1.1.5 Interim Summary I

From highly specialized origins in the field of photochemistry crystal engineering has become diversified over the years. Although a plethora of approaches, both simple and complicated, have been developed, key problems at the heart of research concerning the field could not be holistically solved. The reason for this is the complexity of supramolecular chemistry at the level of crystalline solids. The process of crystallization, even though studied for more than a hundred years, is not fully understood. This is due to the numerous possible mechanisms involved in its stages. Various factors can potentially influence each step of the crystallization. Furthermore, crystalline products exist on a spectrum in large influenced by the intermolecular interactions necessary to form a specific compound. The fluid nature and close relation of these interactions limits reliable predictions of structural outcomes. This is even more true for compound properties. At this point in time, thorough investigation of target species remains the only way to understand aggregation behaviour and property relationships, and general statements concerning a large number of different crystalline entities can hardly be made.

1.2 Experimental, analytical, and computational approaches

1.2.1 Experimental approaches to (pharmaceutical) crystal engineering

It was established that crystallization is a complicated process, and the resulting products exist on a structural continuum that does not necessarily correlate with compound properties. In the following paragraphs, an overview on possible crystal synthesis techniques shall be provided, with an emphasis on the ones that were actually applied in the works related to this thesis.

Crystallization from solution is probably the most common method to perform a crystal synthesis and what most models explaining this process are based on. In addition to the thermodynamic or kinetic factors mentioned earlier, the solvent environment itself is possibly the strongest influence on single as well as multicomponent crystallization from solution. A recent example for research in this area was conducted by Liu et al. in 2022. They investigated how the solvent environment influences molecular conformational preferences on API Gabapentin. It was determined that different solvents favour specific conformations which leads to crystal formation directed by these molecular preferences.^[262] The requirement to crystallize a given substance from a solvent environment is that said compound must be soluble in the chosen solvent. To induce an instance of the possible described crystallization processes, the correct target species saturation level in the solvent environment must be reached. This can be achieved for example through cooling or solvent evaporation.^[263–268] Another possible way to start crystallization from solution is the so-called antisolvent crystallization. For this process, a second solvent in which the solute is badly soluble is required. Crystallization can be induced via layering of the solute/solvent solution with the determined antisolvent. Another possibility instead of layering is to add the antisolvent in a closed system by gas diffusion. In this case, the antisolvent should ideally show a higher vapour pressure than the original solvent.^[269–272] A further common technique is seeding. Here, an already grown crystalline particle of the targeted crystal system is added to a saturated solution of the desired substance. This offers the advantage that a given crystal structure is predetermined, and phase transitions are less likely.^[273–275] One more common way to induce or influence the crystallization process is the use of additives. These include substances which are added to a crystallization solution usually in a smaller, non-stoichiometric amount to

change crystallization behaviour at a specific stage. The range of how these additives alter the usual crystallization route is spread widely, for example blocking of growth faces or supramolecular synthons, directing crystal morphology, or even just changing the pH.^[276–280] Lastly, it is worth mentioning that the described techniques are mostly aimed at a laboratory environment. In an industrial context, these methods must be scaled up and it has to be decided whether a batch crystallization or a continuous flow crystallization should be applied. The latter is a relatively recent development, that offers lower operational costs and generated wastes, better potential for scale up, and better product reliability, as it works continuously. Batch crystallization on the other hand is well established, and investment costs for new continuous operations appear to keep it in place for some time to come, but its batch-by-batch nature can vary product quality. On the other hand, batch crystallization offers a better control of the crystallization steps, especially because of its discontinuous nature.^[281–284]

Mechanochemical crystallization is a technique which has gained increased attention over the last years, especially for multicomponent species or polymorphs that might be inaccessible in a solvent environment.^[285–288] Mechanochemical approaches to crystallization typically involve grinding techniques, either in a mortar and pestle or a ball mill. One advantage of this technique is that no solvent or only a negligible amount of solvent (liquid-assisted grinding) is required, which reduces cost and environmental impact. Additionally, the crystallization process via mechanochemical means is faster than solvent crystallization, typically only taking a few minutes.^[289,290] Unlike solvent crystallization, the solubility of the target system in a given solvent is not necessary. However, solvent crystallization enables formation of single crystals, whereas mechanochemical treatment only yields powders. The mechanism underlying grinding crystallization is still not fully understood, although theories have been proposed. The process is mostly linked to local temperature or pressure changes induced through mechanical stress. This might cause surface defects and therefore changes in surface energy, leading to particle migration that even reaches into the bulk phase to form a new structure. Multiple crystalline or non-crystalline stages can be undergone during this process.^[291–294] There is still additional research necessary to fully understand the mechanochemical crystallization.

Additional common crystallization methods include crystallization via slurry or from a melt. In the case of slurry, a crystal/solvent dispersion is continuously stirred over prolonged time periods. This mixture can be influenced by solvent-based as well as

mechanochemical influences, leading to crystallization products that may not be accessible via the usual solvent or grinding route.^[295–297] Crystallization from melt requires the target compound to be able to melt without decomposing. Where applicable, this method is popular for accessing otherwise non-receivable polymorphs.^[298–300]

All discussed crystallization methods show some distinctive benefits, but in the course of this thesis crystallization through solvent evaporation, antisolvent crystallization, usage of additives upon crystallization and mechanochemical crystallization from a ball mill were used (**Figure 7**).

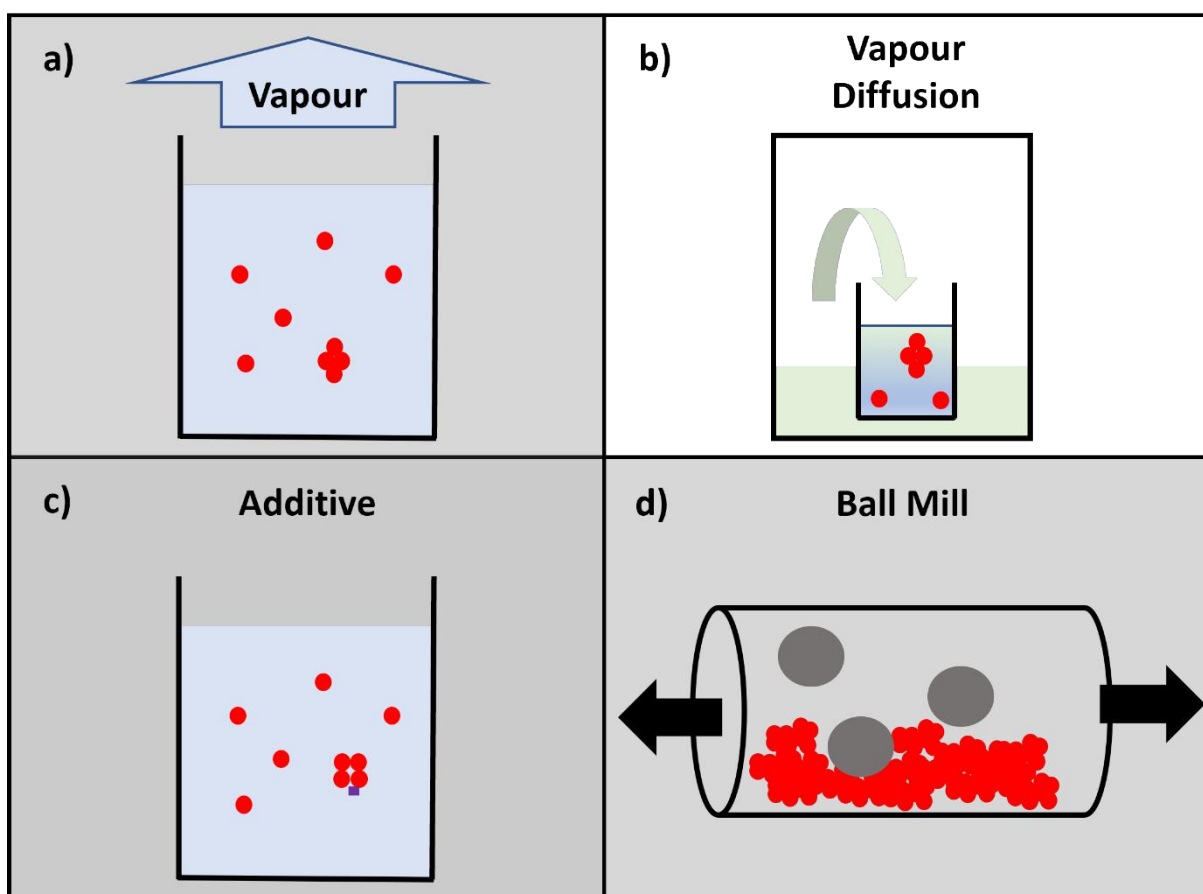


Figure 7. Simplified depiction of the applied crystallization techniques. Crystallization through evaporation of the solvent **a)**, diffusion crystallization **b)**, additive crystallization from solution **c)**, and mechanochemical crystallization in a ball mill **d)**. The chemical target species is depicted in red, the solvent in blue, antisolvent in green, additive in purple and ball milling balls in grey. Arrows indicate vaporization direction or shaking direction of the ball mill.

1.2.2 Analytical approaches to (pharmaceutical) crystal engineering

After a successful crystal synthesis, it is essential to characterize the resulting product. Characterization methods can be roughly divided into two categories: structure determination and investigation of physicochemical properties. In the context of pharmaceutical crystal engineering, structural makeup mostly refers to crystal structure

and supramolecular binding behaviour, as opposed to molecular structure. Further interesting properties to investigate include solubility and thermal behaviour, such as melting point, thermally driven phase transitions, or thermal decomposition. In the following paragraphs, the analytical methods used for characterization will be discussed.

X-ray diffraction methods can be considered the foundation of crystal engineering analytics. In principle, a metal cathode (usually Cu, Mo, or Ag) is used to produce an x-ray beam that is directed at a crystalline sample from various angles. As crystalline samples behave like meshes due to their structurally periodic nature, they interact with the beam. If the correct angles are reached, constructive interference will occur, and a reflected ray can be detected using an appropriate x-ray detector. Bragg's law describes the conditions under which this constructive interference can occur (**Equation 1**).

$$n\lambda = 2d \sin \theta \quad (1)$$

Here, n is an integer number describing the degree of diffraction. The wavelength λ of the x-ray source depends on the specific type of source. The distance between the grid layers is represented by d . Finally, the angle of incidence of the x-ray is represented by θ . This allows for the recording of a two- or three-dimensional pattern, depending on the diffraction method, that is characteristic of the structure.^[301–306]

Diffraction methods can be performed on both crystalline powders and small, favourably well-ordered single crystals. Powder x-ray diffraction (PXRD) is a potentially very fast, non-destructive method that gives a two-dimensional diffraction pattern as a function of diffraction signal intensity in relation to double of the angle position. A recorded powder pattern can be thought of as a fingerprint of a crystalline substance. As such, distinguishing between polymorphs or the formation of a new multicomponent phase becomes possible through simple comparison of powder patterns. Additionally, the signal intensity in the diffraction pattern can provide information about preferential growing directions of crystal surfaces, while Bragg reflection resolution compared to noise can reveal information about the crystallinity of the sample.^[301,302]

Three-dimensional diffraction on single crystals (SCXRD) can reveal even more detailed structural information. In this technique, the single crystal is irradiated with an x-ray beam from up to three different angles (ω , χ , ϕ) in a three-dimensional alignment.

This generates a reciprocal lattice in a so-called reciprocal space. This reciprocal lattice can be understood as a model containing information about how the crystal lattice is composed at the geometric level, without any information about the chemical species. To identify the latter, the signal intensity in the reciprocal space must be evaluated. The interaction of x-ray beams with a crystalline substance can be seen as the interaction of photons with electrons. As the beam wavelength is fixed, the intensity of a reflected ray depends on the number and nature of the electrons present on the irradiated sample. As such it becomes possible to determine the atomic species participating in the investigated lattice. Together with the geometrical information it is possible to generate a detailed description of the crystal structure.^[303,305,306] SCXRD can provide information on various characteristics of the crystal structure, such as axis lengths and angles, cell volume, space group of a unit cell, intermolecular bonding behaviour in the crystal system, and chiral information on molecular species. With the advent of advanced detector technology, SCXRD has become considerably faster. However, if the quality of the single crystal is too low, it can still take hours, days, or even be impossible to determine the structure sufficiently. In such cases, a powder pattern can be recorded, and if intermolecular interactions need to be investigated, infrared spectra can be a helpful tool.

Infrared (IR) spectroscopy is another technique based on the interaction of light and matter. However, contrary to diffraction methods, far less energetic infrared radiation is used. The resulting spectrum of an IR experiment is based on absorption, rather than on irradiation angles and subsequent reflection. Various setups are possible, such as transmittance of light through a sample, reflectance of an evanescent wave on the sample, or interference of reflected beams. The energy level of IR radiation is sufficient to excite molecular vibrations which are characteristic to specific bonds between atomic species and their close environment. After the initial beam transmits through or reflects on the sample, its energetic properties change, depending on the interaction with the matter. One commonly applied setup makes use of attenuated total reflection (ATR) through a reflective crystal over the sample surface. This maximizes sample exposition to the IR-beam and minimizes the beam travel path, leading to better signal-to-noise ratio. The reflected beam in either setup can be recorded with a suitable detector, and Fourier transformation is commonly applied to produce an IR-spectrum that is a function of band intensity dependent on infrared wavelength.^[307–309] By investigating these bands, it is possible, for example, to identify HBs,^[310,311] the

presence of lattice water,^[312,313] or distinguish between salt and co-crystal through examination of carbonyl bands.^[314,315] As such, IR spectroscopy can help classify a received crystalline solid if single crystal diffraction is not an option. The described methods are visualized in **Figure 8**.

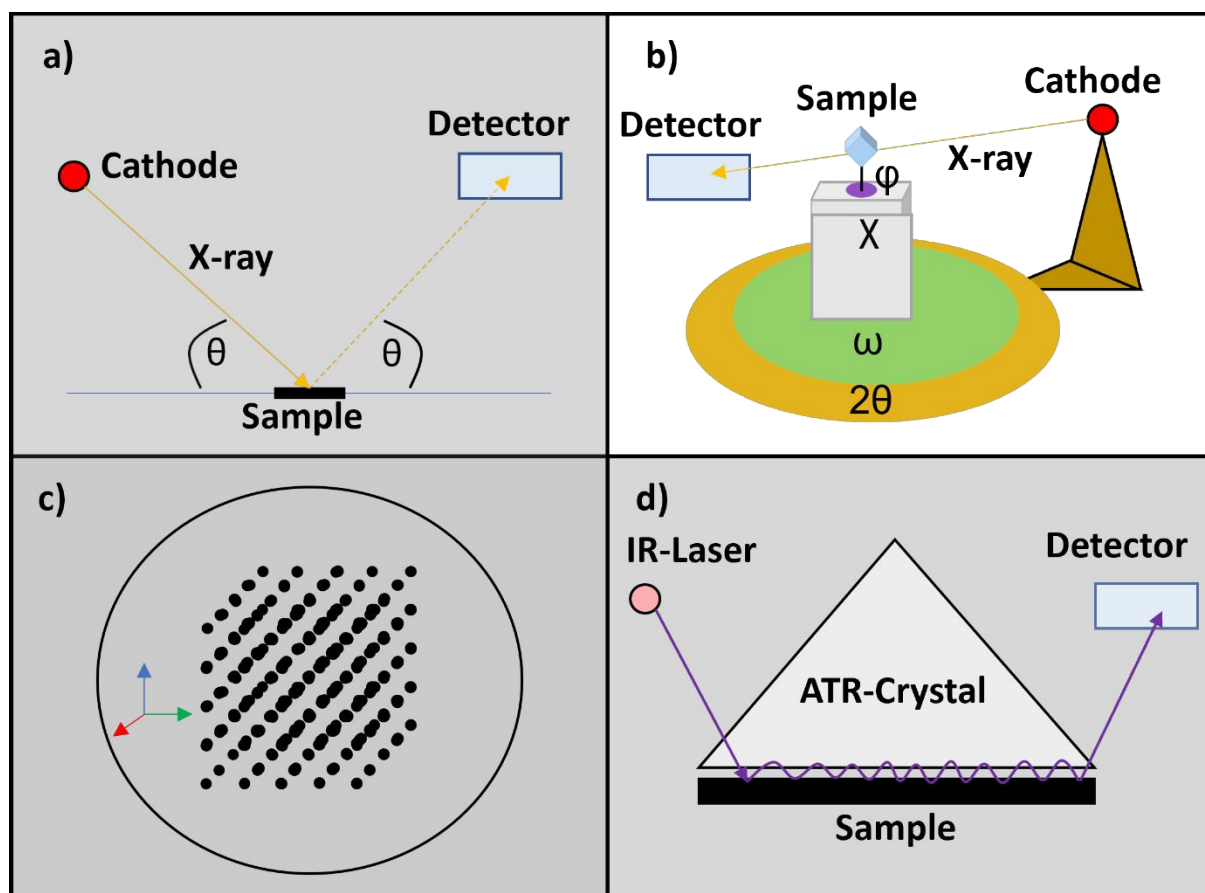


Figure 8. Simplified depiction of described structural characterization methods. X-ray reflectance in $\theta/2\theta$ measurement geometry for PXRD **a)**, SCXRD setup showing the separately movable diffraction angles with χ able to move vertically **b)**, exemplary diffraction pattern in reciprocal space **c)**, and ATR-IR setup **d)**.

The determination of solubility can be achieved by various methods. One simple approach involves removing a specific volume of a saturated solution from a larger sample and allowing the liquid to evaporate. The remaining residue can be weighed to determine the ratio of solute mass to solvent volume.^[316] However, in the pharmaceutical context, there are several commonly used methods for measuring solubility that do not require solvent evaporation. These mostly do not require evaporation of the solvent, but involve microscopic or spectroscopic methods to record the content of the target solute in a given solution.^[317,318] In the context of this thesis, proton magnetic resonance ($^1\text{H-NMR}$) spectroscopy was used to measure product solubility. $^1\text{H-NMR}$ spectroscopy is commonly used for molecular structure characterization and is based on proton excitation through a magnetic field. A Fourier-

transformed spectrum is produced, similar to infrared spectroscopy, which is presented as a one-dimensional spectrum of peaks at their respective chemical shift positions in parts per million (ppm). These peak positions are characteristic for different molecular subgroups in a given molecular environment. For solubility studies, the quantitative nature of $^1\text{H-NMR}$ spectroscopy is useful. Integration of peak areas of different signals in the spectrum reveals the ratio in which the compounds corresponding to the signals are present in a sample.^[319–322] This enables the measurement of the desired species content against the solvent signal or a standard of fixed concentration.

Understanding the thermal properties of pharmaceutical solids is essential for their characterization. Differential scanning calorimetry (DSC) is a powerful method for investigating the behaviour of compounds upon heat treatment. In a typical DSC setup, the sample of interest is put in a metal crucible and placed in a heating chamber. An empty reference crucible is either present during the subsequent measurement, or the reference measurement is conducted beforehand. A temperature regime is then applied in the heating chamber, and via temperature sensors the heat flux on the sample is measured in $\text{Jg}^{-1}\text{s}^{-1}$. If through the applied temperature regime, a phase transition of the sample occurs this heat flux changes. Depending on whether such a phase transition is endothermic and requires energy, or exothermic and releases energy, the heat flux curve as a function of the temperature will show a transition peak. It is common practice to present the direction of exothermic events in a received thermogram.^[323–325] The evaluation of these thermograms thusly reveals solid/solid phase transitions, melting, and whether such processes are endothermic or exothermic.

To investigate decomposition, the thermogravimetric analysis (TGA) is the most common method of choice. Here, the sample is also placed in a metal crucible and exposed to a previously determined temperature regime. However, instead of measuring heat flux changes, the mass change caused by thermal decomposition of the sample is recorded. This enables identification of hydrates or solvates through decomposition events at low temperatures, or general decomposition behaviour at higher temperatures.^[326]

1.2.3 Computational approaches to (pharmaceutical) crystal engineering

Computational modelling methods can provide a deeper understanding of experimentally and analytically determined compound properties. These can include

energetic benchmarks such as lattice energies of different structural embodiments received from a crystallization batch, detailed analyses of intermolecular interaction properties, the electronic structure of a molecular species in a given crystalline system, or even moderately successful structure predictions.^[242,327–331]

Many approaches regarding such applications are based on density functional theory (DFT). In principle, DFT offers an approach to calculate the electronic structure for atoms, molecules, agglomerates or (crystalline) solids based on electron density.^[332,333] Total electronic energy is calculated by summing up different energetic contributions (**Equation 2**).

$$E_{tot} = E_T + E_V + E_J + E_X + E_C \quad (2)$$

Where E_T is the kinetic energy term for the electrons, E_V their potential energy concerning attractive electron/nuclei interactions, E_J their potential energy regarding averaged electron/electron repulsion, E_X the electron exchange energy and E_C the electron correlation energy. While E_J only considers averaged values for electron/electron interactions the DFT evaluates both E_X and E_C , offering a more accurate description of electron behaviour. It is the interpretation of these terms that distinguishes DFT from other available methods. Various functionals that each interpret electronic structure differently have been established over the years. Popular examples include the Becke-3-parameter-Lee-Yang-Paar functional *B3LYP*, or the Perdew-Burke-Ernzerhof *PBE* exchange-correlation functionals.^[334,335] Furthermore, these functionals require a basis-set which usually contains a number of different electronic wave functions for chosen atomic species. The right combination of functional and basis-set is essential for accurate results.^[336] As DFT is only concerned with electronic contributions, energetic descriptions of periodic systems like crystals can become challenging. Contributions of other forces such as dispersion or long-range interactions play a role here as well. To account for such factors, it has become common practice to use dispersion correction models and/or apply periodic-boundary conditions.^[327,337,338] A dispersion correction adds a further energetic contribution for the dispersion to **Equation 2**. Periodic boundary conditions significantly decrease calculation costs of large, quasi-infinite systems such as a crystal by reducing the calculation effort to the unit cell, or equivalently a previously established super cell alone. A quasi-infinite number of cells are approximated by introducing an original unit

cell surrounded by infinite images of itself to simulate interactions between adjacent cells.

The DFT-based electronic property description enables the visualization of electron density on investigated chemical species. However, the obtained energetic values can also be utilized to calculate further properties. By performing a structural optimization on a crystalline system using a DFT method, an E_{tot} value for the electronic structure of the investigated system is received. For the calculation of lattice energies, this value is typically referred to as ideal solid-state energy, or E_{iss} (**Equation 3**).^[339]

$$E_{\text{lat}} = \frac{E_{\text{iss}}}{Z} - E_{\text{isg}} \quad (3)$$

Here, Z is the number of crystallographic entities in the unit cell, and E_{isg} the ideal static gas energy. The latter corresponds to the E_{tot} value for the geometric optimization of a single molecule in an otherwise empty cluster of predetermined size through DFT approaches. The calculation effort is visually highlighted in **Figure 9**. In essence, **Equation 3** compares the energetic effort of the crystallographic entity in the crystalline system with that of the entity on its own in an empty space. Thereby, the gain in energy per entity (kJoule per mol) is received, which is considered the lattice energy. This energetic value is useful for assessing phase stability and could help identify stable crystalline forms of a target species if calculated for theoretical phase geometries.^[329]

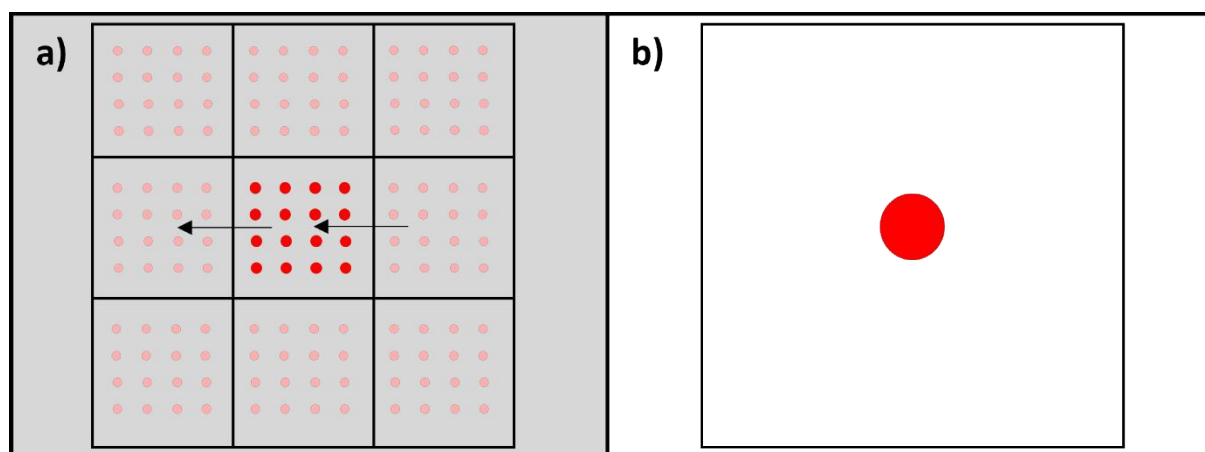


Figure 9. Principle of the unit cell evaluation of a crystalline solid under periodic boundary conditions to account for long-range interactions **a)**, and of a singular entity in an otherwise empty cluster **b)**.

In addition to the energetic evaluations of the solid phase, it is common to investigate the energetic properties of specific bonding interactions such as HBs. The Atoms in Molecules (AIM) model is a common approach for this. After determining the electron density distribution of a system of interest, such as via DFT methods, it is possible to

identify electron density extrema between atomic species. These bond critical points can be interpreted as binding interactions such as covalent bonds, but also HBs depending on the energetic extrema properties.^[340,341] Emamian et al. have developed an approachable method to feasibly use bond critical point evaluation for the calculation of HB bond strength.^[242] They employed a B3LYP method with the Grimme DFT-D3(BJ) dispersion correction to determine electronic properties and applied coupled cluster singles and doubles with perturbative triples correction (CCSD(T))^[342] in conjunction with Boys and Bernadi's counterpoise technique to determine interaction energies at these points. By empirically investigating various electronic properties of 42 HB complexes, they established a linear equation that links bond energies to electron density extrema at the bond critical points, which can be adjusted for neutral and charged HBs (**Equation 4, 4a and 4b**).

$$E_{int} = E_s \times \rho_{BCP} + E_c \quad (4)$$

$$E_{int} = -223.08 \times \rho_{BCP} + 0.7423 \quad (4a)$$

$$E_{int} = -332.34 \times \rho_{BCP} - 1.0661 \quad (4b)$$

Where ρ_{BCP} is the electron density at the bond critical point in atomic units, E_s the empirically determined slope of the linear regression in kcal mol⁻¹, and E_c the empirically determined intercept in kcal mol⁻¹. The linear correlation between interaction energy and electron density produced by this approach allows for easy determination of interaction energies by simply identifying the bond critical point electron density, which saves time and resources compared to fully DFT-based energy calculations.

1.2.4 Interim Summary II

The described well-established methods to determine crystal structure, physicochemical properties and modelling further attributes computationally are powerful and have undergone significant progress over the recent decades. However, they remain mostly descriptive. Although computational methods like DFT-based energetic evaluations have been used to predict possible stable phases, these applications are still in their infancy. It is not yet possible to reveal general laws of crystallization that would enable complete control of the crystallization process. This emphasizes the point previously stated that, at this time, individual systems of interest must be investigated separately.

1.3 γ -amino butanoic acid and its pharmaceutically active derivatives

1.3.1 γ -amino butanoic acid (GABA)

γ -amino butanoic acid (GABA) is a small amino acid consisting of a four carbon alkylic chain and a carboxylate residue on C1 as well as an ammonium residue on C4. This makes it zwitterionic in nature, a common feature of amino acids.^[343–346] Furthermore it is nonessential, which means that it can be produced by the body on its own without the need to be consumed via food uptake. Up to three neuroreceptors are named after GABA: the GABA_A receptor and its subclass GABA_{A ρ} , which is sometimes argued to be its own GABA_C receptor, and GABA_B.^[347–349] All GABA type receptors are linked to inhibition and excitation of the central nervous system in vertebrates. GABA regulates pain and stress experiencing, sleep and immune responses.^[350–353]

Three polymorphic modifications of GABA have been described to date.^[354–357] The first form was described by Tomita et al. in 1973 and crystallizes readily from water. The second polymorph was discovered in 1996 by Dobson et al., compared to the first form it is elusive and may undergo phase transitions. Wang et al. and Lamkowski et al. have described ways to stabilize this form through additive crystallization via mechanochemical means and from solution respectively. Furthermore, Wang et al. also discovered the third modification via mechanochemical additive crystallization. Regarding crystallization of multicomponent species, GABA has received less attention. A solvate and a hydrate are known, as well as a calixarene complex.^[358–360] Losev et al. have described salts with diastereomeric and L-forms of tartaric acid, while Lamkowski et al. have found salts with malic acid species.^[355,361,362]

1.3.2 2-(1-(aminomethyl)-cyclohexyl)acetic acid (Gabapentin)

2-(1-(aminomethyl)-cyclohexyl)acetic acid (Gabapentin) is an API derived from GABA. While retaining the basic GABA-chain, a cyclohexyl residue is introduced in C3, which increases Gabapentin's molecular size compared to GABA, but does not introduce further supramolecular synthons. Marketed as an anticonvulsant agent since 1993 in Europe, its uses today include treatment of neuropathic pain, pain in general and easement of anxiety. As such it can be regarded a blockbuster API, that is still prescribed regularly as of today. Interestingly, it does not interact with any GABA receptors, though some studies have linked it to GABA_B activity. Recently its abuse potential has become cause of concern, primarily abused by opioid users.^[363–368]

The crystallization behaviour of Gabapentin has been extensively studied since its introduction. Three polymorphic modifications and a hydrate have been identified. These can undergo phase transitions between each other through mechanical stress, heat treatment, or recrystallization from different solvents.^[369–372] Numerous patents have been published regarding the stabilization of specific polymorphs, reflecting its status as a commercially viable API.^[373–375] Additionally, research has focused on the formation of multicomponent species of Gabapentin. Thus, salts and co-crystals were described, but also large clathrate-like formulations or complexes involving gold.^[376–383] A notable study was conducted in 2020 by Soliman et al. who co-crystallized Gabapentin with Saccharin. The received compound improved the taste properties of the API, in congruence with other, more classically considered physicochemical attributes.^[384] Furthermore noteworthy is the plethora of patents concerning multicomponent species of Gabapentin.^[385–387]

1.3.3 3-(aminomethyl)-5-methylhexanoic acid (Pregabalin)

3-(aminomethyl)-5-methylhexanoic acid (Pregabalin) is an API that is very similar to Gabapentin. However, instead of a cyclohexyl residue in C3, it has an isobutyl group in this position. This makes Pregabalin chiral, and strictly only the (S)-form, its eutomer, the enantiomer showing the desired pharmaceutical properties, is marketed as Pregabalin. The similarities to Gabapentin go beyond structural level, and the two compounds are sometimes referred to as *Gabapentinoids*. Pregabalin, released in 2004, has similar pharmacokinetic properties to Gabapentin and is not active on GABA receptors. It is used to treat similar diseases as an anticonvulsant, pain inhibitor, and anxiolytic. Its commercial impact is significant, and it has similar addictive properties that have come to light in the past decade. Several studies have been conducted to investigate its abuse potential.^[363,364,368,388–392]

In the case of Pregabalin, much of the research on its crystallization behaviour has been conducted in the form patents.^[393,394] However, there are some works published in scientific journals which mostly concern multicomponent formation or the structure of (S)-Pregabalin.^[395–398] One structure evaluation by Samas et al. presented a co-crystal of (S)-Pregabalin and mandelic acid.^[399] Apparently, this spurred a significant industrial research effort concerning crystallization-based enantiopurification processes of Pregabalin.^[400–406] These methods utilize co-crystallization of racemic Pregabalin with enantiopure mandelic acid to separate Pregabalin enantiomers. The commercial success of (S)-Pregabalin has motivated the development of cost-effective

methods for enantiopurification. A plethora of patented crystallization-based deracemizations demonstrates the potential of these approaches.

1.3.4 γ -Amino-3-phenylbutanoic acid (Phenibut)

γ -Amino-3-phenylbutanoic acid (Phenibut) has the typical zwitterionic GABA chain capable of HB or ionic interaction, and a further phenyl group in C3, which introduces chirality in that position. First marketed in 1963 in the Soviet Union it is primarily sold as a racemate, while research has suggested that the (R)-enantiomer is the eutomer. Phenibut might be considered *the-odd-one-out* among the discussed GABA-derived APIs. It is not authorized on European or US markets, only being officially sold as a medication in some former soviet countries where it is used to treat anxiety, insomnia, and other stress-related symptoms. In contrast to Pregabalin and Gabapentin, it shows affinity for the GABA_B-receptor in combination with pharmacokinetic properties of the Gabapentinoids. In Western countries, it has gained notoriety for its abuse potential, being sold as a *dietary supplement* disregarding its severe pharmaceutical potency.^[407–412]

Research regarding its crystallographic properties is sparse. The crystal structure of Phenibut • HCl was reported by Mao et al. in a CSD communication in 2018.^[413] This structure was furthermore reproduced and used to investigate binding motifs to monoamine transporters by Senior et al. in 2020.^[414] Prior to the works concerning this thesis, there was no significant research conducted on the structural properties of Phenibut.

1.3.5 γ -Amino-3-(4-chlorophenyl)butanoic acid (Baclofen)

γ -Amino-3-(4-chlorophenyl)butanoic acid (Baclofen) is structurally most similar to Phenibut, differing only by the presence of a chloro-group in the para position of the phenyl ring. It shares the zwitterionic GABA chain, a chiral center at C3, and a phenyl residue capable of π -interactions, with the added potential for halogen bonding due to the chloro-substituent. Baclofen was approved by the FDA in 1977 and is commonly used to treat spasticity and related conditions that cause involuntary muscle movement and twitching. Like Phenibut, it targets the GABA_B-receptor and its (R)-enantiomer is considered the eutomer, though it is mostly sold as a racemate. An interesting use of Baclofen, given the abuse potential of the Gabapentinoids and Phenibut, is in the treatment of alcohol and other substance addictions. However, discontinuation of Baclofen treatment can lead to problems, including delirious states.^[415–421]

Maybe due to its success as a medication, investigations on Baclofen's structural properties are plentiful compared to Phenibut and are on a level closer to that of the Gabapentinoids. These investigations include structural determinations of the racemate, polymorphs of the enantiopure (R)-form, and hydrates of Baclofen.^[422–424] Additionally, there is significant interest in multicomponent structures as well. Salts as well as co-crystals with multiple organic structures have been described.^[425–427] It is worth highlighting that processes for chiral resolution were developed by Córdova-Villanueva et al. as well as Songsermawad et al. in 2018 and 2022 respectively.^[428,429] The former proposes the use of malic acid, while the latter uses mandelic acid again to perform the enantiopurification. The interest from an industrial perspective is also high, with processes being patented to enhance Baclofen solubility or resolve the racemate through crystallization.^[430,431]

1.3.6 Co-formers

The choice of co-formers to be used in this work was based on what was known to form multicomponent structures with at least one of the investigated compounds from literature evaluation. As such mandelic acid was chosen, as its potential to resolve racemic structures of Pregabalin and Baclofen was established in the past.^[400–406,429] Malic- as well as tartaric acid multicomponent forms with GABA and Baclofen were shown to exist, as were maleic acid forms with Baclofen and Gabapentin.^[355,361,362,427,429,432] Furthermore, succinic acid and fumaric acid were chosen due to their molecular similarity with maleic acid, malic acid and tartaric acid. If considered at large, an increase of molecular complexity akin to the APIs is present in the co-formers. Succinic acid is the simplest entity, a four carbon aliphatic chain with two carboxyl groups on C1 and C4. Fumaric acid introduces a π -bond, and maleic acid furthermore a cis conformation. This enables intramolecular HB and thus slightly changed properties compared to fumaric acid. Malic acid lacks the π -bond but shows a hydroxy residue in the chiral C2 position. Tartaric acid poses an additional hydroxy group in C3 with another chiral centre here. Mandelic acid is the only non-dicarboxylic acid between the co-formers, but it poses a carboxylic group, a hydroxy residue on the chiral C2 and an aromatic phenyl ring.

1.3.7 Interim Summary III

GABA and some of its relevant derivatives Gabapentin, Pregabalin, Phenibut, and Baclofen are a successful class of APIs. In the stated order they offer increasingly complex molecular makeups. While their crystallization behaviour was investigated

separately to varying degrees, up until this point no one has tried to connect these molecularly very similar entities from a crystallographic point of view. Thus, this group of commercially viable substances shall be evaluated based on the established central problems of crystal engineering under use of the available methods.

2 Motivation

The central problem of modern pharmaceutical crystal engineering, as well as crystal engineering in general, still is the unpredictability of the crystallization process as well as the inability to generalize findings regarding structural and physicochemical properties on a meaningful level. Thus, it remains necessary to investigate target systems piece by piece and further our understanding incrementally.

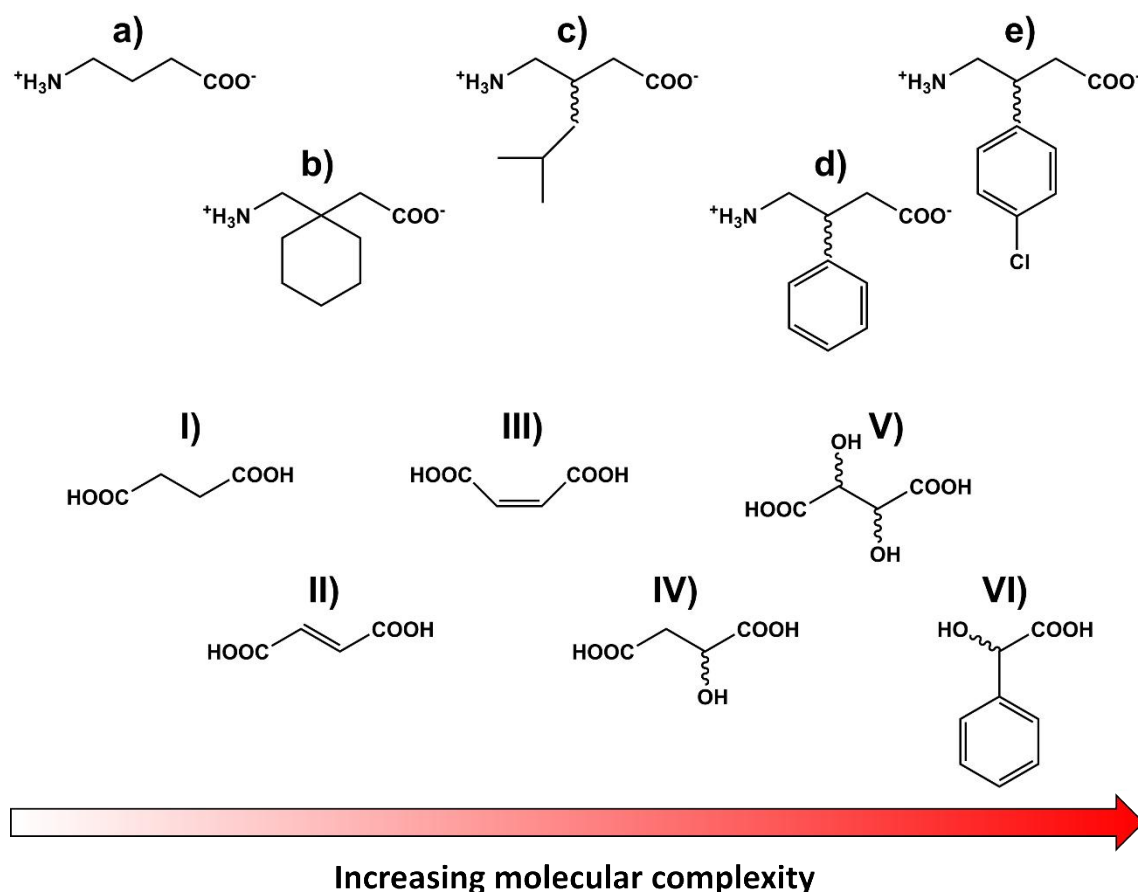


Figure 10. Investigated γ -amino butanoic acid derivatives and dicarboxylic or α -hydroxy carboxylic acid co-formers. Molecular complexity increases in the order a) GABA, b) Gabapentin, c) Pregabalin, d) Phenibut, e) Baclofen and in the order I) succinic acid, II) fumaric acid, III) maleic acid, IV), malic acid, V), tartaric acid, and VI) mandelic acid.

The compounds central to this thesis, GABA and its pharmaceutically relevant derivatives, are a class of successful APIs. They are molecularly small substances that offer limited capacity for intermolecular interactions but increase in complexity from GABA to Baclofen (**Figure 10**). The investigation of their crystallization behaviour is interesting, as it enables the revelation of how slight changes in molecular makeup affect structural properties on the supramolecular level, be it in terms of single component or multicomponent species. The choice of co-formers was undertaken according to established literature and serves to uncover how structural features, physicochemical properties, or crystallization-based processes established regarding

one compound are applicable to the related GABA-derivatives. As such the following questions are central to this thesis:

In how far are structural properties between the investigated species comparable regarding intermolecular interaction motifs in single and multicomponent systems?

Are there co-formers that form a multicomponent entity with each compound, and do these potential forms show similar physicochemical properties?

How does the crystal synthesis route affect the outcome of a crystallization for the central compounds? Are there any similarities between them?

How do established processes for example regarding enantiopurification work? Which structural characteristics enable these methods? Can this be transferred to other similar systems as well?

Answers to these questions on one hand highlight how far along we are in understanding relations between molecular and structural properties. Are we actually able to predict a crystal structure by observations on the molecular level? On the other hand, it offers a deeper understanding regarding solid-phase behaviour of blockbuster medications. Especially the commercial success of Gabapentin, Pregabalin and in a more limited capacity Baclofen serves to indicate that further APIs related to the investigated compounds will be marketed in the future. A sound understanding of their solid-phase behaviour can facilitate the optimization process prior to the product launch.

3 Published works

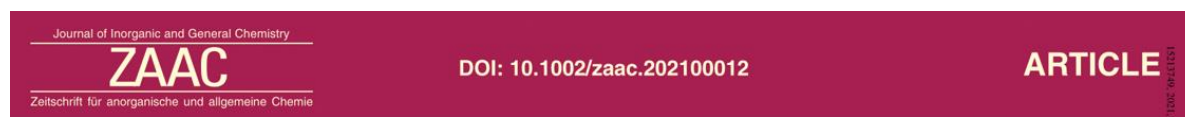
The different works published in, or submitted to a scientific journal will be presented on the upcoming pages. Each publication has an independent list and numeration of references, as well as an independent numeration of figures and tables. At the end of each article, the corresponding supporting information is shown as well.

All works are introduced with a short description of their contents, followed by a list of the authors contributions to the specific publication. The published or submitted articles are presented chronologically.

The published articles are provided in the form they can be accessed online. Submitted articles are presented as the most recent manuscript that is available.

Permissions were acquired where necessary and mentioned in the introductory remarks to each chapter.

3.1 Crystal Structure and Thermal Properties of Phenibut, Phenibut H₂O and Phenibut HCl: a Case for Phase Stability Based on Structural Considerations



Crystal Structure and Thermal Properties of Phenibut, Phenibut H₂O and Phenibut HCl: a Case for Phase Stability Based on Structural Considerations

D. Komisarek,^[a] M. Pallaske,^[a] and V. Vasylyeva*^[a]

Dedicated to Professor Christoph Janiak on the Occasion of his 60th Birthday.

15317796, 2021, 4, Downloaded from https://onlinelibrary.wiley.com/doi/10.1002/zaac.202100012

Komisarek, D.; Pallaske, M.; Vasylyeva, V. Crystal Structure and Thermal Properties of Phenibut, Phenibut H₂O and Phenibut HCl: a Case for Phase Stability Based on Structural Considerations, *Z. Anorg. Allg. Chem.*, **2021**, 647, 984–991.

DOI: 10.1002/zaac.202100012

Republished with Permission of *Zeitschrift für Anorganische und Allgemeine Chemie*
© John Wiley & Sons, Inc.

In this first contribution, the structure of Phenibut and its hydrate was presented and compared to that of the previously described HCl salt. Hirshfeld surfaces and an analysis of the existing HBs were made using *Crystal Explorer*. Thermogravimetric analysis was conducted to determine the heat induced decomposition behaviour of the investigated compounds. Based on this analysis, the stability of the different crystal phases was evaluated.

Contributions-list:

- Conceptualization of this work based on literature research and feedback from Dr. Vera Vasylyeva-Shor.
- Experimental work, including single crystal synthesis of the investigated compounds together with Mark Pallaske.
- Measurement of SCXRD and PXRD, FT-IR spectroscopy, and sample preparation for the TGA together with Mark Pallaske.
- Data evaluation of the recorded analyses.
- *Crystal Explorer*-based evaluation of the determined crystal structures.
- Manuscript preparation, including text writing, figure and table preparation, literature research and providing the supporting information.
- Revision process of the manuscript together with Dr. Vera Vasylyeva-Shor before and after Peer-Review process.

Crystal Structure and Thermal Properties of Phenibut, Phenibut H₂O and Phenibut HCl: a Case for Phase Stability Based on Structural Considerations

D. Komisarek,^[a] M. Pallaske,^[a] and V. Vasylyeva*^[a]

Dedicated to Professor Christoph Janiak on the Occasion of his 60th Birthday.

Phenibut is an anxiolytic drug approved for medical use in many eastern European states. With the exception of the HCl Salt of Phenibut no crystal structure related research has been conducted on this substance. Herein, the crystal structures of Phenibut and Phenibut-H₂O are presented, including crystal packing analysis based on interaction energy calculations. IR spectra are shown alongside powder diffraction data and thermogravimetric analysis to characterize and compare struc-

tural as well as thermal properties of the examined Phenibut forms. Single crystal diffraction is used in conjunction with Crystal Explorer based Hirshfeld analysis to carefully identify the bonding interaction properties in each compound. Finally, a case is made regarding stability of the compared crystalline phases based on the conducted structural analyses and the quantification of the molecular interaction energies.

Introduction

Recent advances in the understanding of neuronal binding motifs as well as drug development options highlight the value of the Crystal Structure Database (CSD).^[1–3] As of 2020 more than a million entries have been submitted to the CSD.^[4] In conjunction with the emergence of tools such as Crystal Explorer^[5] it has become possible to describe, compare or analyze crystalline substances much easier and more thoroughly than in the past. Despite all the progress made there are still many examples of even small molecules about which surprisingly little data is available.

Phenibut, a nootropic and anxiolytic drug^[6] belongs to the family of γ -amino butyric acid (GABA) derivatives. While several eastern European states allow its medical use^[7] it is mostly considered a New Psychoactive Substance (NPS) in the western world.^[8] Although there is an abundance of studies on the abuse potential of Phenibut^[9–13] only one CSD communication by P. Y. Zavalij gives any information on its structural properties, or more specifically on those of the HCl salt form.^[14] Contemplating the possible stigma around NPS or psychoactive substances in general could be an explanation for the

diminutive interest. However, this disregards the impact that related substances have had on the market of pharmaceutical products. Other GABA derivatives including but not limited to Gabapentin, Pregabalin and Baclofen continue to receive much attention. Recent studies are examining the proven antiepileptic and analgesic effects of the former two^[15–20] but also shine a light on their use for the treatment of anxiety disorders.^[21–23] Baclofen, a relaxant which is structurally most similar to Phenibut shows potential in the treatment of substance abuse.^[24–26] Besides the numerous studies on the pharmaceutical benefits of these substances there is also some interest in their structural behavior. Polymorphism,^[27,28] co-crystallization^[29–32] or salt formation^[32–34] of Gabapentin, Pregabalin and Baclofen continue to be current topics. Therefore, knowledge about the structural behavior of GABA related drugs should be furthered by starting to include Phenibut into the research effort. Furthermore, it should be beneficial to start connecting the findings regarding crystal engineering in general and GABA derivatives in particular to come to a better understanding of the crystallization behavior of these substances.

The crystal structure of Phenibut (**A**) and Phenibut-H₂O (**B**) are presented and compared to the respective HCl salt (**C**). The structural properties of each compound are analyzed. **A** as well as **B** and **C** are characterized by powder X-ray diffraction (PXRD), infra-red spectroscopy (IR) and thermogravimetric analysis (TGA). The lattice parameters and the molecular conformation of the GABA moieties in the Phenibut units are compared for all compounds. Crystal Explorer 17.5 is used to create the Hirshfeld surfaces of each compound as a tool to identify bonding interactions more thoroughly. Single crystal X-ray diffraction (SCXRD) is used to describe similarities and differences in their bonding and packing behavior. Stability of the crystalline forms in the case of hydrate and molecular crystal is quantified by Crystal Explorer calculations. The driving

[a] D. Komisarek, M. Pallaske, Dr. V. Vasylyeva
Department of Inorganic and Structural Chemistry I
Heinrich Heine University Duesseldorf
Universitaetsstr. 1, 40225 Duesseldorf
E-mail: vera.vasylyeva-shor@hhu.de

Supporting information for this article is available on the WWW under <https://doi.org/10.1002/zaac.202100012>

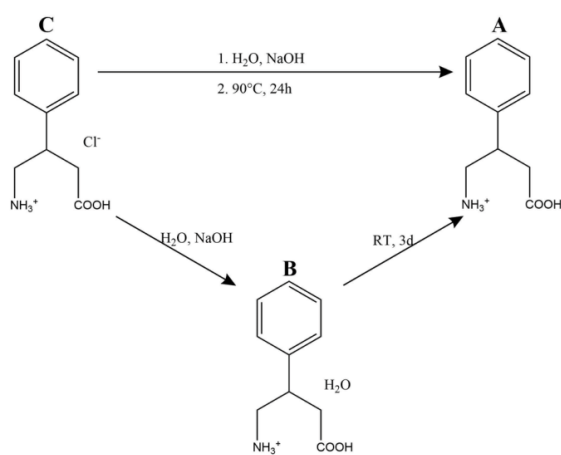
© 2021 The Authors. *Zeitschrift für anorganische und allgemeine Chemie* published by Wiley-VCH GmbH. This is an open access article under the terms of the Creative Commons Attribution Non-Commercial NoDerivs License, which permits use and distribution in any medium, provided the original work is properly cited, the use is non-commercial and no modifications or adaptations are made.

force behind the conversion of **B** to **A** is identified based on the conducted experiments and energy quantifications.

Results and Discussion

Crystal Synthesis

A and **B** were synthesized by reacting the salt **C** with NaOH in aqueous solution. The reaction conditions are presented in Scheme 1. **B** undergoes a relatively fast conversion to **A** when left to dry at room temperature. Based on that it was determined that the conversion of **B** to **A** can serve as an example of stability dependent preferential structure formation for GABA analogues. PXRD analysis was performed on the compounds **A–C** after they were obtained. Different phases were first identified by comparison of their respective powder patterns.



Scheme 1. Synthesis of Phenibut and Phenibut-H₂O from Phenibut-HCl.

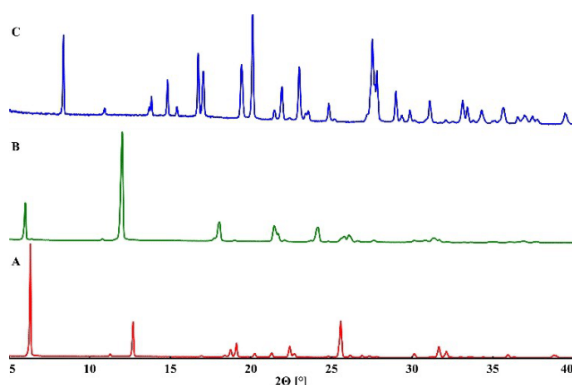


Figure 1. Powder patterns of **A**, **B** and **C** recorded from 5 to 40° 2 θ .

PXRD Analysis

A and **B** show similar powder patterns while **C** poses more distinct reflexes than the former two (Figure 1). The powder pattern **C** does not indicate strong preferential growing directions for the crystal surfaces contrary to **A** and **B**. It should further be noted that traces of **A** are present in **B** which is most prevalent by some shared reflexes in both compounds. This can be attributed to the tendency of **B** to decompose to **A** over time. A zoomed version of the diffraction patterns with a comparison to simulated patterns from SCXRD data is shown in the supporting information. IR spectra of **A–C** were collected to analyse the occurring bonding interactions in the crystal lattices.

IR Analysis

No O-H stretching is detected in the IR-spectra of **A** (Figure 2), which indicates the absence of water in the crystal lattice as well as the absence of any form of hydroxy subunit. This is in congruence with the position of C=O stretching at 1524 cm⁻¹. The shift towards lower wavenumbers is more common for carboxylate than for carboxy groups which means **A** exists in the zwitterionic form often seen for amino acids. A further indication for this is the comparatively weak band at 1162 cm⁻¹ probably attributed to the deprotonated C–O stretching. A similar pattern occurs in **B** with an additional broad band at 3300 cm⁻¹ probably caused by water in the crystal lattice. In **C** a weak broad band at 3163 cm⁻¹ in conjunction with the C=O stretching at 1713 cm⁻¹ indicates a protonation of the acid through HCl in the lattice forming a carboxy subunit. The C–O stretching band is stronger, and blue shifted to 1196 cm⁻¹. The broad band in the range of 3000 cm⁻¹–2300 cm⁻¹ shows the presence of hydrogen bond interactions in **A**, **B** and **C**. The band near 2100 cm⁻¹ in **A** and **B** is a signal common in amino acids and terminal ammonium ions. **A** and **B** show greater

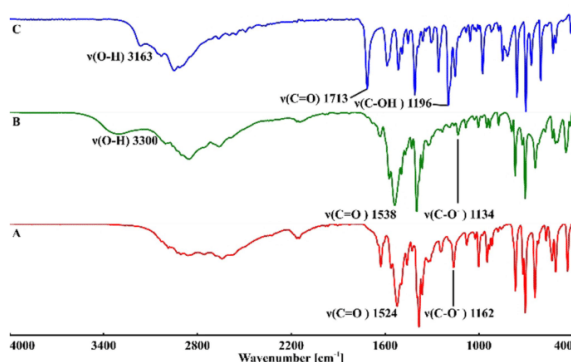


Figure 2. IR spectra of **A**, **B** and **C** recorded from 400 cm⁻¹ to 4000 cm⁻¹.

similarities sub 1600 cm^{-1} in comparison to **C** which indicates a more similar bonding network in **A** and **B**.

TG Analysis

TG analysis of the compounds **A–C** was performed to identify any remarkable features in the decomposition behavior. The decomposition of **A**, **B** and **C** under thermal influence in a range of 50 °C – 300 °C is shown in Figure 3. **A** remains stable until 168 °C when the decomposition starts in two steps. It seems most likely that the alkyl residue starts to break apart at that temperature removing CO_2 or NH_3 from the system. **B** first loses

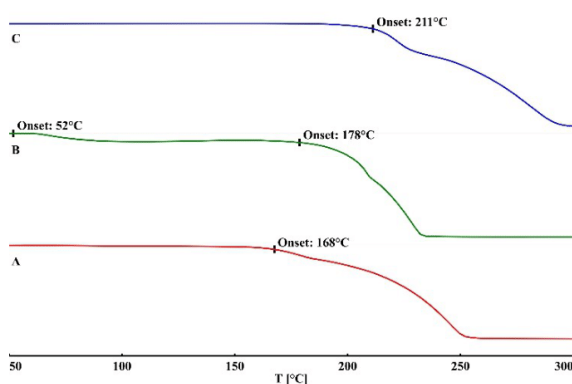


Figure 3. TGA of **A–C**. Onset temperature for decomposition is shown.

its hydrate water at 52 °C and then decomposes more rapidly in roughly the same range as **A**. The HCl salt **C** shows the highest decomposition temperature of 211 °C . All compounds decompose similarly in two steps with an extra step in **B** losing the hydrate water. The thermal analysis therefore indicates a ranking in thermal stability of the order $\text{B} < \text{A} < \text{C}$.

Crystal Structure and Molecular Geometry Analysis

Single crystals of **A**, **B** and **C** could be obtained from solution. Table 1 shows the geometry and measurement parameters of the examined phases. Comparison of the cell parameters reveals a strong similarity between all compounds. Especially **A** and **B** share nearly identical axis length values, *b*– and *c*–axes being switched. **A** as well as **B** are orthorhombic systems and while **C** is monoclinic it only exhibits a very slight deviation from 90° in β . All three compounds share the presence of a GABA moiety in the molecular structure. The molecular geometry of GABA has already gained attention in the past and present. A recent study by Wu and Gong reports on the conformation between C_β and C_γ of the three GABA polymorphs received through different milling conditions. The most frequently obtained form in their experiments posed a gauche conformation in this position.^[35] Earlier studies have linked the gauche conformation in GABA to higher stability in the crystal phase possibly because this geometry favors an intramolecular HB. In contrast to that, a trans conformation between C_β and C_γ does not enable the formation of such a HB.^[36–39] These observations lead to the question whether such findings can be transferred from a simple GABA molecule to its more complex

Table 1. Crystallographic Data for **A**, **B** and **C**

	Phenibut	Phenibut·H ₂ O	Phenibut·HCl
Formula	C ₁₀ H ₁₃ NO ₂	C ₁₀ H ₁₃ NO ₂ ·H ₂ O	C ₁₀ H ₁₄ NO ₂ ·Cl
M [g mol ⁻¹]	179.21	197.23	215.67
Temperature [K]	140(2)	140(2)	140(2)
System	Orthorhombic <i>Pbca</i>	Orthorhombic <i>Aba2</i>	Monoclinic <i>C2/c</i>
Space group			
<i>a</i> [Å]	9.3847(10)	9.7795(10)	15.939(2)
<i>b</i> [Å]	6.9789(9)	29.313(3)	6.4033(11)
<i>c</i> [Å]	27.505(3)	7.1381(7)	21.355(4)
β [°]	90	90	89.857(14)
<i>V</i> [Å ³]	1801.4(4)	2046.3(4)	2179.4(6)
<i>Z</i> / <i>Z'</i>	8/1	8/1	8/1
Density [g cm ⁻³]	1.322	1.280	1.315
μ [mm ⁻¹]	0.092	0.094	0.325
<i>T</i> _{min} / <i>T</i> _{max}	0.7990/1.0000	0.6822/0.7457	0.6921/0.7455
<i>F</i> (000)	768	848	912
Crystal size [mm]	0.06·0.1·0.6	0.07·0.1·0.4	0.08·0.1·0.4
θ range [°]	2.63–25.17	2.78–28.45	3.18–26.85
Completeness [%]	99.8	99.8	99.7
Recorded refl.	6997	8472	8671
Independent refl.	1609	2457	2364
Goodness-of-fit <i>F</i> ²	1.013	0.959	1.056
X-Ray Source	Mo K α	Mo K α	Mo K α
	($\lambda = 0.71073$)	($\lambda = 0.71073$)	($\lambda = 0.71073$)
<i>R</i> ₁ / <i>wR</i> ₂ [%]	4.81/11.97	4.01/11.25	3.74/9.39

derivatives. Further a question arises whether statements regarding phase stability in the presented examples are possible based only on the orientation of the GABA moiety or whether the phenyl subunit in Phenibut would dominate the structural preference. Therefore, the conformation in the GABA moiety is compared between compounds **A**, **B** and **C**. The torsion angles $C_{\alpha}-C_{\beta}-C_{\gamma}-N$ and $COO-C_{\alpha}-C_{\beta}-C_{\gamma}$ of the Phenibut molecules in compounds **A–C** are shown in Figure 4. While a clear gauche conformation including the possibility to form an intramolecular HB is apparent in **C**, both **A** and **B** pose unfavorable trans-angles from the $C_{\alpha}-C_{\beta}-C_{\gamma}-N$ viewpoint. This conformation in **A** and **B** hinders the formation of an intramolecular HB. From the $COO-C_{\alpha}-C_{\beta}-C_{\gamma}$ view it is notable that **A** is more closely related to **C** than to **B**. This relation could be an indicator of a more stable molecular geometry in **A**, but no clear differentiation of a favorable structure between **A** and **B** is possible through this aspect. The intermolecular bonding network in the structures of **A–C** was further analysed. A Hirshfeld analysis was performed to determine the bonding interactions in each system. Hirshfeld surfaces of different Phenibut molecules in **A**, **B**, and **C** as well as the respective fingerprint plots of each compound are shown in Figure 5. A detailed analysis is given in the supporting information. The Hirshfeld analysis for **A** shows that HB donor interactions with the ammonium and HB acceptor interactions with the carboxylate subunits take place. Each NH_3^+ subunit can donate three HB and each COO^- subunit can accept three HB. A plethora of π -bonding interactions with the phenyl subunit are possible including edge-to-face and edge-to-edge interactions. In **B** the total number of HB interaction sites has risen compared to **A**,

but also more binding sites are occupied by water molecules. While the COO^- subunit now participates in four HB acceptor interactions two are blocked by water molecules. The same goes for the ammonium subunit where one of the three donor sites binds a water molecule. The number of possible π -interaction sites is reduced even further ruling out edge-to-face interactions and showing less edge-to-edge interactions than **A**. The Hirshfeld analysis of **C** reveals strong similarities in the interactions of the NH_3^+ subunit compared to **A** and **B**. However, the HB donor sites are now connected in two directions to chloride ions. Furthermore, an additional intramolecular HB occurs that can possibly be linked to more stable crystalline phases of GABA derivatives. The acid group is protonated through the HCl in the structure which distinguishes it from both **A** and **B** COO^- -groups and consequently changes the HB interaction modes. While the phenyl subunit cannot partake in edge-to-face interactions such as in **A**, a phenyl hydrogen is donated towards oxygen of a hydroxy group in the carboxyl subunit. Also, edge-to-edge interactions occur as in **A** and **B**. The inter- and intramolecular interactions in the crystal packing of **A**, **B** and **C** were determined based on the performed Hirshfeld analysis via SCXRD. The bonding interactions of the molecules of each examined compound are shown in Figure 6. **A** exhibits a pattern of hydrogen bonds between its GABA moieties. Hydrogen atoms of the NH_3^+ subunits N, connect via strong HB to two O1 and one O2 of the COO^- subunits. The network is further stabilized by edge-to-face and edge-to-edge π -interactions. The edge-to-edge interactions occur between C6 and C7 as well as C7 and C9 in the phenyl subunit. The edge-to-face interactions are formed

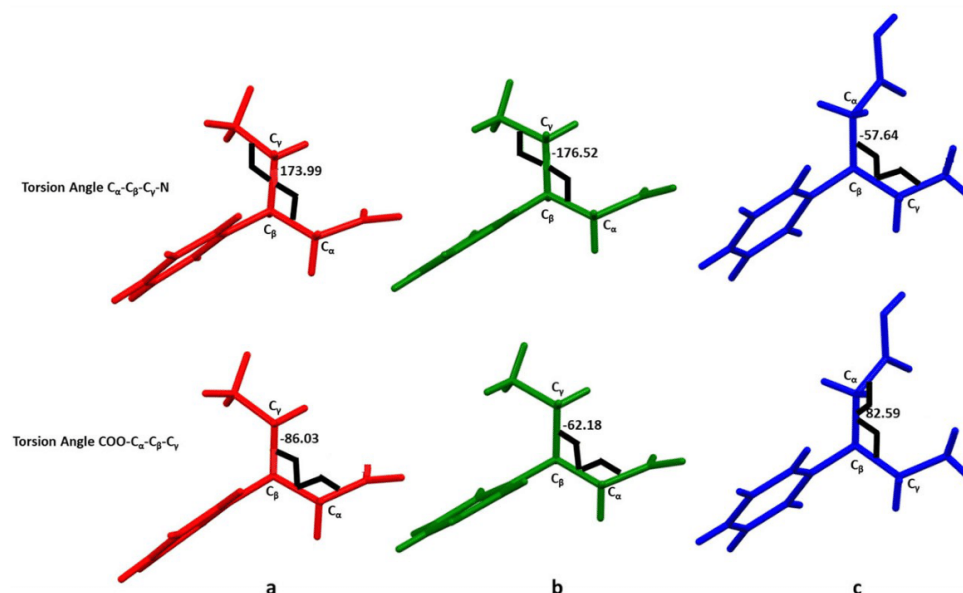


Figure 4. Torsion angles and molecular geometry determined from the crystal structures in Phenibut (a), Phenibut-H₂O (b) and Phenibut-HCl (c). Only Phenibut molecules are shown for clarity.

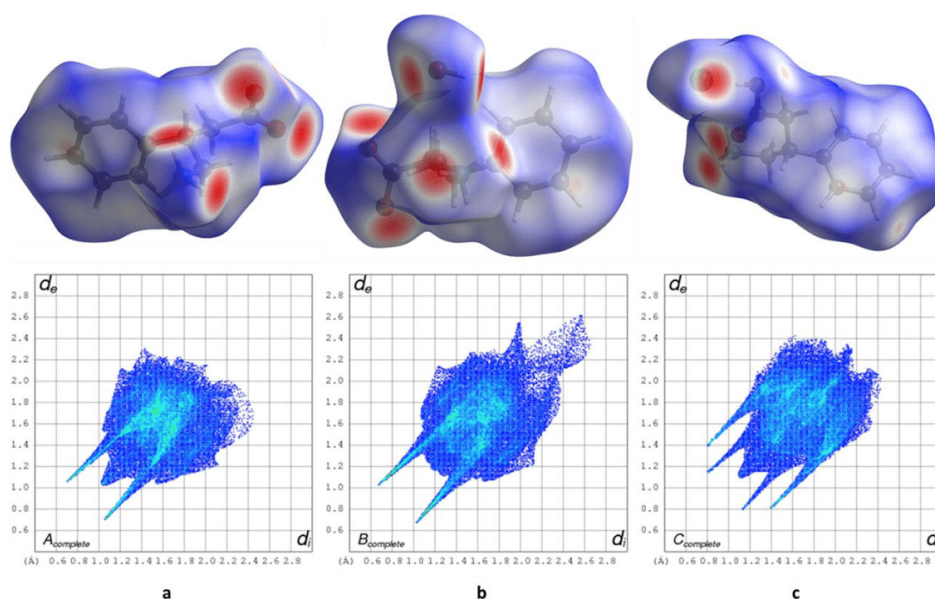


Figure 5. Hirshfeld surface and fingerprint plot of: Phenibut (a), Phenibut-H₂O (b) and Phenibut-HCl (c).

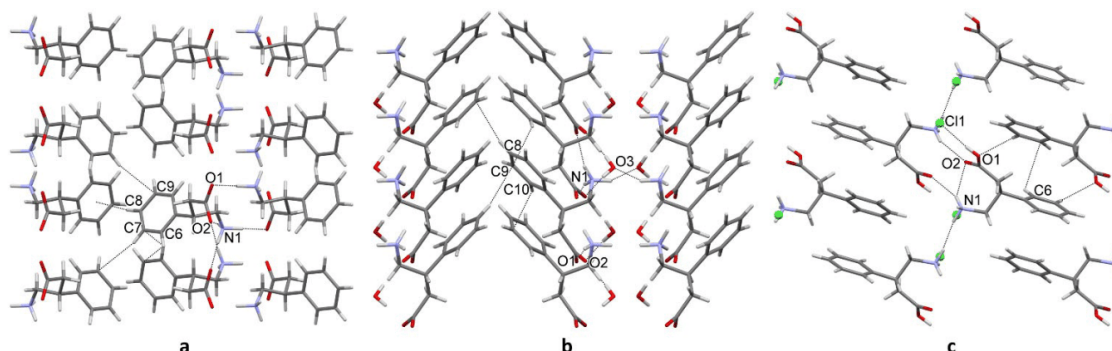


Figure 6. Comparison of interacting modes in crystal structures of Phenibut (a) view along b-axis, Phenibut-H₂O (b) view along a-axis and Phenibut-HCl (c) view along b-axis. Only atoms undergoing selected intermolecular interactions are labeled. C atoms = grey, N atoms = blue, O atoms = red, H atoms = white and Cl⁻ anions = green.

between C8 and the center of the phenyl ring straight ahead. In that regard **A** differs from **B** as well as from **C** where such interactions do not take place. **A** forms chains of Phenibut molecules connected by HB and edge-to-face π -interactions. These chains are extended into further dimensions by the edge-to-edge π -interactions and the HB between N1 and O2. Overall, hydrogen bonds connect Phenibut molecules at the GABA moieties while edge-to-face and edge-to-edge interactions connect the phenyl subunits. In **B** water molecules are intertwined into the HB network of the GABA moieties of Phenibut molecules. The oxygen O3 of the water molecule occupies a HB donor site of N1. The other two HB donor sites interact with O1 atoms of the carboxylate subunits in the

Phenibut molecules. The double acceptor sites in O2 of the carboxylates are occupied by donated HB from two water molecules marked as O3. Edge-to-edge π -interactions are formed between C9 and C10 of Phenibut molecules. The edge-to-face π -interactions cease to take place. Water molecules settle between the HB bonding sites. This forces the phenyl subunits of the Phenibut molecules into a position that makes the edge-to-face interactions less favorable causing a network of edge-to-edge interactions. The bonding interactions in **B** are similar to **A** yet the HB are weakened by synthon/water interactions and the number of possible π -interactions is reduced. Chains comparable to **A** are formed connected by HB between the GABA moieties. Said chains are connected by

edge-to-edge interactions into further dimensions. In **C** the HB network between the GABA moieties of the Phenibut molecules is stabilized by HB interactions between the NH_3^+ subunit and the chloride ion. It is notable that one N1 hydrogen connects to two O2 atoms of the carboxylate subunits. While one of the subunits stems from the same molecule the other comes from a different one combining intra- as well as intermolecular HB in a bifurcated motif. A further chloride ion Cl1 is connected to N1 via purely ionic attraction over a longer distance based on the chloride binding sites in the Hirshfeld analysis. Cl1 is further connected to COOH O1 as an acceptor site for a HB. The quadruple connectivity of chloride seems to be the leading direction in the crystal lattice as quasi-tetrahedral geometry is formed around the ion. O1 is further connected as an HB acceptor to the C7 phenyl hydrogen. Edge-to-edge interactions take place between C6 atoms of the Phenibut molecules. Summarizing **C** there is a network of HB between the GABA moieties similar to **A** and **B** but chloride ions seem to strengthen the interactions instead of weakening them compared to water molecules in **B**. π -interactions occur less than in **A** and are only of an edge-to-edge type which is more similar to **B**. Chains in **C** are further stabilized by incorporated chloride ions that participate in HB and ionic interactions towards ammonium subunits and HB interactions with a carboxyl subunit. The interconnection of these chains to layers occurs through the chloride ions by a HB/ionic hybrid interaction between N1 and Cl1. **A** and **B** share a common layered arrangement of the Phenibut molecules in the lattice (Figure 7) differentiating only by the water molecules in **B** situated between the rows of Phenibut molecules. A similar behaviour is visible in **C** but here the arrangement of the Phenibut ions is tilted in regard to each other. Chloride ions are placed in between of the rows of Phenibut ions in a comparable manner to water molecules in **B**.

Interaction Energy Calculations

When comparing crystalline phases of **A**, **B** and **C** it appears that the least stable form is **B**. The TGA shows that the lattice starts to release water at 52 °C. Many HB interactions are formed between water and Phenibut molecules whereas the phenyl subunits are linked solely by edge-to-edge π -interactions. Also, the conformation between the residues on C_β and C_γ in **B** is gauche in $\text{COO}-\text{C}_\alpha-\text{C}_\beta-\text{C}_\gamma$ direction but trans in $\text{C}_\alpha-\text{C}_\beta-\text{C}_\gamma-\text{N}$ direction. The gauche angle is -62.18° and deviates from both **A** and **C** with angles around $(-)\text{85}^\circ$ in the $\text{COO}-\text{C}_\alpha-\text{C}_\beta-\text{C}_\gamma$ direction. An intramolecular HB cannot be formed in this geometry. This is also the case in **A**. However, more HB-interactions between Phenibut molecules appear as well as edge-to-face in addition to edge-to-edge π -interactions. To quantify these observations of stability Crystal Explorer was used to calculate the interaction energies between different molecules in the lattices of **A** and **B**. The quantification of these energies can elucidate why **B** undergoes a conversion to **A**. For this, the direct interactions of each different molecule in the lattice were identified. The following table compares interaction properties of the molecules in **A** and **B**. More detailed tables are shown in the supporting information. The interaction properties of different molecules in the lattices of **A** and **B** are presented in Table 2. While each Phenibut molecule in both structures interacts directly with nine different molecules, **B** also possesses an additional water molecule with three distinguishable interactions in its lattice. The longest interaction distance in **B** is 2.88(4) Å and slightly longer than in **A** with 2.85(3) Å, but the shortest interaction in **A** is 1.64(3) Å and is decisively shorter than that in **B** with 1.78(6) Å. The short and strong interactions in both molecules are hydrogen bond type interactions while the longer and weaker interactions are π -interactions. The strongest interaction in **A** occurs between two Phenibut molecules where GABA moieties are connected via ammonium/carboxylate donor/acceptor hydrogen bonds. This binding

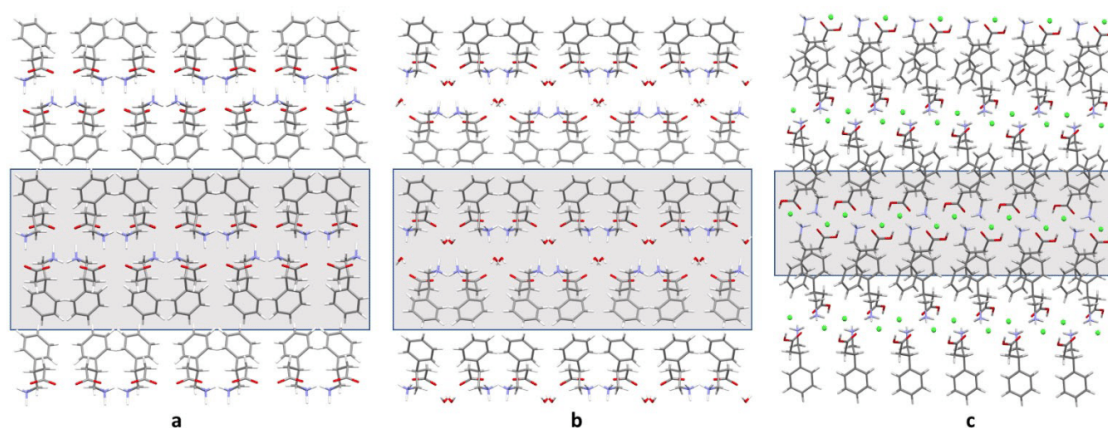


Figure 7. Similarities in the overall crystal packing of Phenibut (a) view along a-axis, Phenibut-H₂O (b) view along c-axis and Phenibut-HCl (c) view along b-axis. Layered motives are highlighted by the background. C atoms = grey, N atoms = blue, O atoms = red, H atoms = white and Cl⁻ anions = green.

Table 2. Comparison of interaction properties in Phenibut and Phenibut-H₂O.

	Phenibut	Phenibut-H ₂ O
Different lattice molecules	1	2
Interactions per molecule	9	9 (Phenibut) 3 (Water)
Longest int. dist. [Å]	2.85(3)	2.88(4)
Interaction type	edge-to-face	edge-to-edge
Shortest int. dist [Å]	1.64(3)	1.78(6)
Interaction type	hydrogen bond	hydrogen bond
E_tot strongest [kJ mol ⁻¹]	-385.3	-149.0
Interaction types	HB, donor/acceptor HB, donor/acceptor	HB, donor HB, acceptor
E_tot weakest [kJ mol ⁻¹]	5.3	-1.9
Interaction types	edge-to-edge	edge-to-edge
Sum of E_tot per molecule [kJ mol ⁻¹]	-863.3	-636.4 (Phenibut) -168.4 (Water)

mode is energetically very much favored resulting in a highly attractive interaction with a minimum of $-385.3 \text{ kJ mol}^{-1}$. The described interaction is missing in **B**. Here the strongest interaction also takes place between two Phenibut molecules, but it is only between one ammonium and one carboxylate subunit. While this interaction still is favorable it does not grant such a beneficial minimum at $-149.0 \text{ kJ mol}^{-1}$. It is notable that the GABA/GABA-moiety connection results in an energetic gain that is more than the sum of two single $\text{NH}_3^+/\text{COO}^-$ HB connections. It is furthermore remarkable that even though the weakest interaction in **A** is of a repulsive nature the total of interaction energies for the direct interactions in each molecule of **A** with $-863.3 \text{ kJ mol}^{-1}$ is more than 200 kJ mol^{-1} higher than for Phenibut molecules in **B** at $-636.4 \text{ kJ mol}^{-1}$. The interaction energies for the water molecules in **B** pose a comparatively low gain at only $-168.4 \text{ kJ mol}^{-1}$. The results of these calculations show that the conversion of **B** to **A** leads to a substantial gain in energetically favorable interactions for each Phenibut molecule. This could be the driving force behind the conversion of the metastable **B** structure to the more stable **A** structure.

Conclusions

In this work the crystal structures of the nootropic and anxiolytic drug Phenibut and its monohydrate were firstly presented. The driving force behind the conversion of the metastable Phenibut-H₂O to the stable Phenibut structure was examined. Both structures were compared to the thermodynamically favorable HCl Salt in their bonding motifs as well as their molecular geometry. The results suggest that the conformation between the C_β and C_γ of the GABA moiety is not a serious indicator for stability in the present case. Even though some similarities between Phenibut and Phenibut-HCl occur along the COO-C_α-C_β-C_γ view the number of examined compounds in this work is too small to lead to a reliable conclusion. It was shown that the number of bonding interactions and more so their energetic favorability can be identified as the most probable driving force behind the phase

transition. Structural considerations and qualitative as well as quantitative bonding analysis can be used as a tool to estimate the stability of crystalline GABA analogues. Crystal explorer enables a quick and facile possibility to check and compare such properties. The observed decomposition behavior of Phenibut H₂O to Phenibut and the thermal stability examined via TGA match the structural considerations and energy calculations. Emphasis should be put on the possibility to compare GABA analogues with each other. This could help to identify desirable crystalline phases in present as well as future commercially viable GABA analogues. Furthermore, a thorough investigation of crystallization behavior of these compounds can also help in the understanding of GABA receptor binding properties.

Experimental Section

Synthesis: Phenibut-HCl was purchased from abcr GmbH and used without further purification. Phenibut and Phenibut-H₂O were synthesized by reacting 1 eq Phenibut-HCl with 1 HCl eq of NaOH. Phenibut-HCl was dissolved in water and mixed with a solution of NaOH. This resulted in a colorless precipitation forming immediately on mixing of the solutions. The residue was filtered and dried at 90 °C for one day. Phenibut-H₂O could be received by drying at RT but decomposed to Phenibut after three days.

Diffraction quality needle shaped single crystals of Phenibut were obtained by dissolving in hexafluoro-2-propanol and slow diffusion of acetonitrile. Diffraction quality needle shaped single crystals of Phenibut-H₂O were obtained by dissolving Phenibut in water and slow diffusion of acetonitrile. Diffraction quality block shaped single crystals of Phenibut-HCl were obtained by dissolving in water and slow evaporation of the solvent.

Single-Crystal X-ray Diffraction: Suited single crystals were selected from the sample and mounted on the loop under oil. Diffraction data were recorded with a Bruker APEX Duo diffractometer with CCD detector using Mo-K α radiation ($\lambda = 0.71073$) at 140(2) K. The single crystal structure was solved by using direct methods and refined with SHELXL crystallographic software package.^[40] Figures were prepared with Mercury software.^[41]

X-ray Powder Diffraction: Measurements were performed on a Rigaku Miniflex diffractometer in $\theta/2\theta$ geometry at ambient temperature using Cu-K α radiation ($\lambda = 1,54182 \text{ \AA}$).

Spectroscopy and thermal analysis: The IR spectra were recorded on Bruker Tensor 37, measured with an ATR unit as FTIR at room temperature. Netzsch DSC600 with LNP96-S was used for the thermogravimetric analysis in the range 30 °C–600 °C with 10 °C min⁻¹ in nitrogen atmosphere.

Hirshfeld analysis and energy calculations: Crystal Explorer 17.5^[5] was used to generate Hirshfeld surfaces, fingerprint plots and calculate interaction energies. The energy model B3LYP/6-31G (d, p) was used.

All obtained crystal structures were deposited to CCDC (depository number CSD Phenibut: 2050677, Phenibut-H₂O: 2050679, Phenibut-HCl: 2050678)

Acknowledgements

Open access funding enabled and organized by Projekt DEAL.

Keywords: GABA-analogues · topological analysis · interaction energy · Hirshfeld analysis · crystal engineering

- [1] P. R. Spackman, L.-J. Yu, C. J. Morton, M. W. Parker, C. S. Bond, M. A. Spackman, D. Jayatilaka, S. P. Thomas, *Angew. Chem. Int. Ed.* **2019**, *58*, 16780.
- [2] M. J. Bryant, S. N. Black, H. Blade, R. Docherty, A. G. P. Maloney, S. C. Taylor, *J. Pharm. Sci.* **2019**, *108*, 1655.
- [3] P. Giastas, M. Zouridakis, S. J. Tzartos, *Br. J. Pharmacol.* **2018**, *175*, 1880.
- [4] P. Willett, J. C. Cole, I. J. Bruno, *CrystEngComm* **2020**.
- [5] C. F. Mackenzie, P. R. Spackman, D. Jayatilaka, M. A. Spackman, *IUCrJ* **2017**, *4*, 575.
- [6] L. Zvejniece, E. Vavers, B. Svalbe, G. Veinberg, K. Rizhanova, V. Liepins, I. Kalvinsh, M. Dambrova, *Pharmacol. Biochem. Behav.* **2015**, *137*, 23.
- [7] I. Lapin, *CNS Drug Rev.* **2001**, *7*, 471.
- [8] D. R. Owen, D. M. Wood, J. R. H. Archer, P. I. Dargan, *Drug and alcohol review* **2016**, *35*, 591.
- [9] T. Ahuja, O. Mgbako, C. Katzman, A. Grossman, *Case reports in psychiatry* **2018**, *2018*, 9864285.
- [10] M. I. Hardman, J. Sprung, T. N. Weingarten, *Bosnian journal of basic medical sciences* **2019**, *19*, 125.
- [11] E. Kupats, J. Vrublevska, B. Zvejniece, E. Vavers, G. Stelfa, L. Zvejniece, M. Dambrova, *Pharmacopsychiatry* **2020**, *53*, 201.
- [12] D. J. McCabe, S. A. Bangh, A. M. Arens, J. B. Cole, *The American journal of emergency medicine* **2019**, *37*, 2066.
- [13] C. Tamarelli, A. Hosanagar, *Pain medicine (Malden, Mass.)* **2020**.
- [14] Y. Mao, P. Y. Zavalij, *CCDC 1821706: Experimental Crystal Structure Determination*, Cambridge Crystallographic Data Centre, **2018**.
- [15] D. Shan, Li Zou, X. Liu, Y. Shen, Y. Cai, J. Zhang, *Am. J. Obstet. Gynecol.* **2020**, *222*, 564–579.e12.
- [16] D. Kapustin, A. Bhatia, A. McParland, A. Trivedi, A. Davidson, R. Brull, M. Singh, *Pain* **2020**, *161*, 476.
- [17] S. Mathieson, C.-W. C. Lin, M. Underwood, S. Eldabe, *BMJ (Clinical research ed.)* **2020**, *369*, m1315.
- [18] L. R. Small, A. Galor, E. R. Felix, D. B. Horn, R. C. Levitt, C. D. Sarantopoulos, *Eye & contact lens* **2020**, *46*, 174; contact lens **2020**, *46*, 174.
- [19] X. Yang, Y. Zhang, H. Yu, J. Sun, Y. He, *Journal of the College of Physicians and Surgeons–Pakistan: JCPSP* **2020**, *30*, 106.
- [20] B. Miziak, A. Konarzewska, M. Ułamek-Kozioł, M. Dudra-Jastrzębska, R. Pluta, S. J. Czuczwar, *Int. J. Mol. Sci.* **2020**, *21*.
- [21] M. Mula, S. Pini, G. B. Cassano, *J. Clin. Psychopharmacol.* **2007**, *27*, 263.
- [22] H. K. Greenblatt, D. J. Greenblatt, *Clinical pharmacology in drug development* **2018**, *7*, 228.
- [23] T. Novais, A. Doutone, C. Gombault, P. Krolak-Salmon, A. Lepetit, C. Mouchoux, *J. Clin. Psychopharmacol.* **2019**, *39*, 261.
- [24] L. Leggio, D. E. Falk, M. L. Ryan, J. Fertig, R. Z. Litten, *Handb. Exp. Pharmacol.* **2020**, *258*, 443.
- [25] C. N. Kent, C. Park, C. W. Lindsley, *ACS Chem. Neurosci.* **2020**, *11*, 1740.
- [26] D. C.-S. Oh, N. Rakesh, B. LaGrant, M. Sein, *A&A practice* **2020**, *14*, e01204.
- [27] I. C. B. Martins, J. R. B. Gomes, M. T. Duarte, L. Mafra, *Cryst. Growth Des.* **2017**, *17*, 428.
- [28] C.-H. Hsu, W.-T. Ke, S.-Y. Lin, *Journal of pharmacy & pharmaceutical sciences : a publication of the Canadian Society for Pharmaceutical Sciences, Societe canadienne des sciences pharmaceutiques* **2010**, *13*, 67.
- [29] I. I. Soliman, S. M. Kandil, E. M. Abdou, *Pharm. Dev. Technol.* **2020**, *25*, 227.
- [30] B. Samas, W. Wang, D. B. Godrej, *Acta Crystallogr. Sect. E* **2007**, *63*, o3938–o3938.
- [31] P. Kavuru, D. Aboarayas, K. K. Arora, H. D. Clarke, A. Kennedy, L. Marshall, T. T. Ong, J. Perman, T. Pujari, Ł. Wojtas et al., *Cryst. Growth Des.* **2010**, *10*, 3568.
- [32] V. André, A. Fernandes, P. P. Santos, M. T. Duarte, *Cryst. Growth Des.* **2011**, *11*, 2325.
- [33] F.-X. Gendron, J. Mahieux, M. Sanselme, G. Coquerel, *Cryst. Growth Des.* **2019**, *19*, 4793.
- [34] I. C. B. Martins, M. Sardo, T. Čendak, J. R. B. Gomes, J. Rocha, M. T. Duarte, L. Mafra, *Magnetic resonance in chemistry : MRC* **2019**, *57*, 243.
- [35] L. Wang, G. Sun, K. Zhang, M. Yao, Y. Jin, P. Zhang, S. Wu, J. Gong, *ACS Sustainable Chem. Eng.* **2020**.
- [36] A. J. Dobson, R. E. Gerkin, *Acta crystallographica. Section C, Crystal structure communications* **1996**, *52* (Pt 12), 3075.
- [37] H.-P. Weber, B. M. Craven, R. K. McMullan, *Acta Crystallogr. Sect. E* **1983**, *39*, 360.
- [38] D. L. Crittenden, M. Chebib, M. J. T. Jordan, *J. Phys. Chem. A* **2004**, *108*, 203.
- [39] I. K. Song, Y. K. Kang, *J. Mol. Struct.* **2012** *1024*, 163.
- [40] a) G. M. Sheldrick, *Acta Crystallogr. Sect. A* **2008** *64*, 112–122; b) G. M. Sheldrick, *Acta Crystallogr. Sect. A* **2015**, *71*, 3–8; c) G. M. Sheldrick, *Acta Crystallogr. Sect. C* **2015**, *71*, 3–8.
- [41] C. F. Macrae, I. Sovago, S. J. Cottrell, P. T. A. Galek, P. McCabe, E. Pidcock, M. Platings, G. P. Shields, J. S. Stevens, M. Towler, P. A. Wood, *J. Appl. Crystallogr. Mercury 4.0: from visualization to analysis, design and prediction*, **2020**, *53*, 226–235.

Manuscript received: January 12, 2021
 Revised manuscript received: March 3, 2021
 Accepted manuscript online: March 8, 2021

Zeitschrift für anorganische und allgemeine Chemie

Supporting Information

**Crystal Structure and Thermal Properties of Phenibut,
Phenibut H₂O and Phenibut HCl: a Case for Phase Stability
Based on Structural Considerations**

D. Komisarek, M. Pallaske, and V. Vasyljeva*

Crystal Structure and Thermal Properties of Phenibut, Phenibut·H₂O and Phenibut·HCl: a case for phase stability based on structural considerations

D. Komisarek, M. Pallaske and V. Vasylyeva*

Supporting Information

In this document further information on PXRD data, Hirshfeld analysis and HB interactions is given.

PXRD

Comparison of recorded and simulated powder patterns of Phenibut, Phenibut·H₂O and Phenibut·HCl.

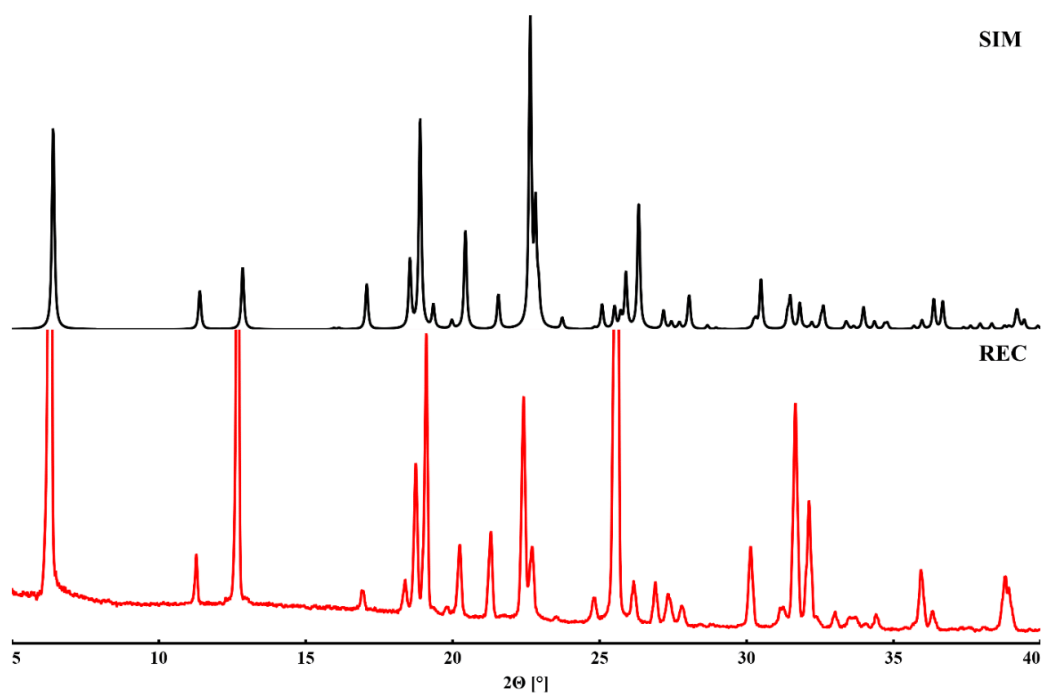


Figure S1. Powder pattern of Phenibut **REC** and **SIM**.

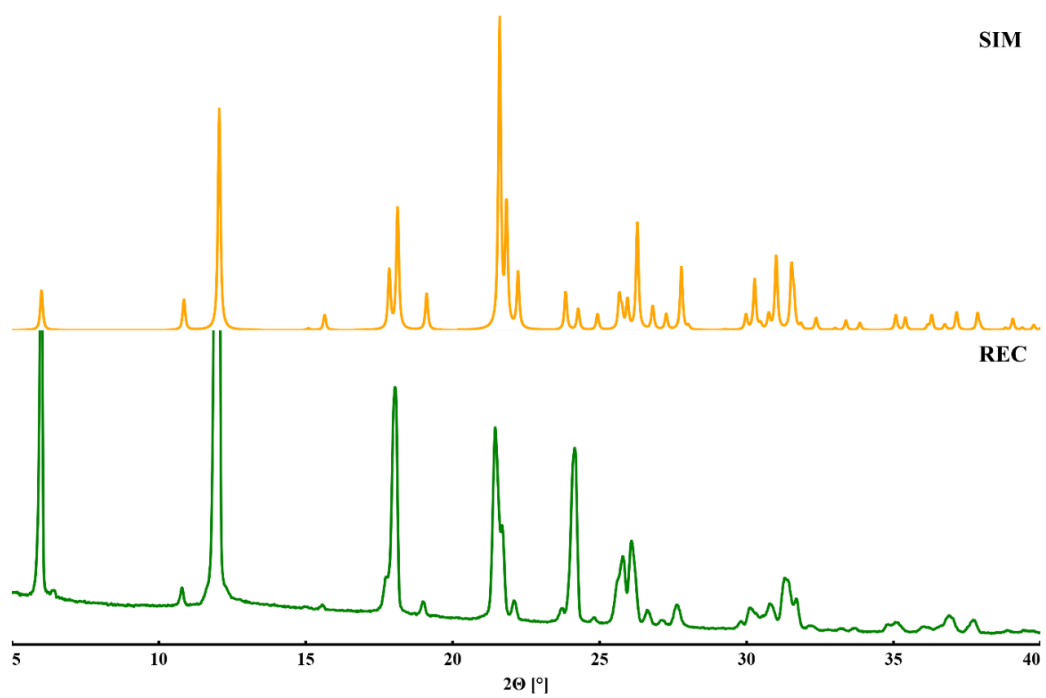


Figure S2. Powder pattern of Phenibut-H₂O REC and SIM.

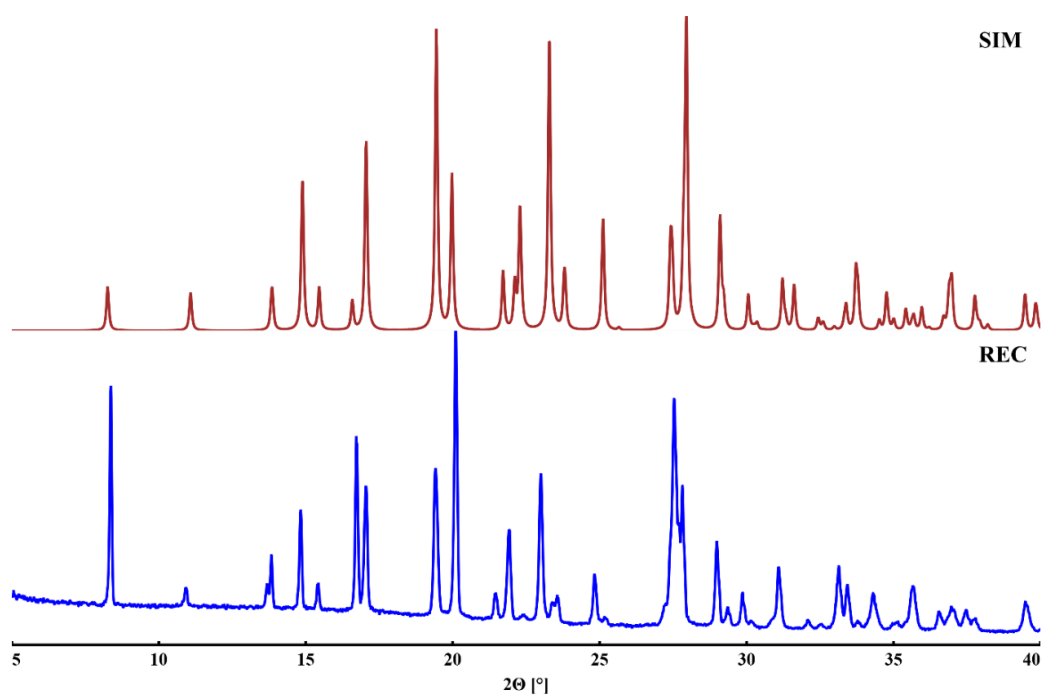


Figure S3. Powder pattern of Phenibut-HCl REC and SIM.

Hirshfeld analysis

Detailed information on Hirshfeld surfaces and fingerprint analysis of Phenibut, Phenibut Monohydrate and Phenibut HCl.

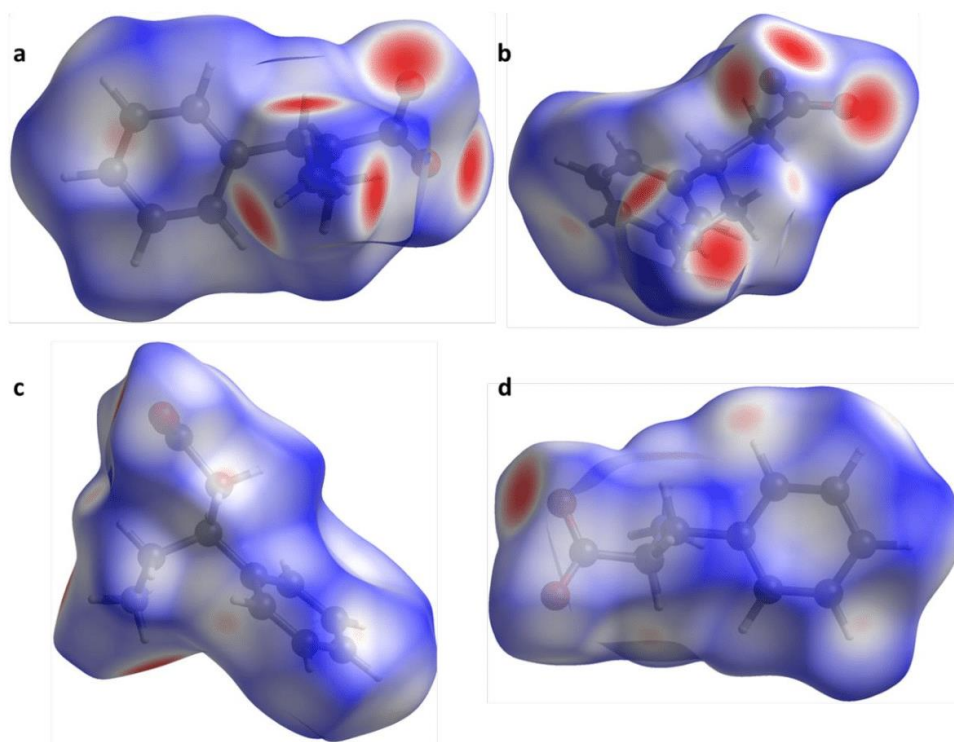


Figure S4. Hirshfeld Surface of Phenibut from different viewpoints.

S4 shows different viewpoints of Phenibut Hirshfeld surfaces. **a** shows the interaction options on the ammonium subunit as well as one side of the Phenyl ring. **b** shows the HB acceptor sides on the carboxylate subunit. **c** shows a sideways depiction of the Phenyl subunit. **d** shows the other face of the Phenyl subunit.

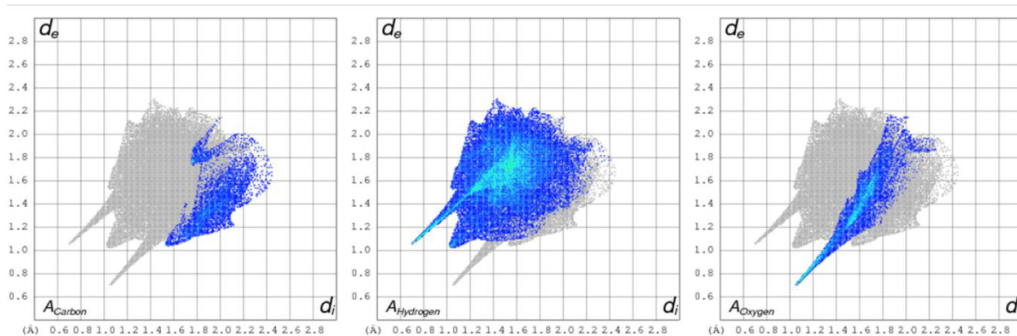


Figure S5. Fingerprint plots of Phenibut, close contacts of inside atoms Carbon, Hydrogen and Oxygen with outside interaction partners.

S5 shows which part of the overall interactions the inside atoms carbon, hydrogen and oxygen make up. It is notable, that Nitrogen only partakes via its hydrogen atoms and is not involved in any close contacts itself.

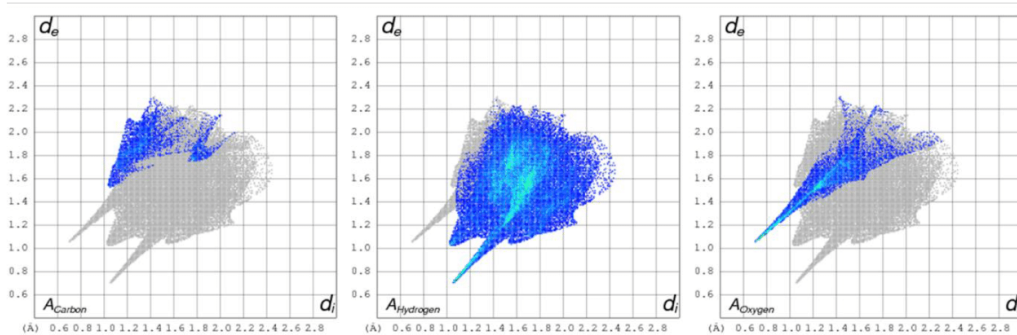


Figure S6. Fingerprint plots of Phenibut, close contacts of outside atoms Carbon, Hydrogen and Oxygen with inside interaction partners.

S6 shows which part of the overall interactions the outside atoms carbon, hydrogen and oxygen make up. It is notable, that Nitrogen only partakes via its hydrogen atoms and is not involved in any close contacts itself.

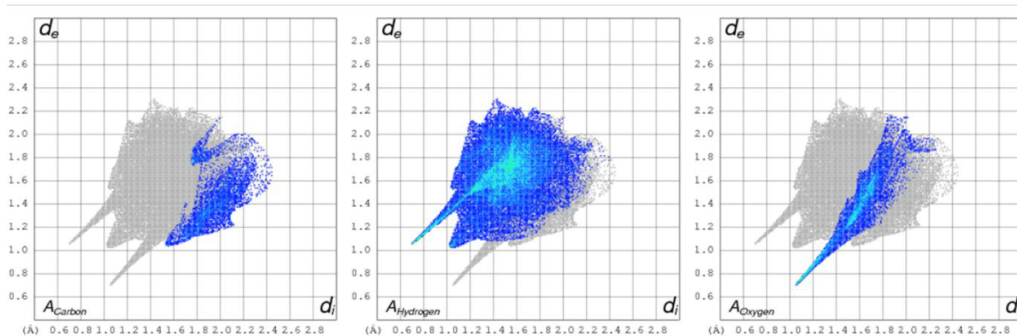


Figure S5. Fingerprint plots of Phenibut, close contacts of inside atoms Carbon, Hydrogen and Oxygen with outside interaction partners.

S5 shows which part of the overall interactions the inside atoms carbon, hydrogen and oxygen make up. It is notable, that Nitrogen only partakes via its hydrogen atoms and is not involved in any close contacts itself.

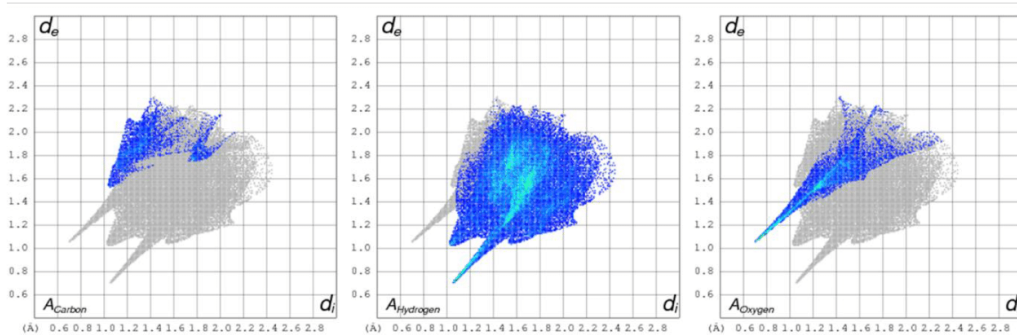


Figure S6. Fingerprint plots of Phenibut, close contacts of outside atoms Carbon, Hydrogen and Oxygen with inside interaction partners.

S6 shows which part of the overall interactions the outside atoms carbon, hydrogen and oxygen make up. It is notable, that Nitrogen only partakes via its hydrogen atoms and is not involved in any close contacts itself.

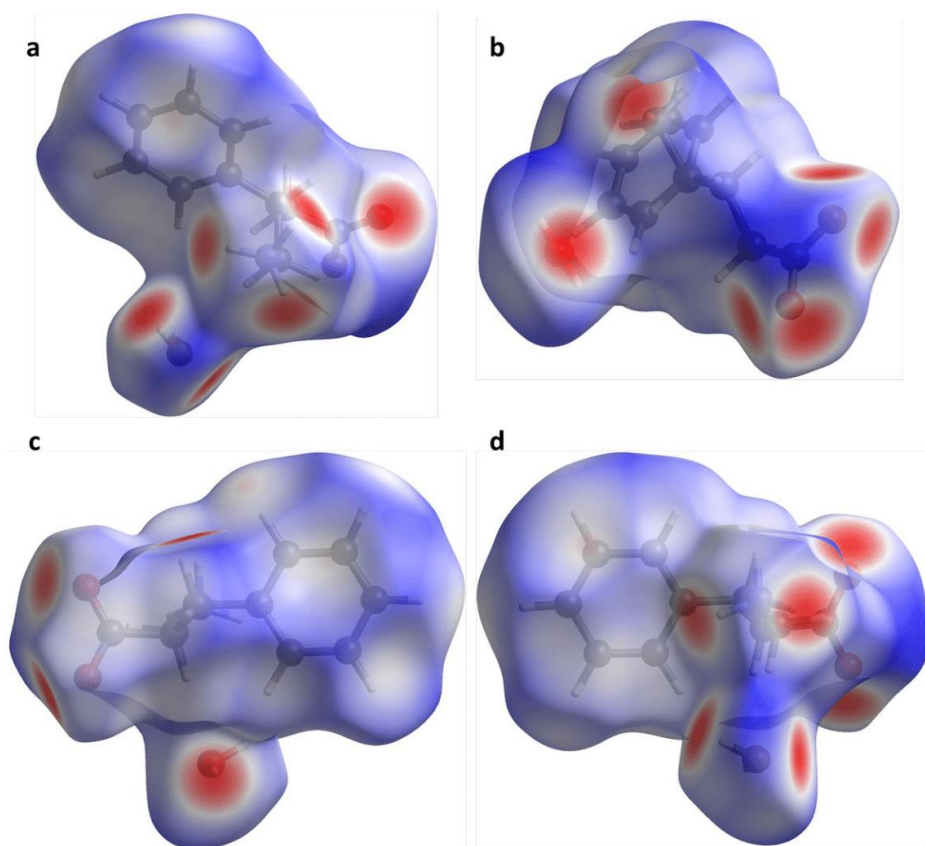


Figure S7. Hirshfeld surface of Phenibut-H₂O from different Viewpoints.

S7 shows different viewpoints of Phenibut-H₂O Hirshfeld surfaces. **a** elucidates on the ammonium interaction possibilities and simultaneously shows water interaction sides. **b** highlights the four HB acceptor sites in the carboxylate subunit. **c** and **d** put emphasis on the phenyl subunit from two sides and further show the water binding sites.

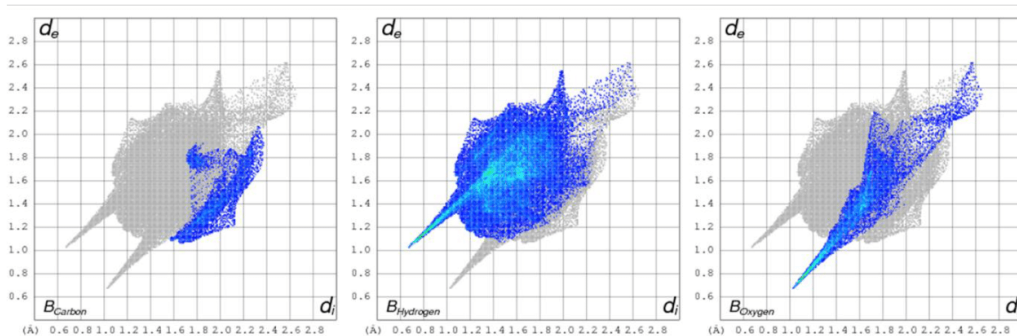


Figure S8. Fingerprint plots of Phenibut-H₂O, close contacts of inside atoms Carbon, Hydrogen and Oxygen with outside interaction partners.

S8 shows which part of the overall interactions the inside atoms carbon, hydrogen and oxygen make up. Same as in Phenibut, Nitrogen only partakes via its hydrogen atoms and is not involved in any close contacts itself.

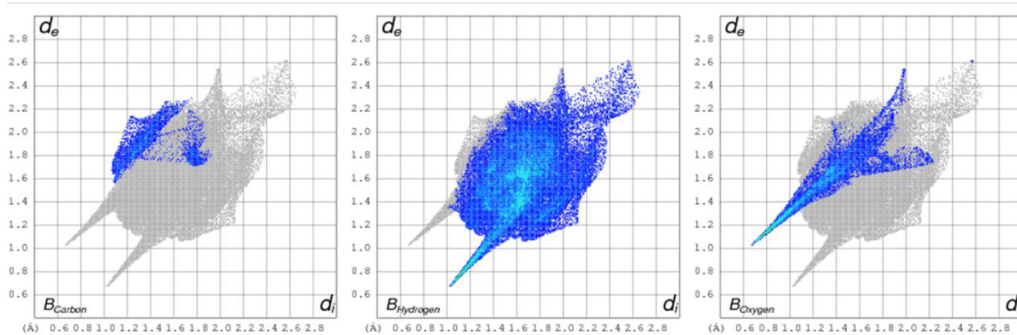


Figure S9. Fingerprint plots of Phenibut-H₂O, close contacts of outside atoms Carbon, Hydrogen and Oxygen with inside interaction partners.

S9 shows which part of the overall interactions the outside atoms carbon, hydrogen and oxygen make up. Same as in Phenibut, Nitrogen only partakes via its hydrogen atoms and is not involved in any close contacts itself.

Energies

Detailed Information on Binding Energies in Phenibut and Phenibut-H₂O.

Table S1. Direct interactions of Phenibut molecules in Phenibut. Energy values in kJ mol⁻¹.

	N	Symop	R	Electron Density	E_ele	E_pol	E_dis	E_rep	E_tot
	1	-x, -y, -z	6.92	B3LYP/6-31G(d,p)	-340.1	-105.5	-31.2	128.9	-385.3
	2	x, y, z	6.98	B3LYP/6-31G(d,p)	-140	-47	-21	59.4	-164.3
	2	-x+1/2, y+1/2, z	5.48	B3LYP/6-31G(d,p)	-41.5	-63.3	-35.7	72.7	-76.8
	2	-x, y+1/2, -z+1/2	8.10	B3LYP/6-31G(d,p)	4.2	-1.2	-13.1	7.6	-3.2
	2	x+1/2, y, -z+1/2	8.67	B3LYP/6-31G(d,p)	8.3	-1.1	-8.2	7.2	5.3

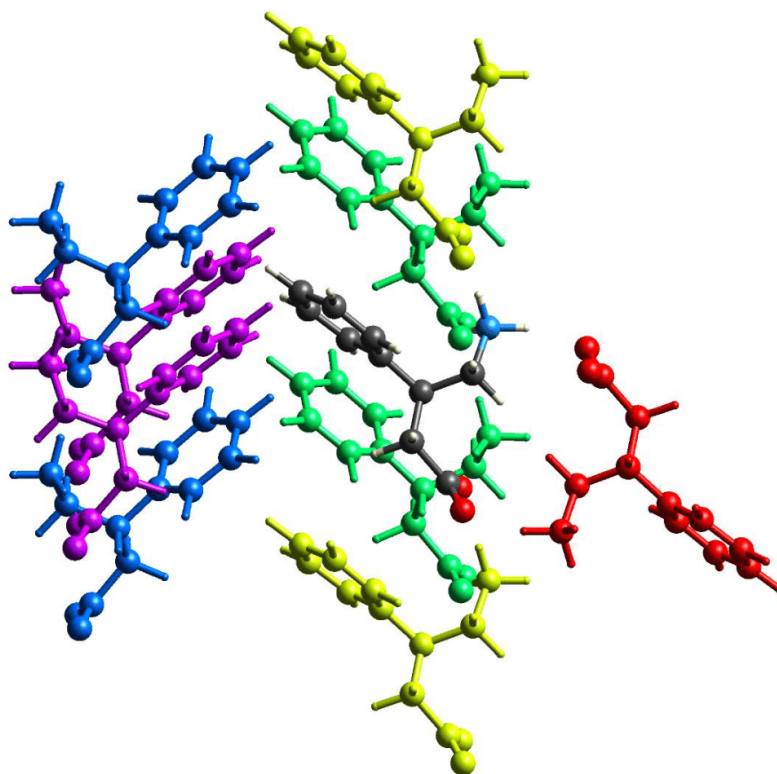


Figure S12. Bonding interactions of Phenibut molecules in Phenibut with direct interaction partners in the lattice. Colours indicate which values belong to which interaction partner.

Table S2. Direct interactions of Phenibut molecules in Phenibut-H₂O. Energy values in kJ mol⁻¹.

	N	Symop	R	Electron Density	E_ele	E_pol	E_dis	E_rep	E_tot
	2	-x+1/2, y, z+1/2	5.65	B3LYP/6-31G(d,p)	-45.3	-66.8	-34.5	71.6	-83.1
	2	x, y, z	7.14	B3LYP/6-31G(d,p)	-120.3	-42.3	-22.2	46.6	-149
	1	-	4.63	B3LYP/6-31G(d,p)	-58.9	-23.7	-8	53.2	-54
	1	-	6.46	B3LYP/6-31G(d,p)	-69.8	-21.5	-3.8	64.9	-53
	1	-	5.36	B3LYP/6-31G(d,p)	-72.1	-18.1	-5.1	53	-61.4
	2	-x, -y+1/2, z+1/2	7.79	B3LYP/6-31G(d,p)	5.2	-1.6	-13.8	9.4	-1.9

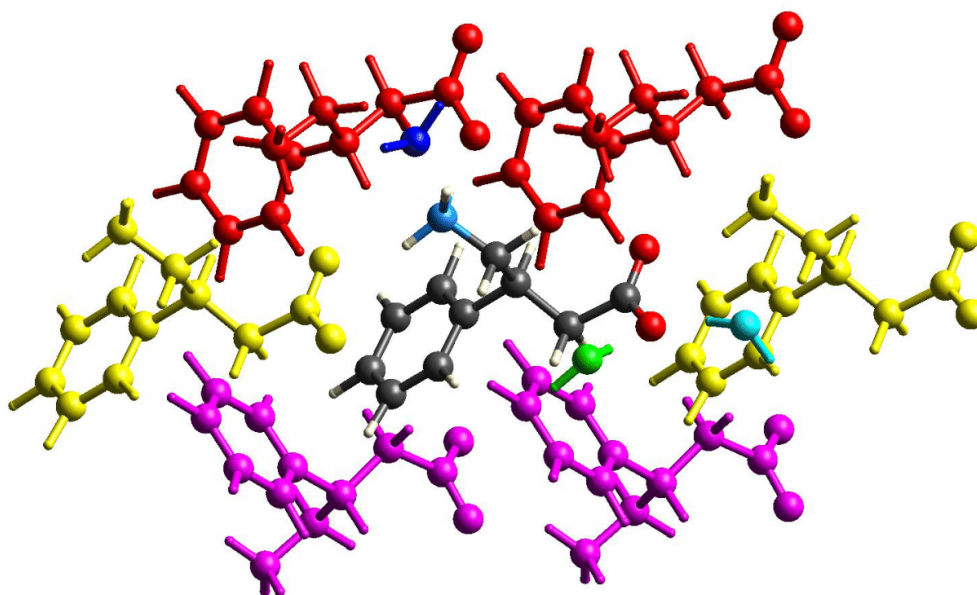


Figure S13. Bonding interactions of Phenibut molecules in Phenibut-H₂O with direct interaction partners in the lattice. Colours indicate which values belong to which interaction partner.

Table S3. Direct interactions of water molecules in Phenibut-H₂O. Energy values in kJ mol⁻¹.

	N	Symop	R	Electron Density	E_ele	E_pol	E_dis	E_rep	E_tot
	1	-	6.46	B3LYP/6-31G(d,p)	-69.8	-21.5	-3.8	64.9	-53
	1	-	4.63	B3LYP/6-31G(d,p)	-58.9	-23.7	-8	53.2	-54
	1	-	5.36	B3LYP/6-31G(d,p)	-72.1	-18.1	-5.1	53	-61.4

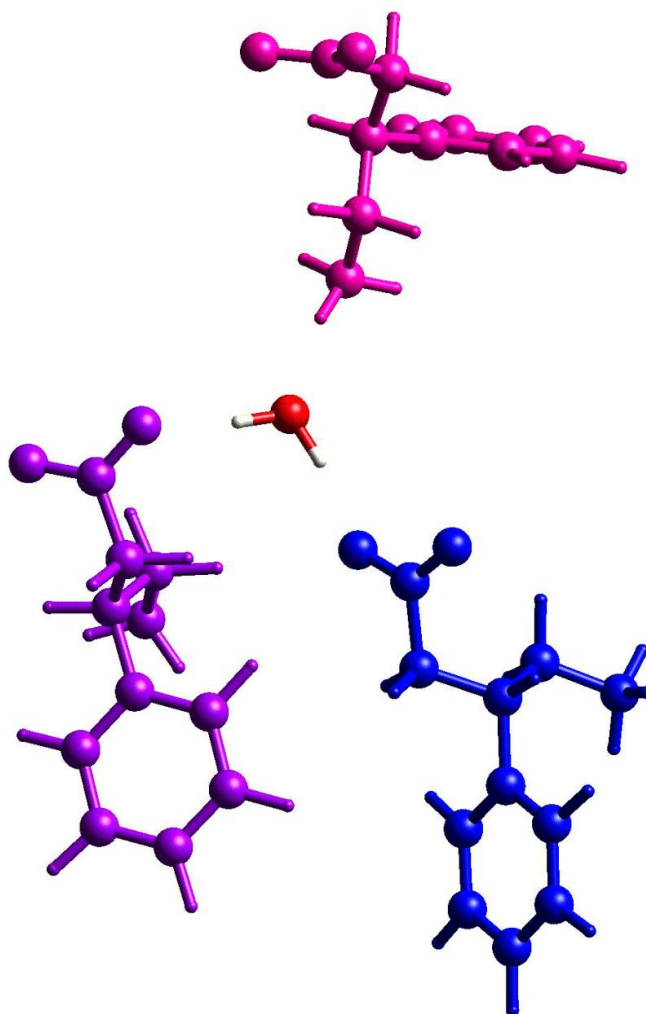


Figure S14. Bonding interactions of water molecules in Phenibut-H₂O with direct interaction partners in the lattice. Colours indicate which values belong to which interaction partner.

Table S3. Direct interactions of water molecules in Phenibut-H₂O. Energy values in kJ mol⁻¹.

	N	Symop	R	Electron Density	E_ele	E_pol	E_dis	E_rep	E_tot
	1	-	6.46	B3LYP/6-31G(d,p)	-69.8	-21.5	-3.8	64.9	-53
	1	-	4.63	B3LYP/6-31G(d,p)	-58.9	-23.7	-8	53.2	-54
	1	-	5.36	B3LYP/6-31G(d,p)	-72.1	-18.1	-5.1	53	-61.4

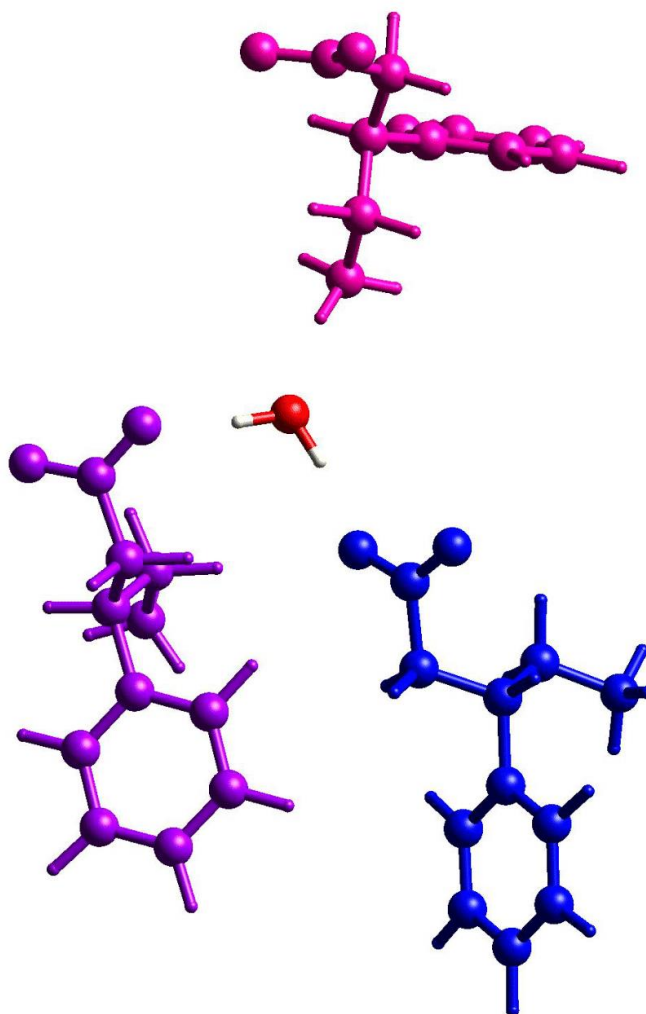


Figure S14. Bonding interactions of water molecules in Phenibut-H₂O with direct interaction partners in the lattice. Colours indicate which values belong to which interaction partner.

HB interactions

Table 4. HB interactions in Phenibut.

Donor-- H..Acceptor	D-H	H...A	D...A	D-H...A
N1--H6..O2	0.95(3)	1.84(3)	2.775(3)	172(3)
N1--H7..O1	1.13(3)	1.64(3)	2.732(3)	160(3)
N1--H8..O2	0.96(4)	1.84(4)	2.795(3)	173(2)

Table 5. HB interactions in Phenibut-H₂O

Donor-- H..Acceptor	D-H	H...A	D...A	D-H...A
N1--H6..O3	1.01(6)	1.78(6)	2.709(3)	151(6)
N1--H7..O1	0.97(4)	1.84(4)	2.788(3)	167(3)
N1--H8..O1	0.94(4)	1.94(4)	2.814(3)	154(3)
O3--H14..O2	0.78(4)	1.90(4)	2.672(3)	172(4)
O3--H15..O2	0.88(6)	1.87(6)	2.751(3)	174(5)

Table 6. HB interactions in Phenibut-HCl

Donor-- H..Acceptor	D-H	H...A	D...A	D-H...A
O1--H1..Cl1	0.87(3)	2.17(3)	3.0350(16)	174(2)
N1--H7..Cl1	0.93(3)	2.27(3)	3.163(2)	161.0(16)
N1--H8..O2	0.86(2)	2.46(2)	2.868(2)	109.9(16)
N1--H8..O2	0.86(2)	2.07(2)	2.860(2)	152.9(19)'
N1--H9..Cl1	0.94(2)	2.27(2)	3.1644(18)	158.7(17)
C7--H11..O1	0.96(3)	2.57(2)	3.331(3)	136.6(18)

3.2 A Lesson in Humbleness: Crystallization of Chiral and Zwitterionic APIs Baclofen and Phenibut



Article

A Lesson in Humbleness: Crystallization of Chiral and Zwitterionic APIs Baclofen and Phenibut

Marco Herbst [†], Daniel Komisarek [†], Till Strothmann and Vera Vasylyeva ^{*†}

Herbst, M. & Komisarek, D.; Strothmann, T.; Vasylyeva, V. A Lesson in Humbleness: Crystallization of Chiral and Zwitterionic APIs Baclofen and Phenibut, *Crystals*, **2022**, *12*, 1393.

DOI: 10.3390/cryst12101393

As per the *MDPI Open Access Information and Policy*, no special permission is required to reuse all or part of article published by MDPI, including figures and tables.


In the second publication, the synthesis of multicomponent systems of Baclofen and Phenibut with chiral malic- as well as tartaric acid was studied. Solution-based and mechanochemical crystallization methods were used and compared. Some single crystal structures of salts, hydrates and salt hydrates of these systems were obtained, and their thermal properties were characterized. The work illustrates how chiral information and the crystal synthesis method exert a complex influence on the crystallization behaviour of these materials and shows that even between molecularly very similar Baclofen and Phenibut, there may be major differences in the product obtained.

Contributions-list:

- Conceptualization of this work based on literature research and feedback from Dr. Vera Vasylyeva-Shor.
- Experimental work, including single crystal synthesis of the investigated compounds via solution or mechanochemically together with Marco Herbst.
- Measurement of SCXRD and PXRD, DSC, FT-IR spectroscopy, and sample preparation for the TGA together with Marco Herbst.
- Measurement of TGA Curves was conducted by Till Strothmann.
- Data evaluation of the recorded analyses.
- Manuscript preparation, including text writing, figure and table preparation and literature research.
- Supporting information was produced together with Marco Herbst.
- Revision process of the manuscript together with Dr. Vera Vasylyeva-Shor before and after Peer-Review process.

Article

A Lesson in Humbleness: Crystallization of Chiral and Zwitterionic APIs Baclofen and Phenibut

Marco Herbst [†], Daniel Komisarek [†], Till Strothmann and Vera Vasylyeva ^{*†} 

Molecular Crystal Engineering Group, Department of Inorganic and Structural Chemistry, Heinrich Heine University, 40225 Duesseldorf, Germany

* Correspondence: vera.vasylyeva-shor@hhu.de

[†] These authors contributed equally to this work.

Abstract: Crystallization and multicomponent crystal formation of active pharmaceutical ingredients Baclofen and Phenibut with dicarboxylic acid co-formers are discussed. The crystallization process of several crystalline entities is elucidated via single crystal—as well as powder X-ray—diffraction, followed by thermal analysis and phase stability studies over time. Both APIs form increasingly complex crystalline phases with co-formers malic and tartaric acid, where phase purity of a desired compound is not necessarily a given. Therefore, the influence of different solution and milling environments during crystallization on the outcome is studied. Emphasis is laid on how molecular influences such as the chirality, propensity to form hydrates as well as low solubility of Baclofen and Phenibut impede attempts to gather high-quality single crystals. The results highlight that targeted crystallization of these compounds with dicarboxylic acids can be difficult and unreliable.

Keywords: crystallization; chirality; GABA; zwitterions; milling



Citation: Herbst, M.; Komisarek, D.; Strothmann, T.; Vasylyeva, V. A Lesson in Humbleness: Crystallization of Chiral and Zwitterionic APIs Baclofen and Phenibut. *Crystals* **2022**, *12*, 1393. <https://doi.org/10.3390/cryst12101393>

Academic Editors: José Gavira, Fiora Artusio and Rafael Contreras-Montoya

Received: 25 August 2022
Accepted: 23 September 2022
Published: 1 October 2022

Publisher's Note: MDPI stays neutral with regard to jurisdictional claims in published maps and institutional affiliations.



Copyright: © 2022 by the authors. Licensee MDPI, Basel, Switzerland. This article is an open access article distributed under the terms and conditions of the Creative Commons Attribution (CC BY) license (<https://creativecommons.org/licenses/by/4.0/>).

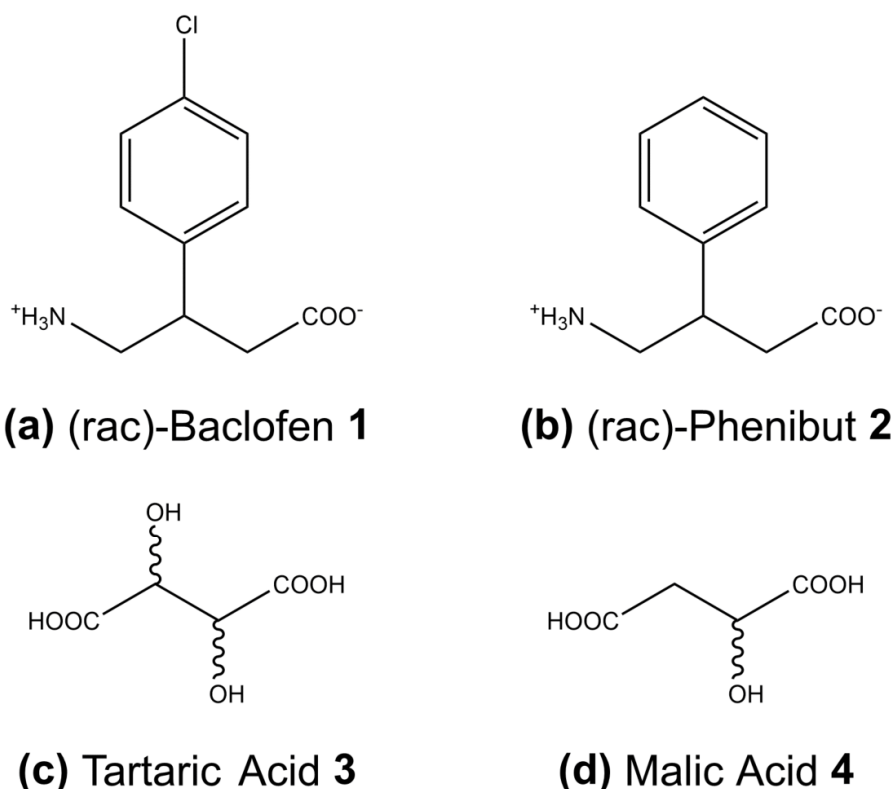
1. Introduction

Targeted synthesis of a desired crystalline modification remains a core objective in crystal engineering, and manifold approaches for various applications are continuously developed [1–4]. Occurrences of polymorphism, hydrate or solvate formation can hinder crystal synthesis of the wanted product, especially if said product is not the thermodynamically most stable variant [5–8]. The underlying challenge is a common tendency among many compounds—to crystallize in varying forms during all stages of the crystallization process. This empirical observation was first conducted by Wilhelm Ostwald in 1897 [9]. Presently, progress is made in understanding how crystal growth occurs from molecular to nanocluster stages [10–13] and how factors such as solvent medium, saturation, temperature or presence of ‘impurities’ impact the crystallization product [14–18]. The influence of molecular chirality on crystal formation, as well as methods to determine the chiral outcome of a crystallization batch, were recently enhanced [19–21]. This is especially important for the pharmaceutical industry, as eutomer, the product of desired chirality, and distomer, the by-product of undesired chirality, can vary widely in their effectiveness. Receiving active pharmaceutical ingredients (APIs) in their desired crystalline phase with the correct chirality must be accomplished to guarantee reliable product effectiveness and, therefore, marketability [6,8,22–24].

APIs Phenibut ((*RS*)-4-amino-3-phenylbutanoic acid) and Baclofen ((*RS*)-4-amino-3-(4-chloro-phenyl) butanoic acid) are structurally similar γ -amino butanoic acid (GABA) derivatives with a phenyl subunit on C3. Both pose a chiral center in that position, with the (*R*)-form being the eutomer [25–28]. The sole difference is a chloro-subunit on the phenyl-ring in Baclofen in the *p*-position in regard to the GABA chain. Baclofen is commonly used in the treatment of spastic diseases [29–31], but its potential in the treatment of alcohol addiction is an additional topic of interest [32–34]. Contrary to that, Phenibut is not actually approved for

medical use in the US, Europe or Australia but is classified as a dietary supplement, research chemical or new psychoactive substance [25,35–38]

Different attempts at multicomponent crystal formation on racemic Baclofen (**1**) and Phenibut (**2**) were conducted from solution with pure enantiomers and racemic mixtures of dicarboxylic acids tartaric acid (**3**) and malic acid (**4**) (Scheme 1). Since **1** and **2** show extremely poor solubility in almost every solvent except for water, limiting the choice of the solvent for the supramolecular synthesis and single crystals growth, a mechanochemical crystallization was performed as an alternative route to access the desired products. Various multicomponent species, including hydrates, salts and salt hydrates, were obtained, eight of which could be characterized via single crystal X-ray diffraction (SC-XRD). Powder X-ray diffraction (PXRD) shows how some of the obtained phases remain stable even after months while others undergo quick phase transitions. Furthermore, differential scanning calorimetry (DSC) investigations highlight that while a similar melting range is present in all compounds, multiple transitions can occur upon heating, and recrystallization by re-cooling can never be achieved. The present study aims to link these findings to molecular peculiarities in Baclofen and Phenibut, namely their chirality, zwitterionic charge status and phenyl-subunit. The latter distinguishes them from other GABA derivative APIs, such as Pregabalin and Gabapentin, with a comparatively reliable crystallization behavior [39,40]. By placing the herein investigated molecules in a larger context of other pharmaceutically active GABA derivatives, the massive influence of small molecular changes in otherwise similar entities is highlighted. Thus, the limits of relatively simple crystallization behavior predictions for these compounds are presented.



Scheme 1. Overview of the investigated APIs: (a) (rac)–Baclofen **1**, (b) (rac)–Phenibut **2** and co-formers (c) tartaric acid **3** and (d) malic acid **4**. The dicarboxylic acids were used as racemic mixtures and enantiomerically pure D– and L–forms.

2. Materials and Methods

2.1. Chemicals

Baclofen and hexafluoropropan-2-ol were purchased from flurochem. Phenibut was purchased from Combi-Blocks (San Diego, United States). Enantiopure tartaric acid was bought from J&K Scientific (Beijing, China). Racemic tartaric acid was purchased from Carl Roth (Karlsruhe, Germany), D-malic acid was purchased from BLD pharm (Shanghai, China) and L-malic acid was purchased from Glentham Life Science (Corsham, United Kingdom). All chemicals were used without further purification.

2.2. Sample Preparation

Single Crystals. Equimolar amounts of the APIs (0.5 mmol) and the chosen co-formers (0.5 mmol) were dissolved in water (all systems); additionally, water: ethyl acetate (1:14) mixture and hexafluoropropan-2-ol were used for Baclofen: malic acid systems. Single crystals suitable for SC-XRD were obtained by diffusion crystallization from aqueous solution using acetonitrile as an antisolvent for Phenibut hydrate and Baclofen hydrate as well as from hexafluoropropan-2-ol solution for Baclofen: malic acid hydrate. All other single crystals were obtained by slow evaporation of the solvent from aqueous solution at room temperature.

Powder samples. Crystalline powder samples were obtained from solution under the same conditions described before. Samples were vacuum dried in a Büchi 585 Drying vacuum oven at 100 °C and 10^{-1} bar for 2 h. Furthermore, liquid-assisted grinding (LAG) experiments were conducted using equimolar amounts of API (0.5 mmol) and co-former (0.5 mmol) with 10 μ L of methanol in a Retsch MM400 ball mill with 10 mL stainless steel containers and 2 ZrO₂ balls (diameter: 1 cm), milling for 30 min at 25 Hz.

2.3. Powder X-ray Diffraction (PXRD)

Powder patterns of the obtained samples were measured on a Rigaku Miniflex 300 using Cu K α radiation ($\lambda = 1.54182$ Å). The measurements were conducted at ambient temperature in $\theta/2\theta$ geometry between 5° and 50° with a runtime of ten minutes.

2.4. Single-Crystal X-ray Diffraction (SC-XRD)

Suitable crystals were carefully selected under a polarized-light microscope, covered in protective oil and mounted on a cryo-loop. Following that, crystals were selected for SC-XRD experiments: a needle-shaped colorless crystal of **1** • H₂O (size 0.87 • 0.06 • 0.05 mm); a plate-shaped colorless crystal of **2** • H₂O (size 0.11 • 0.09 • 0.03 mm); a plate-shaped colorless crystal of **1:L-3** • H₂O (size 0.18 • 0.06 • 0.05 mm); a block-shaped colorless crystal of **1:D-3** • H₂O (size 0.35 • 0.1 • 0.09 mm); plate-shaped colorless crystals of **1:DL-3** • H₂O (size 0.09 • 0.04 • 0.03 mm) and **1:D-4** • H₂O (size 0.16 • 0.07 • 0.06 mm); a block-shaped colorless crystal of **2:L-3** • H₂O (size 0.2 • 0.09 • 0.06 mm) and a plate-shaped colorless crystal of **2:DL-3** (size 0.16 • 0.06 • 0.05 mm). The single crystal diffraction data were collected using a Rigaku XtaLAB Synergy S Diffraction System (Malvern Panalytical, Malvern, United Kingdom) with a Hybrid Pixel Array Detector and a PhotonJet X-ray source for Cu-K α radiation ($\lambda = 1.54184$ Å), with a multilayer mirror monochromator at 100.0 ± 0.1 K using ω -scans. Data reduction and absorption correction were performed with CrysAlisPRO v. 42 (Oxford Diffraction / Agilent Technologies UK Ltd, Yarnton, England) software, using numerical absorption correction based on Gaussian integration over a multifaceted crystal model and empirical absorption correction using spherical harmonics, implemented in SCALE3 ABSPACK scaling algorithm [41]. Structure analysis and refinement: The structures were solved by direct methods (SHELXT-2015), full-matrix least-squares refinements on F₂ were executed using the SHELXL2017/1 program package [42,43]. Structure, as well as disorder solution and refinements were conducted using Olex2-1.5 (Olexsys, Durham, England) software [44]. Disorders are present in **1:D-4** • H₂O and **2:DL-3**. In the former, about two water molecules are disordered over three positions in canal voids (Occu. 0.75:0.64:0.58). Furthermore, malic acid's hydroxyl group O7-H27A and hydrogen H27B were half-occupied

due to an inversion center in the malic acid molecule. In the latter, the GABA subunit (C1, C2, C3) was disordered over two positions (Occu. 0.57:0.43). Hydrogen atoms were freely refined except C-H hydrogens in **1:L-3 • H₂O**, **1:DL-3 • H₂O**, **2:L-3 • H₂O**, **1:D-4 • H₂O** and **2:DL-3**. The rest electron density was found on the N- and O7-atoms, which correspond to hydrogen atoms. However, all attempts to refine these freely failed and led to a structure breakdown, probably due to the present disorder. Accordingly, N-H hydrogens, as well as the O7-H27A hydrogen in **1:D-4 • H₂O**, were also positioned geometrically. The following atomic displacement parameters were used: $U_{\text{iso}}(\text{H}_{\text{CH}}) = 1.2 U_{\text{eq}}$, and further for **1:D-4 • H₂O** $U_{\text{iso}}(\text{H}_{\text{NH}}) = 1.2 U_{\text{eq}}$ and $U_{\text{iso}}(\text{H}_{\text{OH}}) = 1.5 U_{\text{eq}}$. Overviews of the received crystallographic datasets are given in Tables 1–5. Graphics were prepared with the program Mercury [45]. The crystallographic data for the structures were deposited in the Cambridge Crystallographic Data Centre (CCDC-numbers 2201472-2201477) and can be obtained free of charge via: www.ccdc.cam.ac.uk/data_request/cif (access date: 1 August 2022).

Table 1. Crystallographic data obtained by SC-XRD measurements of **1 • H₂O** and **2 • H₂O**.

Parameters	1 • H₂O	2 • H₂O
Formula	C ₁₀ H ₁₂ ClNO ₂ , H ₂ O	C ₁₀ H ₁₃ NO ₂ , H ₂ O
Formula Weight [gmol ⁻¹]	231.67	197.23
T [K]	100	100
Crystal System	orthorhombic	orthorhombic
Space Group	Aea 2	Aea 2
a [Å]	9.5543 (2)	9.7521 (3)
b [Å]	32.6466 (6)	29.3294 (11)
c [Å]	7.1995 (1)	7.1397 (2)
β [°]	90	90
V [Å ³]	2245.64 (7)	2042.12 (11)
Z, Z'	8, 1	8, 1
R1, wR2 [%]	4.56, 12.11	4.42, 10.4
Hoof	0.003 (16)	−0.18 (16)
Source	Cu Kα (λ = 1.54184)	Cu Kα (λ = 1.54184)

Table 2. Overview of the received single crystalline forms. The depicted compounds containing Baclofen (1), Phenibut (2), tartaric acid (3) or malic acid (4) are sorted by their tendency to transit phases. Products in the left column remain stable only until dried. Products in the mid column remain stable for a longer time upon drying or show transition signals other than melting in the DSC. The product in the right column remains stable after six months under dry conditions and only shows a melting signal in the DSC. Additionally, space group information is given, and some important properties are described.

Quick Phase Transition ≤ 3 d	Phase Transition ≥ 3 d or in DSC	Remains Stable, DSC Melting Only
1 • H₂O , <i>Aea2</i> , only stable in mother liquid	1:D-3 • H₂O , <i>P1</i> , transition in about 1 week 1:L-3 • H₂O , <i>P1</i> , transition in about 1 week 1:DL-3 • H₂O , <i>P2₁/n</i> , DSC transition, no decomposition over time	2:DL-3 , <i>P1̄</i> , disorder along GABA subunit
2 • H₂O , <i>Aea2</i> , transition upon drying—slower than 1 • H₂O	1:D-4 • H₂O , <i>P1̄</i> , strongly disordered water molecules; no decomposition over time 2:L-3 • H₂O , <i>P2₁</i> , DSC transition, no decomposition over time	

Table 3. Crystallographic data obtained by SCXRD measurements of 1:L–3 • H₂O, 1:D–3 • H₂O and 1:DL–3 • H₂O.

Parameters	1:L–3 • H ₂ O	1:D–3 • H ₂ O	1:DL–3 • H ₂ O
Formula	C ₁₀ H ₁₃ ClNO ₂ , C ₄ H ₅ O ₆ , H ₂ O	C ₁₀ H ₁₃ ClNO ₂ , C ₄ H ₅ O ₆ , H ₂ O	(C ₁₀ H ₁₃ ClNO ₂) ₂ , C ₁₀ H ₁₂ ClNO ₂ , (C ₄ H ₅ O ₆) ₂ , (H ₂ O) ₃
Formula Weight [g mol ⁻¹]	381.76	381.76	995.19
T [K]	100	100	100
Crystal System	triclinic	triclinic	monoclinic
Space Group	P1	P1	P2 ₁ /n
a [Å]	7.3819 (1)	7.3781 (1)	19.2882 (4)
b [Å]	8.5625 (1)	8.5661 (1)	7.2929 (3)
c [Å]	13.8601 (2)	13.8636 (1)	32.3679 (10)
α [°]	75.551 (1)	75.546 (1)	90
β [°]	88.406 (1)	88.339 (1)	92.378 (2)
γ [°]	89.616 (1)	89.529 (19)	90
V [Å ³]	848.02 (2)	848.111 (17)	4549.2 (3)
Z, Z'	2, 2	2, 2	4, 1
R1, wR2 [%]	2.56, 6.50	2.76, 7.26	6.56, 18.38
Hooft	−0.003 (6)	−0.003 (7)	−
Source	Cu Kα (λ = 1.54184)	Cu Kα (λ = 1.54184)	Cu Kα (λ = 1.54184)

Table 4. Crystallographic data obtained by SCXRD measurements of 1:D–4 • H₂O.

Parameters	1:D–4 • H ₂ O
Formula	C ₁₀ H ₁₂ ClNO ₂ , C ₁₀ H ₁₃ ClNO ₂ , (C ₁₀ H ₁₃ ClNO ₂) _{0.5} , (H ₂ O) ₂
Formula Weight [g mol ⁻¹]	1051.91
T [K]	100
Crystal System	triclinic
Space Group	P $\bar{1}$
a [Å]	6.1571 (1)
b [Å]	11.8661 (2)
c [Å]	17.6166 (5)
α [°]	77.292 (2)
β [°]	82.763 (2)
γ [°]	76.139 (2)
V [Å ³]	1215.34 (5)
Z, Z'	4, 2
R1, wR2 [%]	8.31, 21.28
Hooft	−
Source	Cu Kα (λ = 1.54184)

Table 5. Crystallographic data obtained by SCXRD measurements of 2:L–3 • H₂O and 2:DL–3.

Parameters	2:L–3 • H ₂ O	2:DL–3
Formula	(C ₁₀ H ₁₄ NO ₂) ₃ , (C ₄ H ₅ O ₆) ₃ , H ₂ O	C ₁₀ H ₁₄ NO ₂ , C ₄ H ₅ O ₆
Formula Weight [g mol ⁻¹]	1023.93	329.20
T [K]	100	100
Crystal System	monoclinic	triclinic
Space Group	P2 ₁	P $\bar{1}$
a [Å]	7.4642 (2)	7.2070 (0)
b [Å]	20.0354 (6)	8.2646 (0)
c [Å]	15.8509 (5)	13.2223 (3)

Table 5. Cont.

Parameters	2:L-3 • H ₂ O	2:DL-3
α [°]	90	93.570 (2)
β [°]	100.400 (3)	103.006 (2)
γ [°]	90	97.319 (2)
V [Å ³]	2331.53 (12)	757.73 (2)
Z, Z'	2, 1	2, 1
R1, wR2 [%]	5.89, 13.85	5.01, 12.72
Hooft	0.1 (2)	-
Source	Cu K α (λ = 1.54184)	Cu K α (λ = 1.54184)

2.5. Thermal Analysis

Differential Scanning Calorimetry (DSC) measurements were conducted on a Linkam THMS 600 DSC with a heating rate of 5 °C/min. Additionally, thermogravimetric analysis (TGA) was executed on a Netzsch TG 209 F3 Tarsus in the range from 30 °C to 350 °C with a heating rate of 5 K min⁻¹ under a nitrogen atmosphere. Selected TG curves are presented in the Supplementary Materials.

2.6. IR-Spectra

IR spectra were recorded on a Bruker Tensor 27 FTIR device in attenuated total reflectance mode in the range 4000 cm⁻¹ to 400 cm⁻¹. Spectra are presented in the Supplementary Materials.

3. Results

3.1. Overview of All Received Single Crystals and Pure Hydrates of Baclofen and Phenibut

Indications for a plethora of different phases could be received through solution and milling experiments via PXRD. However, single crystals could be obtained for eight phases, most of which are hydrates (Table 2). This highlights the first encountered problem—nearly all described compounds undergo one or even multiple phase transitions upon crystallization and nearly always involve a hydrate stage. At this stage, single crystals suitable for SC-XRD can sometimes be received from solution.

A commonality in both APIs is the formation of a monohydrate with the same *Aea*2 space group, very similar structural makeup and in both cases, **1** and **2** retain their zwitterionic molecular state. In **1** • H₂O and **2** • H₂O, rows of **1** or **2** molecules connect through hydrogen bonds (HBs) on their GABA subunits and via edge-to-face π -interactions on their phenyl residues. These rows are further interconnected by HB involving water molecules (Figure 1). Both hydrates decompose in a quick time frame, with **1** • H₂O faster than **2** • H₂O, the latter of which could be observed remarkably often. It is notable that they were obtained during attempts to receive multicomponent crystalline compounds, with three or four dissolved species present in the mother liquid. If these samples were left to dry out completely, powdery multicomponent compounds could indeed be obtained as determined via PXRD. This implies that the hydrates form prior to more complex crystalline entities. In the context of GABA derivatives as APIs, it is interesting to mention that similar hydrate formations can be observed in Gabapentin as well as racemic Pregabalin [46–49]. However, contrary to the herein-described hydrates of **1** and **2**, these hydrates remain stable for a long time, even under dry conditions. Diffraction quality single crystals of **1** • H₂O and **2** • H₂O can reliably be grown from an aqueous solution with diffusion techniques, using acetonitrile as an antisolvent.

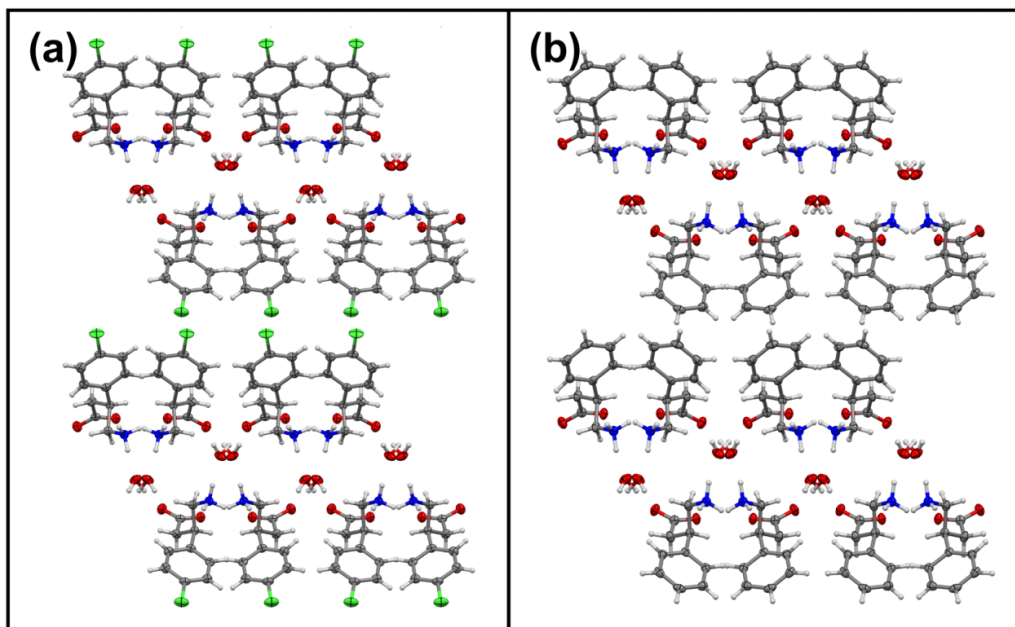


Figure 1. Structure comparison of (a) Baclofen • H₂O and (b) Phenibut • H₂O (re-determined—see Komisarek et al., 2021) [26], view along c-axis. Both compounds are commonly occurring intermediates during attempted crystallizations. Carbon atoms are depicted in grey, hydrogen atoms are depicted in white, oxygen atoms are depicted in red, nitrogen atoms are depicted in blue and chlorine atoms are depicted in green.

3.2. Baclofen and Tartaric Acid Species

Baclofen and tartaric acid were crystallized in equimolar ratios either through slow evaporation from aqueous solution or by methanol-assisted milling crystallization. By crystallization of **1** and **D**– or **L**–**3** from aqueous solution, isostructural salt hydrates in the non-centrosymmetric space group P1 are formed. Here, tartaric acid protonates the former carboxylate group in **1**'s GABA subunit, leading to formal charges on co-formers **1** and **3**. Water molecule positions in the lattice are well defined, such as in the described hydrates of pure **1** and **2** forms, yet a decomposition of these multicomponent species occurs later, after about one week. This stands in opposition to the **1:DL-3 • H₂O** system, which was likewise received by slow evaporation from aqueous solution. In this system, one **1** molecule with zwitterionic charges, as well as two further protonated **1** molecules, interact with two singly deprotonated **3** molecules and three hydrate water molecules. Even though this structure appears more complicated by the number of differently charged molecules in its asymmetric unit, it remains stable after six months under dry conditions. Crystal packings of the discussed **1:3** forms are depicted in Figure 2.

Evidence for additional species was obtained via PXRD. A possibly anhydrous phase of **1:D-3** or **1:L-3** can be observed by comparison of recorded patterns to the simulated pattern from single crystal data (Figure 3).

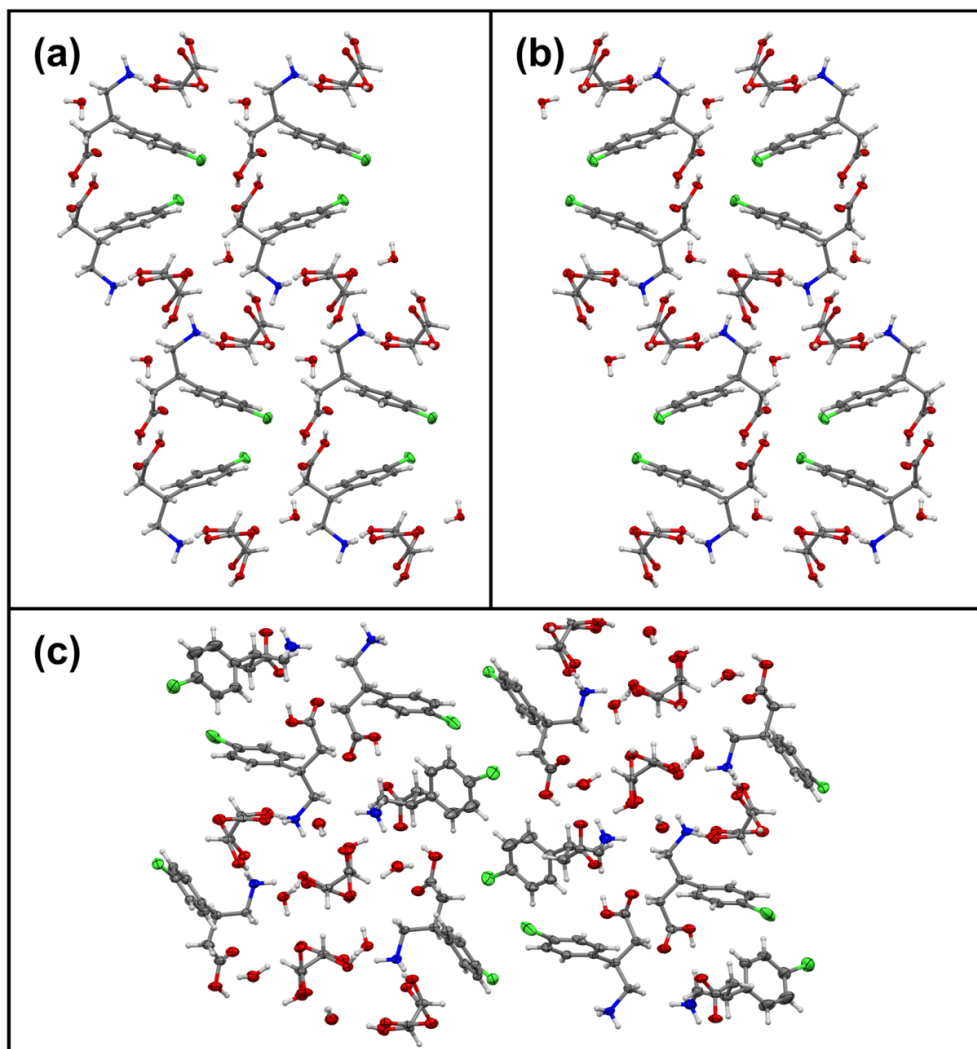


Figure 2. Structure comparison of (a) Baclofen:L-tartaric acid • H₂O (view along a-axis), (b) Baclofen:D-tartaric acid • H₂O (view along a-axis) and (c) Baclofen:DL-tartaric acid • H₂O (view along b-axis). While compounds (a) and (b) behave like mirror images and are composed of hydrate water, single-charged Baclofen and tartaric acid molecules, compound (c) contains additional zwitterionic Baclofen entities. Carbon atoms are depicted in grey, hydrogen atoms are white, oxygen atoms are red, nitrogen atoms are blue and chlorine atoms are green.

A careful comparison of the received patterns shows that complete phase purity for the enantiomerically pure 1:3 systems cannot be achieved in any case. While the fresh sample is still in good agreement with the simulated pattern, traces of a new phase are already visible between 10° and 15° 2 θ , in the small Bragg reflections between 16° and 18° 2 θ as well as at about 25° 2 θ . Patterns recorded after three months shared a good agreement with the presented milling or DSC patterns (see the Supplementary Materials). The possibly anhydrous phase was mostly distinguishable from the SC-XRD-characterized hydrate by its additional small reflections towards low angles at about 5° 2 θ and the prevalent occurrence of reflections between 23° and 26° 2 θ , especially well visible in the pattern recorded after

DSC heating as well as the one from vacuum dried substance. It is notable that even the milling pattern seems to retain characteristics of the hydrate form, visible through the absence of the described signals at lower angles. This highlights how energetically beneficial the hydrate stage for the described systems as an intermediate must be, as trace amounts of water in the methanol or adsorbed water from the milling vessel walls have sufficed to enable its formation. Concerning the racemic **3** forms, aging does not affect the **1:DL-3** hydrate received from solution, which is in opposition to its chiral **3** counterparts. The milling sample shows the most outstanding behavior in comparison to the other received patterns. It seems to be a mixture of **1:DL-3** hydrate and its presumably anhydrous form, possibly including hydrated or anhydrous enantiomerically pure **1:3** forms. This suggests that the formation of anhydrous **1:DL-3** is unfavorable and could explain how next to the hydrated **1:DL-3** system, enantiomerically pure **1:3** entities are formed during milling. Anhydrous **1:DL-3** is probably the most visible in the **1:DL-3** sample recorded after DSC heating. Even though the vacuum-dried sample shows three well-resolved reflections at $4.8\text{--}5.4^\circ 2\theta$, it still retains more similarity to the simulated hydrate pattern than the DSC sample. Furthermore, it does not offer higher overall crystallinity, suggesting that drying does not work as well here as in **1:3** forms with pure **3** enantiomers. Additional comparisons involving all received phases are shown in the Supplementary Materials. To rule out any further phases, DSC data were recorded from a sample obtained from solution as well as through milling (Figure 4).

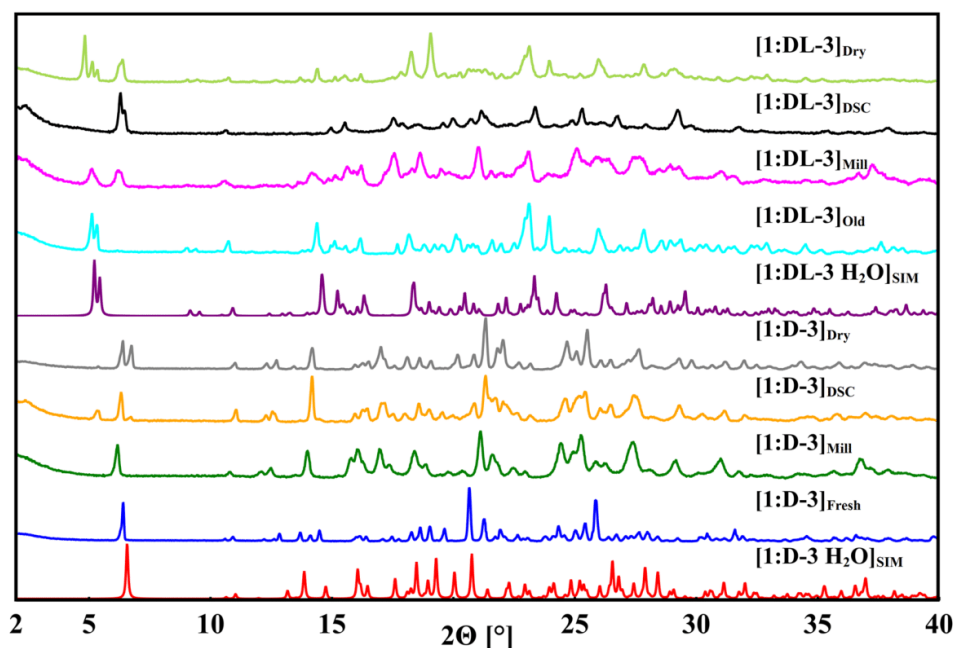


Figure 3. PXRDs of Baclofen:tartaric acid systems under different conditions in a range $2\text{--}40^\circ 2\theta$. Simulated pattern of **1:D-3 • H₂O** from single crystal data (red); recorded pattern from (blue) a fresh sample of said substance shortly after crystallization; LAG sample of Baclofen and D-tartaric acid (dark green); heating a fresh sample of **1:D-3 • H₂O** in a DSC chamber to 140°C and subsequent cooling prior to melting (orange); a vacuum dried sample of **1:D-3 • H₂O** (grey). Simulated pattern of Baclofen:DL-tartaric acid hydrate from single crystal data. (cyan) **1:DL-3 • H₂O** after six months at ambient conditions (purple); after LAG crystallization of Baclofen and DL-tartaric acid (magenta); after heating a fresh sample in a DSC chamber to 135°C and subsequent cooling prior to melting (black) and a vacuum dried sample of **1:DL-3 • H₂O** (light green).

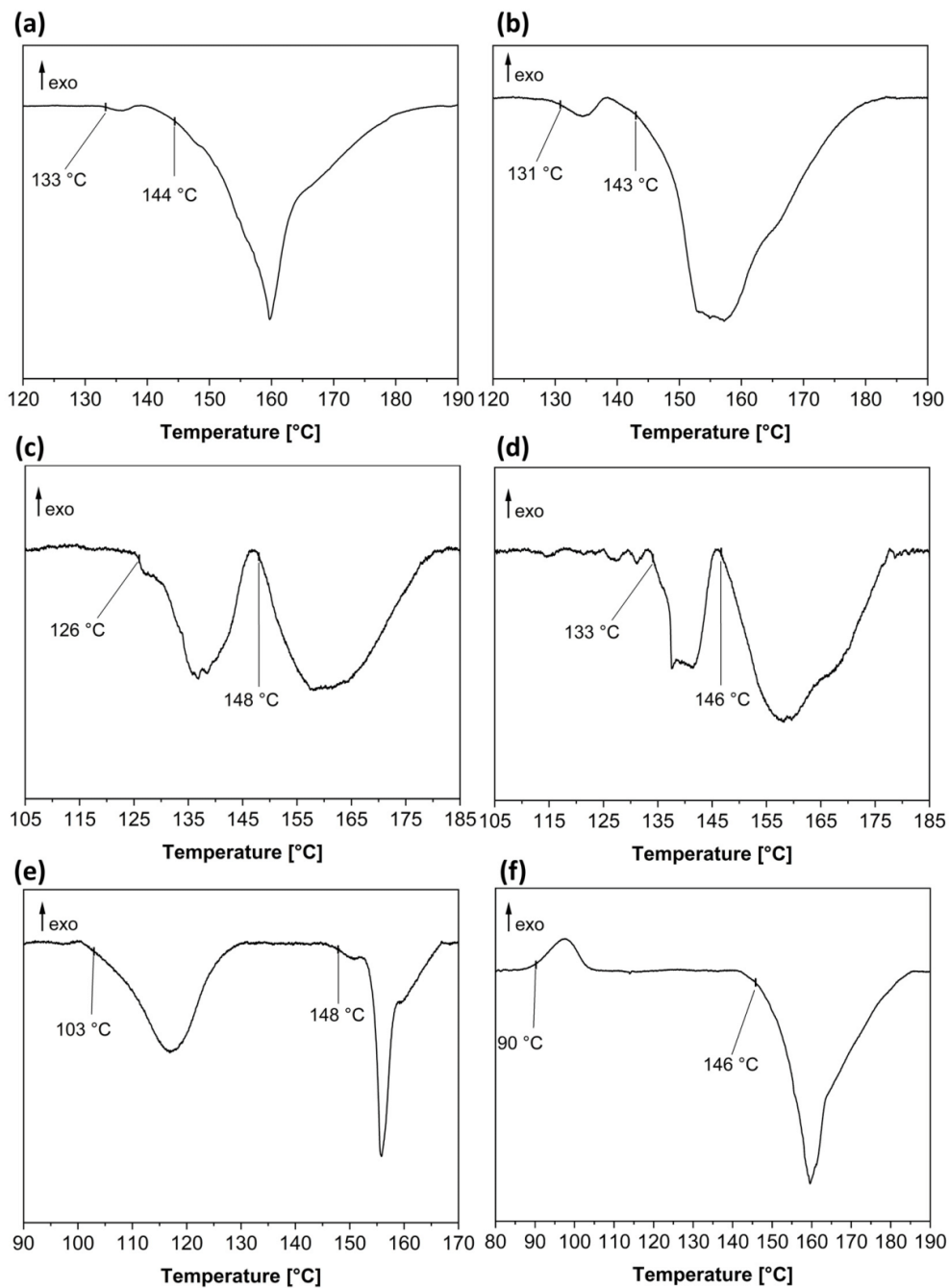


Figure 4. DSC data of the samples grown from aqueous solution. (a) Baclofen:D-tartaric acid hydrate, (b) Baclofen:L-tartaric acid hydrate, (e) Baclofen:DL-tartaric acid hydrate and samples obtained by milling, (c) Baclofen:D-tartaric acid, (d) Baclofen:L-tartaric acid, and (f) Baclofen:DL-tartaric acid. DSC was heated at $5\text{ }^{\circ}\text{C min}^{-1}$; for clarity, only a temperature range of $70\text{ }^{\circ}\text{C}$ (a,b,e), $80\text{ }^{\circ}\text{C}$ (c,d), and $110\text{ }^{\circ}\text{C}$ (f) is shown.

The DSC data suggest that higher quality samples are obtained from aqueous solution compared to LAG experiments in the case of enantiomerically pure **3** entities. The presented signals for samples grown from solution show a better signal-to-noise ratio than those which were obtained by milling. Furthermore, the melting signal is more intense than the signal for the presumed loss of hydrate water. This is not the case in the milling samples, suggesting the presence of a larger amorphous amount of substance. The hydrate water is removed at a comparatively high temperature of 130 °C. This indicates that water molecules are bound strongly into the **1:D-3** (or **1:L-3**) hydrate lattice. Low binding force to hydrate water molecules thus is probably not the reason for the phase transition. Rather than that, the anhydrous lattice is overall energetically more beneficial compared to the hydrate form. Melting of the anhydrous form occurs about 15 °C after the hydrate water loss, between 143 °C and 148 °C. In the **1:DL-3** hydrate grown from an aqueous solution, on the other hand, the presumed loss of hydrate water begins at lower temperatures of 103 °C. However, the anhydrous **1:DL-3** system remains stable for approximately just as long as the **1:3** forms of the determined chirality, resulting in a well-defined melting signal at 148 °C. Interestingly, if **1:DL-3** is produced through milling, an exothermic signal can be observed starting at 90 °C. This indicates further crystallization of amorphous material upon heating. If a powder pattern is recorded after the heating process, but prior to melting, an increase in crystallinity by better resolution of signals can indeed be observed (see the Supplementary Materials). Furthermore, signals corresponding to the **1:DL-3** hydrate are removed from the pattern. However, it still appears to be better to start from a solvent-based sample to receive an anhydrous **1:DL-3** form, indicated through a well-resolved powder pattern and a sharper melting signal.

Baclofen:tartaric acid species, including single crystals, can best be produced from aqueous solution, even though hydrates are formed in the first place. In the case of **1:3** species with enantiopure **3** co-formers, aging of the received hydrate will take place over time. Heating or vacuum drying of the described species should remove hydrate water quicker and help obtain a pure phase. Grinding leads to a product of lower crystallinity, especially visible through the badly resolved DSC data. If **DL-3** is used as a co-former, the hydrate form remains stable for a longer time, but water molecules can also be removed through heating. Milling experiments lead to low crystallinity and phase mixtures in the first step. Subsequent heating interestingly leads to a similar product as the drying of a hydrate product. The described hydrates can be received reliably from aqueous solution, even though they do not remain stable for long. Milling under the exclusion of water and vacuum drying, however, can reliably produce the presumed anhydrous forms.

3.3. Baclofen and Malic Acid Species

Similar experiments with Baclofen and tartaric acid were conducted with Baclofen and malic acid. Equimolar amounts of **1** and **4** were either crystallized by methanol-assisted grinding or from solution. Solution-based crystallization attempts involved solvent water, hexafluoro-2-propanol and ethyl acetate. Through the crystallization of **1** and **D-4** from hexafluoro-2-propanol solution, the **1:D-4** monohydrate with the centrosymmetric space group $P\bar{1}$ was synthesized. Interestingly, while it was actually attempted to reproduce the anhydrous $P2_1$ **1:4** form first described by Córdov-Villanueva et al. in 2018 [50], residual water in the hexafluoro-2-propanol seems to have favored the described hydrate formation. It should be noted that the same experiment with dried hexafluoro-2-propanol could not be performed because of the complete insolubility of **1** in the absence of water. A pure **1:D-4** • H_2O form was not reproducible, neither as a single crystal nor as a crystalline powder. This species contains strongly disordered water molecules in opposition to the previously discussed compounds. An additional oddity is the changing orientation of the **D-4** molecule in the lattice, which is captured by the half occupation of either a hydroxy- or hydrogen subunit on C22 in **D-4**. This variation of the alignment in the **1:D-4** lattice enables the formation of a centrosymmetric space group despite decisive chiral information on a molecular level. Rows of **1** molecules, where default zwitterionic and singly protonated

ones alternate, are connected through HBs on their GABA subunits over deprotonated D-4 species. Canal voids are formed by two D-4 entities and four 1 units filled with disordered water molecules. Towards the chlorophenyl subunits, 1 molecules are stacked offset in regard to each other. Positioning and distance between phenyl-centers-of-gravity and edges or between chlorine atoms makes π -interactions or halogen bonds unlikely. It is more probable that dispersive forces stabilize the structure in that direction (Figure 5).

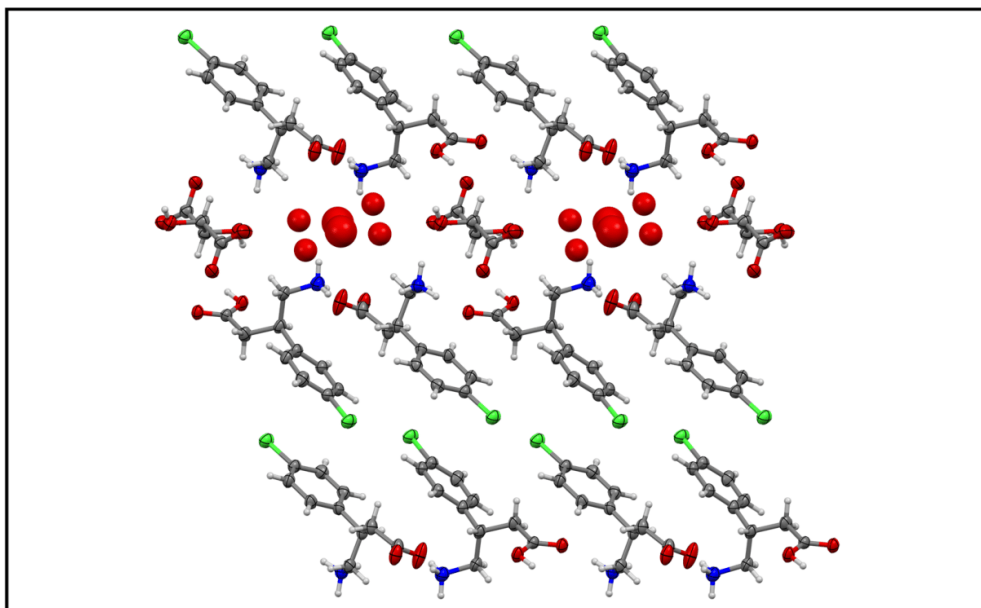


Figure 5. Crystal packing of Baclofen: D-malic acid • H₂O; view from a-axis. Strongly disordered water molecules accumulate in the pores between Baclofen and malic acid entities. Both malic acid molecules are half occupied and invert their alignment at each position. Carbon atoms are depicted in grey, hydrogen atoms are white, oxygen atoms are red, nitrogen atoms are blue and chlorine atoms are green.

The $P2_1$ form already published by Córdova-Villanueva et al. [50] could be obtained from purely aqueous solution in two cases, but more reliably via milling. Next to the described hydrate and previously published anhydrous form, a plethora of different mixtures was obtained, especially from solution and seemingly independent of the chosen conditions. Given the results of numerous experiments, authors are not comfortable in proposing a definitive answer to what phase can be safely obtained under which solvent conditions. However, the received results seem to confirm Córdova-Villanueva et al. in that milling leads to a clean formation of the anhydrous form. Furthermore, the racemic form of **4** does not appear to crystallize in an independent manner compared to enantiomerically pure co-formers. A selection of pure phase powder patterns received under various conditions is presented in Figure 6. Data recordings of some chosen phase mixtures are shown in the Supplementary Materials.

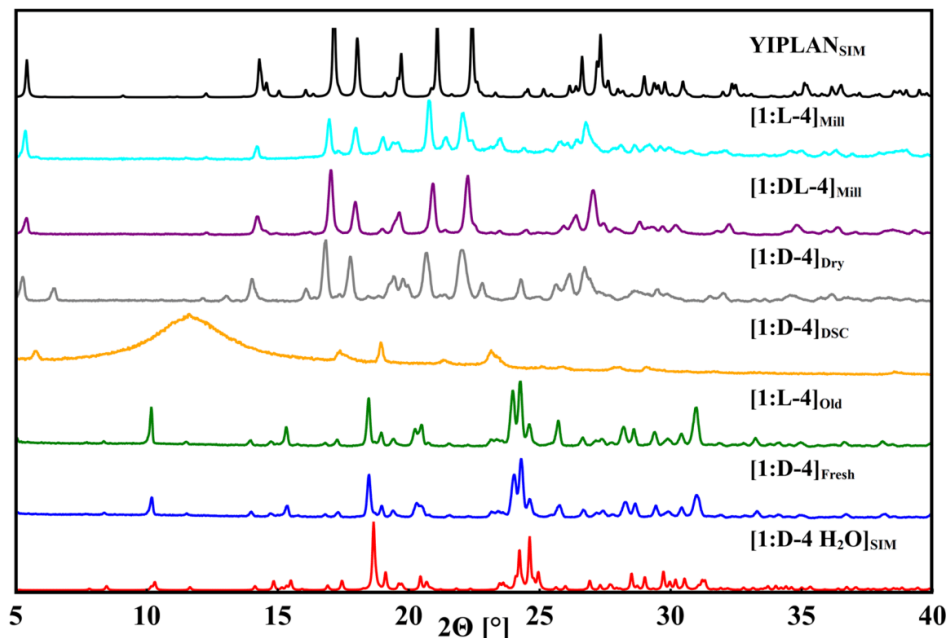


Figure 6. PXRDs of different Baclufen:malic acid systems obtained as pure phases at least once: freshly synthesized sample of **1:D-4 • H₂O** (blue) and a six months old sample of **1:L-4 • H₂O** (green), both obtained from hexafluoro-2-propanol solution contaminated with water; **1:D-4 • H₂O** sample after heating to 140 °C (orange) or vacuum drying (grey); samples of **1:DL-4 • H₂O** (purple) and **1:L-4 • H₂O** (cyan) after methanol-assisted grinding. Simulated patterns of obtained **1:D-4 • H₂O** (red) and previously reported by Córdova-Villanueva et al. [50] (Crystal Structure Database, Ref. Code YIPLAN) (black) are shown for comparison.

While the shown patterns might suggest easily obtainable clean phases, it should again be emphasized that **1:4** hydrates in the shown purity were only received once during the conducted experiments. The hydrate could not be obtained with **DL-4**. It remains stable over time but decomposes to a mixture of amorphous substance and pure **1** near its melting point in the DSC (Figure 7, see the Supplementary Materials for PXRD comparisons regarding DSC products). Milling experiments, on the other hand, led to a relatively reliable formation of the anhydrous form. Even though the shown pattern of vacuum drying suggests that this method works just as well as milling, similar results could not be obtained for any other attempts at vacuum drying (see the Supplementary Materials). It is notable that higher crystallinity seems to be present when using **DL-4**, as compared to enantiomerically pure **4** co-formers, and some slight changes are visible in the pattern. For example, an additional small Bragg reflection is present in **1:L-4** between the two high-intensity reflections at 17° and 18° 2θ, respectively. Furthermore, the whole pattern appears to be shifted slightly towards lower diffraction angles. Similar observations were described by Córdova-Villanueva and colleagues [50]. They theorize the existence of an additional phase, backed by infrared spectroscopy data. We, however, suggest that the visible behavior might be explainable by considerations of chirality. Contrary to the **1:4** hydrate, the anhydrous form crystallizes in the non-centrosymmetric space group *P2₁* and poses a definitive chirality on **1** as well as **4**. Therefore, two isostructural phases are actually formed **R-1:L-4** and **S-1:D-4**. This is not possible if only **L-4** or **D-4** are present during the experiment, which might lead to a larger amorphous amount in the received product or, as proposed by Córdova-Villanueva et al., another crystalline system. Chirality might also explain why a pure phase is hard to obtain from solution. As

previously mentioned, the hydrate crystallizes in the centrosymmetric space group $P\bar{1}$, even though chiral information is present on co-former **4**. Yet, by forcing a disorder that accounts for the chiral directionality, this chiral influence is canceled out. Thus, the hydrate can be formed from solution, which lessens the amount of available **4** molecules for the anhydrous **1:4** formation, and as the powder recordings show, the hydrate of **1:4** remains stable over time, thereby not releasing the necessary molecules back. Furthermore, **1** tends to form its own hydrate, which can often be observed in the received solution crystallization products (see the Supplementary Materials).

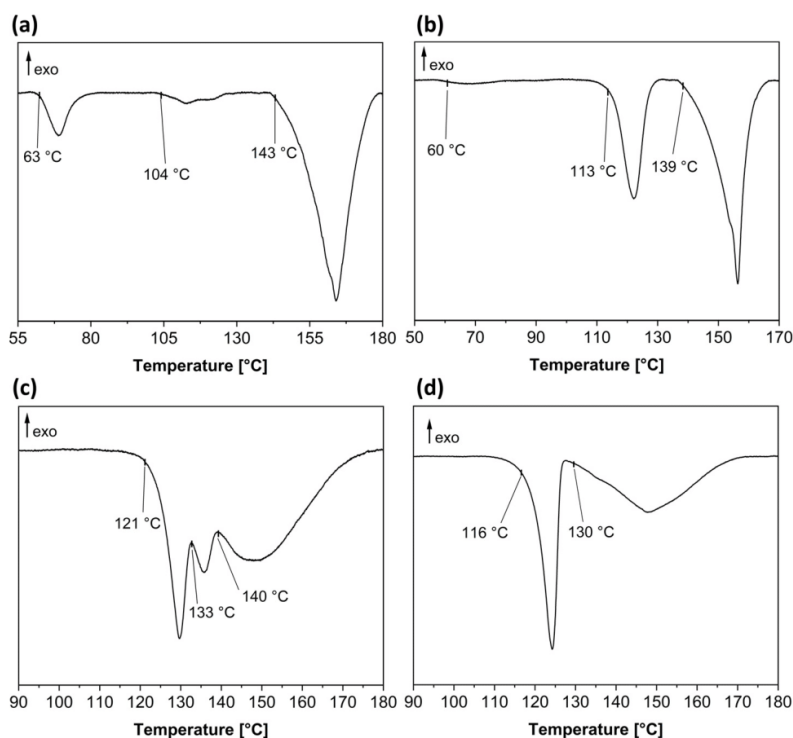


Figure 7. DSC data of **1:D-4 • H₂O** (a) and **1:L-4 • H₂O** (b) samples grown from aqueous hexafluoropropan-2-ol solution; **1:D-4** (c) and **1:DL-4** (d) samples produced by milling. DSC was heated at 5 °C min⁻¹; only important temperature ranges are shown for clarity.

DSC recordings highlight that the composition of the received products must differ. The **1:4** hydrates presented in Figure 7a,b show varying intensities and slight temperature shifts for the presumed same transitions at about 60 °C, as well as 104 °C and 113 °C. Furthermore, the melting signal at 143 °C and 139 °C is irregularly resolved in a comparable manner to the melting signals of the Baclofen:tartaric acid species. As the respective powder patterns show no evidence for impurities of a crystalline nature, possible amorphous substance or varying degrees of incorporated hydrate water might explain this behavior. As was shown, contrary to **1:3** hydrates, water molecules are not incorporated in a fixed network but rather occur as filling in present voids in **1:4** hydrates. If the powder pattern of a sample heated in a DSC-oven up to 140 °C is used for comparison, a phase mixture still remains. This could explain the uneven distribution of signals and the wide range of melting signals. Thermograms in Figure 7c,d show better-resolved phase transitions, and the melting signals for **1:D-4** and **1:L-4** are at the same position (Comparison shown in the Supplementary Materials). However, the received DSC data seem to confirm the theory regarding another phase, as assumed by Córdova-Villanueva and colleagues. **1:DL-4** melts at 116 °C, which is 5 °C prior to the **1:D-4** or **1:L-4** phases. Furthermore, the latter show

previously mentioned, the hydrate crystallizes in the centrosymmetric space group $P\bar{1}$, even though chiral information is present on co-former **4**. Yet, by forcing a disorder that accounts for the chiral directionality, this chiral influence is canceled out. Thus, the hydrate can be formed from solution, which lessens the amount of available **4** molecules for the anhydrous **1:4** formation, and as the powder recordings show, the hydrate of **1:4** remains stable over time, thereby not releasing the necessary molecules back. Furthermore, **1** tends to form its own hydrate, which can often be observed in the received solution crystallization products (see the Supplementary Materials).

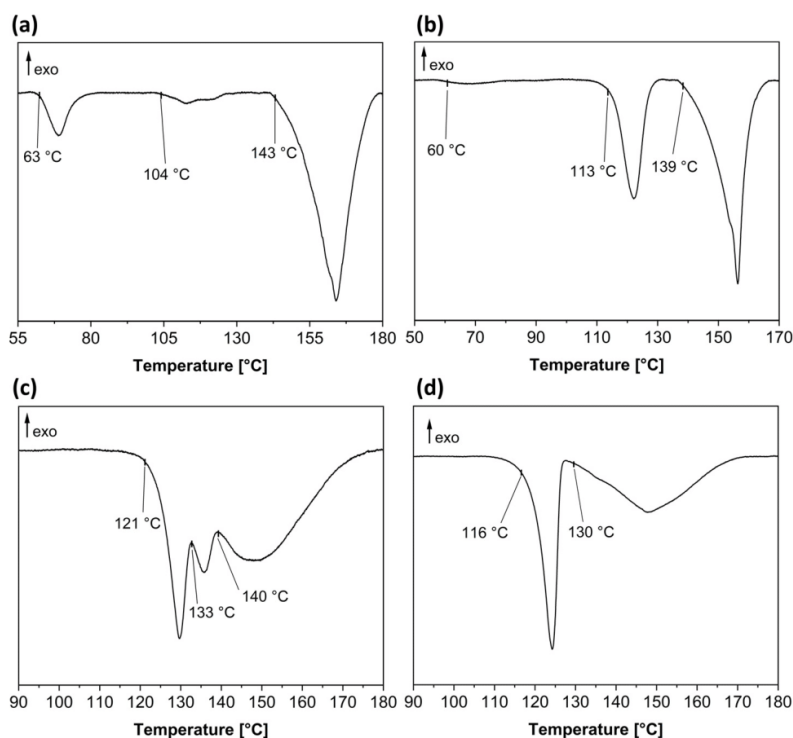


Figure 7. DSC data of **1:D-4 • H₂O** (a) and **1:L-4 • H₂O** (b) samples grown from aqueous hexafluoropropan-2-ol solution; **1:D-4** (c) and **1:DL-4** (d) samples produced by milling. DSC was heated at 5 °C min⁻¹; only important temperature ranges are shown for clarity.

DSC recordings highlight that the composition of the received products must differ. The **1:4** hydrates presented in Figure 7a,b show varying intensities and slight temperature shifts for the presumed same transitions at about 60 °C, as well as 104 °C and 113 °C. Furthermore, the melting signal at 143 °C and 139 °C is irregularly resolved in a comparable manner to the melting signals of the Baclofen:tartaric acid species. As the respective powder patterns show no evidence for impurities of a crystalline nature, possible amorphous substance or varying degrees of incorporated hydrate water might explain this behavior. As was shown, contrary to **1:3** hydrates, water molecules are not incorporated in a fixed network but rather occur as filling in present voids in **1:4** hydrates. If the powder pattern of a sample heated in a DSC-oven up to 140 °C is used for comparison, a phase mixture still remains. This could explain the uneven distribution of signals and the wide range of melting signals. Thermograms in Figure 7c,d show better-resolved phase transitions, and the melting signals for **1:D-4** and **1:L-4** are at the same position (Comparison shown in the Supplementary Materials). However, the received DSC data seem to confirm the theory regarding another phase, as assumed by Córdova-Villanueva and colleagues. **1:DL-4** melts at 116 °C, which is 5 °C prior to the **1:D-4** or **1:L-4** phases. Furthermore, the latter show

an additional signal between the melting signal and the broad, less intense signal at higher temperatures. No powder patterns could be recorded for samples at this point as only a goeey substance was received, but the presence of crystallites of a different phase might be presumed.

Contrary to Baclofen:tartaric acid species, Baclofen:malic acid forms can best be produced using mechanochemical means. However, co-former chirality seems to play a decisive role in the accessibility of exact phases, as shown through PXRD recordings and thermal analysis. The phase with the highest purity is obtained if both **1** and **4** are of a racemic nature. Interestingly, anhydrous phases can possibly be obtained by vacuum drying, but it is not reliable that the outcome will show the desired qualities.

3.4. Phenibut and Tartaric Acid Species

Phenibut and tartaric acid were crystallized in equimolar ratios either through slow evaporation from aqueous solution or by milling crystallization under the addition of 10 μ L methanol at 25 Hz for 30 min. Two multicomponent crystalline single-crystal structures were obtained with **2** and two embodiments of **3**: the monoclinic **2:L-3 • H₂O** with the space group $P2_1$, as well as the triclinic **2:DL-3** with the space group $P\bar{1}$. **2:DL-3** is the only species characterized via SC-XRD, which does not contain any hydrate water in its lattice. It shows a disorder along its GABA subunit on **2** molecules: in half of its occupations, the alignment is akin to an S-chirality of **2**, in the other half to an R-chirality. However, its lattice makeup is relatively simple. A single crystallographically independent protonated Phenibut molecule and a single deprotonated **DL-3** molecule interact via hydrogen bonds. Rows are formed with **2**-phenyl subunits facing away from the HB-network and **DL-3** connecting between two **2**-GABA subunits. The alignment of the phenyl subunits again makes π -interactions unlikely, considering distances between edges and phenyl-centers-of-gravity. While a similar binding motive is present in **2:L-3 • H₂O**, some decisive differences occur: The asymmetric unit consists of three crystallographically distinct protonated **2** and three deprotonated **L-3** molecules in congruence with two additional hydrate water molecules. The latter are incorporated into the HB network that is formed in a similar manner to **2:DL-3** regarding **2** and **3** molecules. However, in **2:L-3 • H₂O**, alignment and distance of edges and centers-of-gravity in **2** phenyl subunits would make π -interactions possible. Although no disorder is present in the Phenibut:L-tartaric acid • H₂O structure, the multitude of crystallographically-independent molecules results in an overall structure perceived as less ordered, yet retaining some similarity to the anhydrous **2:DL-3** form regarding **2** and **3** positioning and interaction motif. A comparison of both lattices is shown in Figure 8.

Especially compared to the previously discussed Baclofen:malic acid entities **2:3** can be obtained with pleasant reliability by solvent crystallization or the mechanochemical approach, even though phase purity cannot be achieved instantly in all cases (Figure 9).

Concerning **2:3** forms with enantiomerically pure **3** entities, it is evident that phase purity is not obtained by crystallization from solution. This is observable by just comparing the first signal at about $5.6^\circ 2\Theta$ in the pattern simulated from the single crystal data. In the solvent-based sample, two Bragg reflections can be observed there, an additional one at $5.8^\circ 2\Theta$. Contrary to that, the shown pattern of the milling sample only poses the latter reflection. Furthermore, a strong reflection at $7.2^\circ 2\Theta$ is present. Even though the pattern received from heating the solution-based sample in a DSC chamber or after vacuum drying does not have the $7.2^\circ 2\Theta$ reflection, and the reflection at lower angles seems to be slightly shifted towards higher angles; careful analysis reveals that these patterns have more in common with each other than with the simulated or solvent-based pattern (see Supplementary Materials for larger comparison of the discussed samples). Two possible explanations seem reasonable: Either the milling pattern is a different phase, or it is just better resolved due to higher crystallinity. The slight amorphous course of the baseline in the PXRD pattern recorded after DSC, as well as the worse signal resolution, suggest a lower crystallinity after heating. This could cover up the $7.2^\circ 2\Theta$ signal, which might

also be more prevalent in the milling sample due to less preferential directionality from smaller crystallites after milling. Therefore, it seems most likely that milling of 2:L-3 and heating of a solution-based 2:L-3 sample in the DSC lead to the same, presumably anhydrous, product. It is noteworthy that the milling sample prepared from D-3 under the same conditions, and at the same time as its L-analog, led to a pattern akin to the solution product. This led us to the assumption that more water must have still been adsorbed on the milling vessel of the 2:D-3 sample. As methanol from the same batch was used in both cases, impurities contained in solvent can be ruled out as a reason for this behavior. While no obvious impurities occur in 2:DL-3, a small reflection that cannot be observed in the simulated pattern appears at $5^\circ 2\Theta$ when grown from solution. This signal is attributable to a non-incorporated precursor and does not disappear upon aging of the sample (see the Supplementary Materials). However, a mechanochemical approach seems to favor the formation of a pure 2:DL-3 phase as opposed to crystallization from solution. The received pattern matches well with the simulated one. To further confirm phase purity, DSC data were recorded (Figure 10).

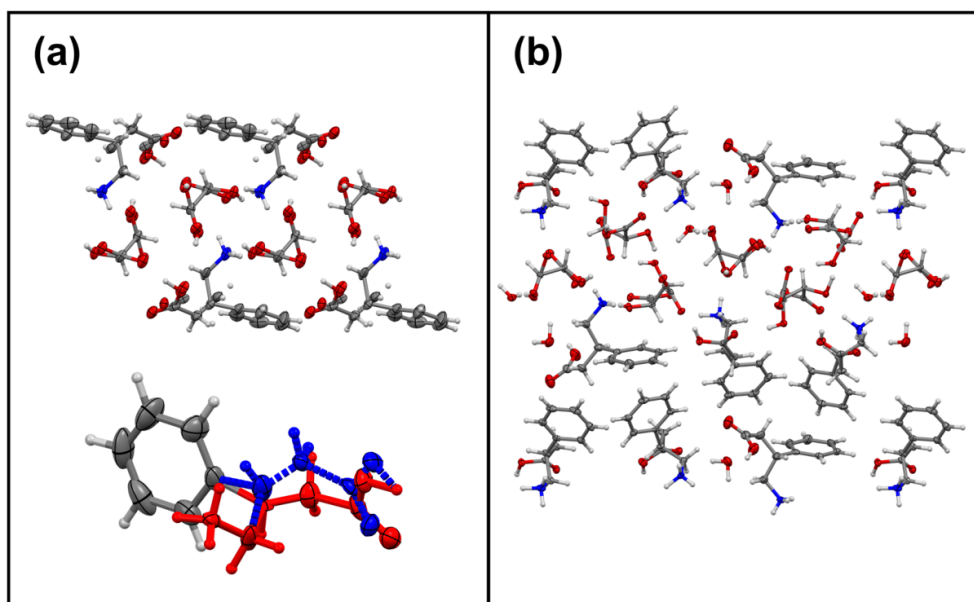


Figure 8. Structure comparison of (a) Phenibut:DL-tartaric acid (view from a-axis) with a highlighted disorder in the GABA subunit and (b) Phenibut:L-tartaric acid \cdot H₂O (view from a-axis). Phenibut occurs in two half-occupied GABA-subunit confirmations in a), as shown through additional atom positions along the chain, which is highlighted between the red and blue colored atoms and bonds on the Phenibut molecule. Carbon atoms are depicted in grey, hydrogen atoms are depicted in white, oxygen atoms are depicted in red and nitrogen atoms are depicted in blue.

Thermal analysis of the discussed compounds containing enantiopure 3 shows that the majority of the obtained samples do not solely contain 2:D-3 or 2:L-3 hydrates. Hydrate decomposition starts between 81 °C and 89 °C and occurs in a wide signal, which contains an additional shoulder at 103 °C or 104 °C. The subsequent melting signal between 131 °C and 136 °C is, in most cases, less intense than its predecessors. This indicates that the phase transition that occurs here does not lead to a more crystalline product, which is further confirmed through the powder pattern received after DSC heating. Here, the crystallinity is lowered, which leads to a less intense melting signal as less energy is released. DSC data analysis further confirms the assumptions regarding the received milling product 2:L-3. No signals occur prior to melting, and the melting signal comes in a well-defined

and intense form. Thus, a pure, presumably anhydrous phase must have been obtained. In the case of **2:DL-3**, the received products show no decisive differences; a melting signal occurs at 164 °C or 165 °C.

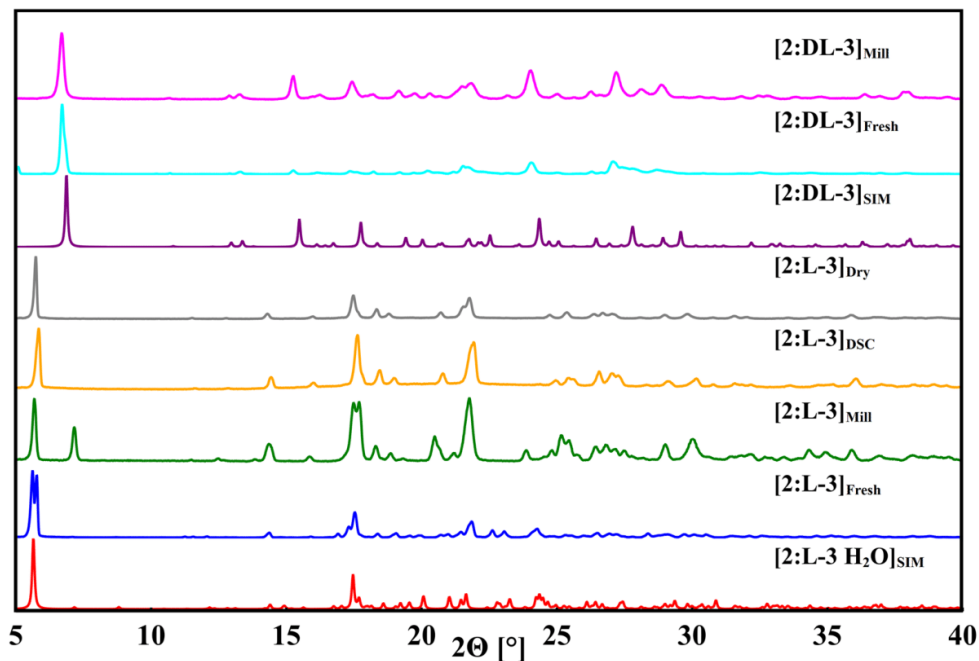


Figure 9. Selected powder patterns received from crystallization experiments involving Phenibut and tartaric acid in a range 2–40° 2 θ are compared to the simulated **2:L-3 • H₂O** (red) and anhydrous **2:DL-3** (purple) pattern: (blue) freshly prepared sample with L–tartaric acid from aqueous solution; (green) methanol-assisted co-milling sample of Phenibut and L–tartaric acid; (orange) **2:L-3 • H₂O** sample from aqueous solution after heating to 120 °C in a DSC chamber; (grey) **2:L-3 • H₂O** after vacuum drying; (cyan) fresh **2:DL-3** sample from aqueous solution crystallization; (magenta) a co-milling sample of Phenibut and D–tartaric acid, methanol-assisted.

Phenibut:tartaric acid species tend to form higher purity phases compared to Baclofen:malic acid species and contain smaller amounts of API-hydrate impurities. However, it is challenging to remove hydrate water from **2:D-3** or **2:L-3** species. Drying comes with a great loss of crystallinity, while milling has to be conducted under the exclusion of water to reliably gain the presumed anhydrous form. The anhydrous **2:DL-3** species appears to be the most easily obtainable within all presented samples. However, solution-based crystallization leads to small impurities. Thus, milling is the authors' recommendation to obtain Phenibut and tartaric acid multicomponent systems.

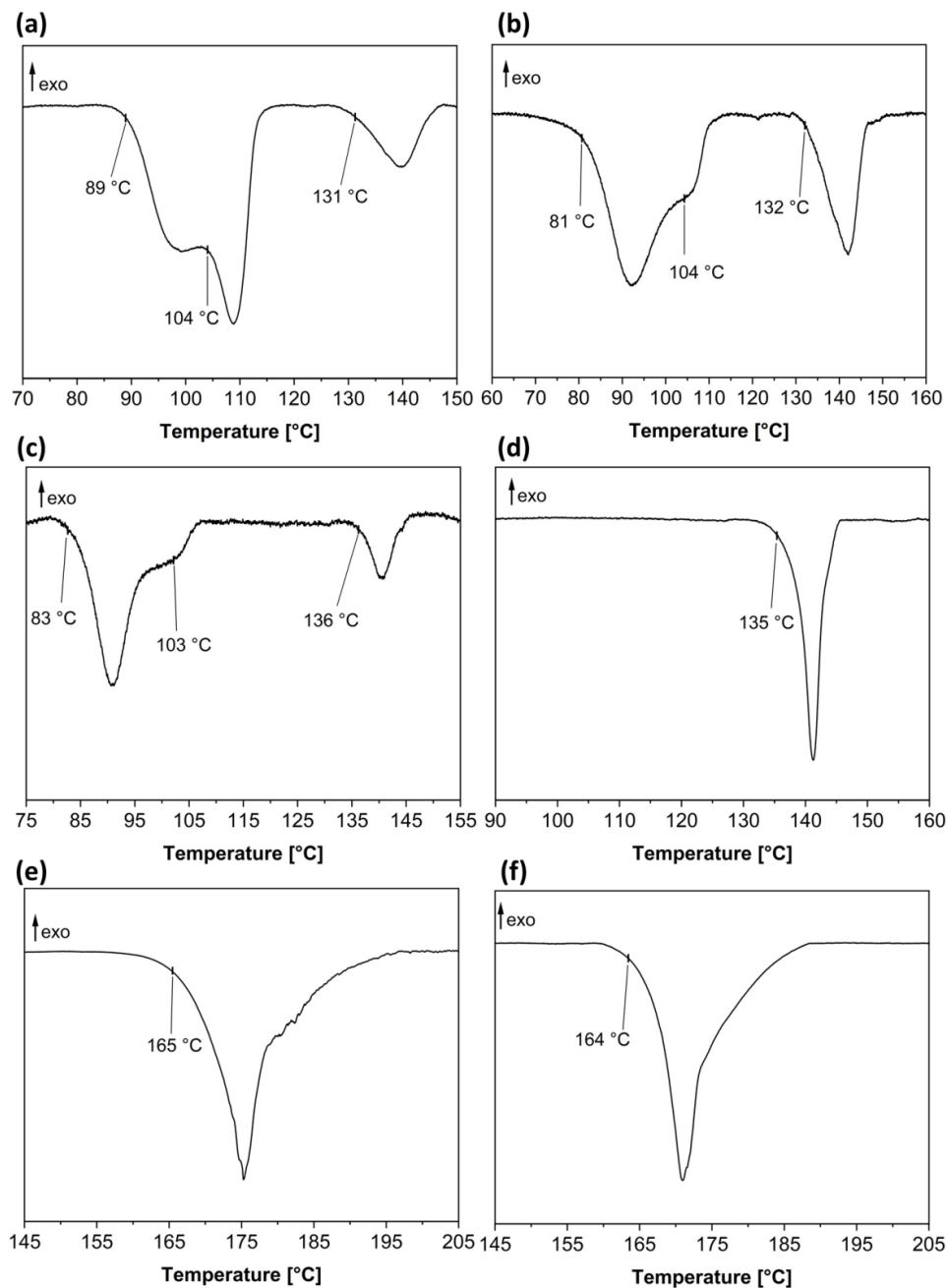


Figure 10. DSC data collected from Phenibut:tartaric acid samples grown from aqueous solution (a) 2:D-3 • H₂O, (b) 2:L-3 • H₂O, (e) 2:DL-3 and samples obtained by milling (c) 2:D-3 • H₂O, (d) 2:L-3 • H₂O and (f) 2:DL-3. DSC was heated at 5 °C min⁻¹; for clarity, only temperature ranges containing signals are shown.

3.5. Phenibut and Malic Acid Species

Attempted crystallization of Phenibut with malic acid proved to be more difficult than with tartaric acid again. Contrary to all other examined combinations, no single crystals suitable for the SC-XRD could be grown during these experiments. However, PXRD data suggest the presence of a multicomponent system of **2** and forms of **4** (Figure 11).

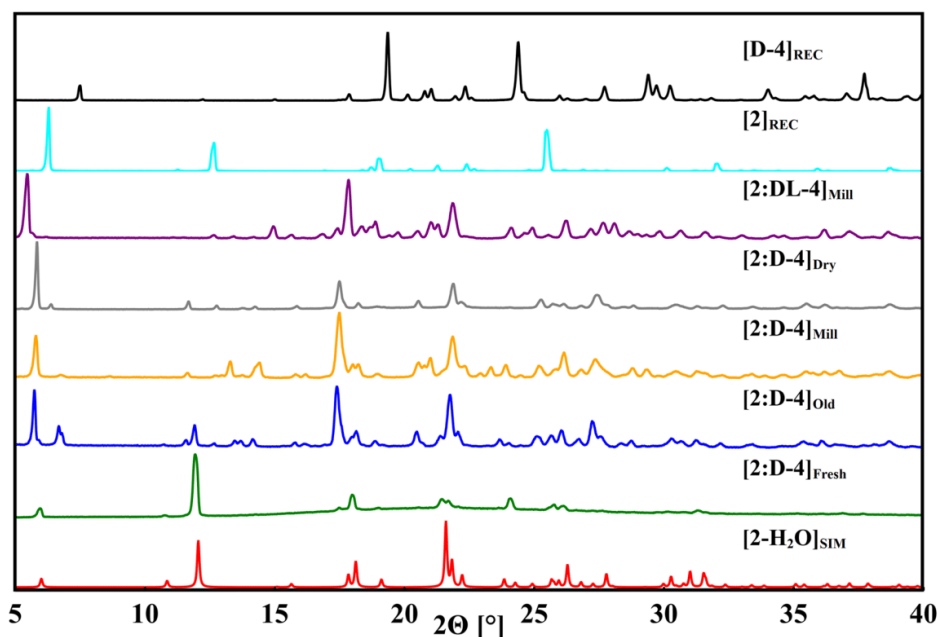


Figure 11. Selected PXRDs received from crystallization experiments involving Phenibut and malic acid in a range $2\text{--}40^\circ$ 2θ are compared to the simulated $2 \bullet \text{H}_2\text{O}$ (red) and recorded **2** (cyan) and **D-4** (black) pattern: (green) freshly prepared sample with **D**-malic acid from aqueous solution; (blue) six months old sample of Phenibut and **D**-malic acid from aqueous solution; (orange) **2:D-4** sample produced by methanol-assisted co-milling; (grey) Phenibut and **D**-malic acid from aqueous solution after vacuum drying; (purple) a co-milling sample of Phenibut and **DL**-malic acid.

The recorded powder patterns reveal the following: fresh samples received from solution crystallization are identifiable as $2 \bullet \text{H}_2\text{O}$ for all combinations (see the Supplementary Materials for (rac)-malic acid), and a new phase is received via milling of **2:DL-4** as compared to **2:D-4** or **2:L-4**. As freshly prepared samples basically only show reflections attributable to $2 \bullet \text{H}_2\text{O}$, obtaining single crystals suitable for SC-XRD proves difficult. Manifold attempts at growing single crystals of the new phase resulted in good quality needle-shaped crystals, which, however, always turned out to be $2 \bullet \text{H}_2\text{O}$. In general, Phenibut hydrate formation represents a strong competitive reaction, which impedes multicomponent system crystallization or occurs concomitantly. Powder patterns of **2:4** forms could only be obtained after prolonged drying of samples for weeks at room temperature after all water evaporated or, at least in the presented grey pattern, after vacuum drying. However, it should be noted that attempting to accelerate this process by vacuum leads to transition of the solid crystalline sample to a goeey substance, which does not recrystallize again. The shown pattern was recorded from left-over solid residues taken from said goeey substance. Traces of **2** hydrate remain visible even in the older sample, for example, in the Bragg reflection at 12° 2θ in the aged **2:D-4** sample. This signal is absent from both milling compounds. Furthermore, no patterns could be recorded after DSC-heating. Even though there are two or three visible signals in DSC from solution, they occur in a close

range (Figure 12). A viscous substance is received even after the first small DSC step, which is not suitable for PXRD analysis.

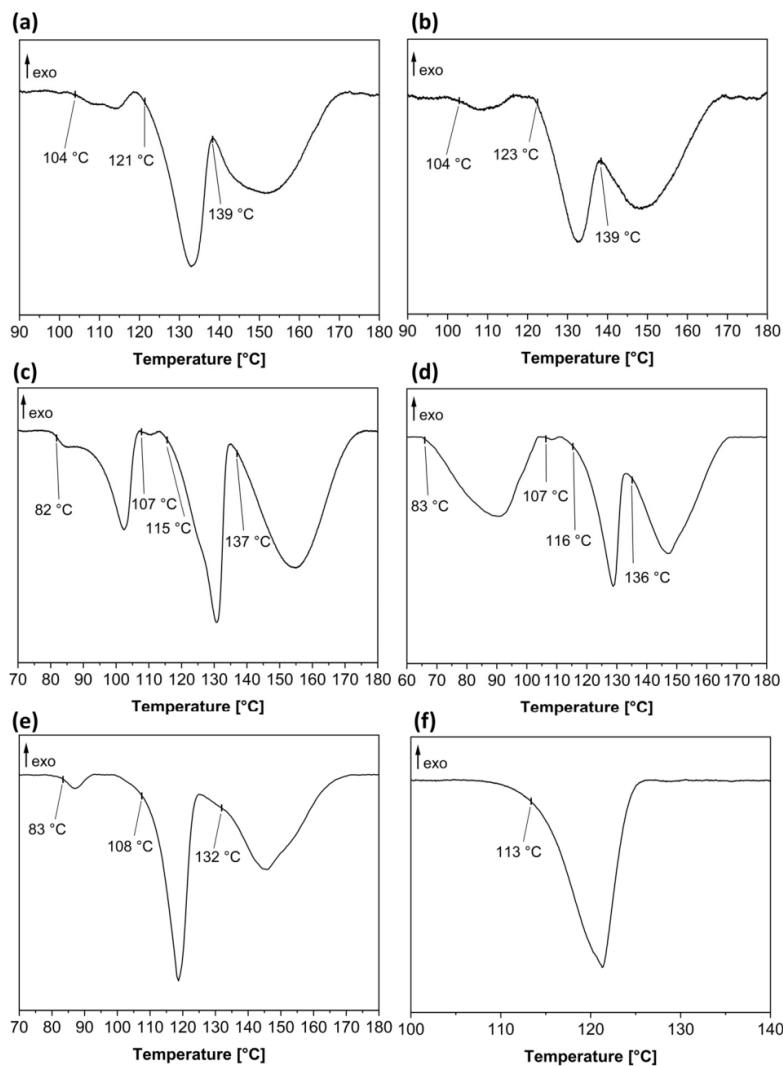


Figure 12. DSC data collected from samples grown from aqueous solution (a) Phenibut:D-malic acid, (b) Phenibut:L-malic acid, (e) Phenibut:DL-malic acid and samples obtained by milling (c) Phenibut:D-malic acid, (d) Phenibut:L-malic acid and (f) Phenibut:DL-malic acid. DSC was heated at $5\text{ }^{\circ}\text{C min}^{-1}$; selected temperature ranges are shown for clarity.

Thermal analysis indicates that the phase purity of 2:4 species containing enantiopure co-former was not achieved. Multiple signals were present, especially in the samples obtained via grinding. Even though the resolution was comparatively high, which indicates high crystallinity, no pure product was obtained under the examined conditions. This could explain why no single crystal could be obtained from solution. As no single crystal data were accessible, it can only safely be concluded by PXRD and DSC analysis that two of the received phases must be 2 hydrate and a novel phase containing an embodiment of 2:D- or L-4. Judging by the previous received results, a hydrate form of 2:4 seems likely to be formed. The melting point of the presumed anhydrous 2:D- or L-4 must be in the

range between 137 °C and 139 °C, as this includes the starting point for the final melting step in all recorded DSC data. Contrary to that, just a single melting signal was obtained in **2:DL-4** at 113 °C. This suggests a pure formation of this form.

Phenibut:malic acid species are difficult to obtain in a single crystalline form, the solvent choice being limited to water based on the poor solubility of **2** in other solvents. The results indicate multiple phases for **2** with enantiopure **4** co-formers, possibly including additional hydrate stages. While in conjunction with **DL-4**, a pure product seems to be obtainable through milling, single crystal growth from solution is still hindered by the formation of **2** hydrate. Without complete drying for prolonged time periods, the discussed phase cannot be obtained from solution, which degrades the quality of single crystals too much to be measured. Attempting to accelerate drying by vacuum or heat results in a gooey substance that might contain some desired product but cannot be analyzed by common solid-state methods. However, if just a quick method to obtain a **2:DL-4** multicomponent system is needed, the authors would recommend grinding, as this system can be regained reliably, at least by comparison of powder patterns, through milling.

4. Discussion

In this study, it was attempted to find similarities or distinctions in the multicomponent crystallization behavior of Baclofen and Phenibut with two simple and similar co-formers, tartaric and malic acid. The goal was to find a feasible method to obtain single crystals as well as pure co-phases for the investigated compounds. The results show that the formation of multicomponent species is possible in all investigated cases. However, a range of difficulties can occur concerning single crystal growth and receiving pure microcrystalline phases. As was shown, the presence of intermediate hydrates is prevalent, be it pure API hydrate forms or multicomponent hydrates, both from solution and liquid-assisted grinding. The zwitterionic GABA moiety present in both APIs offers various HB possibilities to incorporate water into a crystal lattice, same as carboxylic acid or hydroxyl-groups present in the co-formers. Furthermore, as both APIs are nearly insoluble in every solvent except water (where they cannot be considered as “well soluble” either), it becomes obvious why hydrate stages are formed in nearly all cases during crystallization from solution. The stability and predominant formation of the hydrate form become evident, as it occurs even during the grinding process, where water molecules contained in the atmosphere are adsorbed and incorporated into the crystal lattice. The chirality of the investigated compounds brings further complexity into this study. The best results were mainly obtained by milling a racemic API with a racemic co-former, except for Baclofen:tartaric acid systems, where milling as a method should not be preferred. In the case of Phenibut:DL-tartaric acid and Phenibut:DL-malic acid, an anhydrous form could even be received from aqueous solution. Thus, the same chirality on both co-formers seems to be beneficial. An effect of chirality on crystal lattices is visible in Baclofen:D-malic acid hydrate as well as Phenibut:DL-tartaric acid, with the former one being disordered. To compensate for the unfavorable directionality induced by the chiral co-former, the alignment of malic acid shifts by 180° in each position. In the latter, even though chiralities match, the GABA subunit in Phenibut also shifts its alignment constantly to best fit with the corresponding tartaric acid molecule. The formation of the discussed compounds seems to be mostly driven by strong intermolecular interactions. This is also highlighted by the makeup of some other of the received crystalline structures. With the exception of API hydrates and Phenibut:tartaric acid, they all pose a large asymmetric unit consisting of up to eight crystallographically independent molecules. This low symmetry suggests that the raw intermolecular binding force of HB is driving the formation. In Baclofen:DL-tartaric acid hydrate, even the protonation status of Baclofen molecules differs. This could indicate that the formation happens before each Baclofen molecule can be protonated by tartaric acid and just ‘freezes’ in this stage due to beneficial HB interactions. Thus, the formation of hydrates of pure APIs competes with the formation of multicomponent hydrates as well as anhydrous forms. While the exclusion of water via milling is helpful in gaining an anhy-

drous product, in most cases, it is not an absolute solution. Firstly, single crystals cannot be obtained this way if that is the goal. Secondly, milling must occur under dry conditions to guarantee the formation of anhydrous forms, as was shown. In the case of Baclofen:tartaric acid, solvent-based crystallization is the better solution. However, the product still must be dried by heating, as hydrate traces are persistent even after months. This, on the other hand, leads to loss of crystallinity. Lastly, Phenibut and enantiopure malic acid could not be obtained as a pure phase product in all conducted experiments. Even though not all substances could be received as single crystals, it is highly likely that proton transfer occurs in Phenibut:malic acid species and uncharacterized anhydrous forms as well. Some form of protonation/deprotonation occurs in all investigated species except for the Baclofen and Phenibut hydrates. Furthermore, IR-spectra analysis shows a large variation in carbonyl bands in all multicomponent systems; thus, salts or salt hydrates are probably applicable labels to all of them (see the Supplementary Materials). Regarding reproducibility, the best results can be achieved in the phases described herein, which are obtainable in high purity. The API hydrates can be received reliably through diffusion crystallization. Hydrate forms of Baclofen:tartaric acid forms reliably from aqueous solution; however, the drying product depends on the drying method and crystallinity can vary. The Baclofen:malic acid systems behave differently in that solution-based crystallization is unreliable for them. Crystallization through milling can lead to a product that seems pure at first glance, but as the DSC analysis has shown, the varying distributions of peak areas indicate variations in composition. These problems are also true for Phenibut:D- or Phenibut:L-tartaric acid species, even though Phenibut:DL-tartaric acid is the most reliably receivable system by PXRD as well as DSC analysis. Lastly, Phenibut:malic acid forms are probably the hardest to obtain. It takes a long time to overcome the Phenibut hydrate stage if these systems are attempted to grow from solution. This cannot be forcefully achieved through heat or vacuum drying, as the substance tends to become viscous without recrystallization. While grinding seems to be able to produce a reliable phase by powder pattern comparison, DSC analysis shows that composition varies strongly. Thus, trustworthy reproducibility, as confirmed by the conducted investigations, is only present in API hydrates, Baclofen:tartaric acid hydrates and Phenibut:DL-tartaric acid.

Baclofen and Phenibut, molecularly similar, also pose a similar crystallization behavior. Both tend to form pure hydrates and salt hydrates, representing a favorable competing reaction to the anhydrous phase's formation, their chirality has a decisive influence on crystal makeup, and it can require effort to obtain a targeted crystallization product.

Supplementary Materials: The following supporting information can be downloaded at: <https://www.mdpi.com/article/10.3390/cryst12101393/s1>. Table S1: Overview on results obtained by co-crystallization of Baclofen and Phenibut with co-formers tartaric acid and malic acid from solution in solvent water. Table S2: Overview on results obtained by milling co-crystallization of Baclofen and Phenibut with co-formers tartaric acid and malic acid under addition of 10 μ L methanol at 25 Hz for 30 min. Table S3: Overview on results obtained by co-crystallization of Baclofen and malic acid in solvent mixtures of ethyl acetate/water and aqueous hexafluoropropan-2-ol. No experiment was carried out with Baclofen and DL-malic acid in aqueous hexafluoropropan-2-ol. Table S4: Overview on preparation and results of different Baclofen:tartaric acid compounds. 0.5 mmol of Baclofen (107 mg) and 0.5 mmol of tartaric acid (75 mg) were used if not specified otherwise. Table S5: Overview on preparation and results of different Baclofen:malic acid compounds. 0.5 mmol of Baclofen (107 mg) and 0.5 mmol of malic acid (67 mg) were used if not specified otherwise. Table S6: Overview on preparation and results of different Phenibut:tartaric acid compounds. For the preparation of the compounds, 0.5 mmol of Phenibut (90 mg) and 0.5 mmol of tartaric acid (75 mg) were used if not specified otherwise. Table S7: Overview on preparation and results of different Phenibut:malic acid compounds. For the preparation of the compounds, 0.5 mmol of Phenibut (90 mg) and 0.5 mmol of malic acid (67 mg) were used if not specified otherwise. Table S8: Chosen bands corresponding to the carbonyl C=O stretching depicted in Figure S11. Table S9: Chosen bands corresponding to the carbonyl C=O stretching depicted in Figure S12. Table S10: Chosen bands corresponding to the carbonyl C=O stretching depicted in Figure S13. Table S11: Chosen bands corresponding

to the carbonyl C=O stretching depicted in Figure S14. Table S12: Chosen bands corresponding to the carbonyl C=O stretching depicted in Figure S15. Figure S1: Recorded powder patterns of Baclofen: tartaric acid systems under different conditions in a range from 5°–40° 2 θ : (blue) a fresh sample of **1:L-3 • H₂O**, shortly after crystallization, (purple) a sample of the same substance after six months, (green) LAG sample of Baclofen and L-tartaric acid, (grey) a vacuum dried sample of **1:L-3 • H₂O**, (orange) after heating a fresh sample of **1:L-3 • H₂O** in a DSC chamber to 140 °C and subsequent cooling before melting occurs, (cyan) **1:D-3 • H₂O** after six months, (magenta) LAG sample of Baclofen and D-tartaric, (black) after heating a fresh sample **1:D-3 • H₂O** in a DSC chamber to 140 °C and subsequent cooling before melting occurs. Simulated pattern of **1:L-3 • H₂O** hydrate is shown in red. Figure S2: Recorded powder patterns of Baclofen:DL-tartaric acid under different conditions in a range from 5°–40° 2 θ . Baclofen and DL-tartaric acid sample after a methanol-assisted grinding (red) and the same sample after heating in a DSC chamber to 115 °C and subsequent cooling before melting occurs (blue). Figure S3: Recorded powder patterns of Baclofen:malic acid systems in a range from 5°–40° 2 θ : (red) sample of Baclofen and L-malic acid a few days after crystallization occurs; (blue) LAG sample of Baclofen and L-malic acid; (purple) **1:L-4 • H₂O** obtained from hexafluoro-2-propanol solution contaminated with water six months after crystallization occurs; (green) simulated from single crystal data provided by Córdova-Villanueva et al. [50] (Cambridge Crystal Structure Database Ref. Code YIPLAN) and (cyan) simulated pattern of **1:D-4 • H₂O** from collected single crystals data. Figure S4: Overview on some recorded patterns of phase mixtures received by co-crystallization of Baclofen and L-malic acid under different conditions in a range from 2°–40° 2 θ : (red) Baclofen; (blue) L-malic acid; (purple) and (green) both samples of Baclofen and L-malic acid shortly after crystallization occurs; (cyan) **1:L-4** sample received from a solvent mixture of ethyl acetate and water shortly after crystallization occurs; (grey) a vacuum dried sample of **1:L-4**. Simulated powder patterns from single crystal data provided by Córdova-Villanueva et al. [50] (CCDC Ref. Code YIPLAN) (orange), from single crystal data of **1:D-4 • H₂O** (magenta) and from single crystal data of **1 • H₂O** (black) are given for comparison. Figure S5: Recorded patterns of Baclofen:D-malic acid systems under different conditions in a range from 2°–40° 2 θ : Baclofen (red); D-malic acid (blue); different samples of **1:D-4** shortly after crystallization occurs (purple and green); **1:D-4 • H₂O** after heating to 130 °C in a DSC chamber and subsequent cooling before melting (cyan); simulated from single crystal data provided by Córdova-Villanueva et al. [50] (CCDC Ref. Code YIPLAN) (orange); simulated from single crystal data of **1:D-4 • H₂O** (magenta) and of **1 • H₂O** (black). Figure S6: Recorded powder patterns of systems Baclofen:DL-malic in a range from 2°–40° 2 θ : (red) Baclofen, (blue) D-malic acid; (purple) **1:DL-4** shortly after crystallization, (green) **1:DL-4** from a solvent mixture of ethyl acetate and water; (cyan) LAG sample of Baclofen and DL-malic; (grey) a vacuum dried **1:DL-4**; (orange) simulated from single crystal data provided by Córdova-Villanueva et al. [45] (CCDC Ref. Code YIPLAN [46]); (magenta) simulated from single crystal data of **1:D-4 • H₂O** and (black) simulated from single crystal data of **1 • H₂O**. Figure S7: DSC-data of **1:D-4** (a) and **1:L-4** (b) samples obtained by milling crystallization of Baclofen and D- or L-malic acid under addition of 10 μ L methanol at 25 Hz for 30 min. DSC was heated at 5 °C min⁻¹, only important temperature ranges are shown for clarity. Figure S8: Recorded powder patterns of Phenibut:tartaric acid systems in a range from 2°–40° 2 θ : (red) **2:L-3 • H₂O** pattern simulated from single crystal data; (blue) **2:D-3 • H₂O** sample shortly after crystallization occurs; (purple) LAG sample of Phenibut and D-tartaric acid; (green) vacuum dried **2:D-3 • H₂O** sample. Figure S9: Further recorded powder patterns of Phenibut:L-tartaric acid systems under different conditions in a range from 2°–40° 2 θ . Simulated pattern from single crystal data of **2:L-3 • H₂O** (red) is compared to an LAG sample of Phenibut and L-tartaric acid (blue), **2:L-3 • H₂O** sample from aqueous solution after heating to 120 °C in a DSC chamber (purple) and a vacuum dried sample of **2:L-3 • H₂O** (green). Figure S10: Recorded powder patterns of Phenibut:malic acid systems under different conditions in a range from 5°–40° 2 θ : (red) Phenibut; (blue) L-malic acid; (purple and green) different samples of **2:L-4** shortly after crystallization; (cyan) LAG sample of Phenibut and L-malic acid; (grey) a vacuum dried sample of **2:L-4**; (orange) **2:DL-4** shortly after crystallization occurs; (magenta) LAG sample of Phenibut and DL-malic acid; (dark-green) a vacuum dried sample of **2:DL-4** and (black) simulated pattern from single crystal data of **2 • H₂O**. Figure S11: Recorded IR-spectra of used educts (red) Baclofen, (green) Phenibut, (blue) D-tartaric acid, (orange) L-tartaric acid, (purple) D-malic acid and (cyan) L-malic acid in a range from 4000 cm⁻¹ to 400 cm⁻¹. Figure S12: Recorded IR-spectra of Baclofen:tartaric acid systems under different conditions in a range from 4000 cm⁻¹ and 400 cm⁻¹. Samples obtained via crystallization from solution: (red) **1:D-3**, (green)

1:L-3, (blue) 1:DL-3 and samples after methanol-assisted grinding: (orange) Baclofen and D-tartaric acid, (purple) Baclofen and L-tartaric acid, (cyan) Baclofen and DL-tartaric acid. Figure S13: Recorded IR-spectra of Baclofen:malic acid systems under different conditions in a range from 4000 cm^{-1} and 400 cm^{-1} . Samples from solution crystallization of 1:D-4 • H₂O (red), 1:L-4 • H₂O (green) and of 1:D-4 (blue) which showed similarities to the published YIPLAN structure in its powder pattern. Samples after LAG experiments: (orange) Baclofen and D-malic acid, (purple) Baclofen and L-malic acid, (cyan) Baclofen and DL-malic acid. Figure S14: Recorded IR-spectra of Phenibut:tartaric acid systems under different conditions in a range from 4000 cm^{-1} and 400 cm^{-1} . Samples from solution crystallization: (red) 2:D-3, (green) 2:L-3 and (blue) 2:DL-3. Samples from LAG with methanol: (orange) Phenibut and D-tartaric acid, (purple) Phenibut and L-tartaric acid and (cyan) Phenibut and DL-tartaric acid. Figure S15: Recorded IR-spectra of Phenibut:malic acid systems in a range from 4000 cm^{-1} and 400 cm^{-1} . Samples obtained from solution crystallization: (red) 2:D-4, (green) 2:L-4 and from LAG experiments: (orange) Phenibut and D-malic acid, (purple) Phenibut and L-malic acid, (cyan) Phenibut and DL-malic acid. Figure S16: TGA-data of 1:D-3 • H₂O (a), 1:L-3 • H₂O (b) and 1:DL-3 • H₂O (c). TGA was heated at 10 °C min⁻¹ in a range from 30 °C to 350 °C. Figure S17: TGA-data of a LAG sample of Baclofen and D-tartaric acid with methanol (a), a LAG sample of Baclofen and L-tartaric acid with methanol (b), a LAG sample of Baclofen and DL-tartaric acid with methanol (c), a vacuum dried sample of 1:D-3 • H₂O (d), a vacuum dried sample of 1:L-3 • H₂O (e) and a vacuum dried sample of 1:DL-3 • H₂O (f). TGA was heated with 10 °C min⁻¹ in a range from 30 °C–350 °C. Figure S18: TGA-data of a sample of 1:D-4 (a), a sample of 1:L-4 (b) and a sample of 1:DL-4 (c). TGA was heated at 10 °C min⁻¹ in a range from 30 °C to 350 °C. Figure S19: TGA-data of a LAG sample of Baclofen and D-malic acid with methanol (a), a LAG sample of Baclofen and L-malic acid with methanol (b), a LAG sample of Baclofen and DL-malic acid with methanol (c), a vacuum dried sample of 1:D-4 (d), a vacuum dried sample of 1:L-4 (e) and a vacuum dried sample of 1:DL-4 (f). TGA was heated with 10 °C min⁻¹ in a range from 30 °C–350 °C. Figure S20: TGA-data of a LAG sample of Phenibut and D-tartaric acid with methanol (a), a LAG sample of Phenibut and L-tartaric acid with methanol (b), a LAG sample of Phenibut and DL-tartaric acid with methanol (c), a vacuum dried sample of 2:D-3 • H₂O (d), a vacuum dried sample of 2:L-3 • H₂O (e) and a vacuum dried sample of 2:DL-3 (f). TGA was heated with 10 °C min⁻¹ in a range from 30 °C–350 °C. Figure S21: TGA-data of a LAG sample of Phenibut and D-malic acid with methanol (a), a LAG sample of Phenibut and L-malic acid with methanol (b) and a LAG sample of Phenibut and DL-malic acid with methanol (c). TGA was heated with 10 °C min⁻¹ in a range from 30 °C–350 °C.

Author Contributions: Conceptualization, V.V. and D.K.; methodology, M.H. and D.K.; validation, M.H. and D.K.; formal analysis, D.K.; investigation, M.H., D.K. and T.S.; resources, V.V.; writing—original draft preparation, D.K.; writing—review and editing, V.V. and M.H.; visualization, D.K.; supervision, V.V.; project administration, V.V.; funding acquisition, V.V. All authors have read and agreed to the published version of the manuscript.

Funding: Funded by the Deutsche Forschungsgemeinschaft (DFG, German Research Foundation)—440366605.

Data Availability Statement: Not applicable.

Acknowledgments: The authors thank Carsten Schauerte, Kevin Grasmik and the SOLID-CHEM GmbH Team for technical support.

Conflicts of Interest: The authors declare no conflict of interest.

References

- Morrison, G.; zur Loye, H.-C. Expanding the Chemistry of Salt-Inclusion Materials: Utilizing the Titanyl Ion as a Structure Directing Agent for the Targeted Synthesis of Salt-Inclusion Titanium Silicates. *Cryst. Growth Des.* **2020**, *20*, 8071–8078. [[CrossRef](#)]
- Hou, Y.; Sun, X.; Dou, M.; Lu, C.; Liu, J.; Rao, W. Cellulose Nanocrystals Facilitate Needle-like Ice Crystal Growth and Modulate Molecular Targeted Ice Crystal Nucleation. *Nano Lett.* **2021**, *21*, 4868–4877. [[CrossRef](#)]
- Uehara, T. Simulation of Polyhedral Crystal Growth Based on the Estimated Surface Energy of Crystallographic Planes. *MSA* **2021**, *12*, 519–533. [[CrossRef](#)]
- Wu, C.-S.; Ikeyama, J.; Nakabayashi, S.; Sugiyama, T.; Yoshikawa, H.Y. Growth Promotion of Targeted Crystal Face by Nanoprocessing via Laser Ablation. *J. Phys. Chem. C* **2019**, *123*, 24919–24926. [[CrossRef](#)]
- Jain, R.; Mallette, A.J.; Rimer, J.D. Controlling Nucleation Pathways in Zeolite Crystallization: Seeding Conceptual Methodologies for Advanced Materials Design. *J. Am. Chem. Soc.* **2021**, *143*, 21446–21460. [[CrossRef](#)]

6. Orehek, J.; Teslić, D.; Likozar, B. Continuous Crystallization Processes in Pharmaceutical Manufacturing: A Review. *Org. Process Res. Dev.* **2021**, *25*, 16–42. [[CrossRef](#)]
7. Tappan, B.A.; Brutchey, R.L. Polymorphic Metastability in Colloidal Semiconductor Nanocrystals. *ChemNanoMat* **2020**, *6*, 1567–1588. [[CrossRef](#)]
8. Selekman, J.A.; Roberts, D.; Rosso, V.; Qiu, J.; Nolfo, J.; Gao, Q.; Janey, J. Development of a Highly Automated Workflow for Investigating Polymorphism and Assessing Risk of Forming Undesired Crystal Forms within a Crystallization Design Space. *Org. Process Res. Dev.* **2016**, *20*, 70–75. [[CrossRef](#)]
9. Ostwald, W. Studien über die Bildung und Umwandlung fester Körper. *Z. Phys. Chem.* **1897**, *22U*, 289–330. [[CrossRef](#)]
10. Ahn, B.; Bosetti, L.; Mazzotti, M. Accounting for the Presence of Molecular Clusters in Modeling and Interpreting Nucleation and Growth. *Cryst. Growth Des.* **2022**, *22*, 661–672. [[CrossRef](#)]
11. Fu, H.; Gao, X.; Zhang, X.; Ling, L. Recent Advances in Nonclassical Crystallization: Fundamentals, Applications, and Challenges. *Cryst. Growth Des.* **2022**, *22*, 1476–1499. [[CrossRef](#)]
12. Maurya, R.S.; Jayanthi, S.; Chandaluri, C.G.; Radhakrishnan, T.P. Monitoring Molecular Microparticles through the Amorphous-to-Crystalline Transformation and Fluorescence Enhancement/Tuning. *Chem. Mater.* **2022**, *34*, 244–253. [[CrossRef](#)]
13. Weber, J.; Bracco, J.N.; Yuan, K.; Starchenko, V.; Stack, A.G. Studies of Mineral Nucleation and Growth Across Multiple Scales: Review of the Current State of Research Using the Example of Barite (BaSO₄). *ACS Earth Space Chem.* **2021**, *5*, 3338–3361. [[CrossRef](#)]
14. Rizvi, A.K.; Roberts, K.J.; Izumi, T. The Influence of Supersaturation and the Presence of Biuret on the Nucleation, Growth and Morphology of Urea Crystallised from Ethanolic Solutions. *Isr. J. Chem.* **2021**, *61*, 727–742. [[CrossRef](#)]
15. Peng, H.; Tian, N.; Yu, C.; Gao, Y.; Li, K.; Yan, H.; Zhao, P.; Wu, S.; Chen, M.; Gong, J. Insights into the Role of Dipentaerythritol in the Thermodynamics and Nucleation Behavior of a Pentaerythritol–Water System. *Cryst. Growth Des.* **2022**, *22*, 449–460. [[CrossRef](#)]
16. Ouyang, J.; Xing, X.; Chen, J.; Zhou, L.; Liu, Z.; Heng, J.Y. Effects of solvent, supersaturation ratio and silica template on morphology and polymorph evolution of vanillin during swift cooling crystallization. *Particuology* **2022**, *65*, 93–104. [[CrossRef](#)]
17. Chen, Y.-M.; Gao, J. Synthesis and characterization of ZnO nanoparticles in n-hexanol solution. *Mater. Lett. X* **2021**, *12*, 100106. [[CrossRef](#)]
18. Arzig, M.; Künecke, U.; Salamon, M.; Uhlmann, N.; Wellmann, P.J. Influence of the growth conditions on the formation of macro-steps on the growth interface of SiC-Crystals. *J. Cryst. Growth* **2021**, *576*, 126361. [[CrossRef](#)]
19. Zhang, L.; Xu, Y.; Lou, B.; Qin, X.; Zhang, L.; Liu, X.; Yuan, H.; Zhang, Y.; Rohani, S.; Lu, J. Effect of Additives on Preferential Crystallization for the Chiral Resolution of Citrulline: Experimental, Statistical, and Molecular Dynamics Simulation Studies. *Cryst. Growth Des.* **2022**, *22*, 2392–2406. [[CrossRef](#)]
20. Hoffmann, J.; Flannigan, J.; Cashmore, A.; Briuglia, M.L.; Steendam, R.R.E.; Gerard, C.J.J.; Haw, M.D.; Sefcik, J.; Horst, J.H. The unexpected dominance of secondary over primary nucleation. *Faraday Discuss.* **2022**, *235*, 109–131. [[CrossRef](#)]
21. Carpenter, J.E.; Grünwald, M. Pre-Nucleation Clusters Predict Crystal Structures in Models of Chiral Molecules. *J. Am. Chem. Soc.* **2021**, *143*, 21580–21593. [[CrossRef](#)] [[PubMed](#)]
22. Bučar, D.-K.; Lancaster, R.W.; Bernstein, J. Disappearing polymorphs revisited. *Angew. Chem. Int. Ed.* **2015**, *54*, 6972–6993. [[CrossRef](#)] [[PubMed](#)]
23. Liu, Y.; Gabriele, B.; Davey, R.J.; Cruz-Cabeza, A.J. Concerning Elusive Crystal Forms: The Case of Paracetamol. *J. Am. Chem. Soc.* **2020**, *142*, 6682–6689. [[CrossRef](#)] [[PubMed](#)]
24. Malec, L.M.; Gryl, M.; Oszejca, M.T.; Brela, M.Z.; Stadnicka, K.M. Chasing the Co-crystal Disappearing Polymorph with Ab Initio Methods. *Cryst. Growth Des.* **2021**, *21*, 6902–6912. [[CrossRef](#)]
25. Lapin, I. Phenibut (beta-phenyl-GABA): A tranquilizer and nootropic drug. *CNS Drug Rev.* **2001**, *7*, 471–481. [[CrossRef](#)]
26. Komisarek, D.; Pallaske, M.; Vasylyeva, V. Crystal Structure and Thermal Properties of Phenibut, Phenibut H₂O and Phenibut HCl: A Case for Phase Stability Based on Structural Considerations. *Z. Anorg. Allg. Chem.* **2021**, *647*, 984–991. [[CrossRef](#)]
27. Belov, F.; Villinger, A.; Langermann, J. von. (R)-Baclofen (R)-4-amino-3-(4-chloro-phen-yl)butanoic acid. *Acta Crystallogr. E Crystallogr. Commun.* **2022**, *78 Pt 1*, 33–35. [[CrossRef](#)]
28. Gendron, F.-X.; Mahieux, J.; Sanselme, M.; Coquerel, G. Resolution of Baclofenium Hydrogenomaleate By Using Preferential Crystallization. A First Case of Complete Solid Solution at High Temperature and a Large Miscibility Gap in the Solid State. *Cryst. Growth Des.* **2019**, *19*, 4793–4801. [[CrossRef](#)]
29. Takagi, Y.; Yamada, H.; Ebara, H.; Hayashi, H.; Kidani, S.; Toyooka, K.; Ishino, Y.; Kitano, Y.; Nakanami, A.; Kagechika, K.; et al. Intrathecal baclofen therapy for severe spasticity in an adult with tethered cord syndrome: A case report. *J. Med. Case Rep.* **2021**, *15*, 442. [[CrossRef](#)]
30. Romito, J.W.; Turner, E.R.; Rosener, J.A.; Coldiron, L.; Udipi, A.; Nohrn, L.; Tausiani, J.; Romito, B.T. Baclofen therapeutics, toxicity, and withdrawal: A narrative review. *SAGE Open Med.* **2021**, *9*, 20503121211022197. [[CrossRef](#)]
31. Kent, C.N.; Park, C.; Lindsley, C.W. Classics in Chemical Neuroscience: Baclofen. *ACS Chem. Neurosci.* **2020**, *11*, 1740–1755. [[CrossRef](#)] [[PubMed](#)]
32. Agabio, R.; Baldwin, D.S.; Amaro, H.; Leggio, L.; Sinclair, J.M.A. The influence of anxiety symptoms on clinical outcomes during baclofen treatment of alcohol use disorder: A systematic review and meta-analysis. *Neurosci. Biobehav. Rev.* **2021**, *125*, 296–313. [[CrossRef](#)] [[PubMed](#)]

33. Garbutt, J.C.; Kampov-Polevoy, A.B.; Pedersen, C.; Stansbury, M.; Jordan, R.; Willing, L.; Gallop, R.J. Efficacy and tolerability of baclofen in a U.S. community population with alcohol use disorder: A dose-response, randomized, controlled trial. *Neuropsychopharmacology* **2021**, *46*, 2250–2256. [[CrossRef](#)] [[PubMed](#)]
34. Leggio, L.; Litten, R.Z. The GABA-B receptor agonist baclofen helps patients with alcohol use disorder: Why these findings matter. *Neuropsychopharmacology* **2021**, *46*, 2228–2229. [[CrossRef](#)]
35. Levine, M.; Lovecchio, F. New Designer Drugs. *Emerg. Med. Clin. N. Am.* **2021**, *39*, 677–687. [[CrossRef](#)] [[PubMed](#)]
36. Jouney, E.A. Phenibut (β -Phenyl- γ -Aminobutyric Acid): An Easily Obtainable “Dietary Supplement” with Propensities for Physical Dependence and Addiction. *Curr. Psychiatry Rep.* **2019**, *21*, 23. [[CrossRef](#)] [[PubMed](#)]
37. Doyno, C.R.; White, C.M. Sedative-Hypnotic Agents That Impact Gamma-Aminobutyric Acid Receptors: Focus on Flunitrazepam, Gamma-Hydroxybutyric Acid, Phenibut, and Selank. *J. Clin. Pharmacol.* **2021**, *61* (Suppl. S2), S114–S128. [[CrossRef](#)]
38. Kupats, E.; Vrublevska, J.; Zvejniece, B.; Vavers, E.; Stelfa, G.; Zvejniece, L.; Dambrova, M. Safety and Tolerability of the Anxiolytic and Nootropic Drug Phenibut: A Systematic Review of Clinical Trials and Case Reports. *Pharmacopsychiatry* **2020**, *53*, 201–208. [[CrossRef](#)]
39. Liu, Y.; Wang, Y.; Huang, X.; Li, X.; Zong, S.; Wang, N.; Hao, H. Conformational Selectivity and Evolution Affected by the Desolvation Process. *Cryst. Growth Des.* **2022**, *22*, 1283–1291. [[CrossRef](#)]
40. Venu, N.; Vishweshwar, P.; Ram, T.; Surya, D.; Apurba, B. (S)-3-(Ammoniomethyl)-5-methylhexanoate (pregabalin). *Acta Crystallogr. C Struct. Chem.* **2007**, *63 Pt 5*, o306–o308. [[CrossRef](#)]
41. *CrysAlisPRO*; Oxford Diffraction/Agilent Technologies UK Ltd.: Yarnton, England, 2014.
42. Sheldrick, G.M. Crystal structure refinement with SHELXL. *Acta Crystallogr. Sect. C Cryst. Struct. Commun.* **2015**, *C71*, 3–8. [[CrossRef](#)] [[PubMed](#)]
43. Sheldrick, G.M. A short history of SHELX. *Acta Crystallogr. Sect. A Found. Crystallogr.* **2008**, *64*, 112–122. [[CrossRef](#)] [[PubMed](#)]
44. Macrae, C.F.; Sovago, I.; Cottrell, S.J.; Galek, P.T.A.; McCabe, P.; Pidcock, E.; Platings, M.; Shields, G.P.; Stevens, J.S.; Towler, M.; et al. Mercury 4.0: From visualization to analysis, design and prediction. *J. Appl. Crystallogr.* **2020**, *53 Pt 1*, 226–235. [[CrossRef](#)] [[PubMed](#)]
45. Dolomanov, O.V.; Bourhis, L.J.; Gildea, R.J.; Howard, J.A.K.; Puschmann, H. OLEX2: A complete structure solution, refinement and analysis program. *J. Appl. Cryst.* **2009**, *42*, 339–341. [[CrossRef](#)]
46. Ibers, J.A. Gabapentin and gabapentin monohydrate. *Acta Crystallogr. C Struct. Chem.* **2001**, *57 Pt 5*, 641–643. [[CrossRef](#)]
47. Khandavilli, U.B.R.; Lusi, M.; Frawley, P.J. Plasticity in zwitterionic drugs: The bending properties of Pregabalin and Gabapentin and their hydrates. *IUCr* **2019**, *6 Pt 4*, 630–634. [[CrossRef](#)]
48. Vasudev, P.G.; Aravinda, S.; Ananda, K.; Veena, S.D.; Nagarajan, K.; Shamala, N.; Balaram, P. Crystal structures of a new polymorphic form of gabapentin monohydrate and the e and z isomers of 4-tertiarybutylgabapentin. *Chem. Biol. Drug Des.* **2009**, *73*, 83–96. [[CrossRef](#)]
49. Wang, Y.; Du, S.; Wu, S.; Li, L.; Zhang, D.; Yu, B.; Zhou, L.; Bekele, H.K.; Gong, J. Thermodynamic and molecular investigation into the solubility, stability and self-assembly of gabapentin anhydrate and hydrate. *J. Chem. Thermodyn.* **2017**, *113*, 132–143. [[CrossRef](#)]
50. Córdova-Villanueva, E.N.; Rodríguez-Ruiz, C.; Sánchez-Guadarrama, O.; Rivera-Islas, J.; Herrera-Ruiz, D.; Morales-Rojas, H.; Höpfl, H. Diastereomeric Salt Formation by the γ -Amino Acid RS -Baclofen and L -Malic Acid: Stabilization by Strong Heterosynthons Based on Hydrogen Bonds between RNH³⁺ and COOH/COO⁻ Groups. *Cryst. Growth Des.* **2018**, *18*, 7356–7367. [[CrossRef](#)]

Supporting Information

A Lecture in Humbleness: Crystallization of chiral and zwitterionic APIs Baclofen and Phenibut

Marco Herbst & Daniel Komisarek, Till Strothmann, Vera Vasylyeva*

Table S1. Overview on results obtained by co-crystallization of Baclofen and Phenibut with co-formers tartaric acid and malic acid from solution in solvent water.

	D-3	L-3	DL-3	D-4	L-4	DL-4
1	1:D-3 • H ₂ O single crystals	1:D-3 • H ₂ O single crystals	1:DL-3 • H ₂ O single crystals	unreliable, phase mixtures	unreliable, phase mixtures	unreliable, phase mixtures
2	2:D-3 • H ₂ O	2:L-3 • H ₂ O single crystals	2:DL-3 single crystals	Formation of 2 • H ₂ O, phase transition after drying	Formation of 2 • H ₂ O, phase transition after drying	Formation of 2 • H ₂ O, phase transition after drying

Table S2. Overview on results obtained by milling co-crystallization of Baclofen and Phenibut with co-formers tartaric acid and malic acid under addition of 10 µL methanol at 25 Hz for 30 minutes.

	D-3	L-3	DL-3	D-4	L-4	DL-4
1	Possible anhydrous form	Possible anhydrous form	Phase mixture of anhydrous forms 1:L-3, 1:D-3 and 1:DL-3	YIPLAN, phase mixture	YIPLAN	YIPLAN
2	2:D-3 • H ₂ O	2:L-3 • H ₂ O, phase mixture with possible anhydrous form	2:DL-3	Formation of a new co-system	Formation of a new co-system	Formation of a new co-system

Table S3. Overview on results obtained by co-crystallization of Baclofen and malic acid in solvent mixtures of ethyl acetate / water and aqueous hexafluoropropan-2-ol. No experiment was carried out with Baclofen and DL-malic acid in aqueous hexafluoropropan-2-ol.

	D-4	L-4	DL-4
Ethyl acetate	phase mixtures	phase mixtures	phase mixtures
Hexafluoro-2-propanol	1:D-4 • H ₂ O Single crystals after 1 • H ₂ O single crystal formation	1:L-4 • H ₂ O after 1 • H ₂ O single crystal formation	-

Table S4. Overview on preparation and results of different Baclofen:tartaric acid compounds. 0.5 mmol of Baclofen (107 mg) and 0.5 mmol of tartaric acid (75 mg) were used if not specified otherwise.

Compound	Preparation	Result
1:D-3	Crystallization in aqueous solution	Similar to 1:D-3 • H ₂ O but with traces of new phases
1:D-3	LAG with 10 µL methanol	Possible anhydrous phase
1:L-3	Crystallization in aqueous solution	Similar to 1:L-3 • H ₂ O but with large amounts of new phases
1:L-3	LAG with 10 µL methanol	Possible anhydrous phase
1:DL-3	Crystallization in aqueous solution	Similar to 1:DL-3 • H ₂ O
1:DL-3	LAG with 10 µL methanol	Mixture of 1:DL-3 • H ₂ O, 1:D-3 • H ₂ O, 1:L-3 • H ₂ O and possible anhydrous forms

Table S5. Overview on preparation and results of different Baclofen:malic acid compounds. 0.5 mmol of Baclofen (107 mg) and 0.5 mmol of malic acid (67 mg) were used if not specified otherwise.

Compound	Preparation	Result
1 • H ₂ O	Crystallization in aqueous solution with dissolved molecules of 4 present in solution	SCXRD-quality crystals which decompose to 1 after drying
1:D-4	Crystallization in aqueous hexafluoroisopropanol solution, only 0.25 mmol of Baclofen (53 mg) and D-malic acid (34 mg) were used	Similar to 1:D-4 • H ₂ O
1:D-4	Crystallization in aqueous solution	Phase mixture of 1:D-4 • H ₂ O, 1 • H ₂ O and YIPLAN
1:D-4	LAG with 10 µL methanol	Similar to YIPLAN but with slight differences in the powder pattern
1:L-4	Crystallization in aqueous hexafluoroisopropanol solution, only 0.25 mmol of Baclofen (53 mg) and L-malic acid (34 mg) were used	Similar to 1:D-4 • H ₂ O
1:L-4	Crystallization in aqueous solution	Phase mixture of 1:D-4 • H ₂ O, 1 • H ₂ O and YIPLAN
1:L-4	LAG with 10 µL methanol	Similar to YIPLAN but with slight differences in the powder pattern
1:DL-4	Crystallization in aqueous solution	Phase mixture of 1, 1 • H ₂ O, 1:D-4 • H ₂ O and YIPLAN
1:DL-4	LAG with 10 µL methanol	Similar to YIPLAN with slightly higher crystallinity compared to samples with enantiomerically pure 4 molecules

2

Table S6. Overview on preparation and results of different Phenibut:tartaric acid compounds. For the preparation of the compounds, 0.5 mmol of Phenibut (90 mg) and 0.5 mmol of tartaric acid (75 mg) were used if not specified otherwise.

Compound	Preparation	Results
2:D-3	Crystallization in aqueous solution, 0.75 mmol of Phenibut (134 mg) and D-tartaric acid (113 mg) were used	Similar to 2:L-3 • H ₂ O with slight amounts of other phases
2:D-3	LAG with 10 µL methanol	Similar to 2:L-3 • H ₂ O with amounts of other phases
2:L-3	Crystallization in aqueous solution, 0.75 mmol of Phenibut (134 mg) and D-tartaric acid (113 mg) were used	Similar to 2:L-3 • H ₂ O with slight amounts of other phases
2:L-3	LAG with 10 µL methanol	Phase mixture of 2:L-3 • H ₂ O and possible anhydrous phase
2:DL-3	Crystallization in aqueous solution	Similar to 2:DL-3
2:DL-3	LAG with 10 µL methanol	Similar to 2:DL-3

Table S7. Overview on preparation and results of different Phenibut:malic acid compounds. For the preparation of the compounds, 0.5 mmol of Phenibut (90 mg) and 0.5 mmol of malic acid (67 mg) were used if not specified otherwise.

Compound	Preparation	Result
2 • H ₂ O	Crystallization in aqueous solution with dissolved molecules of 4	SCXRD-quality crystals which decompose to 2 after drying
2:D-4	Crystallization in aqueous solution	Similar to 2 • H ₂ O, phase transition after drying
2:D-4	LAG with 10 µL methanol	Formation of new phases
2:L-4	Crystallization in aqueous solution	Similar to 2 • H ₂ O, phase transition after drying
2:L-4	LAG with 10 µL methanol	Formation of new phases
2:DL-4	Crystallization in aqueous solution	Similar to 2 • H ₂ O, phase transition after drying
2:DL-4	LAG with 10 µL methanol	Formation of new phases

PXRD and DSC Data Overview

PXRDs of Baclofen:L-tartaric acid hydrate samples are shown in **Figure S1**. Phase transition of Baclofen:L-tartaric acid hydrate occurs quickly after drying of the sample, which can be seen in the differences between the simulated pattern and the recorded pattern of a fresh sample. The pattern recorded after six months for both Baclofen:L-tartaric acid hydrate and Baclofen:D-tartaric acid hydrate share good agreement with the milling, vacuum dried and DSC patterns of said substances.

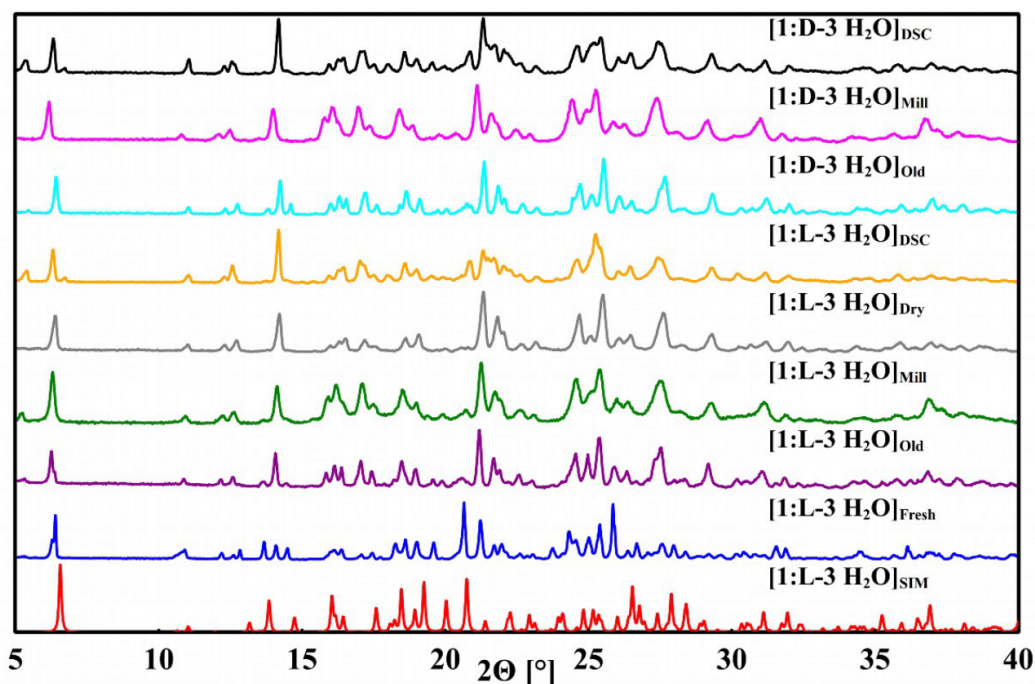


Figure S1. Recorded powder patterns of Baclofen:tartaric acid systems under different conditions in a range from 5°-40° 2 θ : (blue) a fresh sample of 1:L-3 • H₂O, shortly after crystallization, (purple) a sample of the same substance after six months, (green) LAG sample of Baclofen and L-tartaric acid, (grey) a vacuum dried sample of 1:L-3 • H₂O, (orange) after heating a fresh sample of 1:L-3 • H₂O in a DSC chamber to 140 °C and subsequent cooling before melting occurs, (cyan) 1:D-3 • H₂O after six months, (magenta) LAG sample of Baclofen and D-tartaric, (black) after heating a fresh sample 1:D-3 • H₂O in a DSC chamber to 140 °C and subsequent cooling before melting occurs. Simulated pattern of 1:L-3 • H₂O hydrate is shown in red.

Figure S2 shows that heating of a sample of Baclofen:DL-tartaric acid received by milling crystallization leads to small changes in the powder pattern and a slightly higher resolution of the occurring reflections.

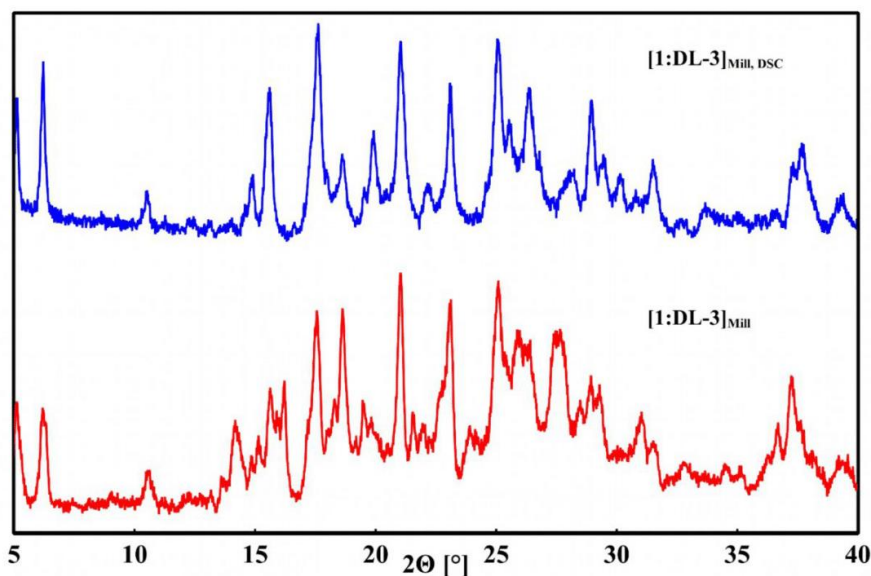


Figure S2. Recorded powder patterns of Baclofen:DL-tartaric acid under different conditions in a range from 5° - 40° 2θ . Baclofen and DL-tartaric acid sample after a methanol-assisted grinding (red) and the same sample after heating in a DSC chamber to 115°C and subsequent cooling before melting occurs (blue).

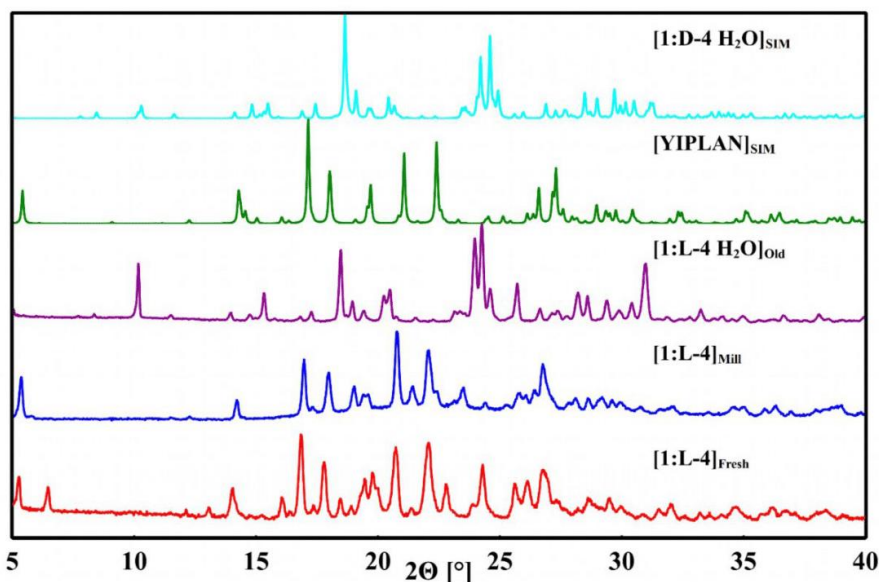


Figure S3. Recorded powder patterns of Baclofen:malic acid systems in a range from 5° - 40° 2θ : (red) sample of Baclofen and L-malic acid a few days after crystallization occurs; (blue) LAG sample of Baclofen and L-malic acid; (purple) $1:L-4 \cdot H_2O$ obtained from hexafluoro-2-propanol solution contaminated with water six months after crystallization occurs; (green) simulated from single crystal data provided by Córdova-Villanueva et al.^[50] (Cambridge Crystal Structure Database Ref. Code YIPLAN) and (cyan) simulated pattern of $1:D-4 \cdot H_2O$ from collected single crystals data.

The red pattern in **Figure S3** is in a good agreement with the blue pattern received by milling crystallization of Baclofen and L-malic acid under addition of 10 μL methanol at 25 Hz for 30 minutes as well as the simulated YIPLAN pattern but shows more reflections than both other patterns, which hints at a received phase mixture.

The purple pattern in **Figure S4** shares signals with the simulated patterns of Baclofen hydrate, Baclofen:D-malic acid hydrate and the YIPLAN pattern which leads to the conclusion, that the received phase is made up of a phase mixture of the named substances. The green and the cyan pattern are in good agreement with each other and both are phase mixtures consisting of Baclofen, Baclofen:L-malic acid hydrate and Baclofen hydrate. The pattern of the vacuum dried sample is amorphous, but the signals are in good agreement with the YIPLAN structure.

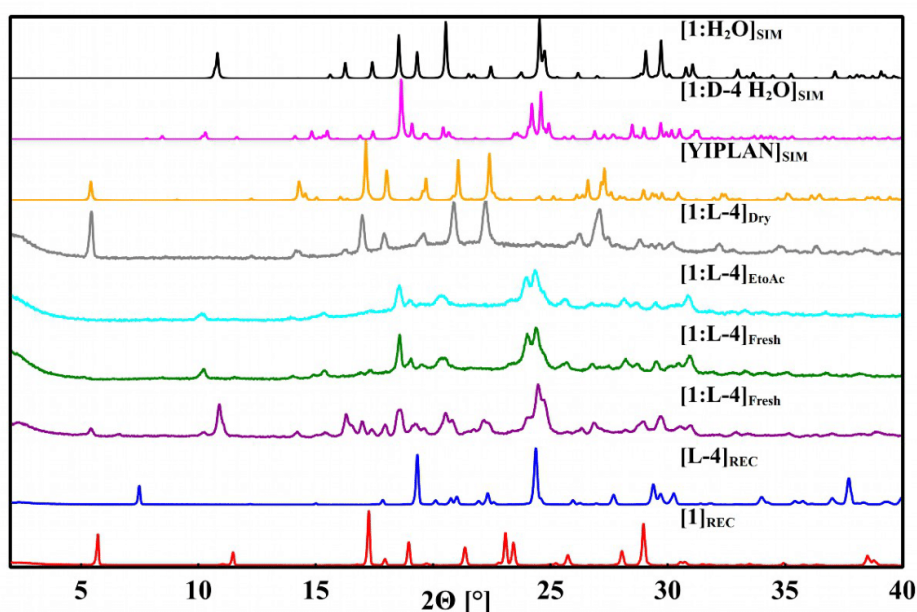


Figure S4. Overview on some recorded patterns of phase mixtures received by co-crystallization of Baclofen and L-malic acid under different conditions in a range from 2° - 40° 2θ : (red) Baclofen; (blue) L-malic acid; (purple) and (green) both samples of Baclofen and L-malic acid shortly after crystallization occurs; (cyan) **1:L-4** sample received from a solvent mixture of ethyl acetate and water shortly after crystallization occurs; (grey) a vacuum dried sample of **1:L-4**. Simulated powder patterns from single crystal data provided by Córdova-Villanueva et al.^[50] (CCDC Ref. Code YIPLAN) (orange), from single crystal data of **1:D-4 • H₂O** (magenta) and from single crystal data of **1 • H₂O** (black) are given for comparison.

The purple pattern in **Figure S5** shows large similarities to the patterns of Baclofen, Baclofen:D-malic acid hydrate and Baclofen hydrate. The green pattern shows similar signals as the YIPLAN pattern, Baclofen:D-malic acid hydrate and Baclofen hydrate. By comparing the cyan pattern to the recorded Baclofen pattern, it can be seen that heating of Baclofen:D-malic acid hydrate leads to decomposition of the sample to a highly amorphous Baclofen sample.

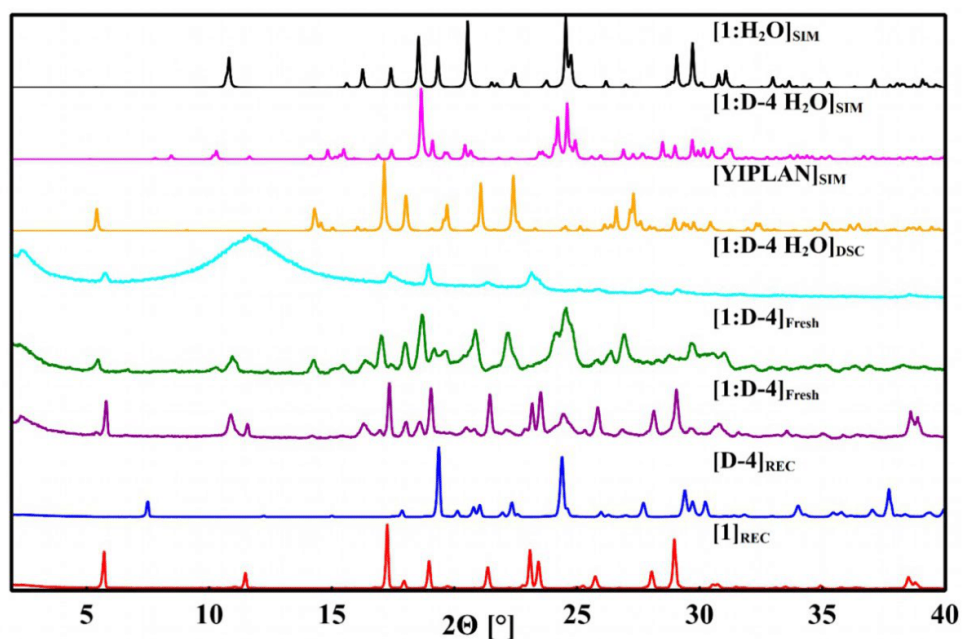


Figure S5. Recorded patterns of Baclofen:D-malic acid systems under different conditions in a range from 2°-40° 2 θ : Baclofen (red); D-malic acid (blue); different samples of 1:D-4 shortly after crystallization occurs (purple and green); 1:D-4 • H₂O after heating to 130 °C in a DSC chamber and subsequent cooling before melting (cyan); simulated from single crystal data provided by Córdova-Villanueva et al.^[50] (CCDC Ref. Code YIPLAN) (orange); simulated from single crystal data of 1:D-4 • H₂O (magenta) and of 1 • H₂O (black).

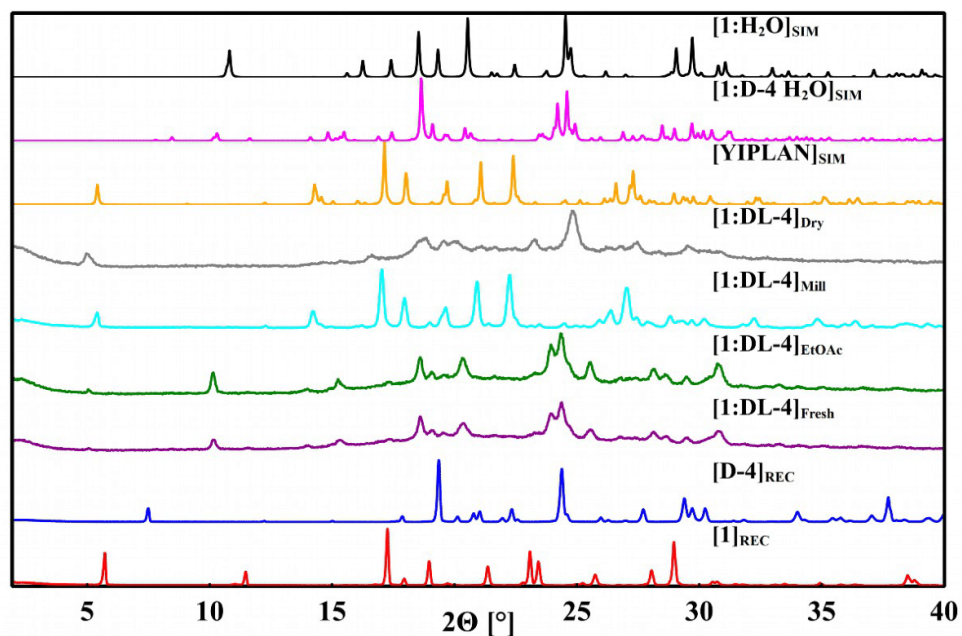


Figure S6. Recorded powder patterns of systems Baclofen:DL-malic in a range from 2°-40° 2 θ : (red) Baclofen, (blue) D-malic acid; (purple) 1:DL-4 shortly after crystallization, (green) 1:DL-4 from a solvent mixture of ethyl acetate and water; (cyan) LAG sample of Baclofen and DL-malic; (grey) a vacuum dried 1:DL-4.; (orange) simulated from single crystal data provided by Córdova-Villanueva et al.^[45] (CCDC Ref. Code YIPLAN^[46]); (magenta) simulated from single crystal data of 1:D-4 • H₂O and (black) simulated from single crystal data of 1 • H₂O .

7

Both patterns of Baclofen:DL-malic acid received from aqueous solution presented in **Figure S6** show large similarities to another. Both samples share signals with Baclofen, Baclofen hydrate, Baclofen:D-malic acid hydrate and the YIPLAN pattern, showing that the co-crystallization from solution lead to a phase mixture of named phases. The pattern of Baclofen:DL-malic acid received by milling crystallization is in good agreement with the simulated YIPLAN-pattern, showing that milling crystallization leads to a pure phase. The pattern of the vacuum dried sample shows that this method leads to a new, amorphous phase.

DSC-data in **Figure S7** obtained from the milling products Baclofen:D-malic acid and Baclofen:L-malic acid show the exact same melting signals only distinguishing in different resolutions of the signals recorded.

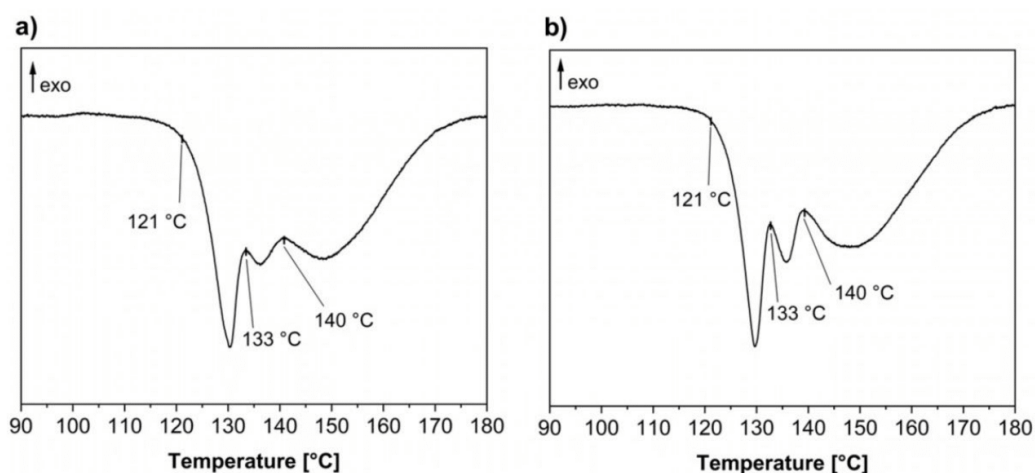


Figure S7. DSC-data of **1:D-4** (a) and **1:L-4** (b) samples obtained by milling crystallization of Baclofen and D- or L-malic acid under addition of 10 μL methanol at 25 Hz for 30 minutes. DSC was heated at 5°C min^{-1} , only important temperature ranges are shown for clarity.

As shown in **Figures S8** and **S9**, the samples produced by crystallization from solution and by milling crystallization are in a good agreement with each other and even with the vacuum dried sample. All samples show strong similarities to the simulated pattern of the Phenibut:L-tartaric acid hydrate, confirming that even by milling crystallization hydrate formation can be observed. It also seems that vacuum drying of the sample does not lead to the formation of an anhydrous system. All three recorded patterns show two signals at about $5.6^\circ 2\theta$, which is in contrast to the simulated pattern, leading to the conclusion that phase mixtures were produced with both methods.

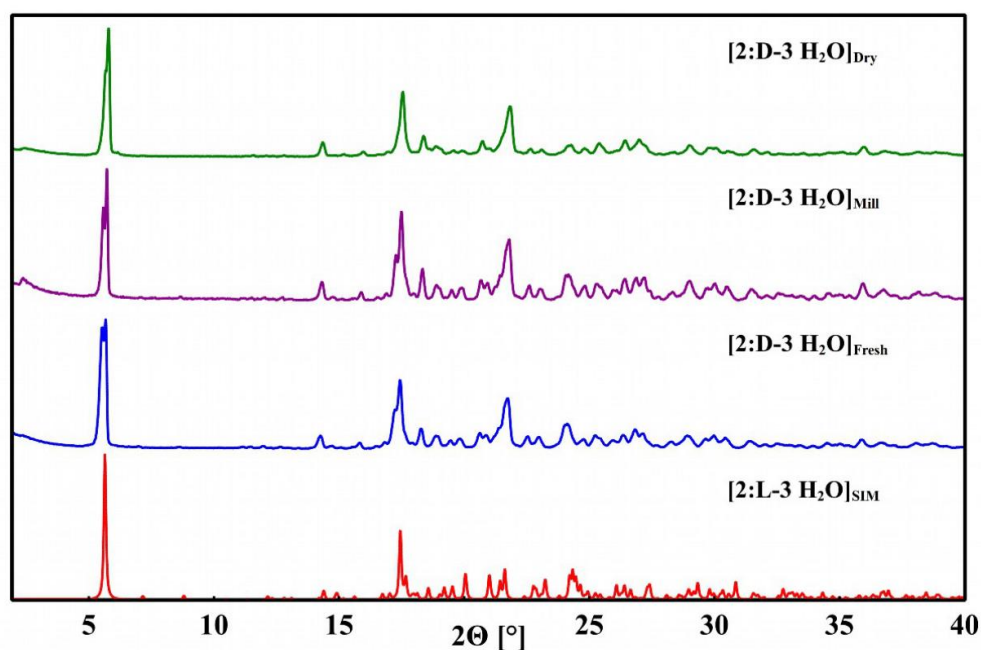


Figure S8. Recorded powder patterns of Phenibut:tartaric acid systems in a range from 2° - 40° 2θ : (red) $2:L-3 \cdot H_2O$ pattern simulated from single crystal data; (blue) $2:D-3 \cdot H_2O$ sample shortly after crystallization occurs; (purple) LAG sample of Phenibut and D-tartaric acid; (green) vacuum dried $2:D-3 \cdot H_2O$ sample.

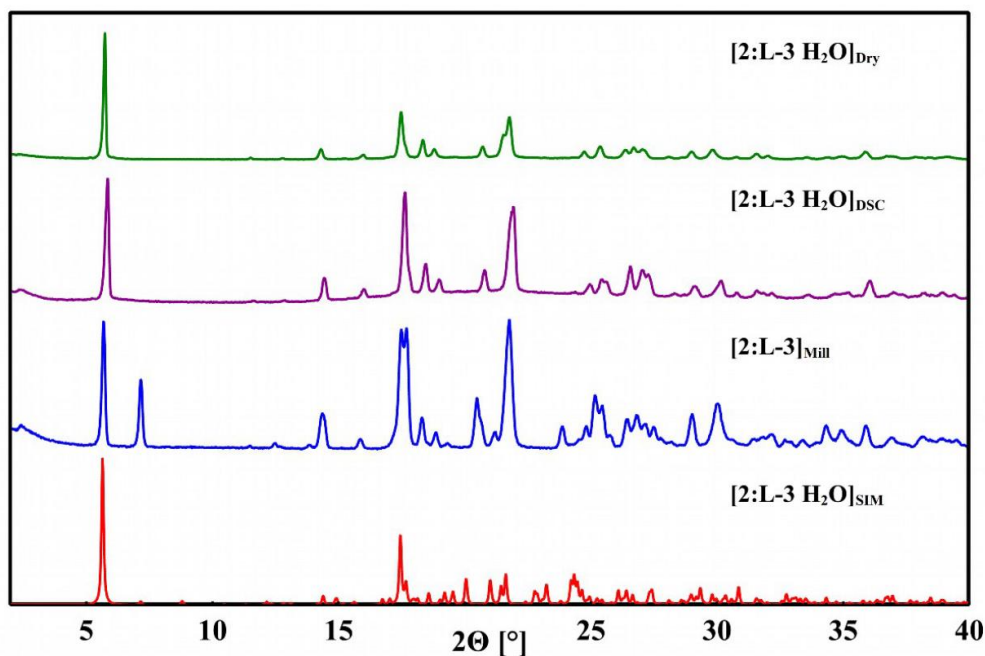


Figure S9. Further recorded powder patterns of Phenibut:L-tartaric acid systems under different conditions in a range from 2° - 40° 2θ . Simulated pattern from single crystal data of $2:L-3 \cdot H_2O$ (red) is compared to an LAG sample of Phenibut and L-tartaric acid (blue), $2:L-3 \cdot H_2O$ sample from aqueous solution after heating to $120^{\circ}C$ in a DSC chamber (purple) and a vacuum dried sample of $2:L-3 \cdot H_2O$ (green).

9

By comparison of the green and the orange pattern in **Figure S10** with the simulated pattern of Phenibut hydrate, it is obvious that in both cases samples of Phenibut hydrate were obtained through co-crystallization from aqueous solution. The purple and the cyan pattern are in good agreement with each other. The purple pattern still has some similarities to the pattern of Phenibut hydrate, showing signals at about 12° and 21.5° which do not occur in the pattern obtained by milling crystallization. The pattern of the vacuum dried sample of Phenibut:L-malic acid shows different signals than all other patterns, showing that vacuum drying lead to a new phase formation. The patten of vacuum dried Phenibut:DL-malic acid is similar to the pattern of pure Phenibut, showing that vacuum drying of this sample leads to decomposition of the Phenibut hydrate obtained from crystallization out of solution.

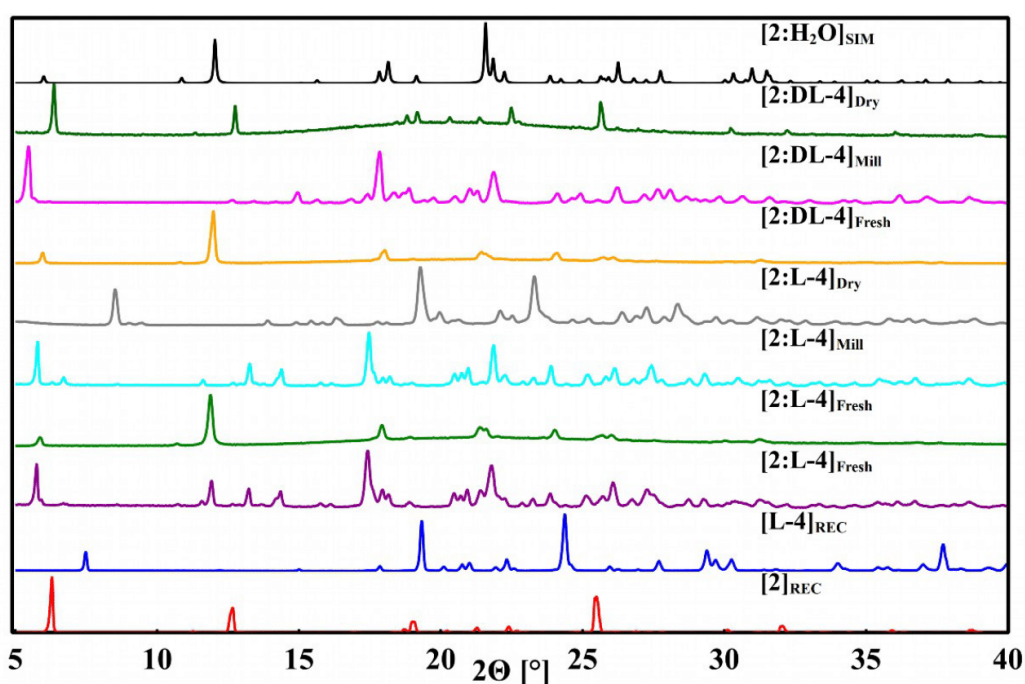


Figure S10. Recorded powder patterns of Phenibut:malic acid systems under different conditions in a range from 5° - 40° 2θ : (red) Phenibut; (blue) L-malic acid; (purple and green) different samples of **2:L-4** shortly after crystallization; (cyan) LAG sample of Phenibut and L-malic acid; (grey) a vacuum dried sample of **2:L-4**; (orange) **2:DL-4** shortly after crystallization occurs; (magenta) LAG sample of Phenibut and DL-malic acid; (dark-green) a vacuum dried sample of **2:DL-4** and (black) simulated pattern from single crystal data of **2 • H₂O**.

Infrared Spectroscopy (IR)

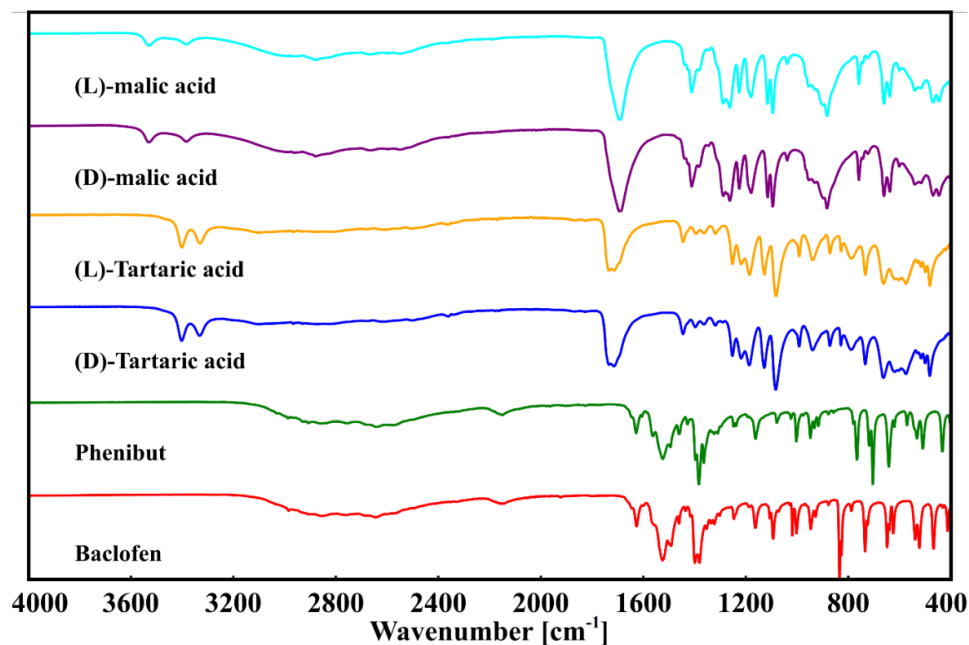


Figure S11. Recorded IR-spectra of used educts (red) Baclofen, (green) Phenibut, (blue) D-tartaric acid, (orange) L-tartaric acid, (purple) D-malic acid and (cyan) L-malic acid in a range from 4000 cm^{-1} to 400 cm^{-1} .

Table S8. Chosen bands corresponding to the carbonyl C=O stretching depicted in **Figure S11**.

Compound	Carbonyl Bands [cm^{-1}]
1	1646/1625/1602
2	1646/1627/1607
D-3	1735/1712
L-3	1735/1712
D-4	1696
L-4	1696

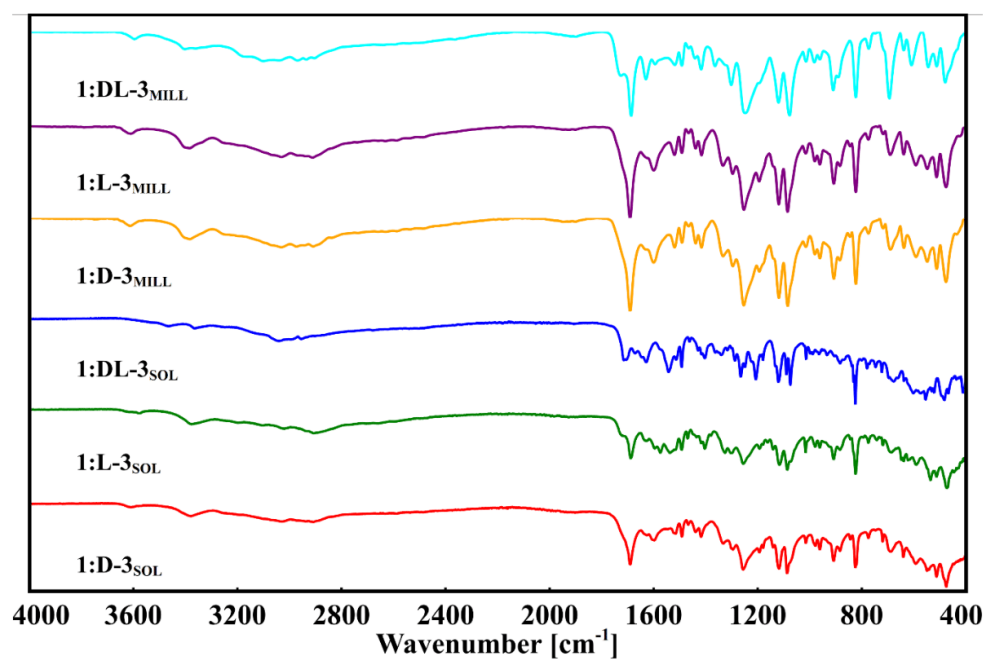


Figure S12. Recorded IR-spectra of Baclofen:tartaric acid systems under different conditions in a range from 4000 cm^{-1} and 400 cm^{-1} . Samples obtained via crystallization from solution: (red) 1:D-3, (green) 1:L-3, (blue) 1:DL-3 and samples after methanol-assisted grinding: (orange) Baclofen and D-tartaric acid, (purple) Baclofen and L-tartaric acid, (cyan) Baclofen and DL-tartaric acid.

Table S9. Chosen bands corresponding to the carbonyl C=O stretching depicted in **Figure S12**.

Compound	Carbonyl Bands [cm^{-1}]			
1:D-3 _{SOL}	1723/1691	1626		1599
1:L-3 _{SOL}	1724/1688	1626		1599
1:DL-3 _{SOL}	1715/1705	1672		1642/1629
1:D-3 _{MILL}	1724/1691	1631		1601
1:L-3 _{MILL}	1723/1691	1631		1601
1:DL-4 _{MILL}	1727/1687	1630		1595

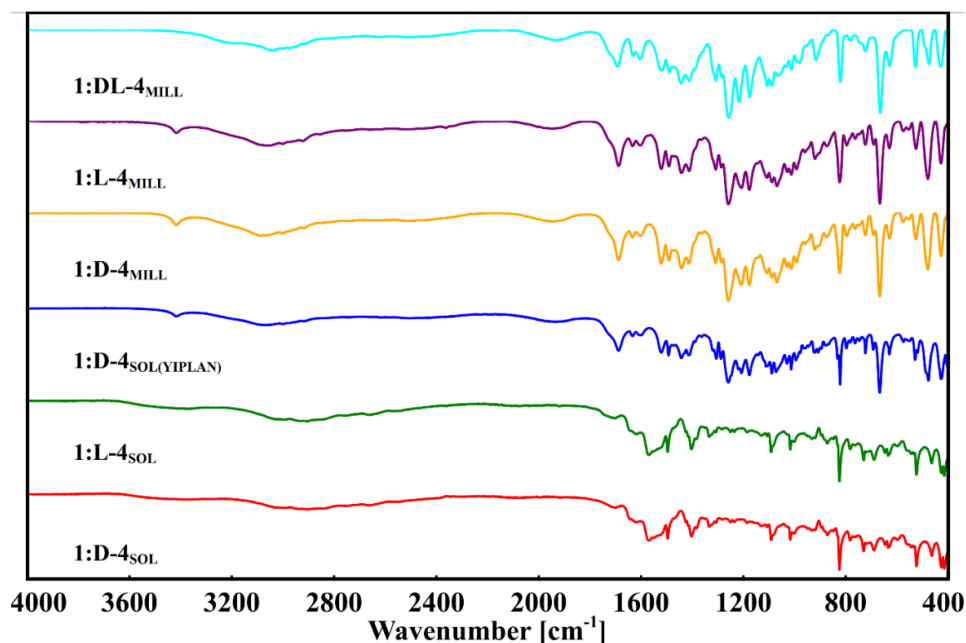


Figure S13. Recorded IR-spectra of Baclofen:malic acid systems under different conditions in a range from 4000 cm^{-1} and 400 cm^{-1} . Samples from solution crystallization of $1:\text{D-4} \cdot \text{H}_2\text{O}$ (red), $1:\text{L-4} \cdot \text{H}_2\text{O}$ (green) and of $1:\text{D-4}$ (blue) which showed similarities to the published YIPLAN structure in its powder pattern. Samples after LAG experiments: (orange) Baclofen and D-malic acid, (purple) Baclofen and L-malic acid, (cyan) Baclofen and DL-malic acid.

Table S10. Chosen bands corresponding to the carbonyl C=O stretching depicted in **Figure S13**.

Compound	Carbonyl Bands [cm^{-1}]		
$1:\text{D-4}_{\text{SOL}}$	1706	1646/1617	1599
$1:\text{L-4}_{\text{SOL}}$	1706	1646/1623	1599
$1:\text{D-4}_{\text{SOL}}(\text{YIPLAN})$	1727/1688	1633	1598
$1:\text{D-4}_{\text{MILL}}$	1728/1688	1633	1603
$1:\text{L-4}_{\text{MILL}}$	1731/1688	1631	1606
$1:\text{D4-4}_{\text{MILL}}$	1727/1693	1631	1603

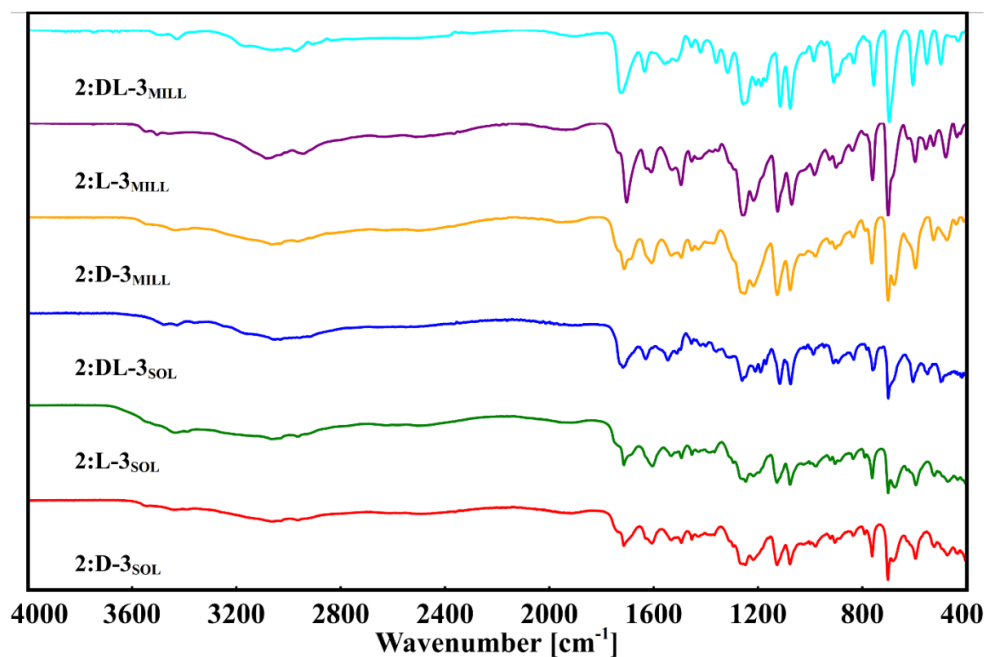


Figure S14. Recorded IR-spectra of Phenibut:tartaric acid systems under different conditions in a range from 4000 cm^{-1} and 400 cm^{-1} . Samples from solution crystallization: (red) **2:D-3**, (green) **2:L-3** and (blue) **2:DL-3**. Samples from LAG with methanol: (orange) Phenibut and D-tartaric acid, (purple) Phenibut and L-tartaric acid and (cyan) Phenibut and DL-tartaric acid.

Table S11. Chosen bands corresponding to the carbonyl C=O stretching depicted in **Figure S14**.

Compound	Carbonyl Bands [cm^{-1}]	
2:D-3_{SOL}	1743/1715	1631/1608
2:L-3_{SOL}	1745/1715	1631/1605
2:DL-3_{SOL}	1731/1718	1631
2:D-3_{MILL}	1741/1714/1686	1631/1608
2:L-3_{MILL}	1739/1703	1629/1609
2:DL-4_{MILL}	1727	1635

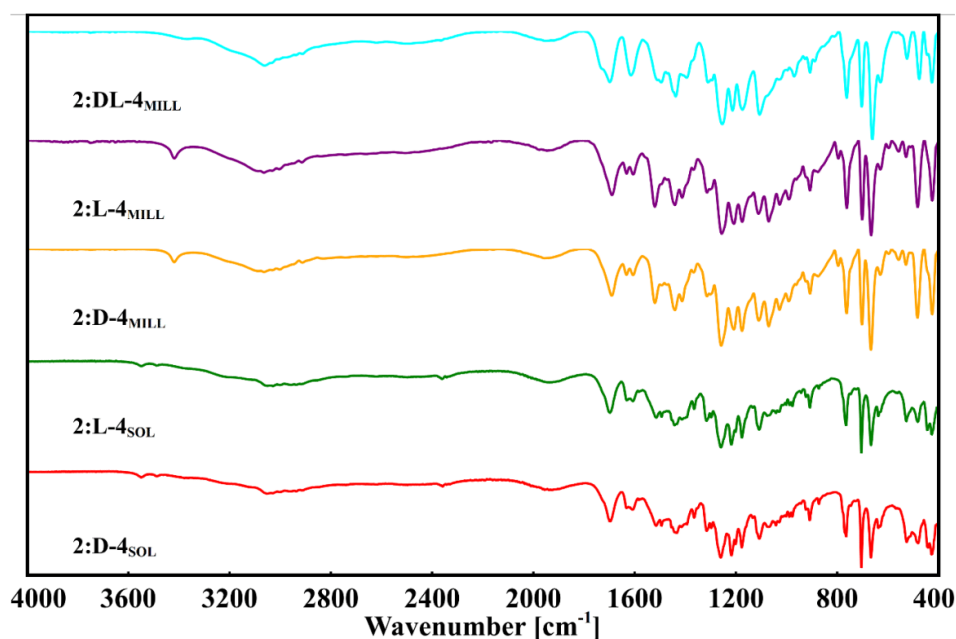


Figure S15. Recorded IR-spectra of Phenibut:malic acid systems in a range from 4000 cm^{-1} and 400 cm^{-1} . Samples obtained from solution crystallization: (red) **2:D-4**, (green) **2:L-4** and from LAG experiments: (orange) Phenibut and D-malic acid, (purple) Phenibut and L-malic acid, (cyan) Phenibut and DL-malic acid.

Table S12. Chosen bands corresponding to the carbonyl C=O stretching depicted in **Figure S15**.

Compound	Carbonyl Bands [cm^{-1}]	
2:D-4_{SOL}	1730/1699	1635/1608
2:L-4_{SOL}	1727/1698	1631/1607
2:D-4_{MILL}	1732/1691	1633/1607
2:L-4_{MILL}	1735/1690	1632/1606
2:DL-4_{MILL}	1733/1698	1614
2:D-4_{SOL}	1730/1699	1635/1608

IR-spectra show that carbonyl vibrational bands in multicomponent systems are multiplied and shifted regarding their positioning. In pure **1** and **2** a triple band at 1646/1625/1602 cm^{-1} and 1646/1627/1607 cm^{-1} is the only discernible carbonyl band. **3** shows a double band in 1735 cm^{-1} and 1712 cm^{-1} . **4** only exhibits a single band in 1696 cm^{-1} . In **1:3** systems, at least four signals are present in each system, ranging between 1727 cm^{-1} and 1599 cm^{-1} . As salt hydrates could be characterized by SCXRD in **1:D-3 • H₂O**, **1:L-3 • H₂O** and **1:DL-3 • H₂O**, and similar IR-bands are present in the milling products, it is probable that analogue compounds have formed as well. The same is true for **1:4** systems where **1:D-4 • H₂O** was characterized as a salt hydrate. Very similar IR-signals are present in **1:L-4 • H₂O**, and while the other systems show differing signals the splitting is similar. Multicomponent species with **2** exhibit less signals than their **1** counterparts, showing a maximum of two multi-signals each. Again, single crystal analysis of **2:L-3 • H₂O** and **2:DL-3** has revealed a proton transfer and herewith an ionized status of the molecules. The IR analysis indicates this for the other species as well. While no single crystals of **2:4** systems were measured, based on observations on all other species and a similar splitting of IR-bands present as in the previously mentioned compounds, it is highly probable that salts or hydrates of salts were obtained.

Thermogravimetric Analysis (TGA)

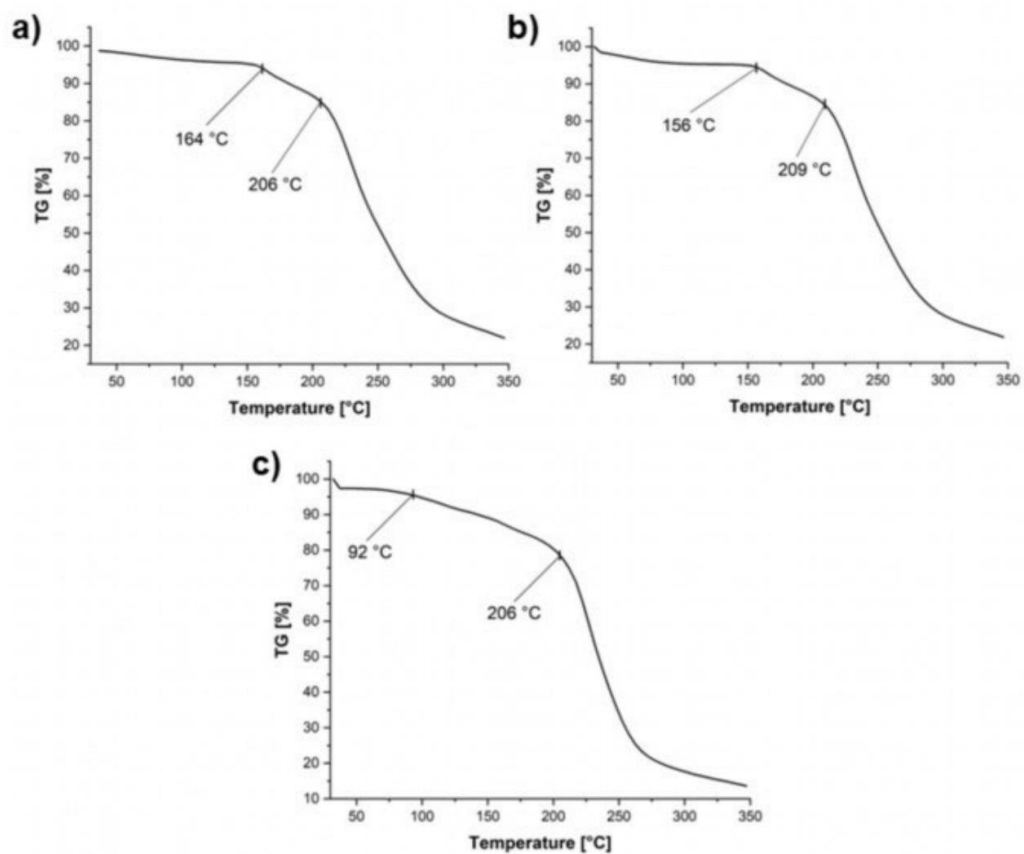


Figure S16. TGA-data of 1:D-3 · H₂O (a), 1:L-3 · H₂O (b) and 1:DL-3 · H₂O (c). TGA was heated at 10 °C min⁻¹ in a range from 30 °C to 350 °C.

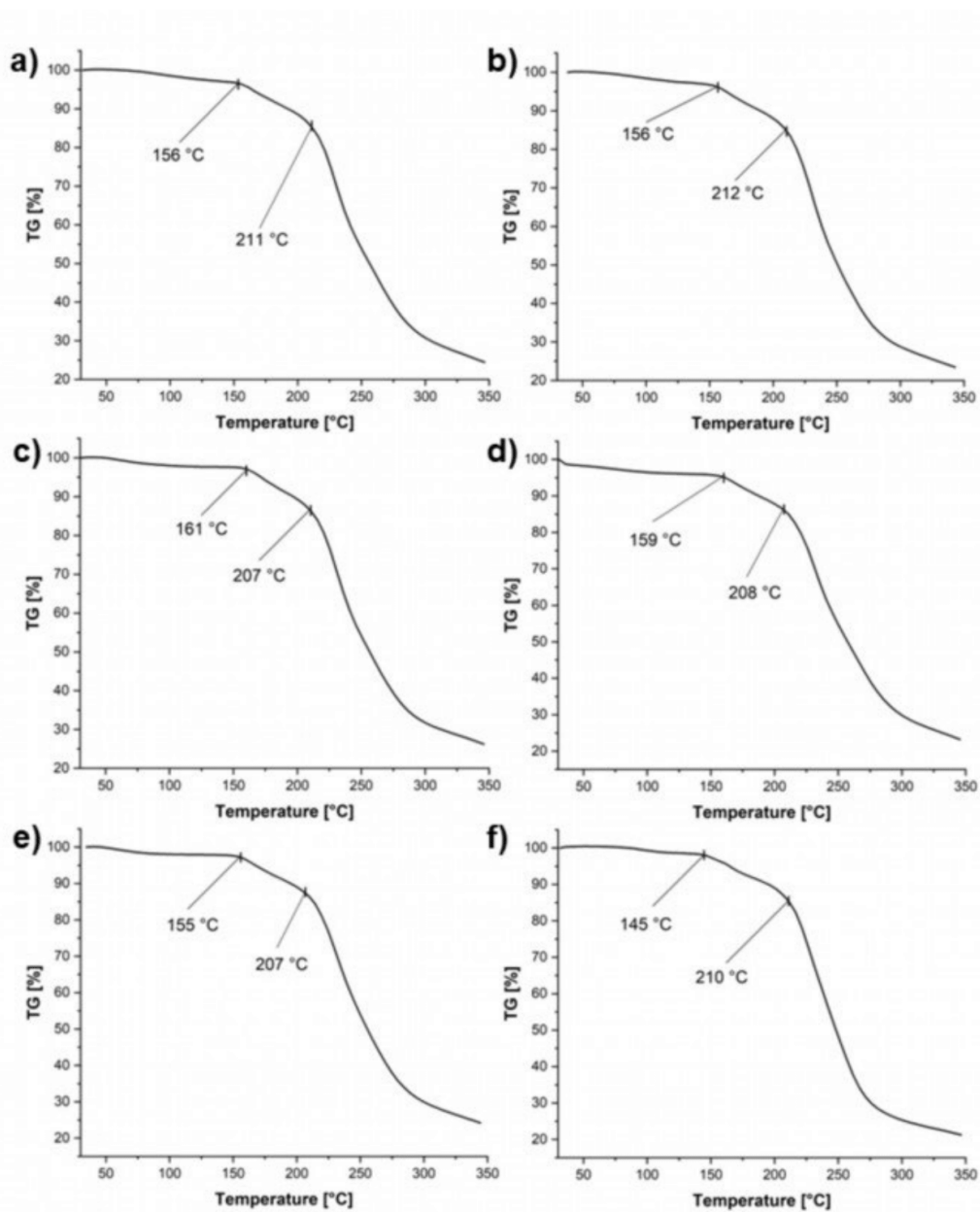


Figure S17. TGA-data of a LAG sample of Baclofen and D-tartaric acid with methanol (a), a LAG sample of Baclofen and L-tartaric acid with methanol (b), a LAG sample of Baclofen and DL-tartaric acid with methanol (c), a vacuum dried sample of 1:D-3 • H₂O (d), a vacuum dried sample of 1:L-3 • H₂O (e) and a vacuum dried sample of 1:DL-3 • H₂O (f). TGA was heated with 10 °C min⁻¹ in a range from 30 °C - 350 °C.

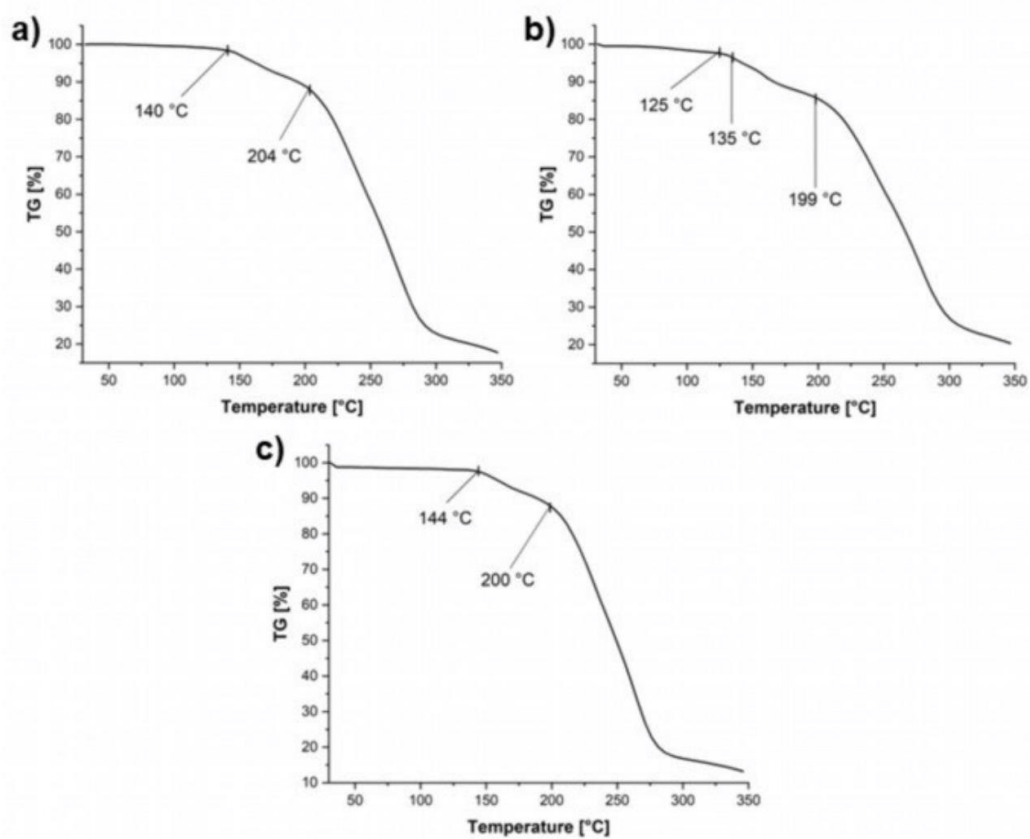


Figure S18. TGA-data of a sample of **1:D-4** (a), a sample of **1:L-4** (b) and a sample of **1:DL-4** (c). TGA was heated at 10 °C min^{-1} in a range from 30 °C to 350 °C .

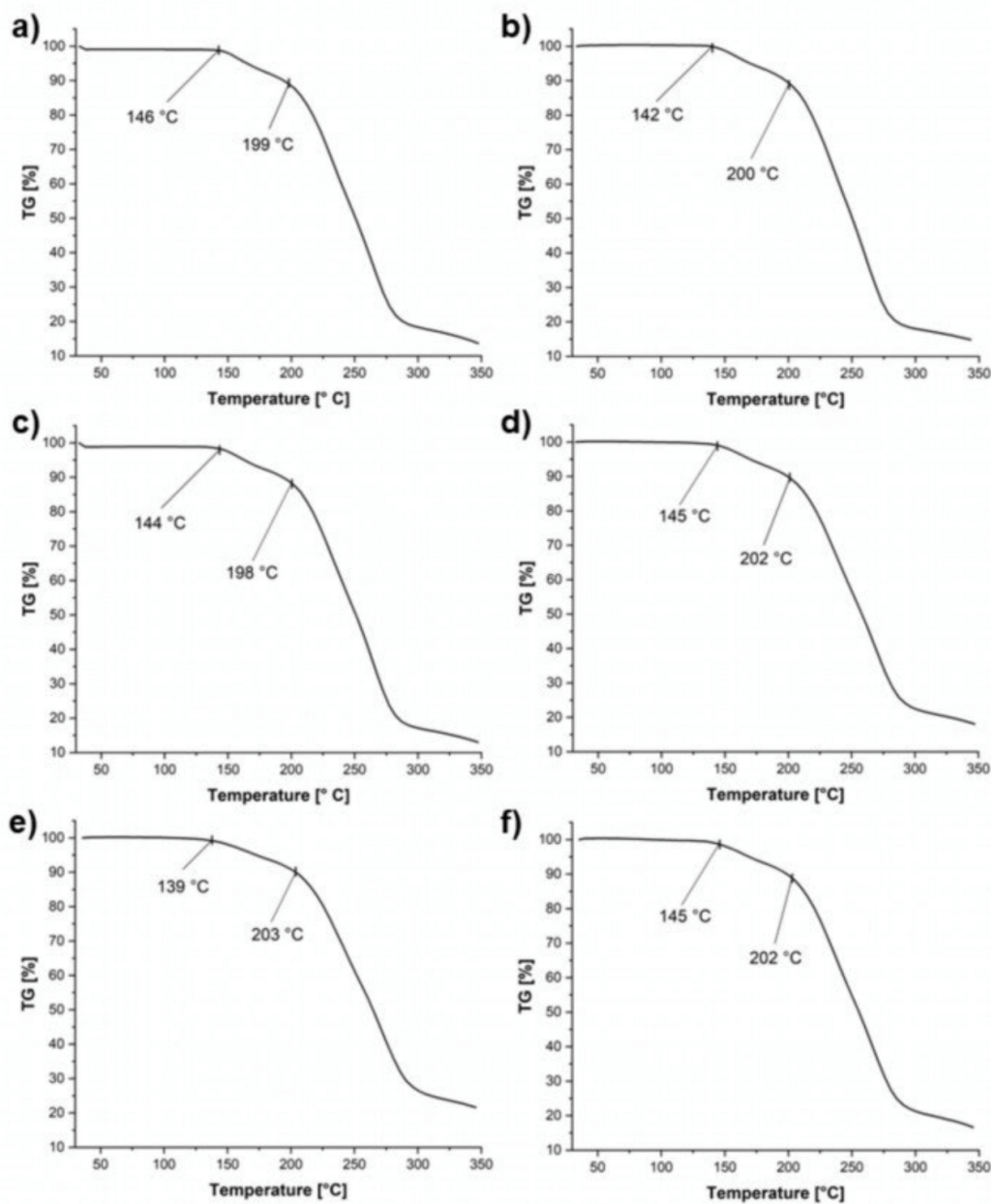


Figure S19. TGA-data of a LAG sample of Baclofen and D-malic acid with methanol (a), a LAG sample of Baclofen and L-malic acid with methanol (b), a LAG sample of Baclofen and DL-malic acid with methanol (c), a vacuum dried sample of 1:D-4 (d), a vacuum dried sample of 1:L-4 (e) and a vacuum dried sample of 1:DL-4 (f). TGA was heated with $10\text{ }^{\circ}\text{C min}^{-1}$ in a range from $30\text{ }^{\circ}\text{C}$ - $350\text{ }^{\circ}\text{C}$.

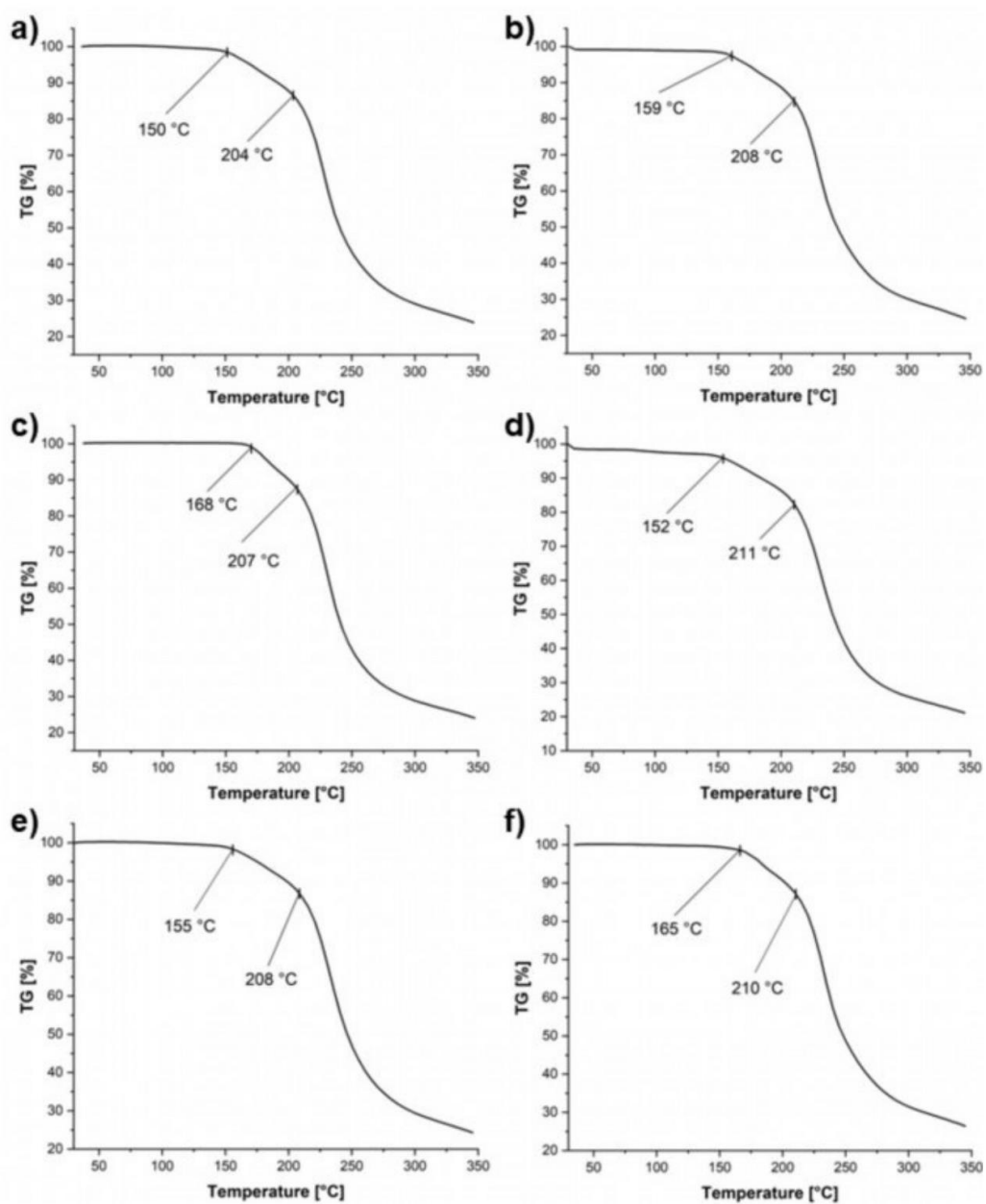


Figure S20. TGA-data of a LAG sample of Phenibut and D-tartaric acid with methanol (a), a LAG sample of Phenibut and L-tartaric acid with methanol (b), a LAG sample of Phenibut and DL-tartaric acid with methanol (c), a vacuum dried sample of 2:D-3 • H₂O (d), a vacuum dried sample of 2:L-3 • H₂O (e) and a vacuum dried sample of 2:DL-3 (f). TGA was heated with 10 °C min⁻¹ in a range from 30 °C - 350 °C.

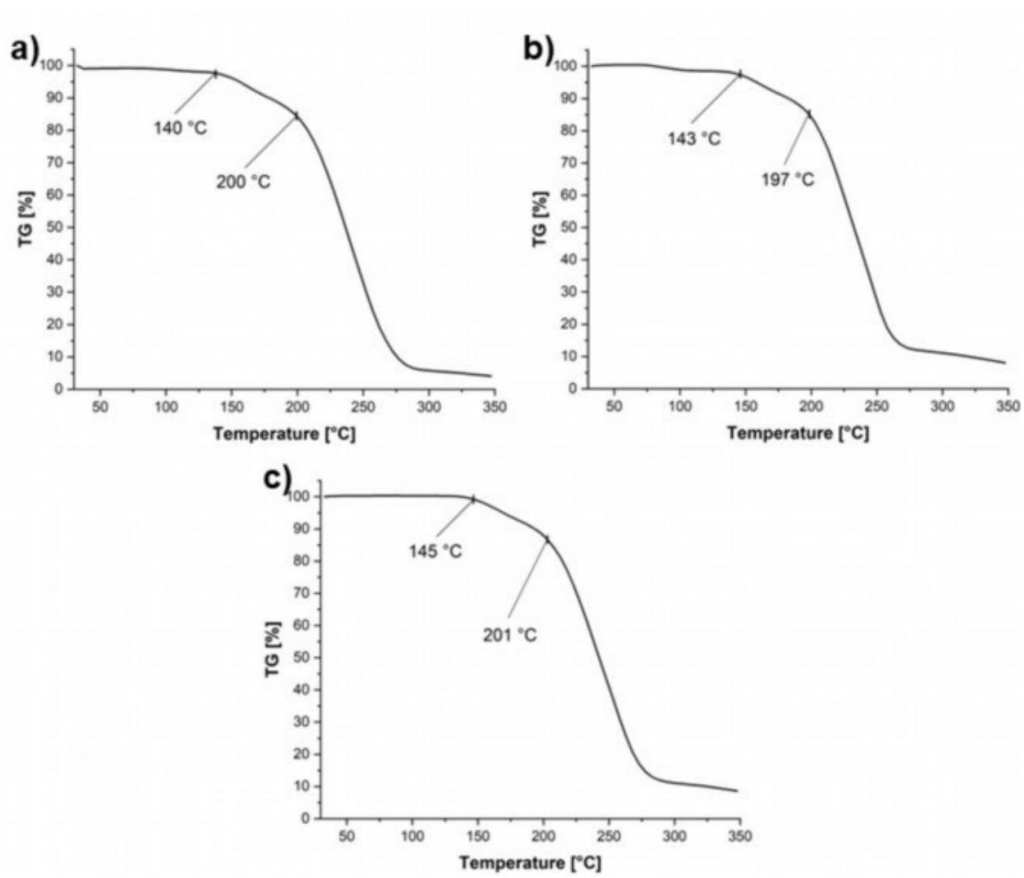


Figure S21. TGA-data of a LAG sample of Phenibut and D-malic acid with methanol (a), a LAG sample of Phenibut and L-malic acid with methanol (b) and a LAG sample of Phenibut and DL-malic acid with methanol (c). TGA was heated with 10 °C min^{-1} in a range from 30 °C - 350 °C .

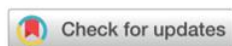
3.3 Co-crystals of zwitterionic GABA API's pregabalin and phenibut: properties and application

CrystEngComm



PAPER

[View Article Online](#)
[View Journal](#) | [View Issue](#)



Co-crystals of zwitterionic GABA API's pregabalin and phenibut: properties and application†

Cite this: *CrystEngComm*, 2022, 24, 8390

Daniel Komisarek, Takin Haj Hassani Sohi and Vera Vasylyeva *

Komisarek, D.; Haj Hassani Sohi, T.; Vasylyeva, V. Co-crystals of zwitterionic GABA API's pregabalin and phenibut: properties and application, *CrystEngComm*, **2022**, 24, 8390-8398.

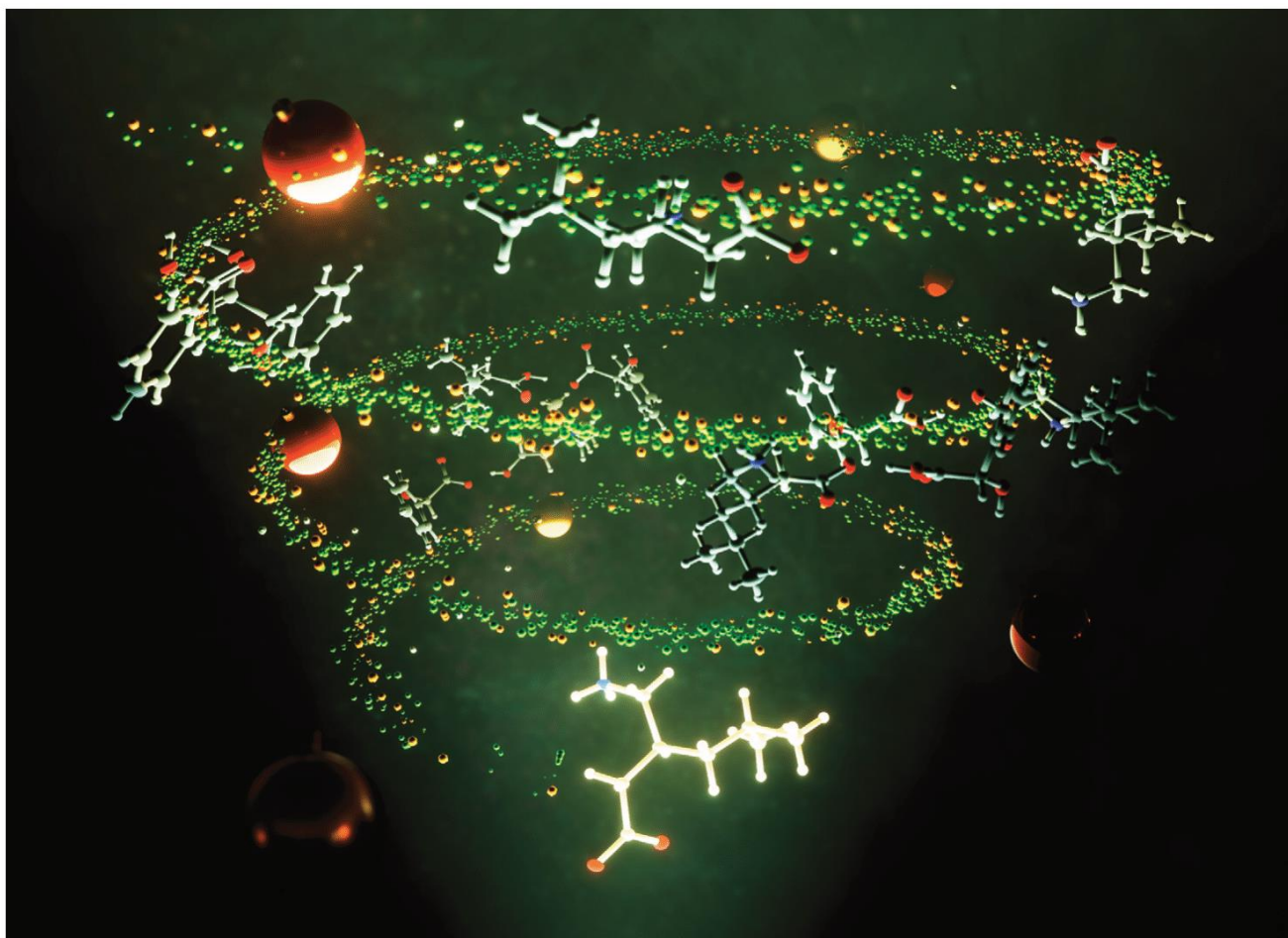
DOI: 10.1039/D2CE01416E

The article is licensed under a Creative Commons Attribution 3.0 Unported License. Material can be used in other publications without requesting further permissions from the RSC, provided that the correct acknowledgement is given.

In this third study, a process for deracemizing pregabalin with mandelic acid was enhanced on, by offering a quicker way of multicomponent species formation through mechanochemical means. In addition, an attempt was made to transfer this same process to Phenibut for comparison. Furthermore, it was shown that mandelic acid is essential for this process and malic acid cannot be used in the same way. *Quantum Espresso* was used to evaluate the energies of all the crystal systems obtained, thermal properties were determined using DSC and solubilities with ¹H-NMR spectroscopy. The work highlights that quite interesting applications can be developed via crystal engineering methods. However, it is also shown that the limits of transferability are quickly reached, since deracemization of Phenibut could not be achieved by the same route as for Pregabalin.

Contributions-list:

- Conceptualization of this work based on literature research and feedback from Dr. Vera Vasylyeva-Shor.
- Experimental work, including single crystal synthesis, mechanochemical and solvent-based crystallization of the investigated compounds and development of the deracemization process for Pregabalin.
- Measurement of SCXRD and PXRD, FT-IR spectroscopy, DSC, and ¹H-NMR solubilities.
- Data evaluation of the recorded analyses.
- *Quantum Espresso*-based evaluation of the determined crystal structures with Takin Haj Hassani Sohi.
- Manuscript preparation, including text writing, figure and table preparation, literature research and providing the supporting information.
- Revision process of the manuscript together with Dr. Vera Vasylyeva-Shor and Takin Haj Hassani Sohi before and after Peer-Review process.

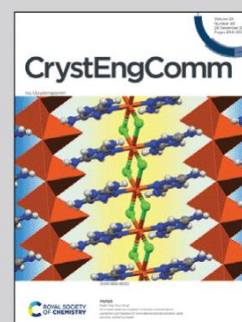


Showcasing research from Dr. Vera Vasylieva's laboratory,
Department of Structural and Inorganic Chemistry,
Heinrich-Heine University Duesseldorf, Germany.

Co-crystals of zwitterionic GABA API's pregabalin and
phenibut: properties and application

A set of multicomponent crystals of chiral, pharmaceutically active γ -amino butanoic acid derivatives pregabalin and phenibut is presented. APIs and co-formers mandelic and malic acid are in a similar pKa-range, which enables formation of either salts or co-crystals. With a detailed analysis of their crystal architecture, thermal properties, solubilities and lattice energies we bring the pieces of a puzzle together. This allows a development of an improved top-down racemic separation process. Mechanochemically synthesised salt/co-crystal mixtures of pregabalin:mandelic acid can be easily separated with water and acetone to give enantiopure pregabalin.

As featured in:



See Vera Vasylieva *et al.*,
CrystEngComm, 2022, **24**, 8390.



Cite this: *CrystEngComm*, 2022, 24, 8390

Received 13th October 2022,
Accepted 17th November 2022

DOI: 10.1039/d2ce01416e

rsc.li/crystengcomm

Co-crystals of zwitterionic GABA API's pregabalin and phenibut: properties and application†

Daniel Komisarek,  Takin Haj Hassani Sohi  and Vera Vasylyeva *

We present several multicomponent crystalline species formed by zwitterionic GABA analogues pregabalin and phenibut. These compounds are evaluated based on their crystal structure in congruence with properties such as melting behaviour, solubility, and lattice energies. Furthermore, it is discussed how major property distinctions between a homo- and heterochiral co-crystalline system enable enantiopurification of pregabalin.

1 Introduction

In crystal engineering of active pharmaceutical ingredients (APIs) the enhancement of attributes such as solubility or drug stability is an ongoing task. Various approaches are used to identify influences on crystal properties and increasingly more sensitive ways are developed to synthesize a desired target product.^{1–10} In many cases, thermodynamic factors such as lattice energies play an important role in the outcome of an attempted crystallization. Computational methods based on density functional theory (DFT) as well as force field applications have proven to be useful in determining energetic properties of single as well as multicomponent species.^{11–15} A common approach in using DFT-methods for lattice energy calculations is to compare energies of larger crystalline slabs to energy sums of occurring crystallographically independent molecules in the unit cell. However, differing molecular charges can make that task difficult. Aside from their effect on energy calculations, molecular charges build a basis for the classification of crystalline solids, for example as either a salt or a neutral co-crystal. Childs *et al.* describe the salt-co-crystal continuum in their 2007 contribution, evaluating molecular influences of the co-formers and their acidity as important factors for the charge status of the received product.¹⁶ In 2010 Braga *et al.* coined the term ionic co-crystal. After describing multicomponent crystalline entities composed of neutral barbituric acid and various alkali bromides or caesium iodide, their publication closes with the suggestion to further examine enthalpic and entropic contributions *via* theoretical

evaluations.¹⁷ They brought up the topic again in 2018, focussing on inorganic and organic co-crystalline systems, highlighting pharmaceutical and agricultural applications and especially the enantiomeric resolution of racemates as interesting uses.¹⁸ Additional discussions on the influence of ionicity on structure, properties or formation of co-crystalline species containing various charged molecular species have been conducted over the years,^{19–21} also in conjunction with organic/organic multicomponent crystalline entities. Various definitions for such structures have been proposed.^{22–26} As the established terminology has found acceptance in the community,^{27–30} methods to explicitly distinguish between salts and ionic co-crystals were designed.^{31,32} Next to varying molecular charges and acidity, a further molecular influence which can impact crystalline structure and lattice makeup is molecular chirality.^{18,33,34} Mandelic acid and its derivatives have shown remarkable chirality-based influences on co-crystalline systems when used as co-formers.^{35–37} In the past, several processes were patented that amongst other compounds use mandelic acid to separate *e.g.* (*S*)-pregabalin ((*S*)-4-amino-3-isobutylbutanoic acid) from its (*R*)-enantiomer. (*S*)-Pregabalin, the eutomer, which is the enantiomer that shows the desired pharmaceutical properties, and (*R*)-pregabalin, its distomer, with no or undesired pharmaceutical effects, can be separated *via* co-crystal formation with mandelic acid and subsequent co-former removal.^{38–44} Pregabalin is a pharmaceutically active γ -amino butanoic acid (GABA) derivative with a considerable amount of uses as an API. Pregabalin remained a staple treatment API for such diseases as epilepsy, neuropathic pain and anxiety disorders over the years since its release.^{45–54} It is chiral, shows zwitterionic charges on its GABA-subunit and being an amino acid is slightly acidic. A further related nootropic and anxiolytic drug is phenibut ((*RS*)-4-amino-3-phenylbutanoic acid) where the (*R*)-enantiomer is the eutomer,^{55–57} that has fallen out of favour for its abuse potential.^{58–62} As another

Department of Inorganic and Structural Chemistry I, Laboratory for Crystal Engineering, Heinrich-Heine-University, Universitätsstraße 1, 40225 Duesseldorf, Germany. E-mail: vera.vasylyeva-shor@hhu.de

† Electronic supplementary information (ESI) available. CCDC 2170100–2170108. For ESI and crystallographic data in CIF or other electronic format see DOI: <https://doi.org/10.1039/d2ce01416e>

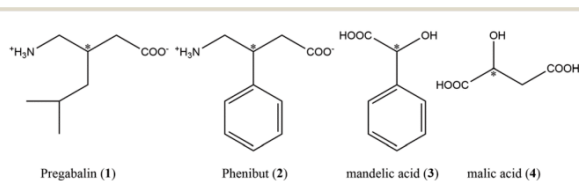


GABA-derivative, it also contains a zwitterionic subunit, poses chirality in C3 and is also a weakly acidic amino acid. In the present work various co-crystalline embodiments of enantiomers of pregabalin (**1**) and racemic phenibut (**2**) with co-formers mandelic acid (**3**) and malic acid (**4**) are examined (Scheme 1). Pregabalin exhibits an unusual behaviour to form a zwitterionic/neutral co-crystal with mandelic acid as first described by Samas *et al.* in 2007,⁶³ or a system composed solely of charged molecules depending on whether a homo- or heterochiral set of co-formers is co-crystallized. For comparison a set of multicomponent systems of pregabalin with malic acid and phenibut with mandelic acid is presented to show that the described behaviour is unique for pregabalin and mandelic acid only. Molecular influences such as zwitterionicity, chiral information and compound acidity in multicomponent entities are discussed in congruence with structural makeup and intermolecular interactions, especially hydrogen bond (HB) as well as properties like melting behaviour, solubility in aqueous medium and lattice energies. These findings are then applied to explain how the enantiopurification of pregabalin according to the established process with mandelic acid can be understood and improved on. It is shown how a specific set of molecular and structural influences enables a useful application.

2 Experimental and computational methods

Single-crystal X-ray diffraction

Suitable single crystals were selected from the sample and mounted on a cryo-loop under protective oil. Diffraction data were recorded with a Rigaku XtaLAB Synergy S diffractometer with Hybrid Pixel Arrow detector and a PhotonJet X-ray source using Cu-K α radiation ($\lambda = 1.54182 \text{ \AA}$) at $100.0 \pm 0.1 \text{ K}$ with ω -scans. Data reduction and absorption correction were conducted on CrysAlisPRO v. 42 software, numerical absorption correction based on Gaussian integration over a multifaceted crystal model and empirical absorption correction using spherical harmonics, implemented in SCALE3 ABSPACK scaling algorithm was used.⁶⁴ The single crystal structures were analyzed and refined by using direct methods (SHELXT-2015), full-matrix least-squares refinements on F^2 were performed using SHELXL2017/01 software package.^{65,66} Structure solution and refinements were conducted with OLEX2-1.5 software package. Hydrogen atoms were experimentally refined, all esds (except the esd in the dihedral angle between two l.s. planes) are estimated



Scheme 1 Compounds used in this work. APIs pregabalin and phenibut as well as cofomers mandelic- and malic acid.

using the full covariance matrix. The cell esds are taken into account individually in the estimation of esds in distances, angles and torsion angles; correlations between esds in cell parameters are only used when they are defined by crystal symmetry. An approximate (isotropic) treatment of cell esds is used for estimating esds involving l.s. planes.⁶⁷ Figures were prepared with Mercury software v. 2020.2.0.⁶⁸

Differential scanning calorimetry

Measurements were performed on a Linkam DSC 600 with nitrogen cooling and heating range from -190 – $600 \text{ }^\circ\text{C}$ in alumina crucibles.

X-ray powder diffraction

Measurements were performed on a Rigaku Miniflex diffractometer in $\theta/2\theta$ geometry at ambient temperature using Cu-K α radiation ($\lambda = 1.54182 \text{ \AA}$).

Lattice energy calculations

Quantum Espresso (QE) PWSCF v. 6.6 was used to perform periodic calculations based on the Perdew–Burke–Ernzerhof (PBE) functional.⁶⁹ The PBEsol basis set was used to describe pseudo potentials. Lattice energies were determined by geometric optimization energies of crystal structures as measured compared to ideal gas states of the participating molecules in a vacuum cluster, similar to the method described by Marchese Robinson *et al.* and Voronin and colleagues.^{12,14}

Diffraction quality single crystals

Multicomponent species (*S,S*)-1:3, (*R,R*)-1:3, (*S,R*)-1:3, (*R,S*)-1:3, (*S,S*)-1:4, (*S,R*)-1:4 and (*R,S*)-2:3 were obtained by co-crystallization of equimolar amounts of co-formers from aqueous solution and subsequent evaporation of the solvent at room temperature. Single crystals of single component species **1** and **2** were obtained by dissolution of powdery substance in aqueous medium and subsequent evaporation of the solvent at room temperature.

Enantiopurification of pregabalin

Two batches of racemic pregabalin hydrate (1.375 g, 7.756 mmol, 1 eq.) and enantiopure mandelic acid (1.180 g, 7.756 mmol, 1 eq.) were co-grinded with a Retsch MM400 ball mill for 40 min at 25 Hz using two 25 mL stainless containers fitted with one PTFE-ball (ϕ 2 cm) each. The received co-crystalline substance was subsequently washed with water and dried at $45 \text{ }^\circ\text{C}$ thrice, using 12 mL water in the first wash, 6 mL water in the second wash and 4 mL water in the third washing instance to remove the more soluble heterochiral species. The remaining residue was then stirred in a mixture of 75 mL acetone and 500 μL water for 40 h at room temperature. Filtration of the powdery residue led to enantiopurified pregabalin.



IR spectra

IR-spectra were recorded on the Bruker Tensor 27 Fourier transformed IR device in attenuated total reflectance mode in the range 4000 cm^{-1} to 400 cm^{-1} . Spectra are shown in the ESI.†

$^1\text{H-NMR}$ spectra

$^1\text{H-NMR}$ spectra for solubility determination were recorded on a Bruker Avance III NMR-spectrometer at 600 MHz and are shown in the ESI.†

Chemicals

The following chemicals were purchased and used without further purification: (*rac*)-pregabalin hydrate from aber, (*rac*)-phenibut from BLDpharm, (*S*)-mandelic acid from G&K, (*R*)-mandelic acid from TCI, (*S*)-malic acid from GLENTHAM LIFE SCIENCES and (*R*)-malic acid from BLDpharm. (*S*)-Pregabalin and (*R*)-pregabalin were produced by enantiomeric enrichment from (*rac*)-pregabalin hydrate according to the described procedure.

3 Results and discussion

3.1 Properties

In 1:3-systems no protonic shift occurs between co-formers if a homochiral (*S,S*) or (*R,R*) chirality is present, while each molecule becomes formally charged in species of (*S,R*) or (*R,S*) chirality in pregabalin:mandelic acid co-crystalline entities (Fig. 1). Homochiral forms crystallize isostructurally in regard to each other as do the heterochiral species. Both homo- and heterochiral pairs can be synthesized from solution as well as through neat grinding. Considering 1 and 3 properties, the only significant difference is their molecular chirality. In terms of acidity, a $\text{p}K_{\text{a}1}$ value of 4.2 is reported for 1 and 3.41 for 3,^{70,71} resulting in a $\Delta\text{p}K_{\text{a}}$ value of 0.79. According to Childs *et al.* this matches a defined murky area of $\Delta\text{p}K_{\text{a}} = 0-3$ for the solid-state protonation where both a salt as well as a co-crystal formation can occur, and additional molecular influences play a role.¹⁶ Similar observations for small structural changes have been conducted in the past. Trifluoroacetic acid becomes an ionic solid at low temperatures when hydrogenated, but a molecular solid when deuterated.⁷² It appears likely that the slight change in molecular chirality has a similar energetic effect in 1:3-species, favouring ionization in heterochiral forms while keeping default charges in homochiral ones. To highlight the uniqueness of the described system, further similar compounds (*S,S*)-1:4, (*S,R*)-1:4 as well as (*R,S*)-2:3, were co-crystallized from aqueous solution. Structural characteristics as well as thermodynamic properties were compared between API's and the received multicomponent species. A detailed comparison of hydrogen bonds shows similar characteristics in all compounds regardless of their protonation status (Table 1). The $\text{p}K_{\text{a}}$ values should be considered to enhance the understanding of the present HB characteristics. The $\text{p}K_{\text{a}1}$ value of 4 is

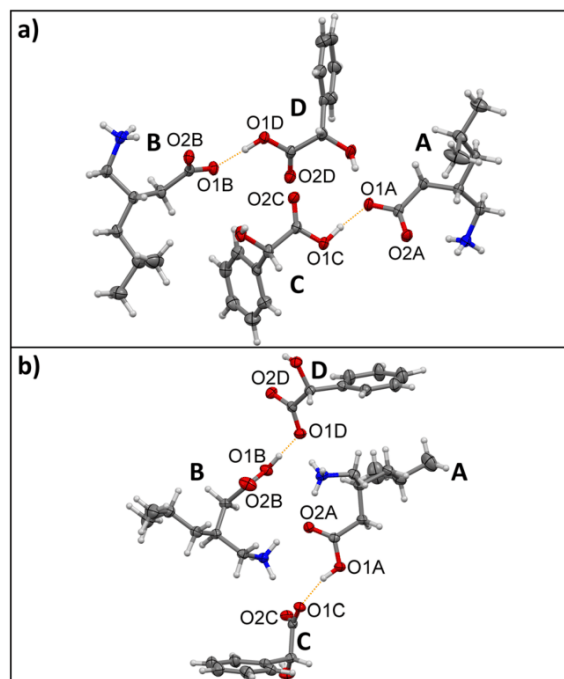


Fig. 1 Illustration of the protonic shift in the asymmetric units of a) homochiral (*S,S*)-1:3 and b) heterochiral (*S,R*)-1:3. Four crystallographically non-equivalent occurring molecules are marked as A, B, C and D respectively. Proton transfer occurs in (*S,R*)-1:3 between pregabalin A's O1A and mandelic acid C's O1C as well as pregabalin B's O1B and mandelic acid D's O1D. Carbon atoms are depicted in grey, hydrogen atoms in white, nitrogen atoms in blue and oxygen atoms in red. The protonic shift is highlighted in a dotted orange line.

3.40,⁷³ and that for 2 is 4.44,⁷⁴ giving $\Delta\text{p}K_{\text{a}}$ values of 0.8 for the 1:4-species and 1.03 for the 2:3 system. All systems are placed in the previously mentioned range of poor definability of the solid-state classification and all form strong – mid

Table 1 An overview of the overall number of hydrogen bonds in the systems, compared to those occurring between two charged subunits. Average, the shortest and the longest HB donor/acceptor distances and their corresponding angles are compared. The average values are calculated for each different occurring HB interaction in the unit cell. Samples composed solely of charged molecules and entries solely involving interactions of charged subunits are written in bold. Carboxylate or ammonium residues in zwitterionic forms are considered charged even though the molecules are overall formally neutral

Sample	Charged HB/all HB	$\bar{\Delta} \text{D}\cdots\text{A}$ [Å]/ $\bar{\Delta}\text{-H}\cdots\text{A}$ [°]	Min. $\text{D}\cdots\text{A}$ [Å]/ $\text{D-H}\cdots\text{A}$ [°]	Max. $\text{D}\cdots\text{A}$ [Å]/ $\text{D-H}\cdots\text{A}$ [°]
(<i>S</i>)-1	3/3	2.751/171	2.728(0)/171(2)	2.771(1)/172(2)
(<i>R</i>)-1	3/3	2.752/172	2.731(2)/174(2)	2.767(2)/172(3)
(<i>rac</i>)-2	3/3	2.767/168	2.732(3)/160(3)	2.795(3)/173(2)
(<i>S,S</i>)-1:3	6/12	2.784/158	2.487(3)/174(2)	3.036(4)/151(4)
(<i>R,R</i>)-1:3	6/14	2.818/152	2.489(7)/172(4)	3.038(2)/148(3)
(<i>S,R</i>)-1:3	4/14	2.799/145	2.570(3)/179(6)	3.012(3)/121(3)
(<i>R,S</i>)-1:3	4/14	2.797/144	2.570(2)/174(4)	3.006(2)/129(2)
(<i>R,S</i>)-2:3	3/7	2.821/151	2.504(2)/175(4)	3.020(2)/117(2)
(<i>S,S</i>)-1:4	2/8	2.827/153	2.446(4)/172(3)	3.154(3)/112(2)
(<i>S,R</i>)-1:4	2/8	2.798/154	2.475(2)/175(3)	3.103(2)/127(3)



strength HBs considering their intermolecular distances. Small ΔpK_a values also facilitate the formation of stronger hydrogen bonds.⁷⁵ This shows why the investigated substances behave structurally similar. Even though some of them are composed of overall neutral molecules and some are charged, they all fall into a range of inconclusive pK_a -influence on protonation behaviour, with the oddity present between homo- and heterochiral 1:3-systems to stay default or protonate/deprotonate apparently solely based on the molecular chirality. Closer examination of HB properties highlights the similarities even further. Except for single species **1** and **2**, where the average HB distance is about 2.75–2.77 Å, the HB average is closer to 2.8 Å in all multicomponent compounds. Interestingly, the shortest interactions never occur between two charged subunits like ammonium and carboxylate. While the shortest HB lengths are observed in malic acid homo- and heterochiral forms (*S,S*)- and (*S,R*)-1:4 which are both composed of charged molecules with 2.446(4) Å and 2.475(2) Å, the mandelic acid overall neutral homochiral (*S,S*)-1:3 Å comes closely thereafter with 2.487(3) Å. The corresponding average HB for this system with 2.784 Å is the shortest among the HB averages in multicomponent entities suggesting the strongest overall HB-motif. Average HB distances in multicomponent systems show a rather large deviation from 0.043 Å up to 0.124 Å. On the other hand, single component species **1** and **2** show a more uniform dispersion of HB distances. Here, the average variation is only 0.016 Å, 0.004 Å in the shortest and 0.028 Å in the longest HB. Hydrogen bonds in single-component structures are not exceptionally short, but on average slightly shorter than in the multicomponent systems. This emphasizes that while molecular charges might shift in the described compounds, they all behave structurally similar regarding their HB characteristics, and multicomponent species stay similar to single component APIs. In general, in the most of these systems it is not possible to discern which structural features are influenced by pK_a distinctions and which by molecular influences, but for the 1:3-species chirality inversion seems to be the most probable cause for the ionization behaviour. Furthermore, ionicity does not appear to have a significant impact on the structural makeup, especially regarding HB lengths and angles. While structurally similar compounds are formed in all investigated species, they do show some significant distinctions in their melting behaviour, solubility and lattice energies (Table 2). As was established in the past, higher melting points correlate with lower solubilities.^{76–78} The highest solubility is present in 1:4 that melt below 100 °C with 85 °C for (*S,S*) and 95 °C for (*S,R*) respectively. In 1:3-systems the heterochiral forms melt 25 °C lower than their homochiral counterparts and their solubility is about nine times higher at 316 ± 18 g L⁻¹ and 307 ± 6 g L⁻¹ for (*S,R*) and (*R,S*) as compared to 37 ± 1 g L⁻¹ and 40 ± 4 g L⁻¹ for (*S,S*)- and (*R,R*)-species. All in all, multicomponent systems composed of charged molecules reach far higher solubilities than their zwitterionic or neutral counterparts. This is interesting especially in the case of 1:3

Table 2 Overview on the determined melting points, solubilities in aqueous phosphate buffer at pH 6.8 and 37 °C as well as lattice energies calculated with quantum espresso. Bold written samples are composed solely of charged molecules. Mandelic and malic acid solubilities are given in ES††

Sample	Melting point [°C]	Solubility [g L ⁻¹]	E_{lat} [kJ mol ⁻¹]
(<i>S</i>)- 1	185	35 ± 0.4	-195.08
(<i>R</i>)- 1	187	33 ± 0.3	-195.17
(<i>rac</i>)- 2	— ^a	18 ± 1	-367.68
(<i>S,S</i>)- 1:3	138	37 ± 1	-320.36
(<i>R,R</i>)- 1:3	132	40 ± 4	-320.99
(<i>S,R</i>)-1:3	111	316 ± 18	-304.66
(<i>R,S</i>)-1:3	105	307 ± 6	-307.77
(<i>R,S</i>)- 2:3	150	71 ± 3	-343.23
(<i>S,S</i>)-1:4	85	>800 ^b	-356.66
(<i>S,R</i>)-1:4	95	>800 ^b	-363.05

^a (*rac*)-Phenibut decomposes prior to melting at about 200 °C, as such no melting point could be determined. ^b The maximum solubility could not be determined. No reliable results could be obtained from the highly viscous substance at higher concentrations.

homo- and heterochiral forms. Even though solubility of **3** is about five times higher than that of **1** with 203 ± 3 g L⁻¹ and 35 ± 0.4 g L⁻¹ or 33 ± 0.3 g L⁻¹ respectively, a substantial increase in solubility is not reached in the homochiral co-crystal forms. In co-crystalline entities the solubility is generally linked to several parameters such as co-former solubility, solvent as well as its pH value, co-former pK_a values, co-former complexation by solvent, co-former ratio and ionicity.^{79–82} As the same pH-stable solvent conditions were used in all cases and neither the co-former, the co-former ratio nor the co-former pK_a was changed, it is highlighted how the chirality induced change in ionicity possibly affects solvent complexation and thereby increases solubility in heterochiral 1:3-forms compared to the homochiral systems. It is furthermore surprising that while the melting point in homochiral 1:3-forms is decreased and **3** is substantially more soluble than **1**, the solubility increase is practically negligible. This indicates that ionicity plays a key role for the dissolution behaviour. In case of 1:4-forms, the mentioned criteria for the co-crystal solubility are fulfilled more uniformly. The solubility of **4** with 2061 ± 76 g L⁻¹ is exceedingly high compared to that of pure **1**, all components are ionized and a very high solubility of more than 800 g L⁻¹ is reached in both cases. In 2:3 an increase of solubility up to 71 ± 3 g L⁻¹ is also achieved, which is comparatively low. Here, the increase is most probably due to the large difference between the solubilities of **2** and **3** with 18 ± 1 g L⁻¹ and 203 ± 3 g L⁻¹ respectively. It is noteworthy that this system is heterochiral, yet here differing chirality does not cause a difference in ionicity as is the case in heterochiral 1:3-species. This further confirms that ionicity plays an important role in the solubility increase in these compounds, having a larger impact than the co-former solubility alone. Lattice energies do not appear to impact solubility in a significant manner, as all multicomponent species are in a similar range, the lowest values present in homochiral 1:3-forms with about -320 kJ



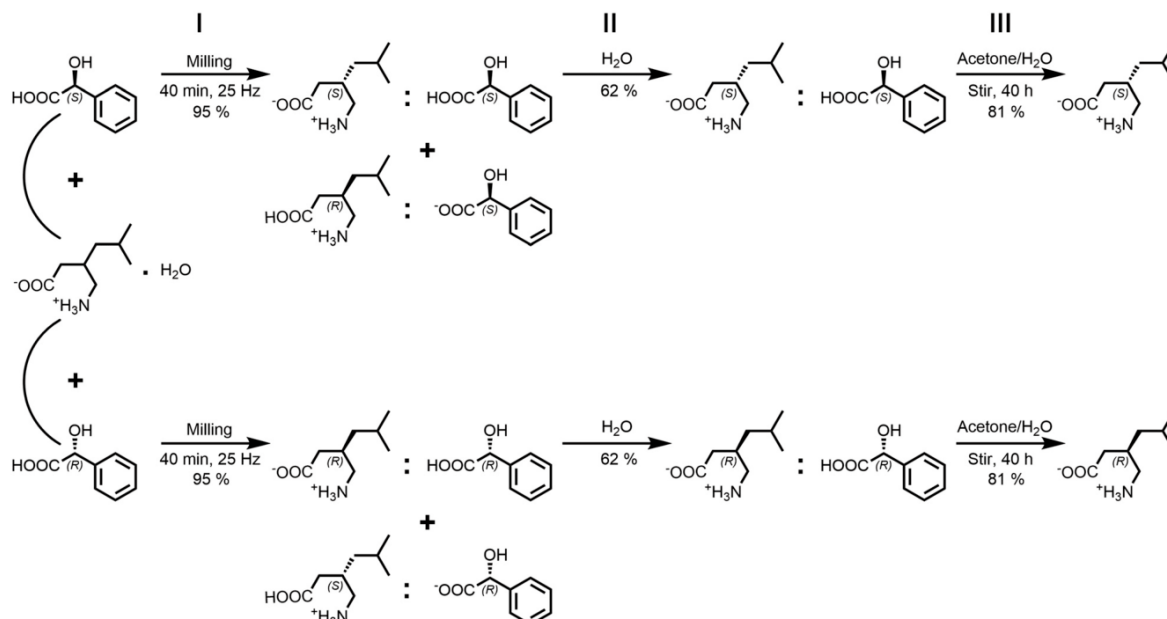
mol⁻¹ and the highest values in 1:4-systems with -356.66 kJ mol⁻¹ in (*S,S*) and -363.05 kJ mol⁻¹ in (*S,R*). As HB-properties are also similar in all investigated compounds, the influence of the charged species on the strength of intermolecular interactions seems to be questionable. While the highest values are present in 1:4-systems composed of charged molecules, the second most favourable energy is given for 2:3 with -343.23 kJ mol⁻¹ composed of zwitterionic and neutral molecules. The calculated lattice energies for the discussed compounds are higher than those established by Marchese Robinson *et al.* for a large number of neutral single component APIs,¹⁴ but lower compared to those for ionic liquids containing inorganic ions,¹³ and far lower than those for inorganic systems.^{83,84} However, the values are slightly higher than values established by Voronin *et al.* for carbendazim maleates.¹² This suggests that (zwitter)ionicity does generally have an influence on lattice energies, even though the final molecular protonation status in multicomponent species of the investigated compounds does not impact structural features meaningfully. The unusually beneficial lattice energy of 2 with -367.68 kJ mol⁻¹ might appear too high especially when compared to 1-forms with about -195 kJ mol⁻¹. However, 2 behaves rather different than 1 in two key aspects: firstly, 2 does not form a stable hydrate as racemic 1 does.^{85,86} Contrary to the latter, 2-hydrate transitions to anhydrous 2 quickly, suggesting a preferable form in the anhydrous species. Furthermore, experimental observations conducted in the presented work suggest a higher stability of 2 as compared to 2:3. While co-crystalline systems of 1 with the used co-formers form readily and without evidence for impurities under the investigated conditions, the 2:3 system cannot be obtained as reliably. 2:3 single crystals could only be received once; neat co-milling did not work under the chosen conditions and co-crystallization from solution still contains impurities visible in the powder pattern (see ESI†). Therefore, a comparatively beneficial lattice energy seems likely. This might stem from an increased connectivity *via* π -interactions enabled by phenyl-subunits in 2. Further support for unusually high lattice energy in 2 is given through its melting behaviour. It is the only discussed compound that decomposes without melting at temperatures above 200 °C which indicates strong intermolecular connectivity. To conclude, the comparison of the presented compounds based on the discussed structural and thermodynamic properties uncover their commonalities. They all behave structurally similar as their co-formers are in a specific murky ΔpK_a range that enables formation of salts as well as co-crystals. Some of the chosen systems retain zwitterionic/neutral molecular makeup and some obtain molecular charges. Energetically, they all are in a similar range, posing more beneficial lattice energies than neutral compounds but less favourable ones than organic/inorganic or purely inorganic compounds. However, this border-region in the *salt-co-crystal continuum* can have high impact on properties such as melting and solubility behaviours. The shown compounds that become charged upon co-

crystallization melt at lower temperatures and are vastly more soluble than their neutral/zwitterionic counterparts. This specific behaviour seems to largely depend on the molecular chirality in case of homo- and heterochiral 1:3-forms and the comparatively low lattice energy in 1 enables easy co-crystallization. As 1 is a commercially viable API the presented results can be used to better understand, modify and improve an established crystallization-based enantiopurification processes.

3.2 Enantiopurification of pregabalin

Based on the described findings, a process for the racemic separation of the racemic pregabalin hydrate ((*rac*)-1·H₂O) could be improved on and simplified (Scheme 2). Similar enantiopurification methods were previously patented,³⁸⁻⁴⁴ that followed a bottom-up approach in their racemic separation processes. By dissolving varying quantities of (*rac*)-pregabalin hydrate with (*S*)-mandelic acid and subsequently cooling or crystallization *via* vaporization the (*S,S*)-species was formed. In the patents it is then removed from solution and further processed. As was shown in the present study the formation of 1:3 is energetically favourable compared to crystallization of 1. Furthermore, (*S,R*)- as well as (*R,S*)-1:3 show ionicity-based increased solubilities compared to the (*S,S*)- and (*R,R*)-species. In opposition, 1:4-compounds are prone to form viscous residue instead of crystalline materials which is one of the reasons those are not suitable for the separation process. Due to the energetic favourability as well as mechanic and thermal stability of 1:3-species they can be prepared in a ball mill *via* mechanochemical synthesis. This enables a top-down approach where the scale depends solely on the largest available milling vessel. By milling of (*rac*)-1·H₂O with either mandelic acid enantiomer (*S*)-3 or (*R*)-3 in equimolar amounts a 1:1 mixture of the (*S,S*)/(*R,S*) or (*R,R*)/(*S,R*) multicomponent systems is formed in good yields (step I in Scheme 2). Missed yield at this point stems from losing some material on the milling vessel walls. As the (*S,R*)- and (*R,S*)-systems pose an about nine times higher solubility in water compared to their homochiral counterparts they can then be removed by subsequent washing and drying steps with increasingly smaller amounts of water. This approach therefore offers the advantage of quickly producing co-crystalline product and necessitates only low amounts of water to remove the unwanted heterochiral species. To give an example, 4.580 g of co-crystal mixture was produced by milling in step I. After three washing and drying steps with 12 mL, 6 mL and 4 mL water, 1.442 g (62%) of enantiopurified homochiral co-crystal were received in step II. Low amounts of washing water further simplify regaining the missed yield: the lost product can be recrystallized by water vaporization. The washing process can then be repeated with even smaller amounts of water. Our approach does not require further additives like organic solvents, additional acidic or caustic compounds nor is heating





Scheme 2 Steps for the racemic separation of *(rac)*-1-H₂O with mandelic acid: step I - mechanochemical co-crystallization, step II - washing powdery product with water and drying the residue, step III - extract mandelic acid by stirring the residue in acetone/water mixture for 40 h.

necessary which is an advantage compared to previously reported procedures. This also allows for an environmentally friendly, low effort process. To separate **3** from **1** in step III a slight variation to the patented process by Pradhan and colleagues,⁴⁰ who proposed a number of different separation methods, is introduced. Washed homochiral co-crystalline product is stirred for 40 h in acetone with catalytic amounts of water added. To follow up on the previous example, 1.442 g of powdery co-crystal were put in a glass vessel with 75 mL

of acetone and 500 μ L of water and stirred for 40 h. The powdery substance was then filtered, washed with additional 20 mL of acetone and 0.612 g (81%) of enantiopurified **1** were received. In contrast to the previously proposed method the stirring process is much longer but does not require heating. Acetone was chosen as it is cheap, easily available and poses less environmental risks than other organic solvents that could be suitable for this process. The proposed enantiopurification can be controlled through powder X-ray diffraction during each step (Fig. 2). The described method relies on property differences unique to the **1:3**-systems. Inversion of molecular chirality leads to related multicomponent species that still differ in their key attributes. Higher solubility in one of the received multicomponent species in congruence with the mechanical stability enables the described process for **1**. The previously discussed properties in malic acid systems deem them unusable for this in contrast to **1:3**-forms, as **1:4**-species preferably form viscous liquids with similar solubilities. On the other end, phenibut co-crystallization with mandelic acid is energetically unfavourable compared to pure **2**-formation. Mechanochemical synthesis under the same herein discussed conditions did not lead to **2:3**. Furthermore, **2** does not show chirality dependent varying crystallization products, a trait inherent only to **1**.

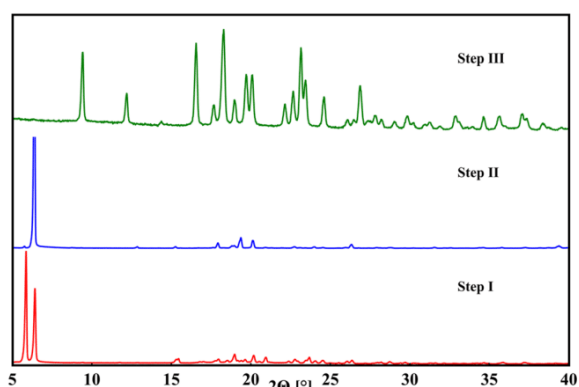


Fig. 2 Powder patterns of products received after enantiopurification process step I (red), step II (blue) and step III (green). In step I, both homo- and heterochiral multicomponent species are present, visible by the two strong diffraction reflexions at 5.9° and 6.4° 2θ . In step II the heterochiral compound was removed by washing, diminishing the 5.9° signal. In step III, mandelic acid was removed, solely leaving enantiopure pregabalin.

4 Conclusions

In this work we presented an atypical case concerning co-crystallization of zwitterionic APIs of the GABA-family. Multicomponent crystalline species of related compounds



pregabalin and phenibut were characterized regarding their structural and thermodynamic properties. Homo- and heterochiral pregabalin:mandelic acid species exhibit a remarkably different solubility and melting behaviour based on molecular charge differences, even though they are structurally very similar. It was shown that this hardly predictable behaviour occurs in a vague range of the *salt-cocystal continuum* and can, in this specific case, be attributed to the co-former chirality inversion. It seems likely that this small change in the molecular makeup crosses an energetic barrier needed for ionization when heterochiral co-formers pregabalin and mandelic acid are used. For the given set of compounds, the results indicate that complex multicomponent crystalline species exist on a spectrum and their properties are influenced more impactfully by molecular makeup rather than their crystal structure. It was further presented how investigations of crystal properties in the borderline regions of the spectrum can offer interesting and unexpected results. An optimized and simplified top-down process of (*rac*)-pregabalin hydrate enantiopurification was developed and its functionality was explained by the previously stated properties. This work shows that careful examination of multicomponent systems composed of similar co-formers in areas where multiple molecular and thermodynamic influences compete to determine product properties can lead to fruitful and surprising results.

Author contributions

Conceptualization: Daniel Komisarek & Vera Vasylyeva. Data curation: Daniel Komisarek. Formal analysis: Daniel Komisarek. Funding acquisition: Vera Vasylyeva. Investigation: Daniel Komisarek. Methodology: Daniel Komisarek, Vera Vasylyeva, Takin Haj Hassani Sohi. Project administration: Vera Vasylyeva. Resources: Vera Vasylyeva. Supervision: Vera Vasylyeva. Validation: Daniel Komisarek, Vera Vasylyeva, Takin Haj Hassani Sohi. Visualization: Daniel Komisarek. Writing: Daniel Komisarek. Review & editing: Vera Vasylyeva.

Conflicts of interest

There are no conflicts to declare.

Acknowledgements

We thank PD Dr. Oliver Weingart and Prof. Dr. Rochus Schmid for valuable discussions on theoretical aspects. Computational support and infrastructure was provided by the "Centre for Information and Media Technology" (ZIM) at the University of Duesseldorf (Germany). Funded by the Deutsche Forschungsgemeinschaft (DFG, German Research Foundation) – 440366605. Thanks to the CeMSA@HHU (Center for Molecular and Structural Analytics@Heinrich Heine University) for recording the NMR-spectroscopic data.

References

- 1 V. Todaro and A. M. Healy, *Drug Dev. Ind. Pharm.*, 2021, **47**, 292–301.
- 2 M. Trampuž, D. Teslić and B. Likozar, *Chem. Eng. Res. Des.*, 2021, **165**, 254–269.
- 3 A. Ainurofiq, K. E. Dinda, M. W. Pangestika, U. Himawati, W. D. Wardhani and Y. T. Sipahutar, *Int. J. Res. Pharm. Sci.*, 2020, **11**, 1621–1630.
- 4 A. J. Al-Ani, C. Herdes, C. C. Wilson and B. Castro-Dominguez, *Cryst. Growth Des.*, 2020, **20**, 1451–1457.
- 5 D. Chen, Q. Sun, W. Huang and B.-S. Yang, *Cryst. Growth Des.*, 2020, **20**, 2251–2265.
- 6 L. Schenck, D. Erdemir, L. Saunders Gorka, J. M. Merritt, I. Marziano, R. Ho, M. Lee, J. Bullard, M. Boukerche and S. Ferguson, *et al.*, *Mol. Pharmaceutics*, 2020, **17**, 2232–2244.
- 7 A. F. Shunnar, B. Dhokale, D. P. Karothu, D. H. Bowskill, I. J. Sugden, H. H. Hernandez, P. Naumov and S. Mohamed, *Chemistry*, 2020, **26**, 4752–4765.
- 8 H.-L. Cao, J.-R. Zhou, F.-Y. Cai, J. Lü and R. Cao, *Cryst. Growth Des.*, 2019, **19**, 3–16.
- 9 S. Chatteraj and C. C. Sun, *J. Pharm. Sci.*, 2018, **107**, 968–974.
- 10 E. Hadjittofis, M. A. Isbell, V. Karde, S. Varghese, C. Ghoroi and J. Y. Y. Heng, *Pharm. Res.*, 2018, **35**, 100.
- 11 F. Yang, C.-X. Yan, X. Yang, D.-G. Zhou and P.-P. Zhou, *CrystEngComm*, 2017, **19**, 1762–1770.
- 12 A. P. Voronin, A. O. Surov, A. V. Churakov, O. D. Parashchuk, A. A. Rykounov and M. V. Vener, *Molecules*, 2020, **25**, 2386.
- 13 U. P. Preiss, D. H. Zaitsau, W. Beichel, D. Himmel, A. Higelin, K. Merz, N. Caesar and S. P. Verevkin, *ChemPhysChem*, 2015, **16**, 2890–2898.
- 14 R. L. Marchese Robinson, D. Geatches, C. Morris, R. Mackenzie, A. G. P. Maloney, K. J. Roberts, A. Moldovan, E. Chow, K. Pencheva and D. R. M. Vatvani, *J. Chem. Inf. Model.*, 2019, **59**, 4778–4792.
- 15 H. K. Buchholz and M. Stein, *J. Comput. Chem.*, 2018, **39**, 1335–1343.
- 16 S. L. Childs, G. P. Stahly and A. Park, *Mol. Pharmaceutics*, 2007, **4**, 323–338.
- 17 D. Braga, F. Grepioni, L. Maini, S. Prosperi, R. Gobetto and M. R. Chierotti, *Chem. Commun.*, 2010, **46**, 7715–7717.
- 18 D. Braga, F. Grepioni and O. Shemchuk, *CrystEngComm*, 2018, **20**, 2212–2220.
- 19 S. P. Kelley, A. Narita, J. D. Holbrey, K. D. Green, W. M. Reichert and R. D. Rogers, *Cryst. Growth Des.*, 2013, **13**, 965–975.
- 20 D. Yang, H. Wang, Q. Liu, P. Yuan, T. Chen, L. Zhang, S. Yang, Z. Zhou, Y. Lu and G. Du, *Chin. Chem. Lett.*, 2021, **33**, 3207–3211.
- 21 T. Alkhalid, Z. M. Saeed, A. F. Shunnar, E. Abujami, R. M. Nyadzayo, B. Dhokale and S. Mohamed, *Cryst. Growth Des.*, 2022, **22**, 485–496.
- 22 M. Gryl, M. Kozieł and K. M. Stadnicka, *Acta Crystallogr., Sect. B: Struct. Sci., Cryst. Eng. Mater.*, 2019, **75**, 53–58.



- 23 N. K. Duggirala, M. L. Perry, Ö. Almarsson and M. J. Zaworotko, *Chem. Commun.*, 2016, **52**, 640–655.
- 24 S. Aitipamula, R. Banerjee, A. K. Bansal, K. Biradha, M. L. Cheney, A. R. Choudhury, G. R. Desiraju, A. G. Dikundwar, R. Dubey, N. Duggirala, P. P. Ghogale, S. Ghosh, P. K. Goswami, N. R. Goud, R. R. K. R. Jetty, P. Karpinski, P. Kaushik, D. Kumar, V. Kumar, B. Moulton, A. Mukherjee, G. Mukherjee, A. Myerson, V. Puri, A. Ramanan, T. Rajamannar, C. M. Reddy, N. Rodriguez-Hornedo, R. D. Rogers, T. N. G. Row, P. Sanphui, N. Shan, G. Shete, A. Singh, C. C. Sun, J. A. Swift, R. Thaimattam, T. S. Thakur, R. K. Thaper, S. Thomas, S. Tothadi, V. R. Vangala, N. Variankaval, P. Vishweshwar, D. R. Weyna and M. J. Zaworotko, *Cryst. Growth Des.*, 2012, **12**, 2147–2152.
- 25 D. J. Berry and J. W. Steed, *Adv. Drug Delivery Rev.*, 2017, **117**, 3–24.
- 26 E. Grothe, H. Meeke, E. Vlieg, J. H. ter Horst and R. de Gelder, *Cryst. Growth Des.*, 2016, **16**, 3237–3243.
- 27 S. Guerin, S. Khorasani, M. Gleeson, J. O'Donnell, R. Sanii, R. Zwane, A. M. Reilly, C. Silien, S. A. M. Tofail, N. Liu, M. Zaworotko and D. Thompson, *Cryst. Growth Des.*, 2021, **21**, 5818–5827.
- 28 J. Nath and J. B. Baruah, *Cryst. Growth Des.*, 2021, **21**, 5325–5341.
- 29 W. Gong, P. K. Mondal, S. Ahmadi, Y. Wu and S. Rohani, *Int. J. Pharm.*, 2021, **608**, 121063.
- 30 T. A. Hegde, A. Dutta, T. C. Sabari Girisun and G. Vinitha, *Chem. Phys. Lett.*, 2021, **781**, 138971.
- 31 A. Kiguchiya, R. Teraoka, T. Sakane and E. Yonemochi, *Chem. Pharm. Bull.*, 2019, **67**, 945–952.
- 32 L. Zhao, M. P. Hanrahan, P. Chakravarty, A. G. DiPasquale, L. E. Sirois, K. Nagapudi, J. W. Lubach and A. J. Rossini, *Cryst. Growth Des.*, 2018, **18**, 2588–2601.
- 33 W. Ji, B. Xue, S. Bera, S. Guerin, L. J. Shimon, Q. Ma, S. A. Tofail, D. Thompson, Y. Cao, W. Wang and E. Gazit, *Mater. Today*, 2021, **42**, 29–40.
- 34 P. Vaňkátová, A. Kubíčková and K. Kalíková, *J. Chromatogr. A*, 2022, **1673**, 463074.
- 35 C. C. Da Silva and F. T. Martins, *RSC Adv.*, 2015, **5**, 20486–20490.
- 36 P. Rajasekar, C. Jose, M. Sarkar and R. Boomishankar, *Angew. Chem., Int. Ed.*, 2021, **60**, 4023–4027.
- 37 L. Zeng, Q. Yi, Q. Liu, K. Tang and B. van der Bruggen, *Sep. Purif. Technol.*, 2021, **257**, 117884.
- 38 V. Gore, D. Datta, M. Gadakar, K. Pokharkar, V. Mankar and S. Wavhal, *WO Pat.*, WO2009122215, 2009.
- 39 V. Gore, D. Datta, M. Gadakar, K. Pokharkar, V. Mankar and S. Wavhal, *US Pat.*, US20110124909, 2011.
- 40 B. S. Pradhan, *IN Pat.*, IN2010CH01584, 2010.
- 41 A. Khaja, V. S. R. Potla, S. Govind, B. R. Konudula, Y. K. Chauhan and D. Datta, *WO Pat.*, WO2009125427, 2009.
- 42 K. B. Mafatlal, K. N. Kagathara, K. Sivaprasad, P. C. Rajendra, V. P. Bhikhalal, B. U. Rajaram and M. I. Ambalal, *IN Pat.*, IN2009MU01587, 2009.
- 43 S. R. D. Reddy, S. R. Velivela and R. R. V. Reddy, *IN Pat.*, IN2010CH00299, 2010.
- 44 R. K. Thaper, M. D. Prabhavat, S. K. Arora, Y. D. Pawar, D. K. P. Varma, V. S. Kamble and V. S. Shinde, *IN Pat.*, IN2008KO00929, 2008.
- 45 D. K. Baidya, A. Agarwal, P. Khanna and M. K. Arora, *J. Anaesthesiol., Clin. Pharmacol.*, 2011, **27**, 307–314.
- 46 M. J. Brodie, *Epilepsia*, 2004, **45**(Suppl 6), 19.
- 47 C. A. Federico, J. S. Mogil, T. Ramsay, D. A. Fergusson and J. Kimmelman, *Pain*, 2020, **161**, 684–693.
- 48 N. M. Gajraj, *Anesth. Analg.*, 2007, **105**, 1805–1815.
- 49 D. R. Guay, *Am. J. Geriatr. Pharmacother.*, 2005, **3**, 274–287.
- 50 R. Kavoussi, *Eur. Neuropsychopharmacol.*, 2006, **16**(Suppl 2), S128–S133.
- 51 N. Kumar, A. Laferriere, J. S. C. Yu, A. Leavitt and T. J. Coderre, *J. Neurochem.*, 2010, **113**, 552–561.
- 52 B. A. Lauria-Horner and R. B. Pohl, *Expert Opin. Invest. Drugs*, 2003, **12**, 663–672.
- 53 R. A. Moore, S. Straube, P. J. Wiffen, S. Derry and H. J. McQuay, *Cochrane Database Syst. Rev.*, 2009, **3**, CD007076.
- 54 P. Ryvlin, E. Perucca and S. Rheims, *Neuropsychiatr. Dis. Treat.*, 2008, **4**, 1211–1224.
- 55 L. Zvejniece, E. Vavers, B. Svalbe, G. Veinberg, K. Rizhanova, V. Liepins, I. Kalvinsh and M. Dambrova, *Pharmacol., Biochem. Behav.*, 2015, **137**, 23–29.
- 56 I. Lapin, *CNS Drug Rev.*, 2001, **7**, 471–481.
- 57 M. Dambrova, L. Zvejniece, E. Liepinsh, H. Cirule, O. Zharkova, G. Veinberg and I. Kalvinsh, *Eur. J. Pharmacol.*, 2008, **583**, 128–134.
- 58 M. A. Downes, I. L. Berling, A. Mostafa, J. Grice, M. S. Roberts and G. K. Isbister, *Clin. Toxicol.*, 2015, **53**, 636–638.
- 59 Y. B. Joshi, S. F. Friend, B. Jimenez and L. R. Steiger, *J. Clin. Psychopharmacol.*, 2017, **37**, 478–480.
- 60 W. Li and B. Madhira, *Am. J. Ther.*, 2017, **24**, e639–e640.
- 61 D. J. McCabe, S. A. Bangh, A. M. Arens and J. B. Cole, *Am. J. Emerg. Med.*, 2019, **37**, 2066–2071.
- 62 D. R. Owen, D. M. Wood, J. R. H. Archer and P. I. Dargan, *Drug Alcohol Rev.*, 2016, **35**, 591–596.
- 63 B. Samas, W. Wang and D. B. Godrej, *Acta Crystallogr., Sect. E: Struct. Rep. Online*, 2007, **63**, o3938–o3938.
- 64 *CrysAlisPRO*, Oxford Diffraction/Agilent Technologies UK Ltd, Yarnton, England.
- 65 G. M. Sheldrick, *Acta Crystallogr., Sect. A: Found. Crystallogr.*, 2008, **64**, 112–122.
- 66 G. M. Sheldrick, *Acta Crystallogr., Sect. C: Struct. Chem.*, 2015, **71**, 3–8.
- 67 O. V. Dolomanov, L. J. Bourhis, R. J. Gildea, J. A. K. Howard and H. Puschmann, *J. Appl. Crystallogr.*, 2009, **42**, 339–341.
- 68 C. F. Macrae, I. Sovago, S. J. Cottrell, P. T. A. Galek, P. McCabe, E. Pidcock, M. Platings, G. P. Shields, J. S. Stevens, M. Towler and P. A. Wood, *J. Appl. Crystallogr.*, 2020, **53**, 226–235.
- 69 P. Giannozzi, O. Barone, P. Bonfà, D. Brunato, R. Car, I. Carnimeo, C. Cavazzoni, S. de Gironcoli, P. Delugas, F. Ferrari Ruffino, A. Ferretti, N. Marzari, I. Timrov, A. Urru and S. Baroni, *Chem. Phys.*, 2020, **152**, 154105.
- 70 *Physicians' desk reference 2007*, ed. Thomson P. D. R., Thomson PDR, Mondvale, NJ, 2007.



Paper

- 71 G. Kortüm, W. Vogel and K. Andrussow, *Pure Appl. Chem.*, 1960, **1**, 187–536.
- 72 D. Mootz and M. Schilling, *J. Am. Chem. Soc.*, 1992, **114**, 7435–7439.
- 73 R. M. Zelle, E. de Hulster, W. A. van Winden, P. de Waard, C. Dijkema, A. A. Winkler, J.-M. A. Geertman, J. P. van Dijken, J. T. Pronk and A. J. A. van Maris, *Appl. Environ. Microbiol.*, 2008, **74**, 2766–2777.
- 74 Chemicalize was used for prediction of pKa properties, 09/2022, <https://chemicalize.com/> developed by ChemAxon (<http://www.chemaxon.com>).
- 75 T. Steiner, *Angew. Chem., Int. Ed.*, 2002, **41**, 48–76.
- 76 E. Batisai, A. Ayamane, O. E. Y. Kilinkissa and N. B. Báthori, *CrystEngComm*, 2014, **16**, 9992–9998.
- 77 K. A. Chu and S. H. Yalkowsky, *Int. J. Pharm.*, 2009, **373**, 24–40.
- 78 G. L. Perlovich, *Cryst. Growth Des.*, 2021, **21**, 5058–5071.
- 79 M. Banik, S. P. Gopi, S. Ganguly and G. R. Desiraju, *Cryst. Growth Des.*, 2016, **16**, 5418–5428.
- 80 S. J. Bethune, N. Huang, A. Jayasankar and N. Rodríguez-Hornedo, *Cryst. Growth Des.*, 2009, **9**, 3976–3988.
- 81 D. J. Good and N. Rodríguez-Hornedo, *Cryst. Growth Des.*, 2009, **9**, 2252–2264.
- 82 D. J. Good and N. Rodríguez-Hornedo, *Cryst. Growth Des.*, 2010, **10**, 1028–1032.
- 83 S. Kaya and C. Kaya, *Inorg. Chem.*, 2015, **54**, 8207–8213.
- 84 S. Kaya, A. Robles-Navarro, E. Mejía, T. Gómez and C. Cardenas, *J. Phys. Chem. A*, 2022, **126**, 4507–4516.
- 85 D. Komisarek, M. Pallaske and V. Vasylyeva, *Z. Anorg. Allg. Chem.*, 2021, **647**, 984–991.
- 86 M. Herbst, D. Komisarek, T. Strothmann and V. Vasylyeva, *Crystals*, 2022, **12**, 1393.



Supporting Information

Co-Crystals of Zwitterionic GABA API's Pregabalin and Phenibut: Properties and Application

Daniel Komisarek, Takin Haj Hassani Sohi, and Vera Vasylyeva

Table of Contents

1 Structural Details	1
1.1 Pregabalin (1)	1
1.2 Phenibut (2)	4
1.3 Homo- and heterochiral Pregabalin:mandelic acid (1:3), ratio (1:1)	7
1.4 Phenibut:mandelic acid (2:3), ratio (1:1).....	16
1.5 Homo- and heterochiral Pregabalin:malic acid (1:4), ratio (1:1).....	19
2 Physical properties	24
2.1 Determination of melting points with differential scanning calorimetry	24
2.2 Determination of solubility with ¹ H-NMR-spectroscopy.....	27
3 Lattice energies	28
3.1 Model description and verification	28
3.2 Compound categorization and model application	32
4 Applications: enantiopurification of (rac)-Pregabalin hydrate	37
5 Addendum	39
6 Sources	57

1 Structural Details

All structures are deposited to CCDC. Deposition Number: 2170100-2170108. Bijvoet analysis was conducted on all received structures with PLATON software v. 1.19 to confirm molecular chirality, shown in **chapter 5**.^[1]

1.1 Pregabalin (1)

Pure Pregabalin is examined as its (S)- and (R)-enantiomer in the context of this work. Single crystals of the enantiomerically pure forms were obtained by slow evaporation of solvent from aqueous solution. Block shaped diffraction quality crystals were obtained. The lattice and measurement parameters are shown in **Table S1**. Interaction distances and angles are shown in **Table S2**.

Table S1. Lattice and measurement parameters of (R)- and (S)-Pregabalin.

Parameters	(R)-Pregabalin	(S)-Pregabalin
Formula	C ₈ H ₁₇ N O ₂	C ₈ H ₁₇ N O ₂
M_r [g mol⁻¹]	159.22	159.22
Temperature [K]	100(2)	100(2)
System/space group	Orthorhombic, <i>P</i> 2 ₁ 2 ₁ 2 ₁	Orthorhombic, <i>P</i> 2 ₁ 2 ₁ 2 ₁
a (Å)	6.368(4)	6.344(4)
b (Å)	7.817(6)	7.809(4)
c (Å)	18.504(4)	18.493(3)
β (°)	90	90
V (Å³)	921.25(5)	916.27(5)
Z/Z'	4/1	4/1
Density [g/cm³]	1.148	1.154
μ [mm⁻¹]	0.656	0.660
T_{min}/T_{max}	0.514/1.000	0.622/1.000
F (000)	352	352
Crystal size [mm]	0.36 · 0.25 · 0.10	0.32 · 0.20 · 0.03
2θ range [°]	4.8 – 77.5	4.8 – 77.5
Completeness [%]	99.7	99.1
Recorded refl.	4569	6940
Independent refl.	1779	1757
Flack x	-0.04(19)	0.03(11)
Goodness-of-fit F²	1.053	1.043
X-Ray Source	Cu Kα (λ = 1.54184)	Cu Kα (λ = 1.54184)
R₁ [%] /wR₂ [%] /S	4.05/ 9.95/ 1.053	3.01/ 7.86/ 1.043

Table S2. Hydrogen bond distances and angles in (R)- as well as (S)-Pregabalin.

	D - H [Å]	H...A [Å]	D...A [Å]	D - H...A [°]
(S)-Pregabalin				
N1-H6...O1	0.90(3)	1.86(3)	2.755(8)	171(2)
N1-H7...O1	0.94(2)	1.79(2)	2.728(0)	171(2)
N1-H8...O2	0.91(2)	1.87(2)	2.771(1)	172(2)
(R)-Pregabalin				
N1-H6...O1	0.91(3)	1.86(3)	2.757(2)	170(3)
N1-H7...O1	0.93(3)	1.80(3)	2.731(2)	174(2)
N1-H8...O2	0.92(3)	1.86(3)	2.767(2)	172(3)

A comparison of the asymmetric unit and lattice packing of both compounds is shown in **Figure S1**. Three distinct HB are formed in both systems. From each donor nitrogen N1 two interactions are formed with acceptor oxygen O1 with a length of 2.755(8) Å (S)/ 2.757(2) Å (R) and 2.728(0) Å (S)/ 2.731(2) Å (R) and one interaction with acceptor oxygen O2 at 2.771(1) Å (S)/ 2.767(2) Å (R). The donor/acceptor distance in each case is short enough to be considered a strong hydrogen bond and the D-H...A angle is around 172.^[2] These values suggest that the ionicity on the ammonium and carboxylate groups may enforce the HB, leading to strong, charge assisted HB. To further elucidate on possible binding interactions, Hirshfeld- as well as electron density surface analysis was conducted with Crystal Explorer 21.5 (**Figure S2**).^[3] In electron density surfaces, red spots suggest high electron density which indicates high probability for binding interactions while white spots suggest surface electron density as expected from not interacting atoms and blue spots indicate low surface electron density most. In Hirshfeld surfaces red spots indicate close contacts between surface atoms shorter than the sum of their respective van der Waals radii, white spots indicate surface atoms close contacts equal to the sum of their van der Waals radii and blue spots indicate that surface atoms are further away from other surface atoms than the sum of their van der Waals radii. Both surface analyses additionally confirm that bonding interactions take place via the ammonium- and carboxylate subunits and molecular vicinity as well as electron density is increased exactly around the HB interaction spots. In congruence with the packing motif depicted in **Figure S1** it can be concluded that rows of symmetrically equivalent Pregabalin molecules connect via charge assisted HB-interactions. As no conspicuous electron density features or close vicinity is present around the isobutyl group and furthermore no π -systems are present in Pregabalin, dispersive forces probably best explain the structural motif with regard to the alkylic residues.

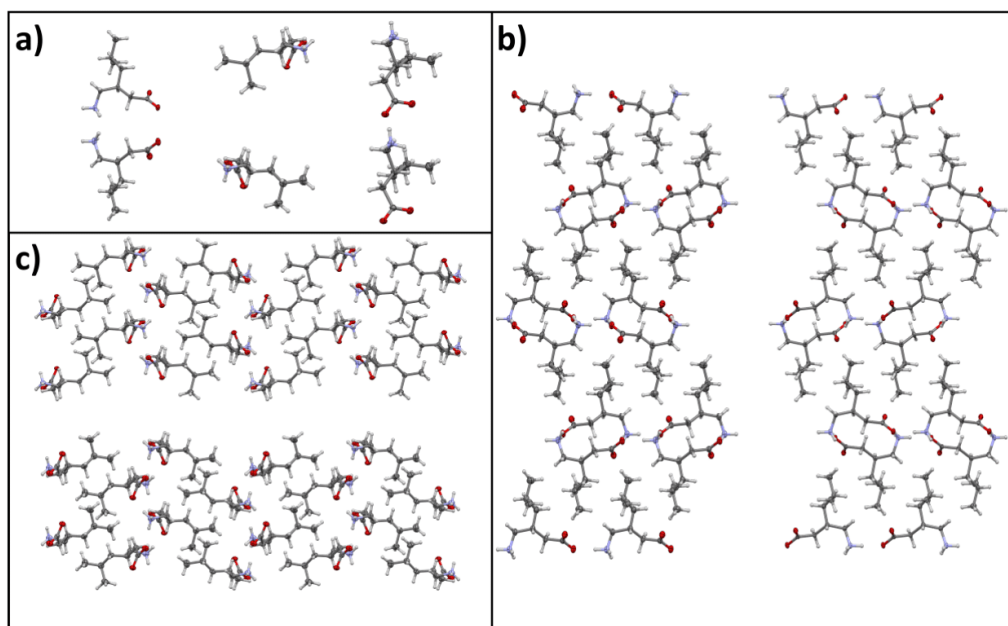


Figure S1. The asymmetric unit of (S)-Pregabalin (**a**), top and (R)-Pregabalin (**a**), bottom is shown: from left to right a-axis, b-axis, c-axis. In **b**) the packing of a $2 \cdot 2 \cdot 2$ unit cell from a-axis view is shown, (S)-Pregabalin top, (R)-Pregabalin bottom. In **c**) the packing of a $2 \cdot 2 \cdot 2$ unit cell from b-axis view is shown, (S)-Pregabalin right, (R)-Pregabalin left. Carbon atoms are depicted in grey, hydrogen atoms in white, nitrogen atoms in blue and oxygen atoms in red.

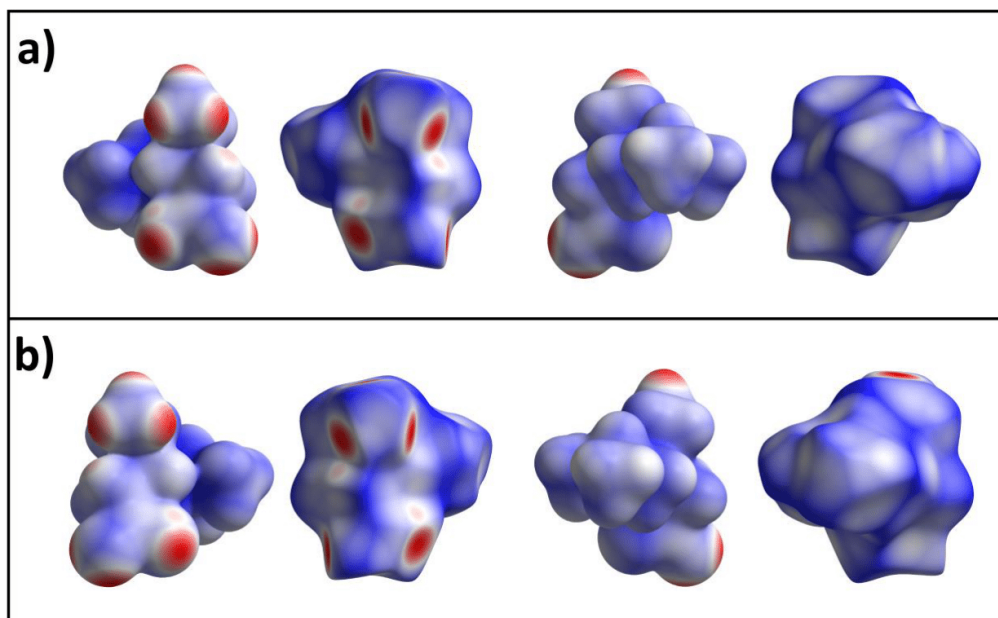


Figure S2. Electron density and Hirshfeld surfaces of (S)- and (R)-Pregabalin. **a**) shows the electron density and Hirshfeld surface of the sole symmetrically inequivalent Pregabalin molecule in the (S)-Pregabalin lattice from two sides. **b**) shows the electron density and Hirshfeld surface of the sole symmetrically inequivalent Pregabalin molecule in the (R)-Pregabalin lattice from two sides.

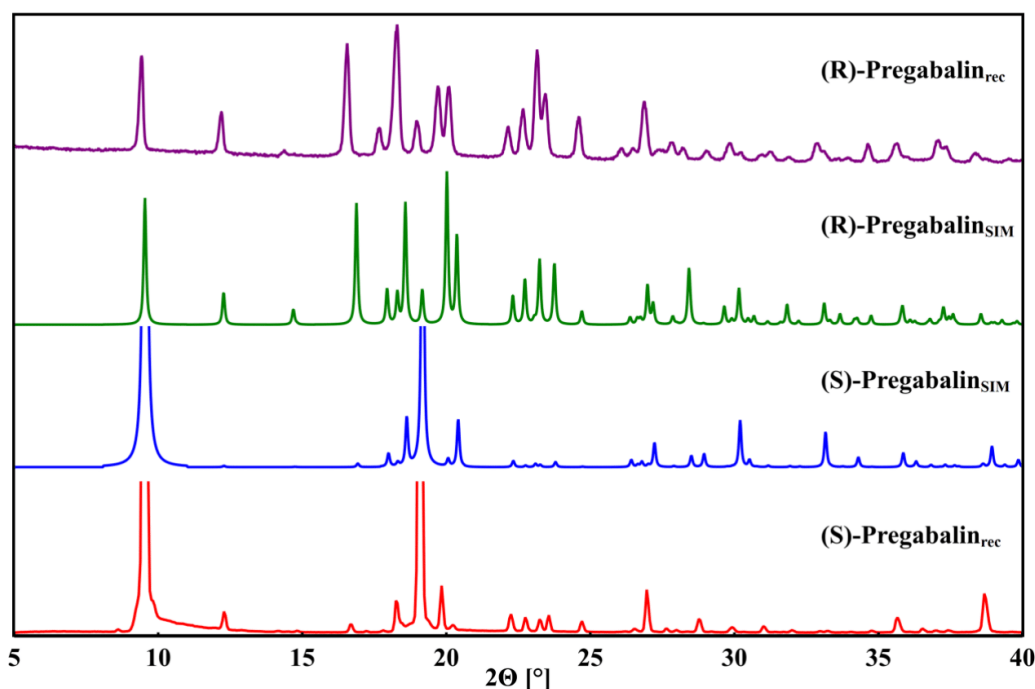


Figure S3. Powder pattern of (S)-Pregabalin recorded (red) compared to a simulated pattern by single crystal data (blue) and powder pattern of (R)-Pregabalin (purple) compared to a simulated pattern by single crystal data (green) in a range of 5° – 40°. (S)-Pregabalin was recrystallized from water leading to preferential directions while (R)-Pregabalin was measured after stirring in acetone/water mixture for 40 h as by the racemic separation process described in this work leading to more uniform sized particles and distribution of signal intensities. The simulated pattern for (S)-Pregabalin was customized regarding hkl distribution to account for preferential directions ($hkl = 4, 4, 0$, March-Dollase parameter = 4).

1.2 Phenibut (2)

The structural properties of (rac)-Phenibut are reevaluated regarding the herein discussed items based on our published structure in ZAAC 2021.^[4] Needle shaped single crystals were obtained from aqueous solution by slow evaporation of the solvent. The lattice and measurement parameters are shown in **Table S3**. Interaction distances and angles, including those for π -interactions, are shown in **Table S4**. The asymmetric unit consisting of a single Phenibut molecule as well as the crystal packing from axis $a - c$ is shown in **Figure S4**. (rac)-Phenibut behaves very similar in terms of its packing compared to the Pregabalin enantiomers. Two axes, in the case of Phenibut the a - and c -axis, are relatively short at below 10 Å considering the large c -axis at 27.505(3) Å. While in Pregabalin the longest axis is 18.504(4) Å the difference is easily explained by the number of molecules in the unit cell, Z . Contrary to enantiomerically pure Pregabalin forms (rac)-Phenibut contains 8 molecules in its unit cell.

Table S3. Lattice and measurement parameters of (rac)-Phenibut.

Parameters	(rac)-Phenibut
Formula	C ₁₀ H ₁₃ N O ₂
M_r [g mol⁻¹]	179.21
Temperature [K]	140(2)
System/space group	Orthorhombic, <i>Pbca</i>
a (Å)	9.384(7)
b (Å)	6.978(10)
c (Å)	27.505(3)
β (°)	90
V (Å³)	1801.4(4)
Z/Z'	8/1
Density [g/cm³]	1.322
μ [mm⁻¹]	0.092
T_{min}/T_{max}	0.7990/ 1.0000
F (000)	768
Crystal size [mm]	0.06 · 0.10 · 0.60
2θ range [°]	2.63 – 25.17
Completeness [%]	99.8
Recorded refl.	6997
Independent refl.	1609
Goodness-of-fit F²	1.013
X-Ray Source	Mo Kα (λ = 0.71073)
R₁ [%] /wR₂ [%] /S	4.81/ 11.97/ 1.013

Table S4. Hydrogen bond and edge-to-face interaction distances and angles in (rac)-Phenibut.

	D - H (Å)	H...A [Å]	D...A [Å]	D - H...A [°]
HB				
N1-H6...O2	0.95(3)	1.84(3)	2.775(3)	172(3)
N1-H7...O1	1.13(3)	1.64(3)	2.732(3)	160(3)
N1-H8...O2	0.96(4)	1.84(4)	2.795(3)	173(2)
C-H...π		H...Cg [Å]	C...Cg [Å]	C-H...Cg [°]
C8-H11...Cg1		2.85(3)	3.845(3)	170(2)

Contrary to Pregabalin, Phenibut has a further phenyl residue as opposed to Pregabalins isobutyl chain. Therefore, next to the HB interactions, π-interactions can be performed possibly strengthening the overall molecular attractions. The HB-network in (rac)-Phenibut is very similar to that in the Pregabalin entities. Three distinct HB with the different ammonium subunit hydrogens towards the two carboxylate oxygens are formed. HB lengths are nearly non-distinguishable from those in Pregabalin at about 2.7 Å between nitrogen and oxygen atoms. The angles in Phenibut are also very close apart from N1-H7...O1 at 160° slightly further from the “ideal” 180° as compared to all other angles in Phenibut and Pregabalin at about 170°. The edge-to-face π-interaction between C8-H11...Cg1 is the distinctive feature of (rac)-Phenibut

interactions compared to Pregabalin. Electron density- and Hirshfeld surface confirm the discussed intermolecular bonding motif (**Figure S5**). Higher-than-average electron density and close atom proximity can be observed right around the relevant molecular subunits. The additional close range or high electron density spots indicate a closer packing as compared to the Pregabalin enantiomers. In the latter, some close ranges could be observed along the GABA chain that do not contribute to attractive interactions but none along the isobutyl subunit. In Phenibut however, more of these spots can be observed on both surface types which also indicates a closer packing as discussed in regard to the lattice properties.

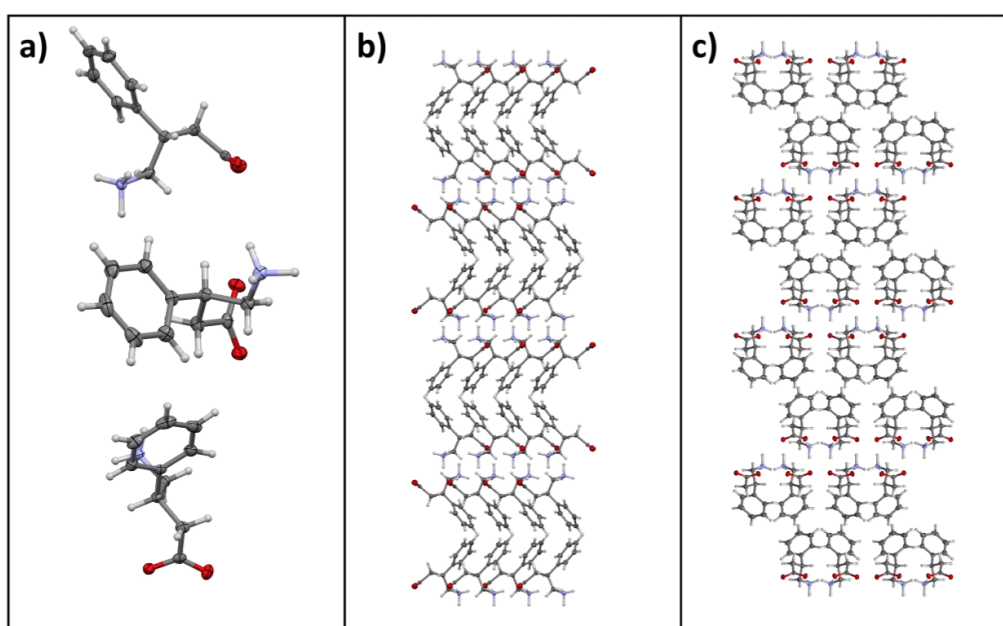


Figure S4. The asymmetric unit of (*rac*)-Phenibut is shown in **a**): from top to bottom *a*-axis, *b*-axis, *c*-axis. In **b**) the packing of a $2 \cdot 2 \cdot 2$ unit cell from *a*-axis view is shown. In **c**) the packing of a $2 \cdot 2 \cdot 2$ unit cell from *b*-axis view is shown. Carbon atoms are depicted in grey, hydrogen atoms in white, nitrogen atoms in blue and oxygen atoms in red.

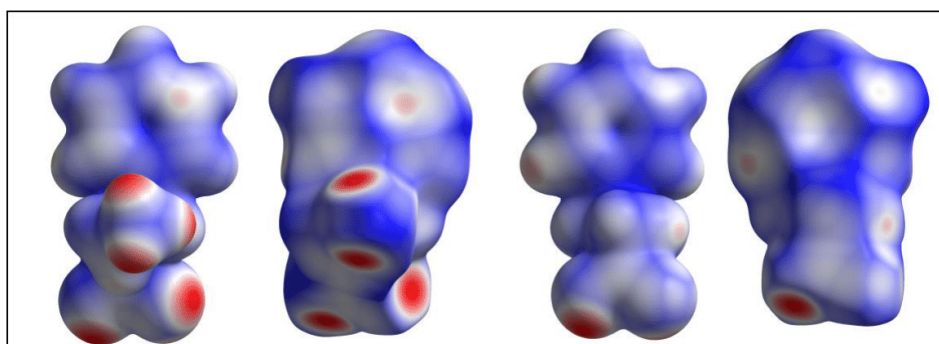


Figure S5. Electron density and Hirshfeld surfaces of (*rac*)-Phenibut. **a**) shows the electron density surface of the sole symmetrically inequivalent Phenibut molecule in the (*rac*)-Phenibut lattice from two sides. **b**) shows the Hirshfeld surface of the same entity.

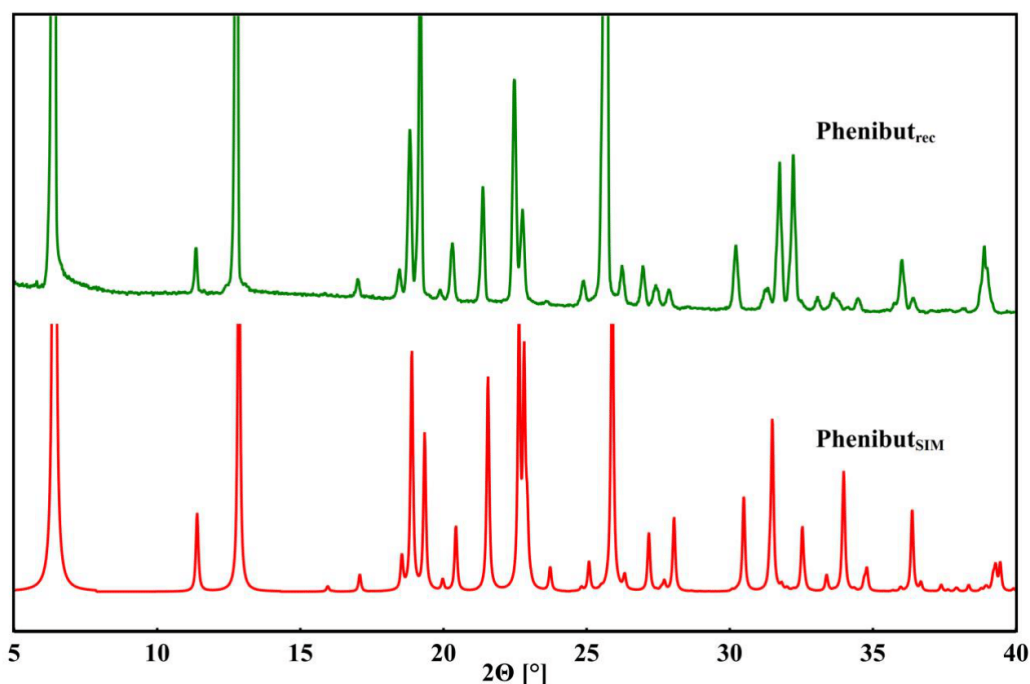


Figure S6. Powder pattern of (*rac*)-Phenibut as recorded (red) compared to a simulated pattern by single crystal data (green) in a range of 5° – 40°.

1.3 Homo- and heterochiral Pregabalin:mandelic acid (1:3), ratio (1:1)

Four Pregabalin:mandelic acid multicomponent systems were obtained. The homochiral (R, R) and (S, S) as well as the heterochiral (R, S) and (S, R) are isostructural. In each case single crystals were obtained by dissolving equimolar amounts of enantiomerically purified Pregabalin and mandelic acid in water and subsequent slow evaporation of the solvent. Thereby, colourless elongated plates were obtained. The lattice and measurement parameters for (R, R) and (S, S) are given in **Table S5** and intermolecular interactions for them are shown in **Table S6** while lattice and measurement parameters for (S, R) and (R, S) are presented in **Table S7** and their intermolecular interactions are depicted in **Table S8**.

The asymmetric unit and packing of homochiral compound (**S, S**)-1:3 is shown in **Figure S7**, heterochiral compound (**R, S**)-1:3 is depicted in **Figure S8**. The homochiral systems crystallize in the same space group with the same unit cell parameters, as do the heterochiral forms respectively. In homochiral forms, Pregabalin and mandelic acid keep their default protonation status, while in heterochiral forms both molecules become formally charged. Notable is the occurrence of an uncommon packing phenomenon in $Z' = 2$. Z' is defined as the number of formula units in the unit cell divided by the number of independent general positions and a

value larger than 1 could indicate a non-optimal structure in terms of stability or symmetry, as defined by Steed and Desiraju respectively.^[5, 6]

Table S5. Lattice and measurement parameters of (R, R)- and (S, S)-Pregabalin:mandelic acid systems.

Parameters	(R, R)-1:3	(S, S)-1:3
Formula	C ₈ H ₁₇ N O ₂ , C ₈ H ₈ O ₃	C ₈ H ₁₇ N O ₂ , C ₈ H ₈ O ₃
M_r [g mol⁻¹]	311.37	311.37
Temperature [K]	100(2)	100(2)
System/space group	Monoclinic, <i>P</i> 2 ₁	Monoclinic, <i>P</i> 2 ₁
a (Å)	6.252(7)	6.245(5)
b (Å)	27.384(8)	27.388(0)
c (Å)	9.960(3)	9.962(4)
β (°)	90.483(0)	90.462(2)
V (Å³)	1705.43(4)	1704.03(5)
Z/Z'	4/2	4/2
Density [g/cm³]	1.221	1.214
μ [mm⁻¹]	0.738	0.739
T_{min}/T_{max}	0.458/1.000	0.560/1.000
F (000)	672	672
Crystal size [mm]	0.40 · 0.11 · 0.09	0.59 · 0.22 · 0.07
2θ range [°]	3.2 – 77.7	3.2 – 77.8
Completeness [%]	99.9	99.9
Recorded refl.	47481	19149
Independent refl.	6627	6561
Flack x	-0.02(5)	0.15(11)
Goodness-of-fit F²	1.035	1.084
X-Ray Source	Cu Kα (λ = 1.54184)	Cu Kα (λ = 1.54184)
R₁ [%] /wR₂ [%] /S	2.78/ 6.89/ 1.035	4.58/ 11.86/ 1.084

There are two symmetrically distinct Pregabalin and mandelic acid molecules. HB are the dominating intermolecular attraction force. Twelve distinct HB interactions occur in the (S, S) variant and fourteen in the (R, R) system. The discrepancy in the number of interactions between (S, S)- and (R, R)-Pregabalin:mandelic acid might have two reasons. In (R, R) an additional interaction is added for N1A-H6A...O3C and N1B-H8B...O3D. Both interaction distances are larger than 3 Å in (R, R) and thus may not have been recognized as interactions by PLATON in (S, S). Mercury however, measures distances of 3.003 Å and 3.033 Å for the former and the latter interaction. It should further be noted that the melting points of both systems differ, which could be accounted to by these differences. It is notable that the shortest interactions occur from the non-ionic mandelic acid oxygens O1C and O3D and to Pregabalin carboxylate Oxygen O1A or B. The distances range from 2.487(3) Å - 2.690(3) Å in (S, S) and from 2.489(7) Å - 2.695(2) Å in (R, R). When these distance values are compared to HB formed between two oppositely charged molecular fragments like N1A-H7A...O2B at 2.770(4) Å in (S, S) or the corresponding N1A-H7A...O2B at 2.767(2) Å in (R, R) it is highlighted that assumed charge assistance between two charged sub molecular entities does not result in the

8

shortest interaction distances in both systems. In the heterochiral (S, R) and (R, S)-forms HB are also the main occurring bonding interaction and the same 14 types are observable in both compounds.

Table S6. Hydrogen bond distances and angles in (S, S) as well as (R, R) Pregabalin:mandelic acid cosystems. Bold written entities are charged at their oxygen or nitrogen atoms. A and B indices mark the different Pregabalin molecules, C and D the different mandelic acid molecules.

	D - H [Å]	H...A [Å]	D...A [Å]	D - H...A [°]
(S, S)-1:3				
N1A-H6A...O2C	0.87(4)	1.93(4)	2.787(4)	165(3)
N1A-H7A...O2B	0.88(5)	1.89(5)	2.770(4)	175(4)
N1A-H8A...O1B	0.88(4)	2.24(4)	3.036(4)	151(4)
N1A-H8A...O2A	0.88(4)	2.40(4)	2.940(4)	120(3)
N1B-H6B...O2A	1.07(6)	1.72(6)	2.780(4)	171(5)
N1B-H7B...O1A	0.90(5)	2.26(4)	3.033(4)	144(4)
N1B-H7B...O2B	0.90(5)	2.30(5)	2.906(4)	125(4)
N1B-H8B...O2D	0.86(4)	1.96(4)	2.802(4)	168(4)
O1C-H1C...O1A	0.97(8)	1.52(8)	2.487(3)	174(2)
O3C-H2C...O1B	0.92(6)	1.80(6)	2.690(3)	161(6)
O1D-H1D...O1B	0.93(6)	1.56(6)	2.492(3)	178(9)
O3D-H2D...O1A	0.87(6)	1.82(6)	2.682(4)	169(5)
(R, R)-1:3				
N1A-H6A...O2C	0.91(3)	1.88(3)	2.786(2)	171(3)
N1A-H6A...O3C	0.91(3)	2.55(3)	3.006(2)	111(2)
N1A-H7A...O2B	0.98(3)	1.79(3)	2.767(2)	171(3)
N1A-H8A...O1B	0.87(3)	2.26(3)	3.038(2)	148(3)
N1A-H8A...O2A	0.87(3)	2.37(3)	2.934(2)	123(2)
N1B-H6B...O2A	0.96(3)	1.83(3)	2.783(2)	176(2)
N1B-H7B...O1A	0.91(3)	2.23(3)	3.035(2)	148(3)
N1B-H7B...O2B	0.91(3)	2.33(3)	2.906(2)	121(2)
N1B-H8B...O2D	0.88(3)	1.92(3)	2.798(2)	172(3)
N1B-H8B...O3D	0.88(3)	2.56(3)	3.031(2)	114(2)
O1C-H1C...O1A	0.97(4)	1.53(4)	2.489(7)	172(4)
O3C-H3C...O1B	0.84(3)	1.88(3)	2.695(2)	166(3)
O1D-H1D...O1B	0.92(3)	1.58(3)	2.497(9)	177(3)
O3D-H2D...O1A	0.89(4)	1.81(4)	2.682(2)	166(4)

Table S7. Lattice and measurement parameters of (S, R) and (R, S) Pregabalin:mandelic acid cosystems.

Parameters	(S, R)-1:3	(R, S)-1:3
Formula	C ₈ H ₁₈ N O ₂ , C ₈ H ₇ O ₃	C ₈ H ₁₈ N O ₂ , C ₈ H ₇ O ₃
M_r [g mol⁻¹]	311.37	311.37
Temperature [K]	100(2)	100(2)
System/space group	Monoclinic, <i>P</i> ₂ ₁	Monoclinic, <i>P</i> ₂ ₁
a (Å)	6.077(1)	6.051(7)
b (Å)	29.926(5)	29.898(9)
c (Å)	9.306(6)	9.306(9)
β (°)	92.662(0)	92.641(0)
V (Å³)	1690.73(4)	1682.19(4)
Z/Z'	4/2	4/2
Density [g/cm³]	1.223	1.229
μ [mm⁻¹]	0.745	0.748
T_{min}/T_{max}	0.351/1.000	0.580/ 1.000
F (000)	672	672
Crystal size [mm]	0.54 · 0.38 · 0.15	0.31 · 0.12 · 0.09
2θ range [°]	3.0 – 77.8	3.0 – 77.1
Completeness [%]	100	99.8
Recorded refl.	21324	25468
Independent refl.	6745	6336
Flack x	-0.05(12)	-0.15(7)
Goodness-of-fit F²	1.050	1.048
X-Ray Source	Cu Kα (λ = 1.54184)	Cu Kα (λ = 1.54184)
R₁ [%] /wR₂ [%] /S	4.97/ 12.05/ 1.05	3.00/ 7.33/ 1.05

Consideration of HB interaction distances shows no especially noticeable deviations from (S, S) and (R, R) systems HB network. The shortest distances occur between carboxyl Pregabalin donors and carboxylate mandelic acid acceptor oxygens at 2.570(3) Å for O1B-H1B...O1D (S, R) and (R, S). This highlights that the shortest contacts occur between a charged and a neutral subunit as is the case in the (S, S) and (R, R) systems. Interactions where both subunits are charged like N1A-H7A...O1D, N1A-H9A...O2D, N1B-H7B...O2C and N1B-H8B...O1C with values around 2.7 – 2.8 Å lie in a median range compared to all shown interactions in **Tables S2, S4, S6 and S8**. To further elucidate on the binding interactions, Hirshfeld surfaces and electron density surfaces of homo- and heterochiral systems were calculated (**Figures S9 & S10**). Again, the closest interactions as derived from the Hirshfeld surface occur around the HB interactions sites, where the highest electron density can also be located. In homochiral forms, neither close distances nor electron density accumulations can be observed around the mandelic acid phenyl subunits. However, C7D-H7D in (S, S) and (R, R) mandelic acid phenyl rings are directed towards the phenyl ring centre of gravity of their respective symmetry unrelated mandelic acid molecule C. While this possible interaction is not recognized by PLATON analysis, Mercury measures a distance C7D-H7D...C_GC of 3.672 Å or

C7D...Cg_C of 4.664 Å for (S, S) and 3.707 Å as well as 4.658 Å in (R, R). This could suggest possible weak edge-to-face C-H... π influences in both systems.

Table S8. Hydrogen bond distances and angles in (S, R) as well as (R, S) Pregabalin:mandelic acid cosystems. Bold written entities are charged at their oxygen or nitrogen atoms. A and B indices mark the different Pregabalin molecules, C and D the different mandelic acid molecules.

	D - H [Å]	H...A [Å]	D...A [Å]	D - H...A [°]
(S, R)-1:3				
N1A-H7A...O1D	0.85(4)	1.91(4)	2.736(3)	163(4)
N1A-H8A...O1B	0.84(4)	2.45(3)	2.916(3)	116(3)
N1A-H8A...O2A	0.84(4)	2.19(4)	2.876(3)	139(3)
N1A-H9A...O2D	0.92(4)	1.92(5)	2.786(3)	158(4)
N1B-H7B...O2C	0.94(4)	1.82(4)	2.757(3)	173(4)
N1B-H8B...O1C	0.96(6)	1.87(5)	2.812(3)	167(5)
N1B-H9B...O2A	0.91(4)	2.35(4)	3.004(3)	129(3)
N1B-H9B...O3D	0.91(4)	2.44(4)	3.012(3)	121(3)
O1A-H1A...O1C	0.89(6)	1.72(6)	2.578(3)	161(5)
O1B-H1B...O1D	0.97(5)	1.60(5)	2.570(3)	179(6)
O3C-H2C...O2B	0.77(4)	2.23(4)	2.880(3)	143(4)
O3C-H2C...O2C	0.77(4)	2.19(4)	2.645(3)	118(4)
O3D-H2D...O1A	0.84(4)	2.19(4)	2.963(3)	152(4)
O3D-H2D...O2D	0.84(4)	2.19(4)	2.645(3)	114(3)
(R, S)-1:3				
N1A-H7A...O1D	0.93(3)	1.83(3)	2.734(2)	163(3)
N1A-H8A...O1B	0.87(3)	2.44(2)	2.905(3)	115(2)
N1A-H8A...O2A	0.87(3)	2.19(3)	2.881(2)	136(2)
N1A-H9A...O2D	0.94(3)	1.92(3)	2.782(2)	153(3)
N1B-H7B...O2C	0.95(3)	1.81(3)	2.758(2)	169(3)
N1B-H8B...O1C	0.98(4)	1.84(4)	2.807(2)	166(3)
N1B-H9B...O2A	0.92(3)	2.35(3)	2.993(2)	127(2)
N1B-H9B...O3D	0.92(3)	2.34(3)	3.006(2)	129(2)
O1A-H1A...O1C	0.92(4)	1.70(4)	2.588(2)	163(3)
O1B-H1B...O1D	0.92(4)	1.66(4)	2.570(2)	174(4)
O3C-H2C...O2B	0.87(4)	2.18(3)	2.881(3)	138(2)
O3C-H2C...O2C	0.87(4)	2.10(3)	2.642(2)	120(3)
O3D-H2D...O1A	0.86(3)	2.17(3)	2.958(2)	152(3)
O3D-H2D...O2D	0.86(3)	2.16(3)	2.648(2)	115(2)

The heterochiral systems contrast the (S, S) and (R, R) forms, the phenyl subunits are not tilted in a favourable angle to engage into C-H... π interactions with each other. As again no such interaction is identified by PLATON analysis, the measured distances between C_{phenyl}-H and close C_{phenyl} atoms lie between 3.060 Å and 3.204 Å with Mercury software calculations. Centroid distances are not taken into consideration this time as the angles between possible C_{phenyl}-H and close centroids are too unfavourable. While the distances of these possible edge-to-edge interactions seem reasonably short the charge distribution, which is alike on all phenyl rings, makes them unlikely.^[7]

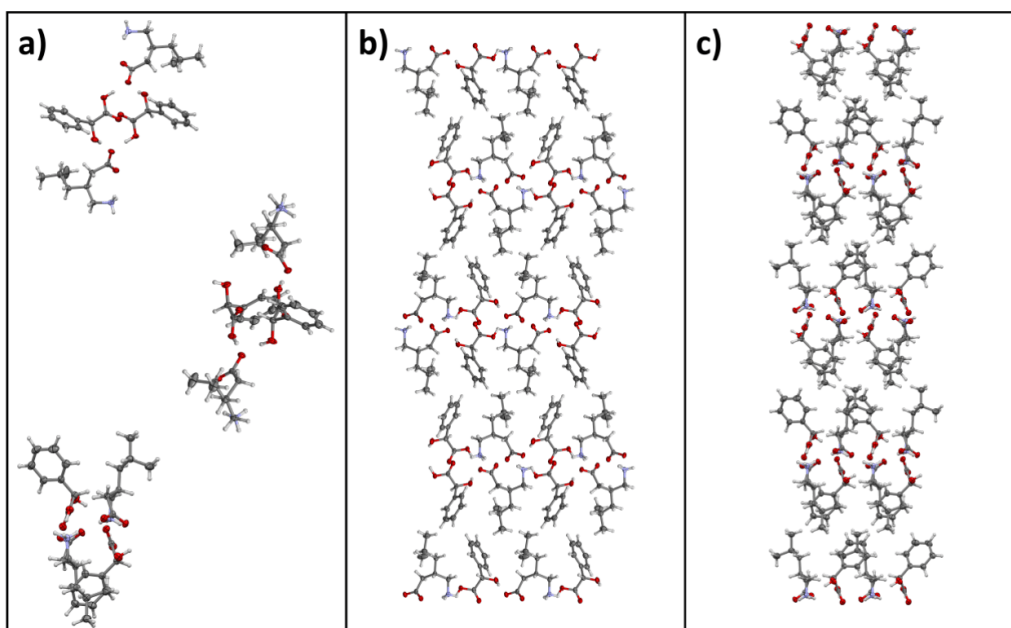


Figure S7. The asymmetric unit of *(S, S)*-Pregabalin:mandelic acid species is shown in **a)**: from top to bottom *a*-axis, *b*-axis, *c*-axis. In **b)** the packing of a $2 \cdot 2 \cdot 2$ unit cell from *a*-axis view is shown. In **c)** the packing of a $2 \cdot 2 \cdot 2$ unit cell from *c*-axis view is shown. Carbon atoms are depicted in grey, hydrogen atoms in white, nitrogen atoms in blue and oxygen atoms in red.

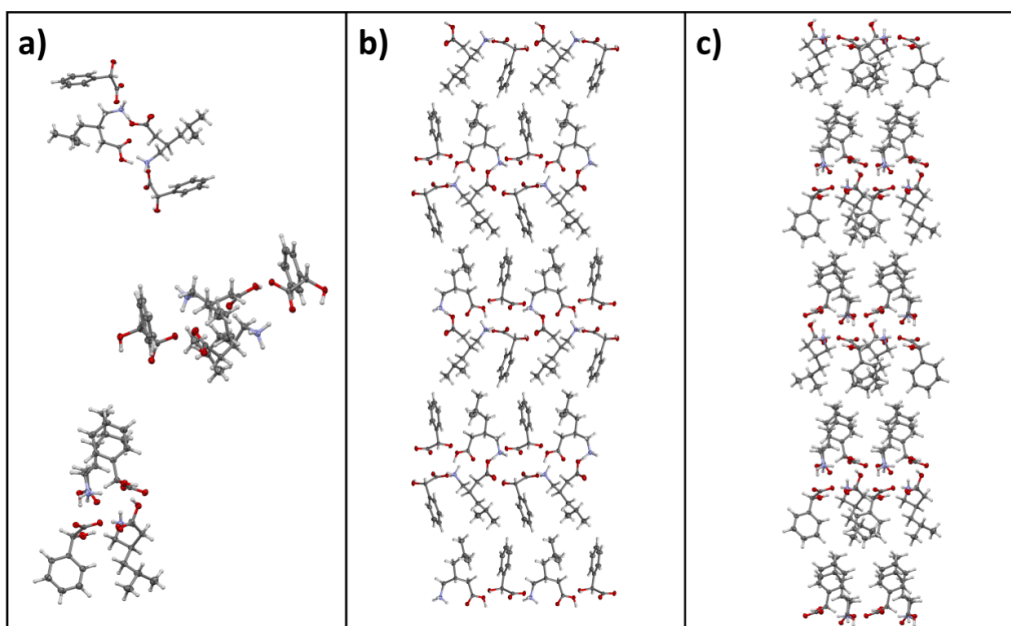


Figure S8. The asymmetric unit of *(R, S)*-Pregabalin:mandelic acid species is shown: from top to bottom *a*-axis, *b*-axis, *c*-axis. In **b)** the packing of a $2 \cdot 2 \cdot 2$ unit cell from *a*-axis view is shown. In **c)** the packing of a $2 \cdot 2 \cdot 2$ unit cell from *c*-axis view is shown. Carbon atoms are depicted in grey, hydrogen atoms in white, nitrogen atoms in blue and oxygen atoms in red.

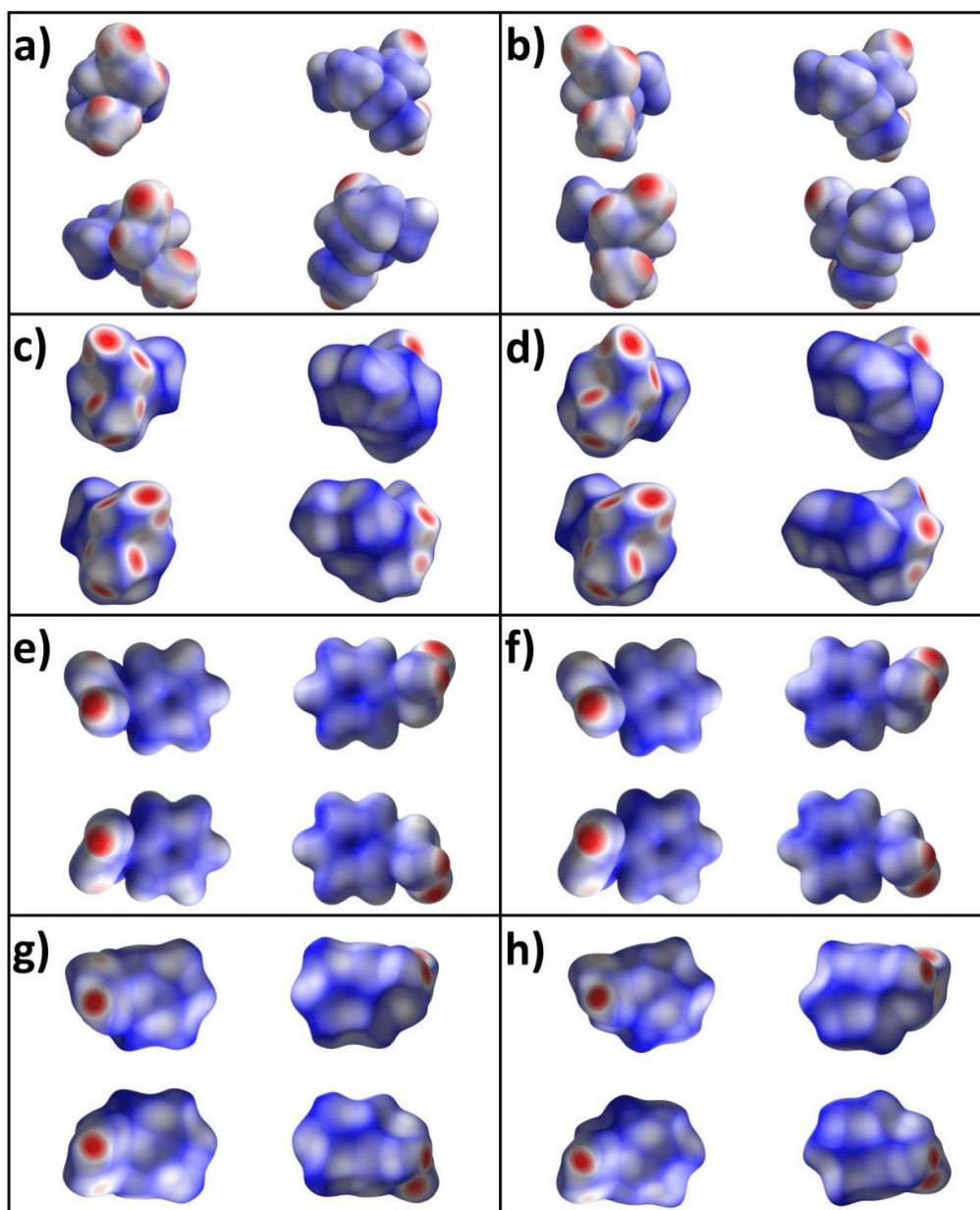


Figure S9. Electron density and Hirshfeld surfaces of *(S, S)*- and *(R, R)* Pregabalin:mandelic acid species. **a)** and **b)** show the electron density surface of the two symmetrically inequivalent Pregabalin molecules in the *(S, S)* and *(R, R)* lattice respectively, from two sides. **c)** and **d)** show the corresponding Hirshfeld surfaces. **e)** and **f)** show the electron density surface of the two symmetrically inequivalent mandelic acid molecules in the *(S, S)* and *(R, R)* lattice respectively, from two sides. **g)** and **h)** show the corresponding Hirshfeld surfaces.

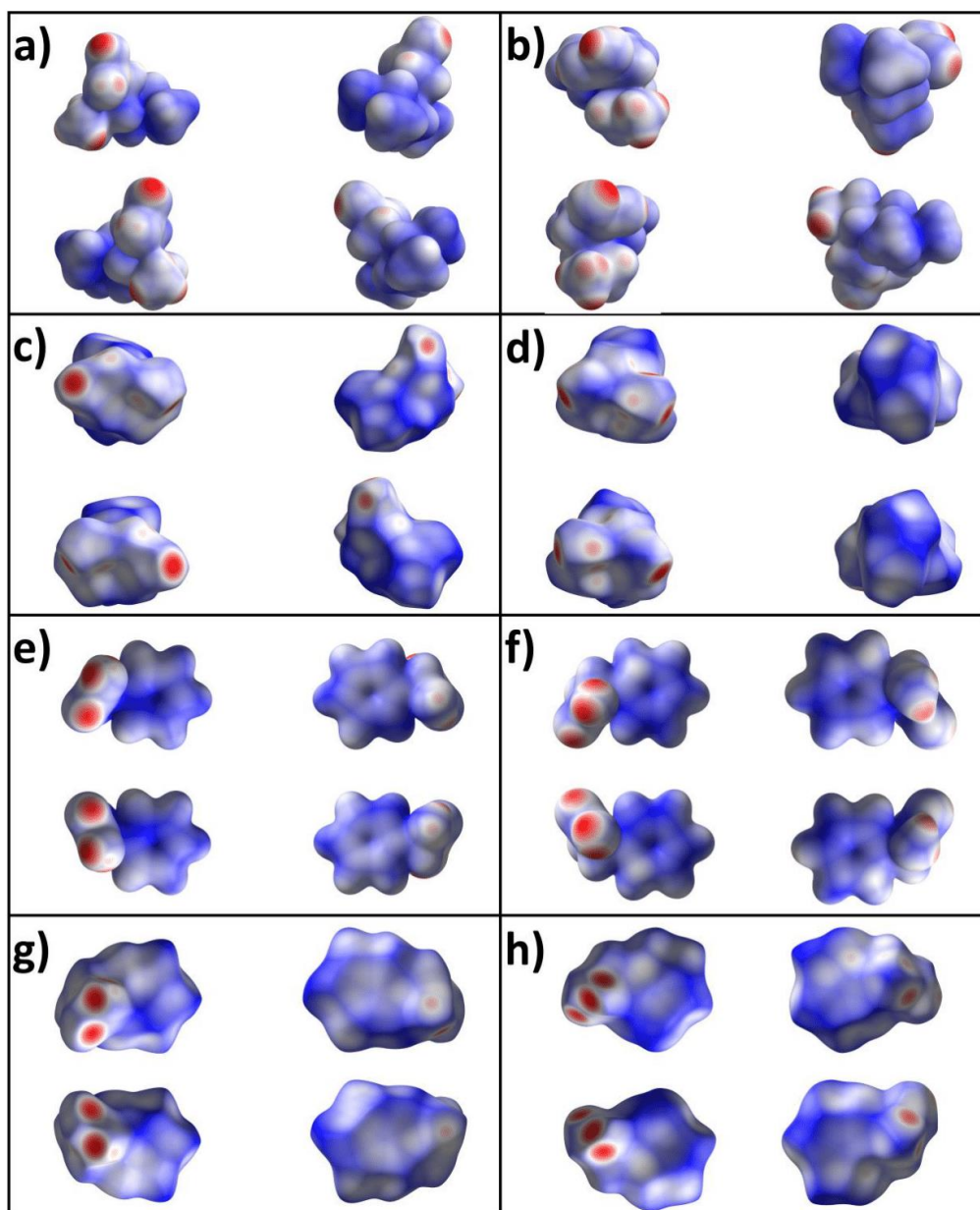


Figure S10. Electron density and Hirshfeld surfaces of (*S*, *R*)- and (*R*, *S*) Pregabalin:mandelic acid species. **a)** and **b)** show the electron density surface of the two symmetrically inequivalent Pregabalin molecules in the (*S*, *R*) and (*R*, *S*) lattice respectively, from two sides. **c)** and **d)** show the corresponding Hirshfeld surfaces. **e)** and **f)** show the electron density surface of the two symmetrically inequivalent mandelic acid molecules in the (*S*, *R*) and (*R*, *S*) lattice respectively, from two sides. **g)** and **h)** show the corresponding Hirshfeld surfaces.

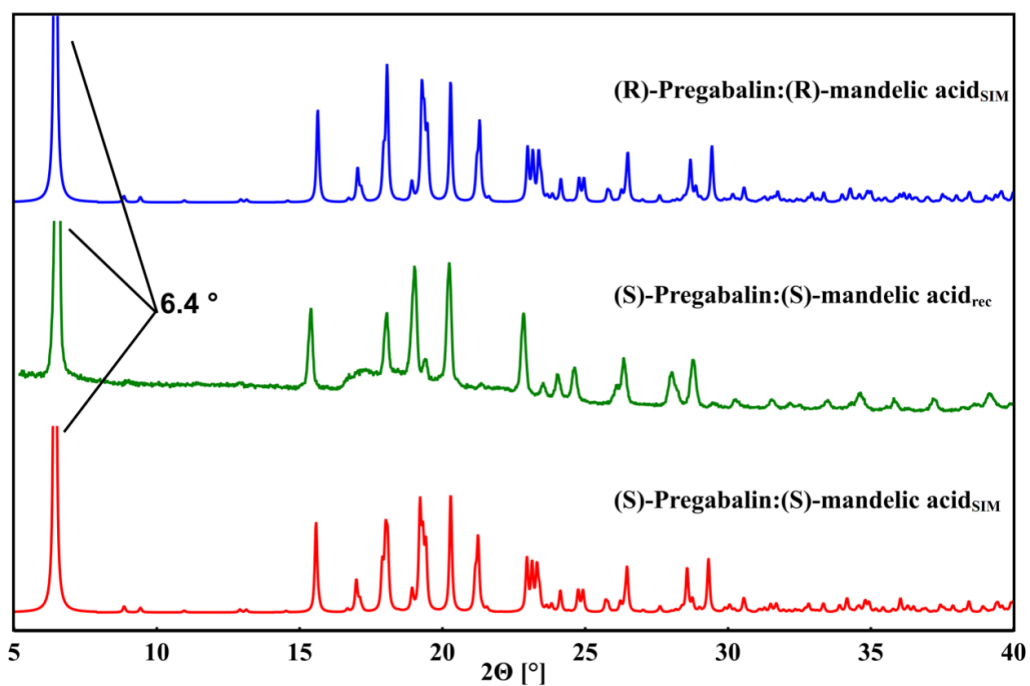


Figure S11. Powder pattern of (S, S) Pregabalin:mandelic acid as recorded (green) compared to simulated patterns of (S, S) (red) and (R, R) (blue) systems single crystal data in a range of 5° – 40°. Only (S, S)_{rec} is shown for clarity.

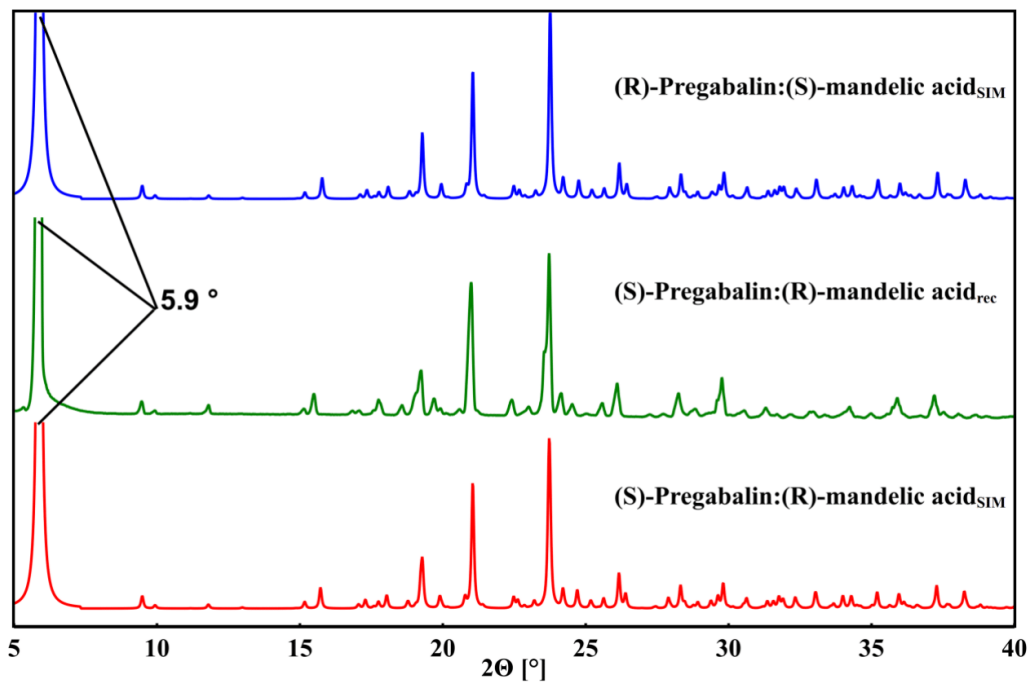


Figure S12. Powder pattern of (S, R) Pregabalin:mandelic acid as recorded (green) compared to simulated patterns of (S, R) (red) and (R, S) (blue) systems single crystal data in a range of 5° – 40°. Only (S, R)_{rec} is shown for clarity.

1.4 Phenibut:mandelic acid (2:3), ratio (1:1)

A single crystal of (R)-Phenibut:(S)-mandelic acid was obtained by dissolving equimolar amounts of (rac)-Phenibut and (S)-mandelic acid in aqueous solution. Elongated, diffraction quality crystalline plates were obtained by slow evaporation of the solvent. **Table S9** shows lattice and measurement parameters. Supramolecular interactions involving HB- and π -interactions are shown in **Table S10**.

Table S9. Lattice and measurement parameters of (R)-Phenibut:(S)-mandelic acid.

Parameters	(R, S)-2:3
Formula	C ₁₀ H ₁₃ N O ₂ , C ₈ H ₈ O ₃
M _r [g mol ⁻¹]	331.36
Temperature [K]	100(2)
System/space group	Monoclinic, P2 ₁
a (Å)	10.130(7)
b (Å)	6.353(9)
c (Å)	13.063(3)
β (°)	95.469(2)
V (Å ³)	837.06(2)
Z/Z'	2/1
Density [g/cm ³]	1.315
μ [mm ⁻¹]	0.794
T _{min} /T _{max}	0.239/ 1.000
F (000)	352
Crystal size [mm]	0.52 · 0.37 · 0.12
2 θ range [°]	3.4 – 77.9
Completeness [%]	99.9
Recorded refl.	19556
Independent refl.	3246
Flack x	0.00(10)
Goodness-of-fit F ²	1.068
X-Ray Source	Cu K α (λ = 1.54184)
R ₁ [%] /wR ₂ [%] /S	3.15/ 8.24/ 1.070

Table S10. Hydrogen bond and edge-to-face interaction distances and angles in (R)-Phenibut:(S)-mandelic acid. Bold written entities are charged at their oxygen or nitrogen atoms. A indices mark Phenibut molecules, B mandelic acid molecules.

	D - H (Å)	H...A [Å]	D...A [Å]	D - H...A [°]
HB				
N1A-H6A...O2A	0.90(3)	2.36(3)	2.929(2)	121(2)
N1A-H6A...O1A	0.90(3)	2.21(3)	2.998(3)	146(3)
N1A-H7A...O2B	0.91(3)	1.92(3)	2.808(2)	163(3)
N1A-H7A...O3B	0.91(3)	2.50(3)	3.020(2)	117(2)
N1A-H8A...O2A	0.97(3)	1.83(3)	2.801(3)	177(3)
O1B-H1B...O1A	0.99(4)	1.52(4)	2.504(2)	175(4)
O3B-H3B...O1A	0.95(4)	1.77(3)	2.689(2)	163(3)
C-H...π		H...Cg [Å]	C...Cg [Å]	C-H...Cg [°]
C5B-H5B...Cg1*		2.57(3)	3.354(2)	136(2)
C7A-H10A...Cg2*		2.88(3)	3.582(2)	133(2)
C9A-H12A...Cg1*		2.98(3)	3.657(2)	129(2)

Asymmetric unit and packing are shown in **Figure S13**. The protonation status of Phenibut and mandelic acid stays in its default state, zwitterionic and neutral respectively. However, contrary to 1:3 species, a heterochiral species with these characteristics is received. The Phenibut:mandelic acid system could not be accessed as readily as its Pregabalin analogues. PXRD data shows that disregarding the mandelic acid chirality in the crystallization attempt if a multicomponent structure is formed at all, all possible chiral permutations lead to an isostructural form (**Figure S15**). The number of HB with 7 distinct types is halved compared to Pregabalin:mandelic acid systems. The shortest interaction distance derives from the carboxyl mandelic acid donor to the carboxylate Phenibut acceptor in the O1B-H1B...O1A interaction with 2.504(2) Å. In this case the corresponding angle at 175(4)° is also close to 180°. It can be noted that this HB is not between two subunits of opposing charges but rather between a charged and a neutral subunit. Interactions formed with the positively charged ammonium subunit lead to median ranged distances of about 2.8 Å – 3 Å which includes charged-charged HB. Furthermore, the angles exhibited for HB in this structure show a distribution of values close to 180°. In contrast to other multicomponent species, strong evidence for π -interactions is shown in the lattice. While each Phenibut phenyl Cg1 is in interaction twice being connected to another Phenibut phenyl and additionally a mandelic acid phenyl Cg2, the latter solely interacts once with Phenibut. The C5B-H5B...Cg1 edge-to-face interaction is also the shortest in H...Cg as well as C...Cg distance at 2.57(3) Å and 3.354(2) Å respectively, between all described compounds. Clear evidence for edge-to-face interactions is visible upon examination of Hirshfeld and electron density surface (**Figure S14**). In the former, close contacts occur around Phenibut and Mandelic Acid phenyl subunits and in the latter, higher electron density can be observed on the same spots.

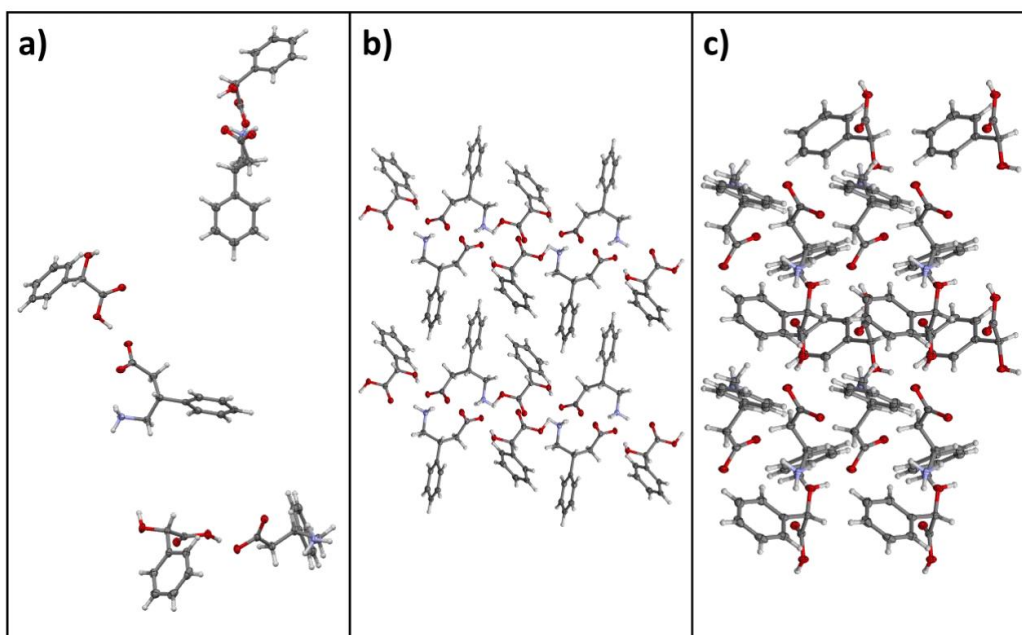


Figure S13. The asymmetric unit of (*R*)-Phenibut:(*S*)-mandelic acid is shown in **a)**: from top to bottom *a*-axis, *b*-axis, *c*-axis. In **b)** the packing of a $2 \cdot 2 \cdot 2$ unit cell from *b*-axis view is shown. In **c)** the packing of a $2 \cdot 2 \cdot 2$ unit cell from *c*-axis view is shown. Carbon atoms are depicted in grey, hydrogen atoms in white, nitrogen atoms in blue and oxygen atoms in red.

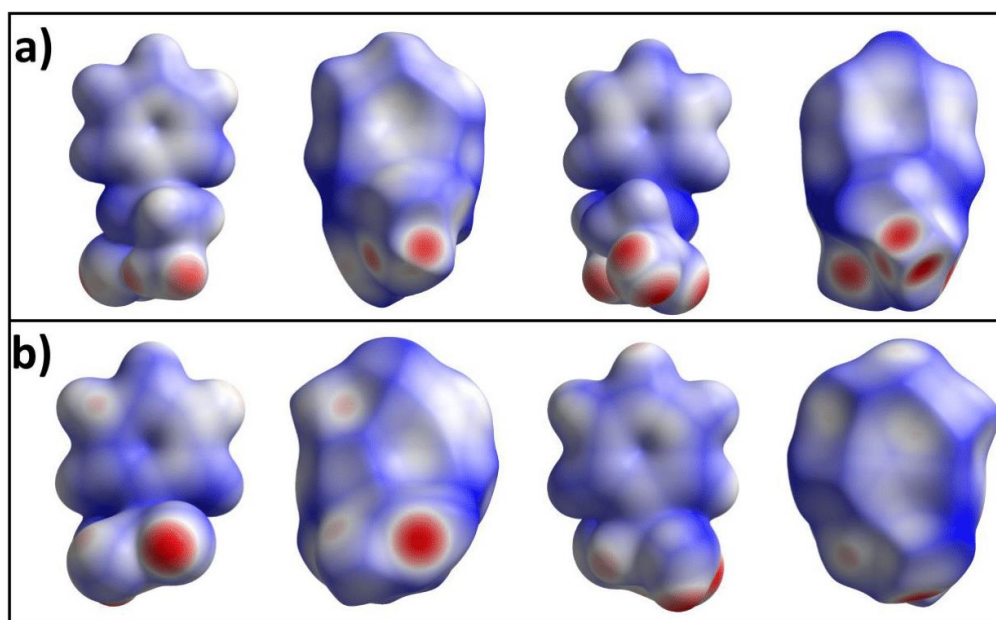


Figure S14. Electron density and Hirshfeld surfaces of (*R*)-Phenibut:(*S*)-mandelic acid. **a)** shows the electron density and Hirshfeld surface of the sole symmetrically inequivalent Phenibut molecule in the lattice from two sides. **b)** shows the electron density and Hirshfeld surface of the sole symmetrically inequivalent mandelic acid molecule in the lattice from two sides.

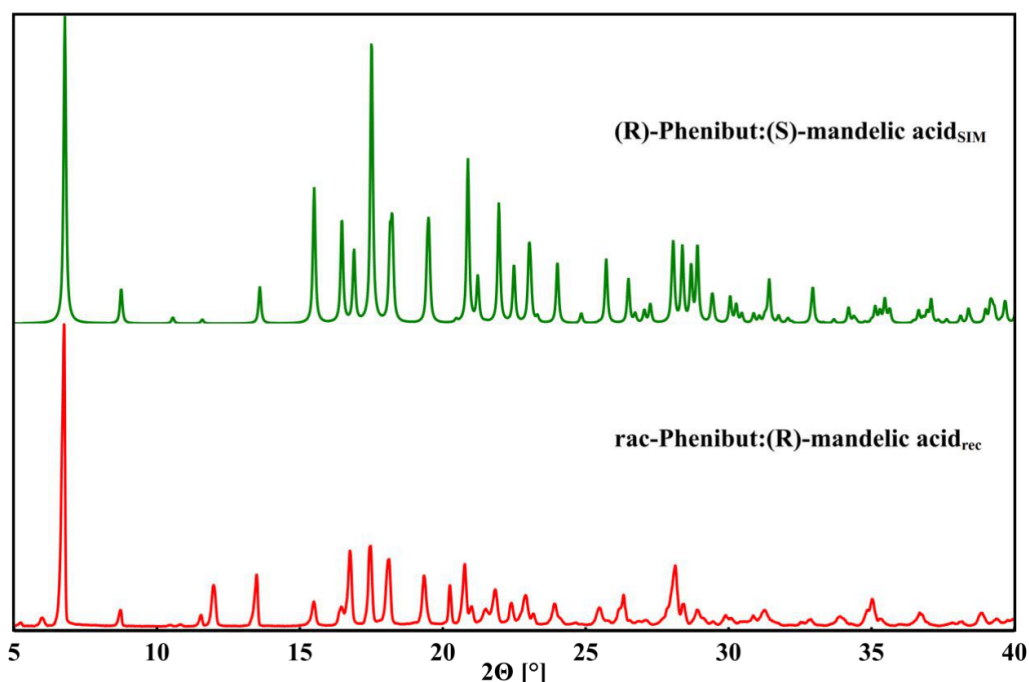


Figure S15. Powder pattern of (*R*)-Phenibut:(*S*)-mandelic acid simulated from single crystal data (green) compared to a recorded pattern of a (*rac*)-Phenibut:(*R*)-mandelic acid co-crystallization attempt (red) in a range of 5° – 40°. The comparison to a pattern received by an attempted crystallization with (*R*)-mandelic acid to the simulated pattern with (*S*)-mandelic acid while (*rac*)-Phenibut was used in both cases highlights isostructural crystallization. The presence of less intense Phenibut and mandelic acid signals at low angles shows the problematic crystallization of the multicomponent system. The multicomponent system seems to be not favourable and cannot always be obtained.

1.5 Homo- and heterochiral Pregabalin:malic acid (1:4), ratio (1:1)

Single crystals of (*S*)-Pregabalin and (*R*)- as well as (*S*)-malic acid were grown from aqueous solution. Diffraction quality, plate shaped crystals were obtained by slow evaporation of the solvent. During the conducted experiments the Pregabalin:malic acid entities exhibited a similarly problematic crystallization behaviour as the Phenibut:mandelic acid system. While the latter could sometimes not be obtained and always showed impurities of its precursors in the powder pattern, the former can take weeks or even months to crystallize. Lattice and measurement parameters for (*S*, *S*) and (*S*, *R*)-Pregabalin:malic acid systems are shown in **Table S11**, HB properties are shown in **Table S12**.

The asymmetric unit shows one symmetry independent and charged Pregabalin and malic acid molecule in both homo- and heterochiral 1:4 (**Figure S16**). Pregabalin units are intertwined with malic acid in closely HB-connected rows, with the alkylic residues of Pregabalin being shifted towards each other and away from the HB interacting subunits. There are 8 distinct HB present in each compound. The shortest interaction in the presented

structures is between two malic acid molecules, connected via carboxyl donor to a carboxylate of an identical molecule via O1B-H1B...O5B in (S, S) and O1B-H1B...O4B in (S, R) at 2.446(4) Å and 2.475(2) Å respectively. Furthermore, as is the case in heterochiral Pregabalin:mandelic acid, uncharged HB interactions are present in both discussed entities even though all participating molecules are formally charged. The comparison between (S, S) and (S, R) reveals differences in the interaction motif that are larger than those present in homochiral Pregabalin:mandelic acid forms and more akin to differences between homo- and heterochiral Pregabalin:mandelic acid.

Table S11. Lattice and measurement parameters of (S, S) and (S, R) Pregabalin:malic acid co-systems.

Parameters	(S, S)-1:4	(S, R)-1:4
Formula	C ₈ H ₁₈ N O ₂ , C ₄ H ₅ O ₅	C ₈ H ₁₈ N O ₂ , C ₄ H ₅ O ₅
M_r [g mol⁻¹]	293.31	293.31
Temperature [K]	100(2)	100(2)
System/space group	Orthorhombic, <i>P</i> 2 ₁ 2 ₁ 2 ₁	Orthorhombic, <i>P</i> 2 ₁ 2 ₁ 2 ₁
a (Å)	7.500(9)	7.440(4)
b (Å)	7.558(1)	7.703(9)
c (Å)	26.180(5)	25.956(6)
β (°)	90	90
V (Å³)	1484.24(3)	1487.83(3)
Z/Z'	4/1	4/1
Density [g/cm³]	1.313	1.309
μ [mm⁻¹]	0.915	0.913
T_{min}/T_{max}	0.535/1.000	0.500/1.000
F (000)	632	632
Crystal size [mm]	0.26 · 0.22 · 0.05	0.36 · 0.16 · 0.08
2θ range [°]	3.4 – 77.7	6.0 – 77.8
Completeness [%]	99.4	99.6
Recorded refl.	8059	22743
Independent refl.	2826	3009
Flack x	0.01(6)	0.01(5)
Goodness-of-fit F²	1.053	1.109
X-Ray Source	Cu Kα (λ = 1.54184)	Cu Kα (λ = 1.54184)
R₁ [%] /wR₂ [%] /S	2.49/ 5.94/ 1.05	3.01/ 7.78/ 1.11

Table S12. Hydrogen bond distances and angles in (S, S) and (S, R) Pregabalin:malic acid cosystems. Bold written entities are charged at their oxygen or nitrogen atoms. A indices mark Pregabalin molecules, B malic acid molecules.

	D - H (Å)	H...A [Å]	D...A [Å]	D - H...A [°]
(S, S)-1:4				
N1A-H7A...O3B	0.90(2)	2.46(3)	3.065(2)	125(2)
N1A-H7A...O4B	0.90(2)	1.94(2)	2.792(6)	157(2)
N1A-H8A...O3B	0.93(2)	2.11(2)	2.976(1)	155(2)
N1A-H9A...O4B	0.93(2)	1.87(2)	2.761(0)	161(2)
O1A-H1A...O2B	0.90(4)	1.85(4)	2.733(4)	168(3)
O1B-H1B... O5B	1.07(4)	1.39(4)	2.446(4)	172(3)
O1B-H1B... O4B	1.07(4)	2.59(3)	3.154(3)	112(2)
O3B-H5B...O2A	0.81(3)	1.88(3)	2.688(9)	175(3)
(S, R)-1:4				
N1A-H7A...O2B	0.86(3)	2.15(3)	2.880(2)	142(3)
N1A-H7A...O3B	0.86(3)	2.52(3)	3.103(2)	127(3)
N1A-H8A...O3B	0.93(3)	1.94(3)	2.850(2)	166(3)
N1A-H9A...O4B	0.87(3)	2.09(3)	2.920(2)	161(3)
N1A-H9A...O4B	0.87(3)	2.33(3)	2.854(2)	119(2)
O1A-H1A... O5B	0.97(4)	1.64(4)	2.609(2)	174(4)
O1B-H1B... O4B	0.90(4)	1.58(4)	2.475(2)	175(3)
O3B-H5B...O2A	0.85(4)	1.86(4)	2.693(2)	166(4)

A Hirshfeld and electron density surface analysis was conducted (**Figure S17**). Close contacts and electron density maxima occur around the HB interaction sites. The close packing of the Pregabalin:malic acid systems leads to closer contacts around alkylic Pregabalin residues, which can be derived from both surface types. However, actual binding interactions with C_{alkyl}-H are highly unlikely. The high connectivity stemming from the large sum of possible HB donors and acceptors leads to close distances for large parts of both molecules which results in these short contacts.

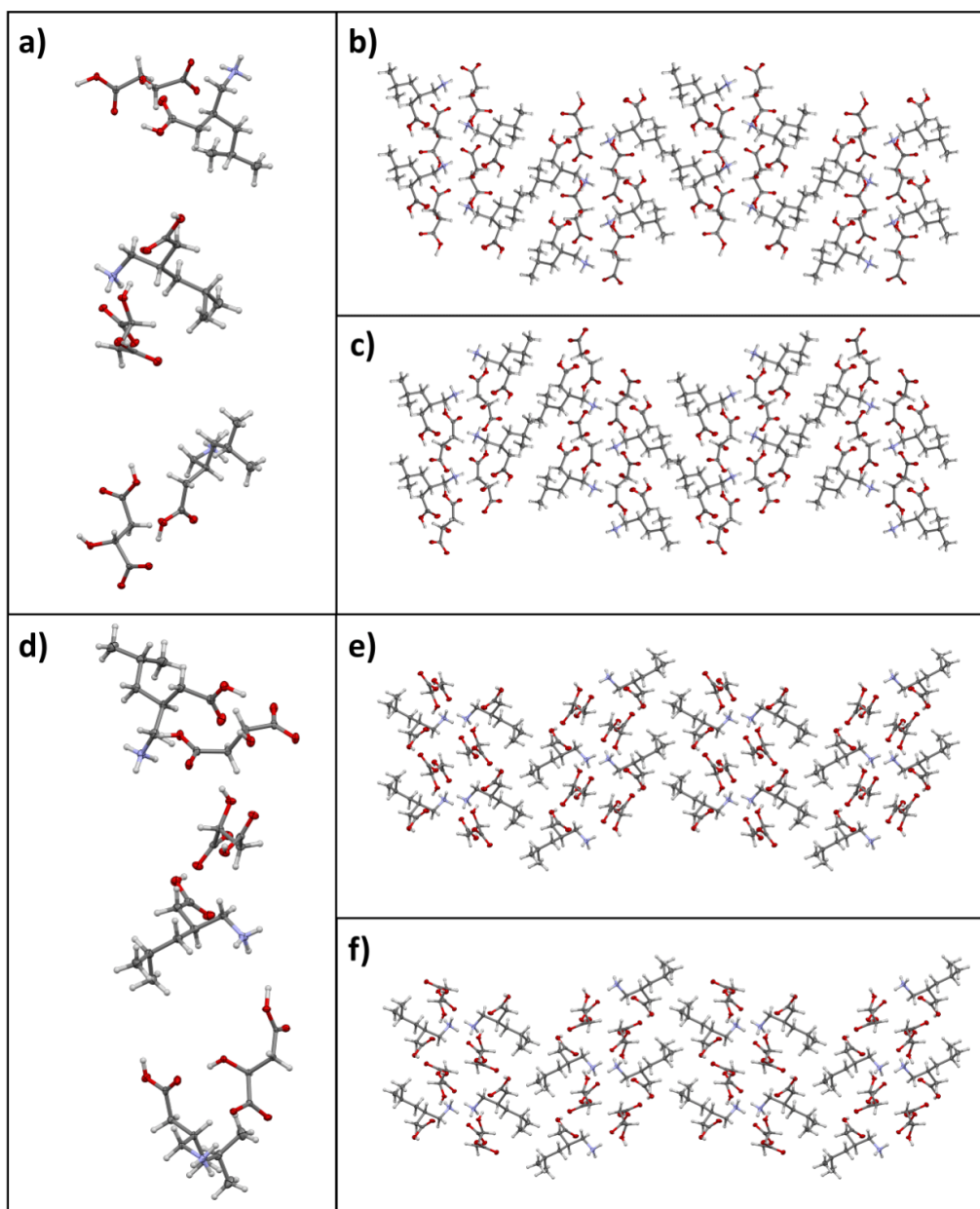


Figure S16. The asymmetric unit of *(S, S)*-Pregabalin:malic acid is shown in **a)**: top to bottom a-axis, b-axis, c-axis. In **e)** the same for *(S, R)*-Pregabalin:malic acid is presented. In **b)** and **e)** the packing of a $2 \cdot 2 \cdot 2$ unit cell from a-axis view is shown, for *(S, S)* and *(S, R)* respectively. In **c)** and **f)** the packing of a $2 \cdot 2 \cdot 2$ unit cell from b-axis view is shown, for *(S, S)* and *(S, R)* respectively. Carbon atoms are depicted in grey, hydrogen atoms in white, nitrogen atoms in blue and oxygen atoms in red.

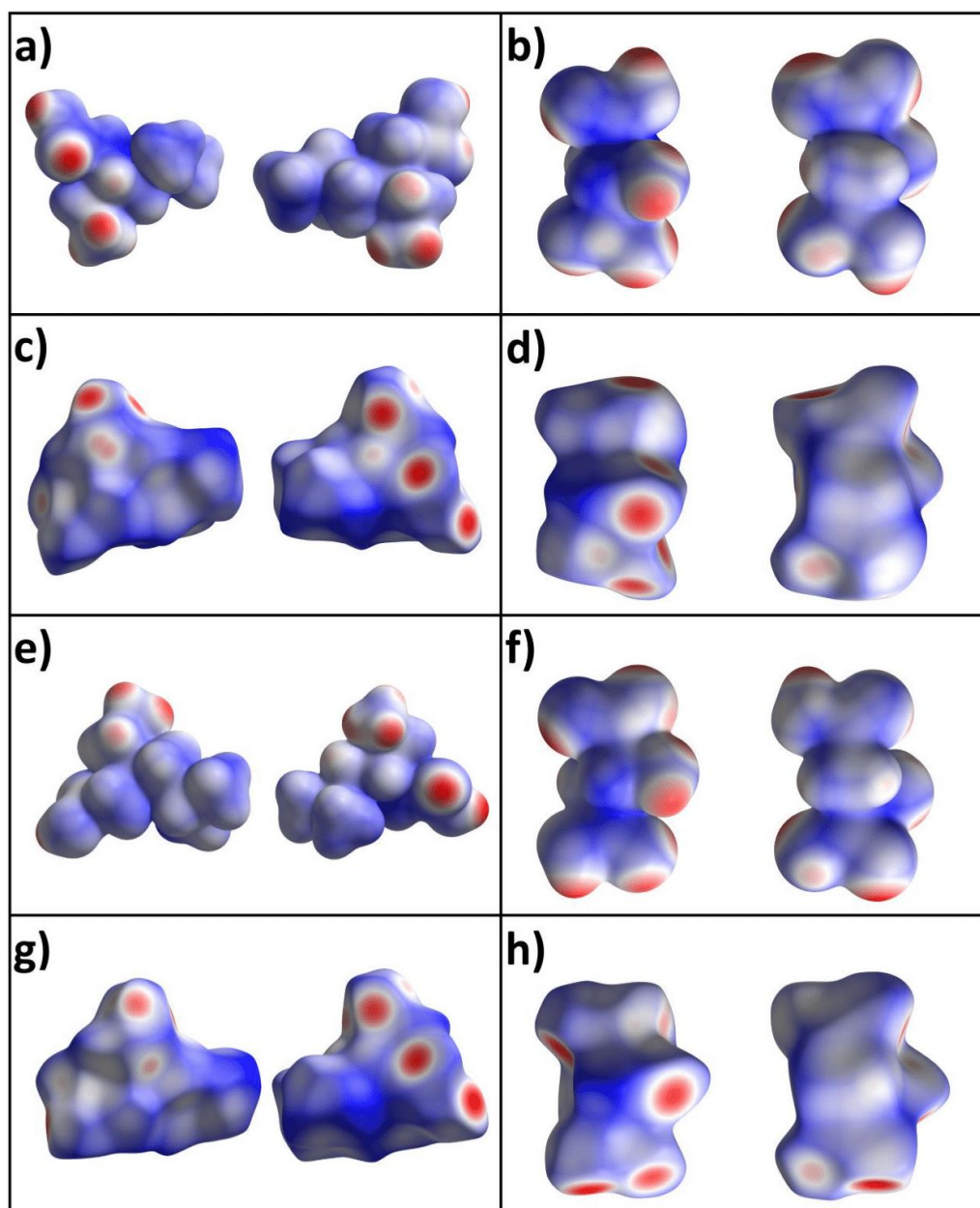


Figure S17. Electron density and Hirshfeld surfaces of (S, S)- and (S, R) Pregabalin:malic acid species. **a)** and **b)** show the electron density surface of the Pregabalin and malic acid molecules in (S, S) from two sides. **c)** and **d)** show the corresponding Hirshfeld surfaces. **e)** and **f)** show the electron density surface of Pregabalin and malic acid molecules in the (S, R) from two sides. **g)** and **h)** show the corresponding Hirshfeld surfaces.

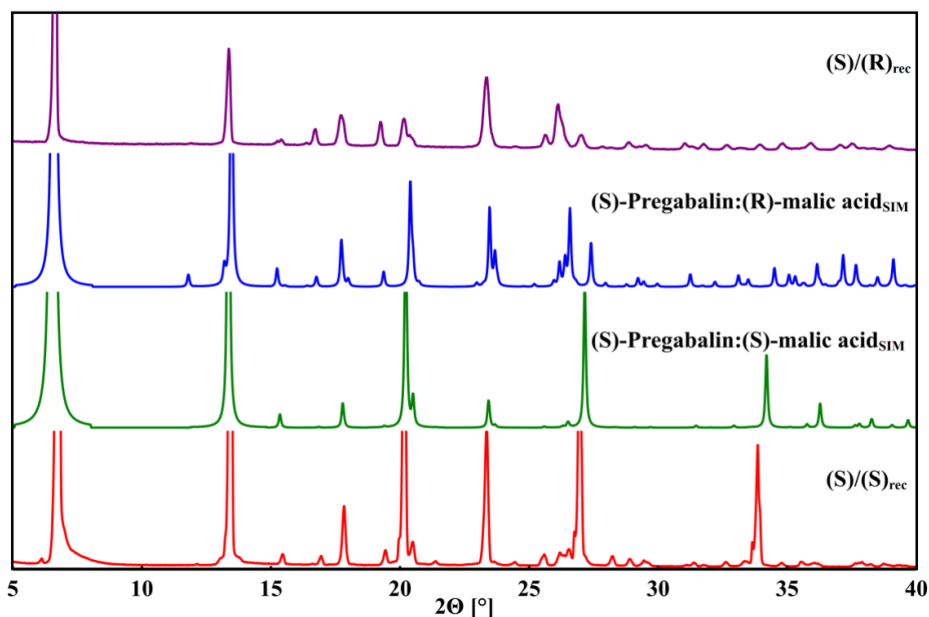


Figure S18. Powder pattern of (S)-Pregabalin:(S)-malic acid (red) and (S)-Pregabalin:(R)-malic acid (purple) as recorded compared simulated from single crystal data of (S)-Pregabalin:(S)-malic acid (green) and (S)-Pregabalin:(R)-malic acid (blue) in a range of 5° – 40°.

2 Physical properties

2.1 Determination of melting points with differential scanning calorimetry

Table S13 shows all melting points that could be determined via DSC.

Table S13. Melting points of all examined substances as determined by DSC.

Substance name	Melting point [°C]
(S)-Pregabalin	185
(R)-Pregabalin	187
(rac)-Phenibut*	-
(S)-mandelic acid	133
(R)-mandelic acid	133
(S)-malic acid	106
(R)-malic acid	106
(S)-Pregabalin:(S)-mandelic acid	138
(R)-Pregabalin:(R)-mandelic acid	132
(S)-Pregabalin:(R)-mandelic acid	111
(R)-Pregabalin:(S)-mandelic acid	105
(S)-Pregabalin:(S)-malic acid	85
(S)-Pregabalin:(R)-malic acid	95
(R)-Phenibut:(S)-mandelic acid	150

* = (rac)-Phenibut decomposes prior to melting at about 200 °C, as such no melting point could be determined.

Corresponding DSC-curves are shown in **Figures S19 – S21**.

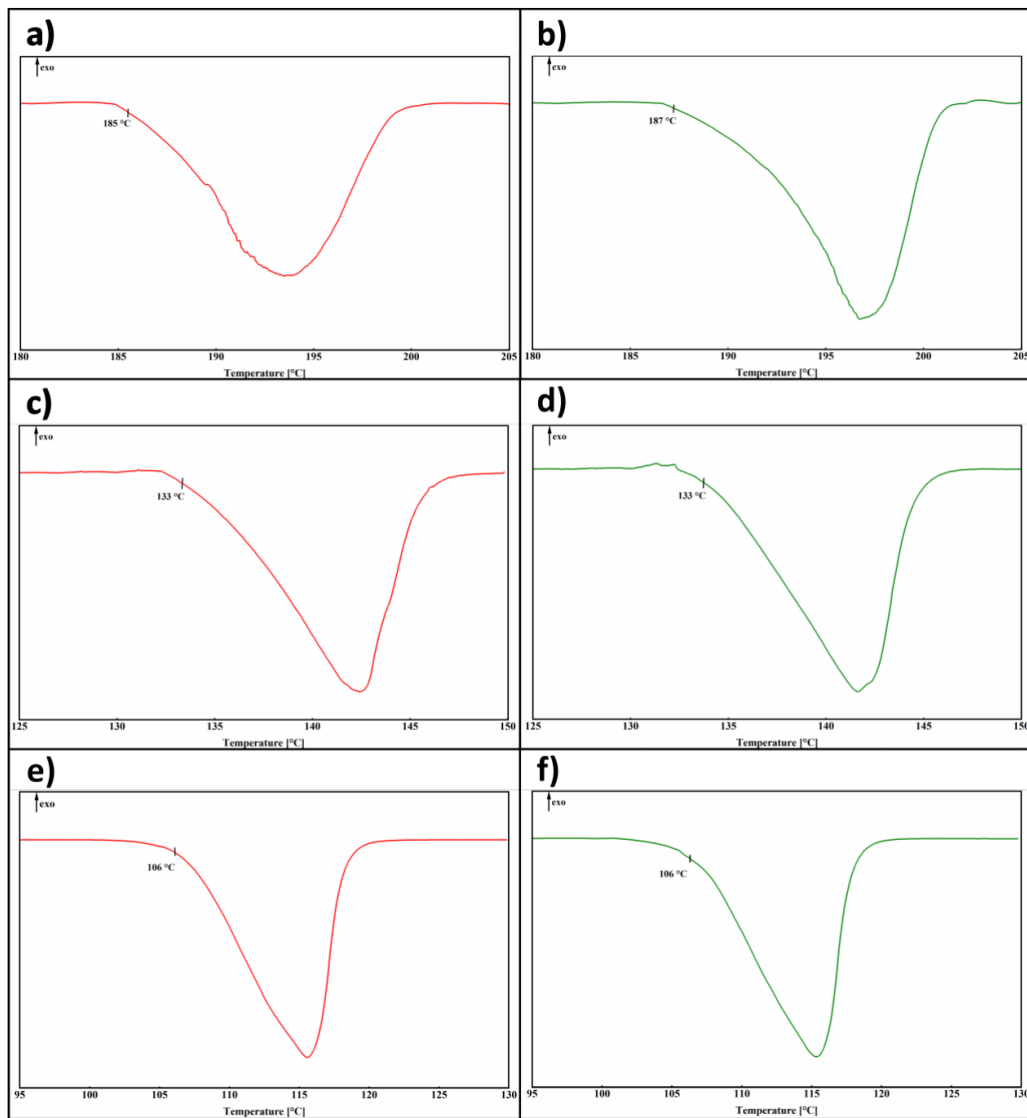


Figure S19. Differential Scanning Calorimetry of **a)** (S)-Pregabalin **b)** (R)-Pregabalin **c)** (S)-mandelic acid, **d)** (R)-mandelic acid, **e)** (S)-malic acid and **f)** (R)-malic acid. The samples were heated with 5 °C/min, specific ranges including the measured melting signal are depicted. Background has been subtracted.

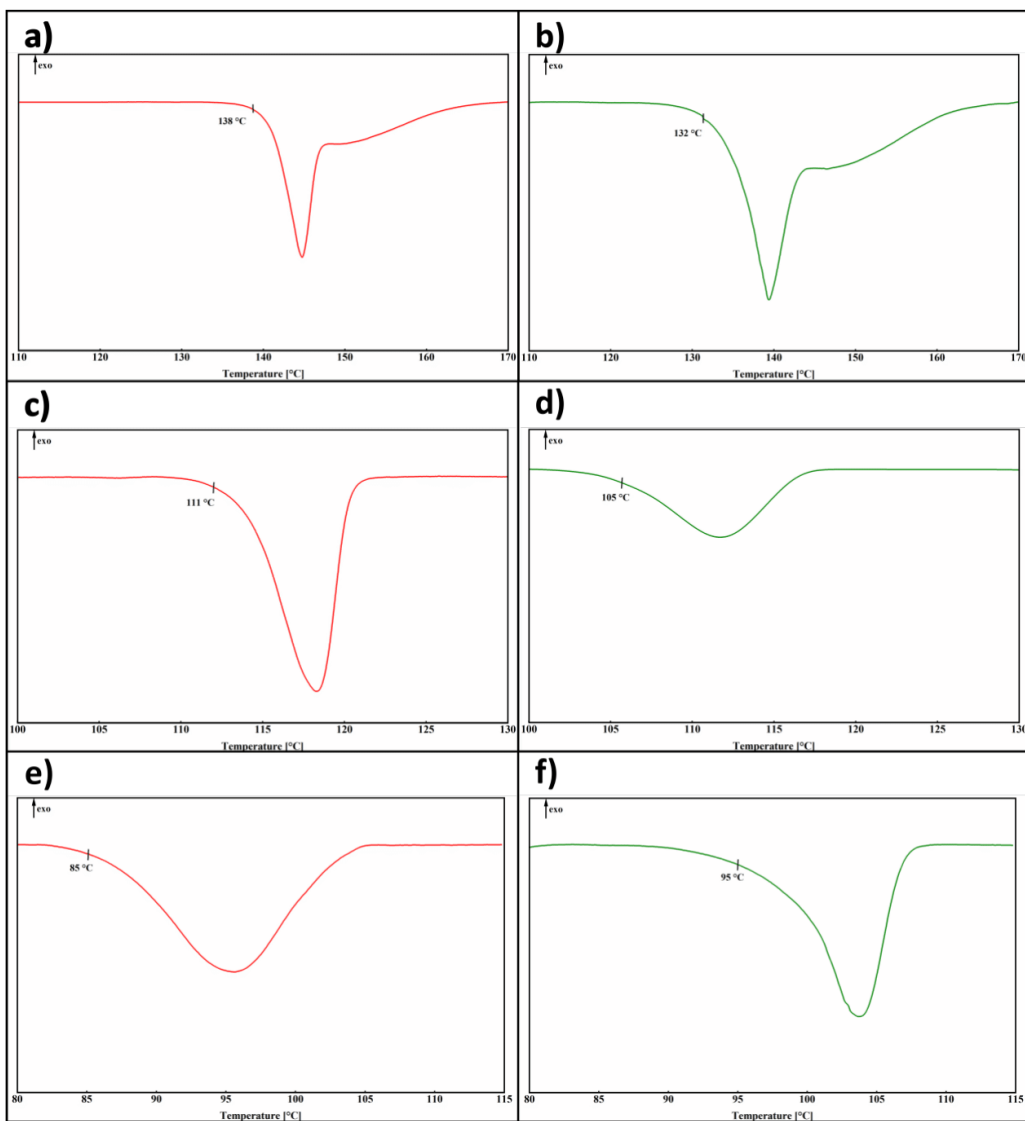


Figure S20. Differential Scanning Calorimetry of **a)** (S, S)-Pregabalin:mandelic acid **b)** (R, R)-Pregabalin:mandelic acid **c)** (S, R)-Pregabalin:mandelic acid, **d)** (R, S)-Pregabalin:mandelic acid, **e)** (S, S)-Pregabalin:malic acid and **f)** (S, R)-Pregabalin:malic acid. The samples were heated with 5 °C/min, specific ranges including the measured melting signal are depicted. Background has been subtracted.

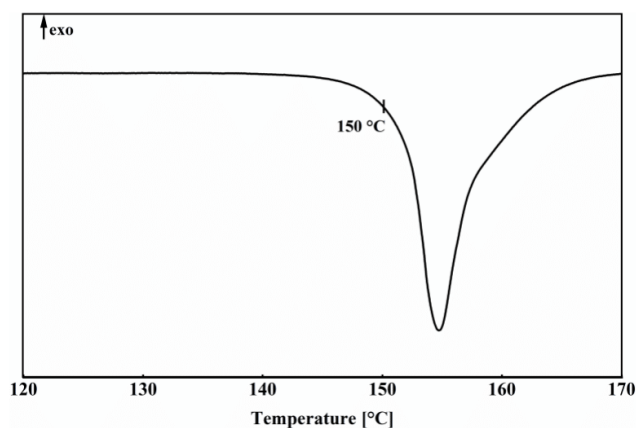


Figure S21. Differential Scanning Calorimetry of (R)-Phenibut:(S)-mandelic acid. The sample was heated with 5 °C/min, the range from 120 °C – 170 °C is depicted. Melting starts at 150 °C. Background has been subtracted.

2.2 Determination of solubility with ¹H-NMR-spectroscopy

Solubilities of the discussed compounds were determined by ¹H-NMR. Powdery samples of each system were layered with phosphate buffer at pH 6.8 in such a way that the solid did not dissolve completely after multiple days. The dispersion was left in an incubator at 37 °C and shaken at 60 min⁻¹. After 1, 2 and in some cases 3 and 4 days 50 μL of solution were taken from the sample and added to 450 μL of D₂O. ¹H-NMR was measured from these samples. The processes were repeated twice for each system. Solubility was determined by comparing the integrals of water to that of the investigated substance. For this, a prevalent signal was integrated and the corresponding value of the water signal was taken from the spectrum. The following **Equation 1** was used to determine the solubility in gL⁻¹.

$$S_p = \left(\frac{M_p}{\frac{I_w}{2} M_w} \rho_w \right) \quad (1)$$

Where S_p is the products solubility in the buffer at pH 6.8 and 37 °C in gL⁻¹, M_p is the molar mass of the investigated substance in gmol⁻¹, I_w is the value of the water integral taken from the ¹H-NMR spectrum, M_w the molar mass of water and ρ_w the density of water at 37 °C of 993.33 gL⁻¹. The used model does not consider trace impurities of water in the D₂O as well as the error of the micropipette. For each system 4 values were calculated based on 2 spectra recorded after 1 and 2 days or 3 and 4 days, based on when stability of the received values was reached. The average of these values is given as the final solubility. A standard deviation on these 4 values was calculated by **Equation 2**.

$$V = \sqrt{\frac{\sum(x - \bar{x})^2}{(n-1)}} \quad (2)$$

With V as the standard deviation, \bar{x} the average of the 4 values, \bar{x} the singular values and n the number of all values, four. **Table S14** shows solubilities and their standard deviations as well as the borders set for the integral of the Pregabalin or Phenibut signal. The water signal was always integrated between 4.830 and 4.750 ppm. A $^1\text{H-NMR}$ spectrum for each compound is shown in **Chapter 5**.

Table S14. Solubilities and their standard deviations for the examined compounds and integral borders set for the $^1\text{H-NMR}$ signal integrals of the investigated substance in the spectra.

Substance name	Solubility/Standard deviation [gL^{-1}]	Integral borders [ppm]
(S)-1	35 \pm 0.4	0.865/0.870 – 0.910
(R)-1	33 \pm 0.3	0.865 – 0.915
(rac)-2* ¹	18 \pm 1	2.520 – 2.665
(S)/(R)-3	203 \pm 3	7.370 – 7.500
(S)/(R)-4	2061 \pm 76	2.760 – 2.900
(S, S)-1:3	37 \pm 1	0.865/0.870 – 0.910/0.915
(R, R)-1:3	40 \pm 4	0.865 – 0.915
(S, R)-1:3	316 \pm 18	0.850/0.860/0.890 – 0.910/0.920/0.950
(R, S)-1:3	307 \pm 6	0.855/0.860 – 0.905/0.910
(S, S)-1:4* ²	>800	0.825/0.845 – 0.890/0.910
(S, R)-1:4* ²	>800	0.835/0.845/0.850 – 0.900/0.910/0.915
(R, S)-2:3	71 \pm 3	2.650 – 2.800

*¹= solubility equilibrium was reached after 3 and 4 days respectively. *² = a maximum solubility could not be determined. Complete dissolution of the substance always occurred. At higher concentrations a highly viscous substance was received with which reliable measurement was impossible.

3 Lattice energies

3.1 Model description and verification

To calculate lattice energies, an adapted method based on Marchese Robinson et al.^[8] and Voronin et al.^[9] was used. Step by step, the following actions were performed:

- Recording of crystal structure in .cif format and subsequent conversion to QE readable .qein input format.
- Self-consistent field (SCF) calculations were performed on the files for (S)-Pregabalin, (rac)-Phenibut, (R, R)/(R, S)-Pregabalin:mandelic acid, (S, S)-Pregabalin:malic acid and (R, S)-Phenibut:mandelic acid to determine a uniform energy convergence threshold (*ecutrho*) and force convergence threshold (*ecutwfc*) (**Table S15**).
- K-points were set to form a grid of about 20 - 25 \AA^3 around the first Brillouin zone for each compound, see **Table S15**.
- Geometric optimization using the 'variable cell relax' (*vc-relax*) command in QE of the examined structures as well as some literature known validation examples was

performed with the determined threshold and K-point grids to receive the ideal static solid energy E_{iss} .

- Geometry parameters for each singular geometrically independent molecule in each structure were gathered from the previously received outputs. For each of these molecules, a further optimization was performed in a fixed 20 \AA^3 otherwise empty cell with the 'relax' command in QE to calculate the energy of the ideal static gas for this molecule, E_{isg} .
- **Equation 3, 5 or 6** were then used to calculate the lattice energy E_{lat} from the received values. These equations shall be explained in detail in the upcoming remarks.

SCF calculations were performed on the described systems with an energy convergence threshold starting at 30 Ry and a force convergence threshold starting at 3 Ry subsequently adding 10 Ry or 1 Ry up until 100 Ry and 10 Ry were reached. Based on the received energy values for these calculations it was determined that 60 Ry and 6 Ry were acceptable values to reach convergence for all examined systems.

Table S15. Variables *ecutrho*, *ecutwfc* and chosen K-point grid for each calculated sample. All values were used in SCF calculations and geometry optimizations. For the simulated gas phase calculations K-points were neglected.

Sample	ecutroh [Ry]	ecutwfc [Ry]	K-point grid
Aspirin ^[10]			2 · 4 · 2
Glycine- α ^[11]			5 · 2 · 5
Glycine- β ^[12]			5 · 4 · 5
Glycine- γ ^[13]			4 · 4 · 4
Benzoic acid ^[14]			4 · 5 · 1
Naphthalene ^[15]			3 · 4 · 3
Carbendazim Maleate ^[9]			3 · 3 · 1
Fenamic acid ^[16]			3 · 3 · 2
(S)-Pregabalin/(1)	60	6	4 · 3 · 2
(R)-Pregabalin/(1)			4 · 3 · 2
(rac)-Phenibut/(2)			3 · 4 · 1
(S, S)-Pregabalin:malic acid/(1:4)			3 · 3 · 1
(S, R)-Pregabalin:malic acid/(1:4)			3 · 3 · 1
(S, S)-Pregabalin:mandelic acid/(1:3)			4 · 1 · 3
(R, R)-Pregabalin:mandelic acid/(1:3)			4 · 1 · 3
(S, R)-Pregabalin:mandelic acid/(1:3)			4 · 1 · 3
(R, S)-Pregabalin:mandelic acid/(1:3)			4 · 1 · 3
(R, S)-Phenibut:mandelic acid/(2:3)			3 · 4 · 2

Naphthalene, aspirin and benzoic acid were chosen as model compounds that are commonly used to verify energy models, they show similar capabilities for intermolecular interactions as the investigated compounds. Glycine polymorphs were chosen because they are well investigated amino acids that exhibit zwitterionicity and as polymorphs should be energetically close regarding each other. Carbendazim maleate was examined by Voronin et al. and serves

to verify that the model works for multicomponent entities. Fenamic acid exhibits $Z' = 2$ and was energetically investigated by Yang et al. in the past,^[17] thus enabling its use as a model compound for systems with this characteristic. The necessary crystallographic information files (.cif) for these compounds were gathered from the crystal structure database via Mercury 2020.2.0.^[9-16] A geometric optimization and subsequent simulated gas phase of the geometrically optimized singular molecules was performed using the determined parameters to receive values for E_{iss} and E_{isg} , sufficient to calculate E_{lat} as shown in **Equation 3** for naphthalene, aspirin, benzoic acid and the glycine polymorphs.

$$E_{lat} = \frac{E_{iss}}{Z} - E_{isg} \quad (3)$$

Where Z is the crystallographic Z , describing the formula units in the unit cell. For further validation purposes, it was assumed that systems that are highly comparable by means of the participating molecules could be used to obtain ΔE_{lat} values without the need to calculate E_{isg} by variation of **Equation 3** under the assumptions that E_{isg} values for the same molecules would be negligible as shown in **Equation 4**.

$$\begin{aligned} \Delta E_{lat} &= E_{lat1} - E_{lat2} \\ \Delta E_{lat} &= \left(\frac{E_{iss1}}{Z_1} - E_{isg} \right) - \left(\frac{E_{iss2}}{Z_2} - E_{isg} \right) \\ \Delta E_{lat} &= \frac{E_{iss1}}{Z_1} - \frac{E_{iss2}}{Z_2} \end{aligned} \quad (4)$$

These values could then be used to verify lattice energy differences calculated by E_{lat} values obtained via **Equation 3**. It was further attempted to consider the influence of Z' . In systems where $Z' > 1$ E_{iss} has to be adjusted by Z' via division to obtain correct values for E_{lat} in the presented model (**Equation 5**).

$$E_{lat} = \frac{E_{iss}}{Z} - \frac{E_{isg}}{Z'} \quad (5)$$

Finally, for multicomponent species each crystallographically distinct molecule has to be considered by their E_{isg} values to obtain E_{lat} , which can be achieved by summation of the different contributions. **Equation 6** considers all discussed influences.

$$E_{lat} = \frac{E_{iss}}{Z} - \frac{\sum E_{isgn}}{Z'} \quad (6)$$

Tables S16 shows E_{iss} and E_{isg} values on the model compounds obtained by the described model, **Table S17** shows corresponding lattice energies.

Table S16. Resulting values of E_{iss} and E_{isg} for the validation compounds. In carbendazim maleate, carbendazim entities are marked with 'C' and maleate entities are marked with 'M'. In fenamic acid, the crystallographically independent molecules are marked as A and B.

Sample	Z	E_{iss} [Ry]	E_{isg} (neutral) [Ry]	E_{isg} (zwitterion/charge) [Ry]
Aspirin	4	-1348.01234	-336.89571	-
Benzoic acid	4	-864.49243	-216.03921	-
Naphthalene	2	-380.81223	-190.34592	-
Carbendazim maleate	4	-2238.98103	-317.81712 ^C -241.69462 ^M	-318.65171 ^C -240.74749 ^M
Fenamic acid	4	-1405.17232	-351.18464 ^A -351.18407 ^B	- -
Glycine- α	4	-580.77370	-145.06565	-145.06563
Glycine- β	2	-290.38351	-145.06570	-145.06570
Glycine- γ	3	-435.58159	-145.05057	-145.06558

Table S17. Resulting values of E_{lat} for the validation compounds. Literature values were obtained from the cited sources.

Sample	E_{lat} (neutral) [Ry]	E_{lat} (zwitterion/charge) [Ry]	E_{lat} (neutral) [kJmol ⁻¹]	E_{lat} (zwitterion/charge) [kJmol ⁻¹]	E_{lat} (lit.) [kJmol ⁻¹]
Aspirin	-0.10737	-	-140.96	-	-131.27 ^{[18]*}
Benzoic acid	-0.08389	-	-110.14	-	-96.0 ^[19]
Naphthalene	-0.06020	-	-79.03	-	-79.4 ^[19]
Carbendazim maleate	-0.23351	-0.34606	-306.54	-454.29	-278.3 ^{[9]*} -625.0 ^{[9]*}
Fenamic acid	-0.10873	-	-142.73	-	-136.5 ^[17]
Glycine- α	-0.12777	-0.12779	-167.73	-167.76	-144.93 ^[20]
Glycine- β	-0.12606	-0.12605	-165.48	-165.48	-143.13 ^[20]
Glycine- γ	-0.14329	-0.12829	-188.11	-168.41	-144.12 ^[20]

* = the cited sources give a plethora of values obtained through differing models and equations. The closest one to the calculated results was picked for this presentation. For Carbendazim maleate the lattice energy values based on neutral molecules and charged molecules are given.

The model's accuracy for polymorphic substances was tested on glycine polymorphs assuming zwitterionic conditions for E_{isg} using **Equations 3 & 4 (Table S18)**.

Table S18. ΔE_{lat} as calculated by Equation 3 & Equation 4 for permutations of the Glycine polymorphs, the zwitterionic state energy values were used.

Sample	ΔE_{lat} (Eq. 3) [kJmol ⁻¹]	ΔE_{lat} (Eq. 4) [kJmol ⁻¹]	Deviation [kJmol ⁻¹]
Glycine- α - Glycine- β	-2.28	-2.19	0.09
Glycine- α - Glycine- γ	0.58	0.65	0.17
Glycine- β - Glycine- γ	2.93	2.77	0.16

3.2 Compound categorization and model application

After verification of the used model its principles were applied to the central Pregabalin and Phenibut based compounds. First, the compounds were categorized based on some of their properties which could influence the calculation results. **Category A** contains (S)-Pregabalin, (R)-Pregabalin and (rac)-Phenibut. These are the simplest examined compounds as they exhibit only one type of molecule in the unit cell, $Z' = 1$ and each molecule is in its default zwitterionic state. In **Category B** only (R, S)-Phenibut:mandelic acid is placed. Here, two different kinds of molecules occur in the unit cell but Z' remains 1 and each molecule keeps its default state with zwitterionic Phenibut and neutral mandelic acid. (S, S)- and (S, R)-Pregabalin:malic acid are placed in **Category C**. Here, two types of molecules occur in the cell, $Z' = 1$ but each species contains a formal charge. **Category D** is composed of (S, S)- and (R, R)-Pregabalin:mandelic acid. These systems are formed from two different molecular species and four crystallographically inequivalent molecules but $Z' = 2$ and default charge status on the molecules is retained. Lastly, **Category E** consists of (S, R)- and (R, S)-Pregabalin:mandelic acid. All previously established complications are applied to this category, as there are two different kinds of molecules and four crystallographically inequivalent ones, $Z' = 2$ and formal charges are present on each molecule. A comprehensive overview on the categories, the involved samples and properties is shown in **Table S19**.

Table S19. Characteristics of the determined categories: contained samples, number of different molecular species, Z' value as determined by PLATON software and information on whether the molecular species are charged (neither zwitterionic nor neutral).

	Samples	Molecule types	Z'	Charge
Category A	(S)-, (R)-Pregabalin, (rac)-Phenibut	1	1	No
Category B	(R)-Phenibut:(S)-mandelic acid	2	1	No
Category C	(S, S)-, (S, R)-Pregabalin:malic acid	2	1	Yes
Category D	(S, S)-, (R, R)-Pregabalin:mandelic acid	2	2	No
Category E	(S, R)-, (R, S)-Pregabalin:mandelic acid	2	2	Yes

It was determined that **Category A** would not require any additional effort to apply the used model on, as its characteristics are the same as those of the model compounds. For **Category B – E** it was assumed that E_{isg} would be determined by summation of $E_{\text{isgA}} + E_{\text{isgB}} + \dots + E_{\text{isgn}}$ for all geometrically independent molecules. For each category it was furthermore examined whether neutral, zwitterionic or, if applicable, charged states on isolated molecules would lead to the most consistent results. Additionally, for **Category D** and **E** it was attempted to consider the influence of Z' .

Category A

Table S20. Resulting values of E_{iss} and E_{isg} for the **Category A** compounds.

Sample	Z	E_{iss} [Ry]	E_{isg} (neutral) [Ry]	E_{isg} (zwitt.) [Ry]
(S)-Pregabalin (1)	4	-1071.82432	-267.79802	-267.80748
(R)-Pregabalin (1)	4	-1071.82525	-267.79161	-267.80764
(rac)-Phenibut (2)	8	-2396.20653	-299.23844	-299.12074

Table S21. Resulting values of E_{lat} as calculated by **Equation 6** for the **Category A** compounds.

Sample	E_{lat} (neutral) [Ry]	E_{lat} (zwitt.) [Ry]	E_{lat} (neutral) [kJmol ⁻¹]	E_{lat} (zwitt.) [kJmol ⁻¹]
(S)-Pregabalin (1)	-0.15806	-0.14860	-207.50	-195.08
(R)-Pregabalin (1)	-0.16470	-0.14867	-216.21	-195.17
(rac)-Phenibut (2)	-0.16238	-0.28008	-213.16	-367.68

Table S22. Comparison of ΔE_{lat} values obtained by **Equation 6** and **Equation 4** for **Category A** compounds (S)- and (R)-Pregabalin.

	ΔE_{lat} (Eq. 3) [kJmol ⁻¹]	ΔE_{lat} (Eq. 4) [kJmol ⁻¹]	Deviation [kJmol ⁻¹]
(S)-1 – (R)-1 (neutral)	-8.71	-0.31	8.40
(S)-1 – (R)-1 (zwitt.)	-0.09		0.22

Category B & C

Table S23. Resulting values of E_{iss} and E_{isg} for the **Category B & C** compounds crystallographically independent occurring molecular species.

Sample	E_{iss} [Ry]	E_{isg} (neutral) [Ry]	E_{isg} (zwitt.) [Ry]	E_{isg} (charged) [Ry]
(S, S)-1:4 (Z = 4)				
(S)-Pregabalin	-2213.33805	-267.79195	-267.80910	-268.61130
(S)-malic acid		-285.25372	-	-284.27132
(S, R)-1:4 (Z = 4)				
(S)-Pregabalin	-2213.34508	-267.79369	-267.80880	-268.61136
(R)-malic acid		-285.25091	-	-284.22893
(R, S)-2:3 (Z = 2)				
(R)-Phenibut	-1154.28106	-299.24119	-299.24904	-
(S)-mandelic acid		-277.63003	-	-

Table S24. Resulting values of E_{lat} as calculated by **Equation 6** for the **Category B & C** compounds using the E_{isg} values of singular molecules depicted in **Table S23**.

Sample	E_{lat} (neutral) [Ry]	E_{lat} (zwitt.) [Ry]	E_{lat} (charged) [Ry]
(S, S)-1:4	-0.28884	-0.27169	-0.45190
(S, R)-1:4	-0.29166	-0.27656	-0.49598
(R, S)-2:3	-0.26931	-0.26146	-
	E_{lat} (neutral) [kJmol ⁻¹]	E_{lat} (zwitt.) [kJmol ⁻¹]	E_{lat} (charged) [kJmol ⁻¹]
(S, S)-1:4	-379.17	-356.66	-593.23
(S, R)-1:4	-382.88	-363.05	-651.10
(R, S)-2:3	-353.54	-343.23	-

Table S25. Comparison of ΔE_{lat} values received by **Equation 6** and **Equation 4** for **Category C** compounds (S, S)- and (S, R)-Pregabalin:malic acid.

Sample	ΔE_{lat} (Eq. 3) [kJmol ⁻¹]	ΔE_{lat} (Eq. 4) [kJmol ⁻¹]	Deviation [kJmol ⁻¹]
(S, S)-1:4 – (S, R)-1:4 (neutral)	3.71		1.40
(S, S)-1:4 – (S, R)-1:4 (zwitt.)	6.39	2.31	4.08
(S, S)-1:4 – (S, R)-1:4 (charged)	57.87		55.66

Category D & E

Table S26. Resulting values of E_{iss} and E_{isg} for the **Category D & E** compounds crystallographically independent occurring molecular species.

Sample	E_{iss} [Ry]	E_{isg} (neutral) [Ry]	E_{isg} (zwitt.) [Ry]	E_{isg} (charged) [Ry]
(S, S)-1:3 (Z = 4)				
(S)-Pregabalin 1	-2182.72832	-267.79208	-267.80897	-
(S)-Pregabalin 2		-267.79387	-267.80898	-
(S)-mandelic acid 1		-277.62920	-	-
(S)-mandelic acid 2		-277.62893	-	-
(R, R)-1:3 (Z = 4)				
(R)-Pregabalin 1	-2182.73030	-267.79375	-267.80898	-
(R)-Pregabalin 2		-267.79208	-267.80900	-
(R)-mandelic acid 1		-277.62918	-	-
(R)-mandelic acid 2		-277.82695	-	-
(S, R)-1:3 (Z = 4)				
(S)-Pregabalin 1	-2182.68327	-267.79976	-267.80809	-268.64999
(S)-Pregabalin 2		-267.81182	-267.80928	-268.59870
(R)-mandelic acid 1		-277.62918	-	-276.65999
(R)-mandelic acid 2		-277.63009	-	-276.63286
(R, S)-1:3 (Z = 4)				
(R)-Pregabalin 1	-2182.68421	-267.79397	-267.80932	-268.59859
(R)-Pregabalin 2		-267.79977	-267.80897	-268.65003
(S)-mandelic acid 1		-277.62918	-	-276.64477
(S)-mandelic acid 2		-277.62575	-	-276.63280

Table S27. Resulting values of E_{lat} as calculated by **Equation 6** for the **Category D & E** compounds using the E_{isg} values of singular molecules depicted in **Table S26**.

Sample	E_{lat} (neutral) [Ry]	E_{lat} (zwitt.) [Ry]	E_{lat} (charged) [Ry]
(S, S)-1:3	-0.26004	-0.24404	-
(R, R)-1:3	-0.26095	-0.24452	-
(S, R)-1:3	-0.23540	-0.23208	-0.40005
(R, S)-1:3	-0.24672	-0.23445	-0.40796
	E_{lat} (neutral) [kJmol ⁻¹]	E_{lat} (zwitt.) [kJmol ⁻¹]	E_{lat} (charged) [kJmol ⁻¹]
(S, S)-1:3	-341.37	-320.36	-
(R, R)-1:3	-342.09	-320.99	-
(S, R)-1:3	-309.02	-305.66	-525.17
(R, S)-1:3	-323.88	-307.77	-535.55

Table S28. Comparison of ΔE_{lat} values received by **Equation 6** and **Equation 4** for **Category D & E** compounds inside the respective categories and between both categories in varying permutations.

Sample	ΔE_{lat} (Eq. 5) [kJmol ⁻¹]	ΔE_{lat} (Eq. 4) [kJmol ⁻¹]	Deviation [kJmol ⁻¹]
(S, S)-1:3 - (R, R)-1:3 (neutral)	0.72		0.07
(S, S)-1:3 - (R, R)-1:3 (zwitt.)	0.63	0.65	0.02
(S, R)-1:3 - (R, S)-1:3 (neutral)	14.86		14.55
(S, R)-1:3 - (R, S)-1:3 (zwitt.)	2.11	0.31	1.80
(S, R)-1:3 - (R, S)-1:3 (charged)	10.38		10.07
(S, S)-1:3 - (S, R)-1:3 (neutral)	-32.35		17.56
(S, S)-1:3 - (S, R)-1:3 (zwitt.)	-15.71	-14.79	0.92
(S, S)-1:3 - (R, S)-1:3 (neutral)	-17.49		3.01
(S, S)-1:3 - (R, S)-1:3 (zwitt.)	-12.59	-14.48	1.89
(R, R)-1:3 - (S, R)-1:3 (neutral)	-33.07		17.63
(R, R)-1:3 - (S, R)-1:3 (zwitt.)	-16.33	-15.44	0.89
(R, R)-1:3 - (R, S)-1:3 (neutral)	-18.21		3.08
(R, R)-1:3 - (R, S)-1:3 (zwitt.)	-13.22	-15.13	1.91

It was determined that the most overall consistent results can be obtained by application of zwitterionicity on Pregablin/Phenibut molecules and neutral charge status on mandelic- or malic acid.

4 Applications: enantiopurification of (rac)-Pregabalin hydrate

Detailed PXRD pattern comparisons of products received during enantiopurification steps I – III are presented in **Figures S22 – S24**.

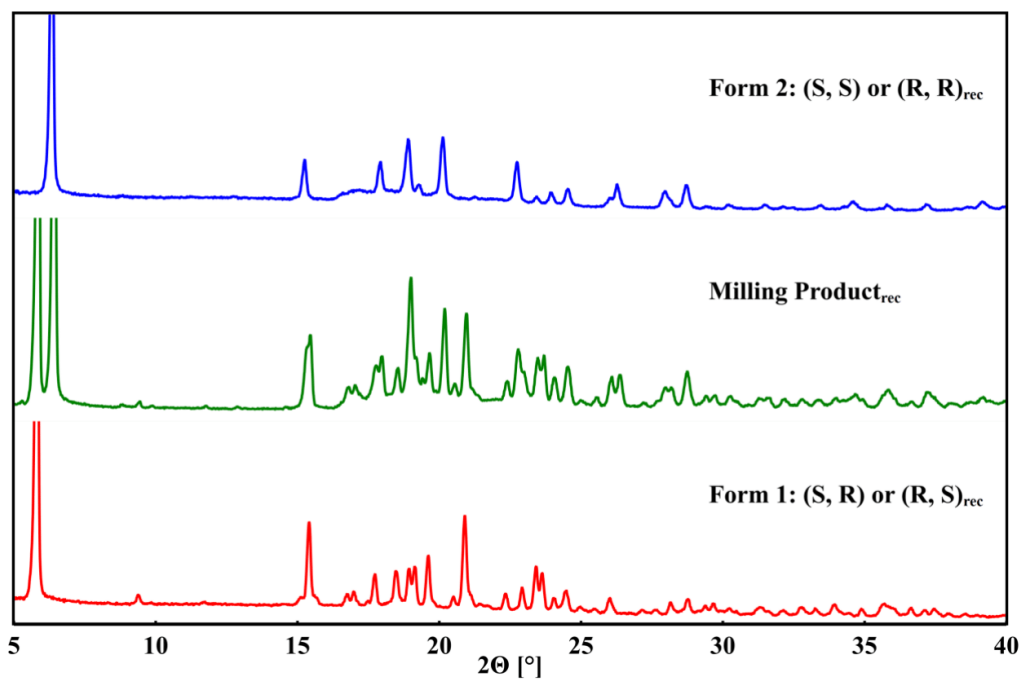


Figure S22. Powder pattern of the milling product of racemic Pregabalin hydrate and (S)-mandelic acid (green). A comparison to the two co-crystalline compounds is shown for (S, R)-Pregabalin:mandelic acid (red) as well as (S, S)-Pregabalin:mandelic acid (blue). Thus, the milling product is identified as a mixture. The depicted angle range is 5° – 40°.

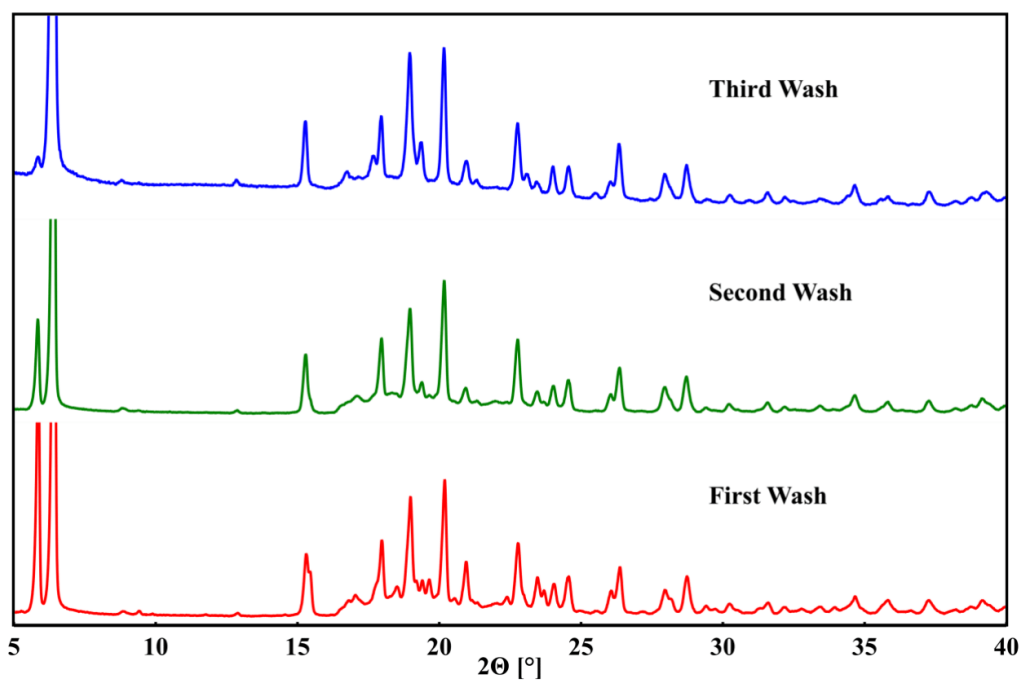


Figure S23. Powder pattern of the milling product of racemic Pregabalin hydrate and (*R*)-mandelic acid after subsequent washing and drying procedure from 5° – 40°. The signals of the more soluble heterochiral co-crystalline entity vanish from red – blue pattern, easily visible in the lowest ° signal.

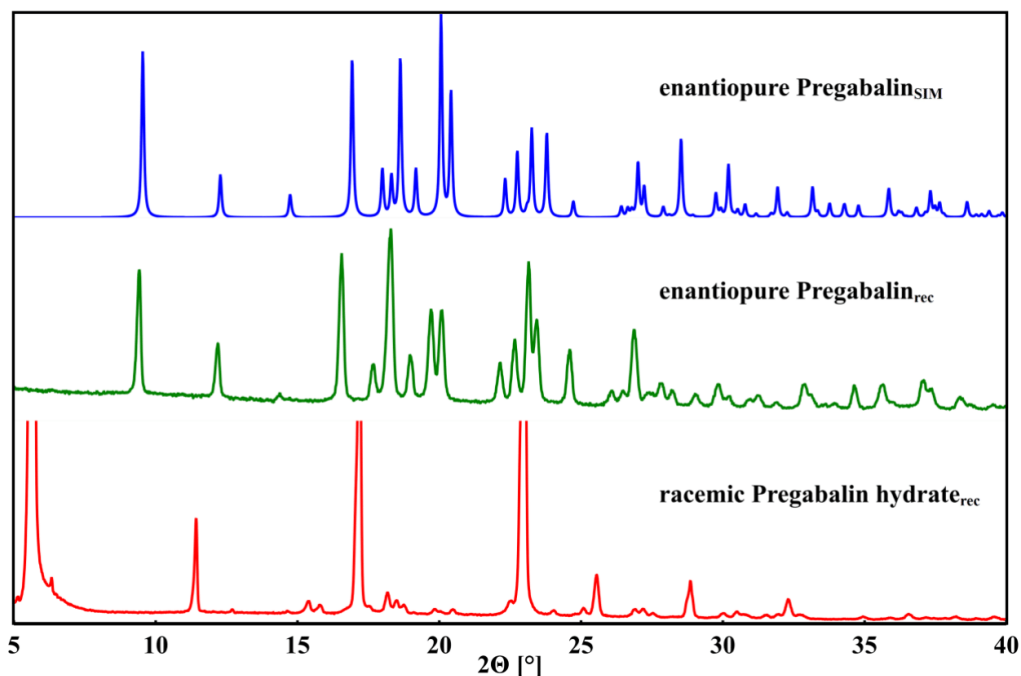


Figure S24. Powder pattern of the final (*R*)-Pregabalin (green) after removal of (*R*)-mandelic acid) compared to a simulated pattern from single crystal data (blue) and the recorded pattern of the racemic Pregabalin hydrate (red) in a range of 5° – 40°.

5 Addendum

Table S29. Bijvoet-analysis for confirmation of chiral purity conducted with PLATON software.

	(S)-1	(R)-1	(S, S)-1:3	(R, R)-1:3	(S, R)-1:3	(R, S)-1:3	(S, S)-1:4	(S, R)-1:4	(R, S)-2:3
Flack x	0.03(11)	-0.04(19)	0.15(11)	-0.02(5)	-0.05(12)	-0.15(7)	0.01(6)	0.01(5)	0.00(10)
Parsons z	0.06(11)	0.00(18)	0.14(9)	-0.04(5)	0.05(8)	-0.17(6)	-0.01(6)	-0.01(4)	-0.01(8)
Bijvoet Pairs	663	696	3038	3150	3209	2991	1133	1210	1412
Coverage	84	88	86	89	91	85	86	91	87
DiffCalcMax.	6.47	6.58	18.43	18.07	28.52	30.71	38.34	39.17	10.17
Outlier Crit.	12.94	13.16	36.85	36.14	57.03	61.43	76.67	78.33	20.34
Sigma Crit.	0.25	0.25	0.25	0.25	0.25	0.25	0.25	0.25	0.25
Select Pairs	84	27	86	528	99	322	280	464	167
Number Plus	55	18	55	352	58	208	179	313	106
Number Minus	29	9	31	176	41	114	101	151	61
Slope	0.908	1.525	0.709	1.024	1.175	1.358	0.949	0.951	1.091
Sample Size	653	686	3028	3140	3199	2981	1123	1200	1402
Corr. Coeff.	0.997	0.999	0.999	1.000	0.999	1.000	0.999	0.998	0.997
Intercept	0.018	-0.065	0.014	-0.034	-0.004	-0.065	-0.076	0.033	-0.151
Slope	0.854	0.840	0.911	0.947	1.009	1.034	0.870	0.944	0.985
Student_T Nu	100	32	9	32	7	32	100	99	19
Select Pairs	663	696	3038	3150	3209	2991	1133	1210	1412
Theta_min	9.32	9.30	5.49	3.23	2.95	2.96	8.50	8.46	7.76
Theta_Max	76.05	76.13	77.15	76.90	77.53	75.38	76.51	77.79	76.14
P2 (true)	1.000	1.000	1.000	1.000	1.000	1.000	1.000	1.000	1.000
P3 (true)	1.000	0.995	1.000	1.000	1.000	1.000	1.000	1.000	1.000
P3 (rac-twin)	0.3E-04	0.005	0.3E-03	0.1E-32	0.9E-06	0.1E-21	0.2E-17	0.9E-30	0.8E-08
P3 (false)	0.2E-20	0.3E-09	0.3E-21	0.1E-121	0.22E-23	0.4E-70	0.3E-70	0.2E-120	0.2E-31
G	0.8773	0.9606	0.7438	1.0754	1.0198	1.3180	1.0004	0.9897	1.0117
G (su)	0.1916	0.2946	0.1728	0.0871	0.1929	0.1270	0.1107	0.0840	0.1652
Hooft y	0.06(10)	0.02(15)	0.13(9)	-0.04(4)	-0.01(10)	-0.16(6)	0.00(6)	0.01(4)	-0.01(8)

¹H-NMR spectroscopy

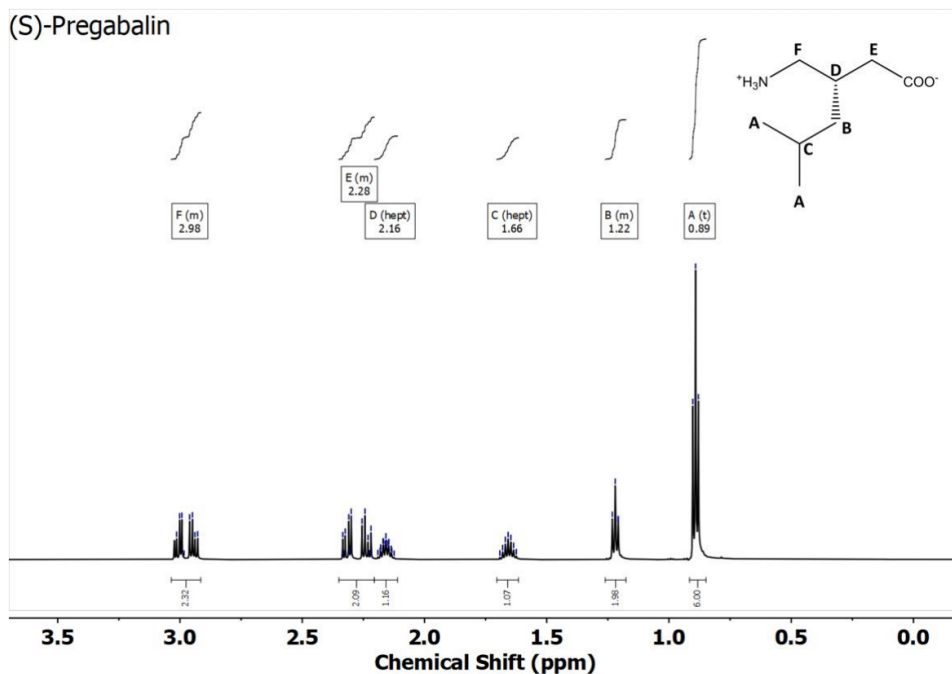


Figure S25. ¹H-NMR spectrum of (S)-Pregabalin recorded in D₂O. The range between 0.25 ppm and 3.75 ppm is depicted, the signals are marked by letters according to the position on the molecule.

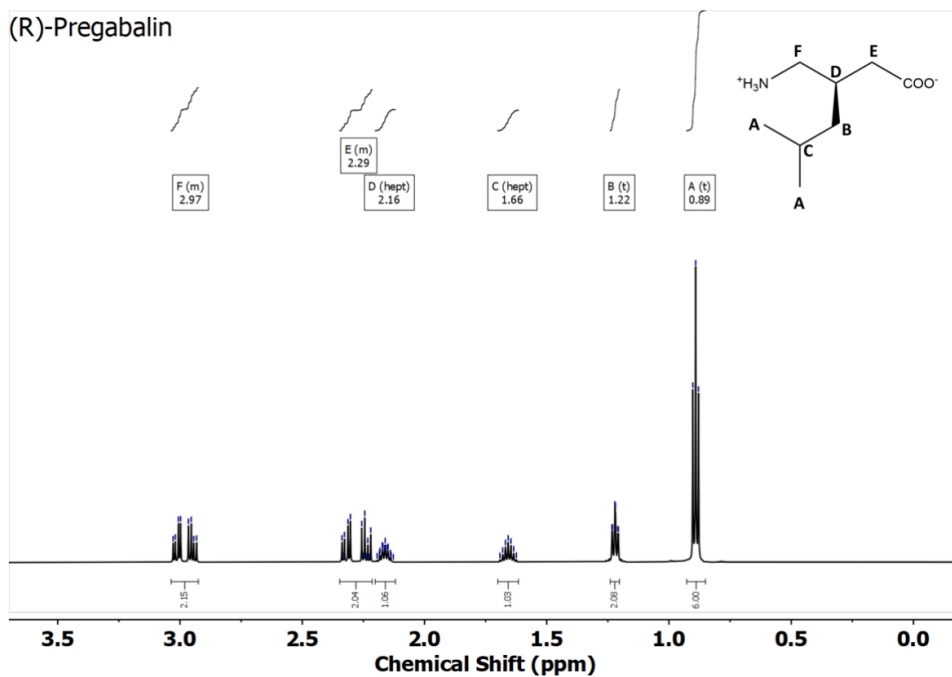


Figure S26. ¹H-NMR spectrum of (R)-Pregabalin recorded in D₂O. The range between 0.25 ppm and 3.75 ppm is depicted, the signals are marked by letters according to the position on the molecule.

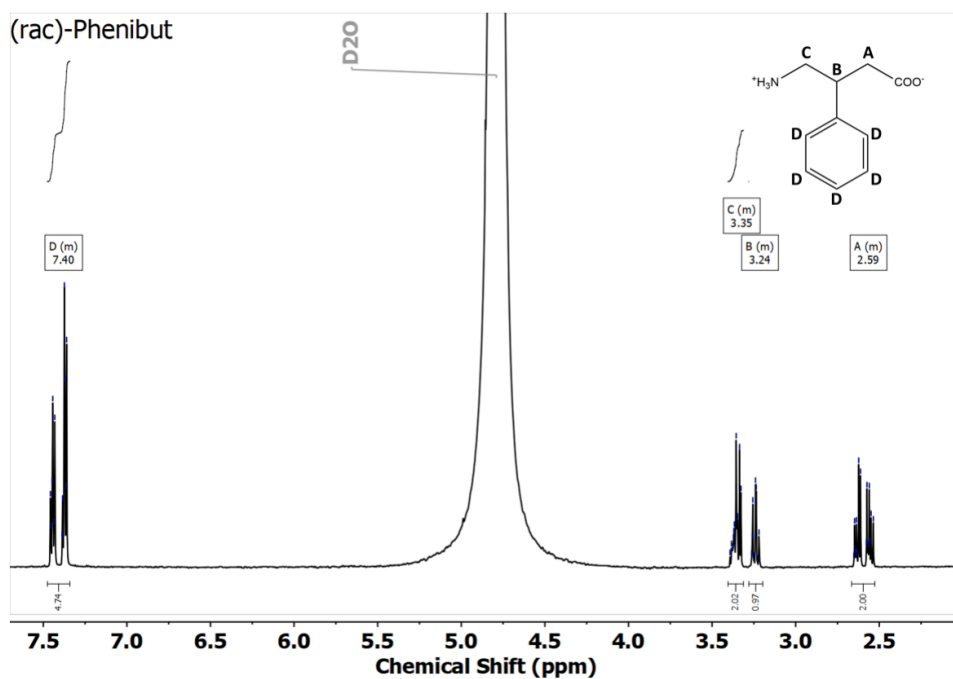


Figure S27. $^1\text{H-NMR}$ spectrum of (rac)-Phenibut recorded in D_2O . The range between 2.00 ppm and 7.75 ppm is depicted, the signals are marked by letters according to the position on the molecule.

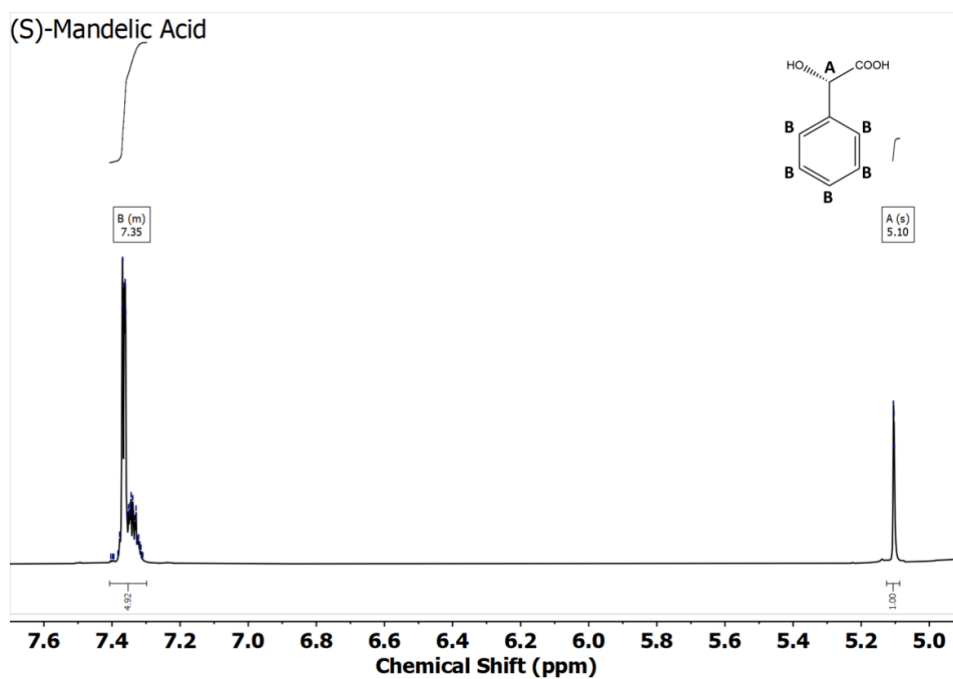


Figure S28. $^1\text{H-NMR}$ spectrum of (S)-mandelic acid recorded in D_2O . The range between 4.8 ppm and 7.8 ppm is depicted, the signals are marked by letters according to the position on the molecule.

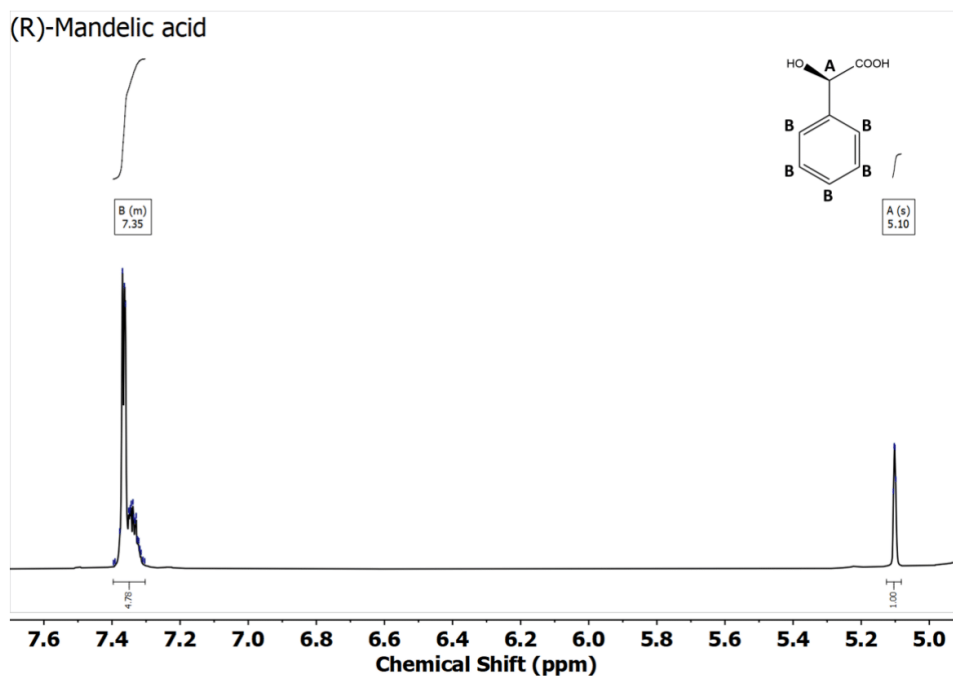


Figure S29. $^1\text{H-NMR}$ spectrum of (R)-mandelic acid recorded in D_2O . The range between 4.8 ppm and 7.8 ppm is depicted, the signals are marked by letters according to the position on the molecule.

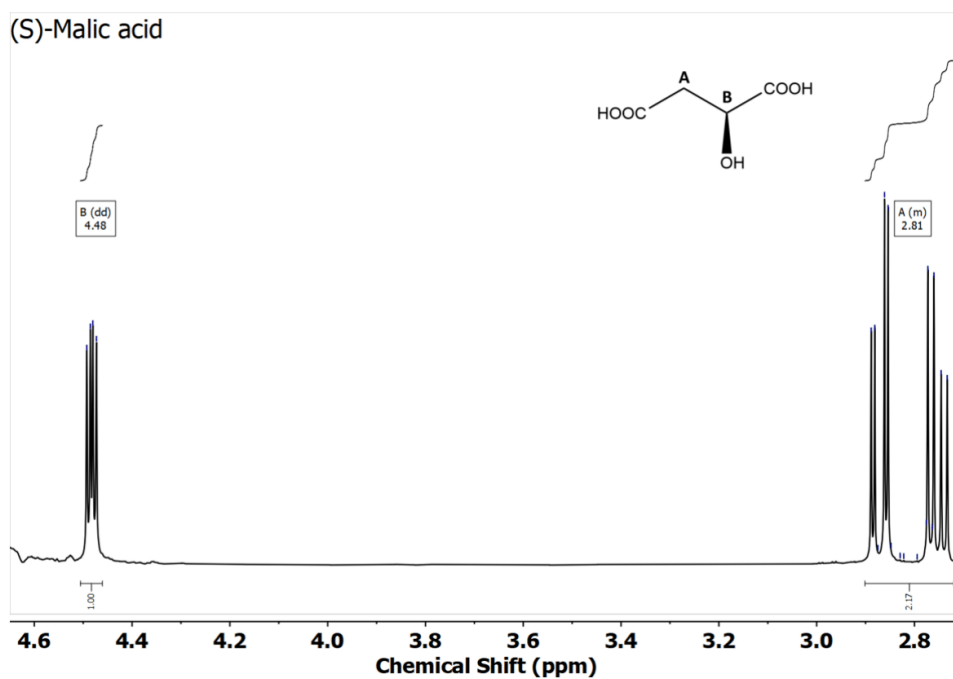


Figure S30. $^1\text{H-NMR}$ spectrum of (S)-Malic acid recorded in D_2O . The range between 2.6 ppm and 4.7 ppm is depicted, the signals are marked by letters according to the position on the molecule.

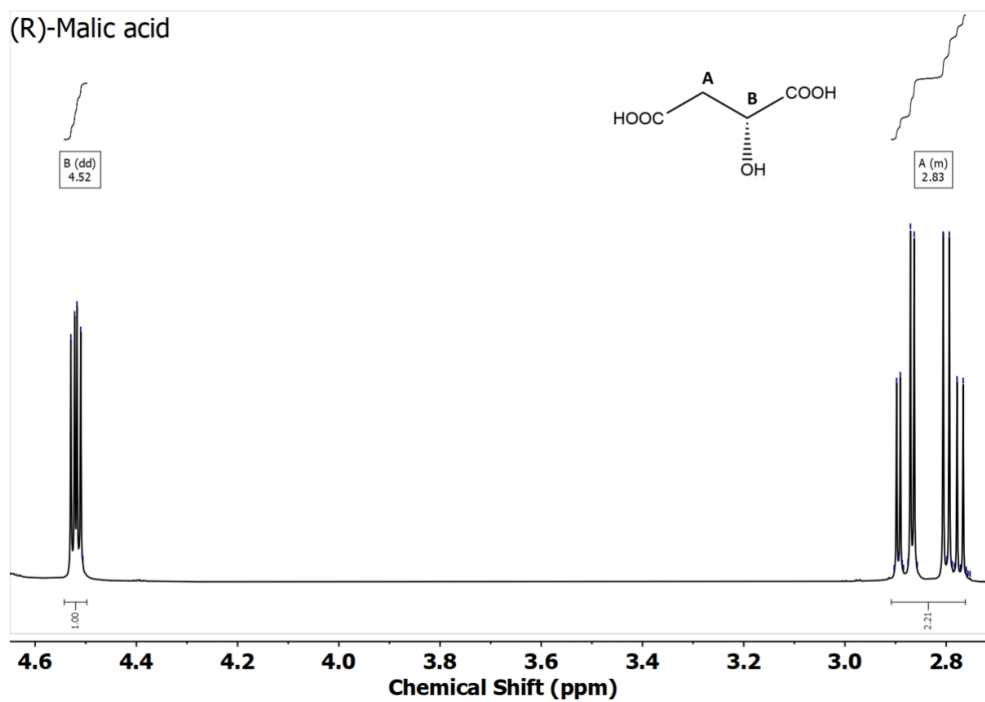


Figure S31. $^1\text{H-NMR}$ spectrum of (R)-Malic acid recorded in D_2O . The range between 2.6 ppm and 4.7 ppm is depicted, the signals are marked by letters according to the position on the molecule.

IR-Spectroscopy

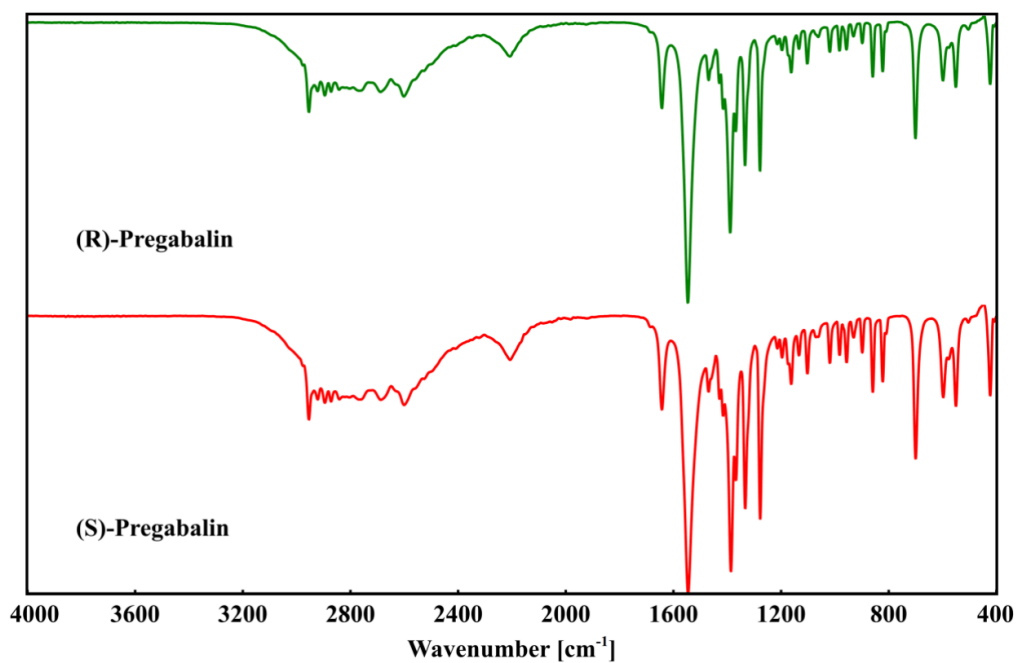


Figure S32. IR-spectra of (S)-Pregabalin (red) and (R)-Pregabalin (green). The range from 400cm^{-1} to 4000cm^{-1} is depicted.

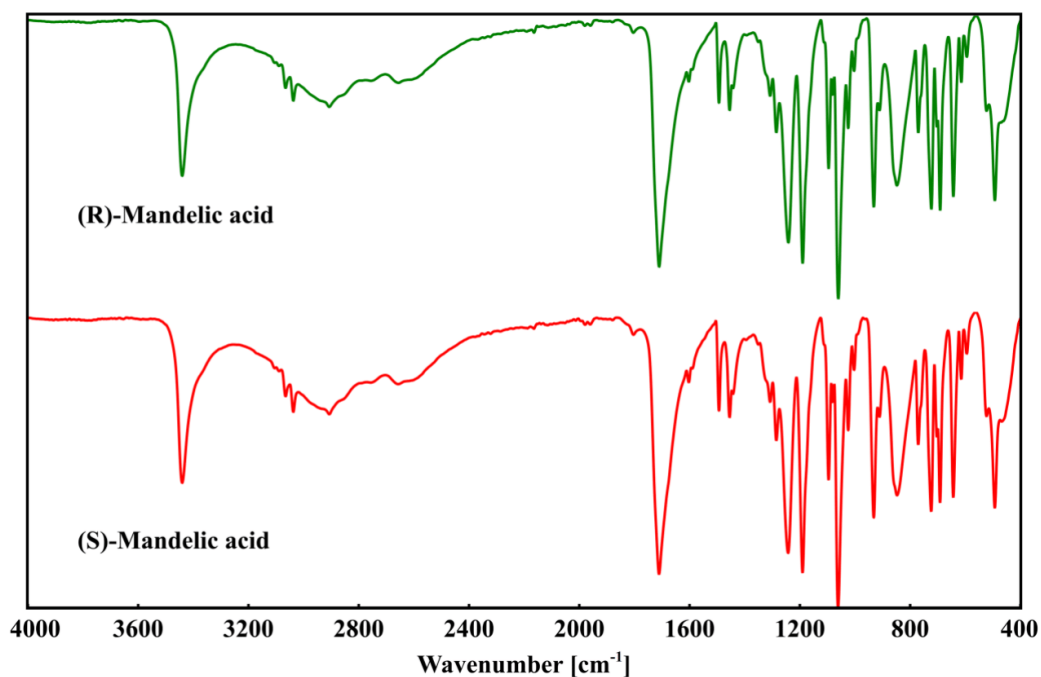


Figure S33. IR-spectra of (S)-mandelic (red) and (R)-mandelic acid (green). The range from 400cm⁻¹ to 4000 cm⁻¹ is depicted.

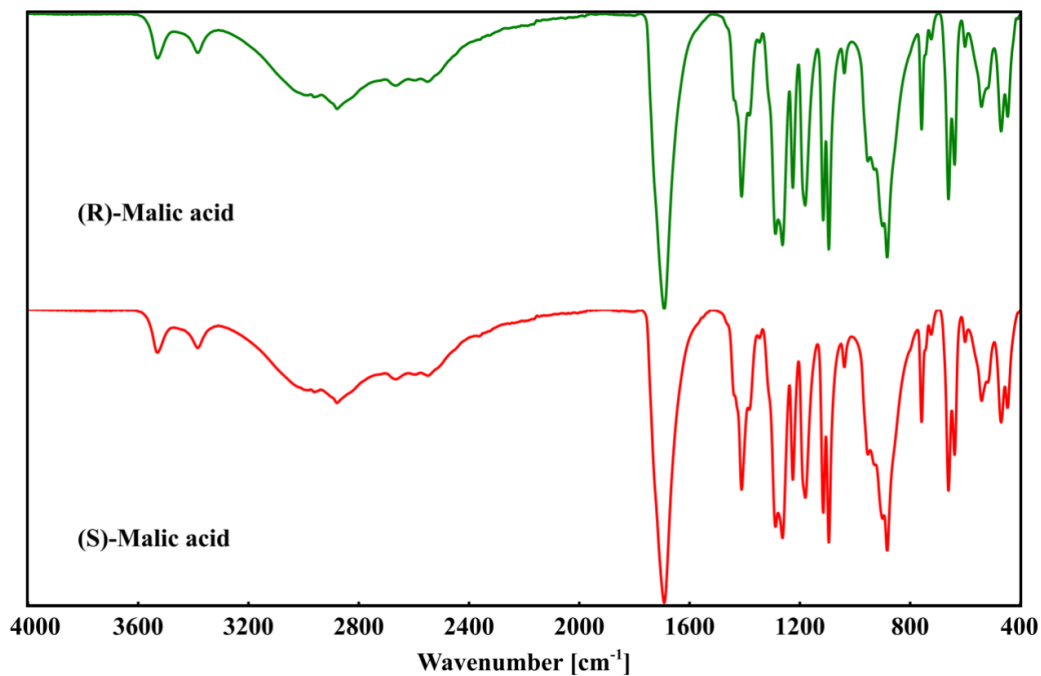


Figure S34. IR-spectra of (S)-malic (red) and (R)-malic acid (green). The range from 400cm⁻¹ to 4000 cm⁻¹ is depicted.

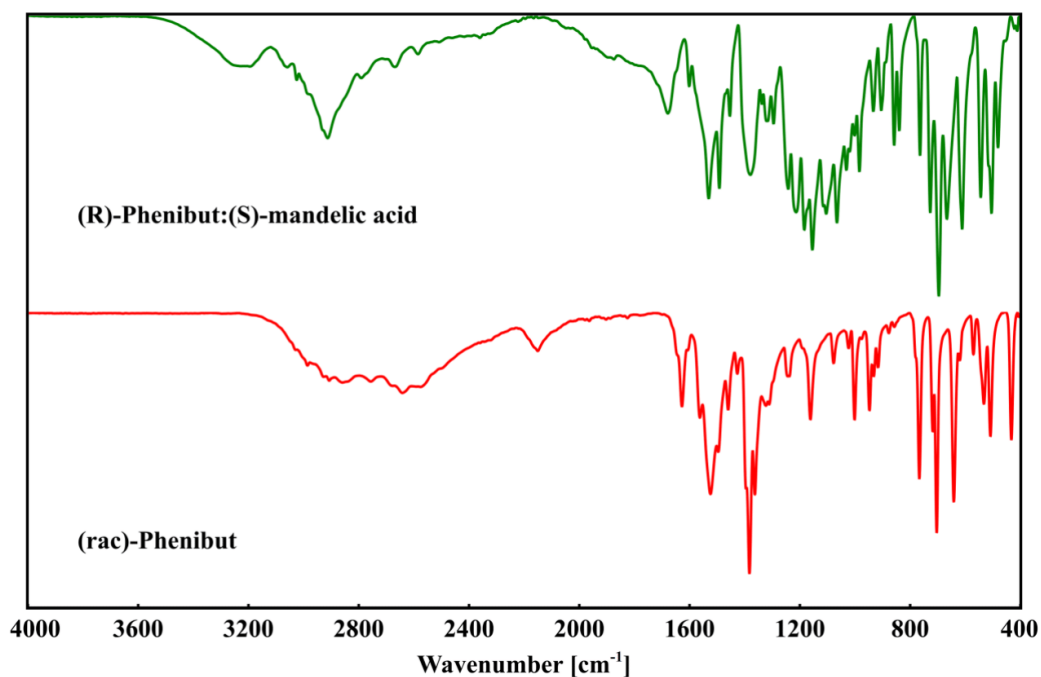


Figure S35. IR-spectra of (rac)-Phenibut (red) and (R, S)-Phenibut:mandelic acid (green). The range from 400cm⁻¹ to 4000 cm⁻¹ is depicted,

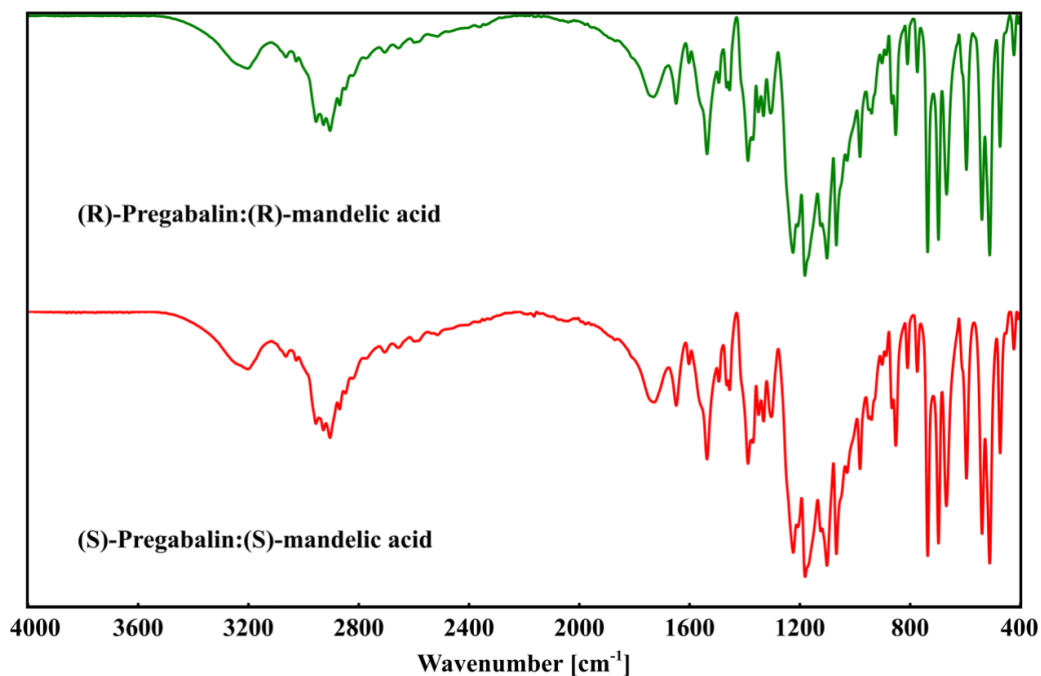


Figure S36. IR-spectra of (S, S)-Pregabalin:mandelic acid (red) and (R, R)-Pregabalin:mandelic acid (green). The range from 400cm⁻¹ to 4000 cm⁻¹ is depicted.

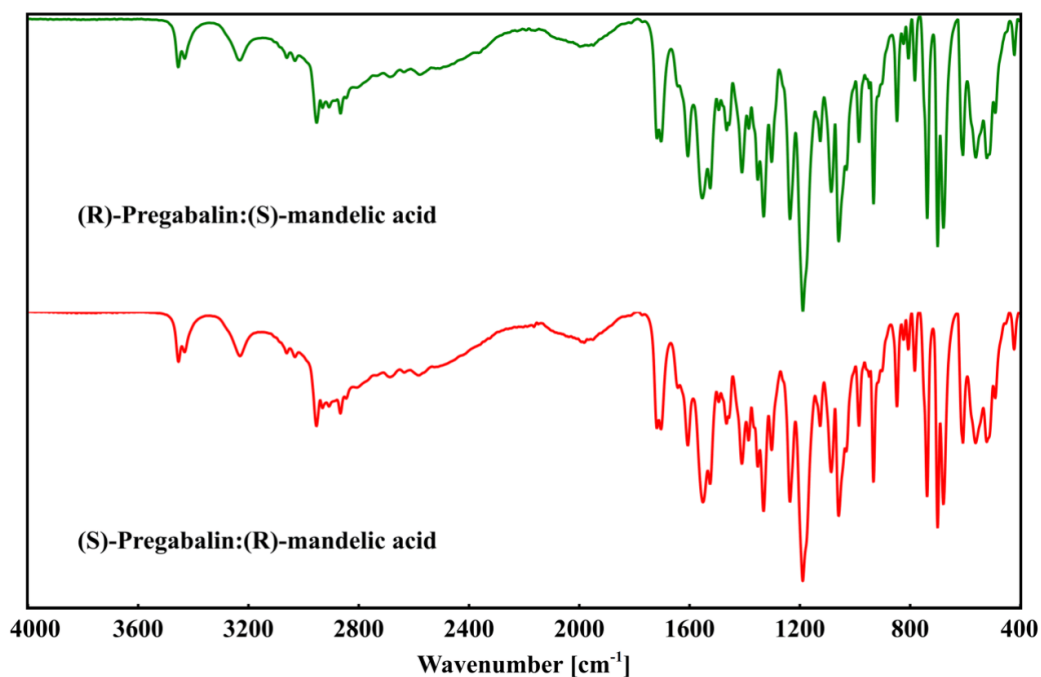


Figure S37. IR-spectra of (S, R)-Pregabalin:mandelic acid (red) and (R, S)-Pregabalin:mandelic acid (green). The range from 400cm^{-1} to 4000 cm^{-1} is depicted.

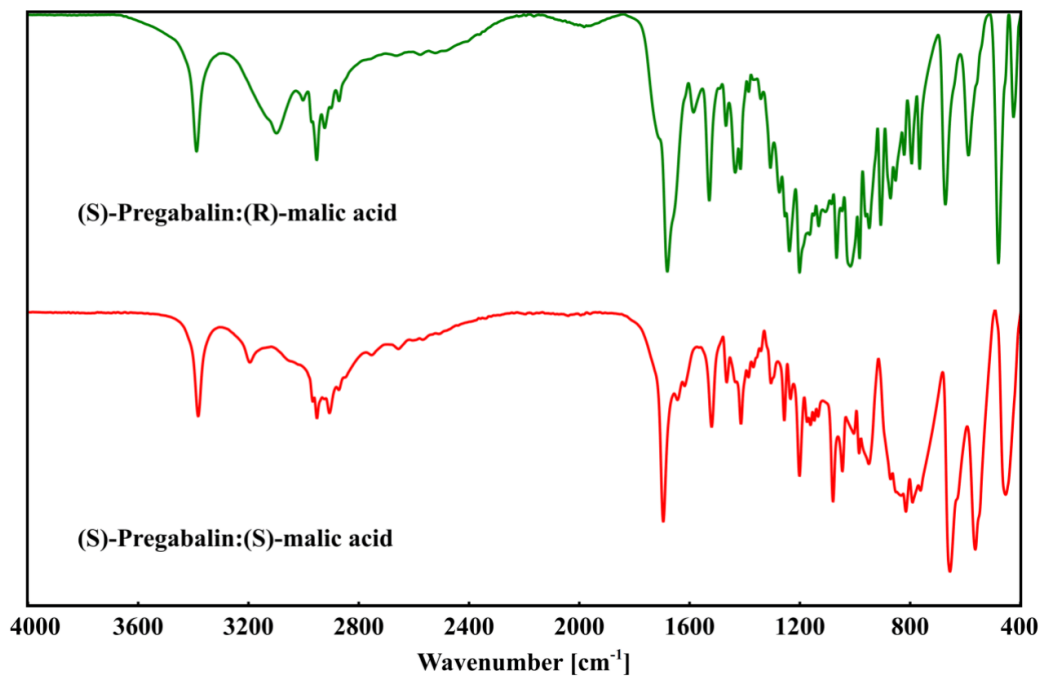


Figure S38. IR-spectra of (S, S)-Pregabalin:malic acid (red) and (S, R)-Pregabalin:malic acid (green). The range from 400cm^{-1} to 4000 cm^{-1} is depicted.

Table S30. *E_{scf}* in aspirin, benzoic acid, naphthalene, carbendazim and fenamic acid.

	Aspirin	Benzoic acid	Naphthalene	Carbendazim Maleate	Fenamic acid
Total energy	-336.89571169 Ry	-864.48414572 Ry	-380.80902318 Ry	-2238.93849076 Ry	-1405.14750341 Ry
Estimated scf accuracy	9.5E-10 Ry	6.3E-09 Ry	4.0E-09 Ry	3.6E-09 Ry	2.5E-09 Ry
One-electron contribution	-1312.88831935 Ry	-431.66148218 Ry	-151.00679470 Ry	-1356.79696542 Ry	-729.97165977 Ry
Hartree contribution	666.38808897 Ry	288.25452830 Ry	111.67278034 Ry	865.02235307 Ry	491.21003984 Ry
Xc contribution	-75.71501968 Ry	-202.93841066 Ry	-102.34427854 Ry	-522.41418926 Ry	-350.97309805 Ry
Ewald contribution	474.77906097 Ry	-280.15301891 Ry	-121.17790015 Ry	-699.48265014 Ry	-435.89581744 Ry
DFT-D3 Dispersion	-0.01546025 Ry	-0.19853529 Ry	-0.12203006 Ry	-0.46184980 Ry	-0.36727809 Ry
One-center paw contribution	-89.444406235 Ry	-237.78722698 Ry	-117.83080007 Ry	-524.80518921 Ry	-379.14968990 Ry
PAW Hartree energy AE	27.95344349 Ry	112.86367996 Ry	46.89218991 Ry	140.64296658 Ry	84.07972051 Ry
PAW Hartree energy PS	-27.92749991 Ry	-112.54564220 Ry	-46.84845552 Ry	-140.30422592 Ry	-84.00187446 Ry
PAW xc energy AE	-30.96576143 Ry	-95.09279017 Ry	-51.66945232 Ry	-126.04609233 Ry	-92.95386241 Ry
PAW xc energy PS	13.26792153 Ry	41.22003547 Ry	22.16801792 Ry	54.48770059 Ry	39.85979623 Ry
Total E _H with PAW	666.41403255 Ry	288.57266606 Ry	111.71651473 Ry	865.36109373 Ry	491.28788589 Ry
Total E _{XC} with PAW	-93.41285959 Ry	-256.81116536 Ry	-131.84571294 Ry	-593.97258100 Ry	-404.06716423 Ry

Table S31. *E_{scf}* in glycine polymorphs $\alpha - \gamma$.

	Glycine α	Glycine β	Glycine γ
Total energy	-580.75928660 Ry	-290.37728560 Ry	-435.57100873 Ry
Estimated scf accuracy	2.5E-09 Ry	1.4E-09 Ry	6.9E-10 Ry
One-electron contribution	-214.06562382 Ry	-110.70421627 Ry	-173.43139417 Ry
Hartree contribution	161.38931511 Ry	82.32377227 Ry	126.72740778 Ry
Xc contribution	-133.72136785 Ry	-66.86096752 Ry	-100.28869051 Ry
Ewald contribution	-274.25350224 Ry	-135.08390726 Ry	-198.50249159 Ry
DFT-D3 Dispersion	-0.15132660 Ry	-0.07472014 Ry	-0.11108147 Ry
One-center paw contribution	-119.95678120 Ry	59.97724668 Ry	-89.96475877 Ry
PAW Hartree energy AE	18.36286775 Ry	18.33019638 Ry	65.24929324 Ry
PAW Hartree energy PS	-18.34599330 Ry	-18.31334187 Ry	-64.97916769 Ry
PAW xc energy AE	-20.57600967 Ry	-20.56792933 Ry	-43.28660728 Ry
PAW xc energy PS	8.78096894 Ry	8.77300925 Ry	18.91587444 Ry
Total E _H with PAW	161.40618955 Ry	82.34062678 Ry	126.99753334 Ry
Total E _{XC} with PAW	-145.51640859 Ry	-78.65588760 Ry	-124.65942334 Ry

Table S32. *E_{int}* in (S)- and (R)-Pregabalin and (rac)-Phenibut

	(S)-1	(R)-1	(rac)-2
Total energy	-1071.80165524 Ry	-1071.80170922 Ry	-2395.20650159 Ry
Estimated scf accuracy	5.1E-09 Ry	5.5E-09 Ry	0.00000016 Ry
One-electron contribution	-577.36224332 Ry	-577.93818768 Ry	-1174.63541450 Ry
Hartree contribution	387.44493557 Ry	387.65747211 Ry	811.05092165 Ry
Xc contribution	-277.66481361 Ry	-277.65938926 Ry	-604.74515244 Ry
Ewald contribution	-342.65463124 Ry	-342.29766682 Ry	-809.28613616 Ry
DFT-D3 Dispersion	-0.32003300 Ry	-0.31943849 Ry	-0.68856853 Ry
One-center paw contribution	-261.24486964 Ry	-261.24449907 Ry	-616.90215161 Ry
PAW Hartree energy AE	129.27305249 Ry	129.26729739 Ry	148.84527047 Ry
PAW Hartree energy PS	-128.94468573 Ry	-128.93889306 Ry	-148.49765287 Ry
PAW xc energy AE	-115.21439958 Ry	-115.21241556 Ry	-136.12237355 Ry
PAW xc energy PS	49.57481541 Ry	49.57288647 Ry	58.66198700 Ry
Total E _H with PAW	387.77330234 Ry	387.98587643 Ry	811.39853925 Ry
Total E _{XC} with PAW	-343.30439778 Ry	-343.29891835 Ry	-682.20553899 Ry

Table S33. *E_{int}* in (S)-, (R)-, (S, R)- and (R, S)-Pregabalin:mandelic acid.

	(S, S)-1,3	(R, R)-1,3	(S, R)-1,3	(R, S)-1,3
Total energy	-2182.72816251 Ry	-2182.72828907 Ry	-2182.68324007 Ry	-2182.68437385 Ry
Estimated scf accuracy	1.3E-09 Ry	1.8E-09 Ry	9.5E-09 Ry	8.0E-09 Ry
One-electron contribution	-1533.51665515 Ry	-1549.49021097 Ry	-1814.50402550 Ry	-1813.82535919 Ry
Hartree contribution	956.64051386 Ry	964.50310881 Ry	1097.70041506 Ry	1097.23254769 Ry
Xc contribution	-534.05440736 Ry	-534.04862113 Ry	-534.00508650 Ry	-533.99359867 Ry
Ewald contribution	-512.26754807 Ry	-504.16306644 Ry	-372.32105602 Ry	-372.54636041 Ry
DFT-D3 Dispersion	-0.55923671 Ry	-0.55880178 Ry	-0.56773385 Ry	-0.56710848 Ry
One-center paw contribution	-558.97082908 Ry	-558.97069756 Ry	-558.98575325 Ry	-558.98449480 Ry
PAW Hartree energy AE	262.04303170 Ry	129.73847311 Ry	270.35132574 Ry	242.94333815 Ry
PAW Hartree energy PS	-261.15762810 Ry	-129.40728577 Ry	-269.46383582 Ry	-242.18723498 Ry
PAW xc energy AE	-202.21748403 Ry	-115.29551401 Ry	-212.40131788 Ry	-196.00997753 Ry
PAW xc energy PS	87.81410231 Ry	49.65568953 Ry	92.09786596 Ry	84.94470266 Ry
Total E _H with PAW	957.52591746 Ry	964.83429615 Ry	1098.58790498 Ry	1097.98865086 Ry
Total E _{XC} with PAW	-648.45778908 Ry	-599.68874561 Ry	-654.30853843 Ry	-645.05887354 Ry

Table S34. *E_{iss}* in (S, S)- and (S, R)-Pregabalin;malic acid and (R, S)-Phenbutir;mandelic acid.

	(S, S)-1:4	(S, R)-1:4	(R, S)-2:3
Total energy	-2213.33656663 Ry	-2213.34434886 Ry	-1154.26774184 Ry
Estimated scf accuracy	1.3E-09 Ry	1.0E-08 Ry	1.6E-09 Ry
One-electron contribution	-1432.30160955 Ry	-1411.01995314 Ry	-662.88344334 Ry
Hartree contribution	901.97731634 Ry	891.31218524 Ry	431.46603161 Ry
Xc contribution	-514.37445599 Ry	-514.40952926 Ry	-279.31815141 Ry
Ewald contribution	-630.60581621 Ry	-641.20468387 Ry	-340.16377027 Ry
DFT-D3 Dispersion	-0.51310661 Ry	-0.51584702 Ry	-0.28393580 Ry
One-center paw contribution	-537.51889461 Ry	-537.50652081 Ry	-303.08447264 Ry
PAW Hartree energy AE	280.18921538 Ry	280.30096324 Ry	159.32291534 Ry
PAW Hartree energy PS	-279.18535867 Ry	-279.29446844 Ry	-158.85326536 Ry
PAW xc energy AE	-208.23496725 Ry	-208.24379479 Ry	-132.16104066 Ry
PAW xc energy PS	90.51428806 Ry	90.52373303 Ry	57.25806117 Ry
Total E _H with PAW	902.98117305 Ry	892.31868004 Ry	431.93568158 Ry
Total E _{XC} with PAW	-632.09513518 Ry	-632.12959102 Ry	-354.22113089 Ry

Table S35. *E_{iss}* in aspirin, benzoic acid and naphthalene.

	Aspirin	Benzoic acid	Naphthalene
Total energy	-336.89571169 Ry	-216.03921007 Ry	-190.34591573 Ry
Estimated scf accuracy	9.5E-10 Ry	4.8E-09 Ry	1.2E-09 Ry
One-electron contribution	-1312.88831935 Ry	-739.41836998 Ry	-736.59527298 Ry
Hartree contribution	666.38808897 Ry	376.18668573 Ry	374.44538692 Ry
Xc contribution	-75.71501968 Ry	-50.59087816 Ry	-51.06730146 Ry
Ewald contribution	474.77906097 Ry	257.24406025 Ry	281.79361367 Ry
DFT-D3 Dispersion	-0.01546025 Ry	-0.00788014 Ry	-0.00959746 Ry
One-center paw contribution	-89.444406235 Ry	-59.45282779 Ry	-58.91274441 Ry
PAW Hartree energy AE	27.95344349 Ry	56.37489016 Ry	28.13589881 Ry
PAW Hartree energy PS	-27.92749991 Ry	-56.11525462 Ry	-28.10975625 Ry
PAW xc energy AE	-30.96576143 Ry	-33.04993323 Ry	-31.01244409 Ry
PAW xc energy PS	13.26792153 Ry	14.57723675 Ry	13.31273914 Ry
Total E _H with PAW	666.41403255 Ry	376.44632128 Ry	374.47152947 Ry
Total E _{XC} with PAW	-93.41285959 Ry	-69.06357463 Ry	-68.76700641 Ry

Table S36. *E_{sig}* in Carbendazim maleate, Carbendazim charged, Carbendazim neutral, maleic acid charged and maleic acid neutral.

	Carbendazim (neutral)	Carbendazim (charge)	Maleic acid (neutral)	Maleic acid (charge)
Total energy	-317.81712031 Ry	-318.65170796 Ry	-241.69462491 Ry	-240.74748977 Ry
Estimated scf accuracy	5.4E-09 Ry	1.4E-09 Ry	8.6E-09 Ry	2.6E-09 Ry
One-electron contribution	-1331.80840675 Ry	-1349.82911878 Ry	-750.38874570 Ry	-741.67106561 Ry
Hartree contribution	675.48840558 Ry	677.97198443 Ry	381.58547061 Ry	383.02285946 Ry
Xc contribution	-80.09207190 Ry	-80.33880782 Ry	-50.11394916 Ry	-49.86629580 Ry
Ewald contribution	489.82645736 Ry	504.77755561 Ry	237.21931250 Ry	227.76142495 Ry
DFT-D3 Dispersion	-0.014329587 Ry	-0.01529829 Ry	-0.00631915 Ry	-0.00561997 Ry
One-center paw contribution	-71.21717873 Ry	-71.21802311 Ry	-59.99039401 Ry	-59.98879279 Ry
PAW Hartree energy AE	0.00000000 Ry	0.00000000 Ry	56.55146170 Ry	55.97546094 Ry
PAW Hartree energy PS	0.00000000 Ry	0.00000000 Ry	-56.29063300 Ry	-55.71544737 Ry
PAW xc energy AE	0.00000000 Ry	0.00000000 Ry	-33.07681606 Ry	-32.98567477 Ry
PAW xc energy PS	0.00000000 Ry	0.00000000 Ry	14.60409227 Ry	14.51384719 Ry
Total E _H with PAW	675.48840558 Ry	677.97198443 Ry	381.84629932 Ry	383.28287303 Ry
Total E _{XC} with PAW	-80.09207190 Ry	-80.33880782 Ry	-68.58667296 Ry	-68.33812339 Ry

Table S37. *E_{sig}* in fenamic acid, molecule A and molecule B as well as Glycine α , neutral and zwitterionic.

	Fenamic acid A	Fenamic acid B	Glycine α (neutral)	Glycine α (zwitterion)
Total energy	-351.18463954 Ry	-351.18406565 Ry	-145.06565496 Ry	-145.06563313 Ry
Estimated scf accuracy	6.6E-09 Ry	8.5E-10 Ry	2.0E-09 Ry	5.3E-09 Ry
One-electron contribution	-1464.34559523 Ry	-1464.03566170 Ry	-444.69888481 Ry	-444.67960905 Ry
Hartree contribution	743.17809909 Ry	743.04041847 Ry	226.93765648 Ry	226.92649777 Ry
Xc contribution	-87.54431237 Ry	-87.54001696 Ry	-33.25141345 Ry	-33.25068021 Ry
Ewald contribution	552.33753090 Ry	552.16178021 Ry	135.94233456 Ry	135.93350594 Ry
DFT-D3 Dispersion	-0.01986038 Ry	-0.01987773 Ry	-0.00368100 Ry	-0.00368579 Ry
One-center paw contribution	-94.79050154 Ry	-94.79070794 Ry	-29.99166675 Ry	-29.99166178 Ry
PAW Hartree energy AE	37.19247007 Ry	27.85123707 Ry	18.22767627 Ry	18.22421611 Ry
PAW Hartree energy PS	-37.15820627 Ry	-27.82543755 Ry	-18.21084902 Ry	-18.20739007 Ry
PAW xc energy AE	-41.26733921 Ry	-30.94234266 Ry	-20.54299767 Ry	-20.54215868 Ry
PAW xc energy PS	17.67303721 Ry	13.24517069 Ry	8.74823976 Ry	8.74740701 Ry
Total E _H with PAW	743.21236288 Ry	743.06621799 Ry	226.95448372 Ry	226.94332381 Ry
Total E _{XC} with PAW	-111.13861438 Ry	-105.23718894 Ry	-45.04617137 Ry	-45.04543188 Ry

Table S38. *E_{sig}* in Glycine β, neutral and zwitterionic as well as Glycine γ, neutral and zwitterionic.

	Glycine β (neutral)	Glycine β (zwitter.)	Glycine γ (neutral)	Glycine γ (zwitter.)
Total energy	-145.06569801 Ry	-145.06570159 Ry	-145.05056883 Ry	-145.06557827 Ry
Estimated scf accuracy	6.9E-09 Ry	1.8E-09 Ry	4.9E-09 Ry	6.8E-09 Ry
One-electron contribution	-444.75995154 Ry	-444.62073980 Ry	-441.73616736 Ry	-444.81722053 Ry
Hartree contribution	226.97201711 Ry	226.90162080 Ry	225.42566450 Ry	226.99643361 Ry
Xc contribution	-33.25476841 Ry	-33.25109138 Ry	-33.22831266 Ry	-33.25077079 Ry
Ewald contribution	135.97232156 Ry	135.89987598 Ry	134.48347770 Ry	136.00136033 Ry
DFT-D3 Dispersion	-0.00367606 Ry	-0.00367672 Ry	-0.00395088 Ry	-0.00368777 Ry
One-center paw contribution	-29.99164066 Ry	-29.99169048 Ry	-29.99128013 Ry	-29.99169313 Ry
PAW Hartree energy AE	18.23912880 Ry	18.22323513 Ry	56.42606530 Ry	56.36291519 Ry
PAW Hartree energy PS	-18.22229626 Ry	-18.20640903 Ry	-56.16667109 Ry	-56.10418032 Ry
PAW xc energy AE	-20.54581868 Ry	-20.54192591 Ry	-33.05806132 Ry	-33.04778665 Ry
PAW xc energy PS	8.75102687 Ry	8.74717092 Ry	14.58523343 Ry	14.57528354 Ry
Total E _H with PAW	226.98884964 Ry	226.91844690 Ry	225.68505871 Ry	227.25516848 Ry
Total E _{XC} with PAW	-45.04956022 Ry	-45.04584637 Ry	-51.70114056 Ry	-51.72327390 Ry

Table S39. *E_{sig}* in (S)-Pregabalin, neutral and zwitterionic. (R)-Pregabalin, neutral and zwitterionic as well as (rac)-Phenbut, neutral and zwitterionic.

	(S)-1 (neutral)	(S)-1 (zwitter.)	(R)-1 (neutral)	(R)-1 (zwitter.)	(rac)-2 (neutral)	(rac)-2 (zwitter.)
Total energy	-267.79801705 Ry	-267.80747791 Ry	-267.79160852 Ry	-267.80763781 Ry	-299.23843736 Ry	-299.12073572 Ry
Estimated scf accuracy	1.0E-09 Ry	8.1E-09 Ry	1.6E-09 Ry	1.1E-09 Ry	3.8E-09 Ry	2.5E-09 Ry
One-electron contribution	-1132.97801838 Ry	-1137.10596586 Ry	-1139.37899930 Ry	-1137.15690002 Ry	-1233.30321001 Ry	-1243.07956735 Ry
Hartree contribution	576.18367680 Ry	577.94914245 Ry	579.17479627 Ry	577.96962803 Ry	626.59819637 Ry	631.59450463 Ry
Xc contribution	-69.16008416 Ry	-69.18545259 Ry	-69.15366478 Ry	-69.18727646 Ry	-75.30456653 Ry	-75.28054105 Ry
Ewald contribution	423.49226678 Ry	425.86835966 Ry	426.90277629 Ry	425.90049677 Ry	459.90584669 Ry	464.78434800 Ry
DFT-D3 Dispersion	-0.02225537 Ry	-0.02261513 Ry	-0.02260823 Ry	-0.02262865 Ry	-0.02054518 Ry	-0.02103308 Ry
One-center paw contribution	-65.31350272 Ry	-65.31094644 Ry	-65.31390877 Ry	-65.31095748 Ry	-77.11415871 Ry	-77.11844687 Ry
PAW Hartree energy AE	65.42093235 Ry	65.47325474 Ry	65.40966588 Ry	65.46862311 Ry	37.40491936 Ry	36.88010451 Ry
PAW Hartree energy PS	-65.15326146 Ry	-65.20405897 Ry	-65.14206060 Ry	-65.19944719 Ry	-37.26504078 Ry	-36.74389647 Ry
PAW xc energy AE	-43.30887949 Ry	-43.31644828 Ry	-43.30718024 Ry	-43.31566576 Ry	-26.80943871 Ry	-26.72862750 Ry
PAW xc energy PS	18.93592371 Ry	18.94489265 Ry	18.93411522 Ry	18.94402132 Ry	11.67352971 Ry	11.59424725 Ry
Total E _H with PAW	576.45134769 Ry	578.21833823 Ry	579.44240155 Ry	578.23880394 Ry	626.73807495 Ry	631.73071267 Ry
Total E _{XC} with PAW	-93.53303994 Ry	-93.55700822 Ry	-93.52672979 Ry	-93.55882090 Ry	-90.44047553 Ry	-90.41492130 Ry

Table S40. E_{seg} in (S), (S)-Pregabalin; mandelic acid, Pregabalin molecule A neutral and zwitterionic, Pregabalin molecule B neutral and zwitterionic, mandelic acid molecule A and mandelic acid molecule B.

	(S)-1_A (neutral)	(S)-1_A (zwitterion)	(S)-1_B (neutral)	(S)-1_B (zwitterion)	(S)-3_A (neutral)	(S)-3_B (neutral)
Total energy	-267.79207687 Ry	-267.80896808 Ry	-267.79386670 Ry	-267.80897994 Ry	-277.62920472 Ry	-277.62892955 Ry
Estimated scf accuracy	8.4E-09 Ry	9.6E-09 Ry	1.4E-09 Ry	7.2E-09 Ry	8.4E-09 Ry	8.2E-09 Ry
One-electron contribution	-1146.57467144 Ry	-1149.129664591 Ry	-1150.27288277 Ry	-1149.76744088 Ry	-1029.52101511 Ry	-1029.30778810 Ry
Hartree contribution	582.84266957 Ry	584.04851409 Ry	584.64607834 Ry	584.36864185 Ry	523.17133645 Ry	523.06281742 Ry
Xc contribution	-69.15187735 Ry	-69.18326169 Ry	-69.16093982 Ry	-69.18745151 Ry	-63.90041076 Ry	-63.89877731 Ry
Ewald contribution	430.42887044 Ry	431.78954630 Ry	432.33012274 Ry	432.1151848 Ry	367.07359829 Ry	366.96757988 Ry
DFT-D3 Dispersion	-0.02309849 Ry	-0.02287750 Ry	-0.022321006 Ry	-0.02290010 Ry	-0.01230029 Ry	-0.01227256 Ry
One-center paw contribution	-65.31396958 Ry	-65.31124336 Ry	-65.31303533 Ry	-65.31134778 Ry	-74.44041329 Ry	-74.44048887 Ry
PAW Hartree energy AE	65.39274545 Ry	65.45833287 Ry	65.43766939 Ry	65.46017095 Ry	84.58268227 Ry	84.58009975 Ry
PAW Hartree energy PS	-65.12532377 Ry	-65.18933924 Ry	-65.16942296 Ry	-65.19119186 Ry	-84.19016010 Ry	-84.18763805 Ry
PAW xc energy AE	-43.30298523 Ry	-43.31464608 Ry	-43.30937372 Ry	-43.31535966 Ry	-49.57454296 Ry	-49.57420263 Ry
PAW xc energy PS	18.93003382 Ry	18.94297919 Ry	18.93652996 Ry	18.94368674 Ry	21.86736942 Ry	21.86699399 Ry
Total E_H with PAW	583.11009124 Ry	584.31750773 Ry	584.91432497 Ry	584.63762094 Ry	523.56385862 Ry	523.45527912 Ry
Total E_XC with PAW	-93.52482877 Ry	-93.55492858 Ry	-93.53378358 Ry	-93.55912444 Ry	-91.60758429 Ry	-91.60598595 Ry

Table S41. E_{seg} in (R), (R)-Pregabalin; mandelic acid, Pregabalin molecule A neutral and zwitterionic, Pregabalin molecule B neutral and zwitterionic, mandelic acid molecule A and mandelic acid molecule B.

	(R)-1_A (neutral)	(R)-1_A (zwitterion)	(R)-1_B (neutral)	(R)-1_B (zwitterion)	(R)-3_A (neutral)	(R)-3_B (neutral)
Total energy	-267.79375084 Ry	-267.808968302 Ry	-267.79208315 Ry	-267.80900234 Ry	-277.62918420 Ry	-277.62894959 Ry
Estimated scf accuracy	4.5E-09 Ry	1.2E-09 Ry	8.4E-09 Ry	1.7E-09 Ry	4.2E-09 Ry	2.3E-09 Ry
One-electron contribution	-1150.18357840 Ry	-1149.37655749 Ry	-1146.61835649 Ry	-1149.27662069 Ry	-1029.64141539 Ry	-1029.31076807 Ry
Hartree contribution	584.60436837 Ry	584.17203235 Ry	582.86745891 Ry	584.12180134 Ry	523.23017098 Ry	523.06429268 Ry
Xc contribution	-69.16129377 Ry	-69.18656757 Ry	-69.15378472 Ry	-69.18739558 Ry	-63.90315362 Ry	-63.89762768 Ry
Ewald contribution	432.28297207 Ry	431.91632775 Ry	430.44963452 Ry	431.86736104 Ry	367.13794787 Ry	366.96786671 Ry
DFT-D3 Dispersion	-0.02319512 Ry	-0.02287986 Ry	-0.02309843 Ry	-0.02287231 Ry	-0.01230760 Ry	-0.01227643 Ry
One-center paw contribution	-65.31302397 Ry	-65.31133819 Ry	-65.31393693 Ry	-65.31127615 Ry	-74.44042645 Ry	-74.44043679 Ry
PAW Hartree energy AE	65.43436647 Ry	65.45507206 Ry	65.39334619 Ry	65.46939876 Ry	84.59206754 Ry	84.57999025 Ry
PAW Hartree energy PS	-65.16609918 Ry	-65.18611142 Ry	-65.12588796 Ry	-65.20034783 Ry	-84.19946124 Ry	-84.18751782 Ry
PAW xc energy AE	-43.30861886 Ry	-43.31433639 Ry	-43.30285552 Ry	-43.31665117 Ry	-49.57601963 Ry	-49.57417644 Ry
PAW xc energy PS	18.93578963 Ry	18.94268044 Ry	18.92991494 Ry	18.94496975 Ry	21.86883673 Ry	21.86697238 Ry
Total E_H with PAW	584.87263565 Ry	584.44099299 Ry	583.13491713 Ry	584.39085227 Ry	523.62277728 Ry	523.45676512 Ry
Total E_XC with PAW	-93.53412301 Ry	-93.55822352 Ry	-93.52672531 Ry	-93.55907699 Ry	-91.61033652 Ry	-91.60483174 Ry

Table S42. E_{sig} in (S, R)-Pregabalin:mandelic acid, Pregabalin molecule A neutral, zwitterionic and charged as well as Pregabalin molecule B neutral, zwitterionic and charged.

	(S)-1_A (neutral)	(S)-1_A (zwitter.)	(S)-1_A (charge)	(S)-1_B (neutral)	(S)-1_B (zwitter.)	(S)-1_B (charge)
Total energy	-267.79975583 Ry	-267.80894456 Ry	-268.64998668 Ry	-267.79703425 Ry	-267.80927522 Ry	-268.59869837 Ry
Estimated scf accuracy	2.6E-09 Ry	3.7E-09 Ry	4.5E-09 Ry	6.3E-09 Ry	1.2E-09 Ry	1.4E-09 Ry
One-electron contribution	-1150.32791801 Ry	-1144.52122571 Ry	-1157.74153844 Ry	-1061.81071755 Ry	-1170.79281370 Ry	-1175.44653807 Ry
Hartree contribution	584.88706105 Ry	581.71822027 Ry	582.42093762 Ry	540.85882190 Ry	594.89073189 Ry	591.44772100 Ry
Xc contribution	-69.16647533 Ry	-69.18155183 Ry	-69.41358892 Ry	-69.16717044 Ry	-69.19667954 Ry	-69.36887551 Ry
Ewald contribution	432.14302255 Ry	429.50919174 Ry	441.41688917 Ry	387.65948308 Ry	442.62496333 Ry	450.10991996 Ry
DFT-D3 Dispersion	-0.02306737 Ry	-0.02269933 Ry	-0.02362598 Ry	-0.02360571 Ry	-0.02410924 Ry	-0.02498421 Ry
One-center paw contribution	-65.31237873 Ry	-65.31087970 Ry	-65.30906012 Ry	-65.31384553 Ry	-65.31136797 Ry	-65.31594154 Ry
PAW Hartree energy AE	65.49651598 Ry	65.35817895 Ry	65.739662312 Ry	65.38430547 Ry	65.41420775 Ry	65.45657948 Ry
PAW Hartree energy PS	-65.22864191 Ry	-65.08926967 Ry	-65.46853461 Ry	-65.11687067 Ry	-65.14561066 Ry	-65.18980703 Ry
PAW xc energy AE	-43.31230587 Ry	-43.27938939 Ry	-43.33943230 Ry	-43.30085731 Ry	-43.30791188 Ry	-43.31980347 Ry
PAW xc energy PS	18.94509686 Ry	18.91257740 Ry	18.97314775 Ry	18.92766341 Ry	18.93618130 Ry	18.94662604 Ry
Total E_H with PAW	585.15493511 Ry	581.98712956 Ry	582.69202613 Ry	541.12625670 Ry	595.15932898 Ry	591.71449345 Ry
Total E_XC with PAW	-93.53368433 Ry	-93.54836382 Ry	-93.77987347 Ry	-93.54036434 Ry	-93.56841013 Ry	-93.74205294 Ry

Table S43. E_{sig} in (S, R)-Pregabalin:mandelic acid, mandelic acid molecule A, neutral and charged, as well as mandelic acid molecule B, neutral and charged.

	(R)-3_A (neutral)	(R)-3_A (charge)	(R)-3_B (neutral)	(R)-3_B (charge)
Total energy	-277.629352062 Ry	-276.65200500 Ry	-277.63008521 Ry	-276.63285774 Ry
Estimated scf accuracy	9.8E-09 Ry	1.8E-09 Ry	5.7E-09 Ry	0.00000095 Ry
One-electron contribution	-984.02556625 Ry	-836.65595354 Ry	-1033.27892563 Ry	-1015.73101764 Ry
Hartree contribution	500.53925577 Ry	431.98760346 Ry	525.05776382 Ry	522.32497785 Ry
Xc contribution	-63.91233143 Ry	-63.65826059 Ry	-63.91244102 Ry	-63.62993845 Ry
Ewald contribution	344.22059760 Ry	266.12644157 Ry	368.95578786 Ry	354.85796838 Ry
DFT-D3 Dispersion	-0.01254664 Ry	-0.01182641 Ry	-0.01256058 Ry	-0.01144589 Ry
One-center paw contribution	-74.43892767 Ry	-74.44000949 Ry	-74.43970966 Ry	-74.44340199 Ry
PAW Hartree energy AE	84.68111468 Ry	83.61206042 Ry	84.64220632 Ry	83.33311012 Ry
PAW Hartree energy PS	-84.28761471 Ry	-83.22235287 Ry	-84.24910181 Ry	-82.94553301 Ry
PAW xc energy AE	-49.58968685 Ry	-49.41921197 Ry	-49.58361938 Ry	-49.37621997 Ry
PAW xc energy PS	21.88259150 Ry	21.71404709 Ry	21.87654439 Ry	21.67079171 Ry
Total E_H with PAW	500.93275574 Ry	432.37731101 Ry	525.45086832 Ry	522.71255496 Ry
Total E_XC with PAW	-91.61942678 Ry	-91.36342547 Ry	-91.61951601 Ry	-91.33536671 Ry

Table S44. E_{seg} in (R, S)-Pregabalin:mandelic acid, Pregabalin molecule A neutral, zwitterionic and charged as well as Pregabalin molecule B neutral, zwitterionic and charged.

	(R)-1_A (neutral)	(R)-1_A (zwitter.)	(R)-1_A (charge)	(R)-1_B (neutral)	(R)-1_B (zwitter.)	(R)-1_B (charge)
Total energy	-267.79396641 Ry	-267.80931677 Ry	-268.59858887 Ry	-267.79977164 Ry	-267.80896960 Ry	-268.65003203 Ry
Estimated scf accuracy	4.0E-09 Ry	7.7E-10 Ry	8.0E-09 Ry	6.1E-09 Ry	2.4E-09 Ry	1.4E-09 Ry
One-electron contribution	-1153.10618141 Ry	-1170.83568908 Ry	-1175.35713834 Ry	-1151.10825527 Ry	-1144.69063057 Ry	-1158.22261487 Ry
Hartree contribution	586.31973900 Ry	594.91086176 Ry	591.41405146 Ry	585.27837240 Ry	581.80257085 Ry	582.65951124 Ry
Xc contribution	-69.15451484 Ry	-69.19512398 Ry	-69.36695264 Ry	-69.16943185 Ry	-69.18286439 Ry	-69.41795409 Ry
Ewald contribution	433.48355758 Ry	442.64608092 Ry	450.05223978 Ry	432.53498839 Ry	429.59556094 Ry	441.66382314 Ry
DFT-D3 Dispersion	-0.02323917 Ry	-0.02411122 Ry	-0.02498764 Ry	-0.02498764 Ry	-0.02270447 Ry	-0.02364287 Ry
One-center paw contribution	-65.31332757 Ry	-65.31133516 Ry	-65.31580150 Ry	-65.31234738 Ry	-65.31090194 Ry	-65.30915459 Ry
PAW Hartree energy AE	65.38648975 Ry	65.42178049 Ry	65.46347958 Ry	65.42252282 Ry	65.47250700 Ry	65.75107390 Ry
PAW Hartree energy PS	-65.11894629 Ry	-65.15316949 Ry	-65.19662209 Ry	-65.15426466 Ry	-65.20327838 Ry	-65.47967284 Ry
PAW xc energy AE	-43.30046885 Ry	-43.30947470 Ry	-43.32057164 Ry	-43.30306322 Ry	-43.31621869 Ry	-43.35300760 Ry
PAW xc energy PS	18.92728254 Ry	18.93772130 Ry	18.94743884 Ry	18.93057606 Ry	18.94465890 Ry	18.98099465 Ry
Total E_H with PAW	586.58728247 Ry	595.17947276 Ry	591.68090895 Ry	585.54663056 Ry	582.07179947 Ry	582.93091231 Ry
Total E_XC with PAW	-93.52770087 Ry	-93.56687738 Ry	-93.74008544 Ry	-93.54191901 Ry	-93.55444218 Ry	-93.78996704 Ry

Table S45. E_{seg} in (R, S)-Pregabalin:mandelic acid, mandelic acid molecule A, neutral and charged, as well as mandelic acid molecule B, neutral and charged.

	(S)-3_A (neutral)	(S)-3_A (charge)	(S)-3_B (neutral)	(S)-3_B (charge)
Total energy	-277.62917802 Ry	-276.64477180 Ry	-277.62574657 Ry	-276.63279628 Ry
Estimated scf accuracy	1.8E-09 Ry	2.3E-09 Ry	1.2E-09 Ry	8.7E-09 Ry
One-electron contribution	-1032.66358245 Ry	-1015.49434460 Ry	-1029.31666511 Ry	-1015.84614954 Ry
Hartree contribution	524.74114097 Ry	522.28819002 Ry	523.03937919 Ry	522.38115878 Ry
Xc contribution	-63.90590518 Ry	-63.64845335 Ry	-63.90083528 Ry	-63.62862274 Ry
Ewald contribution	368.65199764 Ry	354.66134689 Ry	367.00633024 Ry	354.91564817 Ry
DFT-D3 Dispersion	-0.01242153 Ry	-0.01169329 Ry	-0.01226152 Ry	-0.01145176 Ry
One-center paw contribution	-74.444040748 Ry	-74.43981747 Ry	-74.444169408 Ry	-74.44337920 Ry
PAW Hartree energy AE	84.60083134 Ry	83.58818023 Ry	84.51268735 Ry	83.32830041 Ry
PAW Hartree energy PS	-84.20818012 Ry	-83.19857792 Ry	-84.12089990 Ry	-82.94079809 Ry
PAW xc energy AE	-49.57735772 Ry	-49.41527993 Ry	-49.56417359 Ry	-49.37532787 Ry
PAW xc energy PS	21.87018418 Ry	21.71022287 Ry	21.85672289 Ry	21.66997428 Ry
Total E_H with PAW	525.13379219 Ry	522.67779234 Ry	523.43116664 Ry	522.76866110 Ry
Total E_XC with PAW	-91.61307873 Ry	-91.35351042 Ry	-91.60828599 Ry	-91.33397632 Ry

Table S46. E_{sig} in (S, S)-Pregabalin:malic acid, Pregabalin neutral, zwitterionic and charged, as well as malic acid neutral and charged.

	(S)-1 (neutral)	(S)-1 (zwitterion)	(S)-1 (charge)	(S)-4 (neutral)	(S)-4 (charge)
Total energy	-267.79195190 Ry	-267.80910065 Ry	-268.61129733 Ry	-285.25372379 Ry	-284.27132001 Ry
Estimated scf accuracy	6.9E-10 Ry	8.4E-09 Ry	5.7E-09 Ry	1.7E-09 Ry	4.4E-09 Ry
One-electron contribution	-1136.31452856 Ry	-1145.23419082 Ry	-1149.91381033 Ry	-950.21680717 Ry	-935.83302748 Ry
Hartree contribution	577.57489783 Ry	582.07656352 Ry	578.7269549 Ry	483.26247560 Ry	482.11646018 Ry
Xc contribution	-69.15816236 Ry	-69.18910101 Ry	-69.37879494 Ry	-58.94285641 Ry	-58.66689854 Ry
Ewald contribution	425.44242786 Ry	429.87147012 Ry	437.28987967 Ry	309.73863934 Ry	297.20839694 Ry
DFT-D3 Dispersion	-0.02283875 Ry	-0.02227004 Ry	-0.02381648 Ry	-0.00965105 Ry	-0.00883028 Ry
One-center paw contribution	-65.31374792 Ry	-65.31114206 Ry	-65.31345074 Ry	-69.08552410 Ry	-69.08742084 Ry
PAW Hartree energy AE	65.41975252 Ry	65.47797193 Ry	65.59295620 Ry	56.20194601 Ry	56.03295602 Ry
PAW Hartree energy PS	-65.15208371 Ry	-65.20880712 Ry	-65.32452334 Ry	-55.94103201 Ry	-55.77213855 Ry
PAW xc energy AE	-43.30944981 Ry	-43.31787678 Ry	-43.33918912 Ry	-33.02222717 Ry	-32.99354773 Ry
PAW xc energy PS	18.93635720 Ry	18.94625060 Ry	18.96680997 Ry	14.55058100 Ry	14.52276720 Ry
Total E _H with PAW	577.84256664 Ry	582.34572833 Ry	578.99812834 Ry	483.52338960 Ry	482.37727766 Ry
Total E _{XC} with PAW	-93.53125497 Ry	-93.56072719 Ry	-93.75217409 Ry	-77.41450259 Ry	-77.13767908 Ry

Table S47. E_{sig} in (S, R)-Pregabalin:malic acid, Pregabalin neutral, zwitterionic and charged, as well as malic acid neutral and charged.

	(S)-1 (neutral)	(S)-1 (zwitterion)	(S)-1 (charge)	(R)-4 (neutral)	(R)-4 (charge)
Total energy	-267.79369461 Ry	-267.80879947 Ry	-268.61135562 Ry	-285.25091193 Ry	-284.22893057 Ry
Estimated scf accuracy	1.6E-09 Ry	3.6E-09 Ry	1.0E-09 Ry	1.9E-09 Ry	9.8E-10 Ry
One-electron contribution	-1131.28671043 Ry	-1143.86090533 Ry	-1149.82367760 Ry	-952.95477737 Ry	-939.85881162 Ry
Hartree contribution	575.19633096 Ry	581.38466378 Ry	578.68652083 Ry	484.68449087 Ry	484.06054389 Ry
Xc contribution	-69.15608675 Ry	-69.18925831 Ry	-69.37972215 Ry	-58.94229589 Ry	-58.63695052 Ry
Ewald contribution	422.78905988 Ry	429.19015031 Ry	437.24272236 Ry	311.05700150 Ry	299.30453850 Ry
DFT-D3 Dispersion	-0.02257561 Ry	-0.02266884 Ry	-0.02379310 Ry	-0.00974501 Ry	-0.00955013 Ry
One-center paw contribution	-65.31371266 Ry	-65.31078108 Ry	-65.31340595 Ry	-69.08558604 Ry	-69.08870068 Ry
PAW Hartree energy AE	65.43919007 Ry	65.48267393 Ry	65.59452810 Ry	56.82543535 Ry	56.02910396 Ry
PAW Hartree energy PS	-65.17159110 Ry	-65.21334090 Ry	-65.32605466 Ry	-56.56252940 Ry	-55.77055731 Ry
PAW xc energy AE	-43.31264115 Ry	-43.31764738 Ry	-43.33959060 Ry	-33.11632309 Ry	-32.99343133 Ry
PAW xc energy PS	18.93954975 Ry	18.94609891 Ry	18.96723529 Ry	14.64453392 Ry	14.52167757 Ry
Total E _H with PAW	575.46392994 Ry	581.65399680 Ry	578.95499427 Ry	484.94739682 Ry	484.31909053 Ry
Total E _{XC} with PAW	-93.52917815 Ry	-93.56080677 Ry	-93.75207746 Ry	-77.41408506 Ry	-77.10870427 Ry

Table S48. E_{sg} in (R, S)-Phenibut:mandelic acid, Phenibut neutral and zwitterionic as well as mandelic acid neutral.

	(R)- 2 (neutral)	(R)- 2 (zwitterion)	(S)- 3 (neutral)
Total energy	-299.24118523 Ry	-299.24903734 Ry	-277.63003077 Ry
Estimated scf accuracy	2.0E-09 Ry	5.2E-09 Ry	4.4E-09 Ry
One-electron contribution	-1241.39331178 Ry	-1237.67805463 Ry	-1030.68394340 Ry
Hartree contribution	630.84461220 Ry	628.70733242 Ry	523.76518044 Ry
Xc contribution	-75.31692750 Ry	-75.33402510 Ry	-63.90941862 Ry
Ewald contribution	463.75757796 Ry	462.18718074 Ry	367.65037561 Ry
DFT-D3 Dispersion	-0.02048529 Ry	-0.02027812 Ry	-0.01241815 Ry
One-center paw contribution	-77.11265082 Ry	-77.11119265 Ry	-74.43980665 Ry
PAW Hartree energy AE	65.42696385 Ry	65.47298401 Ry	84.63610579 Ry
PAW Hartree energy PS	-65.15878090 Ry	-65.20386654 Ry	-84.24306855 Ry
PAW xc energy AE	-43.30416156 Ry	-43.31677390 Ry	-49.58274610 Ry
PAW xc energy PS	18.93168269 Ry	18.94518322 Ry	21.87563244 Ry
Total E _H with PAW	631.11279515 Ry	628.97644989 Ry	524.15821768 Ry
Total E _{XC} with PAW	-99.68940637 Ry	-99.70561579 Ry	-91.61653228 Ry

6 Sources

- [1] A. L. Spek, *Acta Crystallogr. D*, 2009, **65**, 148.
- [2] S. L. Childs, G. P. Stahly, A. Park, *Mol. Pharm.*, 2007, **4**, 323.
- [3] P. R. Spackman, M. J. Turner, J. J. McKinnon, S. K. Wolff, D. J. Grimwood, D. Jayatilaka, M. A. Spackman, *J. Appl. Crystallogr.*, 2021, **54**, 1006.
- [4] D. Komisarek, M. Pallaske, V. Vasylyeva, *Z. Anorg. Allg. Chem.*, 2021, **647**, 984.
- [5] G. R. Desiraju, *CrystEngComm*, 2007, **9**, 91.
- [6] K. M. Steed, J. W. Steed, *Chem. Rev.*, 2015, **115**, 2895.
- [7] C. R. Martinez, B. L. Iverson, *Chem. Sci.*, 2012, **3**, 2191.
- [8] R. L. Marchese Robinson, D. Geatches, C. Morris, R. Mackenzie, A. G. P. Maloney, K. J. Roberts, A. Moldovan, E. Chow, K. Pencheva, D. R. M. Vatvani, *J. Chem. Inf. Model.*, 2019, **59**, 4778.
- [9] A. P. Voronin, A. O. Surov, A. V. Churakov, O. D. Parashchuk, A. A. Rykounov, M. V. Vener, *Molecules*, 2020, **25**, 2386.
- [10] Y. Kim, K. Machida, T. Taga, K. Osaki, *Chem. Pharm. Bull.*, 1985, **33**, 2641.
- [11] T. Aree, H.-B. Bürgi, S. C. Capelli, *J. Phys. Chem. A*, 2012, **116**, 8092.
- [12] N. A. Tumanov, E. V. Boldyreva, H. Ahsbahs, *Powder Diffr.*, 2008, **23**, 307.
- [13] K. Ishikawa, M. Tanaka, T. Suzuki, A. Sekine, T. Kawasaki, K. Soai, M. Shiro, M. Lahav, T. Asahi, *ChemComm*, 2012, **48**, 6031.
- [14] R. Feld, M. S. Lehmann, *Z. Kristallogr. Cryst. Mater.*, 1981, **157**, 215.
- [15] J. Oddershede, S. Larsen, *J. Phys. Chem. A*, 2004, **108**, 1057.
- [16] T. Zhou, F. Li, Y. Fan, W. Song, X. Mu, H. Zhang, Y. Wang, *ChemComm*, 2009, **22**, 3199.
- [17] F. Yang, C.-X. Yan, X. Yang, D.-G. Zhou, P.-P. Zhou, *CrystEngComm*, 2017, **19**, 1762.
- [18] T. Li, S. Feng, *Pharm. Res.*, 2006, **23**, 2326.
- [19] H. K. Buchholz, M. Stein, *J. Comput. Chem.*, 2018, **39**, 1335.
- [20] N. F. Xavier, A. M. da Silva, G. F. Bauerfeldt, *Cryst. Growth Des.*, 2020, **20**, 4695.

3.4 Maleic Acid as a Co-former for Pharmaceutically Active GABA Derivatives: Mechanochemistry or Solvent Crystallization?



Article

Maleic Acid as a Co-former for Pharmaceutically Active GABA Derivatives: Mechanochemistry or Solvent Crystallization?

Daniel Komisarek ¹, Ebru Taskiran ¹ and Vera Vasylyeva ^{1,*}

Komisarek, D.; Taskiran, E.; Vasylyeva, V. Maleic Acid as a Co-former for Pharmaceutically Active GABA Derivatives: Mechanochemistry or Solvent Crystallization?, Submitted to *Materials*, **Jan. 2023**

No DOI yet available.

As per the *MDPI Open Access Information and Policy*, no special permission is required to reuse all or part of article published by MDPI, including figures and tables.

The fourth paper deals with the crystallization of GABA and all its derivatives studied with maleic acid. It was found that all these substances are capable of forming a maleate salt. Nevertheless, the physicochemical properties of the obtained salts vary greatly, and their supramolecular structure is also not uniform. Furthermore, it was compared whether a solvent crystallization route or a mechanochemical crystallization should be preferred to receive the described maleates. The work shows that similarities in crystallization behaviour of related substances often remain superficial, but for single cases, improvements in desired physicochemical properties are possible. Additionally, it is shown that it can be beneficial to investigate which specific crystal synthesis route to use best, as in some cases a better product quality is attainable mechanochemically and in some cases through the solution crystallization.

Contributions-list:

- Conceptualization of this work based on literature research and feedback from Dr. Vera Vasylyeva-Shor.
- Experimental work, including single crystal synthesis, mechanochemical and solvent-based crystallization of the investigated compounds together with Ebru Taskiran.
- Measurement of SCXRD and PXRD, FT-IR spectroscopy, DSC, and ¹H-NMR solubilities.
- Data evaluation of the recorded analyses.
- Manuscript preparation, including text writing, figure and table preparation, literature research and providing the supporting information.
- Revision process of the manuscript together with Dr. Vera Vasylyeva-Shor.

Article

Maleic Acid as a Co-former for Pharmaceutically Active GABA Derivatives: Mechanochemistry or Solvent Crystallization?

Daniel Komisarek ¹, Ebru Taskiran ¹ and Vera Vasylyeva ^{1,*}¹ Heinrich-Heine-University; Inorganic and Structural Chemistry I

Daniel.Komisarek@hhu.de, Ebru.Taskiran@hhu.de

* Correspondence: Vera.Vasylyeva-Shor@hhu.de

Abstract: In this work we compare mechanochemical and classical solvent crystallization for maleates of GABA and its pharmaceutically active derivatives Pregabalin, Gabapentin, Phenibut and Baclofen. Maleate salt formation is a common and effective tool to increase solubilities of active pharmaceutical ingredients. Structural analysis in the form of single crystal and powder x-ray diffraction is used in conjunction with IR-spectroscopy to identify structural peculiarities of grinding and solvent evaporation products. Thermal properties are investigated by differential scanning calorimetry and in selected cases thermogravimetric analysis. Furthermore, solubilities in aqueous medium for all compounds and their maleates are determined via ¹H-NMR spectroscopy. Our work shows that the crystal synthesis route can potentially have manifold effects. Next to more obvious results such as obtaining of different crystal modifications, the sample condition can be affected impactfully, which in turn influences thermodynamic properties in a nonnegligible manner.

Keywords: Solubility; Crystal Engineering; Mechanochemistry; Crystal Synthesis

1. Introduction

Solubility increase, and therefore improved bioavailability, for active pharmaceutical ingredients (APIs) remains a core objective in medicinal science. Manifold methods addressing this concern have been established, including use of prodrugs,[1–5] nanosuspensions,[6–9] or complexation of an API.[10–14] Modification of the solid API phase itself is another common approach. Formation of API salts, co-crystals, or amorphous systems may enhance the targeted drug solubility properties.[15–25] Product solubility is influenced by various thermodynamic and kinetic factors such as solubilities of the co-formers, solvent environment, and molecular characteristics like polarization or ionization.[17,26,27] Furthermore, when producing salts or co-crystals for pharmaceutical applications the counterion or co-former should not show any unwanted or damaging properties. The list of Generally Recognized As Safe (GRAS) compounds offers a variety of U.S. Food and Drug Administration (FDA) approved substances which can be added to API formulations without need of additional risk assessments.[28] Maleic acid is a simple dicarboxylic acid, a GRAS-list member and a popular choice in salt or co-crystal formation.[29–33] As a dicarboxylic acid maleic acid shows a pK_{a1} value of 1.74 and a pK_{a2} value of 5.81.[34] This makes maleic acid relatively reliable to form maleate salts instead of co-crystalline compounds, as larger ΔpK_a values between maleic acid and possible co-formers shift products in the salt direction on the *salt-cocrystal continuum*.[35] Such predictability is beneficial in the pharmaceutical field. Because of its afore mentioned qualities in conjunction with its low-cost maleic acid, among many other uses, has been applied to form maleates of APIs derived from γ-amino butanoic acid (GABA). GABA is a small non-essential amino acid that plays a role in regulation of sleep, pain and stress impulses in various life forms.[36–40] APIs derived from GABA include for example Gabapentin,

Citation: To be added by editorial staff during production.

Academic Editor: Firstname Last-name

Received: date

Revised: date

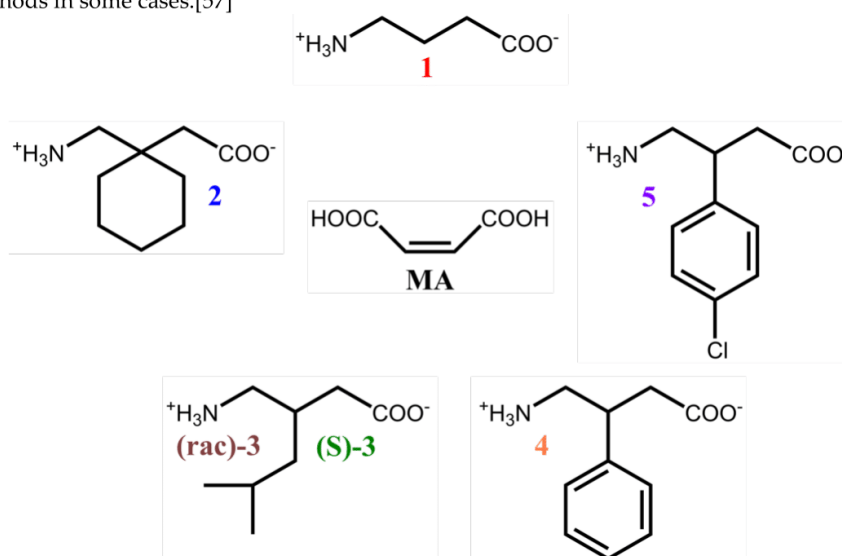
Accepted: date

Published: date



Copyright: © 2023 by the authors. Submitted for possible open access publication under the terms and conditions of the Creative Commons Attribution (CC BY) license (<https://creativecommons.org/licenses/by/4.0/>).

Pregabalin, Baclofen and Phenibut. Gabapentin and Pregabalin are mainly used for treatment of epilepsy, neuropathic pain and anxiolytic effects.[41–43] Baclofen is a muscle relaxant with potential in treatments of different addictions,[44–46] and Phenibut is a anti-convulsant with mood elevating effects.[47–49] Peterson et al. have patented a maleate of Gabapentin received through grinding methods evidenced via powder x-ray diffraction (PXRD) and differential scanning calorimetry (DSC) in 2004.[50] For (S)-Pregabalin, Salaman et al. have described single crystal x-ray structures (SCXRD) of a maleate hydrate and an anhydrous form.[51] Additionally, Gendron et al. and Báthori et al. have described maleates of enantiopure and racemic Baclofen respectively.[52,53] These past works highlight the promising prospect of forming maleates of other related substances as well. GABA, Gabapentin, Pregabalin, Baclofen and Phenibut share similar pKa values around 4 regarding their acid function. [5,52,54–56] According to Childs et al. they should likely form salt like entities with maleic acid by the ΔpK_a values between these substances, which is confirmed through the maleate systems described in the literature.[35,50–53] This establishes maleic acid as a promising candidate for the reliable salt production with pharmaceutically active GABA derivatives, which sets it apart from other GRAS-List co-formers such as tartaric or malic acid. These commonly used dicarboxylic acids have been shown to have a tendency to produce unreliable phase mixtures in the past with Baclofen and Phenibut and the latter tends to form viscous residues with Pregabalin.[56,57] Other important factors in crystal phase production in addition to predictability are time and waste reduction. Classically, salts or other crystalline modifications would be gained through solvent-based methods. Mechanochemistry offers a quick crystallization process and requires no or minimal solvent wastes.[58–60] However, mechanochemically prepared systems may show higher amorphicity, more crystalline defects or morphology changes, which could all affect product properties.[61–63] Similar observations could be conducted by our group for Baclofen and Phenibut, where different thermal properties were detected for multicomponent forms received by grinding or through solvent-based methods in some cases.[57]



Scheme 1. Investigated compounds maleic acid (MA), GABA (1), Gabapentin (2), Pregabalin (3), Phenibut (4) and Baclofen (5).

In the course of the present work, salts of maleic acid (MA) with GABA (1), Gabapentin (2), Pregabalin (3), Phenibut (4) or Baclofen (5) were produced with the goal of improving API solubility. Novel phases were received for a GABA maleate (1-MA), a Gabapentin maleate hydrate (2-MA \cdot H₂O), two (rac)-Pregabalin maleates ((rac)-3-MA-I and

(*rac*)-3-MA-II) as well as a Phenibut maleate (4-MA) and known phases could be reproduced. It was further investigated whether the received maleates could be obtained through grinding as well as by solvent-based methods. The obtained substances were characterized by powder- and single crystal x-ray diffraction (PXRD and SCXRD) as well as Fourier transformed infrared spectroscopy (FTIR). Their thermal properties were investigated via differential scanning calorimetry (DSC) and thermogravimetric analysis (TGA) in selected cases. Solubilities in aqueous medium at 25 °C were determined through proton magnetic resonance spectroscopy (¹H-NMR) for saturated solutions after three days. Solubilities and thermal properties of maleates from their solution crystallization were compared to those gained through the mechanochemical approach. Our work highlights how maleic acid serves as an excellent co-former for simple production of API salts for the investigated compounds. Furthermore, we discuss what pro and contra points might speak for or against the mechanochemical versus solvent-based production of these substances.

2. Materials and Methods

Chemicals: Maleic acid was purchased from TCI, GABA from J&K scientific, Gabapentin and (*rac*)-Pregabalin from abcr, Phenibut from BLDpharm and Baclofen from Flurochem. (*S*)-Pregabalin was synthesized from (*rac*)-Pregabalin hydrate according to our previously reported approach.[56]

Maleate Preparation: All systems 1-MA – 5-MA were prepared by mixing of equimolar ratios of maleic acid and APIs. Solution products were grown from aqueous solution by slow evaporation of the solvent at ambient temperature. Grinding products were produced in a Retsch MM400 ball mill with 10 mL stainless steel vessels and two ZrO₂ balls (diameter: 1 cm) via neat grinding (for (*S*)-3-MA • H₂O liquid-assisted grinding with 54 µL water) at 25 Hz for 30 min. 1-MA was produced using 5 mmol of either substance; 2-MA, 2-MA • H₂O, (*rac*)-3-MA-I, (*rac*)-3-MA-II and 4-MA using 4 mmol of either substance; (*S*)-3-MA • H₂O and 5-MA using 3mmol of either substance. Attempts at producing 2-MA • H₂O by liquid-assisted grinding similar to (*S*)-3-MA • H₂O and producing 2-MA from solution were unsuccessful. It was not possible to successfully separate (*rac*)-3-MA-I and (*rac*)-3-MA-II under the investigated experimental conditions.

PXRD: Powder patterns were recorded on a Rigaku Miniflex 300 powder diffractometer with a Cu-Source and K α radiation at 1.54184 Å in $\Theta/2\Theta$ -geometry. Measurements were conducted at ambient temperature in a range of 5 – 50° 2 Θ .

SCXRD: Crystals suitable for single crystal diffraction were selected under a polarized-light microscope, covered in protective oil, and mounted on a cryo-loop. The single crystal diffraction data were recorded on a Rigaku XtaLAB Synergy S diffractometer with Hybrid Pixel Arrow detector and a PhotonJet X-ray source using Cu-K α radiation ($\lambda = 1.54182 \text{ \AA}$) at 100.0 ± 0.1 K with ω -scans. Plate-shaped colourless crystals were selected for measurement: 1-MA (0.2 • 0.19 • 0.05 mm), 2-MA • H₂O (0.38 • 0.33 • 0.07 mm), (*rac*)-3-MA-I (0.22 • 0.11 • 0.02 mm), (*S*)-3-MA • H₂O (0.52 • 0.1 • 0.06 mm), 4-MA (0.21 • 0.17 • 0.08 mm) and 5-MA (0.21 • 0.11 • 0.06 mm). Data reduction and absorption correction were conducted via CrysAlisPRO v. 42 software, with numerical absorption correction based on gaussian integration over a multifaceted crystal model and empirical absorption correction using spherical harmonics, implemented in SCALE3 ABSPACK scaling algorithm.[64] Structure analysis was performed by direct methods (SHELXT-2015), full-

matrix least-squares refinements on F2 were done using the SHELXL2017/1 program package, and structure solution and refinements were done using Olex2-1.5 software.[65–67] Hydrogen atoms were freely refined except for C-H hydrogens with the following atomic displacement parameter: $U_{\text{iso}}(\text{H}_{\text{CH}})=1.2 U_{\text{eq}}$. Figures were prepared with Mercury software v. 2022.3.0.[68] The crystallographic data for the structures were deposited in the Cambridge Crystallographic Data Centre (CCDC-numbers 2221363- 2221368) and can be obtained free of charge via www.ccdc.cam.ac.uk/data_request/cif.

FT-IR: Infrared spectra were recorded on a Bruker Tensor 27 Fourier transformed IR spectrometer using attenuated total reflectance mode in the range 4000 cm^{-1} to 400 cm^{-1} . Samples grown from solution were measured after evaporation of the solvent and subsequent drying at ambient temperature over two weeks, for (S)-3-MA • H₂O and (rac)-3-MA forms several spectra were recorded at earlier and later points in time.

Thermal properties: Differential scanning calorimetry was performed on a NETZSCH DSC 204F1 Phoenix device in pierced alumina crucibles at heating rates of 5 Kmin^{-1} . Temperature calibration was applied and a reference crucible with a mass of 34.728 mg were used. Crucible and sample masses were recorded, and calculation of peak enthalpies was conducted through NETZSCH Proteus software based on measured DSC curves. Measurements of DSC samples were performed from samples that were dried at ambient conditions for two weeks after removal from the mother liquid. Thermogravimetric analysis was performed for samples (S)-3-MA • H₂O and (rac)-3-MA on a Netzsch TG 209 F3 Tarsus with 10 Kmin^{-1} in a temperature range from $30 \text{ }^{\circ}\text{C}$ – $350 \text{ }^{\circ}\text{C}$.

Solubilities: Determination of substance solubilities was performed through ¹H-NMR spectroscopy with a Bruker Avance III NMR-spectrometer at 600 MHz. Saturated solutions of crystalline material were placed in an incubator at $25 \text{ }^{\circ}\text{C}$ and moved with 60 min^{-1} . Three samples of each investigated substance were left for three days at these conditions. Subsequently, 50 μL of solution were removed from the samples and added to 450 μL of D₂O for ¹H-NMR measurements. Solubility was determined by ratio of integrated solvent to substance peak. Solubility values are presented as averages over the recorded samples with the error margin according to their standard deviation.

3. Results

3.1 Structural Properties

Maleates of GABA and its pharmaceutically active derivatives (**Scheme 1**) were produced by crystallization through evaporation of the solvent from aqueous solution as well as neat- or liquid-assisted grinding. Single crystals could be received by solvent evaporation for most systems. The exceptions are a presumedly anhydrous form of 2-MA, which was only obtainable through neat grinding, and (rac)-3-MA-II which occurs concomitant with (rac)-3-MA-I, disregarding of the crystallization method. Furthermore, in case of 3 crystallization of the enantiomerically pure (S)-form leads to different results than using the racemate. A phase pure maleate hydrate can be obtained by mechanochemical as well as solvent-based synthesis. For the mechanochemical route, liquid-assisted grinding must be performed to receive the product as otherwise crystal synthesis of a new phase fails.

Crystal structures of the various obtained **MA** salts differ in some respects. For example, there are simple rows of molecules present in **1-MA** and **4-MA** (**Figure 1**). These follow the pattern A-B-A-B in the former, while A-B-B-A rows are formed in the latter. Hydrogen bonds (HBs) are the main attractive interaction, but in **4-MA** edge-to-face π -interactions connect phenyl subunits. In **2-MA** • **H₂O** and (*rac*)-**3-MA-I**, pairs of **MA** molecules are surrounded by API molecules, and for **2-MA** • **H₂O** specifically, there are additional water molecules which connect the **MA** pairs via HBs (**Figure 2**). For (*S*)-**3-MA** • **H₂O** and **5-MA** the motif is more complex (**Figure 3**). (*S*)-**3-MA** • **H₂O** breaks the encirclement of maleic acid pairs through the introduction of water in its lattice. Water entities and half of the **MA** molecules form a straight row, thus pushing apart the (*S*)-**3** molecules that surround **MA** pairs in (*rac*)-**3-MA-I**. In (*S*)-**3-MA** • **H₂O** dimers of Pregabalinium cations are formed via carboxyl/carboxyl HBs, while in (*rac*)-**3-MA-I** similar dimers are formed which are connected along their GABA-subunits through carboxyl/ammonium HBs. Exclusive interaction behaviour can also be observed in **5-MA**. The packing could either be interpreted as shifting rows of **5** and **MA** molecules or cavities of Baclofenium cations that are filled with **MA** entities.

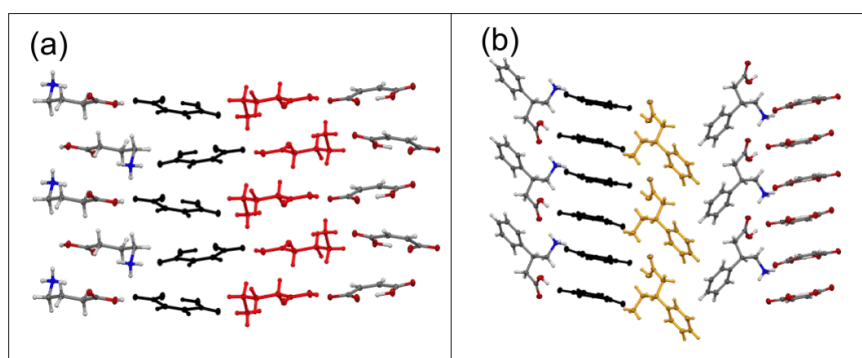


Figure 1. Packing in (a) **1-MA**, view along *a*-axis and (b) **4-MA** view along *b*-axis. Rows are highlighted according to the chosen colour-scheme; oxygen atoms are depicted in red, nitrogen atoms in blue, carbon atoms in grey and hydrogen atoms in white.

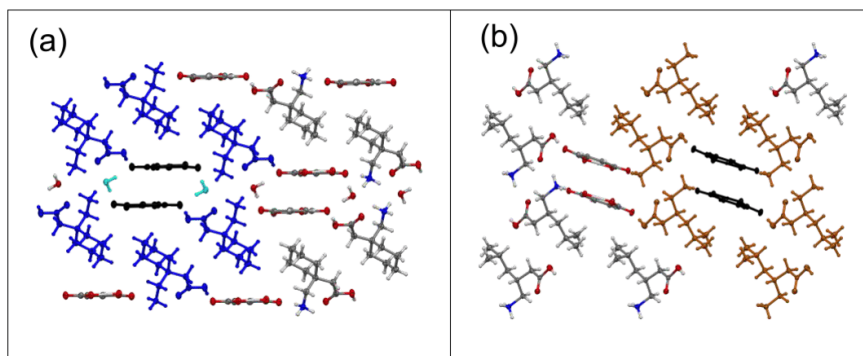


Figure 2. Packing in (a) $2\text{-MA} \cdot \text{H}_2\text{O}$, view along c -axis and (b) $(rac)\text{-3-MA}$ view along b -axis. Motifs are highlighted according to the chosen colour-scheme; oxygen atoms are depicted in red, nitrogen atoms in white, carbon atoms in grey and hydrogen atoms in white.

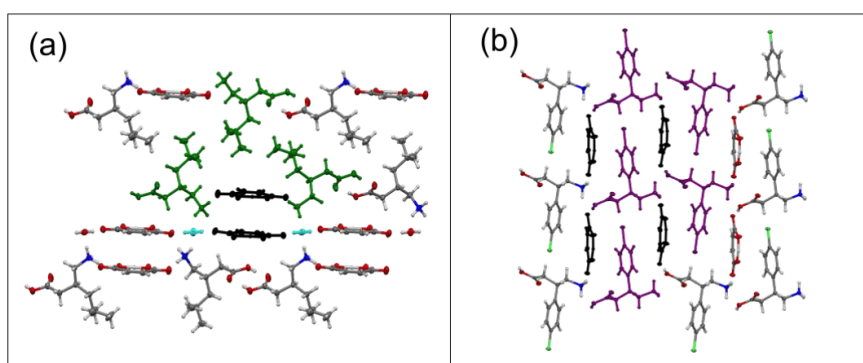


Figure 3. Packing in (a) $(S)\text{-3-MA} \cdot \text{H}_2\text{O}$, view along c -axis and (b) 5-MA view along c -axis. Motifs are highlighted according to the chosen colour-scheme; oxygen atoms are depicted in red, nitrogen atoms in white, carbon atoms in grey and hydrogen atoms in white.

Using either the mechanochemical or the solvent crystallization route can affect which product is formed, the sample condition and properties or the degree of crystallinity of the sample. For **1-MA**, $(S)\text{-3-MA} \cdot \text{H}_2\text{O}$, **4-MA**, and **5-MA** the same system is received by both synthesis routes (see supporting information for **1-MA**, **4-MA** and **5-MA**). Different phases are obtained for **2** and $(rac)\text{-3}$ based maleates. When crystallized from water $2\text{-MA} \cdot \text{H}_2\text{O}$ will form, while mechanochemical synthesis leads to the presumably anhydrous **2-MA** (**Figure 4**). Attempts of liquid-assisted grinding crystallization that work for $(S)\text{-3-MA} \cdot \text{H}_2\text{O}$ are unsuccessful for $2\text{-MA} \cdot \text{H}_2\text{O}$ and lead to phase mixtures. In case of $(rac)\text{-3}$ the distinction of the phases is not as simple as in 2-MA systems. Crystallization via both means leads to a phase mixture, as neither diffraction pattern can be clearly assigned to simulated diffraction data from single crystal analysis (**Figure 5**).

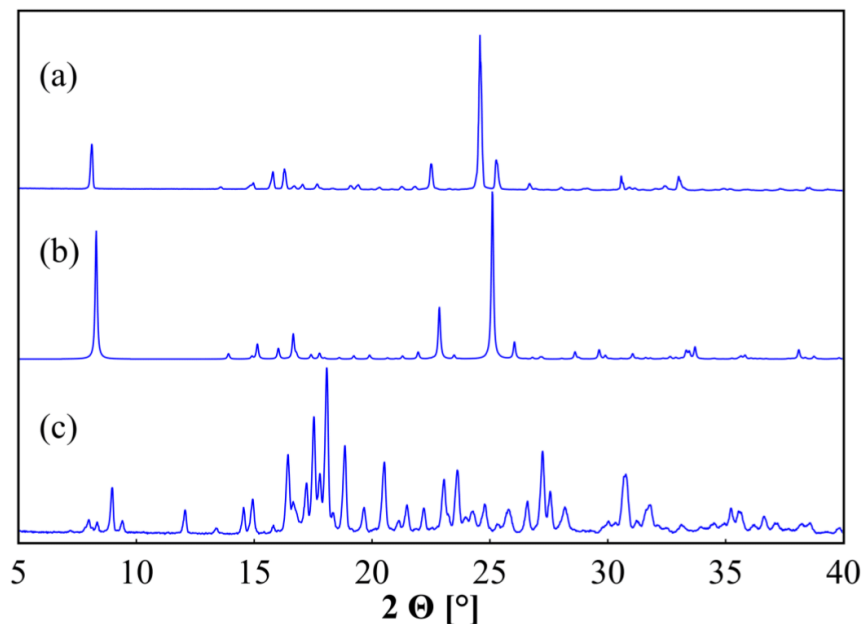


Figure 4. Powder patterns of 2 based maleates. Sample of 2-MA • H₂O obtained by solution crystallization (a), simulated pattern based on single crystal data (b), and sample of 2-MA obtained by mechanochemical crystal synthesis (c). Powder patterns were recorded in a range of 5° – 40° 2 Θ .

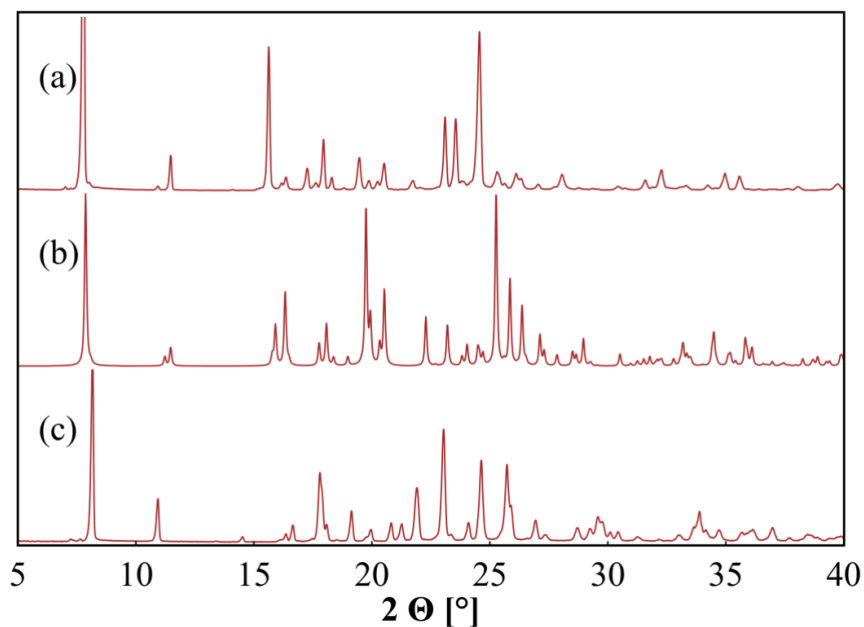


Figure 5. Powder patterns of (rac)-3 based maleates. Sample of (rac)-3-MA obtained by solution crystallization, larger amount of form I (a), simulated pattern of (rac)-3-MA-I based on single crystal data (b), and sample of (rac)-3-MA obtained by mechanochemical crystal synthesis, larger amount of form II (c). Powder patterns were recorded in a range of 5° – 40° 2 Θ .

Contrary to the 2-MA systems the (*rac*)-3-MA forms undergo a phase transition over time. Interestingly, the simulated powder pattern of (*rac*)-3-MA-I fits better with the more commonly obtained but apparently less stable form. During the conducted experiments it was unreliable whether a larger degree of (*rac*)-3-MA-I or (*rac*)-3-MA-II was formed in the samples. Each system was prepared thrice through solvent evaporation and mechanochemically, but only once for a mechanochemical synthesis a larger part of (*rac*)-3-MA-II was formed. Given enough time (*rac*)-3-MA-I converts to (*rac*)-3-MA-II (see supporting information). As such it seems unlikely that (*rac*)-3-MA-II is a hydrate like 2-MA • H₂O or (S)-3-MA • H₂O, and a true polymorphic conversion occurs. While the same phase is received reliably by both crystal synthesis routes, for (S)-3-MA • H₂O their influence on the sample condition is strong. Mechanochemical production with liquid-assisted grinding forms a powder of uniform quality. Crystallization through evaporation from solution is more difficult for this species. A mixture of pasty residue and brittle crystalline material is received that holds water residues for exceedingly long times (Figure 6). Even if solid (S)-3-MA • H₂O is removed from its mother liquid and left to dry at ambient conditions it does not become a uniformly dry substance after days or even weeks. The compound can be dried under vacuum and heating, but the temperature must not be too high because melting occurs at low temperatures, as will be elaborated on in the upcoming paragraphs. Additionally, powder patterns of mechanochemically produced samples show a higher degree of crystallinity by their signal resolution compared to those of samples received through solvent evaporation (Figure 7).

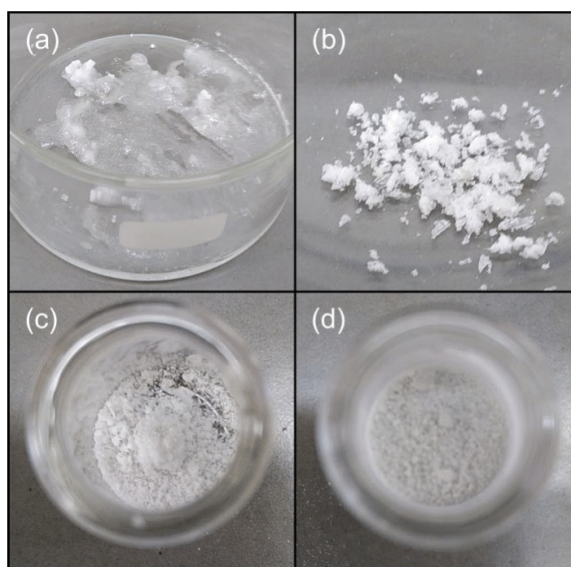


Figure 6. Comparison of 3 products received by solution and grinding crystallization: (S)-3-MA • H₂O three days of drying at ambient temperature after removal from mother liquid (a), and produced mechanochemically (c), (*rac*)-3-MA three days of drying at ambient temperature (b), and (*rac*)-3-MA after grinding (d).

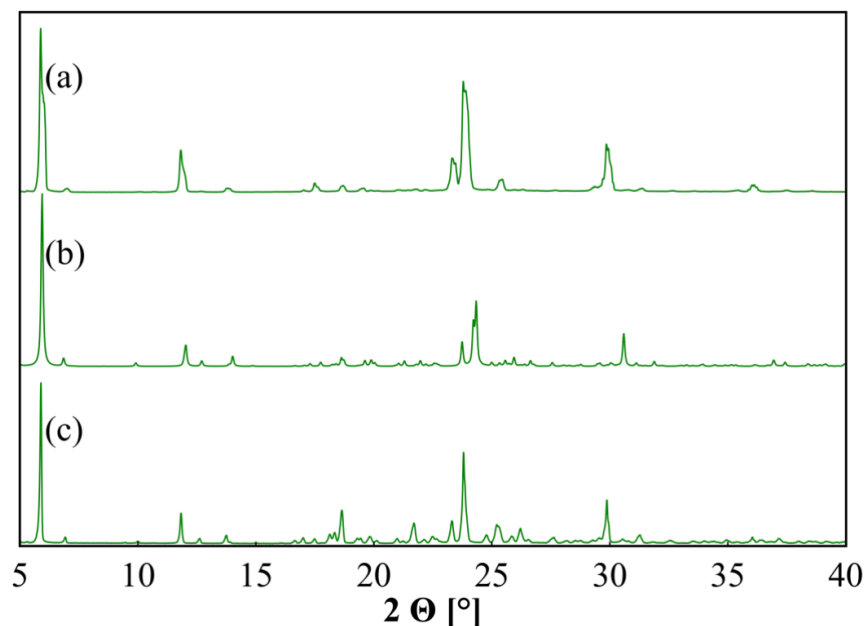


Figure 7. Powder patterns of (S)-3 based maleates. Sample of (S)-3-MA • H₂O obtained by solution crystallization (a), simulated pattern based on single crystal data (b), and sample of (S)-3-MA • H₂O obtained by mechanochemical crystal synthesis (c). Powder patterns were recorded in a range of 5° – 40° 2 Θ .

In case of 4-MA both synthesis routes lead to the same product. However, powder patterns received by mechanochemical and solution crystallization show bad signal resolutions and thus a low degree of crystallinity. Furthermore, even though the same phase is obtained through both means, not all Bragg-reflections can be attributed to the simulated pattern from single crystal data (Figure 8). These signals cannot be assigned to precursor material 4 or MA either. Thus, it appears that an additional crystallization product forms here which is not yet characterized by single crystal diffraction. Past works have shown that 4 tends to form non-pure phases more commonly, probably due to a comparatively high lattice energy that makes formation of a multicomponent phases unfavourable.[56,57]

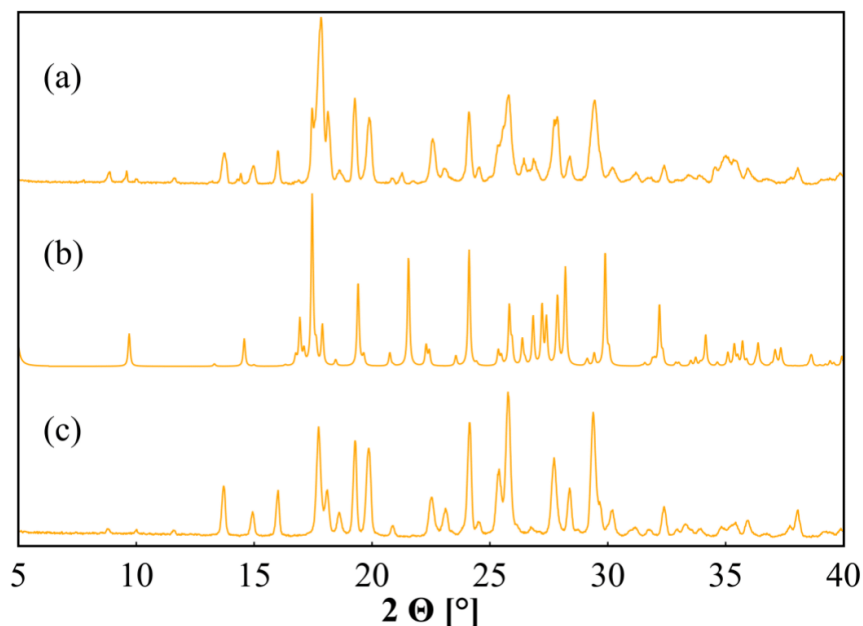


Figure 8. Powder patterns of 4 based maleates. Sample of 4-MA obtained by solution crystallization (a), simulated pattern based on single crystal data (b), and sample of 4-MA obtained by mechanochemical crystal synthesis (c). Powder patterns were recorded in a range of $5^{\circ} - 40^{\circ} 2\Theta$.

3.2. Thermodynamic Properties

Thermodynamic properties are mostly dependent on the received crystal phase, but the crystal synthesis route plays a role as well. What all systems have in common, is that they do not recrystallize upon cooling in a DSC. DSC-thermograms reveal differences in melting behaviour and in some cases indicate the presence of impurities that were not visible in PXRD and IR analyses (Figures 9 & 10, Table 1). For example, a DSC measurement of 2-MA reveals that next to the main signal with an onset of 96°C an additional badly resolved transition signal with an onset of 41°C exists. While this is lower than in 2-MA \cdot H₂O with its well-defined melting signal and an onset of 65°C , it is still probable that hydrate impurities exist in 2-MA. The peak positions of the small signal in 2-MA and the melting signal in 2-MA \cdot H₂O are closer to each other than onsets with 61°C and 68°C for anhydrous phase and hydrate respectively. It appears likely that adsorbed water from the milling vessels was sufficient to form the hydrate at least partially. For (rac)-3-MA species, the distinction is more difficult yet again. Both species (rac)-3-MA-I and (rac)-3-MA-II appear to always exist concomitantly regardless of the synthesis route, and both forms seem to have very closely related melting points. The onset for these products was determined at 98°C , but the signal width in the solvent sample with 7°C is nearly double that of the mechanochemical sample with 4°C . It is possible that the large peak width in the solvent sample covers an additional signal that would otherwise be visible due to the higher content of form I. This would then highlight how thermodynamically similar both forms are and that the difference in phase stability is minimal.

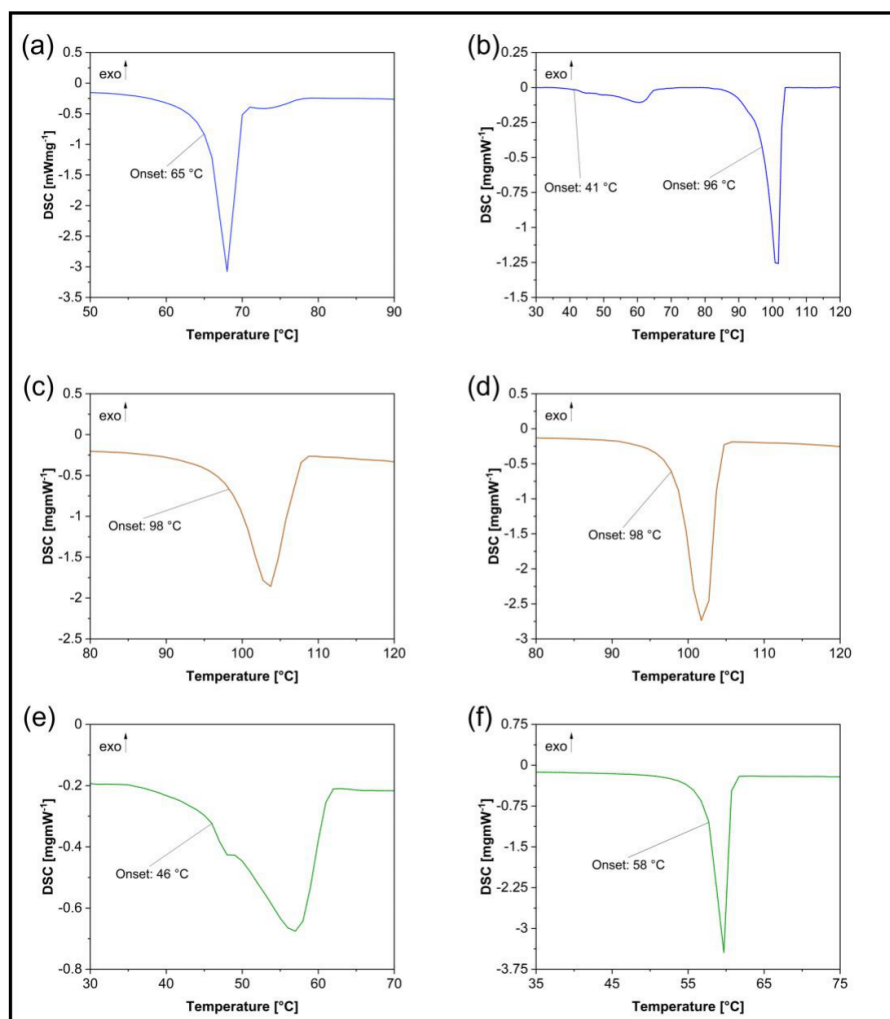


Figure 9. DSC-thermograms of selected MA systems: 2-MA • H₂O synthesized from solution (a), 2-MA obtained mechanochemically (b), (rac)-3-MA synthesized from solution (c), and mechanochemically (d), (S)-3-MA • H₂O synthesized from solution (e), and via grinding (f). For better visibility, only the relevant temperature range is depicted.

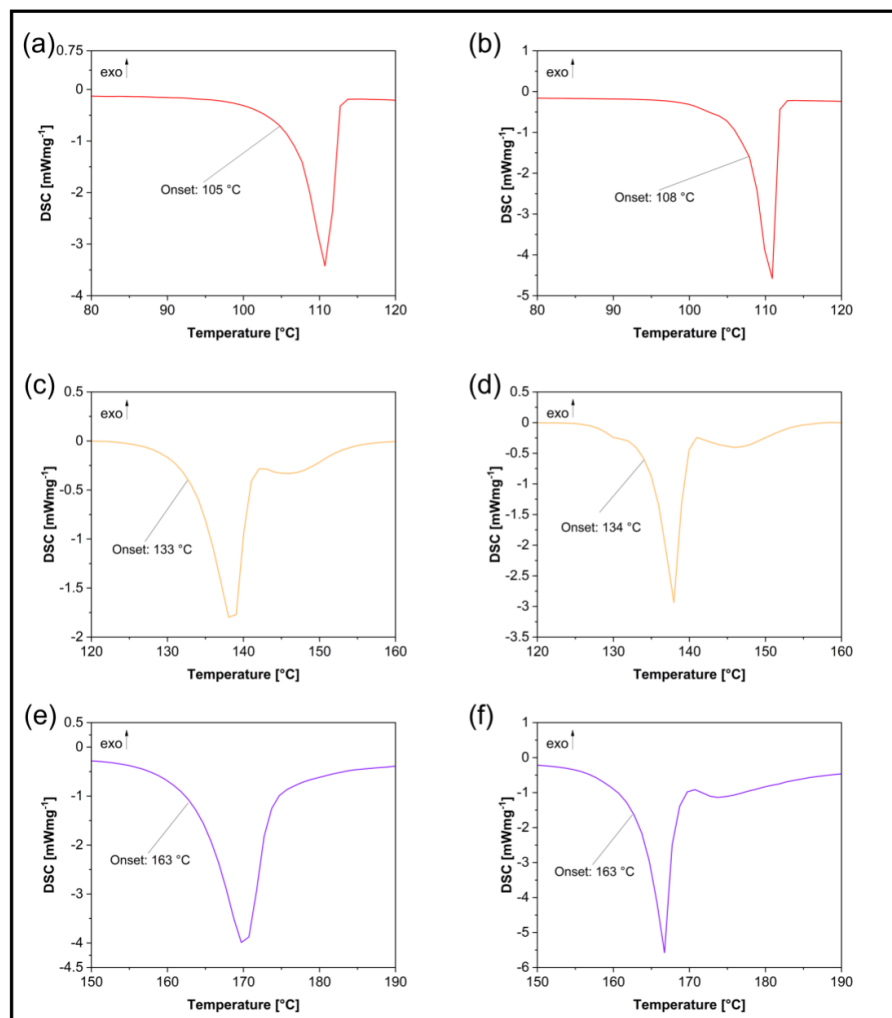


Figure 10. DSC-thermograms of MA systems showing similar thermal behaviour independent of the synthetic route: 1-MA synthesized from solution (a), and mechanochemically (b), 4-MA synthesized from solution (c), and via grinding (d), 5-MA synthesized from solution (e), and mechanochemically (f). For better visibility, only the relevant temperature range is depicted.

A much larger distinction regarding the melting signals is actually present in (S)-3-MA • H₂O entities. The DSC signal confirms the lower degree of crystallinity that was also indicated in powder patterns for the solvent sample. It is not as well resolved as the milling sample melting signal and the melting enthalpy is lowered by 34 Jg⁻¹ to a value of 53 Jg⁻¹ from 87 Jg⁻¹ in the mechanochemically prepared product. The onset with 46 °C for the solvent sample also occurs at lower temperatures than in the grinding one with 58 °C. This might be due to the higher water content still present in the sample even after prolonged drying for two weeks, after which no evidence of excess water was present in any other sample except for 3 forms (see supporting information). The early onset might indicate that dissolution in the residual water starts due to the increase in temperature.

Table 1. Overview on the recorded DSC parameters for all investigated samples. Temperature values have been rounded to full numbers.

Sample	Melting-Enthalpy [Jg ⁻¹]	Onset [°C]	End [°C]	Peak [°C]	Peak-Width [°C]	Peak-Height [mWmg ⁻¹]
1-MA	176	105	113	111	5	3.242
1-MA_M	178	108	112	111	3	4.673
2-MA • H ₂ O	135	65	70	68	3	2.864
2-MA_M (Peak 1)	14	41	65	61	16	0.095
2-MA_M (Peak 2)	85	96	103	101	5	1.345
(rac)-3-MA	125	98	107	104	7	1.619
(rac)-3-MA_M	132	98	104	102	4	2.610
(S)-3-MA • H ₂ O	53	46	61	57	13	0.454
(S)-3-MA • H ₂ O_M	87	58	61	60	2	3.439
4-MA	165	133	141	139	6	1.850
4-MA_M	181	134	139	138	4	2.945
5-MA	376	163	174	170	8	3.708
5-MA_M	362	163	168	167	4	5.252

TGA-analysis was performed for **3** based maleates (**Figure 11**). The thermal decomposition reveals a higher content of water with a mass loss of 7 % at 125 °C in **(S)-3-MA • H₂O** compared to the other **3** maleates that show losses of only 2 – 3 %. The compound can be dried forcefully at 40 °C in a vacuum atmosphere, low temperature has to be chosen due to the low melting point, thus the drying procedure takes a long time (see supporting information). The TGA-analysis further confirms that **(rac)-3-MA** forms **I** and **II** behave rather similar regarding their thermal properties. While the solvent sample starts to lose water at a lower temperature of 57 °C compared to 68 °C in the mechanochemical sample, the mass loss is only at 3 % and 2 % respectively. As the crystal structure of **(rac)-3-MA-I** could be determined and does not incorporate lattice water, this probably stems from adsorbed water. In the grinding sample, this water might be explained by lattice water of **(rac)-3 • H₂O**, with which it was prepared. The slightly higher water content in the solvent sample probably rather stems from excess water from solution. Thermal analyses of the less distinctive maleates reveal some significant characteristics as well. **1-MA** shows slightly different melting points for the different synthesis routes, with onsets of 105 °C and 108 °C for solution crystallization and grinding respectively. However, the peak positions are identical at 111 °C, and as there are no variations in powder patterns or IR-spectra, the most probable explanation is a more uniform dispersion of crystallite sizes in the mechanochemical sample, leading to a sharper melting signal. For **4-MA**, the presence of impurities is confirmed. Next to intense melting signals with onsets of 133 °C and 134 °C there are smaller signals in a very close range to the main one. Both samples show a small phase transition that partly overlaps with the large melting peak, starting at ca. 142 °C. In the mechanochemically prepared sample, an even smaller phase transition occurs at about 127 °C. As the melting signal in the solvent sample is again dispersed over a larger temperature area, it seems possible that it covers the smaller signal here. However, even though no pure phase

is obtainable of **4-MA** by either synthesis route, both means lead to the same, impure end. More surprising is the result for **5-MA**. Diffraction patterns and IR-spectra show no distinctive features regardless of the crystallization method, except for a worse Bragg reflection resolution for the grinding sample. Still, an additional phase transition after the main melting signal with an onset of 163 °C in both samples is visible in the grinding product at ca. 170 °C. It seems possible this signal is again covered in the solvent sample, as the signal peak area with 8 °C is double than that of the milling one with 4 °C.

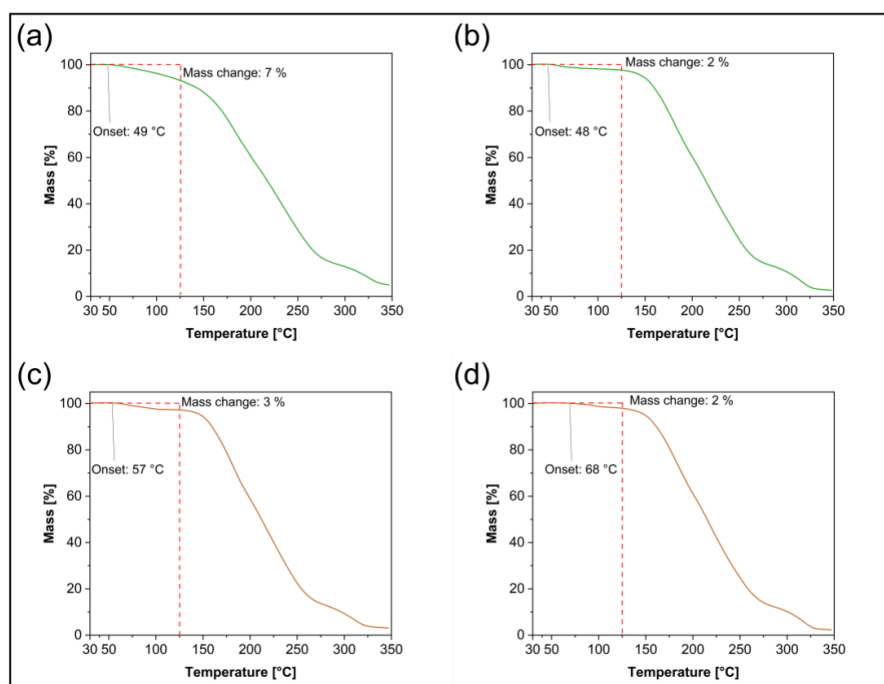


Figure 11. Thermogravimetric analyses of 3 based maleates, recorded after two weeks of drying at ambient conditions. A solvent sample (a) and a mechanochemically prepared sample (b) of (S)-3-MA • H₂O, a solvent sample (c) and a mechanochemically prepared sample (d) of (rac)-3-MA. Decomposition was recorded in a range of 30 °C – 350 °C. The red dotted line indicates the mass loss at 125 °C.

Solubility in aqueous medium determined for the different maleates shows that increases are always present, except for **1-MA** (Figure 12, Table 2). However, **1** alone is exceedingly well soluble in water with a determined solubility of $2261 \pm 23 \text{ gL}^{-1}$. On the other hand, the solubility of **MA** was measured as $687 \pm 44 \text{ gL}^{-1}$. Solubilities of multicomponent crystalline species mostly fall in between that of their co-formers, so it appears this is the probable explanation here. The largest discrepancies occur between different phases for **2** and (rac)-**3** based systems and for (S)-**3** milling and solution crystallization forms. The solubilities of **2-MA • H₂O** and **2-MA** only differ slightly, and they are just outside of each other's error margin with $241 \pm 8 \text{ gL}^{-1}$ and $218 \pm 8 \text{ gL}^{-1}$ respectively. The difference is even higher between (rac)-**3-MA** obtained from solution and by grinding with $719 \pm 10 \text{ gL}^{-1}$ for a sample that contains a larger degree of form **I** and $556 \pm 19 \text{ gL}^{-1}$ for a sample that contains more of form **II**. These values show that both forms increase the content of (rac)-**3** in solution

substantially, but they are influenced by each other's presence and thus it is difficult to say whether form **I** could be even more soluble and form **II** maybe slightly less. The largest influence of the crystal synthesis route on a system that exhibits the same diffraction pattern is present for **(S)-3-MA • H₂O**. The solubility of the solvent product with $977 \pm 79 \text{ gL}^{-1}$ is definitely higher than that of the grinding product with $809 \pm 8 \text{ gL}^{-1}$. As was shown, this can be explained by the sample condition. The solvent product shows a higher degree of amorphicity and contains a higher amount of water from the start. This might ease the hydration of **(S)-3** molecules and thereby increase the dissolution speed compared to mechanochemically produced **(S)-3-MA • H₂O**. All solubilities were determined from three samples stored for three days at 25 °C under slight shaking. However, subsequent observation of the samples showed that **(S)-3-MA • H₂O** samples dissolve even further after longer time. Addition of more solid material led to it dissolving even further. The result is a strongly viscous goo. This observation highlights how viscid residue formation makes it so difficult to obtain a uniform product of **(S)-3-MA • H₂O** from solution. For substances **4-MA** and **5-MA** uniform increases in solubility occur. For the former, this shows that the same phase mixture is received via mechanochemical as well as solvent evaporation crystallization. For the latter, the increase in both cases is high regarding percentage with 100 % each but considering total numbers the solubility is still very low with 6 gL^{-1} . Still, similarly to **1** based forms, the crystallization route for maleate production does not influence the product properties of **4-MA** and **5-MA** meaningfully.

Table 2. Solubility values, error margins and de- or increases of API solubilities in the investigated maleates.

Sample	Solubility [gL^{-1}]	Error [%]	Error [gL^{-1}]
MA	687	6	44
1	2261	1	23
2	174	4	7
<i>(rac)</i> -3 • H ₂ O	33	4	1.3
<i>(S)</i> -3	41	2	0.7
4	15	2	0.3
5	3	3	0.1
1-MA	704	8	60
1-MA_M	680	7	46
2-MA • H ₂ O	241	3	8
2-MA_M	218	4	8
<i>(rac)</i> -3-MA	719	1.4	10
<i>(rac)</i> -3-MA_M	556	3	19
<i>(S)</i> -3-MA • H ₂ O	977	8	79
<i>(S)</i> -3-MA • H ₂ O_M	809	1	8
4-MA	124	3	4
4-MA_M	128	6	8
5-MA	6	4	0.3
5-MA_M	6	10	0.6

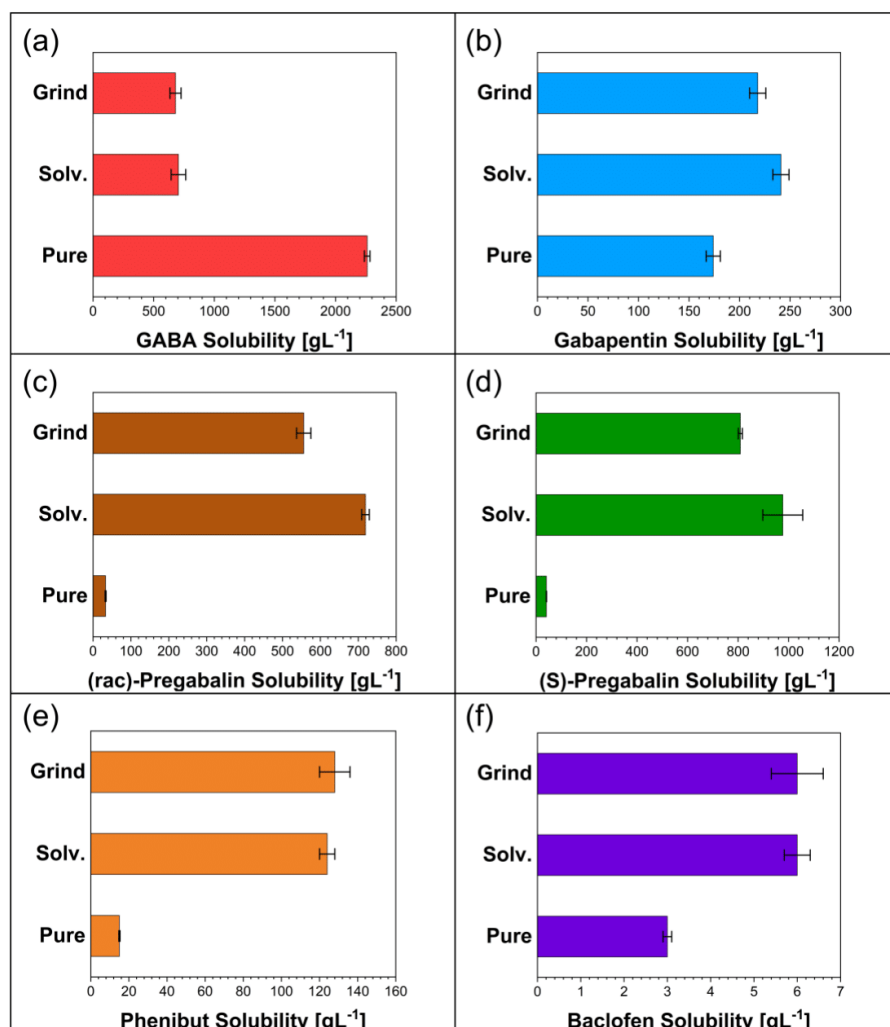


Figure 12. Recorded solubilities of the investigated samples in gL⁻¹ regarding their API solubility of (a) 1, (b) 2, (c) (rac)-3, (d), (S)-3, (e) 4, and (f) 5 based compounds. Solubilities were determined by preparation of saturated dispersions of target compounds in aqueous solution at 25 °C after three days through ¹H-NMR spectroscopy against the water signal.

4. Discussion

The results of this work can be summarized into two key aspects. This first one is that maleic acid can serve as an excellent co-former for GABA related APIs. In many cases there are multiple phases obtainable, sometimes dependant and sometimes independent of the synthesis route. Furthermore, these maleates do not require a high effort to produce, and maleate formation can increase the solubility of the different APIs substantially. The second and arguably more valuable point that can be made is that it is worthwhile to investigate different synthesis routes for various API maleates. It was shown that the synthesis route affects certain properties for 2 and 3 based systems. For 1 and 5 maleates, the synthesis method does not matter, and a similarly good result is obtainable for either way.

In case of **4-MA** a pure, single-phase maleate cannot be obtained regardless of whether mechanochemical or classical solvent crystallization is used. The most interesting effects are certainly present for **2-MA • H₂O** and **2-MA**, (*rac*)-**3-MA-I** and (*rac*)-**3-MA-II**, as well as (*S*)-**3-MA • H₂O**. The 2 maleates are an example where mechanochemically an anhydrous salt is formed, while the solvent route leads to a salt hydrate. However, both systems are easily distinguishable, and we could not find evidence for phase transitioning or decomposition over time in them. Solubility experiments showed that both increase the solubility of **2** in a similar manner. Forms **I** and **II** of (*rac*)-**3-MA** are a more difficult case. In the conducted experiments it was not possible to obtain a completely pure entity of either modification. While it appears that **I**, given enough time, undergoes a phase transition to **II** a full conversion could not be observed. The mechanochemical route can seemingly lead to (*rac*)-**3-MA-I** with greater likelihood, but this could only be achieved once out of three grinding samples and the cause for this is unclear. Here, a completely different route should be established to reliably obtain the observed polymorphs. The highest impact of the synthesis route is maybe present in case of (*S*)-**3-MA • H₂O**. Contrary to its (*rac*)-**3** based counterpart the same phase is always observable by diffraction and IR analyses of grinding and solvent evaporation products. Still, large discrepancies were recorded concerning their thermodynamic properties. The mechanochemical product is a powder, melts higher and with a sharper melting signal but the maximum solubility of the product is lower. The solvent product is of a moist and pasty consistency, melts lower and irregularly, but shows higher overall solubility after the same time frame compared to the grinding sample. Even if maximum solubility is higher in the solution form there is a clear advantage of the milling route in this case. The processability of the milling product is much better and why should time and energy be spent on drying pasty solvent grown (*S*)-**3-MA • H₂O** when it could be produced mechanochemically instantly and in a uniform condition? Both solubilities are very high compared to pure (*S*)-**3** regardless. The choice of the crystal synthesis route can affect the received product quite impactfully and should be reconsidered for each new product.

Supplementary Materials: The following supporting information can be downloaded at: www.mdpi.com/xxx/s1, Figure S1: Powder pattern comparison of (a) recorded GABA pattern, (b) GABA maleate as produced from aqueous solution, (c) GABA maleate pattern simulated by single crystal data, (d) GABA maleate as produced by neat grinding, and (e) recorded maleic acid pattern. A 2θ range from $5 - 40^\circ$ is depicted.; Figure S2: FT-IR spectra of (a) GABA, (b) GABA maleate as produced from aqueous solution, (c) GABA maleate as produced by neat grinding and (d) maleic acid. Spectra are recorded between $4000 \text{ cm}^{-1} - 400 \text{ cm}^{-1}$.; Figure S3: Powder pattern comparison of (a) recorded Gabapentin pattern, (b) Gabapentin maleate hydrate as produced from aqueous solution, (c) Gabapentin maleate hydrate pattern simulated by single crystal data with $hkl = 0\ 4\ 0$ and March-Dollase parameter of 0.5, (d) Gabapentin maleate as produced by neat-grinding, and (e) recorded Gabapentin pattern. A 2θ range from $5 - 40^\circ$ is depicted.; Figure S4: Powder pattern comparison of (a) recorded Gabapentin pattern, (b) Gabapentin maleate as produced by neat grinding, (c) Gabapentin maleate hydrate and maleate mixture as produced by liquid-assisted grinding, (d) Gabapentin maleate hydrate as produced from aqueous solution and (e) recorded maleic acid pattern. A 2θ range from $5 - 40^\circ$ is depicted.; Figure S5: FT-IR spectra of (a) Gabapentin, (b) Gabapentin maleate hydrate as produced from aqueous solution, (c) Gabapentin maleate as produced by neat grinding and (d) maleic acid. Spectra are recorded between $4000 \text{ cm}^{-1} - 400 \text{ cm}^{-1}$.; Figure S6: Powder pattern comparison of (a) recorded (*rac*)-Pregabalin pattern, (b) (*rac*)-Pregabalin maleate as produced from aqueous solution, (c) (*rac*)-Pregabalin maleate I pattern simulated by single crystal data with $hkl = 4\ 15\ 2$ and March-Dollase parameter of 4, (d) (*rac*)-Pregabalin maleate pattern produced via neat grinding with higher content of II, and (e) recorded maleic acid pattern. A 2θ range from $5 - 40^\circ$ is depicted.; Figure S7: Various recorded powder patterns of solvent grown (a), (b) as well as mechanochemically prepared (d), (e) (*rac*)-Pregabalin maleates compared to the once received phase containing more of form II (c).; Figure S8: FT-IR spectra of (a) (*rac*)-Pregabalin hydrate, (b) (*rac*)-Pregabalin maleate as produced from aqueous solution, (c) (*rac*)-Pregabalin maleate as produced by neat grinding containing more of form II and (d) maleic acid. Spectra are recorded between $4000 \text{ cm}^{-1} - 400 \text{ cm}^{-1}$.; Figure S9: FT-IR spectra of (a) (*rac*)-Pregabalin maleate as produced from aqueous solution after, days drying, (b) (*rac*)-Pregabalin maleate as produced from aqueous solution, two weeks

drying, (c) (rac)-Pregabalin maleate as produced from aqueous solution, two weeks drying and subsequent vacuum drying at 40 °C for 2 h, and (d) (rac)-Pregabalin maleate as produced by neat grinding containing more of form II. Spectra are recorded between 4000 cm^{-1} – 400 cm^{-1} ; Figure S10: Powder pattern comparison of (a) recorded (S)-Pregabalin pattern, (b) (S)-Pregabalin maleate hydrate as produced from aqueous solution, (c) (S)-Pregabalin maleate hydrate pattern simulated by single crystal data with $hkl = 0\ 1\ 1$ and March-Dollase parameter of 2, (d) (S)-Pregabalin maleate hydrate as produced by liquid-assisted grinding and (e) recorded maleic acid pattern. A 2θ range from 5 – 40 ° is depicted.; Figure S11: Powder pattern comparison of (a) recorded (S)-Pregabalin pattern, (b) (S)-Pregabalin maleate hydrate as produced by liquid-assisted grinding, (c) (S)-Pregabalin maleate pattern produced by neat grinding and (d) recorded maleic acid pattern. A 2θ range from 5 – 40 ° is depicted.; Figure S12: FT-IR spectra of (a) (S)-Pregabalin, (b) (S)-Pregabalin maleate hydrate as produced from aqueous solution, (c) (S)-Pregabalin maleate hydrate as produced by liquid-assisted grinding and (d) maleic acid. Spectra are recorded between 4000 cm^{-1} – 400 cm^{-1} ; Figure S13: FT-IR spectra of (a) (S)-Pregabalin maleate hydrate as produced from aqueous solution, three days drying, (b) (S)-Pregabalin maleate as produced from aqueous solution, vacuum drying and (c) (S)-Pregabalin maleate hydrate as produced by liquid-assisted grinding. Spectra are recorded between 4000 cm^{-1} – 400 cm^{-1} ; Figure S14: Powder pattern comparison of (a) recorded Phenibut pattern, (b) Phenibut maleate as produced from aqueous solution, (c) Phenibut maleate pattern simulated by single crystal data with $hkl = 1\ 8\ 1$ and March-Dollase parameter of 0.65, (d) Phenibut maleate as produced by neat grinding and (e) recorded maleic acid pattern. A 2θ range from 5 – 40 ° is depicted.; Figure S15: FT-IR spectra of (a) Phenibut, (b) Phenibut maleate as produced from aqueous solution, (c) Phenibut maleate as produced by neat grinding and (d) maleic acid. Spectra are recorded between 4000 cm^{-1} – 400 cm^{-1} ; Figure S16: Powder pattern comparison of (a) recorded Baclofen pattern, (b) Baclofen maleate as produced from aqueous solution, (c) Baclofen maleate pattern simulated by single crystal data with $hkl = 0\ 0\ 7$ and March-Dollase parameter of 4, (d) Baclofen maleate as produced by neat grinding and (e) recorded maleic acid pattern. A 2θ range from 5 – 40 ° is depicted.; Figure S17: FT-IR spectra of (a) Baclofen, (b) Baclofen maleate as produced from aqueous solution, (c) Baclofen maleate as produced by neat grinding and (d) maleic acid. Spectra are recorded between 4000 cm^{-1} – 400 cm^{-1} ; Figure S18: Depiction of the asymmetric unit in each compound that could be characterized by SCXRD: (a) GABA maleate, (b) Gabapentin maleate hydrate, (c) (rac)-Pregabalin maleate, (d) (S)-Pregabalin maleate hydrate, (e) Phenibut maleate, and (f) Baclofen maleate. Carbon atoms are depicted in grey, hydrogen atoms in white, nitrogen atoms in blue, oxygen atoms in red, and chlorine atoms in green. Hydrogen bonds occurring in the asymmetric units are shown as light blue dotted lines.; Figure S19: $^1\text{H-NMR}$ spectrum of GABA recorded in D_2O at 600 MHz.; Figure S20: $^1\text{H-NMR}$ spectrum of Gabapentin recorded in D_2O at 600 MHz.; Figure S21: $^1\text{H-NMR}$ spectrum of (S)-Pregabalin recorded in D_2O at 600 MHz. Also represents (rac)-Pregabalin.; Figure S22: $^1\text{H-NMR}$ spectrum of Phenibut recorded in D_2O at 600 MHz.; Figure S23: $^1\text{H-NMR}$ spectrum of Baclofen recorded in D_2O at 600 MHz.; Figure S24: $^1\text{H-NMR}$ spectrum of GABA maleate recorded in D_2O at 600 MHz. Sample grown from solution.; Figure S25: $^1\text{H-NMR}$ spectrum of Gabapentin maleate hydrate recorded in D_2O at 600 MHz.; Figure S26: $^1\text{H-NMR}$ spectrum of Gabapentin maleate recorded in D_2O at 600 MHz.; Figure S27: $^1\text{H-NMR}$ spectrum of (rac)-Pregabalin maleate recorded in D_2O at 600 MHz. Sample grown from solution.; Figure S28: $^1\text{H-NMR}$ spectrum of (rac)-Pregabalin maleate recorded in D_2O at 600 MHz. Sample grown via grinding.; Figure S29: $^1\text{H-NMR}$ spectrum of (S)-Pregabalin maleate hydrate recorded in D_2O at 600 MHz. Sample grown from solution.; Figure S30: $^1\text{H-NMR}$ spectrum of (S)-Pregabalin maleate hydrate recorded in D_2O at 600 MHz. Sample grown via grinding.; Figure S31: $^1\text{H-NMR}$ spectrum of Phenibut maleate recorded in D_2O at 600 MHz. Sample grown from solution.; Figure S32: $^1\text{H-NMR}$ spectrum of Baclofen maleate recorded in D_2O at 600 MHz. Sample grown from solution.; Table S1: Single crystal measurement details for GABA maleate.; Table S2: Single crystal measurement details for Gabapentin maleate hydrate.; Table S3: Single crystal measurement details for (rac)-Pregabalin maleate.; Table S4: Single crystal measurement details for (S)-Pregabalin maleate hydrate.; Table S5: Single crystal measurement details for Phenibut maleate.; Table S6: Single crystal measurement details for Baclofen maleate.; Table S7: Solubilities of GABA and its derivatives on their own and in form of the investigated maleates and their standard deviations. The integral borders for the product peaks used for solubility calculations of samples S1 – S3 are given.

Author Contributions: Conceptualization, Daniel Komisarek and Vera Vasylyeva; methodology, Daniel Komisarek and Vera Vasylyeva; validation, Daniel Komisarek and Ebru Taskiran; investigation, Daniel Komisarek and Ebru Taskiran; resources, Vera Vasylyeva; data curation, Daniel Komisarek; writing—original draft preparation, Daniel Komisarek; writing—review and editing,

Vera Vasylyeva; visualization, Daniel Komisarek; supervision, Vera Vasylyeva; project administration, Vera Vasylyeva; funding acquisition, Vera Vasylyeva. All authors have read and agreed to the published version of the manuscript.

Funding: Funded by the Deutsche Forschungsgemeinschaft (DFG, German Research Foundation) – 440366605.

Data Availability Statement: not applicable.

Acknowledgments: We want to thank Carsten Schauerte, Kevin Grasmik and the SOLID-CHEM team for technical support.

Computational support and infrastructure were provided by the “Centre for Information and Media Technology” (ZIM) at the University of Duesseldorf (Germany). Further thanks to the CeMSA@HHU (Center for Molecular and Structural Analytics @ Heinrich Heine University) for recording the NMR-spectroscopic data.

Conflicts of Interest: The authors declare no conflict of interest.

References

1. Jornada, D.H.; dos Santos Fernandes, G.F.; Chiba, D.E.; Melo, T.R.F. de; dos Santos, J.L.; Chung, M.C. The Prodrug Approach: A Successful Tool for Improving Drug Solubility. *Molecules* **2015**, *21*, 42.
2. Antraygues, K.; Maingot, M.; Schellhorn, B.; Trebosc, V.; Gitzinger, M.; Deprez, B.; Defert, O.; Dale, G.E.; Bourotte, M.; Lociuro, S.; Willand, N. Design and synthesis of water-soluble prodrugs of rifabutin for intravenous administration. *Eur. J. Med. Chem.* **2022**, *238*, 114515.
3. Liu, J.; Wang, W.; Wang, C.; Zhang, L.; Zhang, X.; Liu, S.; Xu, Y.; Wang, H.; Dai, Q.; Liu, C.; Wang, X.; Yuan, Z.; Gordeev, M.F. Discovery of Antibacterial Contezolid Acefosamil: Innovative O-Acyl Phosphoramidate Prodrug for IV and Oral Therapies. *ACS Med. Chem. Lett.* **2022**, *13*, 1030–1035.
4. Sanches, B.M.A.; Ferreira, E.I. Is prodrug design an approach to increase water solubility? *Int. J. Pharm.* **2019**, *568*, 118498.
5. Yu, Y.; Sun, L.; Tang, Y.; Zhu, H.; Wang, H.; Xiao, H.; Wang, F.; Tao, W. Preparation of cisplatin delivery calcium phosphate nanoparticles using poly(Pt(IV) prodrug) as the payload. *Mater. Today Commun.* **2022**, *33*, 104283.
6. Patel, V.R.; Agrawal, Y.K. Nanosuspension: An approach to enhance solubility of drugs. *J. Adv. Pharm. Technol. Res.* **2011**, *2*, 81–87.
7. Pandey, N.; Bohra, B.S.; Tiwari, H.; Pal, M.; Negi, P.B.; Dandapat, A.; Mehta, S.; Sahoo, N.G. Development of biodegradable chitosan/ graphene oxide nanocomposite via spray drying method for drug loading and delivery application. *Journal of Drug Delivery Science and Technology* **2022**, *74*, 103555.
8. Nora, G.-I.; Venkatasubramanian, R.; Strindberg, S.; Siqueira-Jørgensen, S.D.; Pagano, L.; Romanski, F.S.; Swarnakar, N.K.; Rades, T.; Müllertz, A. Combining lipid based drug delivery and amorphous solid dispersions for improved oral drug absorption of a poorly water-soluble drug. *J. Control. Release* **2022**, *349*, 206–212.
9. Khan, A.A.; Akhtar, S.; Yadav, Y.; Akhtar, A.; Alelwani, W.; Bannunah, A.M.; Mahmood, S. Lopinavir-Loaded Self-Nanoemulsifying Drug Delivery System for Enhanced Solubility: Development, Characterisation and Caco-2 Cell Uptake. *Curr. Drug Deliv.* **2022**, *Online ahead of print*.
10. Pignatello, R.; Corsaro, R.; Bonaccorso, A.; Zingale, E.; Carbone, C.; Musumeci, T. Soluplus® polymeric nanomicelles improve solubility of BCS-class II drugs. *Drug Deliv. Transl. Res.* **2022**, *12*, 1991–2006.
11. Petitprez, J.; Legrand, F.-X.; Tams, C.; Pipkin, J.D.; Antle, V.; Kfoury, M.; Fourmentin, S. Huge solubility increase of poorly water-soluble pharmaceuticals by sulfobutylether- β -cyclodextrin complexation in a low-melting mixture. *Environ. Chem. Lett.* **2022**, *20*, 1561–1568.
12. Loftsson, T. Drug solubilization by complexation. *Int. J. Pharm.* **2017**, *531*, 276–280.
13. Kaur, J.; Singla, P.; Kaur, I. Labrasol mediated enhanced solubilization of natural hydrophobic drugs in Pluronic micelles: Physicochemical and in vitro release studies. *J. Mol. Liq.* **2022**, *361*, 119596.
14. Dadej, A.; Woźniak-Braszak, A.; Bilski, P.; Piotrowska-Kempisty, H.; Józkwiaik, M.; Pawełczyk, A.; Dadej, D.; Łażewska, D.; Jelińska, A. Improved solubility of lornoxicam by inclusion into SBA-15: Comparison of loading methods. *Eur. J. Pharm. Sci.* **2022**, *171*, 106133.
15. Hancock, B.C.; Parks, M. What is the true solubility advantage for amorphous pharmaceuticals? *Pharm. Res.* **2000**, *17*, 397–404.
16. Serajuddin, A.T.M. Salt formation to improve drug solubility. *Adv. Drug Deliv. Rev.* **2007**, *59*, 603–616.
17. Good, D.J.; Rodríguez-Hornedo, N. Solubility Advantage of Pharmaceutical Cocrystals. *Cryst. Growth Des.* **2009**, *9*, 2252–2264.
18. Elder, D.P.; Holm, R.; Diego, H.L. de. Use of pharmaceutical salts and cocrystals to address the issue of poor solubility. *Int. J. Pharm.* **2013**, *453*, 88–100.
19. Jindal, A.; Prashar, M.; Dureja, J.; Dhingra, N.; Chadha, K.; Karan, M.; Chadha, R. Pharmaceutical Cocrystals of Famotidine: Structural and Biopharmaceutical Evaluation. *J. Pharm. Sci.* **2022**, *111*, 2788–2798.
20. Lenschow, I.C.S.; Bazzo, G.C.; Zétola, M.; Stulzer, H.K.; Soares, L.; Pezzini, B.R. Ball-milled valsartan and its combination with mannitol: the case of drug polyamorphism. *J. Therm. Anal. Calorim.* **2022**, *147*, 8765–8777.

21. Vemuri, V.D.; Lankalapalli, S.; Chandra Reddy Guntaka, P. Posaconazole-amino acid cocrystals for improving solubility and oral bioavailability while maintaining antifungal activity and low In vivo toxicity. *J. Drug Deliv. Sci. Technol.* **2022**, *74*, 103491.
22. Wang, Z.; Chen, X.; Li, D.; Bai, E.; Zhang, H.; Duan, Y.; Huang, Y. Platensimycin-berberine chloride co-amorphous drug system: Sustained release and prolonged half-life. *Eur. J. Pharm. Biopharm.* **2022**, *179*, 126–136.
23. Nechipadappu, S.K.; Swain, D. Combined synthetic and solubility aspects of orotate salt of bilastine. *J. Mol. Struct.* **2023**, *1271*, 134148.
24. Liu, L.; An, Q.; Zhang, Y.; Sun, W.; Li, J.; Feng, Y.; Geng, Y.; Cheng, G. Improving the solubility, hygroscopicity and permeability of enrofloxacin by forming 1:2 pharmaceutical salt cocrystal with neutral and anionic co-existing p-nitrobenzoic acid. *J. Drug Deliv. Sci. Technol.* **2022**, *76*, 103732.
25. Neelam, U.K.; Daveedu, B.; Ambabhai, V.N.; Siripragada, M.R.; Kumar, S.R.; Balasubramanian, S. Physicochemical aspects and comparative analysis of Voxelotor and its salt and cocrystal. *J. Mol. Struct.* **2023**, *1271*, 134024.
26. Bethune, S.J.; Huang, N.; Jayasankar, A.; Rodriguez-Hornedo, N. Understanding and Predicting the Effect of Cocrystal Components and pH on Cocrystal Solubility. *Cryst. Growth Des.* **2009**, *9*, 3976–3988.
27. Banik, M.; Gopi, S.P.; Ganguly, S.; Desiraju, G.R. Cocrystal and Salt Forms of Furosemide: Solubility and Diffusion Variations. *Cryst. Growth Des.* **2016**, *16*, 5418–5428.
28. Kruger, C. The relevance of international assessments to GRAS determinations. *Regul. Toxicol. Pharmacol.* **2016**, *79 Suppl 2*, S119–23.
29. Martins, F.T.; Paparidis, N.; Doriguetto, A.C.; Ellena, J. Crystal Engineering of an Anti-HIV Drug Based on the Recognition of Assembling Molecular Frameworks. *Cryst. Growth Des.* **2009**, *9*, 5283–5292.
30. Mittapalli, S.; Mannava, M.K.C.; Khandavilli, U.B.R.; Allu, S.; Nangia, A. Soluble Salts and Cocrystals of Clotrimazole. *Cryst. Growth Des.* **2015**, *15*, 2493–2504.
31. Zhao, Y.; Sun, B.; Jia, L.; Wang, Y.; Wang, M.; Yang, H.; Qiao, Y.; Gong, J.; Tang, W. Tuning Physicochemical Properties of Antipsychotic Drug Aripiprazole with Multicomponent Crystal Strategy Based on Structure and Property Relationship. *Cryst. Growth Des.* **2020**, *20*, 3747–3761.
32. Voronin, A.P.; Surov, A.O.; Churakov, A.V.; Parashchuk, O.D.; Rykounov, A.A.; Vener, M.V. Combined X-ray Crystallographic, IR/Raman Spectroscopic, and Periodic DFT Investigations of New Multicomponent Crystalline Forms of Anthelmintic Drugs: A Case Study of Carbendazim Maleate. *Molecules* **2020**, *25*, 2386.
33. Djaló, M.; Cunha, A.E.S.; Luís, J.P.; Quaresma, S.; Fernandes, A.; André, V.; Duarte, M.T. Sparfloxacin Multicomponent Crystals: Targeting the Solubility of Problematic Antibiotics. *Cryst. Growth Des.* **2021**, *21*, 995–1005.
34. Sun, N.; Avdeef, A. Biorelevant pK(a) (37 °C) predicted from the 2D structure of the molecule and its pK(a) at 25 °C. *J. Pharm. Biomed. Anal.* **2011**, *56*, 173–182.
35. Childs, S.L.; Stahly, G.P.; Park, A. The salt-cocrystal continuum: the influence of crystal structure on ionization state. *Mol. Pharm.* **2007**, *4*, 323–338.
36. Bowery, N.G.; Smart, T.G. GABA and glycine as neurotransmitters: a brief history. *Br. J. Pharmacol.* **2006**, *147 Suppl 1*, S109–19.
37. Bown, A.W.; Shelp, B.J. Plant GABA: Not Just a Metabolite. *Trends Plant Sci.* **2016**, *21*, 811–813.
38. Enna, S.J.; McCarron, K.E. The role of GABA in the mediation and perception of pain. *Adv. Pharmacol.* **2006**, *54*, 1–27.
39. Gottesmann, C. GABA mechanisms and sleep. *Neuroscience* **2002**, *111*, 231–239.
40. Kalueff, A.V.; Nutt, D.J. Role of GABA in anxiety and depression. *Depress. Anxiety* **2007**, *24*, 495–517.
41. Bockbrader, H.N.; Wesche, D.; Miller, R.; Chapel, S.; Janiczek, N.; Burger, P. A comparison of the pharmacokinetics and pharmacodynamics of pregabalin and gabapentin. *Clin. Pharmacokinet.* **2010**, *49*, 661–669.
42. Bramness, J.G.; Sandvik, P.; Engeland, A.; Skurtveit, S. Does Pregabalin (Lyrica®) help patients reduce their use of benzodiazepines? A comparison with gabapentin using the Norwegian Prescription Database. *Basic Clin. Pharmacol. Toxicol.* **2010**, *107*, 883–886.
43. Tomić, M.; Pecikoza, U.; Micov, A.; Vučković, S.; Stepanović-Petrović, R. Antiepileptic drugs as analgesics/adjuvants in inflammatory pain: current preclinical evidence. *Pharmacol. Ther.* **2018**, *192*, 42–64.
44. Ranaldi, R.; Poeggel, K. Baclofen decreases methamphetamine self-administration in rats. *Neuroreport* **2002**, *13*, 1107–1110.
45. Marti-Prats, L.; Belin-Rauscent, A.; Fouyssac, M.; Puaud, M.; Cocker, P.J.; Everitt, B.J.; Belin, D. Baclofen decreases compulsive alcohol drinking in rats characterized by reduced levels of GAT-3 in the central amygdala. *Addict. Biol.* **2021**, *26*, e13011.
46. Kent, C.N.; Park, C.; Lindsley, C.W. Classics in Chemical Neuroscience: Baclofen. *ACS Chem. Neurosci.* **2020**, *11*, 1740–1755.
47. Montoya-Balbás, I.J.; Valentín-Guevara, B.; López-Mendoza, E.; Linzaga-Elizalde, I.; Ordoñez, M.; Román-Bravo, P. Efficient Synthesis of β -Aryl- γ -lactams and Their Resolution with (S)-Naproxen: Preparation of (R)- and (S)-Baclofen. *Molecules* **2015**, *20*, 22028–22043.
48. Lapin, I. Phenibut (beta-phenyl-GABA): a tranquilizer and nootropic drug. *CNS Drug Rev.* **2001**, *7*, 471–481.
49. Dambrova, M.; Zvejniece, L.; Liepinsh, E.; Cirule, H.; Zharkova, O.; Veinberg, G.; Kalvinsh, I. Comparative pharmacological activity of optical isomers of phenibut. *Eur. J. Pharmacol.* **2008**, *583*, 128–134.
50. Peterson, M.; Oliveira, M. Preparation of organic acid salts of gabapentin. WO2004-US10944, filed 8 April 2004, and issued 28 October 2004.
51. Plata Salaman, C.R.; Tesson, N.; Trilla Castano, M.; Cardenas Romana, L. Crystalline forms of pregabalin and co-formers in the treatment of pain. EP2011-384001, filed 24 May 2011, and issued 28 November 2012.

52. Gendron, F.-X.; Mahieux, J.; Sanselme, M.; Coquerel, G. Resolution of Baclofenium Hydrogenomaleate By Using Preferential Crystallization. A First Case of Complete Solid Solution at High Temperature and a Large Miscibility Gap in the Solid State. *Cryst. Growth Des.* **2019**, *19*, 4793–4801.
53. Báthori, N.B.; Kilinkissa, O.E.Y. Are gamma amino acids promising tools of crystal engineering? – Multicomponent crystals of baclofen. *CrystEngComm* **2015**, *17*, 8264–8272.
54. Bloom, R.A.; Sadrieh, N. Environmental Assessment Finding of No Significant Impact NDA 21-446/S-028 Lyrica (Pregabalin) Capsules, 2012. Available online: https://www.accessdata.fda.gov/drugsatfda_docs/nda/2012/021446Orig1s028EA.pdf (accessed on 20 October 2022).
55. Haynes, William M., CRC Handbook of Chemistry and Physics (97th ed.), Boca Raton: CRC Press. 1943-2016 pp. 5–88.
56. Komisarek, D.; Haj Hassani Sohi, T.; Vasylyeva, V. Co-crystals of zwitterionic GABA API's pregabalin and phenibut: properties and application. *CrystEngComm* **2022**, *24*, 8390-8398.
57. Herbst, M.; Komisarek, D.; Strothmann, T.; Vasylyeva, V. A Lesson in Humbleness: Crystallization of Chiral and Zwitterionic APIs Baclofen and Phenibut. *Crystals* **2022**, *12*, 1393.
58. Budny-Godlewski, K.; Leszczyński, M.K.; Tulewicz, A.; Justyniak, I.; Pinkowicz, D.; Sieklucka, B.; Kruczała, K.; Sojka, Z.; Lewiński, J. A Case Study on the Desired Selectivity in Solid-State Mechano- and Slow-Chemistry, Melt, and Solution Methodologies. *ChemSusChem* **2021**, *14*, 3887–3894.
59. Solares-Briones, M.; Coyote-Dotor, G.; Páez-Franco, J.C.; Zermeño-Ortega, M.R.; La O Contreras, C.M. de; Canseco-González, D.; Avila-Sorrosa, A.; Morales-Morales, D.; Germán-Acacio, J.M. Mechanochemistry: A Green Approach in the Preparation of Pharmaceutical Cocrystals. *Pharmaceutics* **2021**, *13*, 790.
60. Wang, L.; Sun, G.; Zhang, K.; Yao, M.; Jin, Y.; Zhang, P.; Wu, S.; Gong, J. Green Mechanochemical Strategy for the Discovery and Selective Preparation of Polymorphs of Active Pharmaceutical Ingredient γ -Aminobutyric Acid (GABA). *ACS Sustainable Chem. Eng.* **2020**, *8*, 16781–16790.
61. Chikhaliya, V.; Forbes, R.T.; Storey, R.A.; Ticehurst, M. The effect of crystal morphology and mill type on milling induced crystal disorder. *Eur. J. Pharm. Sci.* **2006**, *27*, 19–26.
62. Descamps, M.; Willart, J.F. Perspectives on the amorphisation/milling relationship in pharmaceutical materials. *Adv. Drug Deliv. Rev.* **2016**, *100*, 51–66.
63. Mah, P.T.; Laaksonen, T.; Rades, T.; Aaltonen, J.; Peltonen, L.; Strachan, C.J. Unravelling the relationship between degree of disorder and the dissolution behavior of milled glibenclamide. *Mol. Pharm.* **2014**, *11*, 234–242.
64. CrysAlisPRO, Oxford Diffraction /Agilent Technologies UK Ltd, Yarnton, England.
65. Dolomanov, O.V.; Bourhis, L.J.; Gildea, R.J.; Howard, J.A.K.; Puschmann, H. OLEX2 : a complete structure solution, refinement and analysis program. *J. Appl. Crystallogr.* **2009**, *42*, 339–341.
66. Sheldrick, G.M. A short history of SHELX. *Acta Crystallogr. A* **2008**, *64*, 112–122.
67. Sheldrick, G.M. Crystal structure refinement with SHELXL. *Acta Crystallogr. C Struct. Chem.* **2015**, *71*, 3–8.
68. Macrae, C.F.; Sovago, I.; Cottrell, S.J.; Galek, P.T.A.; McCabe, P.; Pidcock, E.; Platings, M.; Shields, G.P.; Stevens, J.S.; Towler, M.; Wood, P.A. Mercury 4.0: from visualization to analysis, design and prediction. *J. Appl. Crystallogr.* **2020**, *53*, 226–235.

Disclaimer/Publisher’s Note: The statements, opinions and data contained in all publications are solely those of the individual author(s) and contributor(s) and not of MDPI and/or the editor(s). MDPI and/or the editor(s) disclaim responsibility for any injury to people or property resulting from any ideas, methods, instructions or products referred to in the content.

Supporting Information

Maleic Acid as a Co-former for Pharmaceutically Active GABA Derivatives

Daniel Komisarek, Ebru Taskiran and Vera Vasylyeva*

1 GABA maleate

Table S1. Single crystal measurement details for GABA maleate.

Parameters	1-MA
Formula	C ₈ H ₁₃ N O ₆
Formula moiety	C ₄ H ₁₀ N O ₂ , C ₄ H ₃ O ₄
M _r [g mol ⁻¹]	219.19
Temperature [K]	100(1)
System/space group	monoclinic, <i>P</i> 2 ₁ / <i>c</i>
a (Å)	5.5757(1)
b (Å)	6.6352 (1)
c (Å)	26.3554(5)
β (°)	94.060(2)
V (Å ³)	972.59(3)
Z/Z'	4/1
Density [g/cm ³]	1.497
μ [mm ⁻¹]	1.121
T _{min} /T _{max}	0.93836/ 0.93836
F (000)	464
Crystal size [mm]	0.2 · 0.19 · 0.05
2θ range [°]	3.4 – 67.0
Completeness [%]	100.0
Recorded refl.	9108
Independent refl.	1744
Goodness-of-fit F ²	1.050
X-Ray Source	Cu Kα (λ = 1.54184)
R ₁ [%] /wR ₂ [%] /S	2.96/ 8.02/ 1.05

GABA maleate was received by either crystallization from aqueous solution or neat grinding of equimolar amounts of GABA and maleic acid (516 mg, 5 mmol and 581 mg, 5 mmol). The same product is received in both cases.

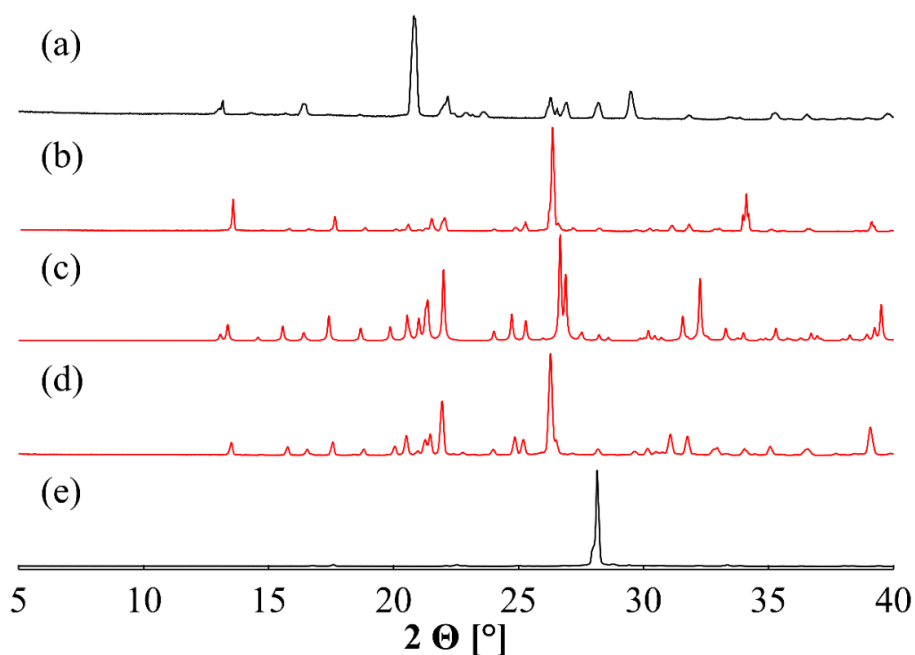


Figure S1. Powder pattern comparison of (a) recorded GABA pattern, (b) GABA maleate as produced from aqueous solution, (c) GABA maleate pattern simulated by single crystal data, (d) GABA maleate as produced by neat grinding, and (e) recorded maleic acid pattern. A 2Θ range from 5 – 40 ° is depicted.

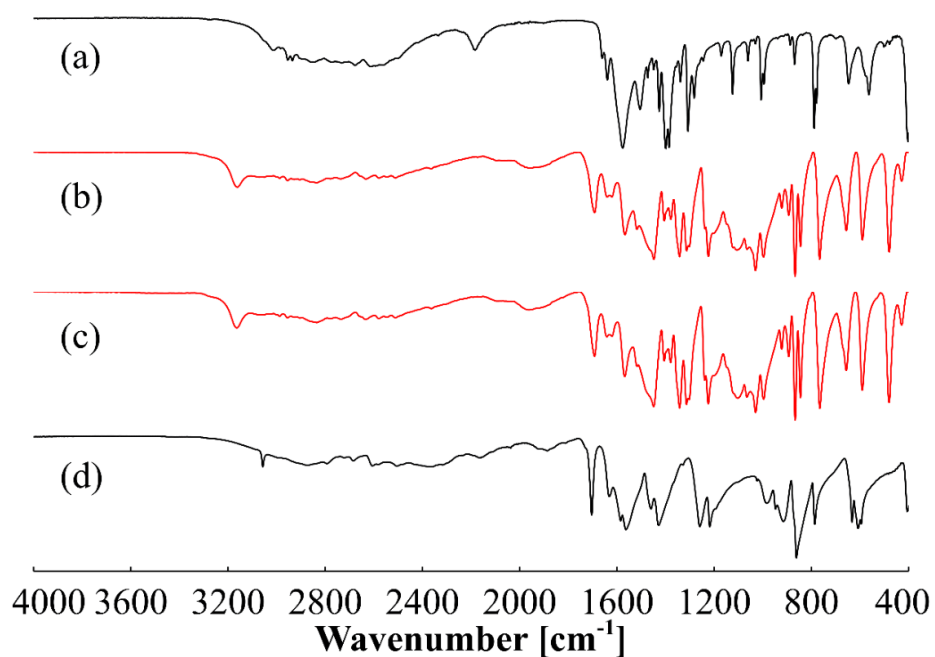


Figure S2. FT-IR spectra of (a) GABA, (b) GABA maleate as produced from aqueous solution, (c) GABA maleate as produced by neat grinding and (d) maleic acid. Spectra are recorded between 4000 cm^{-1} – 400 cm^{-1} .

2 Gabapentin maleate hydrate

Table S2. Single crystal measurement details for Gabapentin maleate hydrate.

Parameters	2-MA • H ₂ O
Formula	C ₁₃ H ₂₃ N O ₇
Formula moiety	C ₉ H ₁₈ N O ₂ , C ₄ H ₃ O ₄ , H ₂ O
M _r [g mol ⁻¹]	305.32
Temperature [K]	100(1)
System/space group	triclinic, <i>P</i> $\bar{1}$
a (Å)	6.0214(2)
b (Å)	11.7991(6)
c (Å)	12.1015(5)
α (°)	64.406(4)
β (°)	80.251(3)
γ (°)	83.629(4)
V (Å ³)	763.52(6)
Z/Z'	2/1
Density [g/cm ³]	1.328
μ [mm ⁻¹]	0.913
T _{min} /T _{max}	0.88604/ 0.88604
F (000)	328
Crystal size [mm]	0.38 · 0.33 · 0.07
2θ range [°]	4.2 – 67.1
Completeness [%]	98.8
Recorded refl.	7622
Independent refl.	2686
Goodness-of-fit F ²	1.053
X-Ray Source	Cu Kα (λ = 1.54184)
R ₁ [%] /wR ₂ [%] /S	3.71/ 10.27/ 1.05

Gabapentin maleate hydrate was received by crystallization of equimolar amounts of Gabapentin and maleic acid from aqueous solution and an anhydrous form was received via neat grinding of equimolar amounts of Gabapentin and maleic acid (685 mg, 4 mmol and 464 mg, 4 mmol). Both products show clear differences in PXRD patterns as well as FT-IR spectra. Attempts at producing Gabapentin maleate hydrate through liquid-assisted grinding result in a phase mixture of the maleate and the maleate hydrate.

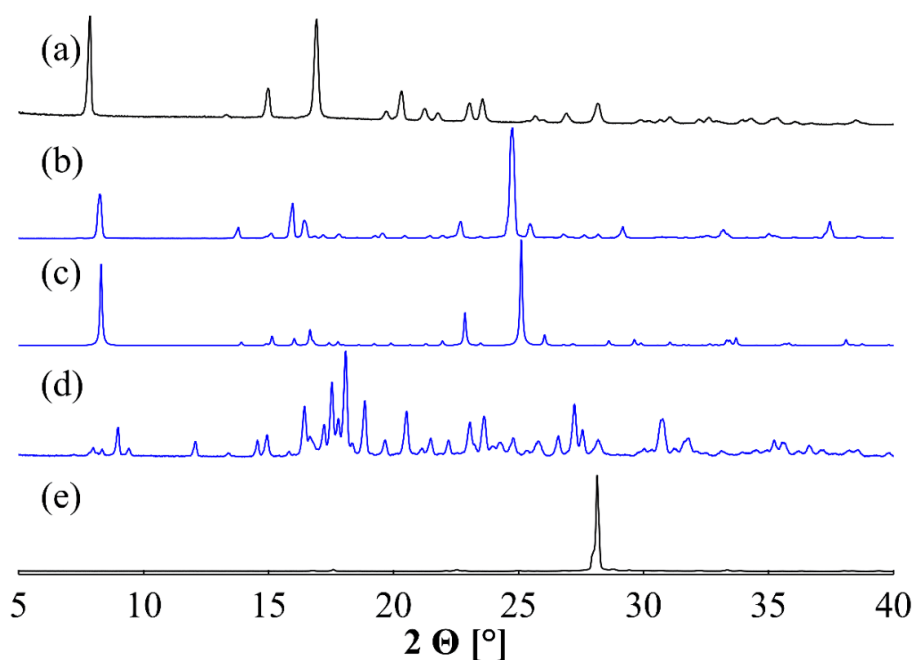


Figure S3. Powder pattern comparison of (a) recorded Gabapentin pattern, (b) Gabapentin maleate hydrate as produced from aqueous solution, (c) Gabapentin maleate hydrate pattern simulated by single crystal data with $hkl = 0\ 4\ 0$ and March-Dollase parameter of 0.5, (d) Gabapentin maleate as produced by neat-grinding, and (e) recorded Gabapentin pattern. A 2θ range from $5 - 40^\circ$ is depicted.

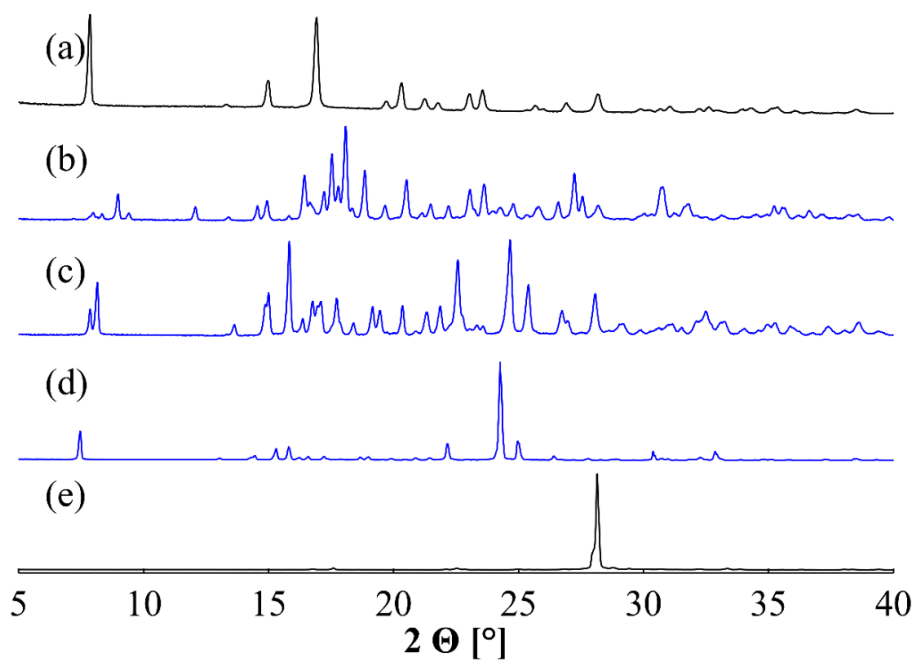


Figure S4. Powder pattern comparison of (a) recorded Gabapentin pattern, (b) Gabapentin maleate as produced by neat grinding, (c) Gabapentin maleate hydrate and maleate mixture as produced by liquid-assisted grinding, (d) Gabapentin maleate hydrate as produced from aqueous solution and (e) recorded maleic acid pattern. A 2θ range from $5 - 40^\circ$ is depicted.

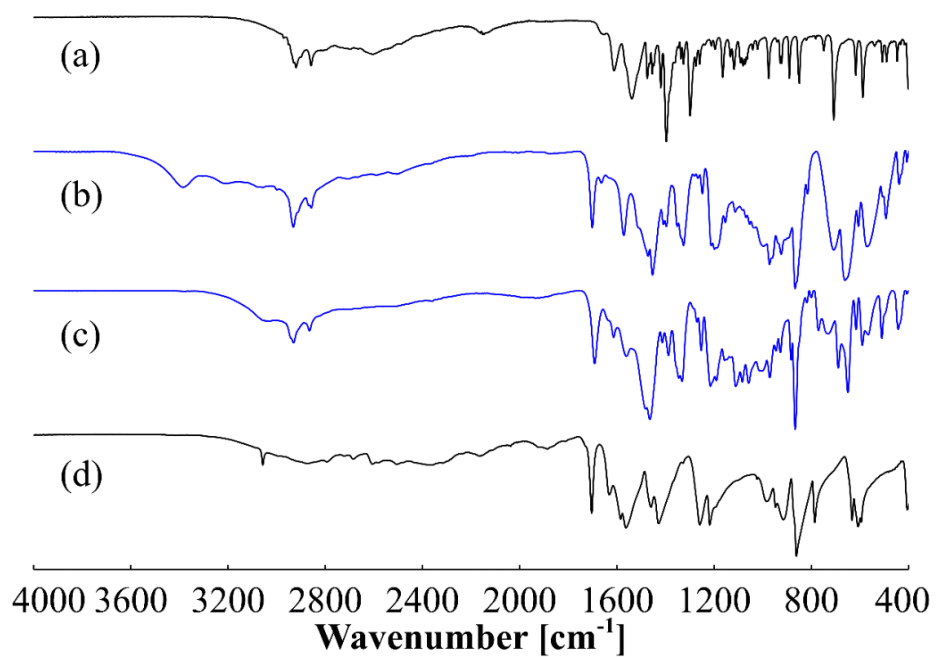


Figure S5. FT-IR spectra of (a) Gabapentin, (b) Gabapentin maleate hydrate as produced from aqueous solution, (c) Gabapentin maleate as produced by neat grinding and (d) maleic acid. Spectra are recorded between 4000 cm^{-1} – 400 cm^{-1} .

3 (*rac*)-Pregabalin maleate

Table S3. Single crystal measurement details for (*rac*)-Pregabalin maleate.

Parameters	(<i>rac</i>)-3-MA-I
Formula	C ₁₂ H ₂₁ N O ₆
Formula moiety	C ₈ H ₁₈ N O ₂ , C ₄ H ₃ N O ₄
M _r [g mol ⁻¹]	275.30
Temperature [K]	100(1)
System/space group	triclinic, <i>P</i> $\bar{1}$
a (Å)	5.8681(2)
b (Å)	11.1369(3)
c (Å)	11.2720(3)
α (°)	88.527(2)
β (°)	79.402(2)
γ (°)	75.521(2)
V (Å ³)	700.93(4)
Z/Z'	2/1
Density [g/cm ³]	1.304
μ [mm ⁻¹]	0.882
T _{min} /T _{max}	0.97036/ 0.97036
F (000)	296
Crystal size [mm]	0.22 · 0.11 · 0.02
2θ range [°]	4.0 – 67.1
Completeness [%]	99.5
Recorded refl.	16382
Independent refl.	2484
Goodness-of-fit F ²	1.075
X-Ray Source	Cu Kα (λ = 1.54184)
R ₁ [%] /wR ₂ [%] /S	4.23/ 11.35/ 1.08

(*rac*)-Pregabalin maleate mixtures of form I and II were received by either crystallization from aqueous solution or neat grinding of equimolar amounts of (*rac*)-Pregabalin hydrate and maleic acid (637 mg, 4 mmol and 464 mg, 4 mmol). The same product is received in both cases, though in one grinding experiment the content of form II was higher. IR-spectra highlight phase shifts between the two forms.

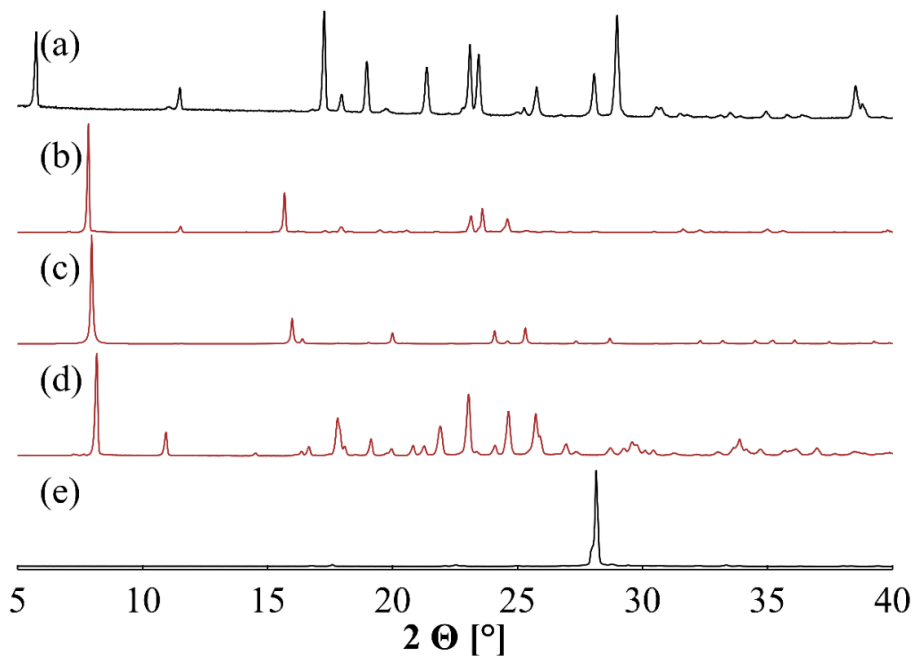


Figure S6. Powder pattern comparison of (a) recorded (rac)-Pregabalin pattern, (b) (rac)-Pregabalin maleate as produced from aqueous solution, (c) (rac)-Pregabalin maleate I pattern simulated by single crystal data with $hkl = 4\ 15\ 2$ and March-Dollase parameter of 4, (d) (rac)-Pregabalin maleate pattern produced via neat grinding with higher content of II, and (e) recorded maleic acid pattern. A 2θ range of $5 - 40^\circ$ is depicted.

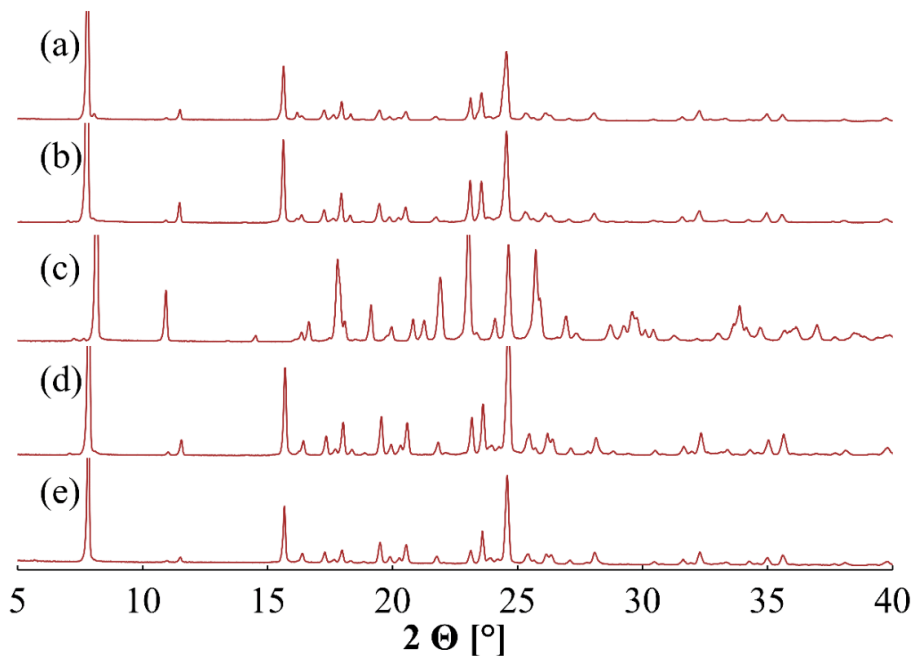


Figure S7. Various recorded powder patterns of solvent grown (a), (b) as well as mechanochemically prepared (d), (e) (rac)-Pregabalin maleates compared to the once received phase containing more of form II (c).

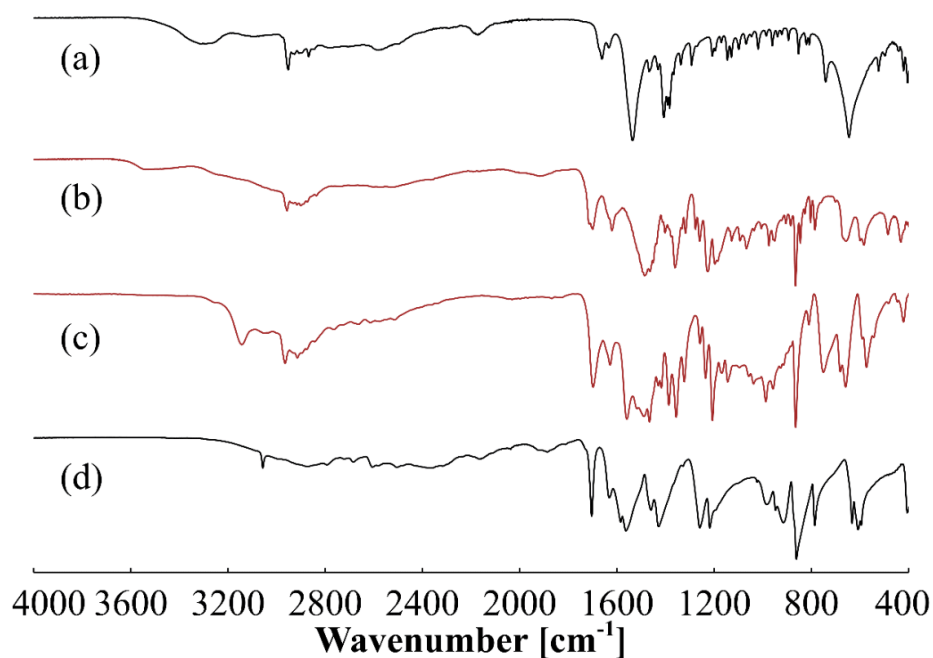


Figure S8. FT-IR spectra of (a) (rac)-Pregabalin hydrate, (b) (rac)-Pregabalin maleate as produced from aqueous solution, (c) (rac)-Pregabalin maleate as produced by neat grinding containing more of form II and (d) maleic acid. Spectra are recorded between 4000 cm^{-1} – 400 cm^{-1} .

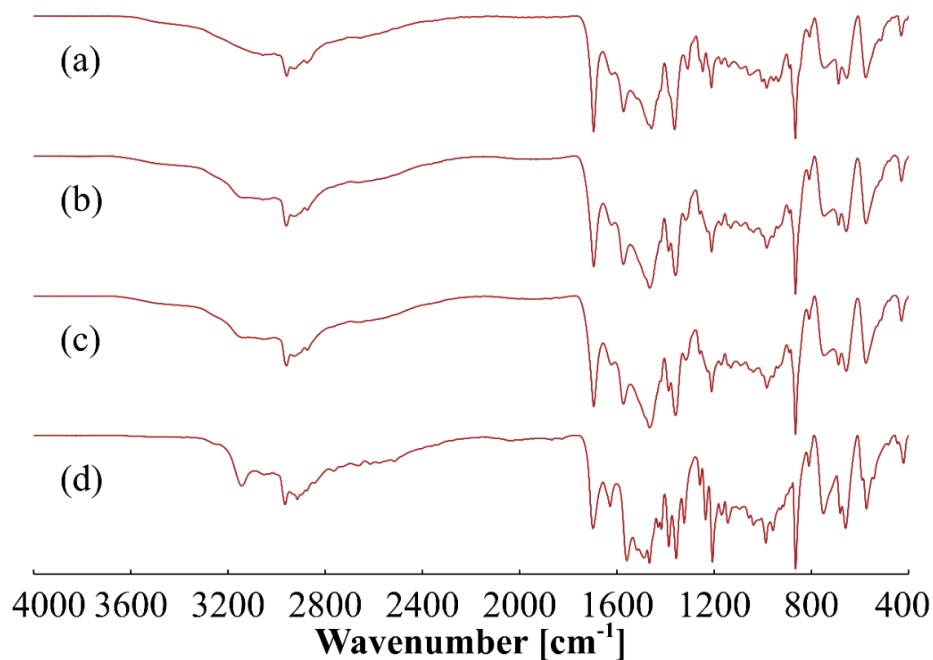


Figure S9. FT-IR spectra of (a) (rac)-Pregabalin maleate as produced from aqueous solution after, days drying, (b) (rac)-Pregabalin maleate as produced from aqueous solution, two weeks drying, (c) (rac)-Pregabalin maleate as produced from aqueous solution, two weeks drying and subsequent vacuum drying at $40\text{ }^{\circ}\text{C}$ for 2 h, and (d) (rac)-Pregabalin maleate as produced by neat grinding containing more of form II. Spectra are recorded between 4000 cm^{-1} – 400 cm^{-1} .

4 (S)-Pregabalin maleate • H₂O

Table S4. Single crystal measurement details for (S)-Pregabalin maleate hydrate.

Parameters	(S)-3-MA • H ₂ O
Formula	C ₂₄ H ₄₄ N ₂ O ₁₃
Formula moiety	2(C ₈ H ₁₈ N O ₂), 2(C ₄ H ₃ O ₄), 2(H ₂ O * 0.5)
M _r [g mol ⁻¹]	568.61
Temperature [K]	100(1)
System/space group	monoclinic, C2
a (Å)	29.9006(3)
b (Å)	5.5788(1)
c (Å)	18.0925(2)
β (°)	102.615(1)
V (Å ³)	2945.14(7)
Z/Z'	4/2
Density [g/cm ³]	1.282
μ [mm ⁻¹]	0.881
T _{min} /T _{max}	0.629/ 1.000
F (000)	1224
Crystal size [mm]	0.52 · 0.10 · 0.06
2θ range [°]	2.5 – 67.1
Completeness [%]	99.9
Recorded refl.	44205
Independent refl.	5271
Flack x	0.01(3)
Goodness-of-fit F ²	1.033
X-Ray Source	Cu Kα (λ = 1.54184)
R ₁ [%] /wR ₂ [%] /S	3.50/ 9.02/ 1.03

(S)-Pregabalin maleate hydrate was received by either crystallization from aqueous solution or liquid-assisted grinding of equimolar amounts of (S)-Pregabalin and maleic acid (477 mg 3 mmol and 384 mg 3 mmol). The same product is received in both cases, though the presence of water is visible in FT-IR spectra of samples grown through solvent evaporation. Attempts at producing (S)-Pregabalin maleate hydrate through neat grinding result in lower crystallinity and an incomplete conversion of the co-formers. The solvent product can be dried at 40 °C under vacuum conditions of 10⁻³ bar.

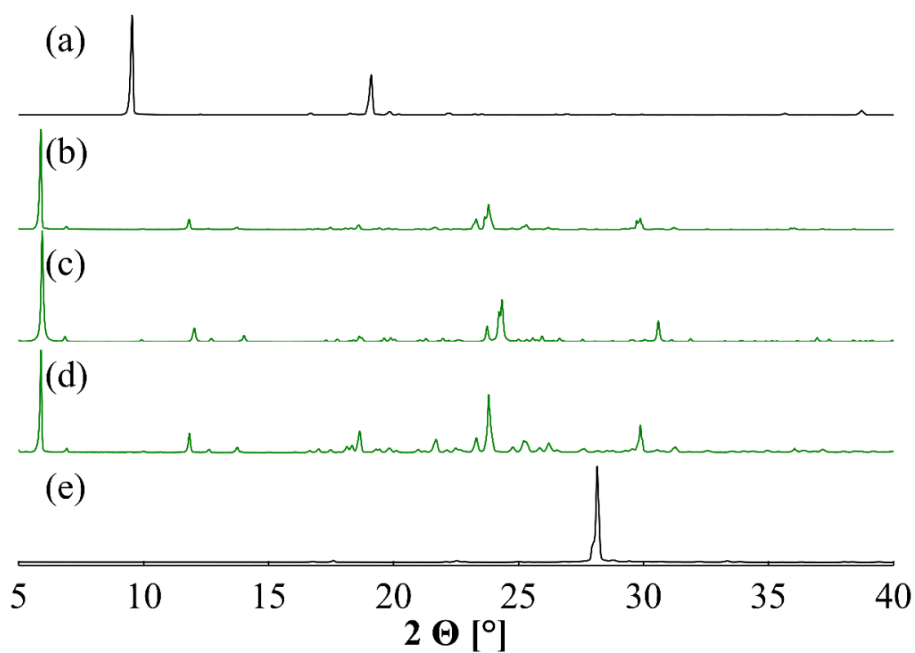


Figure S10. Powder pattern comparison of (a) recorded (S)-Pregabalin pattern, (b) (S)-Pregabalin maleate hydrate as produced from aqueous solution, (c) (S)-Pregabalin maleate hydrate pattern simulated by single crystal data with $hkl = 0\ 1\ 1$ and March-Dollase parameter of 2, (d) (S)-Pregabalin maleate hydrate as produced by liquid-assisted grinding and (e) recorded maleic acid pattern. A 2θ range from $5 - 40^\circ$ is depicted.

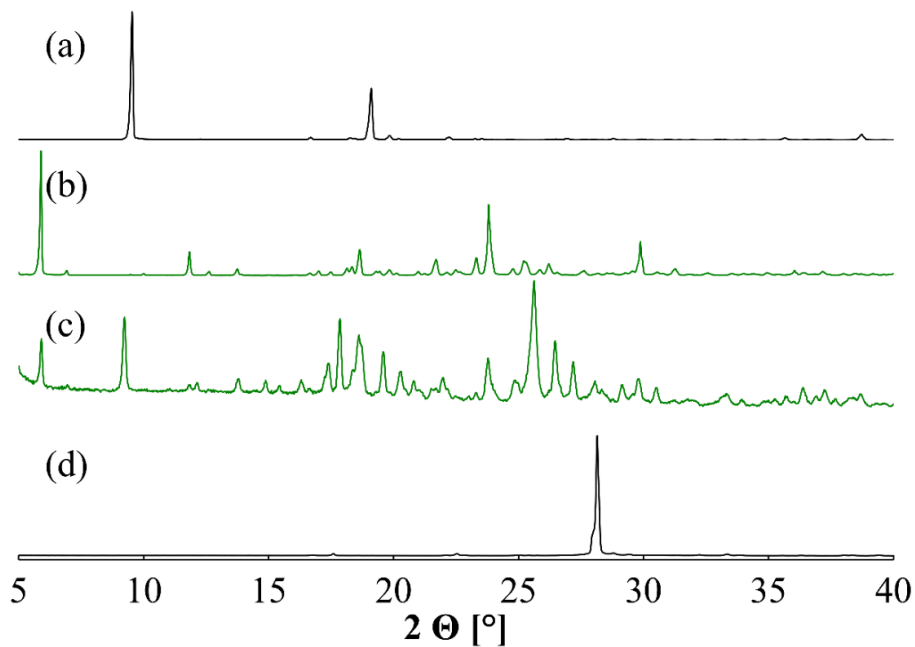


Figure S11. Powder pattern comparison of (a) recorded (S)-Pregabalin pattern, (b) (S)-Pregabalin maleate hydrate as produced by liquid-assisted grinding, (c) (S)-Pregabalin maleate pattern produced by neat grinding and (d) recorded maleic acid pattern. A 2θ range from $5 - 40^\circ$ is depicted.

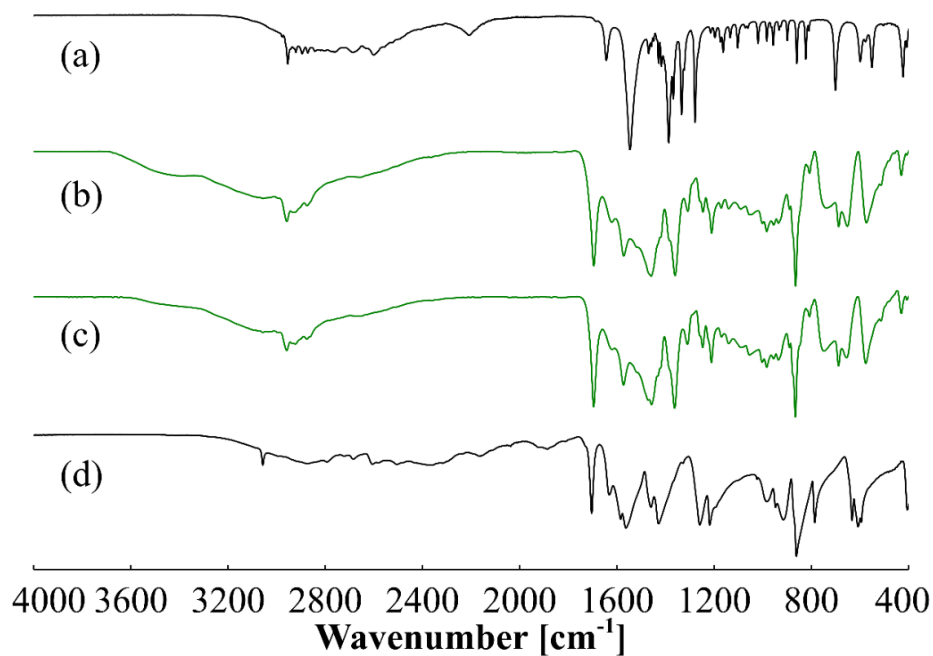


Figure S12. FT-IR spectra of (a) (S)-Pregabalin, (b) (S)-Pregabalin maleate hydrate as produced from aqueous solution, (c) (S)-Pregabalin maleate hydrate as produced by liquid-assisted grinding and (d) maleic acid. Spectra are recorded between 4000 cm^{-1} – 400 cm^{-1} .

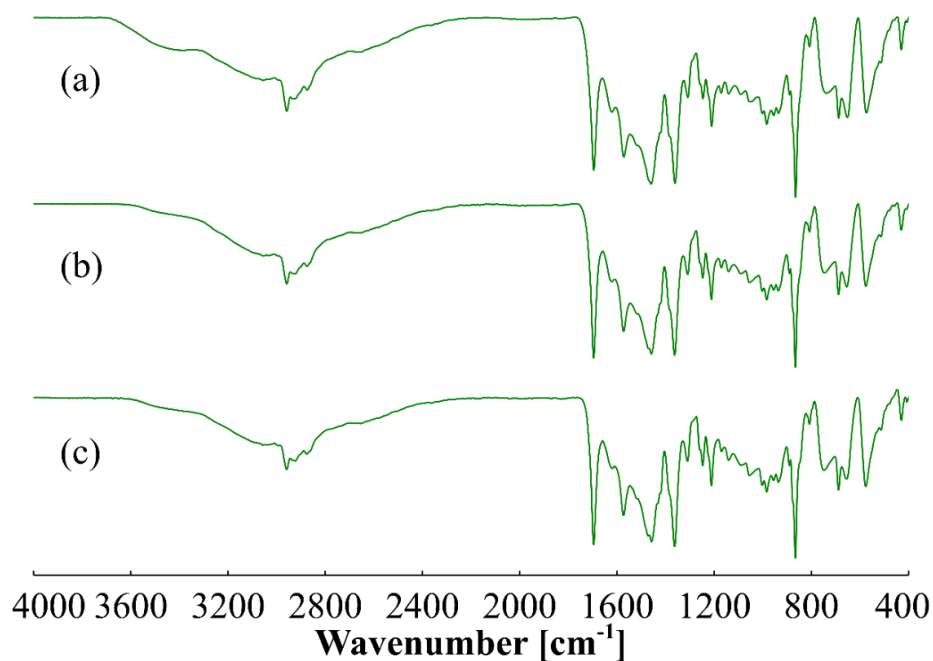


Figure S13. FT-IR spectra of (a) (S)-Pregabalin maleate hydrate as produced from aqueous solution, three days drying, (b) (S)-Pregabalin maleate as produced from aqueous solution, vacuum drying and (c) (S)-Pregabalin maleate hydrate as produced by liquid-assisted grinding. Spectra are recorded between 4000 cm^{-1} – 400 cm^{-1} .

11

5 Phenibut maleate

Table S5. Single crystal measurement details for Phenibut maleate.

Parameters	4-MA
Formula	C ₁₄ H ₁₇ N O ₆
Formula moiety	C ₁₀ H ₁₄ N O ₂ , C ₄ H ₃ O ₄
M _r [g mol ⁻¹]	295.28
Temperature [K]	100(1)
System/space group	monoclinic, <i>P</i> 21/ <i>c</i>
a (Å)	5.7053(1)
b (Å)	36.4004(5)
c (Å)	7.2941(2)
β (°)	112.200(2)
V (Å ³)	1402.51(5)
Z/Z'	4/1
Density [g/cm ³]	1.398
μ [mm ⁻¹]	0.932
T _{min} /T _{max}	0.77073/ 1.00000
F (000)	624
Crystal size [mm]	0.21 · 0.17 · 0.08
2θ range [°]	2.4 – 77.9
Completeness [%]	98.9
Recorded refl.	15078
Independent refl.	2748
Goodness-of-fit F ²	1.117
X-Ray Source	Cu Kα (λ = 1.54184)
R ₁ [%] /wR ₂ [%] /S	4.22/ 10.10/ 1.12

Phenibut maleate was received by either crystallization from aqueous solution or liquid-assisted grinding of equimolar amounts of Phenibut and maleic acid (717 mg, 4 mmol and 464 mg, 4 mmol). Both received phases must be considered impure as they do not fit the powder pattern simulated by single crystal data.

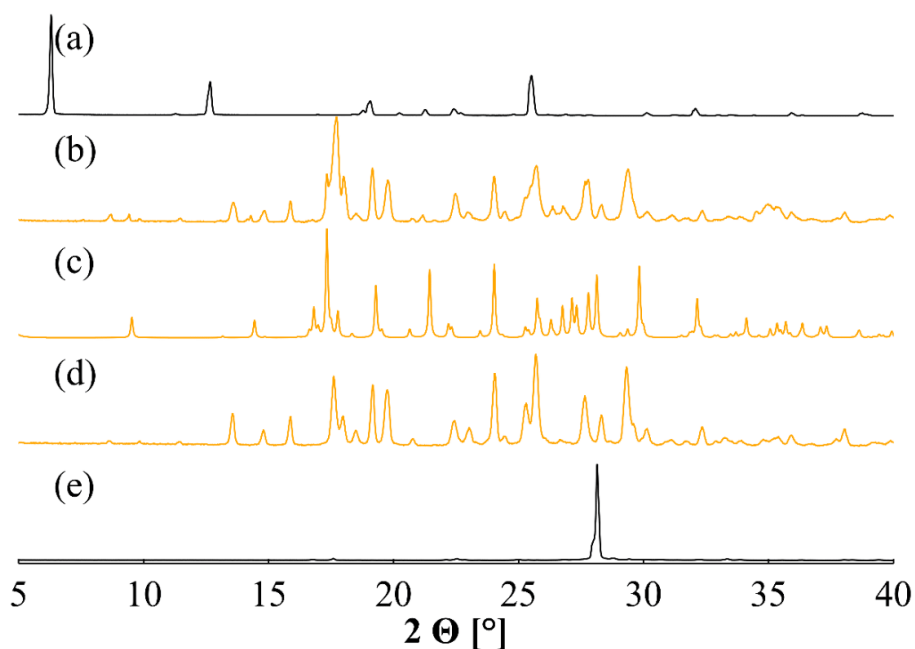


Figure S14. Powder pattern comparison of (a) recorded Phenibut pattern, (b) Phenibut maleate as produced from aqueous solution, (c) Phenibut maleate pattern simulated by single crystal data with $hkl = 1\ 8\ 1$ and March-Dollase parameter of 0.65, (d) Phenibut maleate as produced by neat grinding and (e) recorded maleic acid pattern. A 2θ range from $5 - 40^\circ$ is depicted.

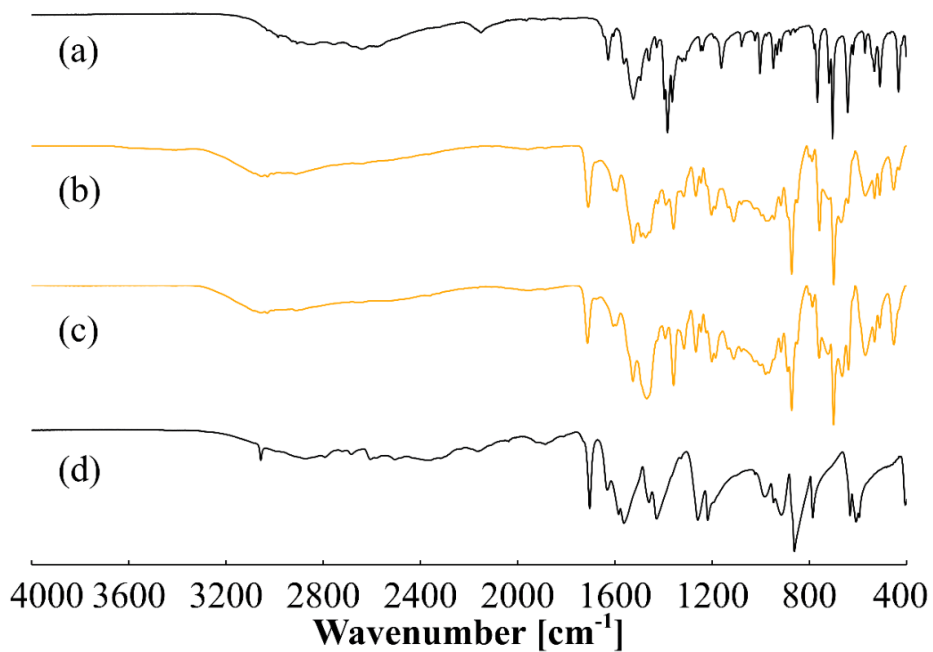


Figure S15. FT-IR spectra of (a) Phenibut, (b) Phenibut maleate as produced from aqueous solution, (c) Phenibut maleate as produced by neat grinding and (d) maleic acid. Spectra are recorded between $4000\text{ cm}^{-1} - 400\text{ cm}^{-1}$.

6 Baclofen maleate

Table S6. Single crystal measurement details for Baclofen maleate.

Parameters	5-MA
Formula	C ₁₄ H ₁₆ Cl N O ₆
Formula moiety	C ₁₀ H ₁₃ Cl N O ₂ , C ₄ H ₃ O ₄
M_r [g mol⁻¹]	329.73
Temperature [K]	100(1)
System/space group	monoclinic, <i>P</i> 21
a (Å)	5.7000(1)
b (Å)	13.5881(2)
c (Å)	9.6176(1)
β (°)	106.886(1)
V (Å³)	712.787(18)
Z/Z'	2/1
Density [g/cm³]	1.536
μ [mm⁻¹]	2.667
T_{min}/T_{max}	0.96014/ 0.96014
F (000)	344
Crystal size [mm]	0.21 · 0.11 · 0.06
2θ range [°]	4.8 – 67.1
Completeness [%]	99.8
Recorded refl.	7998
Independent refl.	2279
Goodness-of-fit F²	1.093
X-Ray Source	Cu Kα (λ = 1.54184)
R₁ [%] /wR₂ [%] /S	2.71/ 6.85/ 1.09

Baclofen maleate was received by either crystallization from aqueous solution or neat grinding of equimolar amounts of Baclofen and maleic acid (641 mg, 3 mmol and 348 mg, 3 mmol). The same product is received in both cases, though the crystallinity is lower in the milling product of Baclofen maleate.

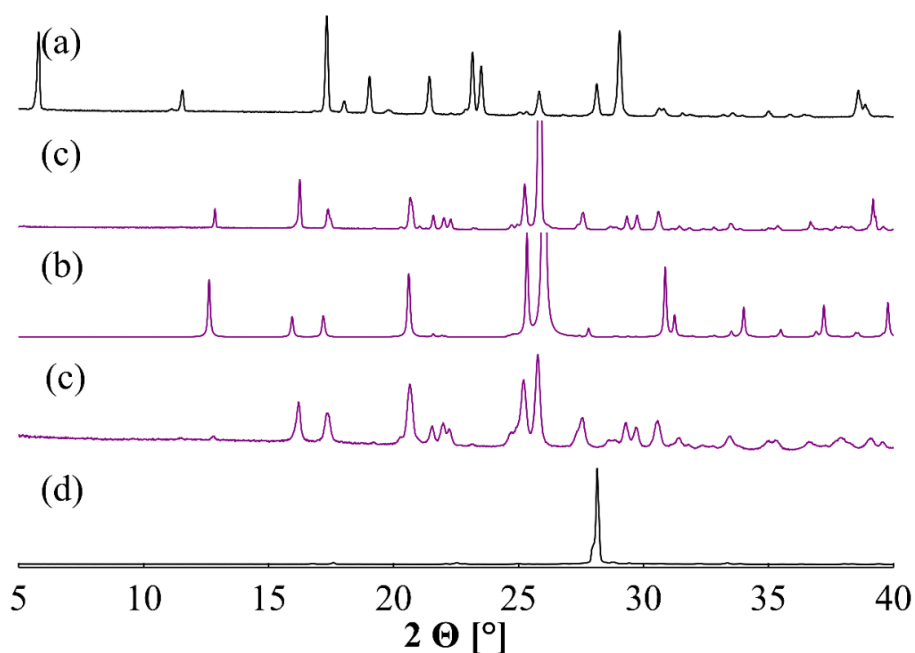


Figure S16. Powder pattern comparison of (a) recorded Baclofen pattern, (b) Baclofen maleate as produced from aqueous solution, (c) Baclofen maleate pattern simulated by single crystal data with $hkl = 0\ 0\ 7$ and March-Dollase parameter of 4, (d) Baclofen maleate as produced by neat grinding and (e) recorded maleic acid pattern. A 2θ range from 5 – 40 ° is depicted.

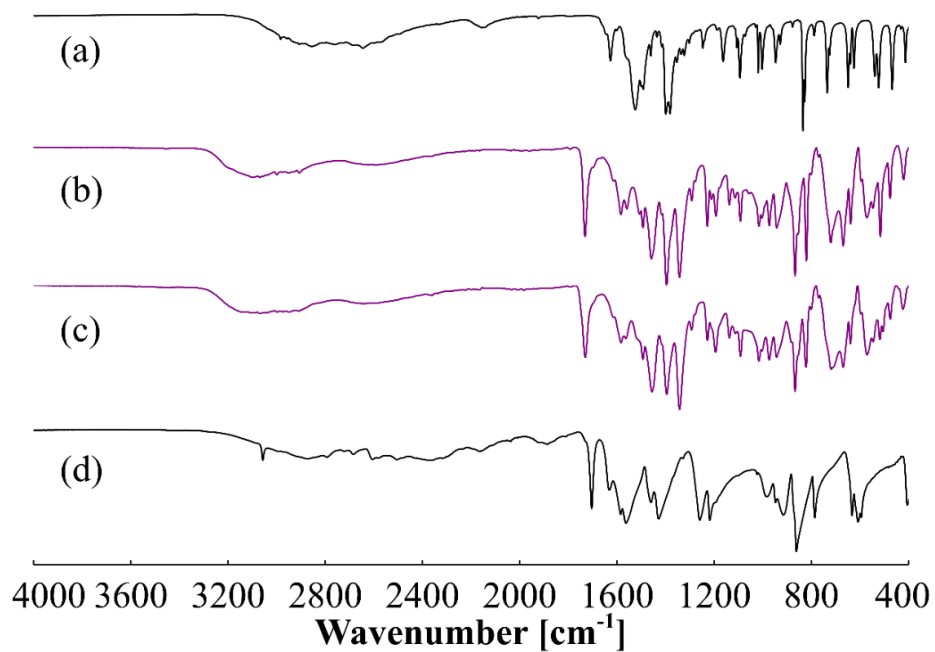


Figure S17. FT-IR spectra of (a) Baclofen, (b) Baclofen maleate as produced from aqueous solution, (c) Baclofen maleate as produced by neat grinding and (d) maleic acid. Spectra are recorded between 4000 cm^{-1} – 400 cm^{-1} .

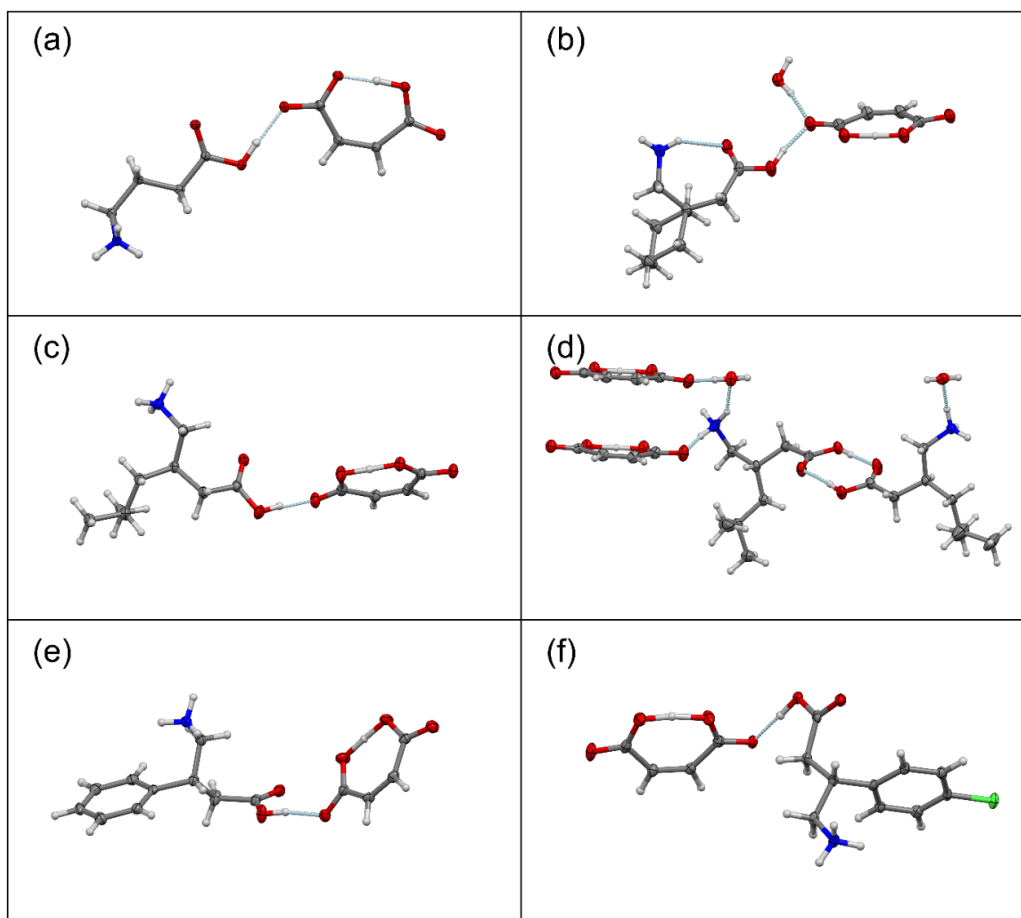


Figure S18. Depiction of the asymmetric unit in each compound that could be characterized by SCXRD: (a) GABA maleate, (b) Gabapentin maleate hydrate, (c) (rac)-Pregabalin maleate, (d) (S)-Pregabalin maleate hydrate, (e) Phenibut maleate, and (f) Baclofen maleate. Carbon atoms are depicted in grey, hydrogen atoms in white, nitrogen atoms in blue, oxygen atoms in red, and chlorine atoms in green. Hydrogen bonds occurring in the asymmetric units are shown as light blue dotted lines.

7 Solubility determination details

Solubilities were determined with $^1\text{H-NMR}$. Three samples for each single compound and three samples for each received maleate gained through grinding or solvent crystallization were prepared. For this, dispersions of the investigated compounds in water were prepared in such a way that no complete dissolution would occur after three days at $25\text{ }^\circ\text{C}$ in an incubator shaking with 60 min^{-1} . Subsequently, $50\text{ }\mu\text{L}$ of liquid were removed from the samples and added to $450\text{ }\mu\text{L}$ of D_2O prepared in an NMR-tube. $^1\text{H-NMR}$ measurements were conducted on a Bruker Avance III NMR-spectrometer at 600 MHz . Solubilities were determined by phase and baseline correction of the received spectrum in MestReNova software x64 14.2.0, application of D_2O shift on the solvent peak from the MestReNova database. Integration of a

chosen signal in the received spectrum and further integration of the solvent signal. The latter signal was always integrated in the borders of 5.000 – 4.600 ppm, the product signals were integrated in as narrow a range as possible (**Table S7**). Trace water in D₂O was considered negligible. Solubilities were calculated by the following equation:

$$S_p = \left(\frac{M_p}{\frac{I_w}{n} M_w} \rho_w \right) \quad (1)$$

Where S_p is the solubility of the API in gL⁻¹, M_p is the molar mass of the targeted API in g mol⁻¹, I_w is the value of the water integral received, n is an adjustment factor necessary if the product integration value is not one (if integral product = 1, $n = 1$, if integral product > 1, $n = 2$ because solvent is water), M_w is the molar mass of water in g mol⁻¹ and ρ_w is the density of water at 25 °C in gL⁻¹. Error was calculated as the standard deviation of the three recorded samples according to **Equation 2**.

$$V = \sqrt{\frac{\sum(x - \bar{x})^2}{(n-1)}} \quad (2)$$

Here V is the standard deviation, x is the average of the three solubility values, \bar{x} each single solubility value and n the number of samples, three.

Table S7. Solubilities of GABA and its derivatives on their own and in form of the investigated maleates and their standard deviations. The integral borders for the product peaks used for solubility calculations of samples S1 – S3 are given.

Sample	$S_p \pm V$ [gL ⁻¹]	Int. S1 [ppm]	Int. S2 [ppm]	Int. S3 [ppm]
MA	687 ± 44	6.380 – 6.300	6.380 – 6.300	6.380 – 6.300
1	2261 ± 22	1.875 – 1.800	1.875 – 1.800	1.875 – 1.800
2	174 ± 7	2.440 – 2.410	2.440 – 2.410	2.440 – 2.410
(rac)-3 • H₂O	33 ± 1	0.915 – 0.870	0.925 – 0.880	0.915 – 0.870
(S)-3	41 ± 1	0.915 – 0.870	0.915 – 0.870	0.920 – 0.875
4	15 ± 0.3	7.475 – 7.340	7.475 – 7.340	7.475 – 7.340
5	3 ± 0.1	7.475 – 7.340	7.475 – 7.340	7.475 – 7.340
1-MA_sol	704 ± 60	1.930 – 1.850	1.930 – 1.850	1.920 – 1.840
1-MA_mill	680 ± 46	1.930 – 1.850	1.930 – 1.850	1.925 – 1.845
2-MA • H₂O_sol	241 ± 8	2.530 – 2.500	2.530 – 2.500	2.530 – 2.500
2-MA_mill	218 ± 8	2.530 – 2.500	2.530 – 2.500	2.530 – 2.500
(rac)-3-MA_sol	719 ± 10	0.870 – 0.815	0.870 – 0.815	0.870 – 0.815
(rac)-3-MA_mill	559 ± 19	0.880 – 0.800	0.880 – 0.800	0.880 – 0.800
(S)-3-MA • H₂O_sol	977 ± 79	0.860 – 0.805	0.860 – 0.805	0.860 – 0.805
(S)-3-MA • H₂O_mill	809 ± 8	0.860 – 0.805	0.860 – 0.805	0.860 – 0.805
4-MA_sol	124 ± 4	7.475 – 7.340	7.475 – 7.340	7.475 – 7.340
4-MA_mill	128 ± 8	7.475 – 7.340	7.475 – 7.340	7.475 – 7.340
5-MA_sol	6 ± 0.3	7.475 – 7.340	7.475 – 7.340	7.475 – 7.340
5-MA_mill	6 ± 0.6	7.480 – 7.330	7.480 – 7.330	7.480 – 7.330

Chosen ¹H-NMR spectra recorded for these solubility measurements are shown in **Figures S18 – S31**.

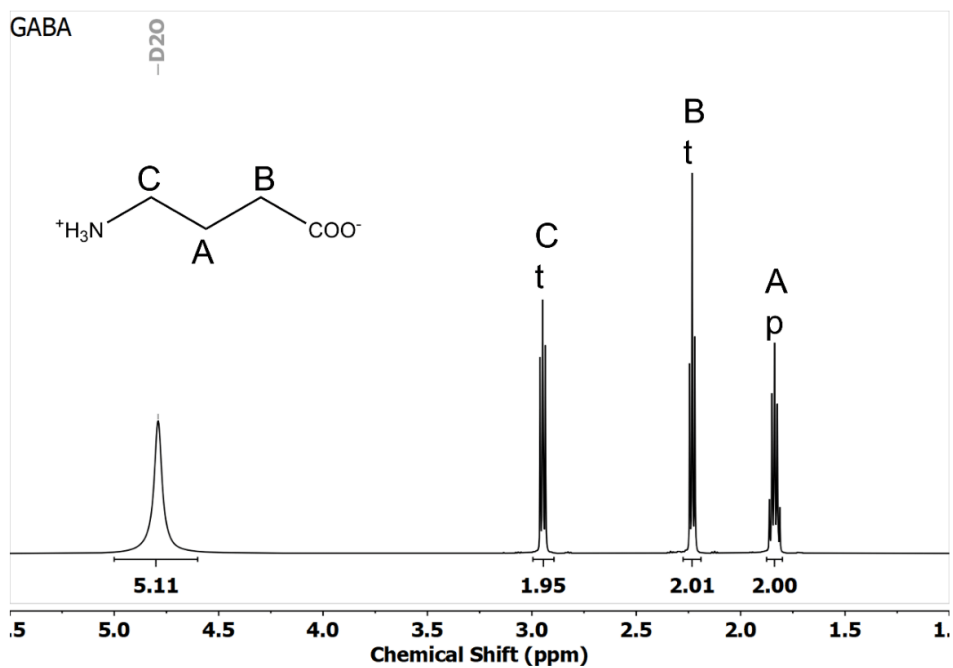


Figure S19. $^1\text{H-NMR}$ spectrum of GABA recorded in D_2O at 600 MHz.

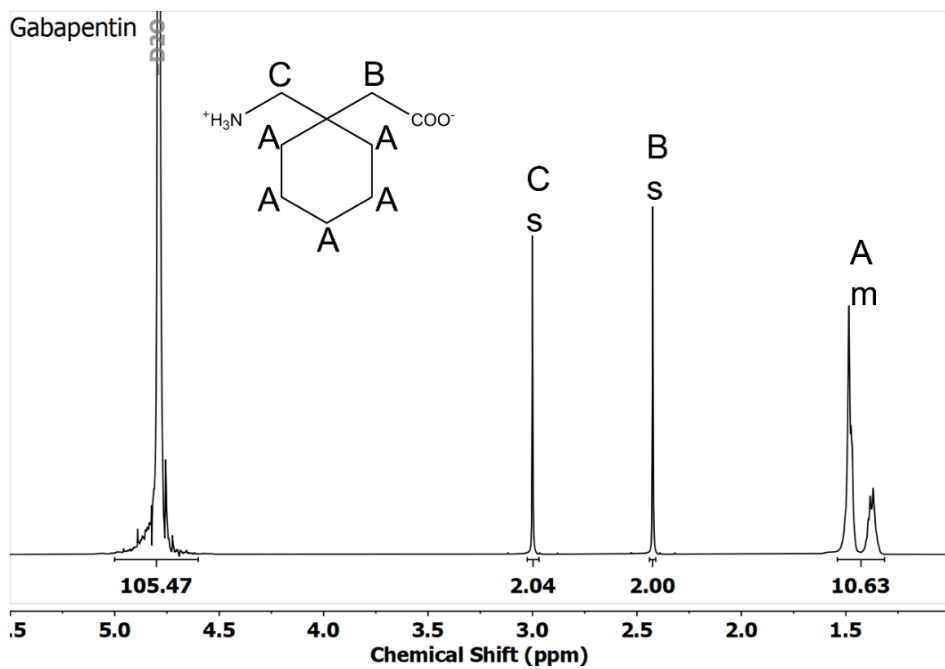


Figure S19. $^1\text{H-NMR}$ spectrum of Gabapentin recorded in D_2O at 600 MHz.

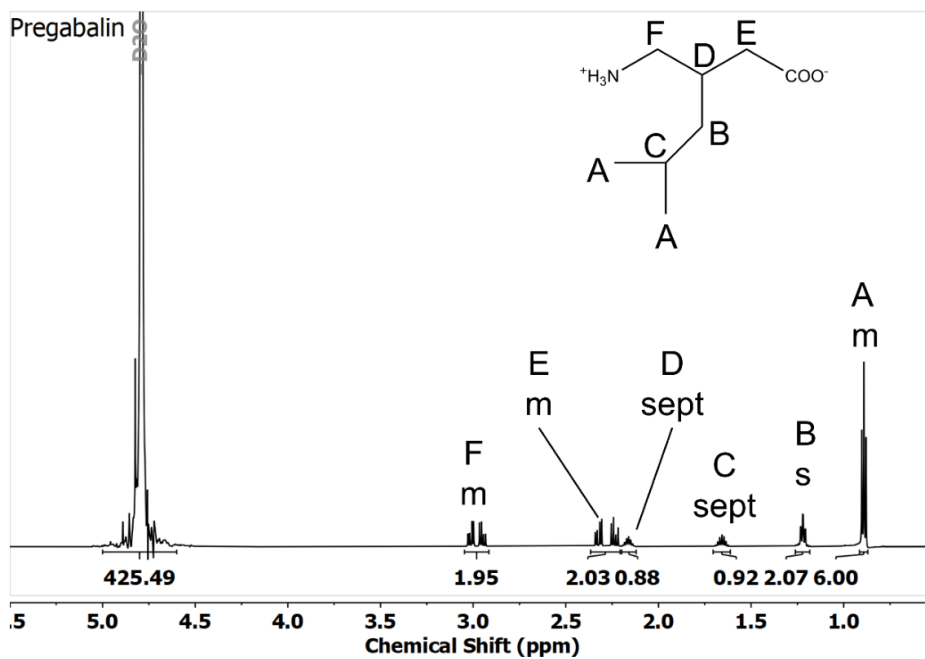


Figure S20. ¹H-NMR spectrum of (S)-Pregabalin recorded in D₂O at 600 MHz. Also represents (rac)-Pregabalin.

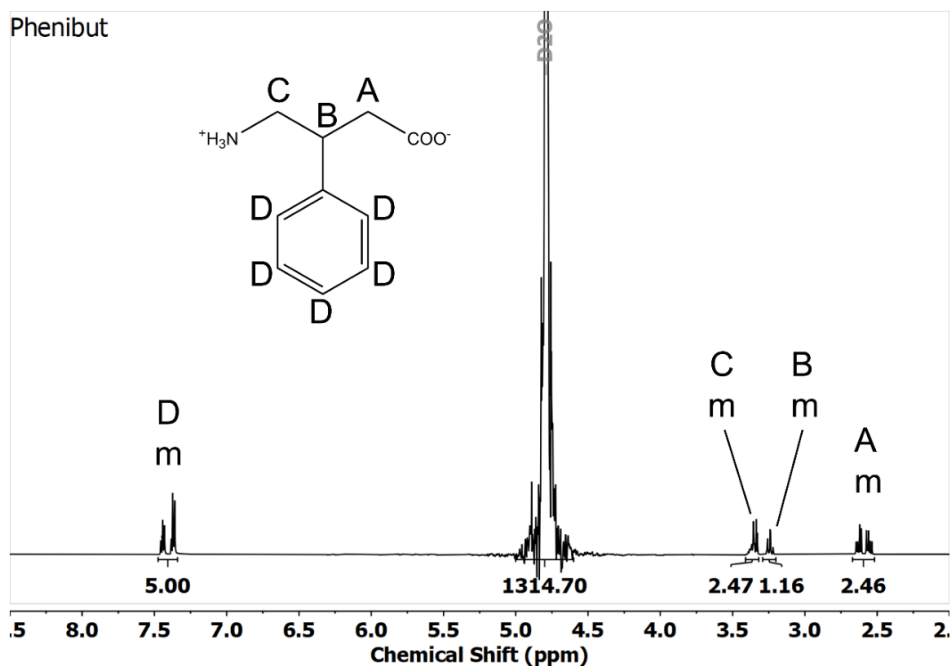


Figure S21. ¹H-NMR spectrum of Phenibut recorded in D₂O at 600 MHz.

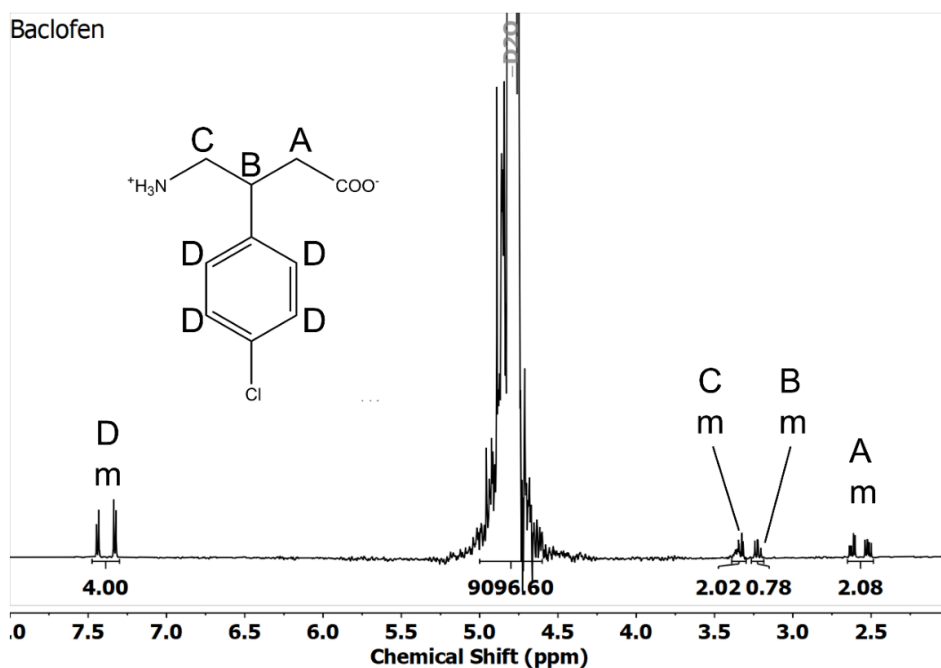


Figure S22. ¹H-NMR spectrum of Baclofen recorded in D₂O at 600 MHz.

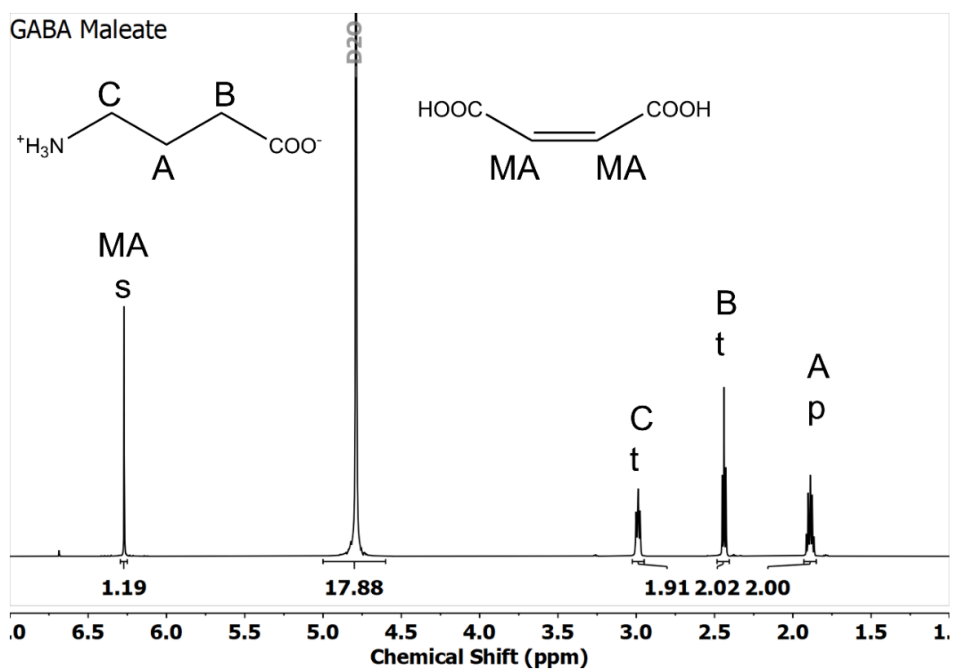


Figure S23. ¹H-NMR spectrum of GABA maleate recorded in D₂O at 600 MHz. Sample grown from solution.

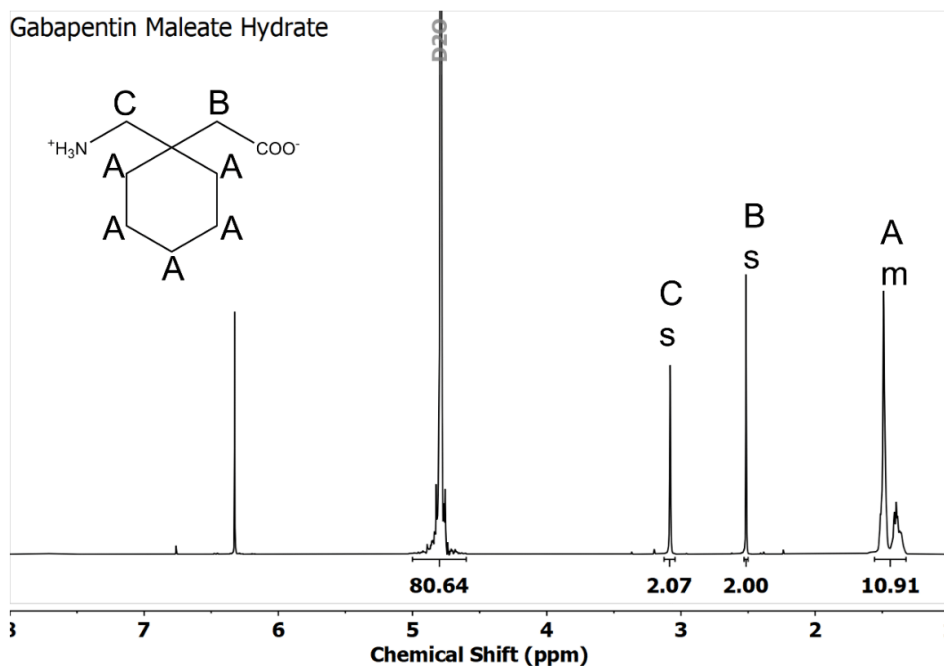


Figure S24. ¹H-NMR spectrum of Gabapentin maleate hydrate recorded in D₂O at 600 MHz.

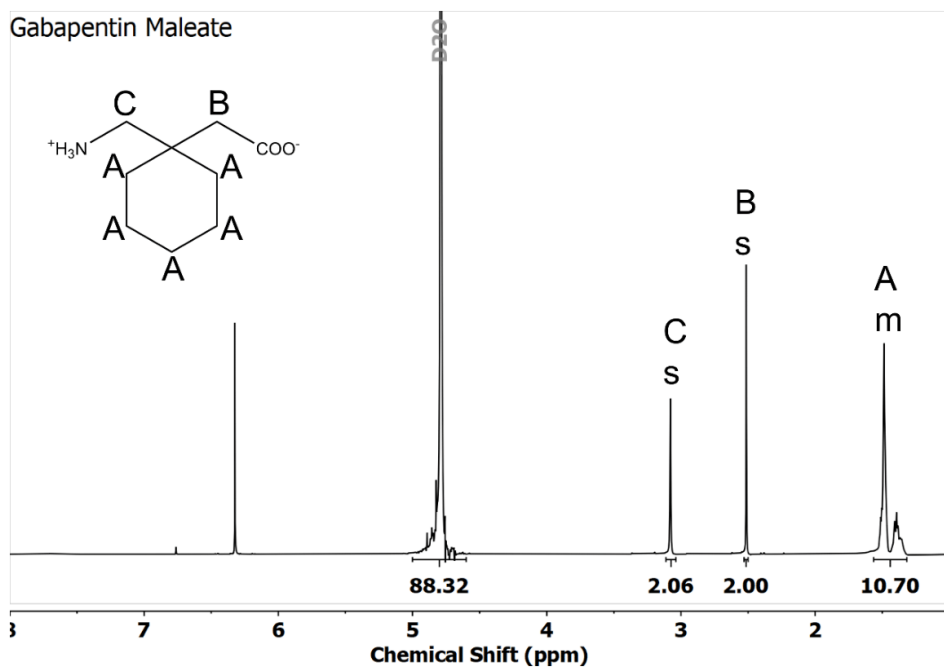


Figure S25. ¹H-NMR spectrum of Gabapentin maleate recorded in D₂O at 600 MHz.

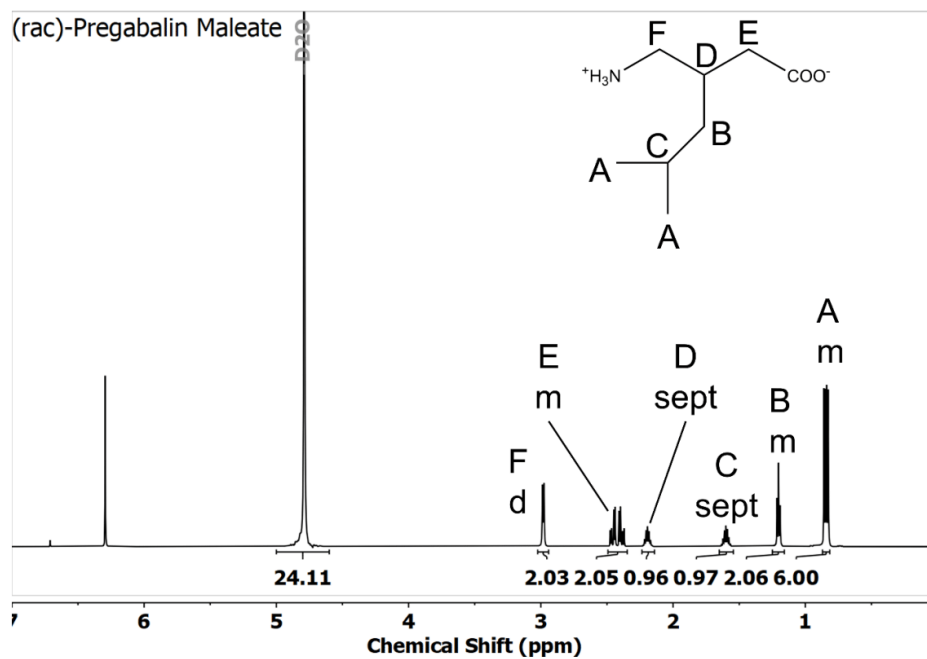


Figure S26. $^1\text{H-NMR}$ spectrum of (rac)-Pregabalin maleate recorded in D_2O at 600 MHz. Sample grown from solution.

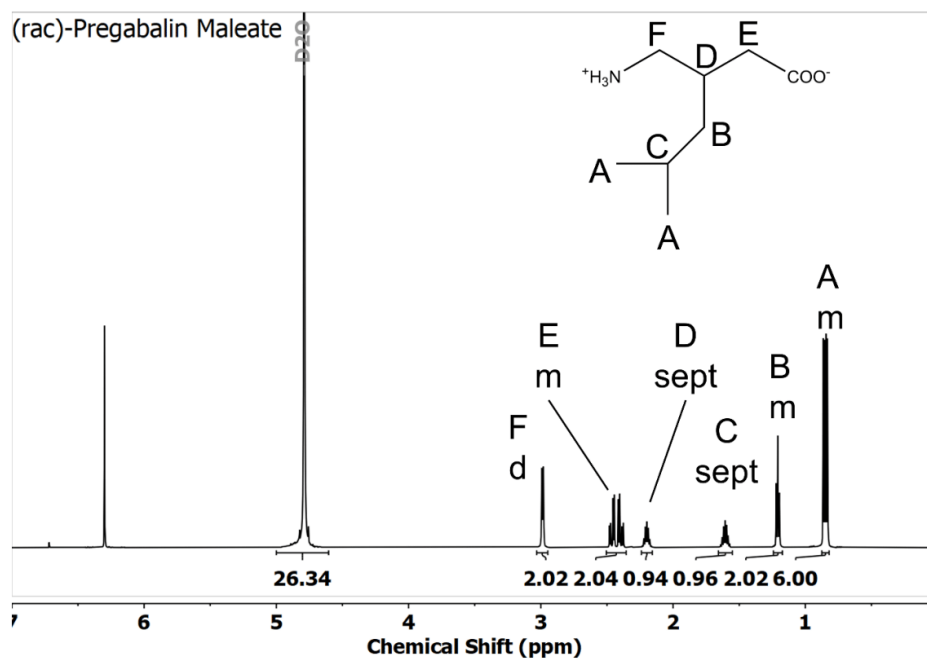


Figure S27. $^1\text{H-NMR}$ spectrum of (rac)-Pregabalin maleate recorded in D_2O at 600 MHz. Sample grown via grinding.

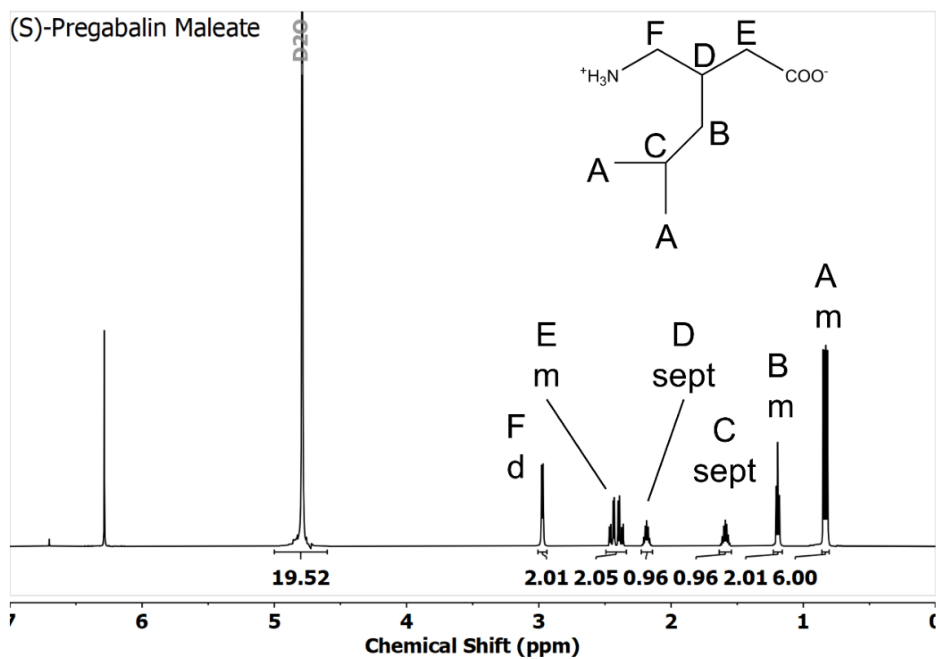


Figure S29. $^1\text{H-NMR}$ spectrum of (S)-Pregabalin maleate hydrate recorded in D_2O at 600 MHz. Sample grown from solution.

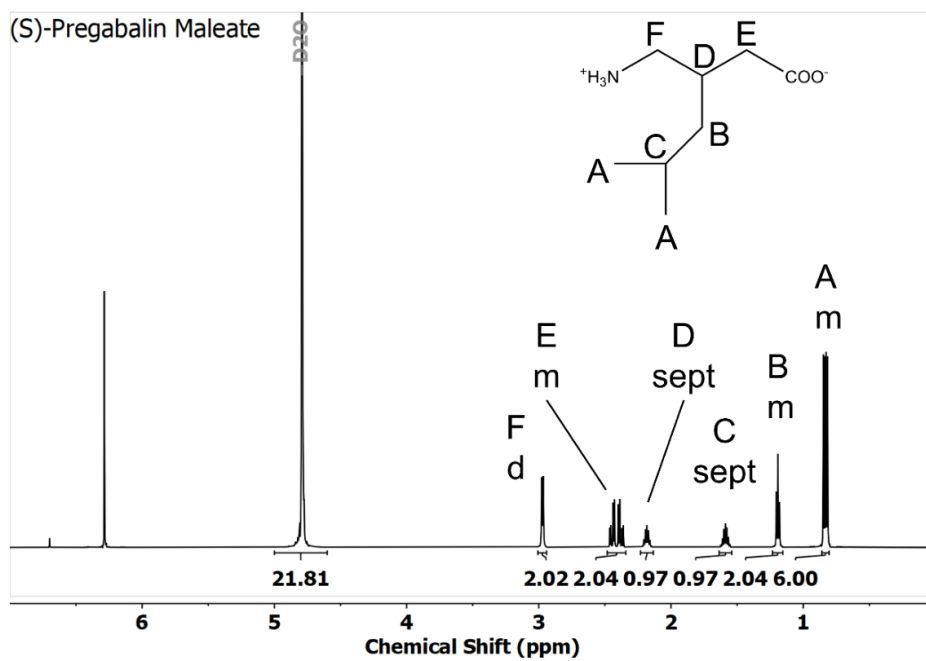


Figure S28. $^1\text{H-NMR}$ spectrum of (S)-Pregabalin maleate hydrate recorded in D_2O at 600 MHz. Sample grown via grinding.

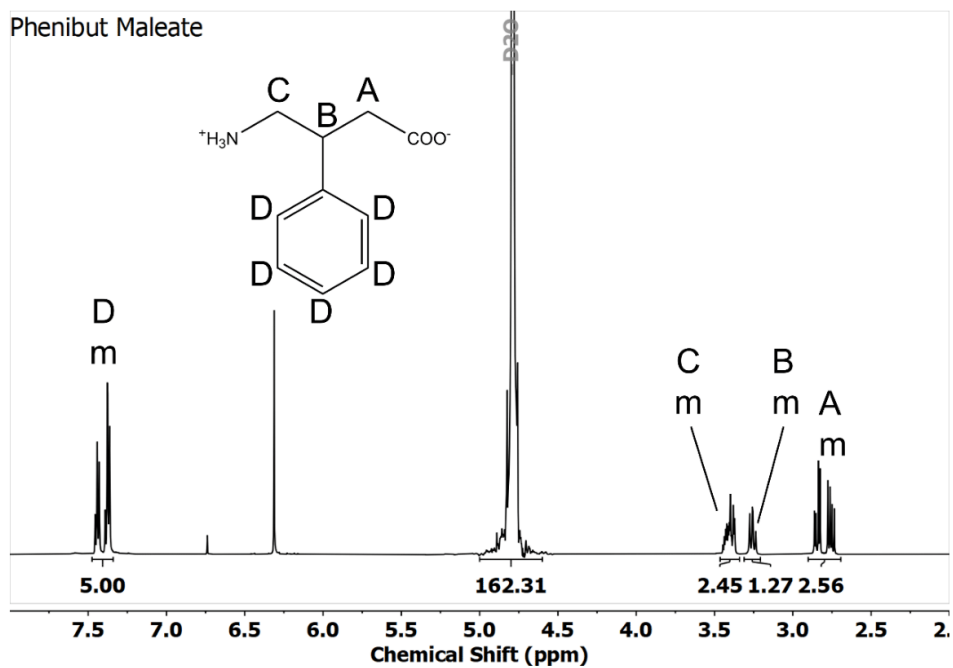


Figure S29. 1H -NMR spectrum of Phenibut maleate recorded in D_2O at 600 MHz. Sample grown from solution.

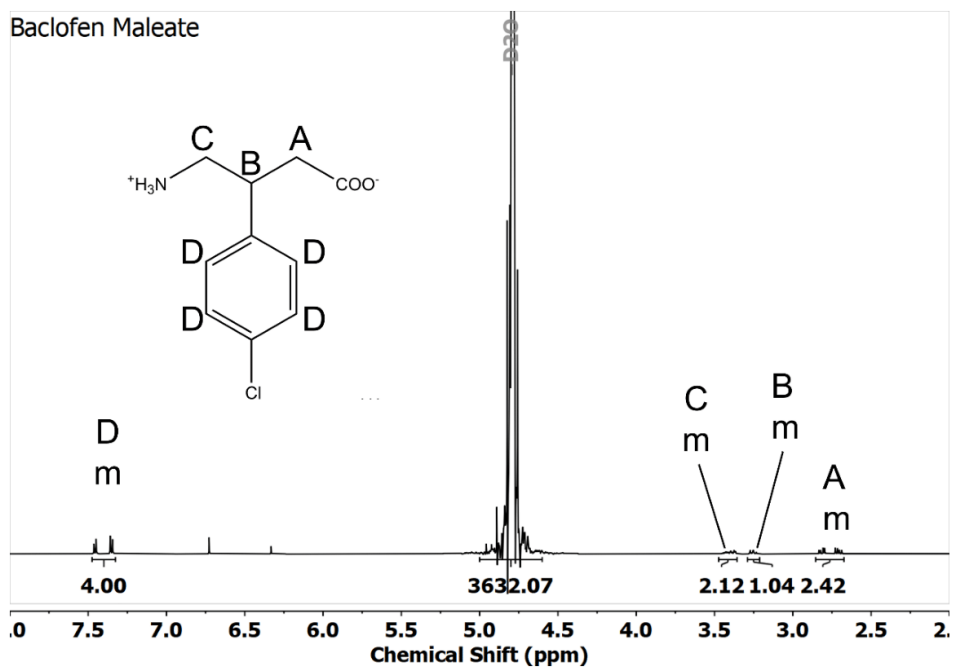


Figure S30. 1H -NMR spectrum of Baclofen maleate recorded in D_2O at 600 MHz. Sample grown from solution.

3.5 Understanding Polymorphism and Multicomponent Crystal Formation of GABA and Gabapentin

Understanding Polymorphism and Multicomponent Crystal Formation of GABA and Gabapentin

AUTHOR NAMES

Daniel Komisarek^a, Fulya Demirbas^a, Takin Haj Hassani Sohi^a, Klaus Merz^b, Carsten

Schauerte^c and Vera Vasylyeva^{a}*

Komisarek, D.; Demirbas, F.; Merz, K.; Schauerte, C.; Vasylyeva, V. Understanding Polymorphism and Multicomponent Crystal Formation of GABA and Gabapentin, Submitted to *Cryst. Growth Des.*, **Feb. 2023**

No DOI yet available.

Reprinted with permission under the *American Chemical Society Terms and Rights in the Journal Publishing Agreement* for republication in a printed thesis. Copyright 2023 American Chemical Society.

In the last paper, the polymorphism and multicomponent system formation behaviour with fumaric and succinic acids of GABA and Gabapentin were investigated. Using *multiwfn*, a comprehensive analysis of the non-covalent interactions in the crystal lattices of eleven crystal species was carried out. It was shown how the HBs in the polymorphs of GABA and Gabapentin exhibit very similar patterns and bond strengths. On the basis of this, an explanation for polymorphic phase changes in these substances was presented. For comparison, it was shown that the introduction of carboxylic acids into the crystallization process leads to the formation of a very strong HB, which subsequently has a directing influence on the remaining binding motif. The publication highlights a possible solution to the problem of unstable polymorphs via multicomponent phase formation.

Contributions-list:

- Conceptualization of this work based on literature research and feedback from Dr. Vera Vasylyeva-Shor.
- Experimental work, including single crystal synthesis, mechanochemical and solvent-based crystallization of the investigated compounds together with Fulya Demirbas.
- Measurement of SCXRD and PXRD, and FT-IR spectroscopy.
- Data evaluation of the recorded analyses.
- Analysis of structure via multiwfn together with Takin Haj Hassani Sohi.
- Manuscript preparation, including text writing, figure and table preparation, literature research and providing the supporting information.
- Revision process of the manuscript together with Dr. Vera Vasylyeva-Shor.

Understanding Polymorphism and Multicomponent Crystal Formation of GABA and Gabapentin

AUTHOR NAMES

Daniel Komisarek^a, Fulya Demirbas^a, Takin Haj Hassani Sohi^a, Klaus Merz^b, Carsten Schauerte^c and Vera Vasylyeva^{a}*

AUTHOR ADDRESS

^a Department of Inorganic and Structural Chemistry I, Laboratory for Crystal Engineering, Heinrich-Heine-University, UniversitaetsstraÙe 1, 40225 Duesseldorf, Germany

^b Inorganic Chemistry, Ruhr-University Bochum, Inorganic Chemistry I, Universitaetstrasse 150, 44801 Bochum, Germany

^c Solid-Chem GmbH, Universitaetstrasse 136, 44799 Bochum, Germany

KEYWORDS

GABA, Gabapentin, non-covalent interactions, pharmaceutical crystal engineering, hydrogen bond, polymorphism

ABSTRACT

This study aims to enhance the understanding of polymorphism and multicomponent crystal formation in single- and multicomponent species of γ -amino butanoic acid (GABA) and its pharmaceutically active derivative Gabapentin. Indicators of phase stability in these compounds are discussed around intermolecular interactions, molecular conformations, and crystallization environment. Through the atoms in molecules (AIM) model in conjunction with non-covalent interactions (NCIs) analyses of polymorphs, hydrates and multicomponent crystals, hydrogen bond (HB) strengths are quantified. Salts and co-crystals of both GABA and Gabapentin with fumaric- as well as succinic acid serve as models to highlight how strong HBs in solid-phase GABA analogues serve as the motif directing force. Reoccurring comparisons to recent literature point out decisive commonalities in crystallization behavior of zwitterionic GABA-derivatives, which shows how they can and should be understood as a whole, for possible related future products.

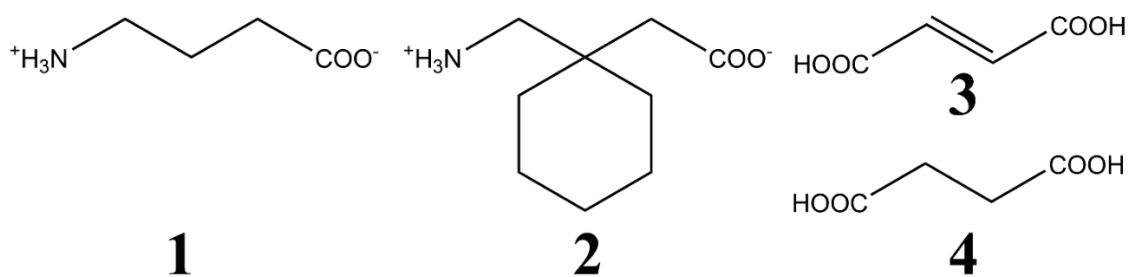
INTRODUCTION

Understanding of the solid phase remains a topic of high interest in crystal engineering of manifold applications and co-crystallization and polymorphism control are in demand for optimization of materials such as polymers¹, batteries,² luminescent compounds,³ or high energy substances.^{4,5} However, production of a reliable phase is a core objective especially in pharmaceuticals. Bernstein and Dunitz's work on disappearing polymorphs of 1995 as well as Bernstein's 2015 follow up on the same topic could be considered classics of literature in crystal engineering at this point.^{6,7} Still, more recent research is conducted providing either a broad overview,^{8,9} or specific outlook concerning single substances.^{10,11} Additionally, emerging as well as established techniques in crystal synthesis control are continuously updated.¹²⁻¹⁴ With growing accessibility and increasingly higher performances of computational methods they become more prevalent, refined, and more numerous in their uses. Examples include approachable programs like T. Lus *multiwfn* which enables atoms in molecules (AIM) analyses as well as non-covalent interaction (NCI) plotting and other useful applications.¹⁵⁻¹⁷ Furthermore, there are many tools implemented into the popular Cambridge Crystallographic Data Centre's (CCDC) *Mercury* software which provide, among numerous other uses, applications such as polymorphic- or co-crystal screening.¹⁸ Even Density Functional Theory (DFT) based programs like Giannozzi's *Quantum Espresso* (QE) or the popular *Gaussian* software show increased usage as well as performance.^{19,20} Recent advancements on computational crystal structure evaluations include insights in basics of the crystallization process,²¹⁻²⁴ but also in-depth studies specifically aimed to describe properties of singular compounds of interest.²⁵⁻³⁰ A specific compound class that receives attention for its structural behavior is that of small, zwitterionic amino acids. Glycine, which is the simplest amino acid, has acclaimed some notoriety over the years for its unpredictability regarding

its crystallization, being called ‘The Gift that Keeps on Giving’ by Boldyreva in 2021.^{31–37} While not less interesting, the structurally related γ -amino butanoic acid (GABA) has received less attention. A *Scifinder-n* search of the terms ‘Glycine AND crystal’ and ‘GABA AND crystal’ leads to 12331 and 858 results respectively, as of November 2022. GABA is a nonessential amino acid acting as a neurotransmitter inhibitor and is linked to sleep and stress relieve, with a variety of GABA-receptors named after the compound.^{38–41} Crystal structure determinations of the polymorphic **I**- and **II**-GABA forms reach back as far as to the 1970’s and 90’s,^{42,43} but recently, Wang et al. have found strong evidence on the existence of a **III**-form in their 2020 contribution.⁴⁴ In their work, they discuss the dihedral angle on GABA in congruence with interaction motifs in the different polymorphs lattices. The topic of GABA polymorphs was last discussed by Lamkowski et al. in a 2022 publication in light of pH-influences for the stabilization of **II**-GABA.⁴⁵ A plethora of Pharmaceutically Active Ingredients (APIs) are derived from GABA, such as Pregabalin, Phenibut, Baclofen and Gabapentin, which have all been discussed regarding their crystal structure over time.^{46–57} Gabapentin stands out as a reliable medication, popularly used for nearly 30 years. It’s primary applications include anti-epileptic capabilities as well as uses in the treatment of neuropathic- and inflammatory pain.^{58–60} Its crystallization was widely studied over time including its polymorphism,^{61–66} as well as co-crystallization behavior.^{67–70} Regarding its polymorphism the conformational direction in its GABA moiety is brought up time and again, lastly in 2022 by Liu and colleagues.⁷¹ In their study the polymorphic phase transfer is explained by careful analysis of Gabapentin conformations in solvent environments. The present study aims

its crystallization, being called ‘The Gift that Keeps on Giving’ by Boldyreva in 2021.^{31–37} While not less interesting, the structurally related γ -amino butanoic acid (GABA) has received less attention. A *Scifinder-n* search of the terms ‘Glycine AND crystal’ and ‘GABA AND crystal’ leads to 12331 and 858 results respectively, as of November 2022. GABA is a nonessential amino acid acting as a neurotransmitter inhibitor and is linked to sleep and stress relieve, with a variety of GABA-receptors named after the compound.^{38–41} Crystal structure determinations of the polymorphic **I**- and **II**-GABA forms reach back as far as to the 1970’s and 90’s,^{42,43} but recently, Wang et al. have found strong evidence on the existence of a **III**-form in their 2020 contribution.⁴⁴ In their work, they discuss the dihedral angle on GABA in congruence with interaction motifs in the different polymorphs lattices. The topic of GABA polymorphs was last discussed by Lamkowski et al. in a 2022 publication in light of pH-influences for the stabilization of **II**-GABA.⁴⁵ A plethora of Pharmaceutically Active Ingredients (APIs) are derived from GABA, such as Pregabalin, Phenibut, Baclofen and Gabapentin, which have all been discussed regarding their crystal structure over time.^{46–57} Gabapentin stands out as a reliable medication, popularly used for nearly 30 years. It’s primary applications include anti-epileptic capabilities as well as uses in the treatment of neuropathic- and inflammatory pain.^{58–60} Its crystallization was widely studied over time including its polymorphism,^{61–66} as well as co-crystallization behavior.^{67–70} Regarding its polymorphism the conformational direction in its GABA moiety is brought up time and again, lastly in 2022 by Liu and colleagues.⁷¹ In their study the polymorphic phase transfer is explained by careful analysis of Gabapentin conformations in solvent environments. The present study aims

to enhance the existing understanding of polymorphism in GABA (**1**) and Gabapentin (**2**) and some of their salts and co-crystals with fumaric- (**3**) and succinic acid (**4**) (**Scheme 1**).



Scheme 1. Overview on the examined compounds. **1** = γ -amino butanoic acid (GABA), **2** = Gabapentin, **3** = fumaric acid, **4** = succinic acid.

The **I**- and **II**-modifications (*P21/c* and *I4_{1cd}*) of GABA as well as the **II**- and **IV**-modifications (*P2₁/c* and *C2/c*) of Gabapentin are examined together with Gabapentin monohydrate (**I**-Gabapentin) and six multicomponent entities. Nomenclature for GABA and Gabapentin is based on the works by Liu et al. and Lamkowski et al. and their respective 2022 publications.^{45,71} In many previously held discussions on the present topic, factors like crystallization conditions and molecular conformations as well as energetic contributions on a molecular as well as crystal phase level were taken into consideration to describe phase stability for GABA and Gabapentin.^{24,44,45,61,63–66,71,72} On GABAs **I**- and **II**-forms it was shown that **I**-GABA crystallizes readily from aqueous solution, while **II**-GABA requires the presence of an additive like acetic acid for crystallization from solution or through liquid-assisted grinding. In case of Gabapentin the **II**- as well as the **IV**-form remain stable on their own once they are crystallized from the respective solvents. However, Gabapentin readily converts to its hydrate modification when water is present during the crystallization process. To enhance the understanding of how and why these processes occur, different crystalline embodiments of GABA and Gabapentin were synthesized, including polymorphs, a hydrate, salts and a co-crystal. The AIM model was used to calculate energy values

for the direct sphere of interaction of each crystallographically independent molecule in all investigated species. NCI based scatterplots were generated for these spheres of interactions and single molecule/molecule interactions to understand the influence of strong hydrogen bonds (HBs) on the crystallization product. Furthermore, the molecular dihedral angles on the GABA moieties are compared. Influences on phase stability are evaluated under consideration of experimental crystal growth conditions, energetic differences in polymorphs and energetic contributions of strong and weak hydrogen bonds and molecular conformation of the GABA moiety in each species.

EXPERIMENTAL SECTION

Synthesis:

Polymorphs & Hydrate of GABA and Gabapentin were synthesized via slow evaporation of the solvent from different solution environments: **I**-GABA and Gabapentin • H₂O were grown from aqueous solution, **II**-Gabapentin was received from methanol, **II**-GABA and **IV**-Gabapentin were obtained from aqueous solution with 2 vol% acetic acid as an additive.

Salts and Co-Crystal were all synthesized by slow evaporation of the solvent from aqueous solution. The 1:1-forms were prepared by dissolving equimolar amounts of either API with a dicarboxylic acid, the 2:1-forms with double the amount of API. The following measures were used: GABA fumarate (2:1) (**1-3**) with 206 mg (2 mmol) of **1** and 116 mg (1 mmol) of **3**; Gabapentin fumarate (2:1) (**2-3a**) with 342 mg (2 mmol) of **2** and 116 mg (1 mmol) of **3**; Gabapentin fumarate (1:1) (**2-3b**) with 171 mg (1 mmol) of **2** and 116 mg (1 mmol) of **3**; GABA succinate (2:1) (**1-4a**) 206 mg (2 mmol) of **1** and 118 mg (1 mmol) of **4**; GABA succinate (1:1)

(1-4b) 103 mg (1 mmol) of **1** and 118 mg (1 mmol) of **4**; Gabapentin:succinic acid (2:1) (**2-4**) with 342 mg (2 mmol) of **2** and 118 mg (1 mmol) of **4**.

Characterization:

PXRD measurements were conducted on Rigaku Miniflex diffractometer in $\theta/2\theta$ geometry at ambient temperature using Cu-K α radiation ($\lambda = 1.54182 \text{ \AA}$).

SCXRD measurements were conducted by choosing suited crystals from a sample and mounting under oil. Diffraction data was collected using a Rigaku Synergy S diffractometer with Hybrid Pixel Arrow detector with Cu-K α radiation ($\lambda = 1.54182 \text{ \AA}$) at 100 K, or in the case of II-GABA a Bruker Apex-II with Bruker Kappa APEX-II CCD area detector at 140 K. In each case, a colorless plate-shaped crystal was measured. Data reduction and absorption correction were performed using CrysAlisPRO v. 42 software, with numerical absorption correction based on gaussian integration over a multifaceted crystal model and empirical absorption correction with spherical harmonics, implemented in SCALE3 ABSPACK scaling algorithm.⁷³ Structure analysis was performed through direct methods (SHELXT-2015), full-matrix least-squares refinements on F2 were done using the SHELXL2017/1 program package, and structure solution and refinements were executed using Olex2-1.5 software.⁷⁴⁻⁷⁶ Hydrogen atoms were freely refined except for C-H hydrogens in GABA-succinates (1:1) and (2:1) where the following atomic displacement parameters were used: $U_{\text{iso}}(\text{H}_{\text{CH}}) = 1.2 U_{\text{eq}}$. Furthermore, O1-H1 distance was fixed in GABA-succinate 1:1 at 0.9 \AA with σ of 0.09 \AA . The proton position could not be decisively determined by single crystal x-ray analysis and thus the more likely variant (deprotonation of succinic acid, protonation of GABA) based on similar systems was chosen. Lastly, a disorder is present on Gabapentin-fumarate (2:1). A carboxyl oxygen O2 on Gabapentin is split over two positions parts

O2A (Occu: 0.58) and O2B (Occu: 0.42). For calculations a version of the file in which the disorder was not resolved was used. CCDC numbers: 2240263-2240273.

FT-IR measurements were conducted on a Bruker Tensor 27 Fourier transformed IR spectrometer in attenuated total reflectance mode in the range of 4000 cm⁻¹ to 400 cm⁻¹.

Computational methods:

Energy calculations for lattice energy differences were executed with *Quantum Espresso* (QE) *PWSCF* v. 6.6 with Perdew–Burke–Ernzerhof (PBE) model to calculate lattice energy differences between the polymorphs of GABA and Gabapentin.²⁰ The PBEsol basis set was used for atomic pseudo potentials. Our approach described in a previous publication was applied.⁵⁰ Calculations of wave functions for further processing in *multiwfn* were performed with *Gaussian* v. 16, on the B3LYP level of theory with the def2-TZVP basis set.¹⁹ AIM and scatter-plot analyses were conducted through *multiwfn* v. 3.8 and figures of NCI as well as the scatterplots were prepared in VMD v. 1.9.4 and *gnuplot* v. 5.4 respectively.^{15,77} AIM analysis was applied for molecular coordinates received from crystal structure analysis. Energy values were calculated for every distinct hydrogen bond between each crystallographically independent molecule in the crystal lattices of the investigated compounds. Interactions energies for charged and uncharged hydrogen bonds were calculated based on the model proposed by Emamian et al. in 2019.¹⁷

Additional software used includes *Mercury 2022.3.0* for structural depictions based on received .cif files and calculation of torsions,¹⁸ and *PLATON* for hydrogen bond analysis.⁷⁸

Chemicals were obtained from the following suppliers: GABA J&K Scientific, Gabapentin aber, succinic acid and fumaric acid TCI.

RESULTS AND DISCUSSION

Polymorphs of GABA and Gabapentin

To evaluate phase stability in polymorphs of **1** and **2**, three common discussion points shall be investigated: i) differences in lattice energy, ii) molecular conformations in dependence of the crystallization environment and in the final product and iii) intermolecular interactions in the crystal lattices of the various polymorphic modifications. Relative differences in lattice energies (ΔE_{lat}) between polymorphs **I-1** and **II-1** as well as **II-2** and **IV-2** were calculated by applying geometry optimization through QE on the recorded crystal structures of these compounds. Subsequently, an energy value for the ideal solid state (E_{iss}) of each system was received. By adjusting such E_{iss} values for the number of formula units in the unit cell (Z) and subtraction according to **Equation 1** ΔE_{lat} values are received.

$$\Delta E_{lat} = \frac{E_{iss1}}{Z_1} - \frac{E_{iss2}}{Z_2} \quad (1)$$

The obtained ΔE_{lat} values are in a typical range for polymorphic substances as determined by Nyman et al. in 2015.⁷⁹ Evaluation of lattice energy differences shows that polymorph **I** of **1** is more stable by -1.94 kJmol^{-1} compared to form **II-1**, and that **II-2** is more stable by -3.49 kJmol^{-1} compared to **IV-2**. If lattice energies were the only indicator of phase stability, **II-1** and **IV-2** should undergo phase transitions to **I-1** and **II-2** respectively. However, while such a transition occurs for sublimation products of **II-1**,⁸⁰ crystallization of this form from aqueous solution with acetic acid or by liquid-assisted grinding with acetic acid leads to a stable **II-1** product.^{44,45} The same can be said for **2** polymorphs, which are both obtainable by various means, but influences such as temperature treatment or mechanical stress can induce solid-solid phase transitions here as well.⁶¹⁻⁶³ Thus, a monotropic transition of **II-1** to **I-1**, given the right crystal synthesis conditions,

and differing enantiotropic transitions of **2** polymorphs have been reported in the literature. In this work the less stable **IV-2** was also produced from aqueous solution with acetic acid and remains stable over time once synthesized via this method. Previously, conformational changes on GABA moieties of **1** and **2** have been connected to stability in different crystallization environments. A depiction of torsion angles φ_1 (N1-C4-C3-C2) and φ_2 (C1-C2-C3-C4) commonly used to characterize GABA-conformations in conjunction with distinctive HBs in the discussed **1** and **2** modifications are presented in **Figure 1**. For **1** in form-**I** and **II** an eclipse conformation is present, φ_1 and φ_2 values are shifted, however. Song et al. have found that neither of both conformations is especially favorable for dissolved zwitterionic **1** in an aqueous environment, but the state of **I-1** can be considered more beneficial than that of **II-1**.⁷⁴ This is in accordance with our experimental observations for **I-1**. In case of **2** Liu and colleagues have investigated conformational changes of

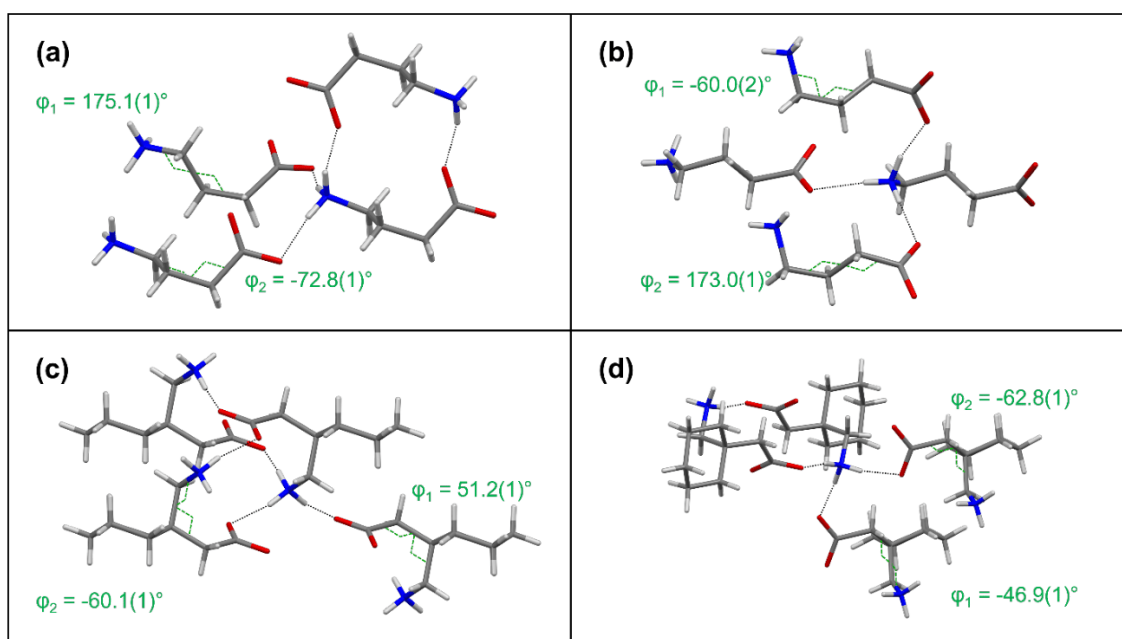


Figure 1. Torsion angles and distinctive hydrogen bonds in (a) *I*-GABA, (b) *II*-GABA, (c) *II*-Gabapentin and (d) *IV*-Gabapentin. Hydrogen bonds are depicted as black dotted lines, torsion angles as green dotted, oxygen atoms in red, nitrogen atoms in blue, carbon atoms in grey and hydrogen atoms in white.

the GABA moieties and cyclohexyl-residue in **2** polymorphs during crystallization in different environments. They have established the role conformational changes play during the nucleation and crystal growth process for these substances and explain how saturation and solvent environment favor or disfavor the formation of various **2** polymorphs.⁷¹ Thus, the formation process of the received form of **1** or **2** is significantly impacted by the crystallization environment via stabilization of a conformational state that does not necessarily lead to the most stable solid modification. The question remains, which factors lead to the higher energetic stabilization of form **I-1** and **II-2** compared to **II-1** and **IV-2** respectively? To identify factors of stability in the solid-state it is necessary to understand the intermolecular interaction motifs. Strong charge-assisted HBs stemming from the zwitterionic nature of all systems are the main occurring attractive force. In each compound, three distinct HBs are formed that show very similar lengths and angles with donor-acceptor distances between 2.7 – 2.8 Å and angles between 158° – 179°. To quantify these observations, AIM analyses was conducted on the various polymorphs and the model established by Emamian et al. in 2019 was used to calculate bonding energies for the occurring HBs (**Table 1**).¹⁷ Calculated interaction energies for the assumed charged hydrogen bonds in **II-1** quantify values between -42.87 kJmol⁻¹ for the N1-H7...O1 interaction and -56.37 kJmol⁻¹ for the N1-H8...O1 interaction. All received interaction energies can be considered as strong HBs, and except for **II-1**, two HBs in all the systems are >50 kJmol⁻¹. Even though the described HB characteristics of all investigated species do not vary too much, the connectivity of each crystallographically independent molecule does. In **I-1** a dimer interaction motif connecting two GABA molecules via their carboxylate as well as their ammonium units takes place. A similar interaction is also present in **IV-2**, and in **II-2** three Gabapentin molecules are connected in this manner. This HB motif is common among other GABA-related APIs as well and can be seen for

Table 1. Overview on the strong, distinctive hydrogen bonds in the investigated GABA and Gabapentin polymorphs. The proton acceptor distance, the donor acceptor distance, the bond angle and the binding energy calculated based on AIM analysis. Dimeric or trimeric interactions are highlighted in bold script.

Compound	H...A [Å]	D...A [Å]	D - H...A [°]	E _{bond} [kJ mol ⁻¹]
I-1				
N1-H7...O1	1.82(0)	2.734(2)	169(3)	-54.83
N1-H8...O1	1.81(1)	2.760(3)	168(5)	-55.37
N1-H9...O2	1.85(3)	2.755(7)	163(1)	-47.52
II-1				
N1-H7...O1	1.94(3)	2.790(1)	172(2)	-42.87
N1-H8...O1	1.82(2)	2.753(3)	164(8)	-56.37
N1-H9...O2	1.90(2)	2.743(9)	179(4)	-46.88
II-2				
N1-H5...O1	1.80(2)	2.753(5)	168(0)	-55.48
N1-H6...O1	1.88(2)	2.778(3)	158(6)	-48.73
N1-H7...O2	1.83(8)	2.746(7)	168(2)	-52.97
IV-2				
N1-H5...O1	1.83(0)	2.769(2)	168(2)	-53.87
N1-H6...O1	1.87(9)	2.796(2)	164(1)	-47.05
N1-H7...O2	1.81(6)	2.733(8)	164(4)	-54.65

example in Pregabalin forms,^{50,56} Phenibut,⁴⁹ or Baclofen.⁵² This motif is noticeably missing in **II-1** and could be an explanation for why **I-1** is more stable by ΔE_{lat} values. Similarly, the **II-2** trimer compared to the **IV-2** dimer might explain the ΔE_{lat} here. However, HBs are not the only interaction-type that occurs for these systems. NCI based scatterplot analyses of Interaction Region Indicator (IRI) type as proposed by Lu et al.¹⁶ of the distinctive HBs in the discussed compounds reveal the distribution of attractive and repulsive interactions in their structures (**Figure 2**). The scatterplots highlight similarities on the distribution of strong HBs are in **1** and **2** polymorphs. Additionally, it becomes obvious that repulsion is least prevalent in **II-1** as a characteristic spike in the repulsive region is entirely missing. Considerations of the interaction motif could explain this observation. The otherwise very beneficial dimeric interaction brings GABA-chains into close contact with each other, and not only subgroups with attractive potential (**Figure 3**). The molecular orientation that enables the strongly binding HB motif also causes a larger degree of repulsion. While strong HBs remain the most important force of attraction in the crystal structures of all the discussed compounds, it could be the minimization of repulsion in congruence with a beneficial

crystallization environment for the observed conformation that enables the formation of **II-1** under the right conditions compared to **I-1** in the same environment.

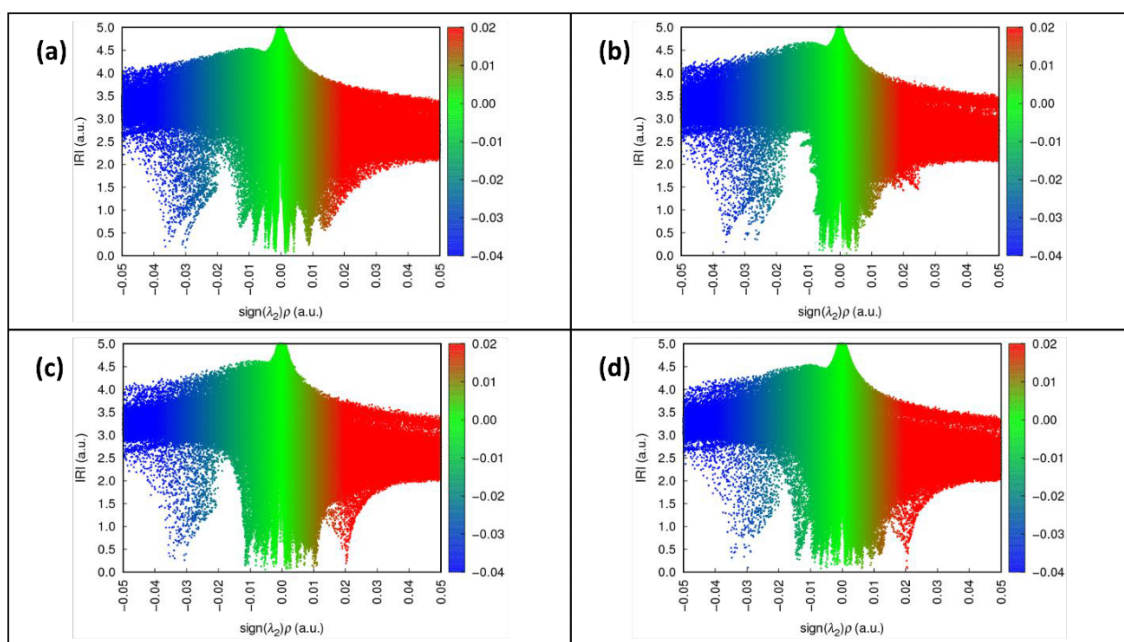


Figure 2. Scatterplots of HB-interaction spheres of **I-1** (a), **II-1** (b), **II-2** (c) and **IV-2** (d). On the x-axis, the dimensionless $\text{sign}(\lambda_2)\rho$ function describes whether a close contact is attractive or repulsive. On the y-axis, the dimensionless Interaction Region Indicator (IRI) function describes the deviation of the electron density from homogenous distribution. Colors indicate occurring interaction types: blue corresponds to hydrogen bonds, green to van-der-Waals interactions and red to intermolecular repulsion.

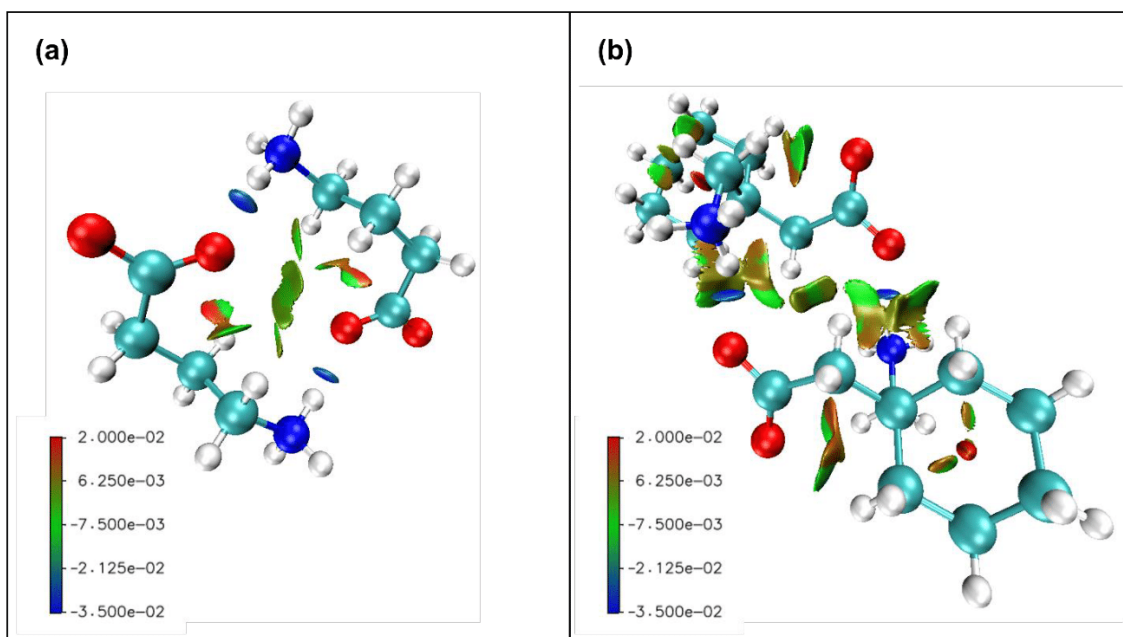


Figure 3. NCI visualisation of a dimeric hydrogen bond interaction mode in **I-1** (a) and **II-2** (b). The color scale represents where contacts are strongly attractive such as hydrogen bonds (blue), weakly attractive like van-der-Waals (green), or repulsive (red).

Monohydrate of Gabapentin (Gabapentin I)

The monohydrate of **2** is classified as its **I**-form,⁶³ and given its propensity to form if water is present this does not seem surprising. While Lin et al. have reported that **I-2** can be converted to **II-2** under dry milling conditions for 2 h, we have found that the opposite can also be the case (**Figure 4**). Attempting to neat grind **II-2** for 30 min at 25 Hz with no additional additive's led to the formation of a phase mixture of **II-2** and **I-2**.

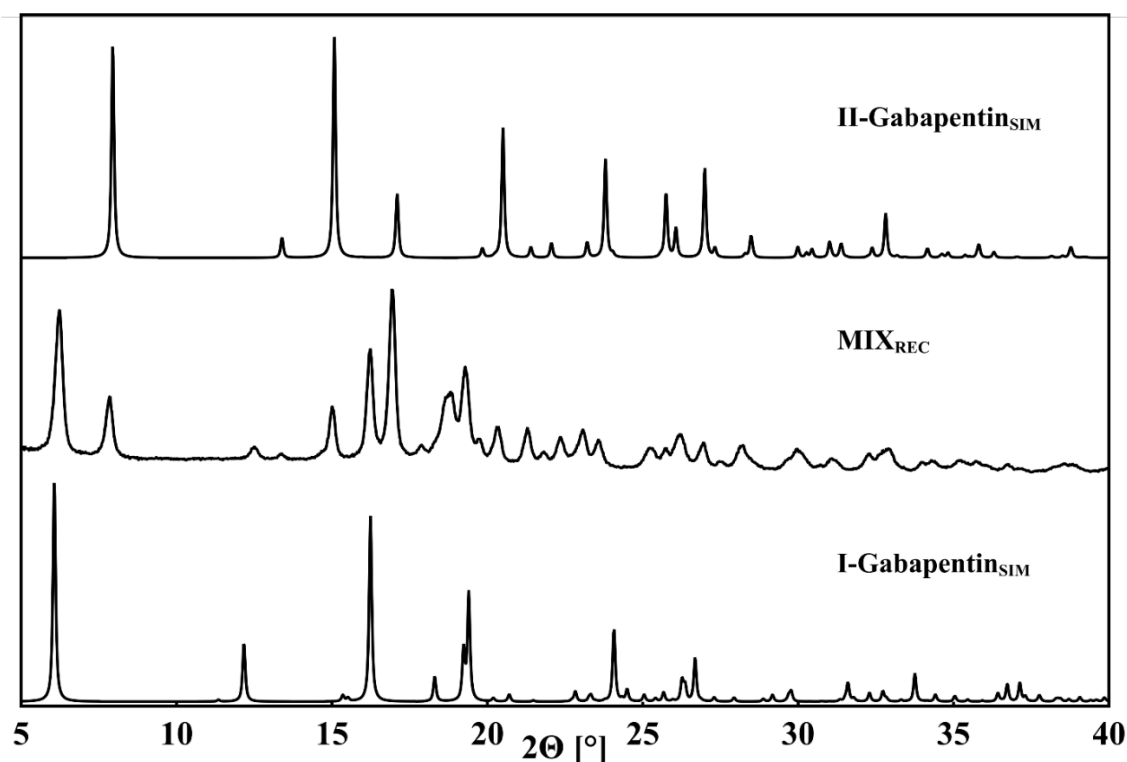


Figure 4. Powder pattern of a mixture of I- and II-Gabapentin received after 30 min of neat grinding at 25 Hz. Patterns were recorded in a range of 5° – 40°.

The milling vessel was not heat-dried prior to this experiment and thus adsorbed water from either the vessel walls or vapor from the air must have enabled the hydrate formation. Similar behavior was observed for Baclofen and Phenibut in the past.⁴⁸ Furthermore, solvent crystallization of **2** from aqueous solution without the using right additives leads to the formation of the hydrate. Taking into consideration the conducted structural observations on **1** and **2** polymorphs the formation of **I-2** appears unlikely at first (**Figure 5**). Investigation of the interaction motif reveals the absence of any dimers which were deemed as a beneficial interaction motif in **I-1**, **II-2** and **IV-2**. Additionally, the scatter plot indicates no noteworthy absence of repulsion. Instead of only three distinctive HBs all occurring between ammonium and carboxylate subgroups there are six different HBs formed.

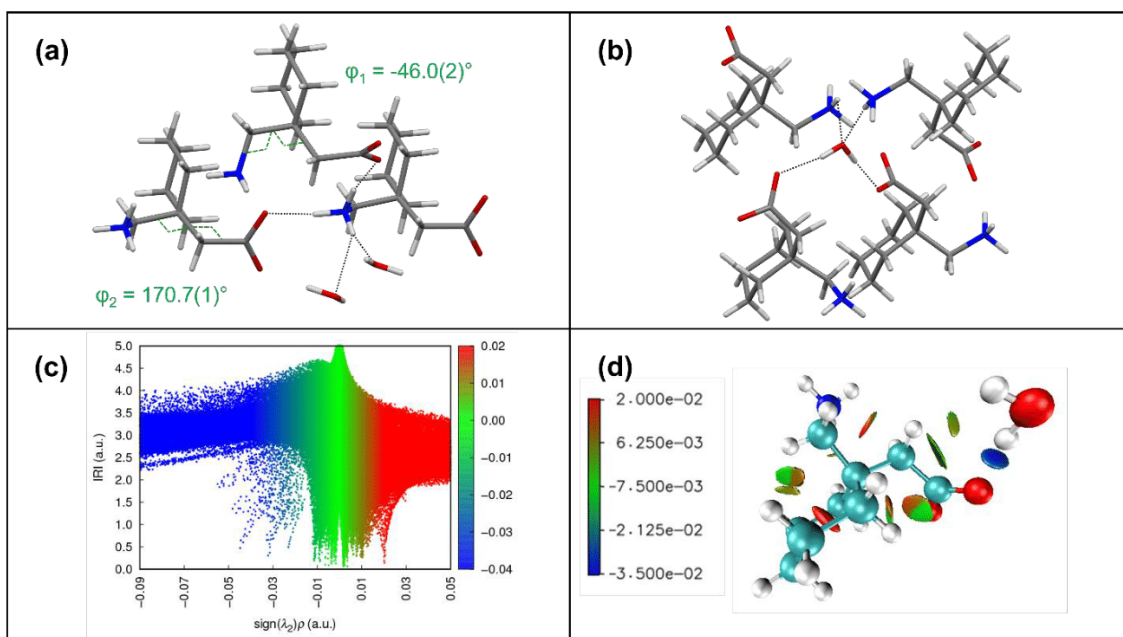


Figure 5. Selected structural properties of **I-2**. The distinctive hydrogen bonds for each independent **2** molecule and their torsions φ_1 and φ_2 (a), distinctive hydrogen bonds for each independent water molecule (b), scatterplot of interactions for motif depicted in (b) (c), and hydrogen bond between water and **2** with water as donor, highlighting the strength of this interaction (d).

Two HBs occur between carboxylate and ammonium subunits of **2** molecules, a bifurcated HB exists between N1-H7...O3 of two water molecules and water further connects to two carboxylate oxygens through its hydrogens. The scatterplot indicates the presence of stronger HBs than in the anhydrous polymorphs. Quantification of the hydrogen bond strengths shows that N1-H6...O1 and those involving water as a HB-donor are surprisingly beneficial (**Table 2**).

Table 2. Overview on the strong, distinctive hydrogen bonds in Gabapentin monohydrate. The proton acceptor distance, the donor acceptor distance, the bond angle and the binding energy calculated for charged HBs are shown.

I-2	H...A [Å]	D...A [Å]	D - H...A [°]	E_{bond} [kJ mol⁻¹]
N1-H5...O1	1.88(3)	2.842(2)	166(2)	-51.46
N1-H6...O1	1.73(2)	2.752(2)	173(2)	-66.71
N1-H7...O3	1.99(3)	2.802(2)	152(3)	-37.01
N1-H7...O3	2.53(3)	3.051(2)	118(2)	-16.67
O3-H18...O2	1.85(3)	2.746(2)	170(3)	-48.70
O3-H19...O2	1.82(3)	2.752(2)	176(2)	-49.12

With a binding energy of $-66.71 \text{ kJmol}^{-1}$, N1-H6...O1 surpasses any HB in anhydrous **1** or **2** forms by more than 10 kJmol^{-1} . As such it seems likely that the multitude of strong HBs formed, even those involving water as a donor and especially the strong N1-H6...O1 interaction are the reason why **I-2** has such a propensity to form in the presence of water. The HB motif of **I-2** indicates that intermolecular attraction strength becomes the main force in dictating the structural makeup as no sufficiently strong competing influences take place.

Multicomponent systems with fumaric acid (3)

The introduction of a co-former with the potential to form strong hydrogen bonds appears to confirm the conducted observations regarding the crystal structural makeup for **1** and **2** based systems. In all presented fumarates an anhydrous salt is formed, where **3** is deprotonated once or twice and carboxylate residues of **1** or **2** are protonated to carboxyl groups. However, the influence of the crystallization environment remains intact in so far that the chosen amount of **3** can affect which salt of **2** is received, the 2:1-form **2-3a** or its 1:1 modification **2-3b**. Depending on the amount of **3** introduced into the supramolecular crystallization, one or the other form is favored (**Figure 6**). Salt **2-3b** is formed once enough **3** is present, with **2-3a** only being produced when this amount is exceeded. The packing motif is more comparable in **1-3** and **2-3b** than between the **2** salts. There are four distinctive HBs formed in each case, one via the **1** or **2** carboxyl to a **3** carboxylate and further three for each ammonium hydrogen to a different **3** carboxylate oxygen (**Figure 7**). Thus, it appears that in a 2:1 system **3** molecules become deprotonated from both sides and adducts with either **1** or **2** molecules are formed. The ammonium residue enables a three-dimensional connection of this motif. Concerning the torsion angles, no clear relation to polymorphs or hydrate of **1** and **2** can be observed.

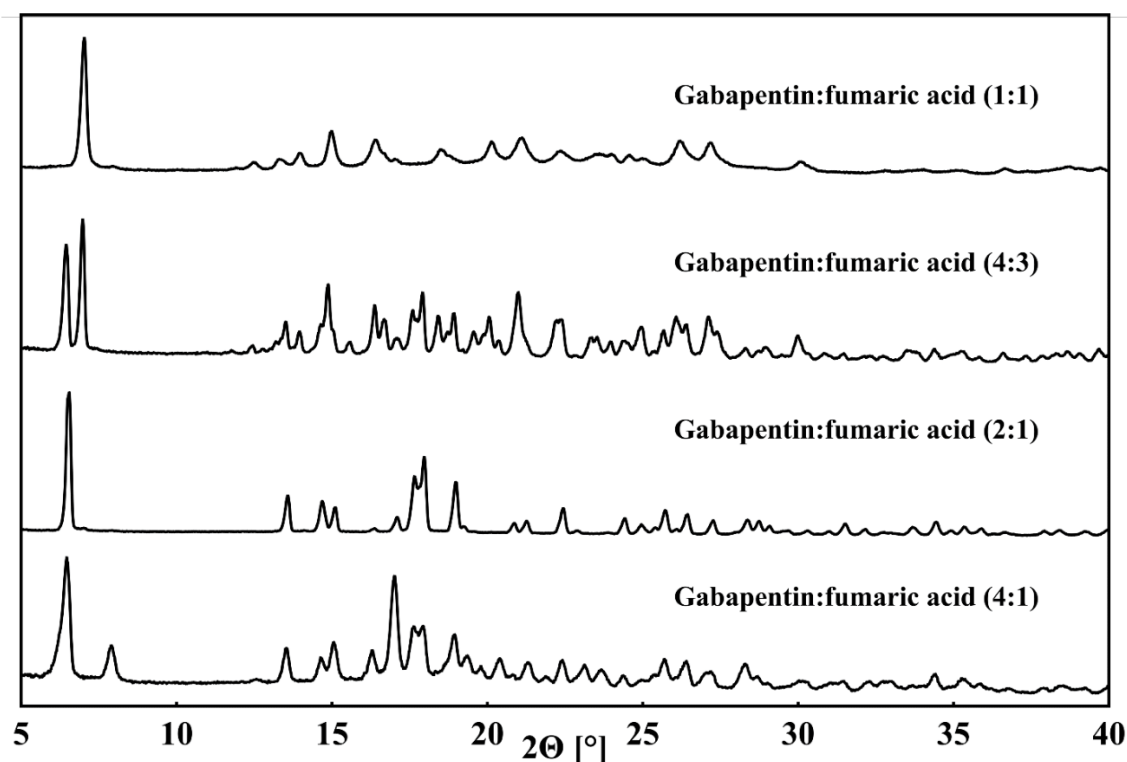


Figure 6. Selected powder patterns of neat grinding crystallizations of Gabapentin and fumaric acid. Products received by compound ratios of 1:1, 4:3, 2:1 and 4:1 are shown. Patterns were recorded in a range of 5° – 40°.

This highlights how the changed crystallization conditions and interactions overshadow molecular conformations that are favorable for single component phases. A quantification of energy values for the occurring HBs indicates how strong HBs favor the formation of the salts over the single component polymorphs (**Table 3, Figure 8**). A strong carboxyl/carboxylate HB with an interaction energy of 65.80 kJmol⁻¹ in **1-3** and -73.09 kJmol⁻¹ in **2-3a** supports the argument of acid/base adduct formation and subsequent growing around the ammonium subunit. With these various hydrogens a uniform HB motif comparable in strength to single component polymorphs is formed. Maybe the most interesting out of the three presented fumarates is **2-3b**. Its motif is more complex than in the other fumarates, consisting of two independent **2** and **3** molecules each.

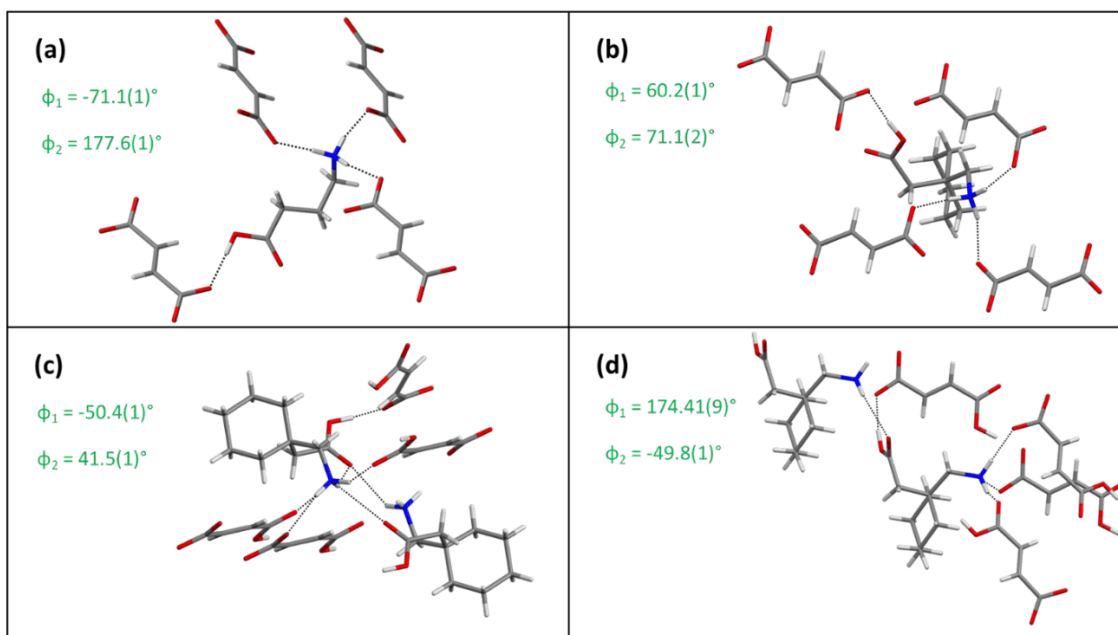


Figure 7. Torsion angles and selected hydrogen bonds for (a) **1-3**, (b) **2-3a**, (c) first distinctive Gabapentin molecule in **2-3b** and (d) second distinctive Gabapentin molecule in **2-3b**. Hydrogen bonds are depicted as black dotted lines, torsion angles are only depicted as values for better visibility, oxygen atoms in red, nitrogen atoms in blue, carbon atoms in grey and hydrogen atoms in white.

Furthermore, it forms 13 distinctive HBs that show a much higher variation in bond strengths, lengths, and angles than any of the afore mentioned systems. It is striking how these bonds are nearly evenly split between the distinctive **2** and **3** molecules. The two different **2** molecules never interact with each other and neither do the two independent **3** molecules. The connection between these two symmetrically unrelated motifs is realized with HBs among **2** and **3** entities. HBs formed between carboxyl O-H and carboxylate oxygen stand out, with bond strengths between $-65.75 \text{ kJmol}^{-1}$ and $-111.08 \text{ kJmol}^{-1}$. The favorability of these interactions apparently allows for more weaker interactions and less uniformity compared to the other discussed systems. IRI scatterplots confirm the strength of HB, especially prevalent by the spike in the highly attractive region in **2-3b**. These occurring spikes in regions of highly attractive HBs visually

highlight how strong the described carboxyl/carboxylate bonds for this system, but also the other fumarates, are.

Table 3. Overview on the strong, distinctive hydrogen bonds in the fumarates of GABA and Gabapentin. The proton acceptor distance, the donor acceptor distance, the bond angle and the binding energy calculated for charged HBs are shown.

Compound	H...A [Å]	D...A [Å]	D - H...A [°]	E _{bond} [kJmol ⁻¹]
1-3				
N1-H8...O3	1.89(9)	2.785(9)	163(6)	-48.84
N1-H9...O4	1.91(0)	2.785(1)	164(3)	-49.63
N1-H10...O4	1.94(2)	2.849(2)	166(1)	-44.02
O1-H1...O3	1.72(2)	2.606(7)	179(2)	-65.80
2-3a				
N1-H6...O4	1.81(2)	2.761(0)	174(6)	-58.11
N1-H7...O4	1.836(16)	2.746(4)	162(2)	-53.54
N1-H8...O3	1.935(18)	2.807(7)	151(7)	-45.58
O1-H1...O3	1.68(3)	2.644(3)	174(2)	-73.09
2-3b				
N1-H6...O2	2.043(15)	2.806(0)	141(0)	-35.27
N1-H7...O10	2.534(17)	3.166(6)	126(8)	-14.97
N1-H7...O12	2.005(15)	2.800(1)	144(6)	-37.23
N1-H8...O2	2.486(16)	2.933(8)	109(5)	-17.06
N1-H8...O12	1.973(16)	2.813(2)	148(5)	-38.97
N2-H24...O4	2.597(15)	3.160(8)	130(8)	-14.74
N2-H24...O8	2.032(16)	2.798(1)	142(0)	-33.00
N2-H25...O9	1.948(15)	2.838(7)	163(0)	-41.64
N2-H26...O6	1.875(17)	2.816(6)	178(1)	-48.08
O1-H1...O5	1.51(2)	2.507(0)	175(2)	-111.08
O3-H19...O9	1.73(2)	2.644(7)	172(9)	-65.75
O7-H39...O6	1.65(2)	2.559(0)	170(5)	-76.81
O11-H42...O10	1.50(2)	2.525(5)	178(3)	-110.63

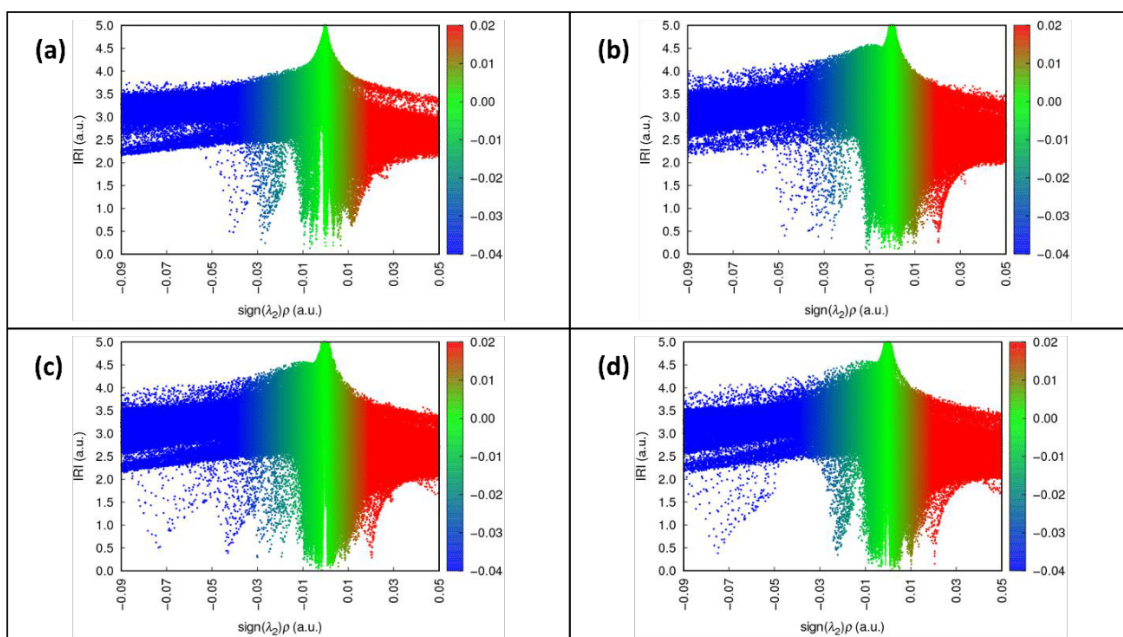


Figure 8. Scatterplots of HB-interaction spheres of **1-3** (a), **2-3a** (b), the interaction sphere around the first distinctive **2** molecule in **2-3b** (c) and the same for the second distinctive **2** molecule in **2-3b** (d). Colors indicate occurring interaction types: blue corresponds to hydrogen bonds, green to van-der-Waals interactions and red to intermolecular repulsion.

Multicomponent systems with succinic acid (**4**)

Multicomponent crystalline systems formed with **4** show many similarities to the described fumarates (**Figure 9**). Consideration of the torsion angles highlights a behavior that could be observed in **3**-forms as well, in so far that no real comparison to single component polymorphs of **1** or **2** can be made. It appears the crystallization conditions involving **4** favor other molecular orientations for **1** or **2** than with **3** or without additional co-formers. However, contrary to **3** based salts there are two entities produced with **1** instead of **2**, the 2:1 **1-4a** phase and its 1:1 modification **1-4b**. These systems also mirror another property of the **2-3** salts, in that one of them, namely **1-4a**, shows a more complex motif with more crystallographically distinct molecules while **1-4b** is simpler and consists of one independent **1** and **4** molecule each. In case

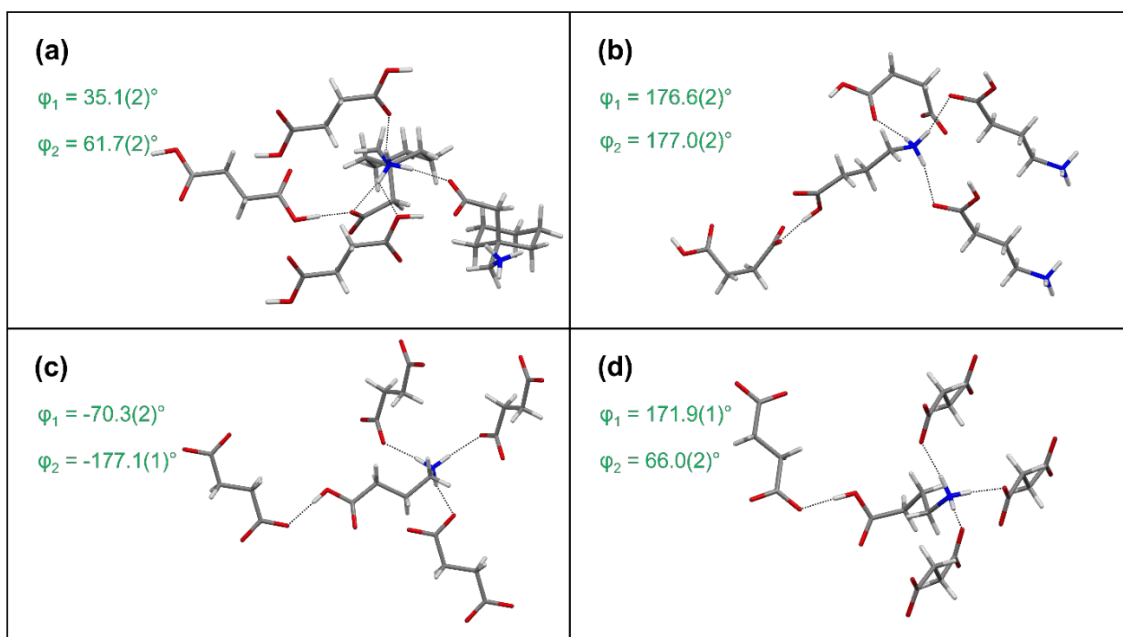


Figure 9. Torsion angles and selected hydrogen bonds for (a) **2-4**, (b) **1-4a**, (c) first distinctive GABA molecule in **1-4b** and (d) second distinctive GABA molecule in **1-4b**. Hydrogen bonds are depicted as black dotted lines, torsion angles are only depicted as values for better visibility, oxygen atoms in red, nitrogen atoms in blue, carbon atoms in grey and hydrogen atoms in white.

of **2-4** a co-crystal instead of a salt is received. Even though this is less common for the discussed compounds and similar entities, exceptions exist for example in homochiral Pregabalin and mandelic acid co-crystals.^{50,54} All **4** based compounds again show at least one comparatively strong hydrogen bond and a secondary network of additional connections that seemingly form around the directional carboxyl/carboxylate interaction (**Table 4**, **Figure 10**). The binding energy of these strong carboxyl to carboxylate interactions are in the same range as those calculated for fumarates. The weakest of them occurs in **1-4b** (O3-H11...O7) with $-64.86 \text{ kJmol}^{-1}$ and the most attractive in **2-4** with $-111.50 \text{ kJmol}^{-1}$ (O3-H18...O1). The latter shows that even if a co-crystal instead of a salt is formed a HB of similar strength can be received due to ionic presence on subgroups in zwitterionic systems.

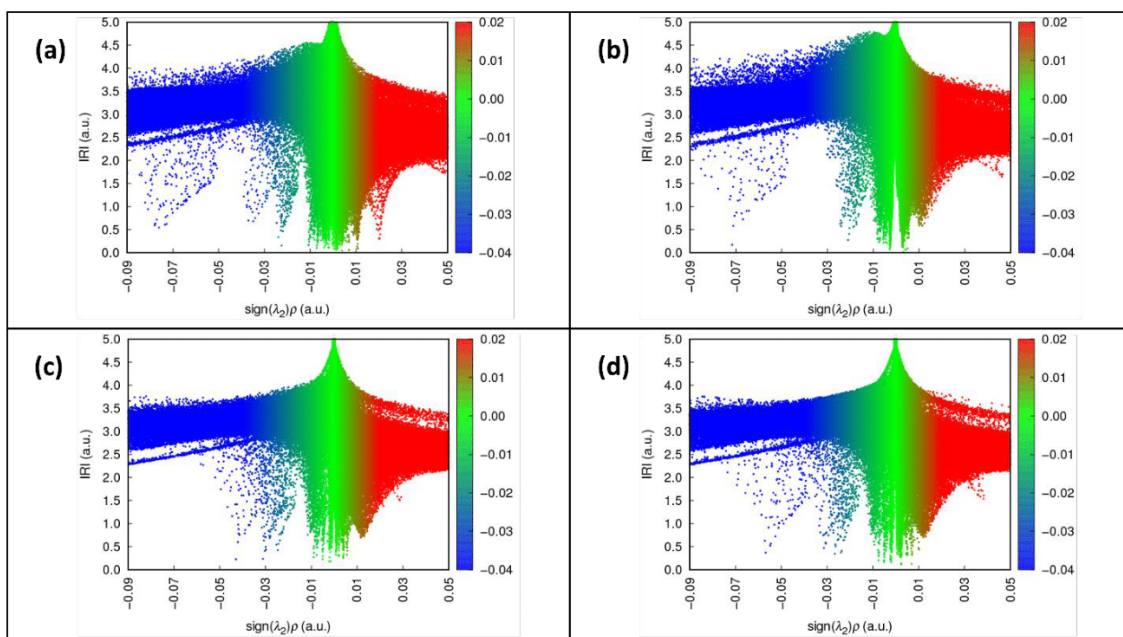


Figure 10. Scatterplots of HB-interaction spheres of 2-4 (a), 1-4a (b), the interaction sphere around the first distinctive 1 molecule in 1-4b (c) and the same for second distinctive 1 molecule in 1-4b (d). Colors indicate occurring interaction types: blue corresponds to hydrogen bonds, green to van-der-Waals interactions and red to intermolecular repulsion.

Table 4. Overview on the strong, distinctive hydrogen bonds in the succinates of GABA and the Gabapentin:succinic acid co-crystal. The proton acceptor distance, the donor acceptor distance, the bond angle and the binding energy calculated for charged HBs are shown.

Compound	H...A [Å]	D...A [Å]	D - H...A [°]	E _{bond} [kJmol ⁻¹]
1-4a				
N1-H8...O5	1.84(2)	2.783(8)	173(2)	-52.26
N1-H9...O6	1.98(2)	2.900(2)	172(8)	-41.14
N1-H10...O6	1.90(2)	2.816(5)	173(2)	-43.73
N2-H18...O7	1.87(2)	2.765(1)	165(2)	-49.47
N2-H19...O8	1.94(3)	2.845(2)	171(7)	-41.51
N2-H20...O8	1.88(2)	2.836(6)	163(2)	-51.29
O1-H1...O5	1.62(3)	2.543(6)	173(2)	-84.68
O3-H11...O7	1.72(3)	2.581(3)	178(2)	-64.86
1-4b				
N1-H8...O2	1.95(3)	2.861(3)	161(3)	-38.57
N1-H9...O2	2.02(3)	2.931(3)	166(2)	-33.56
N1-H10...O6	2.05(3)	2.861(3)	156(2)	-30.40
O1-H1...O3	1.52(3)	2.455(2)	175(4)	-104.67
O5-H11...O4	1.78(4)	2.583(2)	163(3)	-52.74
2-4				
N1-H5...O1	2.06(2)	2.811(2)	137(6)	-36.47
N1-H5...O3	2.51(2)	3.036(7)	116(4)	-16.71
N1-H6...O4	1.94(2)	2.776(0)	155(2)	-38.62
N1-H7...O2	1.79(3)	2.734(3)	175(2)	-56.03
O3-H18...O1	1.50(3)	2.522(0)	175(2)	-111.50

CONCLUSION

The results regarding the investigated structural characteristics paint a picture of complexity, especially concerning single component polymorphs of GABA and Gabapentin. A delicate balance of influences of the crystallization environment favors the formation of one form or the other. Previous works have shown that solid-solid phase transitions can occur for GABA in a monotropic manner, while Gabapentin can even exhibit enantiotropic behavior. We have shown that the occurring HBs in all forms are of a similar strength. Modes of higher connectivity present in **I**-GABA compared to its **II**-form, and **II**-Gabapentin compared to its **IV**-form may lead to more beneficial overall lattice energies. However, if the crystallization environment favors growth of seeds not incorporating said motif, the result will disregard the slight gain in energy. Other past contributions have shown that there appears to be a connection with the molecular conformation of the GABA chain, changing under such environmental influences. The formation of **I**-Gabapentin indicates how easily this polymorphic equilibrium can be disturbed. The introduction of water breaks the uniform dispersion of HB strengths and leads to more distinctive HBs formed. This becomes even more prevalent if dicarboxylic acids capable of being strong hydrogen bond donor or acceptor are introduced. The variation of HB characteristics increases, and at least one hydrogen bond of a much higher binding force than in single components is formed. It appears likely that during crystallization these interactions occur first and everything else subordinates accordingly, which could be derived from the high variations of torsion angles that do not have anything in common with single component entities anymore. The crystallization environment still remains the superordinate influence. Where multicomponent species of different ratios can be formed, they will form according to the amount of co-former available. Thus, polymorphism in these compounds should be considered carefully if a reliable product is the desired target. While

if the right conditions are chosen the wanted phase forms readily, the conversion of II-Gabapentin to its hydrate form is an unnecessary risk. Multicomponent species like salts or co-crystals can minimize phase transition potential by introducing exceedingly beneficial intermolecular interactions that make such transitions unlikely.

ASSOCIATED CONTENT

Supporting Information contains further crystallographic and powder data, IR-spectra, IRI-plots and NCI surfaces for the discussed compounds.

AUTHOR INFORMATION

Corresponding Author

Vera Vasylyeva

Department of Inorganic and Structural Chemistry I, Laboratory for Crystal Engineering,
Heinrich-Heine-University, Universitaetsstraße 1, 40225 Duesseldorf, Germany

E-mail: vera.vasylyeva-shor@hhu.de

Author Contributions

The manuscript was written by Daniel Komisarek and revised by Vera Vasylyeva. Laboratory work was conducted by Daniel Komisarek and Fulya Demirbas. Computational methods were applied by Daniel Komisarek and Takin Haj Hassani Sohi. Figure preparation and result evaluation was conducted by Daniel Komisarek. Important resources were made available by Klaus Merz, Carsten Schauerte and Vera Vasylyeva. Funding acquisition and project supervision was performed by Vera Vasylyeva. All authors have given approval to the final version of the manuscript.

FUNDING SOURCES

Funded by the Deutsche Forschungsgemeinschaft (DFG, German Research Foundation) – 440366605.

ACKNOWLEDGMENT

Computational support and infrastructure was provided by the “Centre for Information and Media Technology” (ZIM) at the University of Duesseldorf (Germany).

ABBREVIATIONS

AIM, Atoms in molecules; NCI, non-covalent interactions; HB, hydrogen bond; CCDC, Cambridge Crystallographic Data Centre; DFT, density functional theory; QE, Quantum Espresso; API, active pharmaceutical ingredient; 1, γ -amino butanoic acid (GABA); 2, Gabapentin; 3, fumaric acid; 4, succinic acid; 1-3, GABA fumarate (2:1); 2-3a; Gabapentin fumarate (2:1); 2-3b, Gabapentin fumarate (1:1); 1-4a, GABA succinate (2:1); 1-4b, GABA succinate (1:1); 2-4, Gabapentin:succinic acid (2:1); PXRD, powder x-ray diffraction; SCXRD, single crystal x-ray diffraction; FT-IR, Fourier transformed infrared spectroscopy; IRI, interaction region indicator.

REFERENCES

1. De Rosa, C.; Scoti, M.; Di Girolamo, R.; Ballesteros, O. R.; Auriemma, F.; Malafronte, A. Polymorphism in polymers: A tool to tailor material's properties. *Polym. Cryst.* **2020**, 3 No. 10101.
2. Shi, W.; Lee, W. S. V.; Xue, J. Recent Development of Mn-based Oxides as Zinc-Ion Battery Cathode. *ChemSusChem* **2021**, 14, 1634–1658.

3. Jia, W.; Wang, Q.; Shi, H.; An, Z.; Huang, W. Manipulating the Ultralong Organic Phosphorescence of Small Molecular Crystals. *Chemistry* **2020**, *26*, 4437–4448.
4. Bennion, J. C.; Matzger, A. J. Development and Evolution of Energetic Cocrystals. *Acc. Chem. Res.* **2021**, *54*, 1699–1710.
5. Bu, R.; Li, H.; Zhang, C. Polymorphic Transition in Traditional Energetic Materials: Influencing Factors and Effects on Structure, Property, and Performance. *Cryst. Growth Des.* **2020**, *20*, 3561–3576.
6. Dunitz, J. D.; Bernstein, J. Disappearing Polymorphs. *Acc. Chem. Res.* **1995**, *28*, 193–200.
7. Bučar, D.-K.; Lancaster, R. W.; Bernstein, J. Disappearing polymorphs revisited. *Angew. Chem. Int. Ed. Engl.* **2015**, *54*, 6972–6993.
8. Chistyakov, D.; Sergeev, G. The Polymorphism of Drugs: New Approaches to the Synthesis of Nanostructured Polymorphs. *Pharmaceutics* **2020**, *12*, 34.
<https://doi.org/10.3390/pharmaceutics1201003>
9. Thakuria, R.; Thakur, T. S. Crystal Polymorphism in Pharmaceutical Science. In *Comprehensive Supramolecular Chemistry II*; Wilson, A., Jayawickramarajah, J., Eds.; Elsevier, 2017; pp 283–309.
10. Cruz, P. C.; Rocha, F. A.; Ferreira, A. M. Application of Selective Crystallization Methods To Isolate the Metastable Polymorphs of Paracetamol: A Review. *Org. Process Res. Dev.* **2019**, *23*, 2592–2607.

11. Nugrahani, I.; Parwati, R. D. Challenges and Progress in Nonsteroidal Anti-Inflammatory Drugs Co-Crystal Development. *Molecules* **2021**, *26*, 4185.
<https://doi.org/10.3390/molecules26144185>
12. Jia, S.; Gao, Z.; Tian, N.; Li, Z.; Gong, J.; Wang, J.; Rohani, S. Review of melt crystallization in the pharmaceutical field, towards crystal engineering and continuous process development. *Chem. Eng. Res. Des.* **2021**, *166*, 268–280.
13. Sparenberg, M.-C.; Chergaoui, S.; Sang Sefidi, V.; Luis, P. Crystallization control via membrane distillation-crystallization: A review. *Desalination* **2021**, *519*, 115315.
14. Xu, S.; Zhang, H.; Qiao, B.; Wang, Y. Review of Liquid–Liquid Phase Separation in Crystallization: From Fundamentals to Application. *Cryst. Growth Des.* **2021**, *21*, 7306–7325.
15. Lu, T.; Chen, F. Multiwfn: a multifunctional wavefunction analyzer. *J. Comput. Chem.* **2012**, *33*, 580–592.
16. Lu, T.; Chen, Q. Interaction Region Indicator: A Simple Real Space Function Clearly Revealing Both Chemical Bonds and Weak Interactions**. *Chem. Methods* **2021**, *1*, 231–239.
17. Emamian, S.; Lu, T.; Kruse, H.; Emamian, H. Exploring Nature and Predicting Strength of Hydrogen Bonds: A Correlation Analysis Between Atoms-in-Molecules Descriptors, Binding Energies, and Energy Components of Symmetry-Adapted Perturbation Theory. *J. Comput. Chem.* **2019**, *40*, 2868–2881.

18. Macrae, C. F.; Sovago, I.; Cottrell, S. J.; Galek, P. T. A.; McCabe, P.; Pidcock, E.; Platings, M.; Shields, G. P.; Stevens, J. S.; Towler, M.; Wood, P. A. Mercury 4.0: from visualization to analysis, design and prediction. *J. Appl. Crystallogr.* **2020**, *53*, 226–235.
19. Gaussian 16, Revision C.01, Frisch, M. J.; Trucks, G. W.; Schlegel, H. B.; Scuseria, G. E.; Robb, M. A.; Cheeseman, J. R.; Scalmani, G.; Barone, V.; Petersson, G. A.; Nakatsuji, H.; Li, X.; Caricato, M.; Marenich, A. V.; Bloino, J.; Janesko, B. G.; Gomperts, R.; Mennucci, B.; Hratchian, H. P.; Ortiz, J. V.; Izmaylov, A. F.; Sonnenberg, J. L.; Williams-Young, D.; Ding, F.; Lipparini, F.; Egidi, F.; Goings, J.; Peng, B.; Petrone, A.; Henderson, T.; Ranasinghe, D.; Zakrzewski, V. G.; Gao, J.; Rega, N.; Zheng, G.; Liang, W.; Hada, M.; Ehara, M.; Toyota, K.; Fukuda, R.; Hasegawa, J.; Ishida, M.; Nakajima, T.; Honda, Y.; Kitao, O.; Nakai, H.; Vreven, T.; Throssell, K.; Montgomery, J. A., Jr.; Peralta, J. E.; Ogliaro, F.; Bearpark, M. J.; Heyd, J. J.; Brothers, E. N.; Kudin, K. N.; Staroverov, V. N.; Keith, T. A.; Kobayashi, R.; Normand, J.; Raghavachari, K.; Rendell, A. P.; Burant, J. C.; Iyengar, S. S.; Tomasi, J.; Cossi, M.; Millam, J. M.; Klene, M.; Adamo, C.; Cammi, R.; Ochterski, J. W.; Martin, R. L.; Morokuma, K.; Farkas, O.; Foresman, J. B.; Fox, D. J. Gaussian, Inc., Wallingford CT, 2016.
20. Giannozzi, P.; Barone, S.; Bonfà, P.; Brunato, D.; Car, R.; Carnimeo, I.; Cavazzoni, C.; Gironcoli, S. de; Delugas, P.; Ferrari Ruffino, F.; Ferretti, A.; Marzari, N.; Timrov, I.; Urru, A.; Baroni, S. Quantum ESPRESSO toward the exascale. *J. Chem. Phys.* **2020**, *152*, 154105.

21. Higashi, K.; Ueda, K.; Moribe, K. Recent progress of structural study of polymorphic pharmaceutical drugs. *Adv. Drug Deliv. Rev.* **2017**, 117, 71–85.
22. Chethan, B. S.; Lokanath, N. K. Study of the crystal structure, H-bonding and noncovalent interactions of novel cocrystal by systematic computational search approach. *J. Mol. Struct.* **2022**, 1251, 131936.
23. Cappuccino, C.; Cusack, D.; Flanagan, J.; Harrison, C.; Holohan, C.; Lestari, M.; Walsh, G.; Lusi, M. How Many Cocrystals Are We Missing? Assessing Two Crystal Engineering Approaches to Pharmaceutical Cocrystal Screening. *Cryst. Growth Des.* **2022**, 22, 1390–1397.
24. Dhibar, M.; Chakraborty, S.; Basak, S. Assessment of Effects of Solvents on Cocrystallization by Computational Simulation Approach. *Curr. Drug. Deliv.* **2021**, 18, 44–53.
25. Ali, A.; Kuznetsov, A.; Khan, M. U.; Tahir, M. N.; Ashfaq, M.; Raza, A. R.; Muhammad, S. 2-Amino-6-methylpyridine based co-crystal salt formation using succinic acid: Single-crystal analysis and computational exploration. *J. Mol. Struct.* **2021**, 1230, 129893.
26. Barbas, R.; Font-Bardia, M.; Frontera, A.; Prohens, R. Polymorphism in the 1/1 Pterostilbene/Picolinic Acid Cocrystal. *Cryst. Growth Des.* **2022**, 22, 590–597.
27. Misaela, F.-M.; La Alexander, P. d. L.; Catalina, S.-C.; Carolina, B.-S.; Ignacio, S.-D. C. Tautomerism and IR spectroscopy of arylsulfonamides by quantum mechanical calculations. *J. Mol. Struct.* **2022**, 1250, 131717.

28. Roselló, Y.; Benito, M.; Barceló-Oliver, M.; Frontera, A.; Molins, E. 1-Ethyluracil, a New Scaffold for Preparing Multicomponent Forms: Synthesis, Characterization, and Computational Studies. *Cryst. Growth Des.* **2021**, *21*, 4857–4870.
29. Stanton, S. A.; Du, J. J.; Lai, F.; Stanton, G.; Hawkins, B. A.; Ong, J. A.; Groundwater, P. W.; Platts, J. A.; Hibbs, D. E. Understanding Hygroscopicity of Theophylline via a Novel Cocrystal Polymorph: A Charge Density Study. *J. Phys. Chem. A* **2021**, *125*, 9736–9756.
30. Zhang, Y.; Zhu, B.; Ji, W.-J.; Guo, C.-Y.; Hong, M.; Qi, M.-H.; Ren, G.-B. Insight into the Formation of Cocrystals of Flavonoids and 4,4'-Vinylenedipyridine: Heteromolecular Hydrogen Bonds, Molar Ratio, and Structural Analysis. *Cryst. Growth Des.* **2021**, *21*, 2720–2733.
31. Boldyreva, E. Glycine: The Gift that Keeps on Giving. *Isr. J. Chem.* **2021**, *61*, 828–850.
32. Bhat, M.; Dharmaprakash, S. Growth of nonlinear optical γ -glycine crystals. *J. Cryst. Growth* **2002**, *236*, 376–380.
33. Dawson, A.; Allan, D. R.; Belmonte, S. A.; Clark, S. J.; David, W. I. F.; McGregor, P. A.; Parsons, S.; Pulham, C. R.; Sawyer, L. Effect of High Pressure on the Crystal Structures of Polymorphs of Glycine. *Cryst. Growth & Des.* **2005**, *5*, 1415–1427.
34. Kim, K.; Centrone, A.; Hatton, T. A.; Myerson, A. S. Polymorphism control of nanosized glycine crystals on engineered surfaces. *CrystEngComm* **2011**, *13*, 1127–1131.

35. Li, L.; Rodríguez-Hornedo, N. Growth kinetics and mechanism of glycine crystals. *J. Cryst. Growth* **1992**, 121, 33–38.
36. Srinivasan, K. Crystal growth of α and γ glycine polymorphs and their polymorphic phase transformations. *J. Cryst. Growth* **2008**, 311, 156–162.
37. Towler, C. S.; Davey, R. J.; Lancaster, R. W.; Price, C. J. Impact of molecular speciation on crystal nucleation in polymorphic systems: the conundrum of gamma glycine and molecular 'self poisoning'. *J. Am. Chem. Soc.* **2004**, 126, 13347–13353.
38. Gottesmann, C. GABA mechanisms and sleep. *Neuroscience* **2002**, 111, 231–239.
39. Ham, S.; Bhatia, S. K.; Gurav, R.; Choi, Y.-K.; Jeon, J.-M.; Yoon, J.-J.; Choi, K.-Y.; Ahn, J.; Kim, H. T.; Yang, Y.-H. Gamma aminobutyric acid (GABA) production in *Escherichia coli* with pyridoxal kinase (pdxY) based regeneration system. *Enzyme Microb. Technol.* **2022**, 155, 109994.
40. Bouché, N.; Fromm, H. GABA in plants: just a metabolite? *Trends Plant Sci.* **2004**, 9, 110–115.
41. Kalueff, A. V.; Nutt, D. J. Role of GABA in anxiety and depression. *Depress. Anxiety* **2007**, 24, 495–517.
42. Tomita, K.; Higashi, H.; Fujiwara, T. Crystal and Molecular Structure of ω -Amino Acids, ω -Amino Sulfonic Acids and Their Derivatives. IV. The Crystal and Molecular Structure of γ -Aminobutyric Acid (GABA), a Nervous Inhibitory Transmitter. *Bull. Chem. Soc. Jpn.* **1973**, 46, 2199–2204.

43. Dobson, A. J.; Gerkin, R. E. gamma-Aminobutyric acid: a novel tetragonal phase. *Acta Crystallogr. C* **1996**, *52*, 3075–3078.
44. Wang, L.; Sun, G.; Zhang, K.; Yao, M.; Jin, Y.; Zhang, P.; Wu, S.; Gong, J. Green Mechanochemical Strategy for the Discovery and Selective Preparation of Polymorphs of Active Pharmaceutical Ingredient γ -Aminobutyric Acid (GABA). *ACS Sustain. Chem. Eng.* **2020**, *8*, 16781–16790.
45. Lamkowski, L.; Komisarek, D.; Merz, K. GABA-Controlled Synthesis of the Metastable Polymorphic Form and Crystallization Behavior with a Chiral Malic Acid. *Cryst. Growth Des.* **2022**, *22*, 356–362.
46. Malapile, R. J.; Nyamayaro, K.; Nassimbeni, L. R.; Báthori, N. B. Multicomponent crystals of baclofen with acids and bases—conformational flexibility and synthon versatility. *CrystEngComm* **2021**, *23*, 91–99.
47. Mirza, S.; Miroshnyk, I.; Rantanen, J.; Aaltonen, J.; Harjula, P.; Kiljunen, E.; Heinämäki, J.; Yliruusi, J. Solid-state properties and relationship between anhydrate and monohydrate of baclofen. *J. Pharm. Sci.* **2007**, *96*, 2399–2408.
48. Herbst, M.; Komisarek, D.; Strothmann, T.; Vasylyeva, V. A Lesson in Humbleness: Crystallization of Chiral and Zwitterionic APIs Baclofen and Phenibut. *Crystals* **2022**, *12*, 1393. <https://doi.org/10.3390/cryst12101393>
49. Komisarek, D.; Pallaske, M.; Vasylyeva, V. Crystal Structure and Thermal Properties of Phenibut, Phenibut H₂O and Phenibut HCl: a Case for Phase Stability Based on Structural Considerations. *Z. Anorg. Allg. Chem.* **2021**, *647*, 984–991.

50. Komisarek, D.; Haj Hassani Sohi, T.; Vasylyeva, V. Co-crystals of zwitterionic GABA API's pregabalin and phenibut: properties and application. *CrystEngComm* **2022**, *24*, 8390–8398.
51. Khandavilli, U. B. R.; Lusi, M.; Frawley, P. J. Plasticity in zwitterionic drugs: the bending properties of Pregabalin and Gabapentin and their hydrates. *IUCrJ* **2019**, *6*, 630–634.
52. Couvrat, N.; Sanselme, M.; Poupard, M.; Bensakoun, C.; Drouin, S. H.; Schneider, J.-M.; Coquerel, G. Solid-State Overview of R-Baclofen: Relative Stability of Forms A, B and C and Characterization of a New Heterosolvate. *J. Pharm. Sci.* **2021**, *110*, 3457–3463.
53. Córdova-Villanueva, E. N.; Rodríguez-Ruiz, C.; Sánchez-Guadarrama, O.; Rivera-Islas, J.; Herrera-Ruiz, D.; Morales-Rojas, H.; Höpfl, H. Diastereomeric Salt Formation by the γ -Amino Acid RS -Baclofen and L -Malic Acid: Stabilization by Strong Heterosynthons Based on Hydrogen Bonds between RNH^3+ and COOH/COO^- Groups. *Cryst. Growth Des.* **2018**, *18*, 7356–7367.
54. Samas, B.; Wang, W.; Godrej, D. B. 1:1 Cocrystal of (S)-3-(ammoniomethyl)-5-methylhexanoate and (S)-mandelic acid. *Acta Crystallogr. E Struct. Rep. Online* **2007**, *63*, o3938-o3938.
55. Steendam, R. R. E.; Khandavilli, U. B. R.; Keshavarz, L.; Frawley, P. J. Solution versus Crystal Hydration: The Case of γ -Amino Acid Pregabalin. *Cryst. Growth Des.* **2019**, *19*, 4483–4488.

56. Venu, N.; Vishweshwar, P.; Ram, T.; Surya, D.; Apurba, B. (S)-3-(Ammoniomethyl)-5-methylhexanoate (pregabalin). *Acta Crystallogr. C* **2007**, 63, o306-o308.
57. Gendron, F.-X.; Mahieux, J.; Sanselme, M.; Coquerel, G. Resolution of Baclofenium Hydrogenomaleate By Using Preferential Crystallization. A First Case of Complete Solid Solution at High Temperature and a Large Miscibility Gap in the Solid State. *Cryst. Growth Des.* **2019**, 19, 4793–4801.
58. Bennett, M. I.; Simpson, K. H. Gabapentin in the treatment of neuropathic pain. *Palliat. Med.* **2004**, 18, 5–11.
59. Cheng, J.-K.; Chiou, L.-C. Mechanisms of the antinociceptive action of gabapentin. *J. Pharmacol. Sci.* **2006**, 100, 471–486.
60. Nicholson, B. Gabapentin use in neuropathic pain syndromes. *Acta Neurol. Scand.* **2000**, 101, 359–371.
61. Delaney, S. P.; Smith, T. M.; Korter, T. M. Conformation versus cohesion in the relative stabilities of gabapentin polymorphs. *RSC Adv.* **2014**, 4, 855–864.
62. Dempah, K. E.; Barich, D. H.; Kaushal, A. M.; Zong, Z.; Desai, S. D.; Suryanarayanan, R.; Kirsch, L.; Munson, E. J. Investigating gabapentin polymorphism using solid-state NMR spectroscopy. *AAPS PharmSciTech* **2013**, 14, 19–28.
63. Lin, S.-Y.; Hsu, C.-H.; Ke, W.-T. Solid-state transformation of different gabapentin polymorphs upon milling and co-milling. *Int. J. Pharm.* **2010**, 396, 83–90.

64. Martins, I. C. B.; Gomes, J. R. B.; Duarte, M. T.; Mafra, L. Understanding Polymorphic Control of Pharmaceuticals Using Imidazolium-Based Ionic Liquid Mixtures as Crystallization Directing Agents. *Cryst. Growth Des.* **2017**, *17*, 428–432.
65. Tulli, L. G.; Moridi, N.; Wang, W.; Helttunen, K.; Neuburger, M.; Vaknin, D.; Meier, W.; Shahgaldian, P. Polymorphism control of an active pharmaceutical ingredient beneath calixarene-based Langmuir monolayers. *ChemComm* **2014**, *50*, 3938–3940.
66. Reece, H. A.; Levendis, D. C. Polymorphs of gabapentin. *Acta Crystallogr. C* **2008**, *64*, o105-o108.
67. André, V.; Fernandes, A.; Santos, P. P.; Duarte, M. T. On the Track of New Multicomponent Gabapentin Crystal Forms: Synthons Competition and pH Stability. *Crystal Growth & Design* **2011**, *11*, 2325–2334.
68. Kumari, H.; Zhang, J.; Erra, L.; Barbour, L. J.; Deakyne, C. A.; Atwood, J. L. Cocrystals of gabapentin with C-alkylresorcin[4]arenes. *CrystEngComm* **2013**, *15*, 4045.
69. Soliman, I. I.; Kandil, S. M.; Abdou, E. M. Gabapentin-saccharin co-crystals with enhanced physicochemical properties and in vivo absorption formulated as oro-dispersible tablets. *Pharm. Dev. Technol.* **2020**, *25*, 227–236.
70. Wenger, M.; Bernstein, J. An Alternate Crystal Form of Gabapentin: A Cocrystal with Oxalic Acid. *Cryst. Growth Des.* **2008**, *8*, 1595–1598.

71. Liu, Y.; Wang, Y.; Huang, X.; Li, X.; Zong, S.; Wang, N.; Hao, H. Conformational Selectivity and Evolution Affected by the Desolvation Process. *Cryst. Growth Des.* **2022**, *22*, 1283–1291.
72. Song, I. K.; Kang, Y. K. Conformational preferences of γ -aminobutyric acid in the gas phase and in water. *J. Mol. Struct.* **2012**, *1024*, 163–169.
73. CrysAlisPRO, Oxford Diffraction /Agilent Technologies UK Ltd, Yarnton, England.
74. Sheldrick, G. M. A short history of SHELX. *Acta Crystallogr. A* **2008**, *64*, 112–122.
75. Sheldrick, G. M. Crystal structure refinement with SHELXL. *Acta Crystallogr. C Struct Chem* **2015**, *71*, 3–8.
76. Dolomanov, O. V.; Bourhis, L. J.; Gildea, R. J.; Howard, J. A. K.; Puschmann, H. OLEX2: a complete structure solution, refinement and analysis program. *J. Appl. Cryst.* **2009**, *42*, 339–341.
77. Humphrey, W.; Dalke, A.; Schulten, K. VMD: visual molecular dynamics. *J. Mol. Graph.* **1996**, *14*, 33-8, 27-8.
78. Spek, A. L. Single-crystal structure validation with the program PLATON. *J. Appl. Crystallogr.* **2003**, *36*, 7–13.
79. Nyman, J.; Day, G. M. Static and lattice vibrational energy differences between polymorphs. *CrystEngComm* **2015**, *17*, 5154–5165.
80. Vamecq, J.; Feutelais, Y.; Maurois, P.; Sghaier, M.; Dichi, E.; German-Fattal, M.; Herrenknecht, C.; Gressens, P.; Cecchelli, R.; Dehouck, L.; Stables, J. P.; Pages, N.;

Legendre, B.; Bac, P. Engineering a GABA endowed with pharmacological CNS activity when given by an extracerebral route. *Med. Chem. Res.* **2009**, 18, 255–267.

Supporting Information

Understanding Polymorphism and Multicomponent Crystal Formation of GABA and Gabapentin

*D. Komisarek, F. Demirbas, T. Haj Hassani Sohi, K. Merz, C. Schauerte and V. Vasylyeva**

Contents

I-GABA (I-1).....	1
II-GABA (II-1).....	4
II-Gabapentin (II-2).....	7
IV-Gabapentin (IV-2).....	10
Gabapentin • H ₂ O (I-Gabapentin) (I-2).....	13
GABA Fumarate (2:1) (1-3).....	17
Gabapentin Fumarate (2:1) (2-3a).....	21
Gabapentin Fumarate (1:1) (2-3b).....	25
GABA Succinate (2:1) (1-4a).....	31
GABA Succinate (1:1) (1-4b).....	36
Gabapentin:Succinic acid (2:1) (2-4).....	40

I-GABA (I-1)

Table S1. Crystallographic data for I-GABA.

Parameters	I-GABA
Formula	C ₄ H ₉ N O ₂
Formula Moiety	C ₄ H ₉ N O ₂
M _r [g mol ⁻¹]	103.12
Temperature [K]	100.00(1)
System/space group	monoclinic, <i>P</i> 2 ₁ / <i>c</i>
a (Å)	7.2196(8)
b (Å)	9.9985(7)
c (Å)	8.2154(8)
α (°)	90
β (°)	110.609(10)
γ (°)	90
V (Å ³)	555.08(10)
Z/Z'	4/1
Density [g/cm ³]	1.234
μ [mm ⁻¹]	0.826
T _{min} /T _{max}	0.749/1.000
F (000)	224
Crystal size [mm]	0.05 · 0.11 · 0.17
2θ range [°]	6.6 – 77.2
Completeness [%]	99.6
Recorded refl.	3100
Independent refl.	1064
Goodness-of-fit F ²	1.112
X-Ray Source	Cu Kα (λ = 1.54184)
R ₁ [%] /wR ₂ [%] /S	3.47/ 8.70/ 1.11

Table S2. Distinctive energy values for the occurring HB obtained by AIM analysis via multiwfn conducted as assumed charged HB for two molecules (*E*₁), and complete interaction sphere of distinctive HB around one molecule (*E*₂), and as assumed neutral HB under the same conditions for *E*₁^{*}, *E*₂^{*}.

Hydrogen Bond	<i>E</i> ₁ [kJ mol ⁻¹]	<i>E</i> ₂ [kJ mol ⁻¹]
N1-H7...O1	-54.83	-53.05
N1-H8...O1	-55.37	-55.37
N1-H9...O2	-47.52	-46.32
	<i>E</i> ₁ [*] [kJ mol ⁻¹]	<i>E</i> ₂ [*] [kJ mol ⁻¹]
N1-H7...O1	-30.71	-29.51
N1-H8...O1	-31.07	-31.07
N1-H9...O2	-25.80	-25.00

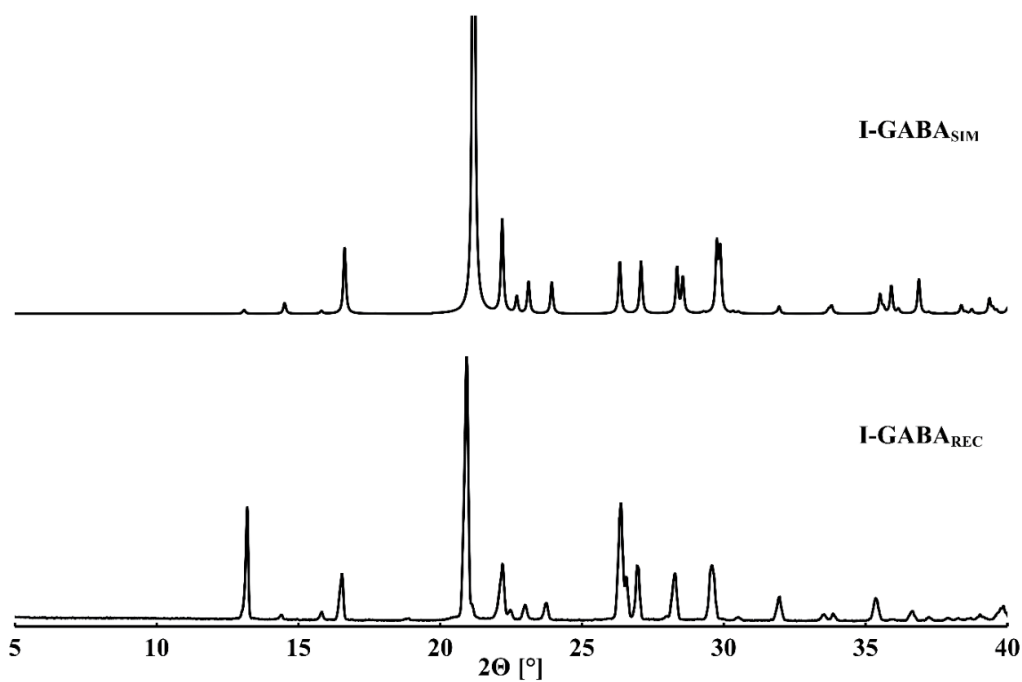


Figure S1. Powder pattern comparison of I-GABA. Simulated from single crystal data (top), recorded substance (bottom). A range between $5^\circ 2\theta$ and $40^\circ 2\theta$ is depicted.

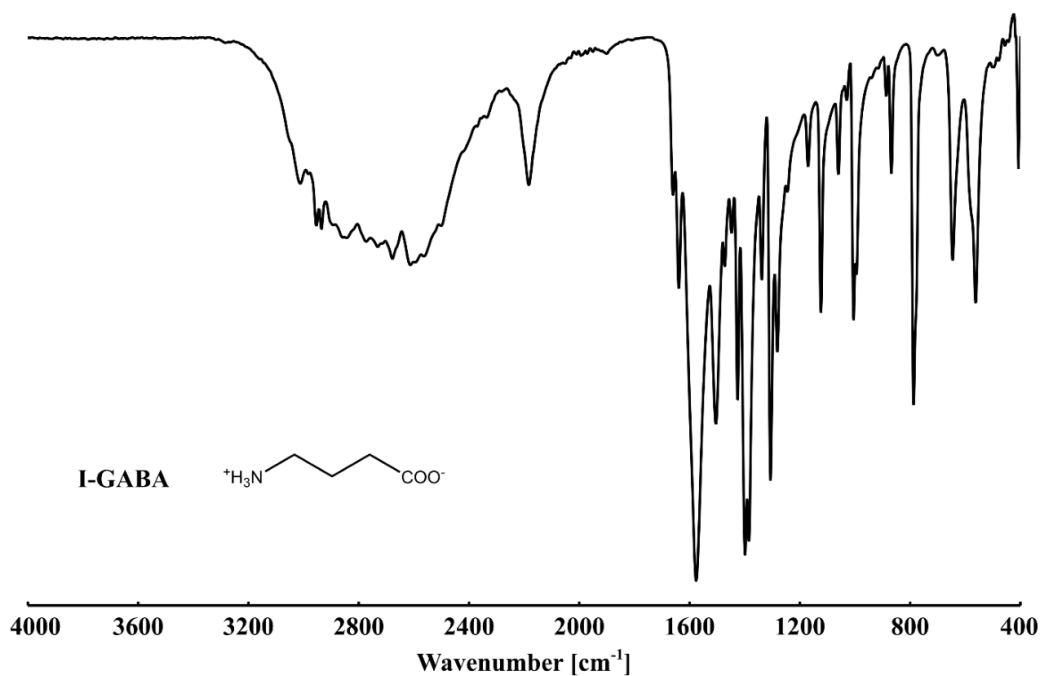


Figure S2. IR spectrum of I-GABA, shown in a range between 4000 cm^{-1} – 400 cm^{-1} . Broad ammonium hydrogen bond network and C-H stretch band between 3200 cm^{-1} and 2270 cm^{-1} , carboxylate stretch band at 1610 cm^{-1} .

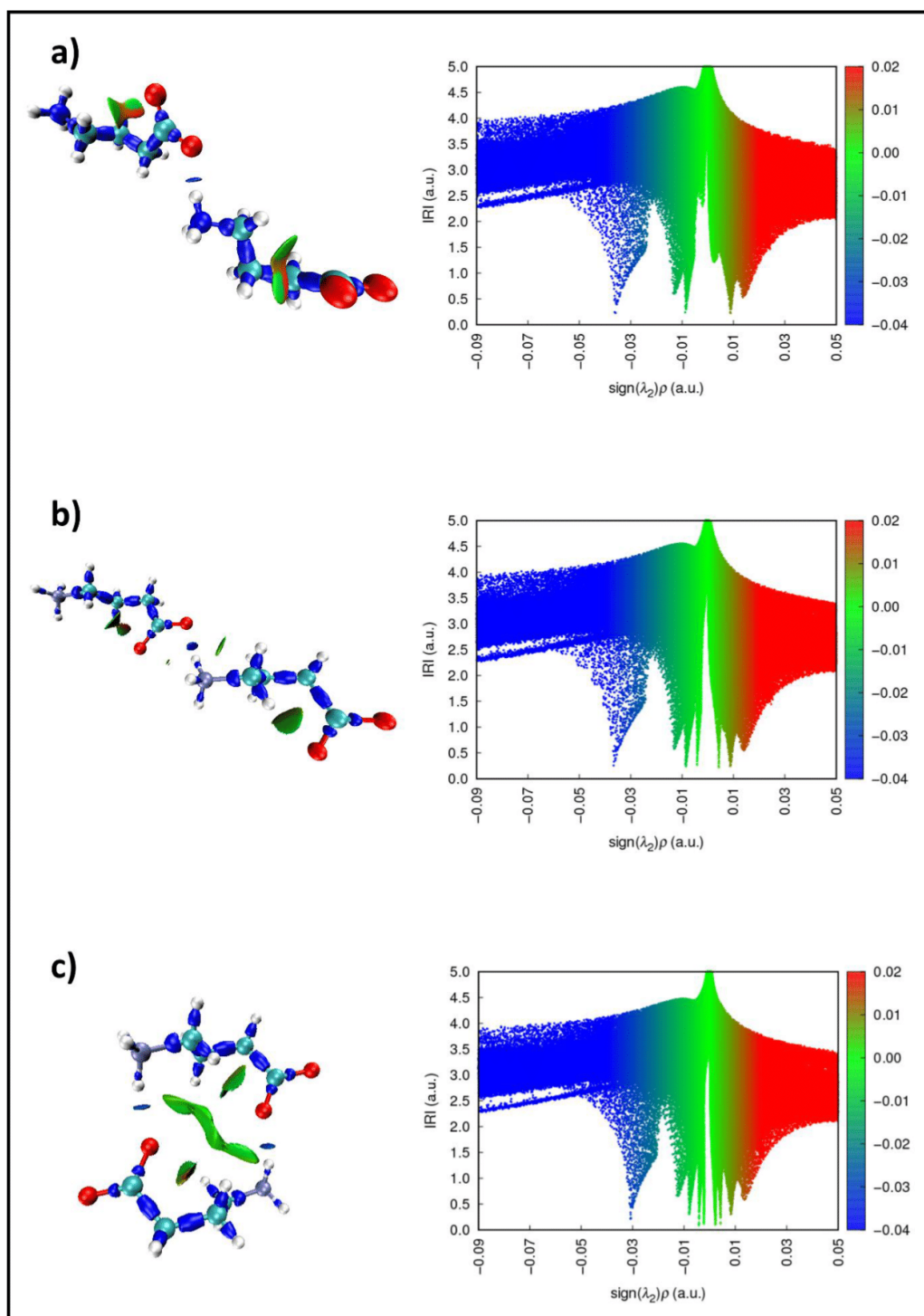


Figure S3. Interaction Region Indicator surfaces and related scatter plots of the distinctive hydrogen bonds in I-GABA: N1-H7...O1 a), N1-H8...O1 b), and N1-H9...O2 c). Blue regions signify strong attraction, green regions weak attraction and red regions repulsion.

II-GABA (II-1)

Table S3. Crystallographic data for II-GABA.

Parameters	II-GABA
Formula	C ₄ H ₉ N O ₂
Formula Moiety	C ₄ H ₉ N O ₂
M _r [g mol ⁻¹]	103.12
Temperature [K]	140(2)
System/space group	tetragonal, <i>I4₁cd</i>
a (Å)	11.8658(4)
b (Å)	11.8658(4)
c (Å)	15.2642(6)
α (°)	90
β (°)	90
γ (°)	90
V (Å ³)	2149.16(17)
Z/Z'	16/1
Density [g/cm ³]	1.275
μ [mm ⁻¹]	0.101
T _{min} /T _{max}	0.6874/0.7463
F (000)	896
Crystal size [mm]	0.12 · 0.17 · 0.26
2θ range [°]	3.4 – 31.8
Completeness [%]	99.2
Recorded refl.	6406
Independent refl.	1707
Goodness-of-fit F ²	1.058
X-Ray Source	Mo Kα (λ = 0.71073)
Flack x	-0.4(5)
R ₁ [%] /wR ₂ [%] /S	3.15/ 7.66/ 1.06

Table S4. Distinctive energy values for the occurring HB obtained by AIM analysis via multiwfn conducted as assumed charged HB for two molecules (E_1), and complete interaction sphere of distinctive HB around one molecule (E_2), and as assumed neutral HB under the same conditions for E_1^* , E_2^* .

Hydrogen Bond	E_1 [kJ mol ⁻¹]	E_2 [kJ mol ⁻¹]
N1-H7...O1	-42.87	-41.51
N1-H8...O1	-56.37	-55.02
N1-H9...O2	-48.88	-46.06
	E_1^* [kJ mol ⁻¹]	E_2^* [kJ mol ⁻¹]
N1-H7...O1	-22.67	-21.76
N1-H8...O1	-31.74	-30.83
N1-H9...O2	-25.37	-24.81

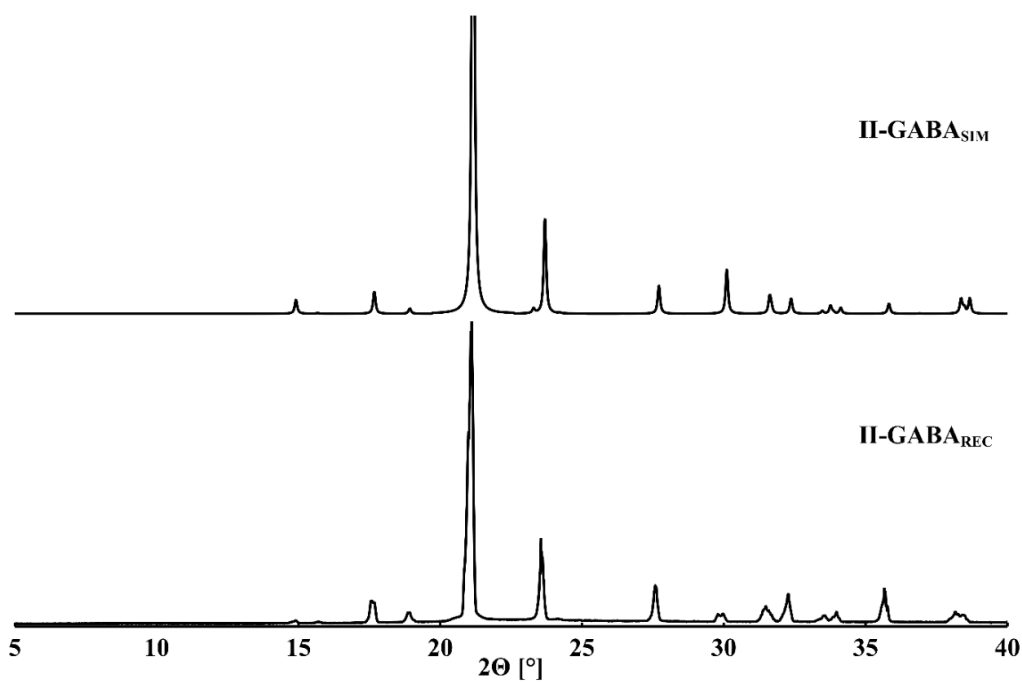


Figure S4. Powder pattern comparison of II-GABA. Simulated from single crystal data (top), recorded substance (bottom). A range between $5^\circ 2\theta$ and $40^\circ 2\theta$ is depicted.

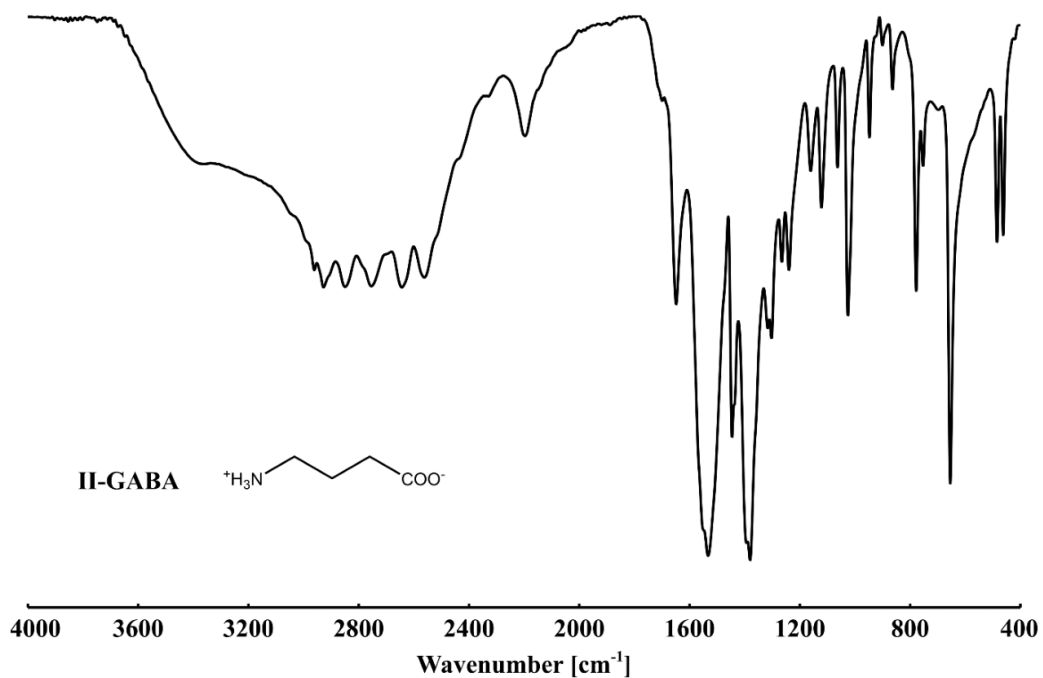


Figure S5. IR spectrum of II-GABA, shown in a range between 4000 cm^{-1} – 400 cm^{-1} . Broad ammonium hydrogen bond network and C-H stretch band between 3700 cm^{-1} and 2270 cm^{-1} , carboxylate stretch band at 1649 cm^{-1} .

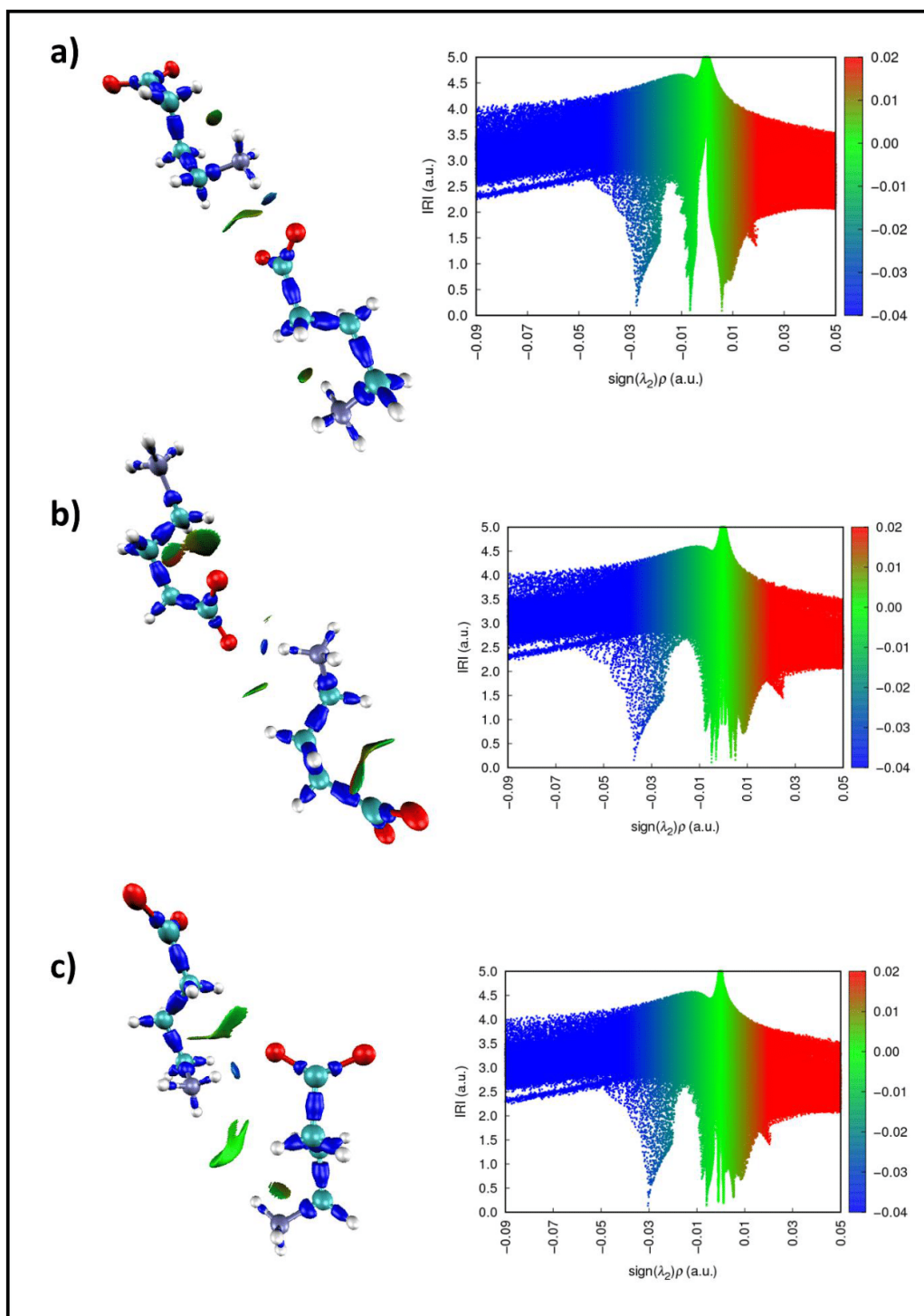


Figure S6. Interaction Region Indicator surfaces and related scatter plots of the distinctive hydrogen bonds in II-GABA: N1-H7...O1 a), N1-H8...O1 b), and N1-H9...O2 c). Blue regions signify strong attraction, green regions weak attraction and red regions repulsion.

II-Gabapentin (II-2)

Table S5. Crystallographic data for II-Gabapentin.

Parameters	II-Gabapentin
Formula	C ₉ H ₁₇ N O ₂
Formula Moiety	C ₉ H ₁₇ N O ₂
M _r [g mol ⁻¹]	171.23
Temperature [K]	100.00(1)
System/space group	monoclinic, <i>P</i> 2 ₁ / <i>c</i>
a (Å)	5.8605(2)
b (Å)	6.9140(3)
c (Å)	22.1954(7)
α (°)	90
β (°)	89.888(3)
γ (°)	90
V (Å ³)	899.34(6)
Z/Z'	4/1
Density [g/cm ³]	1.265
μ [mm ⁻¹]	0.712
T _{min} /T _{max}	0.745/0.865
F (000)	376
Crystal size [mm]	0.21 · 0.26 · 0.44
2θ range [°]	6.7 – 76.7
Completeness [%]	99.7
Recorded refl.	5300
Independent refl.	1591
Goodness-of-fit F ²	1.068
X-Ray Source	Cu Kα (λ = 1.54184)
R ₁ [%] /wR ₂ [%] /S	3.44/ 9.36/ 1.07

Table S6. Distinctive energy values for the occurring HB obtained by AIM analysis via multiwfn conducted as assumed charged HB for two molecules (E_1), and complete interaction sphere of distinctive HB around one molecule (E_2), and as assumed neutral HB under the same conditions for E_1^* , E_2^* .

Hydrogen Bond	E_1 [kJ mol ⁻¹]	E_2 [kJ mol ⁻¹]
N1-H5...O1	-55.48	-54.33
N1-H6...O1	-48.73	-47.52
N1-H7...O2	-52.97	-51.74
	E_1^* [kJ mol ⁻¹]	E_2^* [kJ mol ⁻¹]
N1-H5...O1	-31.14	-30.37
N1-H6...O1	-26.61	-25.79
N1-H7...O2	-29.45	-28.63

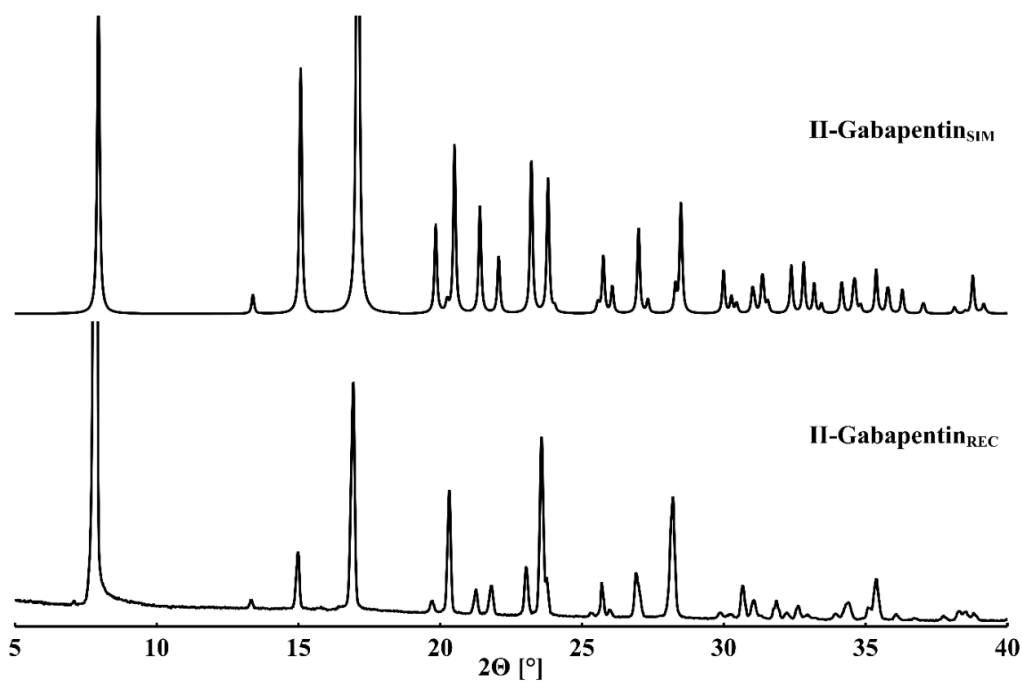


Figure S7. Powder pattern comparison of **II-Gabapentin**. Simulated from single crystal data (top), recorded substance (bottom). A range between $5^\circ 2\theta$ and $40^\circ 2\theta$ is depicted.

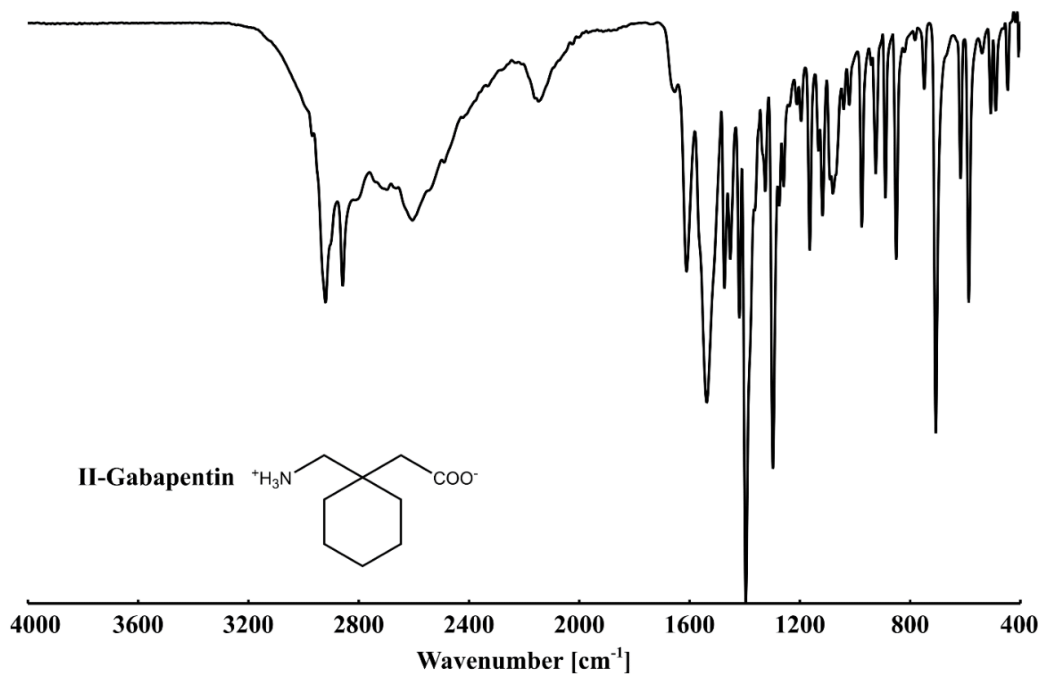


Figure S8. IR spectrum of **II-Gabapentin**, shown in a range between 4000 cm^{-1} – 400 cm^{-1} . Broad ammonium hydrogen bond network and C-H stretch band between 3200 cm^{-1} and 2240 cm^{-1} , carboxylate band at 1611 cm^{-1} .

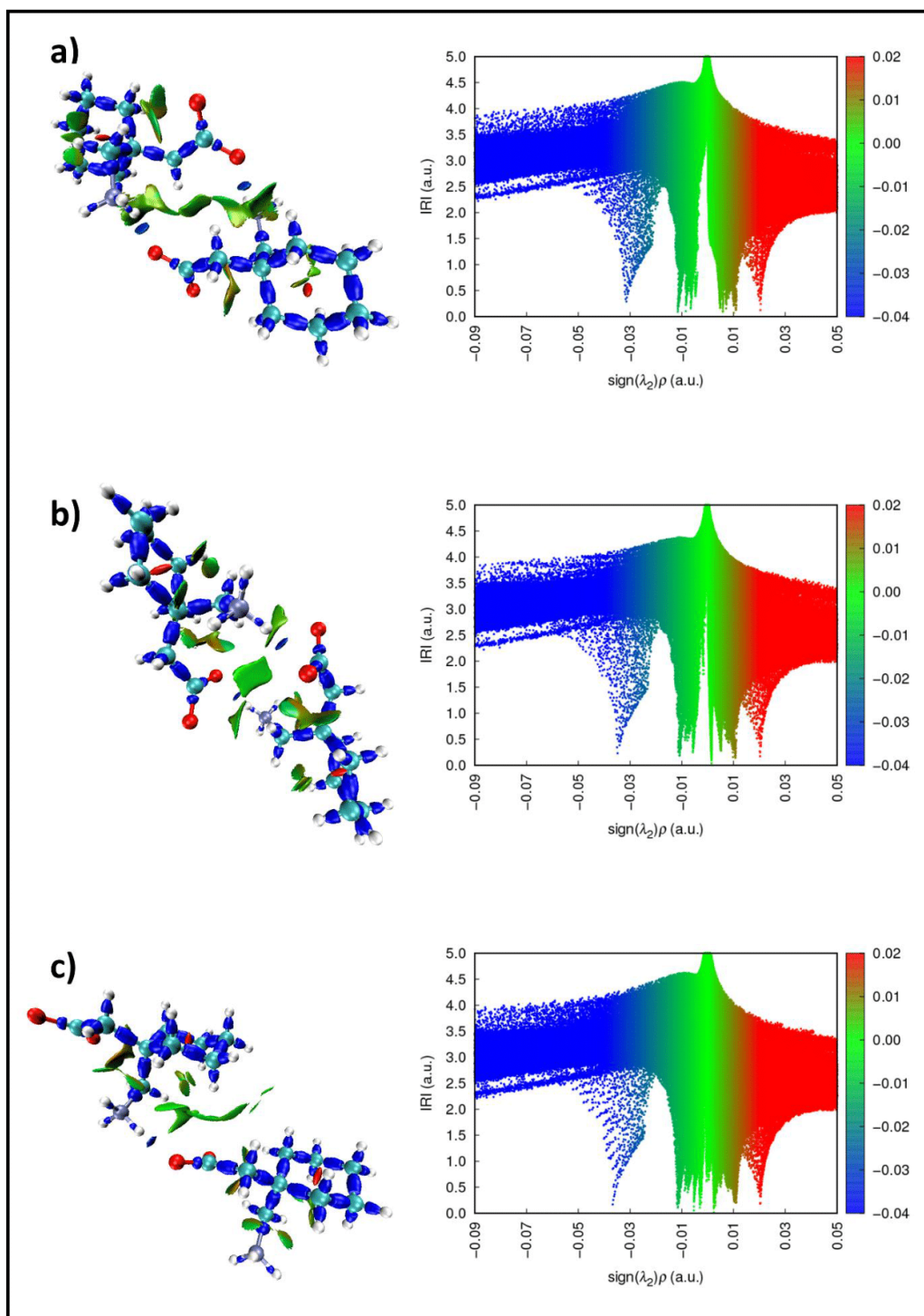


Figure S9. Interaction Region Indicator surfaces and related scatter plots of the distinctive hydrogen bonds in II-Gabapentin: HB N1-H5...O1 a), N1-H6...O1 b), and N1-H7...O2 c). Blue regions signify strong attraction, green regions weak attraction and red regions repulsion.

IV-Gabapentin (IV-2)

Table S7. Crystallographic data for IV-Gabapentin.

Parameters	IV-Gabapentin
Formula	C ₉ H ₁₇ N O ₂
Formula Moiety	C ₉ H ₁₇ N O ₂
M _r [g mol ⁻¹]	171.23
Temperature [K]	100.00(1)
System/space group	monoclinic, C2/c
a (Å)	31.3806(7)
b (Å)	5.8999(1)
c (Å)	10.7957(2)
α (°)	90
β (°)	113.041(3)
γ (°)	90
V (Å ³)	1839.29(7)
Z/Z'	8/1
Density [g/cm ³]	1.237
μ [mm ⁻¹]	0.696
T _{min} /T _{max}	0.921/0.979
F (000)	752
Crystal size [mm]	0.03 · 0.08 · 0.12
2θ range [°]	3.1 – 77.3
Completeness [%]	100
Recorded refl.	10650
Independent refl.	1641
Goodness-of-fit F ²	1.084
X-Ray Source	Cu Kα (λ = 1.54184)
R ₁ [%] /wR ₂ [%] /S	2.81/ 6.97/ 1.08

Table S8. Distinctive energy values for the occurring HB obtained by AIM analysis via multiwfn conducted as assumed charged HB for two molecules (E_1), and complete interaction sphere of distinctive HB around one molecule (E_2), and as assumed neutral HB under the same conditions for E_1^* , E_2^* .

Hydrogen Bond	E_1 [kJ mol ⁻¹]	E_2 [kJ mol ⁻¹]
N1-H5...O1	-53.87	-52.67
N1-H6...O1	-47.05	-45.83
N1-H7...O2	-54.65	-53.62
	E_1^* [kJ mol ⁻¹]	E_2^* [kJ mol ⁻¹]
N1-H5...O1	-30.06	-29.26
N1-H6...O1	-25.48	-24.66
N1-H7...O2	-30.58	-29.89

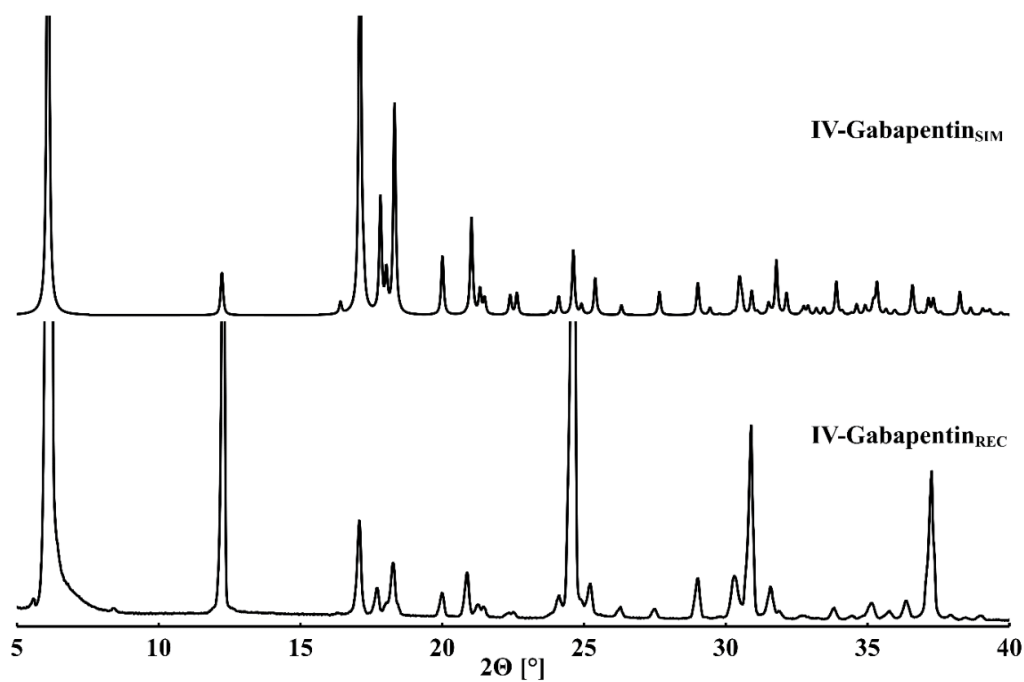


Figure S10. Powder pattern comparison of IV-Gabapentin. Simulated from single crystal data (top), recorded substance (bottom). A range between $5^\circ 2\theta$ and $40^\circ 2\theta$ is depicted.

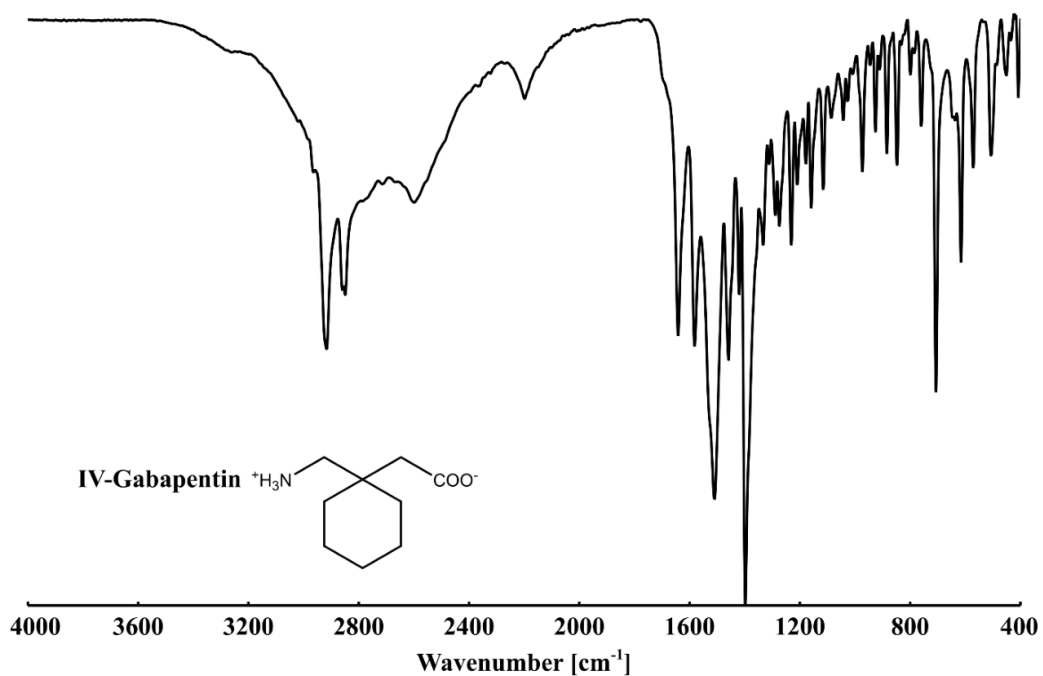


Figure S11. IR spectrum of IV-Gabapentin, shown in a range between 4000 cm^{-1} – 400 cm^{-1} . Broad ammonium hydrogen bond network and C-H stretch band between 3500 cm^{-1} and 2270 cm^{-1} , carboxylate band at 1641 cm^{-1} .

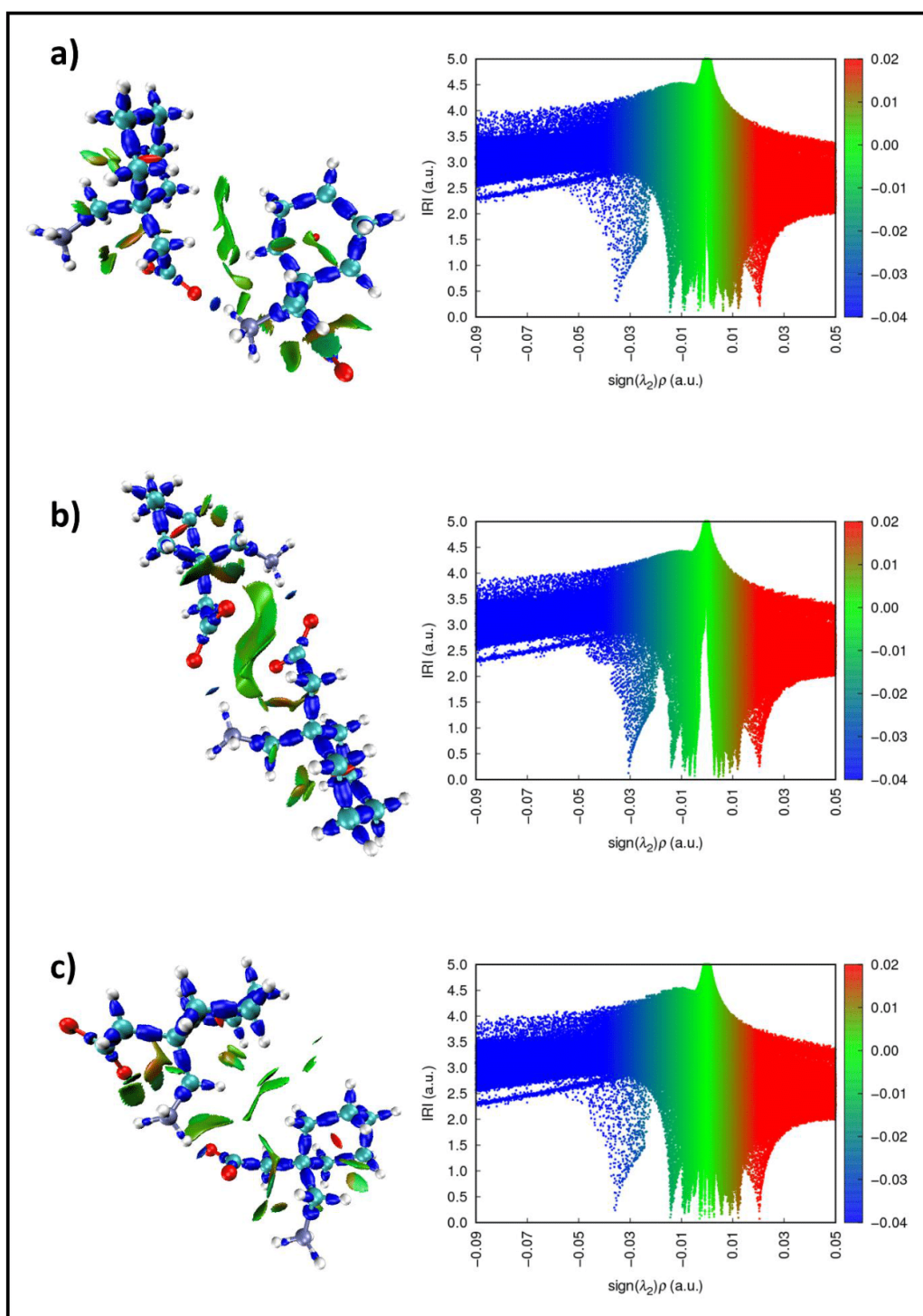


Figure S12. Interaction Region Indicator surfaces and related scatter plots of the distinctive hydrogen bonds in IV-Gabapentin: N1-H5...O1 a), N1-H6...O1 b), and N1-H7...O2 c). Blue regions signify strong attraction, green regions weak attraction and red regions repulsion.

Gabapentin • H₂O (I-Gabapentin) (I-2)

Table S9. Crystallographic data for Gabapentin • H₂O (I-Gabapentin).

Parameters	Gabapentin • H ₂ O (I-Gabapentin)
Formula	C ₉ H ₁₉ N O ₃
Formula Moiety	C ₉ H ₁₇ N O ₂ , H ₂ O
M _r [g mol ⁻¹]	189.25
Temperature [K]	100.01(1)
System/space group	orthorhombic, <i>Pbca</i>
a (Å)	9.2188(3)
b (Å)	7.6384(3)
c (Å)	29.0462(12)
α (°)	90
β (°)	90
γ (°)	90
V (Å ³)	2045.34(13)
Z/Z'	8/1
Density [g/cm ³]	1.229
μ [mm ⁻¹]	0.746
T _{min} /T _{max}	0.902/1.000
F (000)	832
Crystal size [mm]	0.02 · 0.06 · 0.08
2θ range [°]	3.0 – 77.9
Completeness [%]	99.8
Recorded refl.	7406
Independent refl.	1982
Goodness-of-fit F ²	1.062
X-Ray Source	Cu Kα (λ = 1.54184)
R ₁ [%] /wR ₂ [%] /S	4.91/ 13.85/ 1.06

Table S10. Distinctive energy values for the occurring HB obtained by AIM analysis via multiwfn conducted as assumed charged HB for two molecules (E_1), and complete interaction sphere of distinctive HB around one molecule (E_2), and as assumed neutral HB under the same conditions for E_1^* , E_2^* .

Hydrogen Bond	E_1 [kJ mol ⁻¹]	E_2 [kJ mol ⁻¹]
N1-H5...O1	-66.71	-66.55
N1-H6...O1	-51.46	-41.46
N1-H7...O3	-37.01	-37.86
N1-H7...O3	-16.67	-16.81
O3-H18...O2	-48.70	-49.10
O3-H19...O2	-49.12	-49.78
	E_1^* [kJ mol ⁻¹]	E_2^* [kJ mol ⁻¹]
N1-H5...O1	-38.68	-38.57
N1-H6...O1	-28.44	-21.73
N1-H7...O3	-18.75	-19.31
N1-H7...O3	-5.09	-5.18
O3-H18...O2	-26.59	-26.86
O3-H19...O2	-26.87	-27.31

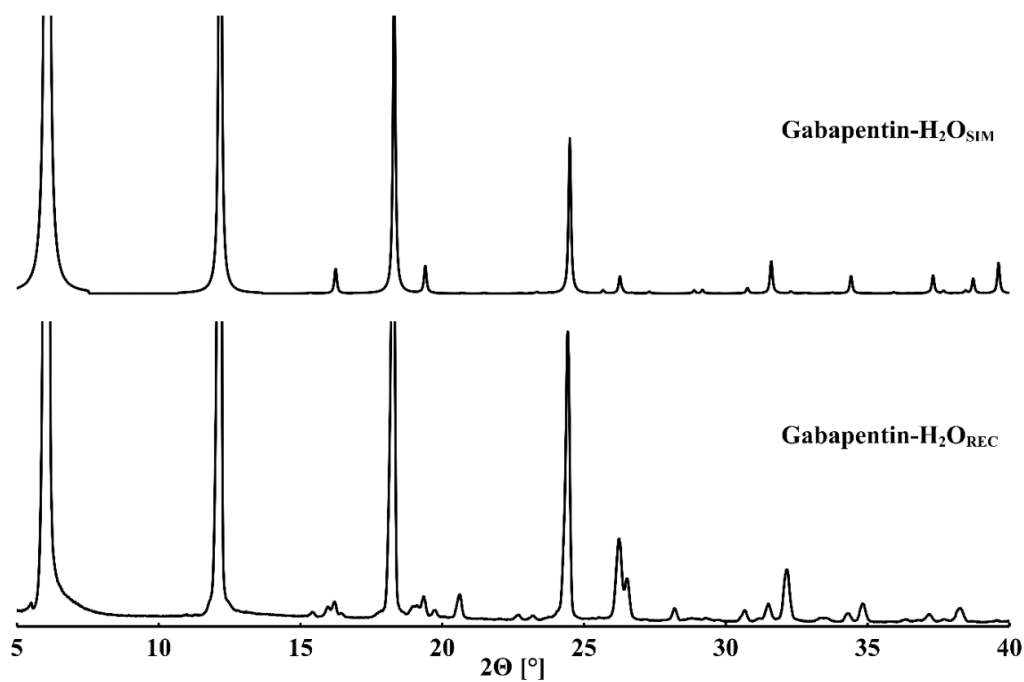


Figure S13. Powder pattern comparison of *I*-Gabapentin. Simulated from single crystal data (top), recorded substance (bottom). A range between $5^\circ 2\theta$ and $40^\circ 2\theta$ is depicted.

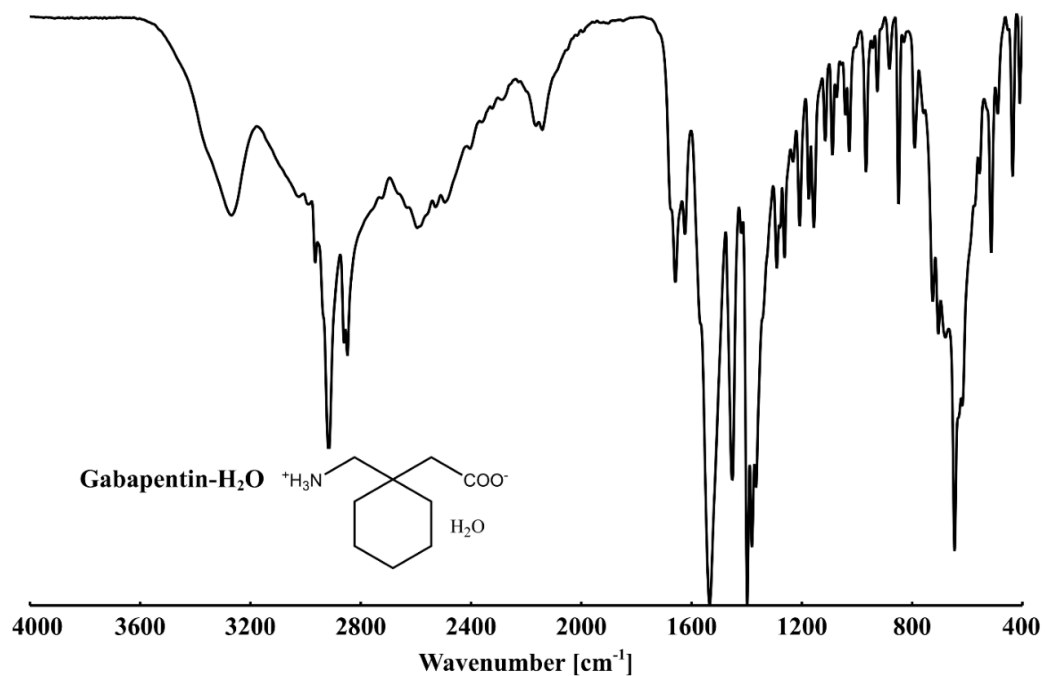


Figure S14. IR spectrum of *I*-Gabapentin, shown in a range between 4000 cm^{-1} – 400 cm^{-1} . Broad ammonium hydrogen bond network and C-H stretch band between 3625 cm^{-1} and 2240 cm^{-1} , water band at 3270 cm^{-1} and carboxylate band at 1659 cm^{-1} .

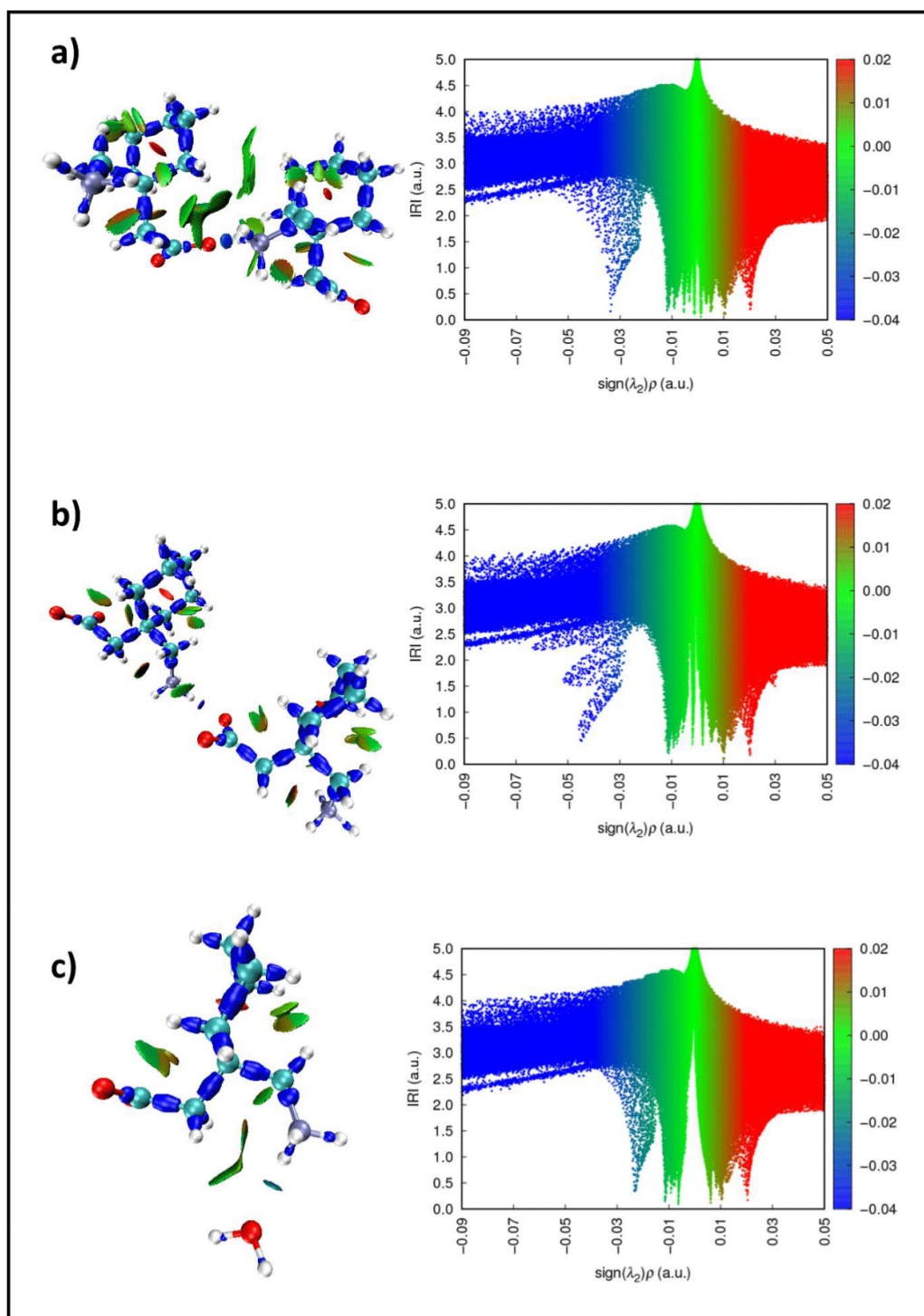


Figure S15. Interaction Region Indicator surfaces and related scatter plots of three distinctive hydrogen bonds in I-Gabapentin: HB N1-H5...O1 a), N1-H6...O1 b), and N1-H7...O3 c). Blue regions signify strong attraction, green regions weak attraction and red regions repulsion.

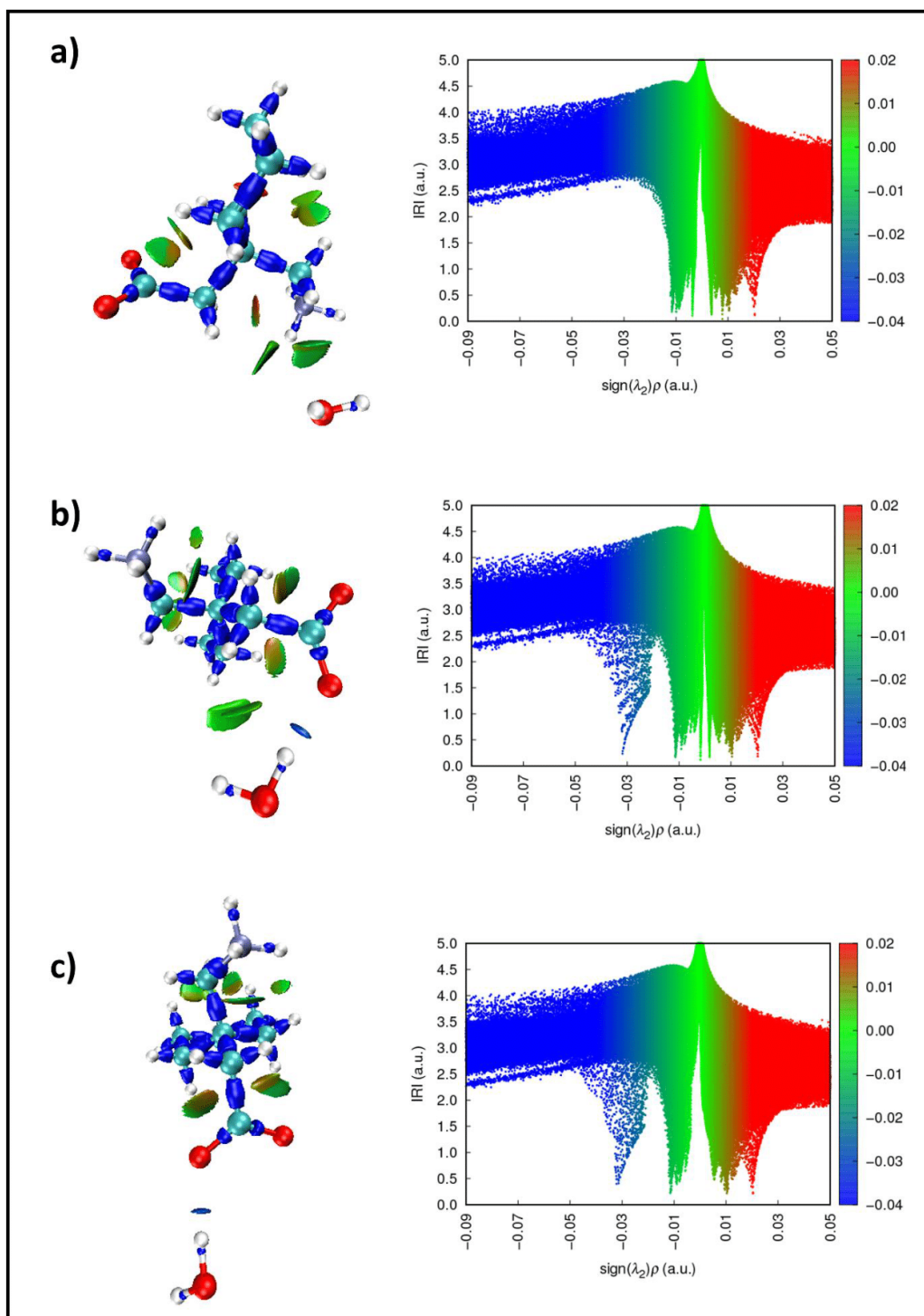


Figure S16. Interaction Region Indicator surfaces and related scatter plots of three distinctive hydrogen bonds in I-Gabapentin: HB N1-H7...O3 a), O3-H18...O2 b), and O3-H19...O2 c). Blue regions signify strong attraction, green regions weak attraction and red regions repulsion.

GABA Fumarate (2:1) (1-3)

Table S11. Crystallographic data for GABA Fumarate (2:1).

Parameters	GABA Fumarate (2:1)
Formula	C ₁₂ H ₂₂ N ₂ O ₈
Formula Moiety	2(C ₄ H ₁₀ N O ₂), C ₄ H ₂ O ₄
M _r [g mol ⁻¹]	322.31
Temperature [K]	100.00(1)
System/space group	monoclinic, <i>P</i> 2 ₁ / <i>n</i>
a (Å)	7.2196(8)
b (Å)	6.5760(1)
c (Å)	14.4204(2)
α (°)	90
β (°)	98.617(1)
γ (°)	90
V (Å ³)	785.562(19)
Z/Z'	2/1
Density [g/cm ³]	1.363
μ [mm ⁻¹]	0.986
T _{min} /T _{max}	0.558/0.866
F (000)	344
Crystal size [mm]	0.15 · 0.39 · 0.67
2θ range [°]	5.3 – 77.7
Completeness [%]	99.7
Recorded refl.	4875
Independent refl.	1504
Goodness-of-fit F ²	1.067
X-Ray Source	Cu Kα (λ = 1.54184)
R ₁ [%] /wR ₂ [%] /S	3.23/ 8.32/ 1.07

Table S12. Distinctive energy values for the occurring HB obtained by AIM analysis via multiwfn conducted as assumed charged HB for two molecules (*E*₁), and complete interaction sphere of distinctive HB around one molecule (*E*₂), and as assumed neutral HB under the same conditions for *E*₁^{*}, *E*₂^{*}.

Hydrogen Bond	<i>E</i> ₁ [kJ mol ⁻¹]	<i>E</i> ₂ [kJ mol ⁻¹]
N1-H8...O3	-48.84	-43.92
N1-H9...O4	-49.63	-44.40
N1-H10...O4	-44.02	-41.46
O1-H1...O3	-65.80	-62.72
	<i>E</i> ₁ [*] [kJ mol ⁻¹]	<i>E</i> ₂ [*] [kJ mol ⁻¹]
N1-H8...O3	-26.69	-23.38
N1-H9...O4	-27.21	-23.70
N1-H10...O4	-23.45	-21.73
O1-H1...O3	-38.07	-36.00

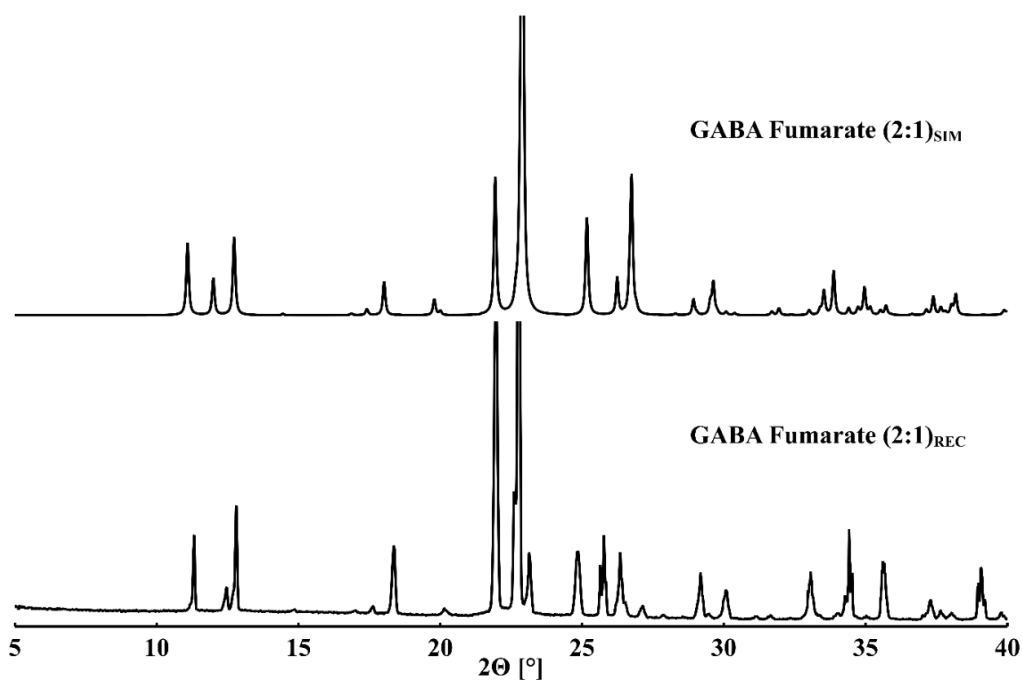


Figure S17. Powder pattern comparison of GABA Fumarate (2:1). Simulated from single crystal data (top), recorded substance (bottom). A range between $5^\circ 2\theta$ and $40^\circ 2\theta$ is depicted.

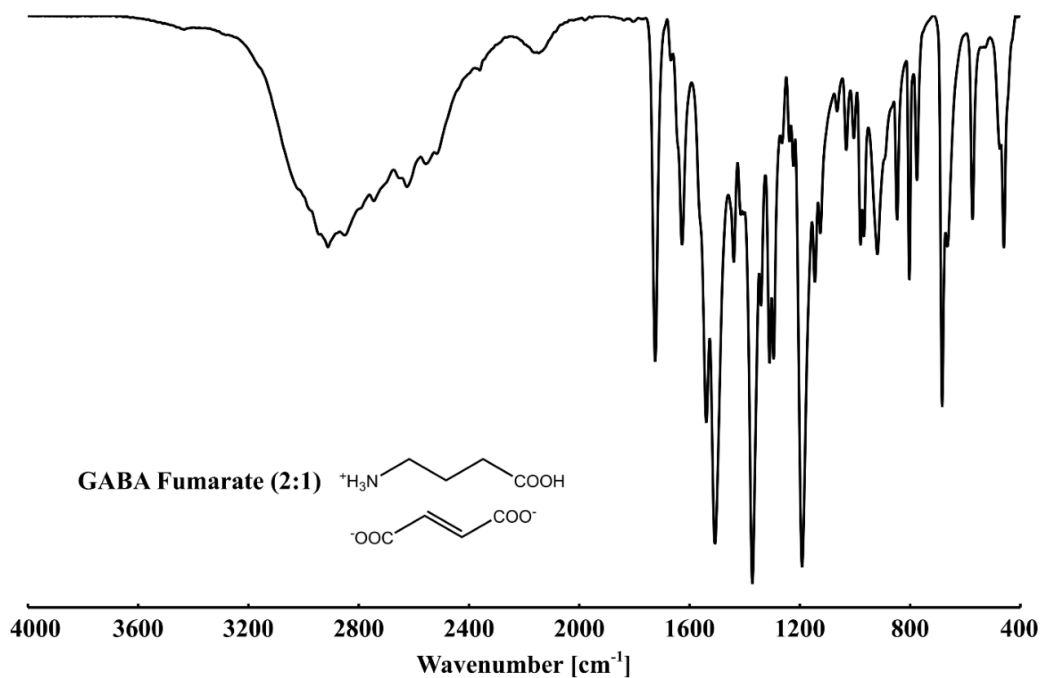


Figure S18. IR spectrum of GABA Fumarate (2:1), shown in a range between 4000 cm^{-1} – 400 cm^{-1} . Broad ammonium hydrogen bond network and C-H stretch band between 3640 cm^{-1} and 2240 cm^{-1} ; carboxyl band at 1724 cm^{-1} carboxylate band at 1626 cm^{-1} .

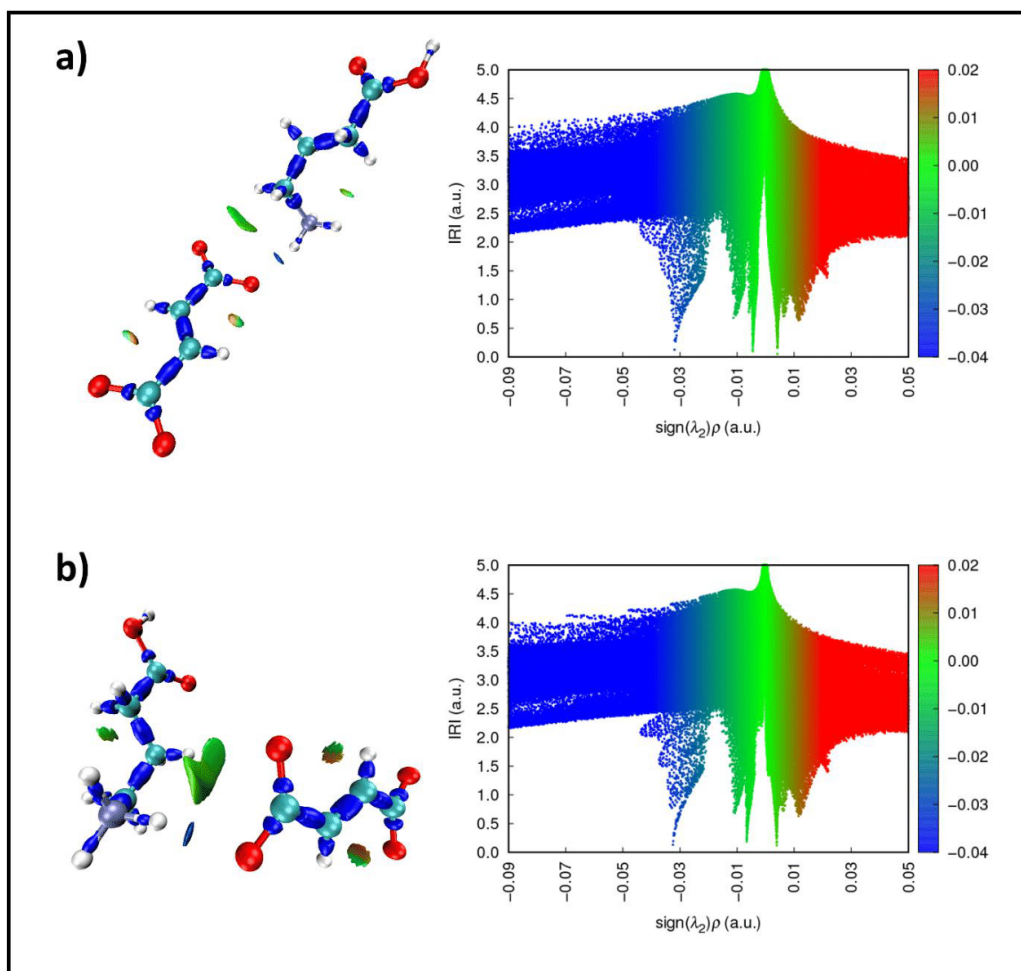


Figure S19. Interaction Region Indicator surfaces and related scatter plots of two distinctive hydrogen bonds in GABA Fumarate (2:1): N1-H8...O3 a), and N1-H9...O4 b). Blue regions signify strong attraction, green regions weak attraction and red regions repulsion.

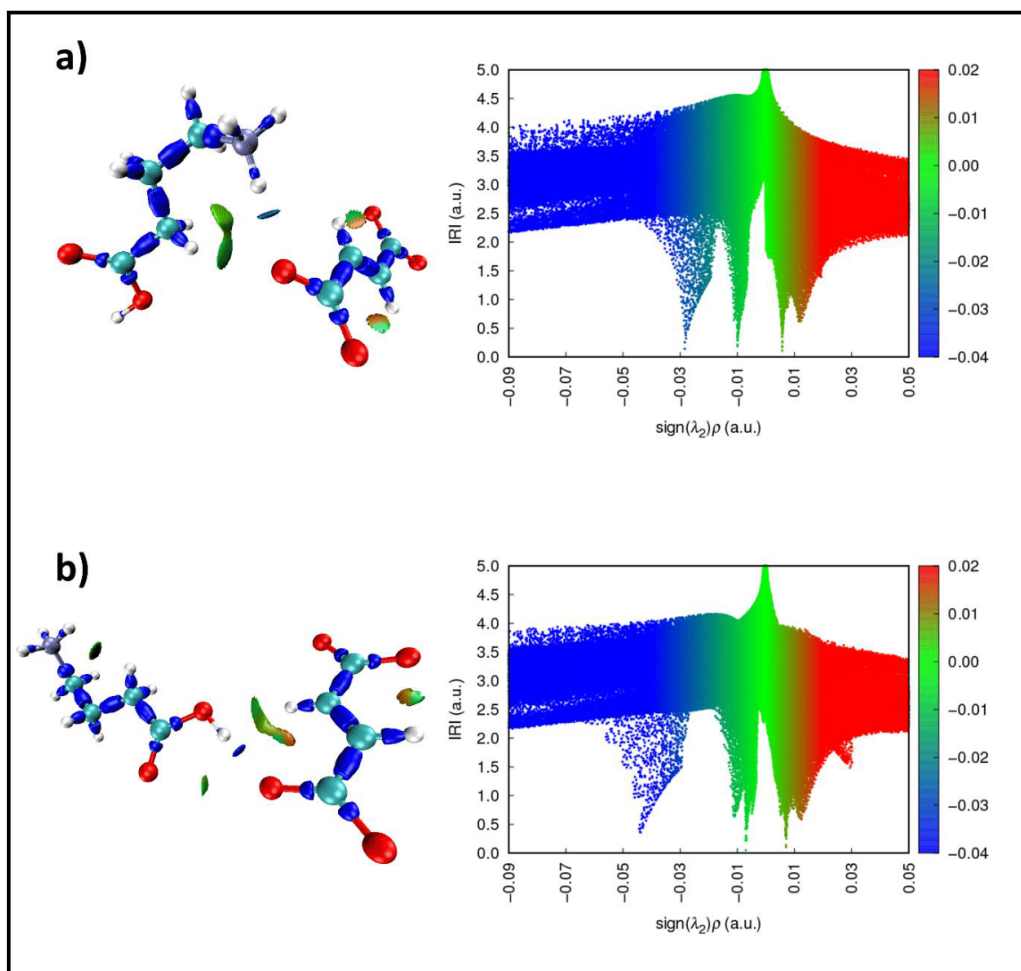


Figure S20. Interaction Region Indicator surfaces and related scatter plots of two distinctive hydrogen bonds in GABA Fumarate (2:1): N1-H10...O4 a), and O1-H1...O3 b). Blue regions signify strong attraction, green regions weak attraction and red regions repulsion.

Gabapentin Fumarate (2:1) (2-3a)

Table S13. Crystallographic data for Gabapentin Fumarate (2:1).

Parameters	Gabapentin Fumarate (2:1)
Formula	C ₁₁ H ₁₉ N O ₄
Formula Moiety	C ₉ H ₁₇ N O ₂ , 0.5(C ₄ H ₂ O ₄)
M _r [g mol ⁻¹]	229.27
Temperature [K]	100.00(1)
System/space group	monoclinic, <i>P</i> 2 ₁ / <i>c</i>
a (Å)	14.1264(6)
b (Å)	7.4699(2)
c (Å)	12.2122(4)
α (°)	90
β (°)	105.751(4)
γ (°)	90
V (Å ³)	1240.28(8)
Z/Z'	4/1
Density [g/cm ³]	1.228
μ [mm ⁻¹]	0.771
T _{min} /T _{max}	0.920/0.970
F (000)	496
Crystal size [mm]	0.04 · 0.04 · 0.11
2θ range [°]	3.2 – 76.3
Completeness [%]	99.7
Recorded refl.	8403
Independent refl.	2200
Goodness-of-fit F ²	1.067
X-Ray Source	Cu Kα (λ = 1.54184)
R ₁ [%] /wR ₂ [%] /S	3.57/ 9.04/ 1.07

Table S14. Distinctive energy values for the occurring HB obtained by AIM analysis via multiwfn conducted as assumed charged HB for two molecules (*E*₁), and complete interaction sphere of distinctive HB around one molecule (*E*₂), and as assumed neutral HB under the same conditions for *E*₁^{*}, *E*₂^{*}.

Hydrogen Bond	<i>E</i> ₁ [kJ mol ⁻¹]	<i>E</i> ₂ [kJ mol ⁻¹]
N1-H6...O4	-58.11	-55.86
N1-H7...O4	-53.54	-50.50
N1-H8...O3	-45.58	-42.41
O1-H1...O3	-73.09	-71.59
	<i>E</i> ₁ [*] [kJ mol ⁻¹]	<i>E</i> ₂ [*] [kJ mol ⁻¹]
N1-H6...O4	-32.91	-31.39
N1-H7...O4	-29.84	-27.80
N1-H8...O3	-24.50	-22.37
O1-H1...O3	-42.96	-41.95

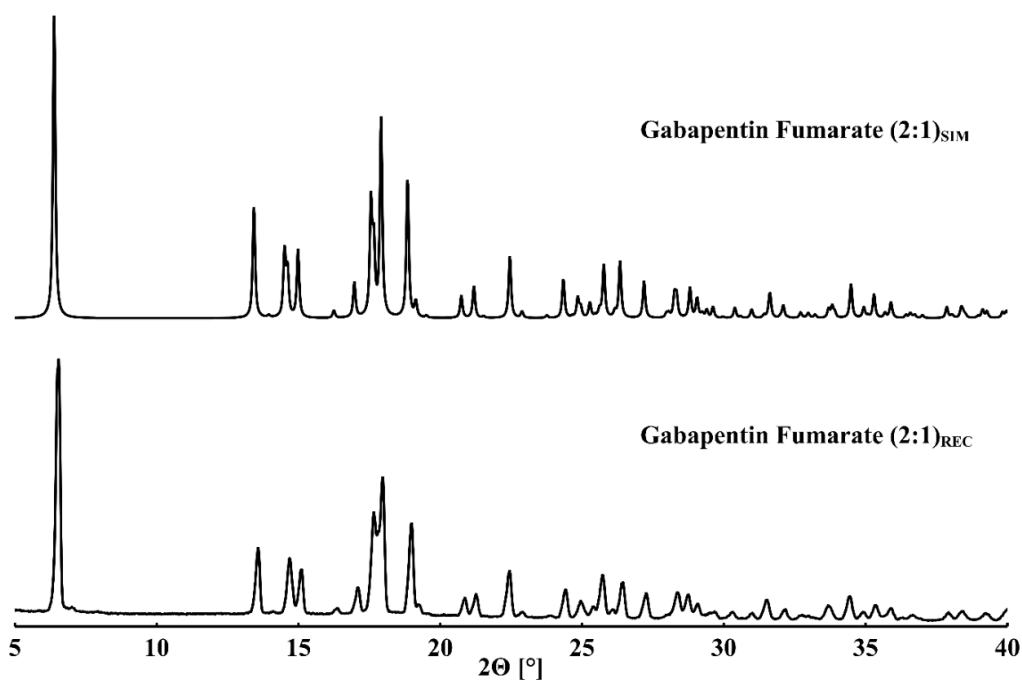


Figure S21. Powder pattern comparison of Gabapentin Fumarate (2:1). Simulated from single crystal data (top), recorded substance (bottom). A range between 5° 2θ and 40° 2θ is depicted.

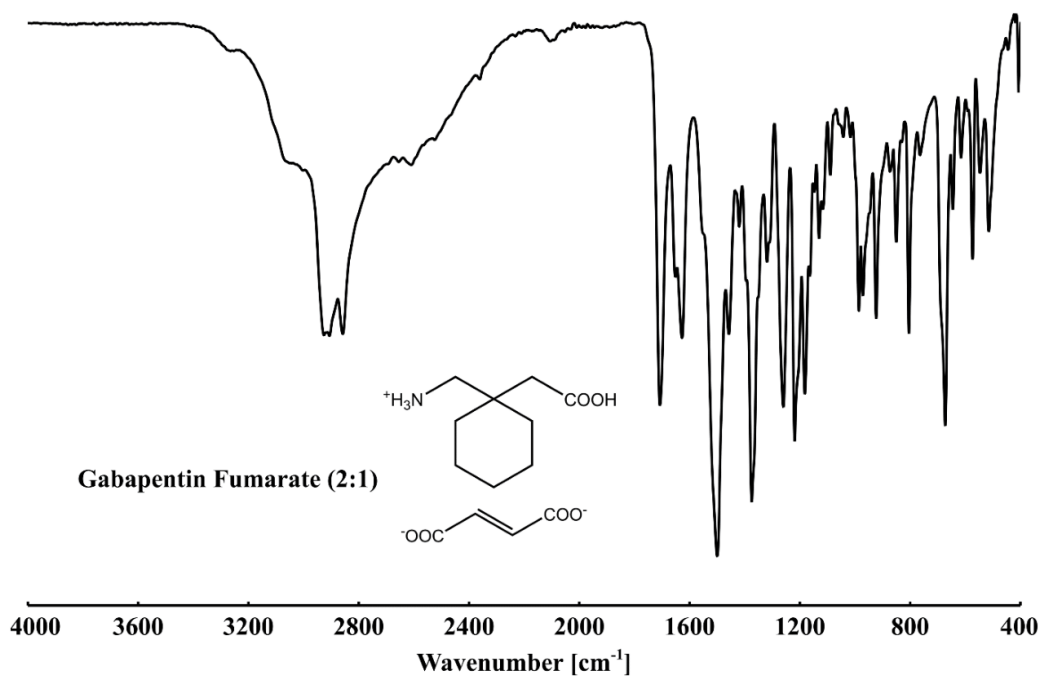


Figure S22. IR spectrum of Gabapentin Fumarate (2:1), shown in a range between 4000 cm⁻¹ – 400 cm⁻¹. Broad ammonium hydrogen bond network and C-H stretch band between 3435 cm⁻¹ and 2170 cm⁻¹, carboxyl band at 1708 cm⁻¹ carboxylate band at 1627 cm⁻¹.

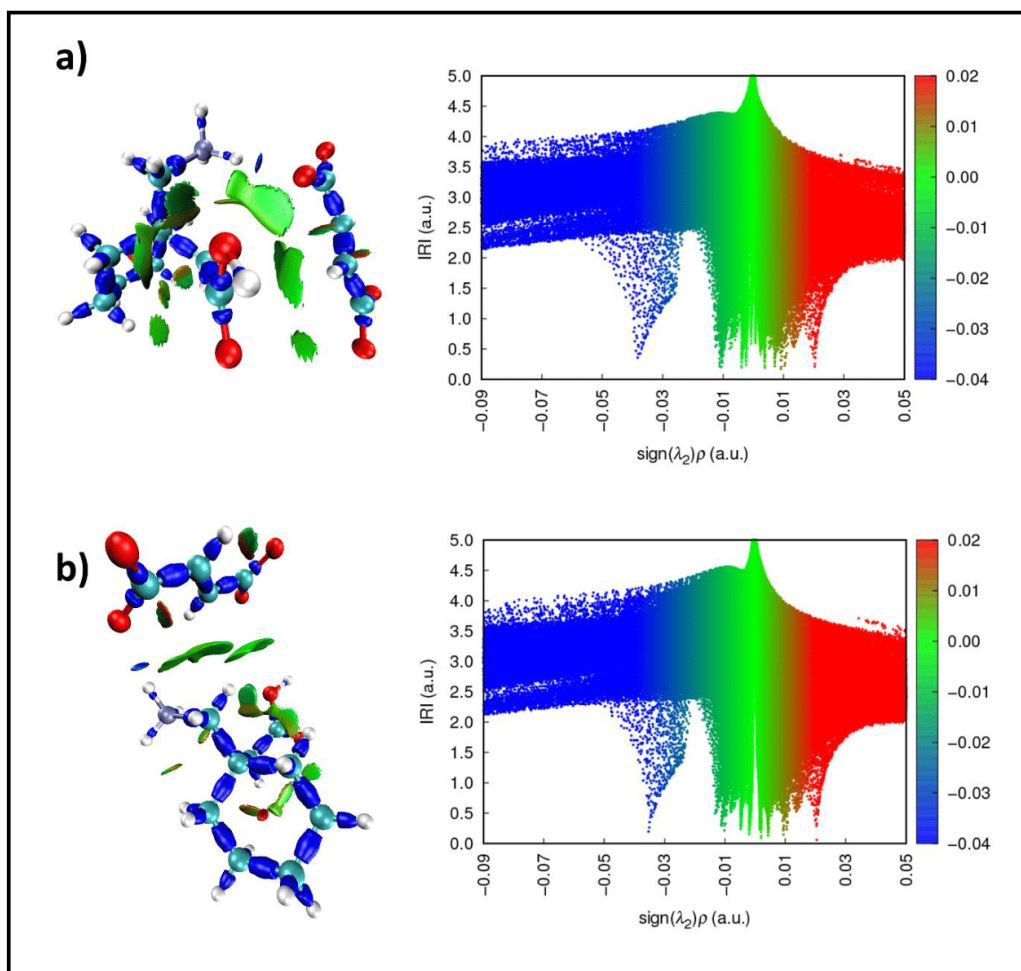


Figure S23. Interaction Region Indicator surfaces and related scatter plots of two distinctive hydrogen bonds in Gabapentin Fumarate (2:1): N1-H6...O4 a), and N1-H7...O4 b). Blue regions signify strong attraction, green regions weak attraction and red regions repulsion.

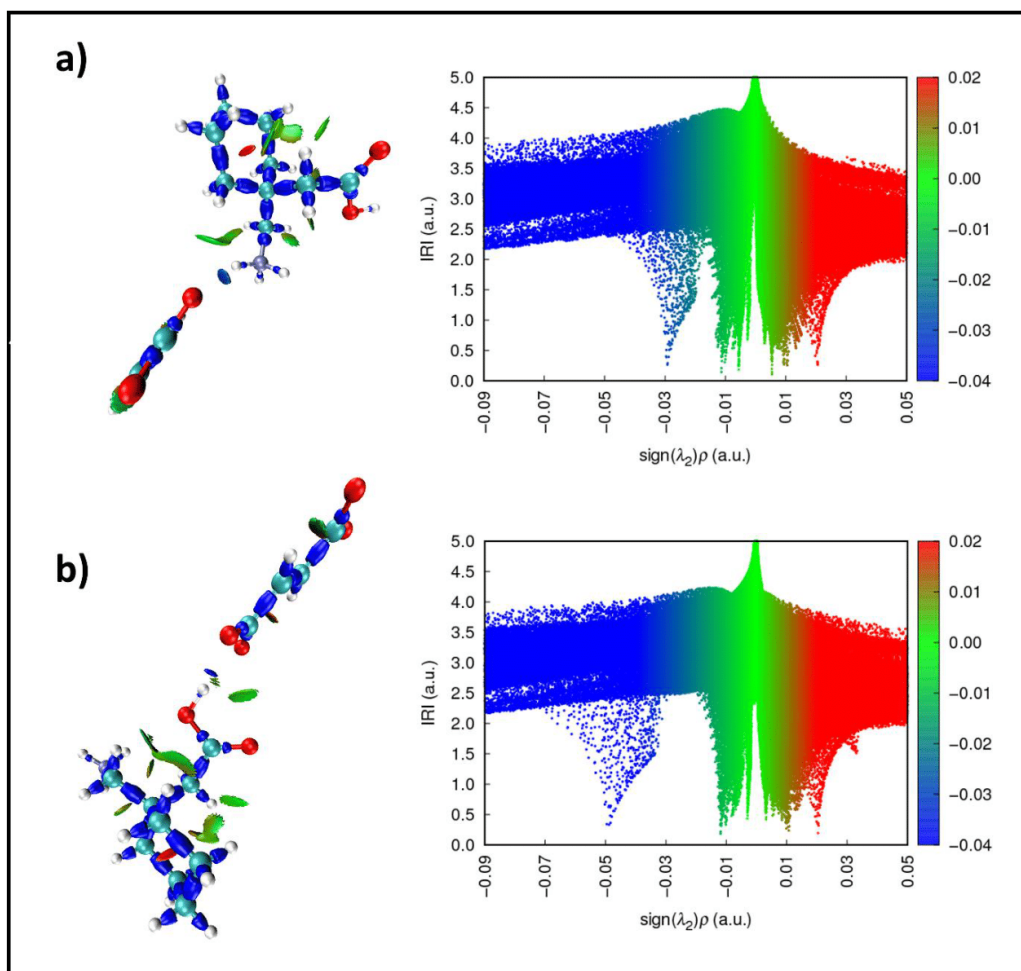


Figure S24. Interaction Region Indicator surfaces and related scatter plots of two distinctive hydrogen bonds in Gabapentin Fumarate (2:1): N1-H8...O3 a), and O1-H1...O3 b). Blue regions signify strong attraction, green regions weak attraction and red regions repulsion.

Gabapentin Fumarate (1:1) (2-3b)

Table S15. Crystallographic data for Gabapentin Fumarate (1:1).

Parameters	Gabapentin Fumarate (1:1)
Formula	C ₁₃ H ₂₁ N O ₆
Formula Moiety	C ₉ H ₁₈ N O ₂ , (C ₄ H ₃ O ₄)
M _r [g mol ⁻¹]	287.31
Temperature [K]	100.00(1)
System/space group	monoclinic, <i>P</i> 2 ₁ / <i>n</i>
a (Å)	15.1587(2)
b (Å)	7.4724(1)
c (Å)	25.7692(3)
α (°)	90
β (°)	102.285(1)
γ (°)	90
V (Å ³)	2852.09(6)
Z/Z'	8/2
Density [g/cm ³]	1.338
μ [mm ⁻¹]	0.892
T _{min} /T _{max}	0.835/0.957
F (000)	1232
Crystal size [mm]	0.05 · 0.15 · 0.21
2θ range [°]	3.1 – 77.8
Completeness [%]	100
Recorded refl.	35528
Independent refl.	5073
Goodness-of-fit F ²	1.038
X-Ray Source	Cu Kα (λ = 1.54184)
R ₁ [%] /wR ₂ [%] /S	2.85/ 7.59/ 1.04

Table S16. Distinctive energy values for the occurring HB obtained by AIM analysis via multiwfn conducted as assumed charged HB for two molecules (*E*₁), and complete interaction sphere of distinctive HB around one molecule (*E*₂), and as assumed neutral HB under the same conditions for *E*₁^{*}, *E*₂^{*}.

Hydrogen Bond	<i>E</i> ₁ [kJ mol ⁻¹]	<i>E</i> ₂ [kJ mol ⁻¹]
N1-H6...O2	-35.31	-35.95
N1-H7...O10	-14.97	-14.28
N1-H7...O12	-37.22	-36.26
N1-H8...O2	-17.06	-16.46
N1-H8...O12	-38.97	-37.89
N2-H24...O4	-14.74	-14.74
N2-H24...O8	-33.00	-31.73
N2-H25...O9	-41.64	-39.53
N2-H26...O6	-48.08	-46.56
O1-H1...O5	-111.08	-111.02
O3-H19...O9	-65.75	-64.82
O7-H39...O6	-76.81	-79.08
O11-H42...O10	-110.63	-110.63
	<i>E</i> ₁ [*] [kJ mol ⁻¹]	<i>E</i> ₂ [*] [kJ mol ⁻¹]
N1-H6...O2	-17.60	-18.03
N1-H7...O10	-3.95	-3.49
N1-H7...O12	-18.89	-18.24
N1-H8...O2	-5.35	-4.95
N1-H8...O12	-20.06	-19.34
N2-H24...O4	-3.80	-3.80
N2-H24...O8	-16.05	-15.20
N2-H25...O9	-21.85	-20.43
N2-H26...O6	-26.17	-25.16
O1-H1...O5	-68.46	-68.42
O3-H19...O9	-38.04	-37.41
O7-H39...O6	-45.46	-46.98
O11-H42...O10	-68.16	-68.16

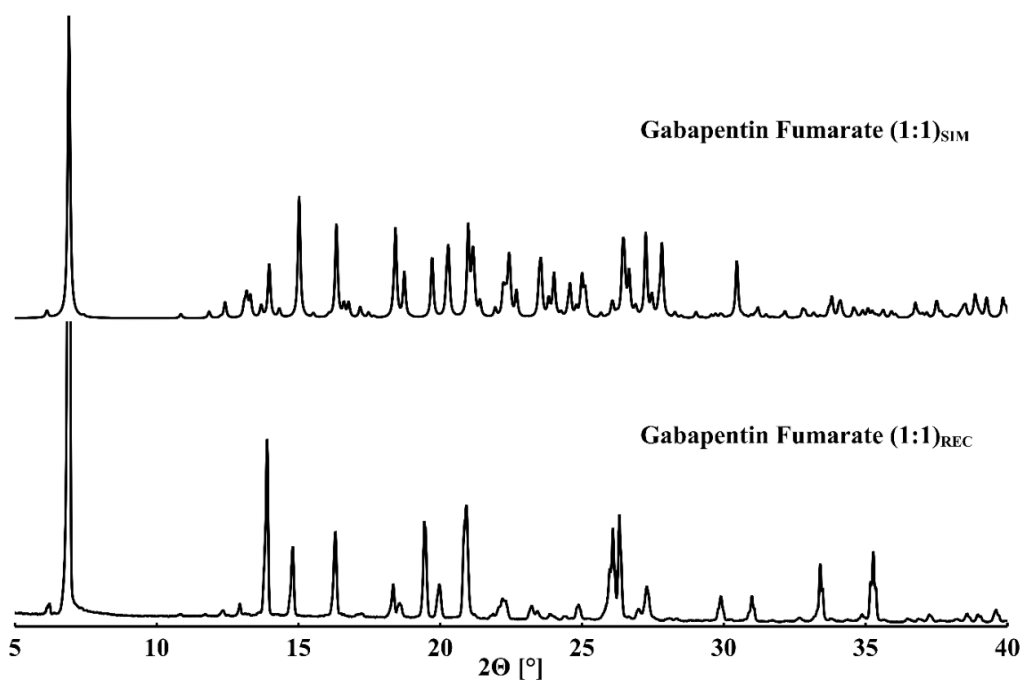


Figure S25. Powder pattern comparison of Gabapentin Fumarate (1:1). Simulated from single crystal data (top), recorded substance (bottom). A range between 5° 2 θ and 40° 2 θ is depicted.

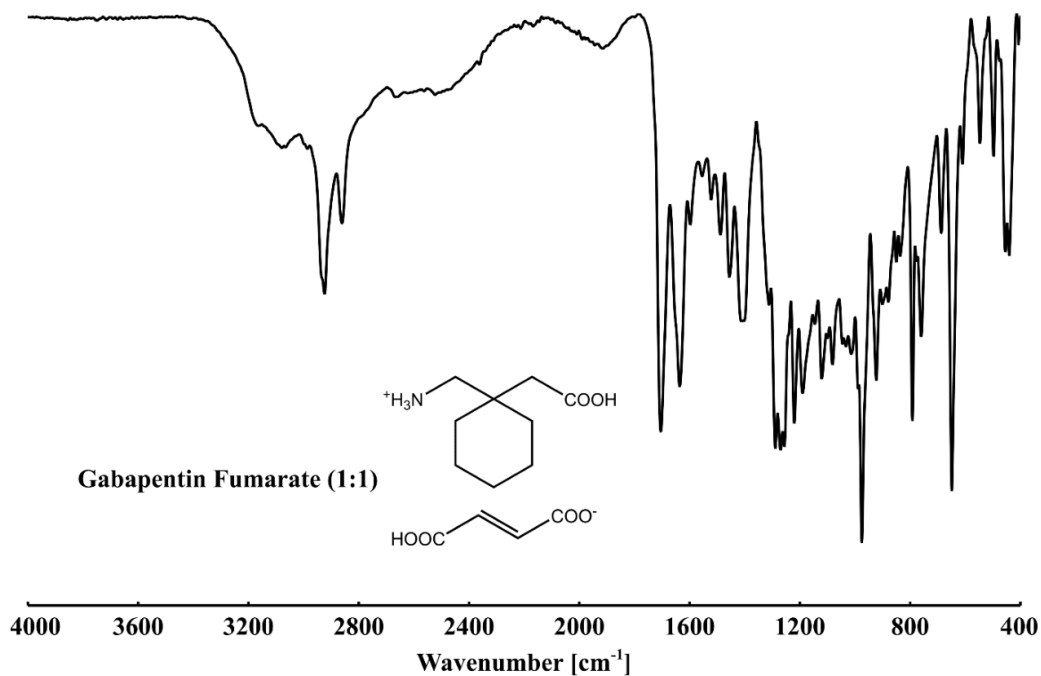


Figure S26. IR spectrum of Gabapentin Fumarate (1:1), shown in a range between 4000 cm⁻¹ – 400 cm⁻¹. Broad ammonium hydrogen bond network and C-H stretch band between 3400 cm⁻¹ and 2195 cm⁻¹, carboxyl band at 1704 cm⁻¹ carboxylate band at 1636 cm⁻¹.

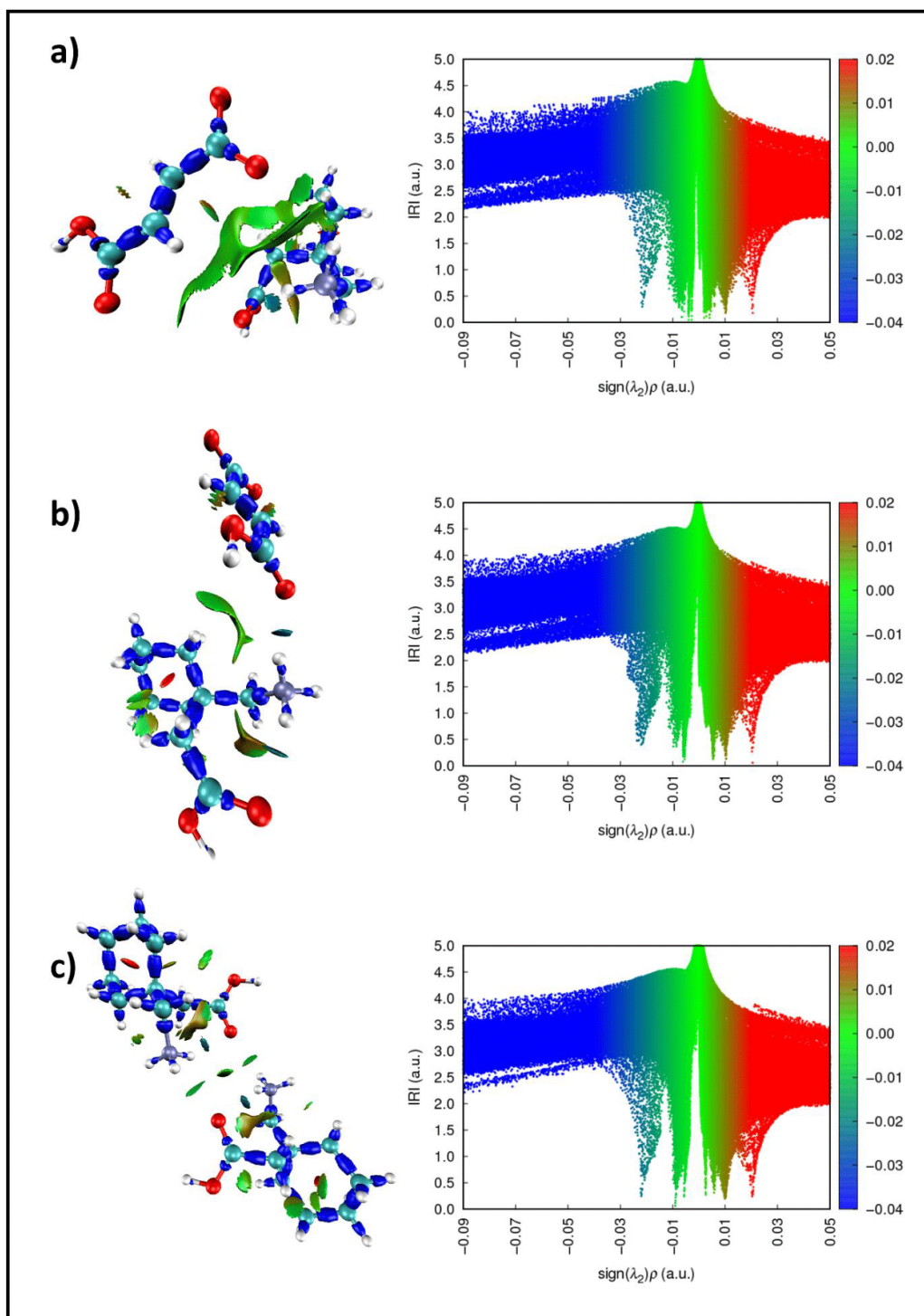


Figure S27. Interaction Region Indicator surfaces and related scatter plots of three distinctive hydrogen bonds in Gabapentin Fumarate (1:1): N1-H7...O10 a), N1-H7...O12 b), and N1-H8...O2 c). The intramolecular hydrogen bond N1-H6...O2 is best visible in c), but present in each depiction. Blue regions signify strong attraction, green regions weak attraction and red regions repulsion.

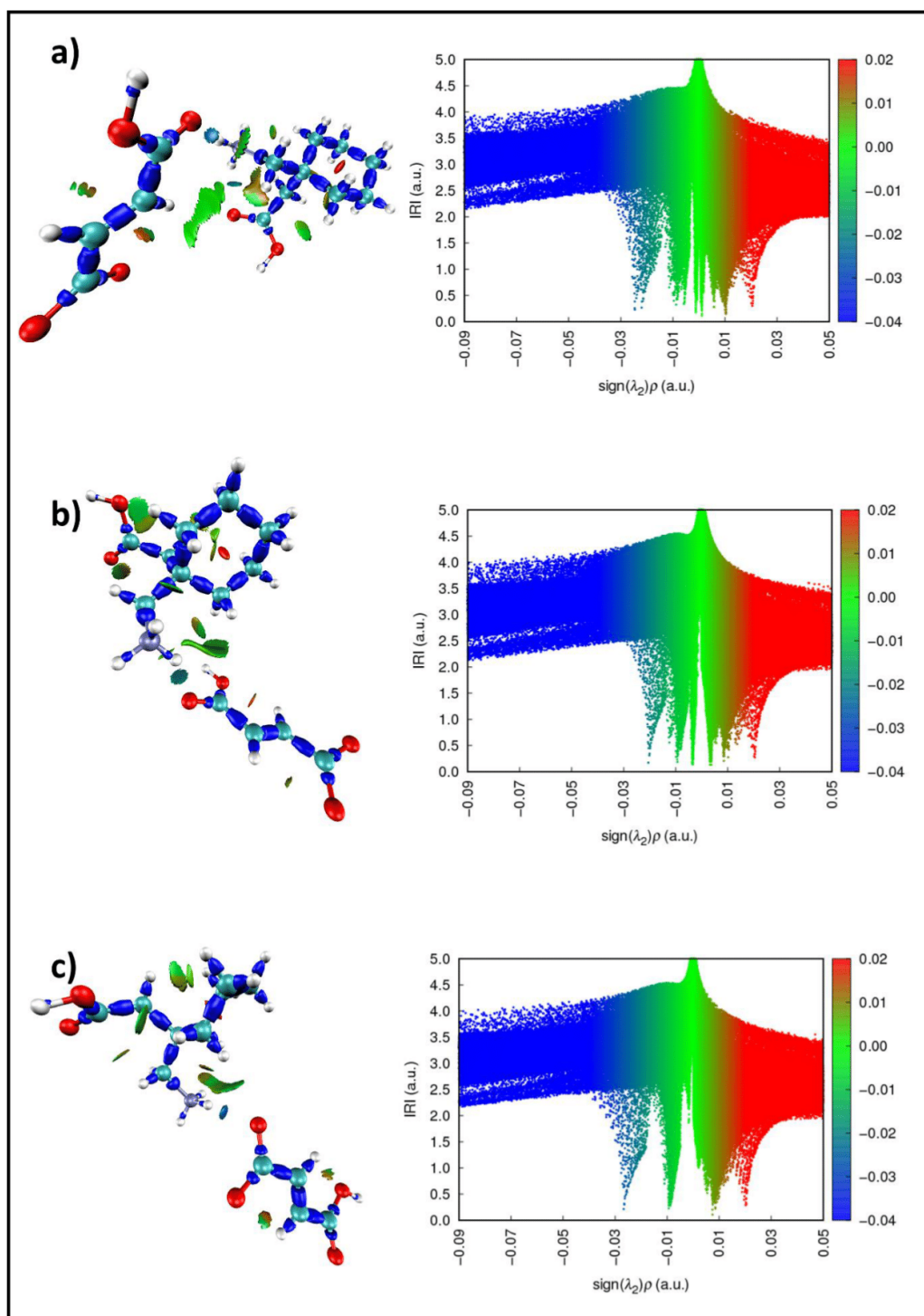


Figure S28. Interaction Region Indicator surfaces and related scatter plots of three distinctive hydrogen bonds in Gabapentin Fumarate (1:1): N1-H8...O12 a), N2-H24...O8 b), and N2-H25...O9 c). The intramolecular hydrogen bond N1-H6...O2 is best visible in a). Blue regions signify strong attraction, green regions weak attraction and red regions repulsion.

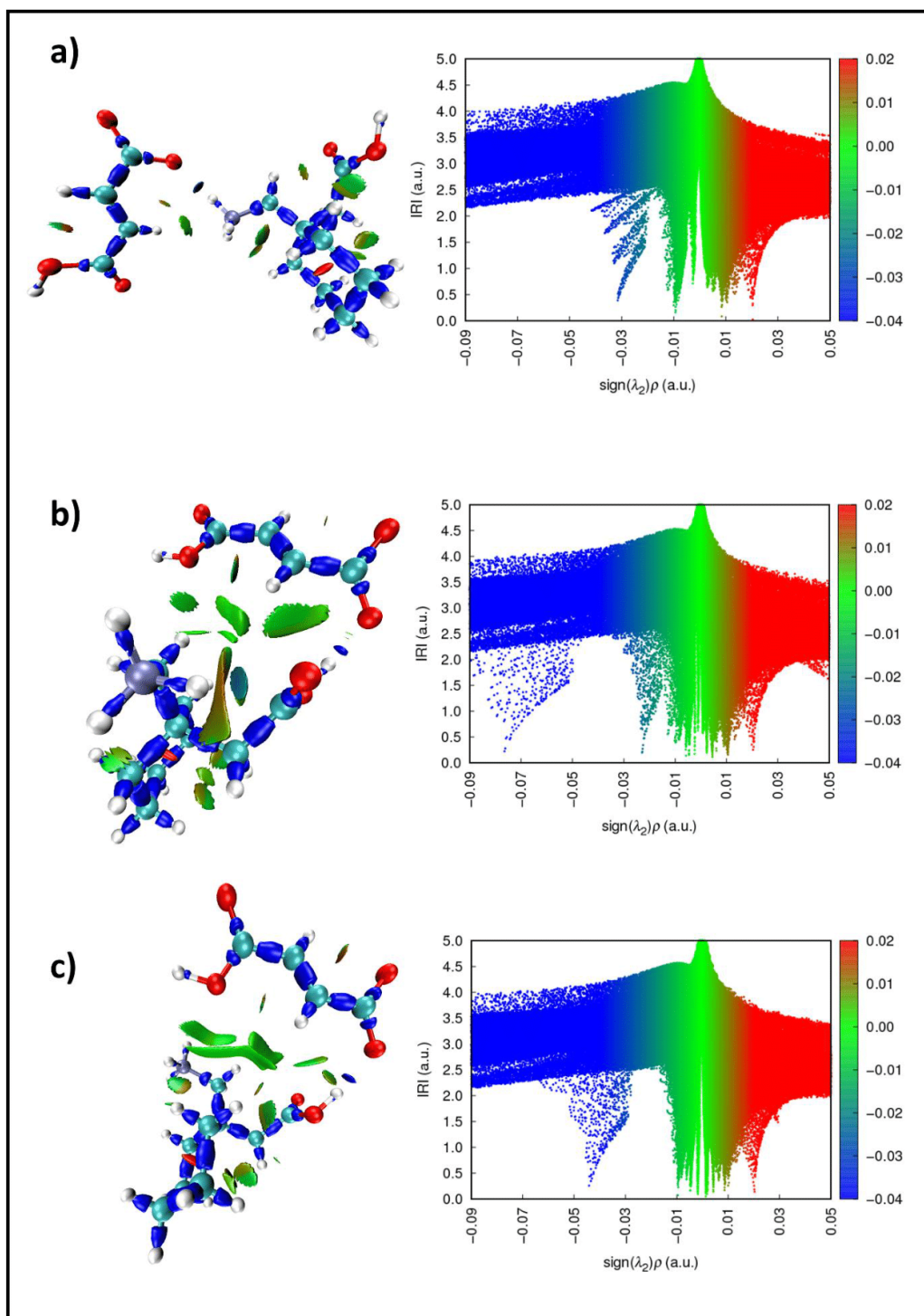


Figure S29. Interaction Region Indicator surfaces and related scatter plots of three distinctive hydrogen bonds in Gabapentin Fumarate (1:1): N2-H26...O6 a), O1-H1...O5 b), and O3-H19...O9 c). The weak hydrogen bond N2-H24...O4 is visible in c). Blue regions signify strong attraction, green regions weak attraction and red regions repulsion.

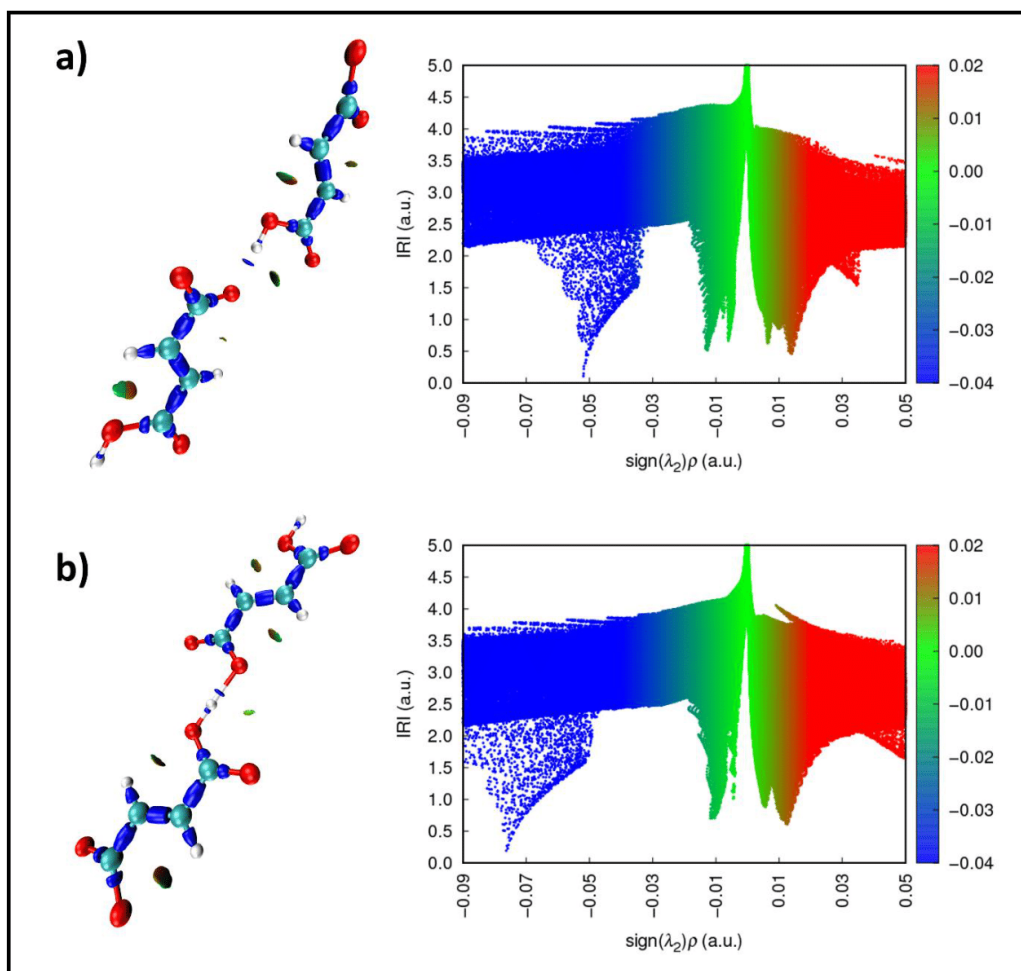


Figure S30. Interaction Region Indicator surfaces and related scatter plots of two distinctive hydrogen bonds in Gabapentin Fumarate (1:1): O7-H39...O6 a), and O11-H42...O10 b). The hydrogen bond strength in b) crossed the threshold for weak covalent interactions. Blue regions signify strong attraction, green regions weak attraction and red regions repulsion.

GABA Succinate (2:1) (1-4a)

Table S17. Crystallographic data for GABA Succinate (2:1).

Parameters	GABA Succinate (2:1)
Formula	C ₁₂ H ₂₄ N ₂ O ₈
Formula Moiety	2(C ₄ H ₁₀ N O ₂), C ₄ H ₄ O ₄
M _r [g mol ⁻¹]	324.33
Temperature [K]	100(1)
System/space group	monoclinic, <i>P</i> 2 ₁ / <i>c</i>
a (Å)	16.2100(6)
b (Å)	6.3619(2)
c (Å)	15.9402(5)
α (°)	90
β (°)	101.211(4)
γ (°)	90
V (Å ³)	1612.49(10)
Z/Z'	4/1
Density [g/cm ³]	1.336
μ [mm ⁻¹]	0.961
T _{min} /T _{max}	0.877/ 0.981
F (000)	696
Crystal size [mm]	0.02 · 0.11 · 0.14
2θ range [°]	2.7 – 67.0
Completeness [%]	99.0
Recorded refl.	10163
Independent refl.	2864
Goodness-of-fit F ²	1.072
X-Ray Source	Cu Kα (λ = 1.54184)
R ₁ [%] /wR ₂ [%] /S	3.89/ 9.35/ 1.07

Table S18. Distinctive energy values for the occurring HB obtained by AIM analysis via multiwfn conducted as assumed charged HB for two molecules (*E*₁), and complete interaction sphere of distinctive HB around one molecule (*E*₂), and as assumed neutral HB under the same conditions for *E*₁^{*}, *E*₂^{*}.

Hydrogen Bond	<i>E</i> ₁ [kJ mol ⁻¹]	<i>E</i> ₂ [kJ mol ⁻¹]
N1-H8...O5	-52.26	-49.35
N1-H9...O6	-41.14	-38.06
N1-H10...O6	-43.73	-42.08
N2-H18...O7	-49.47	-46.97
N2-H19...O8	-41.51	-39.58
N2-H20...O8	-51.29	-47.73
O1-H1...O5	-84.68	-83.81
O3-H11...O4	-64.86	-64.37
	<i>E</i> ₁ [*] [kJ mol ⁻¹]	<i>E</i> ₂ [*] [kJ mol ⁻¹]
N1-H8...O5	-28.98	-27.02
N1-H9...O6	-21.52	-19.44
N1-H10...O6	-23.26	-22.15
N2-H18...O7	-27.11	-25.43
N2-H19...O8	-21.76	-20.47
N2-H20...O8	-28.32	-25.94
O1-H1...O5	-50.74	-50.16
O3-H11...O4	-37.44	-37.11

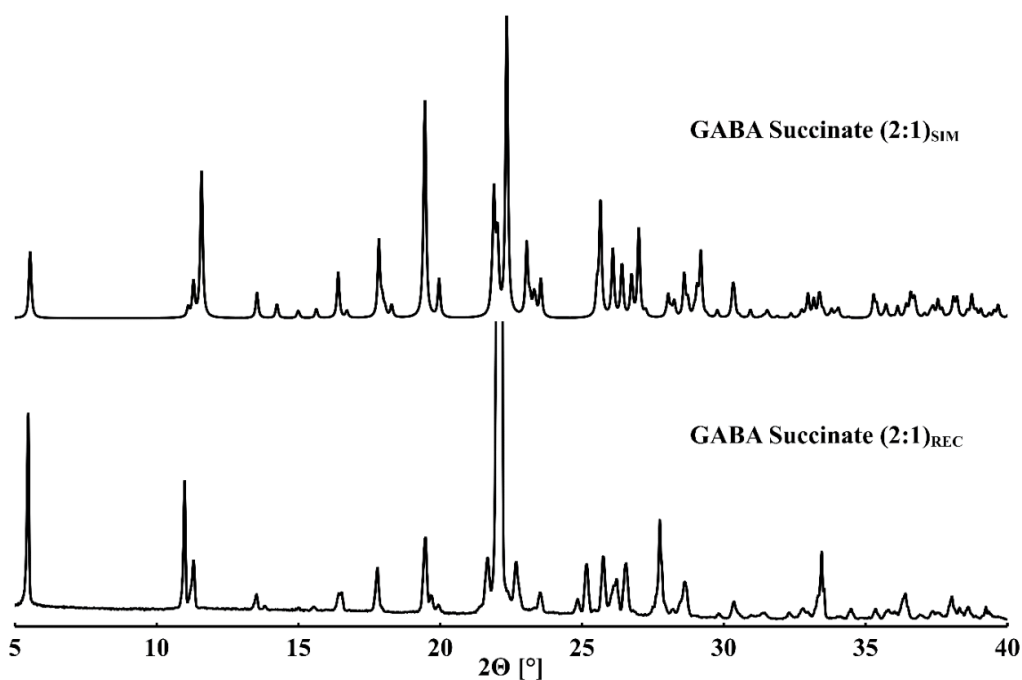


Figure S31. Powder pattern comparison of GABA Succinate (2:1). Simulated from single crystal data (top), recorded substance (bottom). A range between 5° 2 θ and 40° 2 θ is depicted.

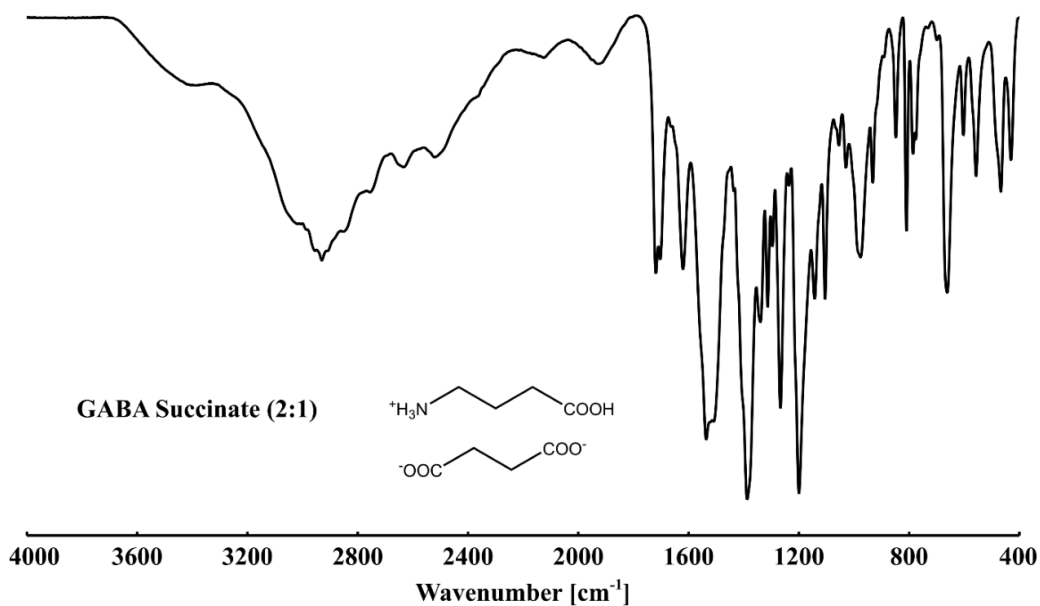


Figure S32. IR spectrum of GABA Succinate (2:1), shown in a range between 4000 cm^{-1} – 400 cm^{-1} . Broad ammonium hydrogen bond network and C-H stretch band between 3700 cm^{-1} and 2240 cm^{-1} , carboxyl band at 1718 cm^{-1} carboxylate band at 1620 cm^{-1} .

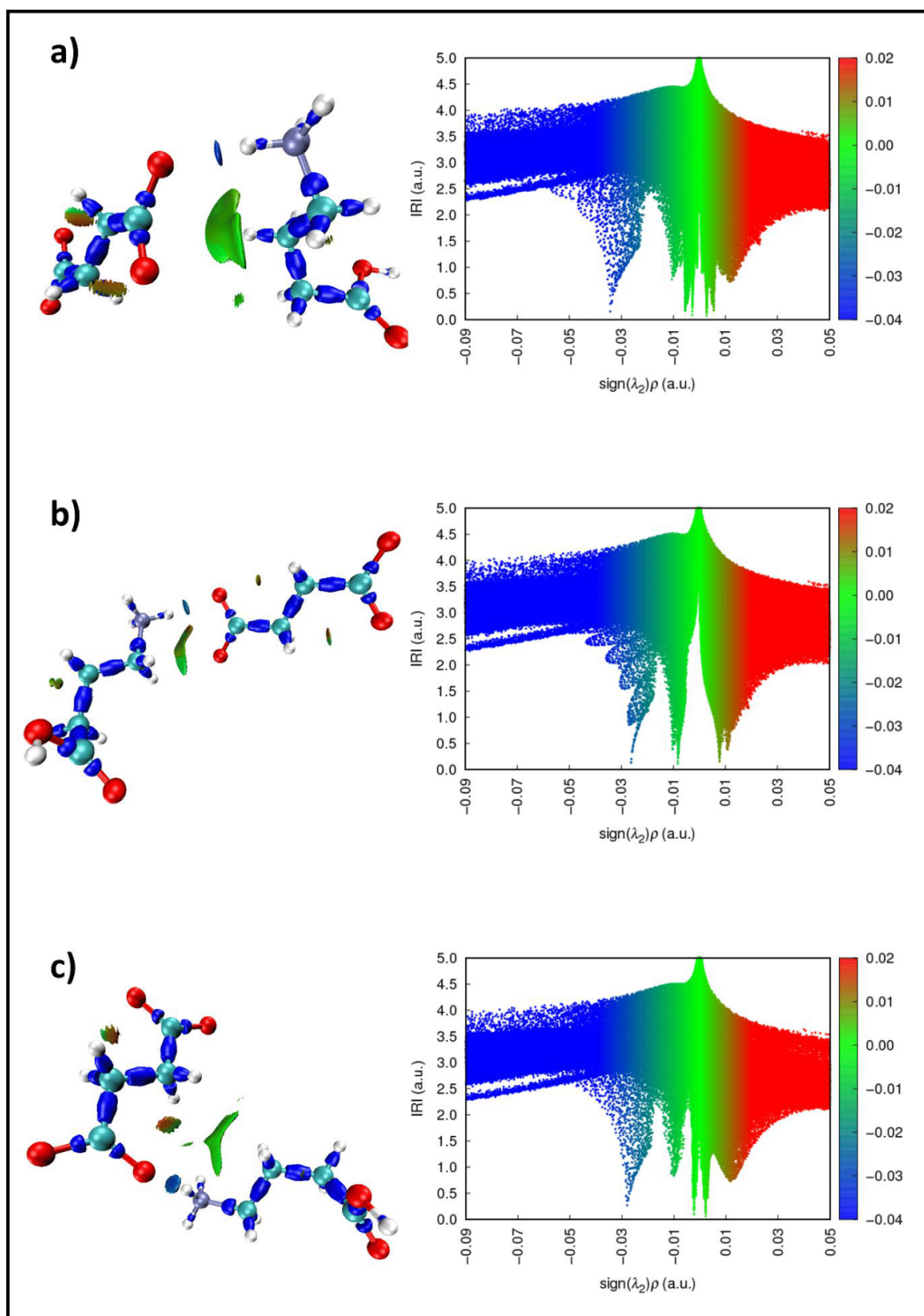


Figure S33. Interaction Region Indicator surfaces and related scatter plots of three distinctive hydrogen bonds in GABA Succinate (2:1): N1-H8...O5 a), N1-H9...O6 b), and N1-H10...O6 c). Blue regions signify strong attraction, green regions weak attraction and red regions repulsion.

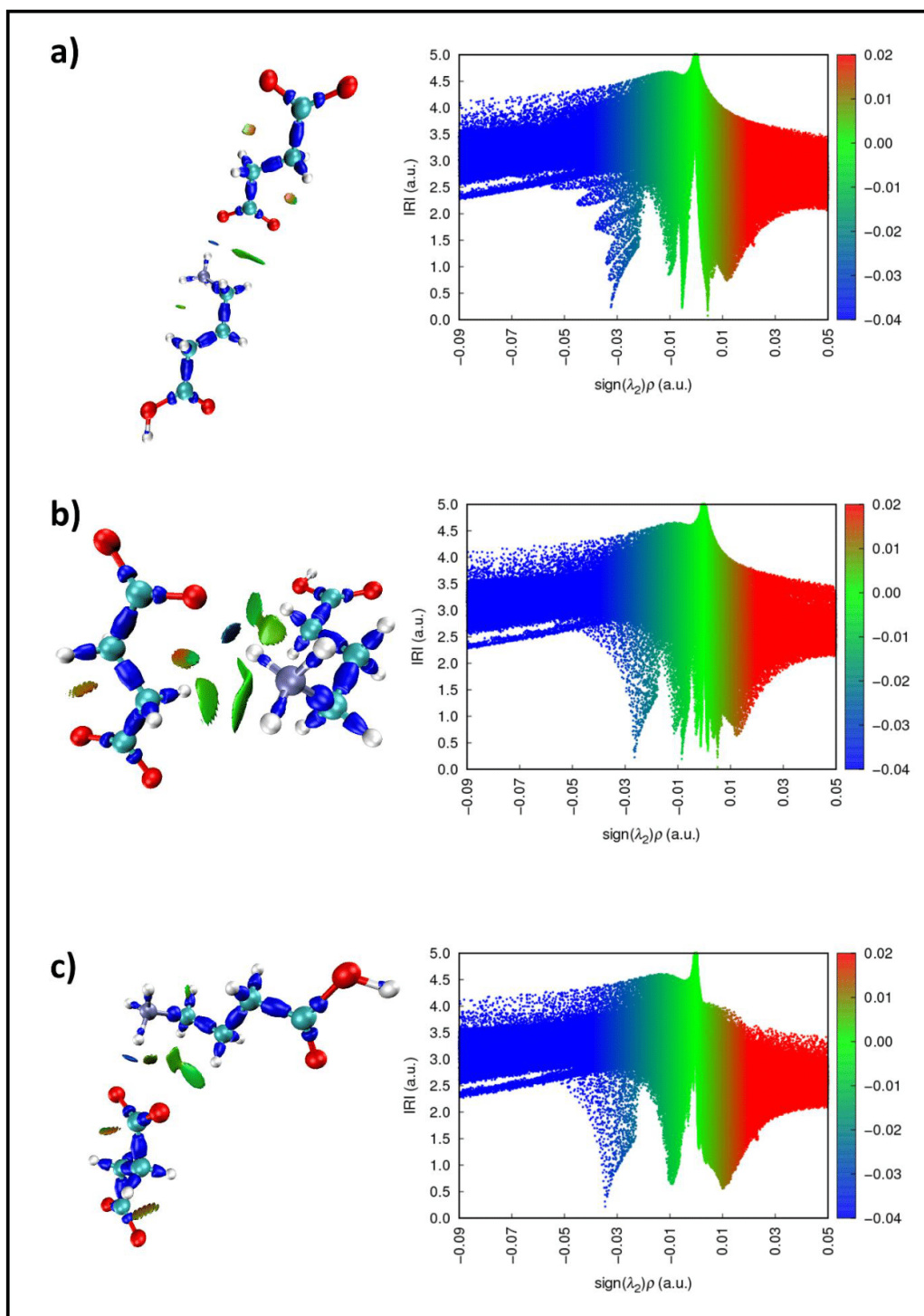


Figure S34. Interaction Region Indicator surfaces and related scatter plots of three distinctive hydrogen bonds in GABA Succinate (2:1): N2-H18...O7 a), N2-H19...O8 b), and N2-H20...O8 c). Blue regions signify strong attraction, green regions weak attraction and red regions repulsion.

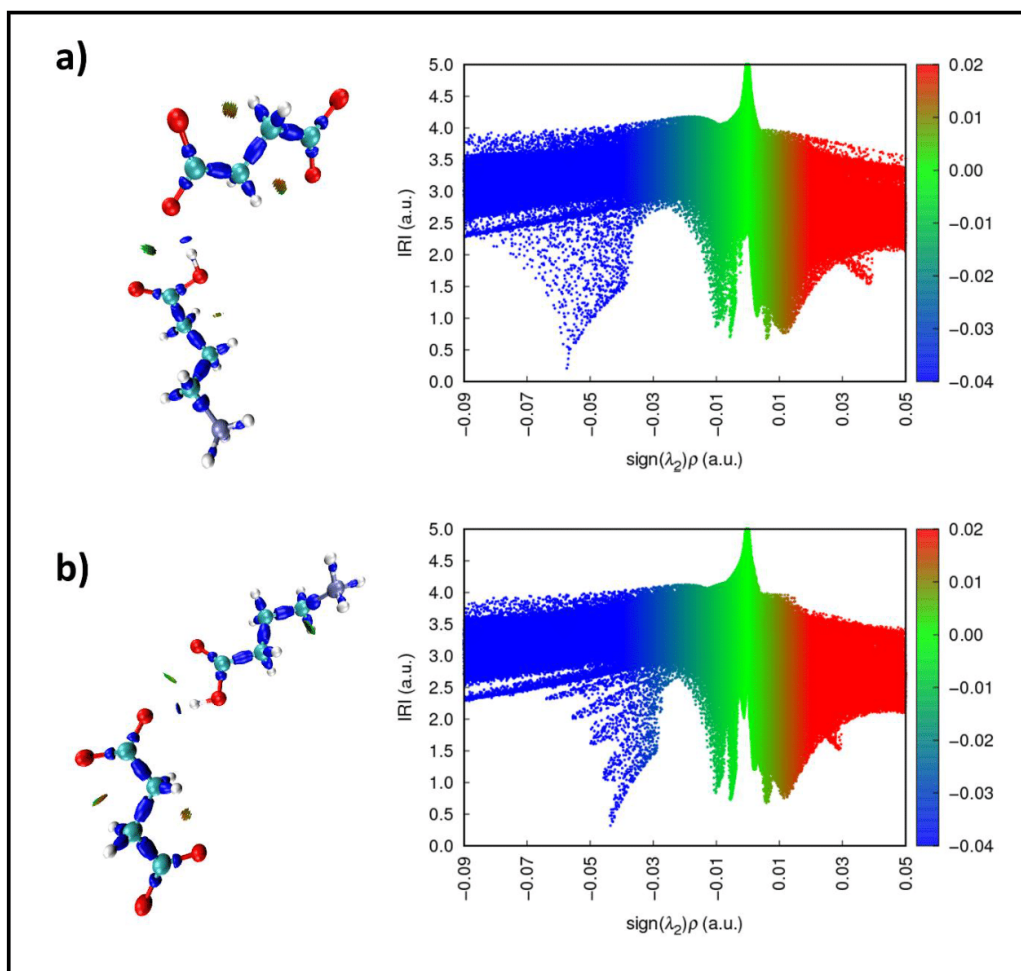


Figure S35. Interaction Region Indicator surfaces and related scatter plots of two distinctive hydrogen bonds in GABA Succinate (2:1): O1-H1...O5 a), and O3-H11...O7 b). Blue regions signify strong attraction, green regions weak attraction and red regions repulsion.

GABA Succinate (1:1) (1-4b)

Table S19. Crystallographic data GABA Succinate (1:1).

Parameters	GABA Succinate (1:1)
Formula	C ₈ H ₁₅ N O ₆
Formula Moiety	C ₄ H ₁₀ N O ₂ , C ₄ H ₅ O ₄
M _r [g mol ⁻¹]	221.21
Temperature [K]	99.8(3)
System/space group	monoclinic, <i>P</i> 2 ₁
a (Å)	5.1129(1)
b (Å)	13.3267(2)
c (Å)	7.1747(1)
α (°)	90
β (°)	95.396(1)
γ (°)	90
V (Å ³)	486.704(14)
Z/Z'	2/1
Density [g/cm ³]	1.509
μ [mm ⁻¹]	1.120
T _{min} /T _{max}	0.558/0.824
F (000)	236
Crystal size [mm]	0.18 · 0.22 · 0.59
2θ range [°]	3.3 – 77.5
Completeness [%]	99.8
Recorded refl.	4662
Independent refl.	1730
Goodness-of-fit F ²	1.108
X-Ray Source	Cu Kα (λ = 1.54184)
Flack x	0.07(7)
R ₁ [%] /wR ₂ [%] /S	2.32/ 5.93/ 1.11

Table S20. Distinctive energy values for the occurring HB obtained by AIM analysis via multiwfn conducted as assumed charged HB for two molecules (*E*₁), and complete interaction sphere of distinctive HB around one molecule (*E*₂), and as assumed neutral HB under the same conditions for *E*₁^{*}, *E*₂^{*}.

Hydrogen Bond	<i>E</i> ₁ [kJ mol ⁻¹]	<i>E</i> ₂ [kJ mol ⁻¹]
N1-H8...O2	-38.57	-38.24
N1-H9...O2	-33.56	-33.86
N1-H10...O6	-30.40	-30.26
O1-H1...O3	-104.67	-104.44
O5-H11...O4	-52.74	-53.37
	<i>E</i> ₁ [*] [kJ mol ⁻¹]	<i>E</i> ₂ [*] [kJ mol ⁻¹]
N1-H8...O2	-19.79	-19.57
N1-H9...O2	-16.43	-16.63
N1-H10...O6	-14.30	-14.21
O1-H1...O3	-64.16	-64.01
O5-H11...O4	-29.30	-29.73

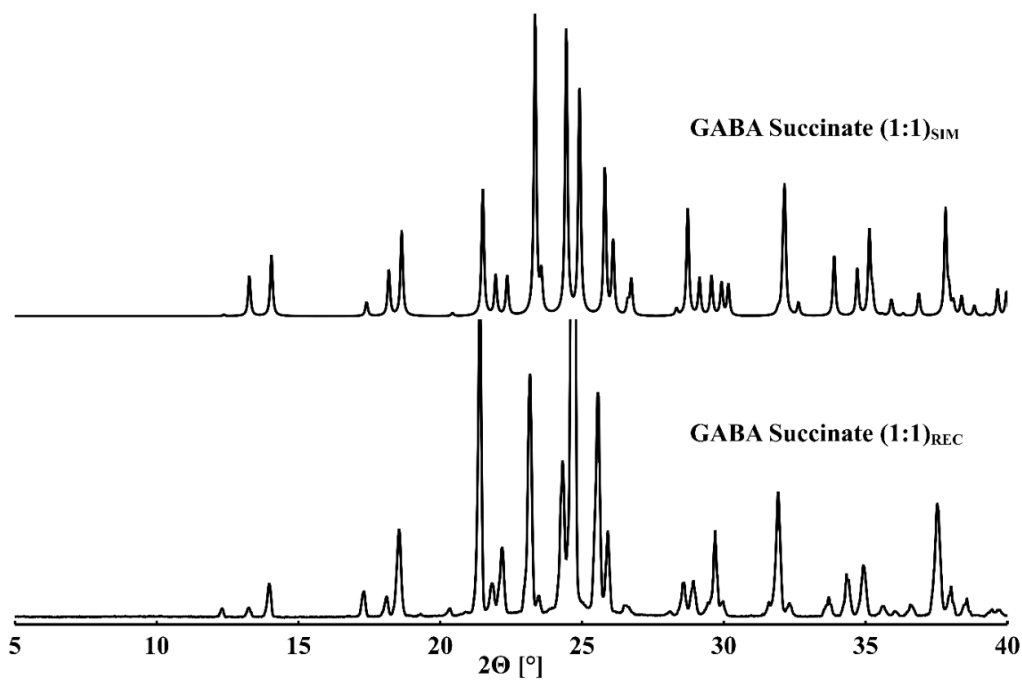


Figure S36. Powder pattern comparison of GABA Succinate (1:1). Simulated from single crystal data (top), recorded substance (bottom). A range between 5° 2 θ and 40° 2 θ is depicted.

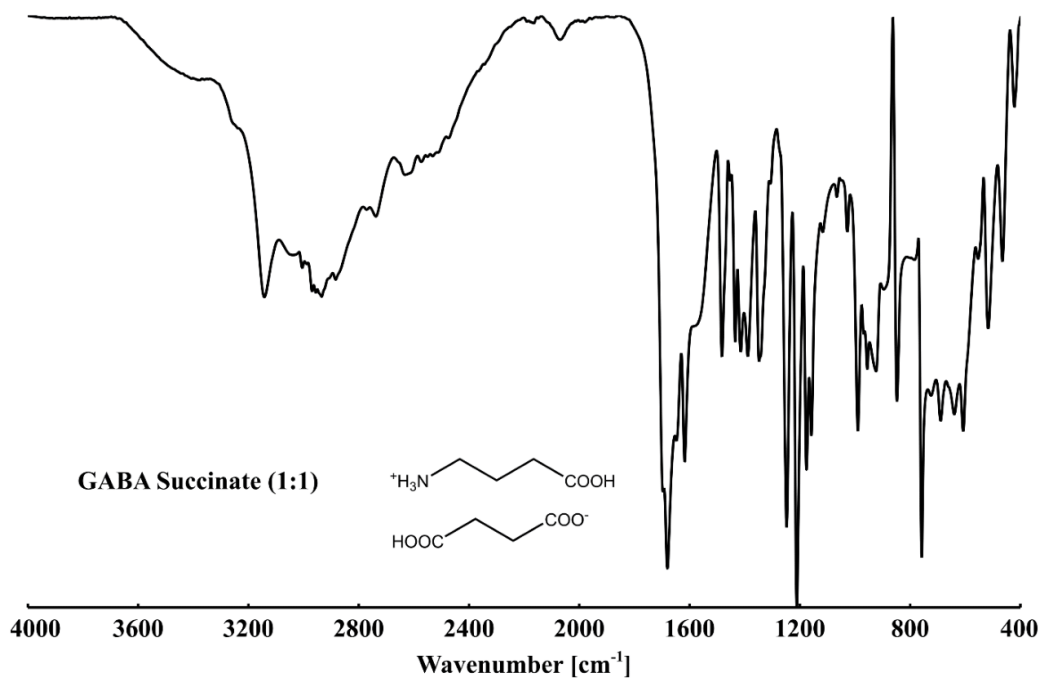


Figure S37. IR spectrum of GABA Succinate (1:1), shown in a range between 4000 cm^{-1} – 400 cm^{-1} . Broad ammonium hydrogen bond network and C-H stretch band between 3690 cm^{-1} and 2210 cm^{-1} ; carboxyl band at 1680 cm^{-1} carboxylate band at 1618 cm^{-1} .

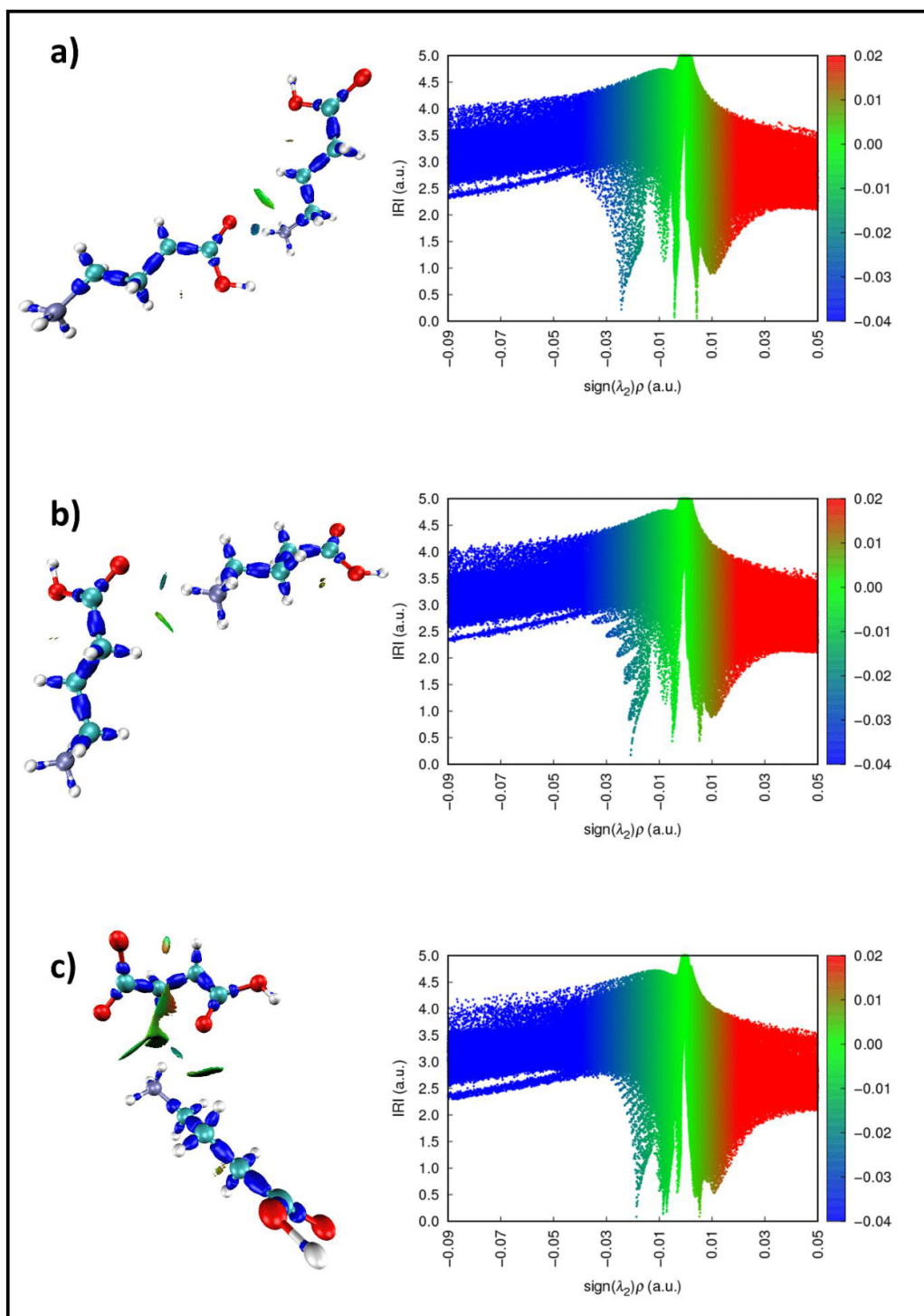


Figure S38. Interaction Region Indicator surfaces and related scatter plots of three distinctive hydrogen bonds in GABA Succinate (1:1): N1-H8...O2 a), N1-H9...O2 b), and N1-H10...O6 c). Blue regions signify strong attraction, green regions weak attraction and red regions repulsion.

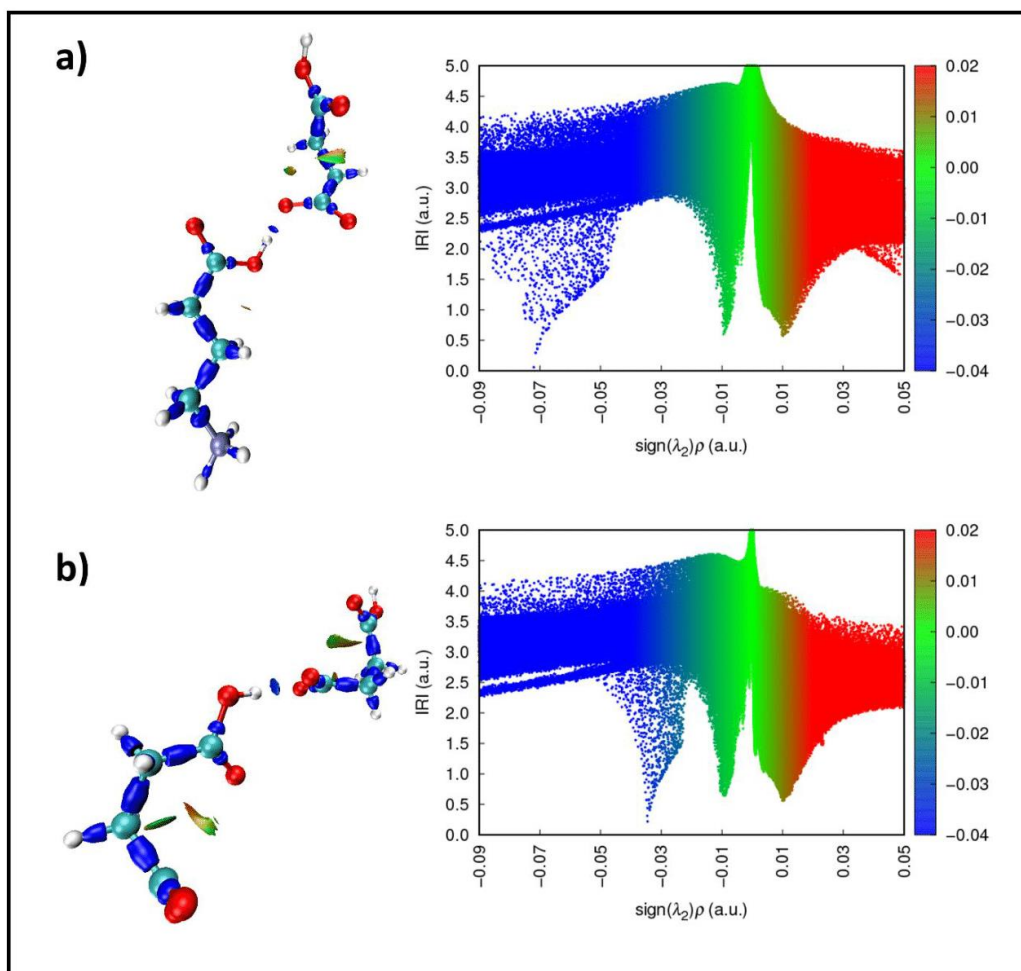


Figure S39. Interaction Region Indicator surfaces and related scatter plots of two distinctive hydrogen bonds in GABA Succinate (1:1): O1-H1...O3 a), and O5-H11...O4 b). Blue regions signify strong attraction, green regions weak attraction and red regions repulsion.

Gabapentin:Succinic acid (2:1) (2-4)

Table S21. Crystallographic data for Gabapentin:Succinic acid (2:1).

Parameters	Gabapentin:Succinic acid (2:1)
Formula	C ₁₁ H ₂₀ N O ₈
Formula Moiety	C ₉ H ₁₇ N O ₂ , 0.5(C ₄ H ₆ O ₄)
M _r [g mol ⁻¹]	230.28
Temperature [K]	100.01(1)
System/space group	monoclinic, <i>P</i> 2 ₁ / <i>c</i>
a (Å)	18.4497(5)
b (Å)	6.4446(1)
c (Å)	10.3289(3)
α (°)	90
β (°)	103.111(3)
γ (°)	90
V (Å ³)	1196.10(5)
Z/Z'	4/1
Density [g/cm ³]	1.279
μ [mm ⁻¹]	0.800
T _{min} /T _{max}	1.000/1.000
F (000)	500
Crystal size [mm]	0.06 · 0.10 · 0.22
2θ range [°]	2.4 – 77.8
Completeness [%]	99.7
Recorded refl.	12538
Independent refl.	2134
Goodness-of-fit F ²	1.077
X-Ray Source	Cu Kα (λ = 1.54184)
R ₁ [%] /wR ₂ [%] /S	5.32/ 13.55/ 1.08

Table S22. Distinctive energy values for the occurring HB obtained by AIM analysis via multiwfn conducted as assumed charged HB for two molecules (*E*₁), and complete interaction sphere of distinctive HB around one molecule (*E*₂), and as assumed neutral HB under the same conditions for *E*₁^{*}, *E*₂^{*}.

Hydrogen Bond	<i>E</i> ₁ [kJ mol ⁻¹]	<i>E</i> ₂ [kJ mol ⁻¹]
N1-H5...O1	-36.47	-36.02
N1-H5...O3	-16.71	-16.67
N1-H6...O4	-38.62	-38.37
N1-H7...O2	-56.03	-55.59
O3-H18...O1	-111.50	-112.78
	<i>E</i> ₁ [*] [kJ mol ⁻¹]	<i>E</i> ₂ [*] [kJ mol ⁻¹]
N1-H5...O1	-18.38	-18.08
N1-H5...O3	-5.12	-5.09
N1-H6...O4	-19.82	-19.66
N1-H7...O2	-31.51	-31.22
O3-H18...O1	-68.74	-69.60

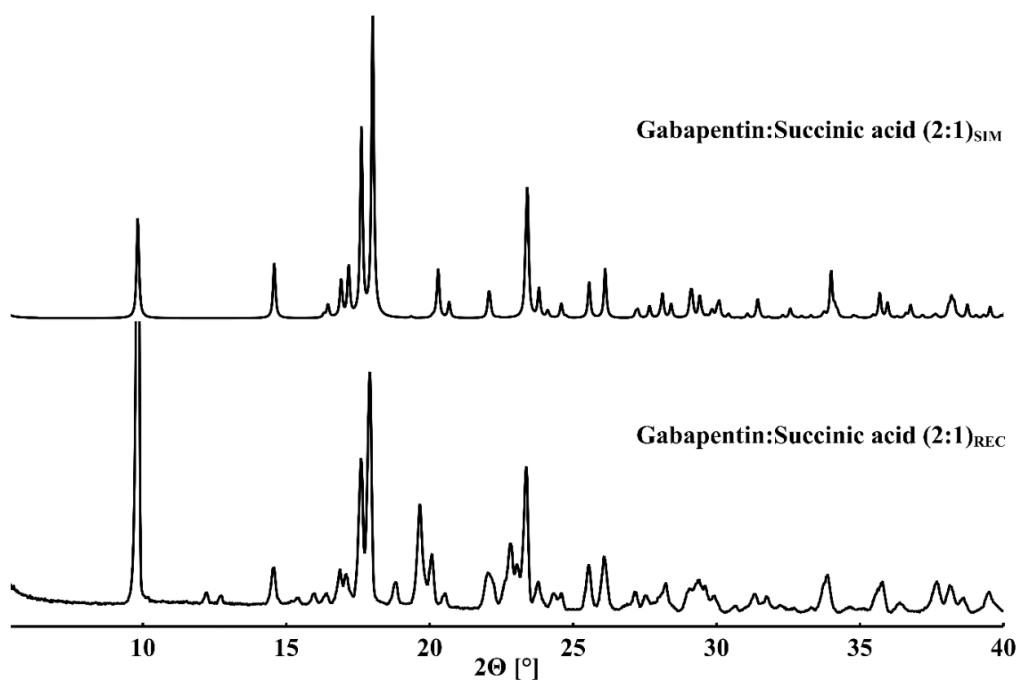


Figure S40. Powder pattern comparison of Gabapentin:Succinic acid (2:1). Simulated from single crystal data (top), recorded substance (bottom). A range between 5° 2 θ and 40° 2 θ is depicted.

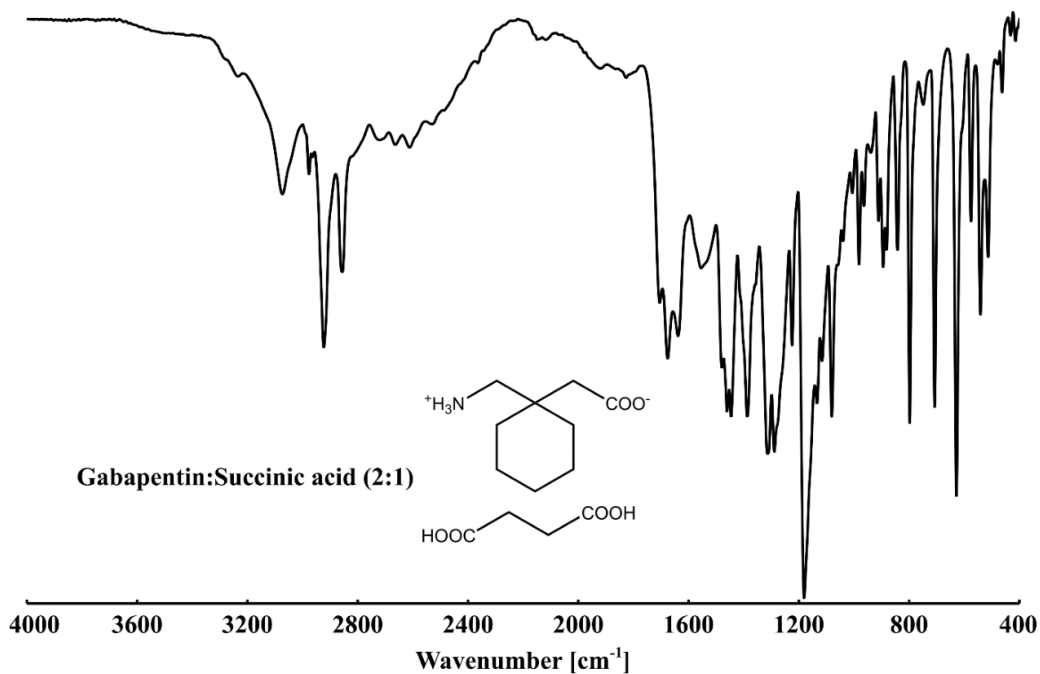


Figure S41. IR spectrum of Gabapentin:Succinic acid (2:1), shown in a range between 4000 cm^{-1} – 400 cm^{-1} . Broad ammonium hydrogen bond network and C-H stretch band between 3660 cm^{-1} and 2225 cm^{-1} , carboxyl band at 1704 cm^{-1} carboxylate band at 1676 cm^{-1} .

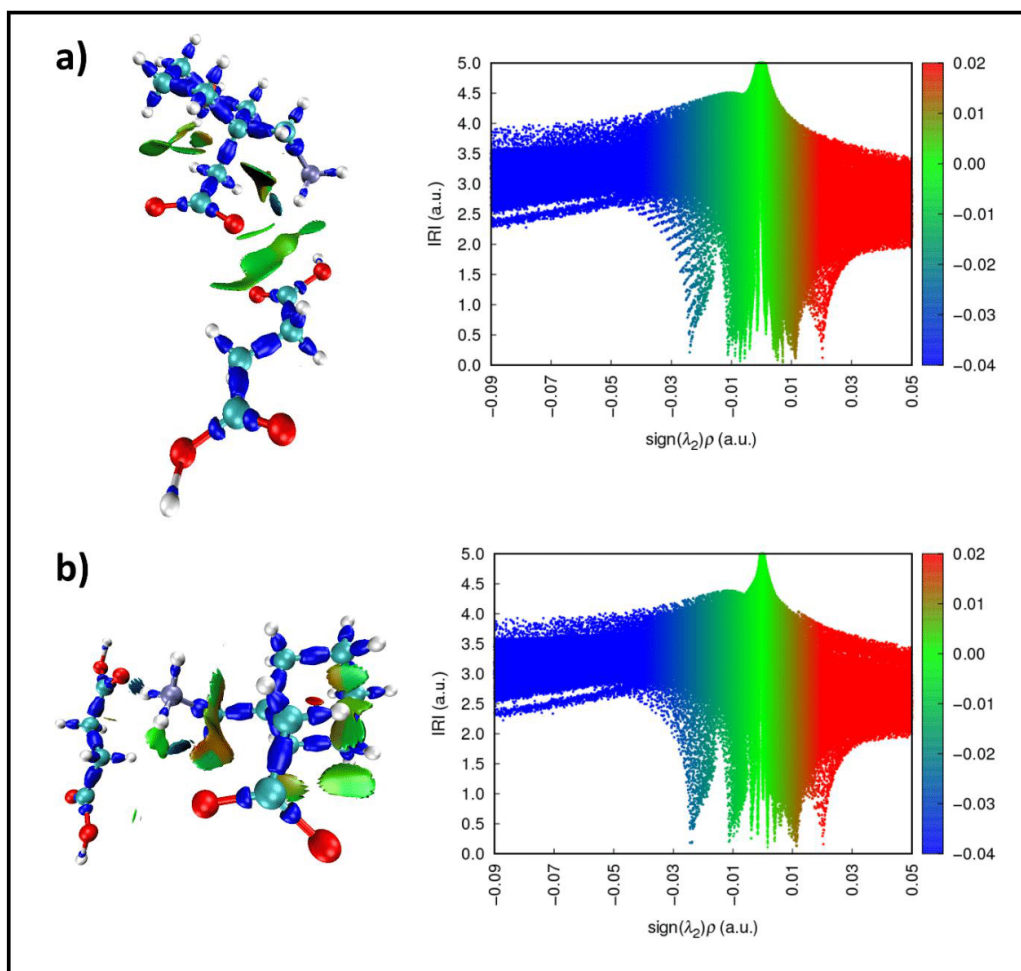


Figure S42. Interaction Region Indicator surfaces and related scatter plots of two distinctive hydrogen bonds in Gabapentin:Succinic acid (2:1): N1-H5...O3 a), and N1-H6...O4 b). The intramolecular hydrogen bond N1-H5...O1 is best visible in a), but present in both. Blue regions signify strong attraction, green regions weak attraction and red regions repulsion.

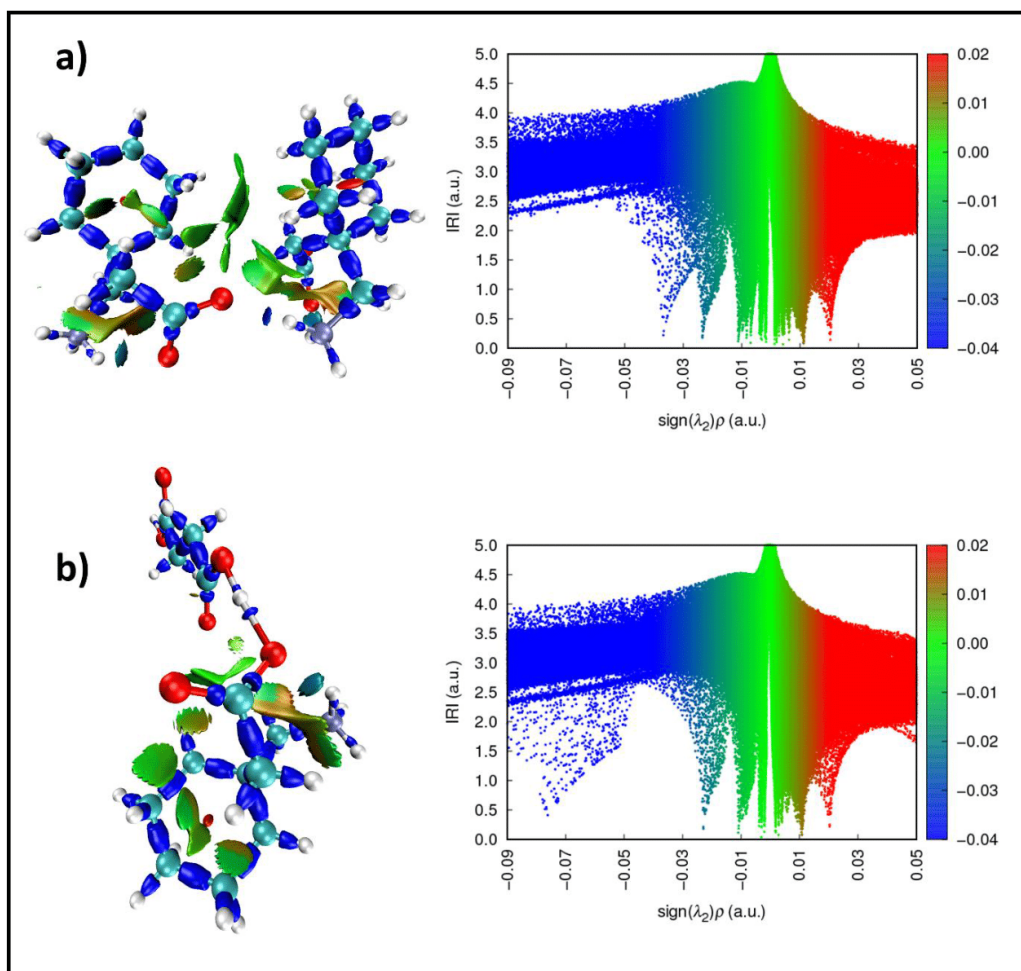


Figure S43. Interaction Region Indicator surfaces and related scatter plots of two distinctive hydrogen bonds in Gabapentin:Succinic acid (2:1): N1-H7...O2 a), and O3-H18...O1 b). The intramolecular hydrogen bond N1-H5...O1 is best visible in a), but present in both. The hydrogen bond strength in b) crossed the threshold for weak covalent interactions. Blue regions signify strong attraction, green regions weak attraction and red regions repulsion.

4 Summary and Outlook

The conducted thesis on GABA and its pharmaceutically active derivatives emphasizes the inherent problem of crystal engineering: even the slightest distinctions on target molecules, crystal synthesis process or crystallization conditions can have grave effects on the crystal structure. An evaluation of the published works based on the previously formulated questions summarizes the point.

In how far are structural properties between the investigated species comparable regarding intermolecular interaction motifs in single and multicomponent systems?

This question was discussed to some degree in all presented publications. For single component entities, some similarities can be observed in most compounds. In GABA, Gabapentin, Pregabalin, Phenibut, and Baclofen singular species a very prevalent basic interaction motif is present. The ammonium subunit serves as a threefold HB donor, while the carboxylate entity serves as a HB acceptor, once on one of the carboxylate oxygens, twice on the other one (**Figure 11**).

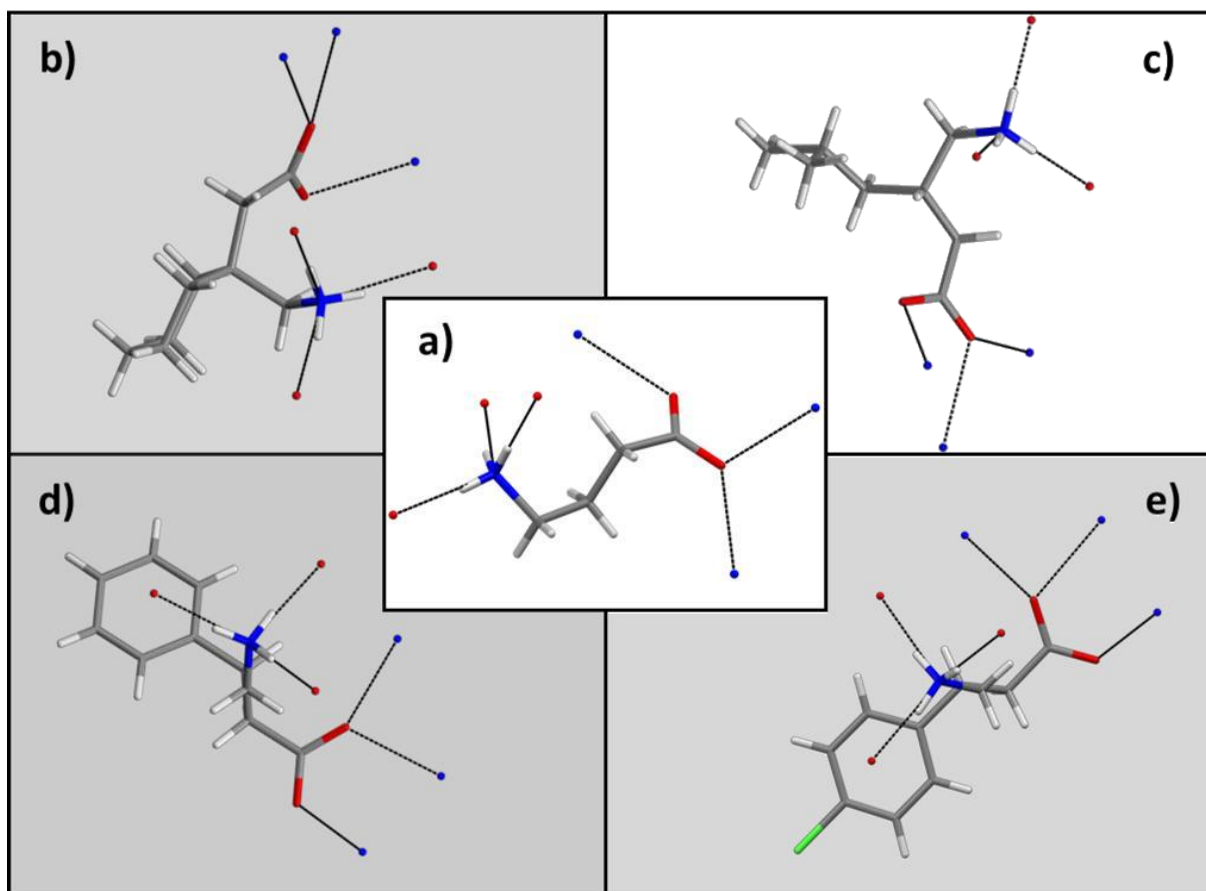


Figure 11. Visualisation of the HB properties on the GABA chain of the investigated APIs, with **a)** GABA form II, **b)** Gabapentin form II, **c)** (S)-Pregabalin, **d)** Phenibut, and **e)** Baclofen,⁴²³ as proposed by Maniukiewicz and colleagues.

However, the identification of this simple motif is where the structural commonalities end. The different described polymorphs of GABA and Gabapentin for example already show some decisive distinctiveness regarding their crystal makeup between I and II or II and IV-forms respectively. The HBs they form are similar in ways such as lengths, angles, and even energetic contributions, but different overall lattice motives are undertaken. Concerning multicomponent entities like co-crystals or salts this behaviour becomes even more pronounced. In many of the described structures of GABA-derivatives with carboxylic acids a strong HB between a carboxyl and carboxylate group is observed, as well as a threefold HB-donor function in ammonium subunits. But the crystal structures are very diverse depending for example on the API and co-former ratio, the solvent or crystal preparation method. As was shown, even the inversion of a chirality centre can make the difference between a salt and a co-crystal. The conducted investigations showcase how such molecularly similar entities can pose a vast variability in their supramolecular aggregation behaviour, and that while their interaction mode may be similar, their final structures need not be.

Are there co-formers that form a multicomponent entity with each compound, and do these potential forms show similar physicochemical properties?

The first part of this question can be answered affirmatively. It was possible to synthesize maleates of all compounds. However, while solubility increases and melting point decreases could be recorded, these are by no means intuitive. For the described Pregabalin species the solubility increases are exceedingly vast while for Baclofen the increase is percentual high but negligible in total. These differences can probably be attributed to the structural distinctions on a molecular as well as crystal level to some degree. They remain unpredictable however: Phenibut, structurally very similar to Baclofen, shows quite a high solubility increase, similar to that of Gabapentin. Gabapentin, on the other hand, is structurally closer related to Pregabalin, yet the solubility increase is marginal compared to that of the investigated Pregabalin forms. The conducted experiments highlight that multicomponent formation can improve desired physicochemical properties substantially, but assumptions about similar enhancements for structurally related compounds can hardly be made.

How does the crystal synthesis route affect the outcome of a crystallization for the central compounds? Are there any similarities between them?

It was shown that the crystal synthesis route can significantly affect the crystallization product. It can be worthwhile to investigate which method leads to not only the desired outcome but may also be the quickest, most resourceful, and offers a uniform quality of the target species. However, it is again almost impossible to predict whether a synthesis route that works well for one compound is also beneficial for the other. Aside from stating a further polymorph or anhydrous phase, that is otherwise not accessible, could be obtained for example via mechanochemical means, more profound predictions are hardly possible. Polymorphic phase shifts can be induced for example in GABA and Gabapentin mechanochemically, but the other substances apparently remain unaffected. Other examples are the mechanochemically produced maleates of (rac)-Pregabalin and Gabapentin. In the latter, a hydrate is received from solution and as such it can be assumed an anhydrous phase is produced in the ball mill. However, (rac)-Pregabalin rather seems to undergo a polymorphic phase shift, as the solution product already is an anhydrous phase. For all the other investigated species, no phase differences occur at all between solution and mechanochemical crystallization. Thus, the crystal synthesis route plays a crucial role to obtain a desired product but offers no means of profoundly predicting any crystallization behaviour.

How do established processes for example regarding enantiopurification work? Which structural characteristics enable these methods? Can this be transferred to other similar systems as well?

Structural differences between multicomponent systems of Pregabalin and mandelic acid enantiomers that enable the deracemization of Pregabalin were identified and the established process was improved. The formation of a salt and a co-crystal of different solubility properties depending on the chiral information in mandelic acid makes it possible to remove the more soluble variant by washing. Even though a similar example exists in the literature for Baclofen, this process could not be transferred to Phenibut under the investigated conditions. Why does the ability to form a salt or co-crystal depending on molecular chirality skip Phenibut? Does the investigated process even work the same for Baclofen? This question is not definitively answered by Songsermawad et al., and patents remain deliberately unclear. This again demonstrates the central point of this thesis: It is important and fruitful to investigate crystallization properties of APIs, but even between extremely similar compounds vastly different behaviour can occur.

Even among molecularly related species such as the investigated GABA-derivatives, strong distinctions in the crystallization behaviour occur. The following connections may be stated regarding their commonalties with some certainty:

The investigated compounds form the same HB-interactions if they remain singular. However, the structural realization of this motif might differ. If a multicomponent formation or crystallization-based process such as an enantiopurification works for one of the investigated species, it is likely that it might work for another one as well, but this is not necessarily a given. Multicomponent species formation with carboxylic acids can likely cause solubility increases and melting point decreases. Formation of such compounds is energetically favoured in many cases, but not always. It is definitively possible to research interesting crystallization behaviours and applications for each compound, but the results do not necessarily transfer from one to another.

It is the authors opinion that significant breakthroughs in crystal engineering depend on collection of huge dataset and suitable means to analyse them. At this point in time, the CSD is a great collection of crystallographic data. However, further information should be collected in a similar manner, and be standardized. Phase transition behaviour should be recorded, as should be solubility, energetic properties, and concerning other substance classes luminescence properties, crystal habitus, hardness, elasticity, and more possible properties that may be interesting in material and pharmaceutical sciences. As we near artificial intelligence and deep learning applications capable of forming connections between all these recorded properties we may be able to perform actual predictions in the near future. Until this point crystal engineering remains a Sisyphus task, with the necessity to understand each single system on its own.

5 References

- [1] Pepinsky, R. Crystal Engineering - New Concept in Crystallography. *Phys. Rev.* **1955**, 100, 971.
- [2] Schmidt, G. M. J. Photodimerization in the solid state. *Pure Appl. Chem.* **1971**, 27, 647–678.
- [3] Gnanaguru, K.; Murthy, G. S.; Venkatesan, K.; Ramamurthy, V. A study in Crystal engineering: Solid-state photodimerization of chloro- and methyl-coumarins. *Chem. Phys. Lett.* **1984**, 109, 255–258.
- [4] Gnanaguru, K.; Ramasubbu, N.; Venkatesan, K.; Ramamurthy, V. A study on the photochemical dimerization of coumarins in the solid state. *J. Org. Chem.* **1985**, 50, 2337–2346.
- [5] Trotter, J. Structural aspects of the solid-state photochemistry of tetrahydronaphthoquinones. *Acta Crystallogr. B Struct. Sci.* **1983**, 39, 373–381.
- [6] Danielmeyer, H. G.; Jeser, J. P.; Schönherr, E.; Stetter, W. The growth of laser quality NdP5O14 crystals. *J. Cryst. Growth* **1974**, 22, 298–302.
- [7] Jiang, Z. Q.; Scheffer, J. R.; Secco, A. S.; Trotter, J. Crystal engineering in the solid state photochemistry of cyclohexenones. *Tetrahedron Lett.* **1981**, 22, 891–894.
- [8] Jones, W.; Ramdas, S.; Theocharis, C. R.; Thomas, J. M.; Thomas, N. W. Crystal engineering of photodimerizable cyclopentanones. Comparison of chloro- and methyl-substitution as solid-state steering groups. *J. Phys. Chem.* **1981**, 85, 2594–2597.
- [9] Adams, J. M.; Pritchard, R. G.; Thomas, J. M. Preparation and X-ray crystal structure of guanidinium oxalate dihydrate monoperhydrate: a novel example of crystal engineering. *J. Chem. Soc., Chem. Commun.* **1976**, 358.
- [10] Brown, G. M.; Frazier, C. C. The structure of tricarbonyl(styrene)chromium, a crystal active in second-harmonic generation. *Acta Crystallogr. C Cryst. Struct. Commun.* **1989**, 45, 1158–1161.
- [11] Sankaran, H.; Sharma, S. M.; Sikka, S. K.; Chidambaram, R. High pressure phase transitions in organic solids II: X-ray diffraction study of p-dichlorobenzene at high pressures. *Pramana - J. Phys.* **1986**, 27, 835–839.
- [12] Theocharis, C. R.; Desiraju, G. R.; Jones, W. The use of mixed crystals for engineering organic solid-state reactions: application to benzylbenzylidenecyclopentanones. *J. Am. Chem. Soc.* **1984**, 106, 3606–3609.
- [13] Sarma, J. A.; Desiraju, G. R. The chloro-substituent as a steering group: A comparative study of non-bonded interactions and hydrogen bonding in crystalline chloro-aromatics. *Chem. Phys. Lett.* **1985**, 117, 160–164.
- [14] Sarma, J. A. R. P.; Desiraju, G. R. Crystal engineering via Cl ... Cl non-bonded interactions. The novel 2 : 1 complex, 6-chloro-3,4-(methylenedioxy)cinnamic acid–2,4-

- dichlorocinnamic acid. Topochemical conversion into an unsymmetrical cyclobutane and kinetics of the reaction. *J. Chem. Soc., Chem. Commun.* **1984**, 145–147.
- [15] Radha Kishan, K. V.; Desiraju, G. R. Crystal engineering: a solid state Diels-Alder reaction. *J. Org. Chem.* **1987**, 52, 4640–4641.
- [16] Nalini, V.; Desiraju, G. R. Crystal engineering through non-bonded contacts to sulphur. *Tetrahedron* **1987**, 43, 1313–1320.
- [17] Ganguly, S.; Fernandes, J. R.; Desiraju, G. R.; Rao, C. Phase transition in malonic acid: An infrared study. *Chem. Phys. Lett.* **1980**, 69, 227–229.
- [18] Desiraju, G. R.; Sarma, J. A. R. P. Crystal engineering via donor–acceptor interactions. X-Ray crystal structure and solid state reactivity of the 1 : 1 complex, 3,4-dimethoxycinnamic acid–2,4-dinitrocinnamic acid. *J. Chem. Soc., Chem. Commun.* **1983**, 45–46.
- [19] Desiraju, G. R.; Paul, I. C.; Curtin, D. Y. Conversion in the solid state of the yellow to the red form of 2-(4'-methoxyphenyl)-1,4-benzoquinone. X-ray crystal structures and anisotropy of the rearrangement. *J. Am. Chem. Soc.* **1977**, 99, 1594–1601.
- [20] Desiraju, G. R.; Luss, H. R.; Smith, D. L. Resonance interactions in metal chelates of o-hydroxyazo compounds. Crystal growth, structure, and spectra of 1-(2-pyridylazo)-2-naphtholato-chlorocopper(II). *J. Am. Chem. Soc.* **1978**, 100, 6375–6382.
- [21] Desiraju, G. R.; Curtin, D. Y.; Paul, I. C. Synthesis and interconversion by hydrogen exchange of isomeric quinhydrones. *J. Org. Chem.* **1977**, 42, 4071–4075.
- [22] Desiraju, G. R.; Curtin, D. Y.; Paul, I. C. Crystal growth by nonaqueous gel diffusion. *J. Am. Chem. Soc.* **1977**, 99, 6148.
- [23] Desiraju, G. R. Carrying out organic chemistry within crystalline solids. *Endeavour* **1984**, 8, 201–206.
- [24] Duncan-Hewitt, W. C.; Weatherly, G. C. Modeling the uniaxial compaction of pharmaceutical powders using the mechanical properties of single crystals. II: Brittle materials. *J. Pharm. Sci.* **1990**, 79, 273–278.
- [25] Ganesan, T.; Muthudoss, P.; Voguri, R. S.; Ghosal, S.; Ann, E. Y. C.; Kwok, J.; Shahnawaz, S. S.; Omar, M. F.; Allada, R.; See, H. H. A new Febuxostat-Telmisartan Drug-Drug Cocrystal for Gout-Hypertension Combination Therapy. *J. Pharm. Sci.* **2022**, 111, 3318–3326.
- [26] Karamertzanis, P. G.; Kazantsev, A. V.; Issa, N.; Welch, G. W. A.; Adjiman, C. S.; Pantelides, C. C.; Price, S. L. Can the Formation of Pharmaceutical Cocrystals Be Computationally Predicted? 2. Crystal Structure Prediction. *J. Chem. Theory Comput.* **2009**, 5, 1432–1448.
- [27] Kawashima, Y.; Cui, F.; Takeuchi, H.; Niwa, T.; Hino, T.; Kiuchi, K. Improvements in flowability and compressibility of pharmaceutical crystals for direct tableting by spherical crystallization with a two-solvent system. *Powder Technol.* **1994**, 78, 151–157.

- [28] Li, Z. J.; Grant, D. J. Relationship between physical properties and crystal structures of chiral drugs. *J. Pharm. Sci.* **1997**, *86*, 1073–1078.
- [29] OTSUKA, M.; HASEGAWA, H.; MATSUDA, Y. Effect of Polymorphic Forms of Bulk Powders on Pharmaceutical Properties of Carbamazepine Granules. *Chem. Pharm. Bull.* **1999**, *47*, 852–856.
- [30] Sanphui, P.; Mishra, M. K.; Ramamurty, U.; Desiraju, G. R. Tuning mechanical properties of pharmaceutical crystals with multicomponent crystals: voriconazole as a case study. *Mol. Pharm.* **2015**, *12*, 889–897.
- [31] Sheth, A. R.; Grant, D. J. Relationship between the Structure and Properties of Pharmaceutical Crystals. *KONA* **2005**, *23*, 36–48.
- [32] Sorensen, R. A.; Liao, W. B.; Kesner, L.; Boyd, R. H. Prediction of polymer crystal structures and properties: polyethylene and poly(oxymethylene). *Macromolecules* **1988**, *21*, 200–208.
- [33] Steed, J. W. The role of co-crystals in pharmaceutical design. *Trends Pharmacol. Sci.* **2013**, *34*, 185–193.
- [34] Thakur, T. S.; Thakuria, R. Crystalline Multicomponent Solids: An Alternative for Addressing the Hygroscopicity Issue in Pharmaceutical Materials. *Cryst. Growth Des.* **2020**, *20*, 6245–6265.
- [35] Vishweshwar, P.; McMahon, J. A.; Bis, J. A.; Zaworotko, M. J. Pharmaceutical co-crystals. *J. Pharm. Sci.* **2006**, *95*, 499–516.
- [36] Walsh, R. D. B.; Bradner, M. W.; Fleischman, a. S.; Morales, L. A.; Moulton, a. B.; Rodríguez-Hornedo, N.; Zaworotko, M. J. Crystal engineering of the composition of pharmaceutical phases. *Chem. Commun.* **2003**, 186–187.
- [37] York, P. Crystal Engineering and Particle Design for the Powder Compaction Process. *Drug Dev. Ind. Pharm* **1992**, *18*, 677–721.
- [38] Dunitz, J. D.; Bernstein, J. Disappearing Polymorphs. *Acc. Chem. Res.* **1995**, *28*, 193–200.
- [39] Beldjoudi, Y.; Arauzo, A.; Palacio, F.; Pilkington, M.; Rawson, J. M. Studies on a “Disappearing Polymorph”: Thermal and Magnetic Characterization of α -p-NCC6F4CNSSN. *J. Am. Chem. Soc.* **2016**, *138*, 16779–16786.
- [40] Bernstein, J.; Henck, J.-O. Disappearing and reappearing polymorphs—an anathema to crystal engineering? *Cryst. Eng.* **1998**, *1*, 119–128.
- [41] Cuppen, H. M.; Smets, M. M. H.; Krieger, A. M.; van den Ende, J. A.; Meekes, H.; van Eck, E. R. H.; Görbitz, C. H. The Rich Solid-State Phase Behavior of L-Phenylalanine: Disappearing Polymorphs and High Temperature Forms. *Cryst. Growth Des.* **2019**, *19*, 1709–1719.

- [42] Hasa, D.; Marosa, M.; Bučar, D.-K.; Corpinot, M. K.; Amin, D.; Patel, B.; Jones, W. Mechanochemical Formation and “Disappearance” of Caffeine–Citric-Acid Cocrystal Polymorphs. *Cryst. Growth Des.* **2020**, *20*, 1119–1129.
- [43] Henck, J. O.; Bernstein, J.; Ellern, A.; Boese, R. Disappearing and reappearing polymorphs. The benzocaine:picric acid system. *J. Am. Chem. Soc.* **2001**, *123*, 1834–1841.
- [44] Liu, Y.; Gabriele, B.; Davey, R. J.; Cruz-Cabeza, A. J. Concerning Elusive Crystal Forms: The Case of Paracetamol. *J. Am. Chem. Soc.* **2020**, *142*, 6682–6689.
- [45] Lucaioli, P.; Nauha, E.; Gimondi, I.; Price, L. S.; Guo, R.; Iuzzolino, L.; Singh, I.; Salvalaglio, M.; Price, S. L.; Blagden, N. Serendipitous isolation of a disappearing conformational polymorph of succinic acid challenges computational polymorph prediction. *CrystEngComm* **2018**, *20*, 3971–3977.
- [46] Malec, L. M.; Gryl, M.; Oszejca, M. T.; Brela, M. Z.; Stadnicka, K. M. Chasing the Co-crystal Disappearing Polymorph with Ab Initio Methods. *Cryst. Growth Des.* **2021**, *21*, 6902–6912.
- [47] Prashad, M.; Sutton, P.; Wu, R.; Hu, B.; Vivello, J.; Carosi, J.; Kapa, P.; Liang, J. Process Research and Development of a MTP Inhibitor: Another Case of Disappearing Polymorphs upon Scale-up. *Org. Process Res. Dev.* **2010**, *14*, 878–882.
- [48] Rubin-Preminger, J. M.; Bernstein, J. 3-Aminobenzenesulfonic Acid: A Disappearing Polymorph. *Cryst. Growth Des.* **2005**, *5*, 1343–1349.
- [49] Speight, I. R.; Huskić, I.; Arhangelkis, M.; Titi, H. M.; Stein, R. S.; Hanusa, T. P.; Friščić, T. Cover Feature: Disappearing Polymorphs in Metal–Organic Framework Chemistry: Unexpected Stabilization of a Layered Polymorph over an Interpenetrated Three-Dimensional Structure in Mercury Imidazolate (Chem. Eur. J. 8/2020). *Chem. Eur. J.* **2020**, *26*, 1696.
- [50] Lancaster, R. W.; Karamertzanis, P. G.; Hulme, A. T.; Tocher, D. A.; Lewis, T. C.; Price, S. L. The polymorphism of progesterone: stabilization of a ‘disappearing’ polymorph by co-crystallization. *J. Pharm. Sci.* **2007**, *96*, 3419–3431.
- [51] Bučar, D.-K.; Lancaster, R. W.; Bernstein, J. Disappearing polymorphs revisited. *Angew. Chem. Int. Ed. Engl.* **2015**, *54*, 6972–6993.
- [52] Byrn, S. R.; Siew, P. Y. Crystal structure and solid-state behavior of aspirin anhydride crystals. *J. Pharm. Sci.* **1981**, *70*, 280–283.
- [53] Cohen, M. L. Prediction of new materials and properties of solids. *Int. J. Quantum Chem.* **1986**, *29*, 843–854.
- [54] Blackwell, J.; Quay, J. R.; Nagarajan, M. R.; Born, L.; Hespe, H. Molecular parameters for the prediction of polyurethane structures. *J. Polym. Sci. Polym. Phys. Ed.* **1984**, *22*, 1247–1259.

- [55] Gdanitz, R. J. Prediction of molecular crystal structures by Monte Carlo simulated annealing without reference to diffraction data. *Chem. Phys. Lett.* **1992**, 190, 391–396.
- [56] Pannetier, J.; Bassas-Alsina, J.; Rodriguez-Carvajal, J.; Caignaert, V. Prediction of crystal structures from crystal chemistry rules by simulated annealing. *Nature* **1990**, 346, 343–345.
- [57] Payne, R. S.; Roberts, R. J.; Rowe, R. C.; Docherty, R. Examples of successful crystal structure prediction: polymorphs of primidone and progesterone. *Int. J. Pharm.* **1999**, 177, 231–245.
- [58] van Eijck, B. P.; Kroon, J. Fast clustering of equivalent structures in crystal structure prediction. *J. Comput. Chem.* **1997**, 18, 1036–1042.
- [59] Desiraju, G. R. Supramolecular Synthons in Crystal Engineering—A New Organic Synthesis. *Angew. Chem. Int. Ed. Engl.* **1995**, 34, 2311–2327.
- [60] Desiraju, G. R. The supramolecular concept as a bridge between organic, inorganic and organometallic crystal chemistry. *J. Mol. Struct.* **1996**, 374, 191–198.
- [61] Reddy, D. S.; Craig, D. C.; Desiraju, G. R. Supramolecular Synthons in Crystal Engineering. 4. Structure Simplification and Synthon Interchangeability in Some Organic Diamondoid Solids 1. *J. Am. Chem. Soc.* **1996**, 118, 4090–4093.
- [62] Reddy, D. S.; Ovchinnikov, Y. E.; Shishkin, O. V.; Struchkov, Y. T.; Desiraju, G. R. Supramolecular Synthons in Crystal Engineering. 3. Solid State Architecture and Synthon Robustness in Some 2,3-Dicyano-5,6-dichloro-1,4-dialkoxybenzenes 1. *J. Am. Chem. Soc.* **1996**, 118, 4085–4089.
- [63] Jin, S.; Sanii, R.; Song, B.-Q.; Zaworotko, M. J. Crystal Engineering of Ionic Cocrystals Sustained by the Phenol-Phenolate Supramolecular Heterosynthon. *Cryst. Growth Des.* **2022**, 22, 4582–4591.
- [64] Li, D.; Li, J.; Deng, Z.; Zhang, H. The discovery of new cocrystals of 5-fluorocytosine using amine–carboxylate supramolecular synthon. *J. Drug Deliv. Sci. Technol.* **2022**, 78, 103934.
- [65] Lin, Z.-J.; Mahammed, S. A. R.; Liu, T.-F.; Cao, R. Multifunctional Porous Hydrogen-Bonded Organic Frameworks: Current Status and Future Perspectives. *ACS Cent. Sci.* **2022**, 8, 1589–1608.
- [66] Marcela, L.-C.; Everardo, J.-A.; Perla, R.-B.; Gabriela, V.-P.; Vojtech, J.; Margarita I, B.-U.; Raymundo, C.-O.; Hugo, T. Is the phosphorous atom a stereogenic center? Crystallographic findings in five new dithiophosphonate compounds supported with non covalent interaction index (NCI), theoretical approach and spectroscopic analysis. *J. Mol. Struct.* **2022**, 1270, 133987.

- [67] Sadhukhan, A.; Brandão, P.; Saha, S.; Mal, D.; Sepay, N. Insight into non-covalent interactions in 1D Gd-based coordination polymer for solid-state self-assembly through a new supramolecular synthon. *J. Mol. Struct.* **2023**, 1272, 134204.
- [68] Bučar, D.-K.; Henry, R. F.; Zhang, G. G. Z.; MacGillivray, L. R. Synthon Hierarchies in Crystal Forms Composed of Theophylline and Hydroxybenzoic Acids: Cocrystal Screening via Solution-Mediated Phase Transformation. *Cryst. Growth Des.* **2014**, 14, 5318–5328.
- [69] Corpinot, M. K.; Stratford, S. A.; Arhangelskis, M.; Anka-Lufford, J.; Halasz, I.; Judaš, N.; Jones, W.; Bučar, D.-K. On the predictability of supramolecular interactions in molecular cocrystals – the view from the bench. *CrystEngComm* **2016**, 18, 5434–5439.
- [70] Chen, J.; Sarma, B.; Evans, J. M. B.; Myerson, A. S. Pharmaceutical Crystallization. *Cryst. Growth Des.* **2011**, 11, 887–895.
- [71] Kitamura, M. Strategy for control of crystallization of polymorphs. *CrystEngComm* **2009**, 11, 949.
- [72] Thakur, A. K.; Kumar, R.; Vipin Kumar, V. K.; Kumar, A.; Kumar Gaurav, G.; Naresh Gupta, K. A critical review on thermodynamic and hydrodynamic modeling and simulation of liquid antisolvent crystallization of pharmaceutical compounds. *J. Mol. Liq.* **2022**, 362, 119663.
- [73] Yao, C.; Zhang, S.; Wang, L.; Tao, X. Recent Advances in Polymorph Discovery Methods of Organic Crystals. *Cryst. Growth Des.* **2023**, 23, 637–654.
- [74] Hagler, A. T.; Bernstein, J. Conformational polymorphism. 2. Crystal energetics by computational substitution. Further evidence for the sensitivity of the method. *J. Am. Chem. Soc.* **1978**, 100, 6349–6354.
- [75] Piela, L.; Stolarczyk, L. Z. On the relativity of short- and long-range effects in calculations for periodic systems. *Chem. Phys. Lett.* **1982**, 86, 195–198.
- [76] Hopfinger, A. J.; Pearlstein, R. A.; Mabilia, M.; Tripathy, S. K. Estimation of thermodynamic and spatial properties of organic compounds for quantitative molecular design. *Pure Appl. Chem.* **1988**, 60, 271–276.
- [77] Krogh-Jespersen, K.; Zhang, X.; Ding, Y.; Westbrook, J. D.; Potenza, J. A.; Schugar, H. J. Molecular and electronic structures of pentaammineruthenium(II)-thioether complexes. The nature of Ru(II)-S back bonding elucidated by structural, electronic spectral, and molecular orbital studies. *J. Am. Chem. Soc.* **1992**, 114, 4345–4353.
- [78] Perlstein, J. Molecular self-assemblies. 2. A computational method for the prediction of the structure of one-dimensional screw, glide, and inversion molecular aggregates and implications for the packing of molecules in monolayers and crystals. *J. Am. Chem. Soc.* **1994**, 116, 455–470.

- [79] Zimmerman, H. E.; Sebek, P.; Zhu, Z. Ab Initio Computations of Reacting Species in Crystal Lattices; Mechanistic and Exploratory Organic Photochemistry 1,2. *J. Am. Chem. Soc.* **1998**, 120, 8549–8550.
- [80] van de Bovenkamp, J.; Matxain, J. M.; van Duijneveldt, F. B.; Steiner, T. Combined ab Initio Computational and Statistical Investigation of a Model C–H···O Hydrogen Bonded Dimer as Occurring in 1,4-Benzoquinone. *J. Phys. Chem. A* **1999**, 103, 2784–2792.
- [81] Madsen, G. K. H.; Wilson, C.; Nymand, T. M.; McIntyre, G. J.; Larsen, F. K. The Structure of Nitromalonamide: A Combined Neutron-Diffraction and Computational Study of a Very Short Hydrogen Bond. *J. Phys. Chem. A* **1999**, 103, 8684–8690.
- [82] Gavezzotti, A. Molecular Aggregation of Acetic Acid in a Carbon Tetrachloride Solution: A Molecular Dynamics Study with a View to Crystal Nucleation. *Chem. Eur. J.* **1999**, 5, 567–576.
- [83] Chin, D. N.; Palmore, G. T. R.; Whitesides, G. M. Predicting Crystalline Packing Arrangements of Molecules That Form Hydrogen-Bonded Tapes. *J. Am. Chem. Soc.* **1999**, 121, 2115–2122.
- [84] Braun, D. E.; Ardid-Candel, M.; D’Oria, E.; Karamertzanis, P. G.; Arlin, J.-B.; Florence, A. J.; Jones, A. G.; Price, S. L. Racemic Naproxen: A Multidisciplinary Structural and Thermodynamic Comparison with the Enantiopure Form. *Cryst. Growth Des.* **2011**, 11, 5659–5669.
- [85] D’Oria, E.; Karamertzanis, P. G.; Price, S. L. Spontaneous Resolution of Enantiomers by Crystallization: Insights from Computed Crystal Energy Landscapes. *Cryst. Growth Des.* **2010**, 10, 1749–1756.
- [86] Davey, R. J.; Schroeder, S. L. M.; Horst, J. H. ter. Nucleation of organic crystals—a molecular perspective. *Angew. Chem. Int. Ed. Engl.* **2013**, 52, 2166–2179.
- [87] Dey, D.; Mohan, T. P.; Vishalakshi, B.; Chopra, D. Computational Study of the Formation of Short Centrosymmetric N–H···S Supramolecular Synthons and Related Weak Interactions in Crystalline 1,2,4-Triazoles. *Cryst. Growth Des.* **2014**, 14, 5881–5896.
- [88] Dudek, M. K.; Jeziorna, A.; Potrzebowski, M. J. Computational and experimental study of reversible hydration/dehydration processes in molecular crystals of natural products – a case of catechin. *CrystEngComm* **2016**, 18, 5267–5277.
- [89] Foces-Foces, C.; Echevarría, A.; Jagerovic, N.; Alkorta, I.; Elguero, J.; Langer, U.; Klein, O.; Minguet-Bonvehí, M.; Limbach, H. H. A solid-state NMR, X-ray diffraction, and ab initio computational study of hydrogen-bond structure and dynamics of pyrazole-4-carboxylic acid chains. *J. Am. Chem. Soc.* **2001**, 123, 7898–7906.
- [90] Gavezzotti, A. Ten years of experience in polymorph prediction: what next? *CrystEngComm* **2002**, 4, 343–347.

- [91] Issa, N.; Karamertzanis, P. G.; Welch, G. W. A.; Price, S. L. Can the Formation of Pharmaceutical Cocrystals Be Computationally Predicted? I. Comparison of Lattice Energies. *Cryst. Growth Des.* **2009**, 9, 442–453.
- [92] Lewis, T. C.; Tocher, D. A.; Price, S. L. Investigating Unused Hydrogen Bond Acceptors Using Known and Hypothetical Crystal Polymorphism. *Cryst Growth Des* **2005**, 5, 983–993.
- [93] Lewis, T. C.; Tocher, D. A.; Day, G. M.; Price, S. L. A computational and experimental search for polymorphs of parabanic acid – a salutary tale leading to the crystal structure of oxo-ureido-acetic acid methyl. *CrystEngComm* **2003**, 5, 3–9.
- [94] Liu, C.; Wang, C.; Wan, S.; Liu, L.; Sun, C. C.; Qian, F. An Elusive Drug–Drug Cocrystal Prepared Using a Heteroseeding Strategy. *Cryst. Growth Des.* **2021**, 21, 5659–5668.
- [95] McKinnon, J. J.; Mitchell, A. S.; Spackman, M. A. Hirshfeld Surfaces: A New Tool for Visualising and Exploring Molecular Crystals. *Chem. Eur. J.* **1998**, 4, 2136–2141.
- [96] Sallum, L. O.; Napolitano, H. B.; Carvalho, P. d. S.; Cidade, A. F.; Aquino, G. L. B. de; Coutinho, N. D.; Camargo, A. J.; Ellena, J.; Oliveira, H. C. B. de; Silva, V. H. C. Effect of the methanol molecule on the stabilization of C₁₈H₁₈O₄ crystal: combined theoretical and structural investigation. *J. Phys. Chem. A* **2014**, 118, 10048–10056.
- [97] Sciortino, F.; Zaccarelli, E. Computational materials science: Soft heaps and clumpy crystals. *Nature* **2013**, 493, 30–31.
- [98] Shruti, I.; Almehairbi, M.; Saeed, Z. M.; Alkhidir, T.; Ali, W. A.; Vishwakarma, R.; Mohamed, S.; Chopra, D. Unravelling the Origin of Solvate Formation in the Anticancer Drug Trametinib: Insights from Crystal Structure Analysis and Computational Modeling. *Cryst. Growth Des.* **2022**, 22, 5861–5871.
- [99] Taylor, C. R.; Mulvee, M. T.; Perenyi, D. S.; Probert, M. R.; Day, G. M.; Steed, J. W. Minimizing Polymorphic Risk through Cooperative Computational and Experimental Exploration. *J. Am. Chem. Soc.* **2020**, 142, 16668–16680.
- [100] Tremayne, M.; Grice, L.; Pyatt, J. C.; Seaton, C. C.; Kariuki, B. M.; Tsui, H. H. Y.; Price, S. L.; Cherryman, J. C. Characterization of complicated new polymorphs of chlorothalonil by X-ray diffraction and computer crystal structure prediction. *J. Am. Chem. Soc.* **2004**, 126, 7071–7081.
- [101] Woo, X. Y.; Tan, R. B. H.; Chow, P. S.; Braatz, R. D. Simulation of Mixing Effects in Antisolvent Crystallization Using a Coupled CFD-PDF-PBE Approach. *Cryst. Growth Des.* **2006**, 6, 1291–1303.
- [102] Zhang, P.; Wood, G. P. F.; Ma, J.; Yang, M.; Liu, Y.; Sun, G.; Jiang, Y. A.; Hancock, B. C.; Wen, S. Harnessing Cloud Architecture for Crystal Structure Prediction Calculations. *Cryst. Growth Des.* **2018**, 18, 6891–6900.

- [103] Groom, C. R.; Bruno, I. J.; Lightfoot, M. P.; Ward, S. C. The Cambridge Structural Database. *Acta Crystallogr. B Struct. Sci. Cryst. Eng. Mater.* **2016**, *72*, 171–179.
- [104] Fang, L.; Liu, J.; Han, D.; Gao, Z.; Gong, J. Revealing the role of polymer in the robust preparation of the 2,4-dichlorophenoxyacetic acid metastable crystal form by AI-based image analysis. *Powder Technol.* **2023**, *413*, 118077.
- [105] Altomare, A.; Billinge, S. J. L. Modern crystallography and its foundations. *Acta Crystallogr. A Found. Adv.* **2021**, *77*, 1.
- [106] Liu, J.; Zhang, Q.; Chen, M.; Gao, Z.; Rohani, S.; Gong, J. A verified open-access AI-based chemical microparticle image database for in-situ particle visualization and quantification in multi-phase flow. *J. Chem. Eng.* **2023**, *451*, 138940.
- [107] Heng, T.; Yang, D.; Wang, R.; Zhang, L.; Lu, Y.; Du, G. Progress in Research on Artificial Intelligence Applied to Polymorphism and Cocrystal Prediction. *ACS Omega* **2021**, *6*, 15543–15550.
- [108] W. Ostwald. Studien über die Bildung und Umwandlung fester Körper. *Z. Phys. Chem.* **1897**, 289–330.
- [109] Yoreo, J. J. de. Casting a bright light on Ostwald's rule of stages. *Proc. Natl. Acad. Sci. U. S. A.* **2022**, *119*, e2121661119.
- [110] Gebauer, D.; Cölfen, H. Prenucleation clusters and non-classical nucleation. *Nano Today* **2011**, *6*, 564–584.
- [111] Mangin, D.; Puel, F.; Veessler, S. Polymorphism in Processes of Crystallization in Solution: A Practical Review. *Org. Process Res. Dev.* **2009**, *13*, 1241–1253.
- [112] Paul, E. L.; Tung, H.-H.; Midler, M. Organic crystallization processes. *Powder Technol.* **2005**, *150*, 133–143.
- [113] Oxtoby, D. W. Nucleation of First-Order Phase Transitions. *Acc. Chem. Res.* **1998**, *31*, 91–97.
- [114] Xu, S.; Di Cao; Liu, Y.; Wang, Y. Role of Additives in Crystal Nucleation from Solutions: A Review. *Cryst. Growth Des.* **2022**, *22*, 2001–2022.
- [115] Zahn, D. Thermodynamics and Kinetics of Prenucleation Clusters, Classical and Non-Classical Nucleation. *Chemphyschem* **2015**, *16*, 2069–2075.
- [116] Yoreo, J. de. Crystal nucleation: more than one pathway. *Nat. Mater.* **2013**, *12*, 284–285.
- [117] Thanh, N. T. K.; Maclean, N.; Mahiddine, S. Mechanisms of nucleation and growth of nanoparticles in solution. *Chem. Rev.* **2014**, *114*, 7610–7630.
- [118] Jreidini, P.; Kocher, G.; Provatas, N. Classical nucleation Theory in the phase-field crystal model *Phys. Rev. E*, **2018**, *97*, 042802.
- [119] Li, J.; Deepak, F. L. In Situ Kinetic Observations on Crystal Nucleation and Growth. *Chem. Rev.* **2022**, *122*, 16911–16982.

- [120] Karthika, S.; Radhakrishnan, T. K.; Kalaichelvi, P. A Review of Classical and Nonclassical Nucleation Theories. *Cryst. Growth Des.* **2016**, *16*, 6663–6681.
- [121] Gebauer, D.; Kellermeier, M.; Gale, J. D.; Bergström, L.; Cölfen, H. Pre-nucleation clusters as solute precursors in crystallisation. *Chem. Soc. Rev.* **2014**, *43*, 2348–2371.
- [122] Fu, H.; Gao, X.; Zhang, X.; Ling, L. Recent Advances in Nonclassical Crystallization: Fundamentals, Applications, and Challenges. *Cryst. Growth Des.* **2022**, *22*, 1476–1499.
- [123] Chen, J.; Zhu, E.; Liu, J.; Zhang, S.; Lin, Z.; Duan, X.; Heinz, H.; Huang, Y.; Yoreo, J. J. de. Building two-dimensional materials one row at a time: Avoiding the nucleation barrier. *Science* **2018**, *362*, 1135–1139.
- [124] Delach, D. L.; Dukes, M. J.; Varano, A. C.; Kelly, D. F.; Dukes III, A. D. Real-time imaging of lead nanoparticles in solution – determination of the growth mechanism. *RSC Adv.* **2015**, *5*, 104193–104197.
- [125] Rodríguez-Navarro, C.; Ruiz-Agudo, E.; Harris, J.; Wolf, S. E. Nonclassical crystallization in vivo et in vitro (II): Nanogranular features in biomimetic minerals disclose a general colloid-mediated crystal growth mechanism. *J. Struct. Biol.* **2016**, *196*, 260–287.
- [126] Ostwald, W. Über die vermeintliche Isomerie des roten und gelben Quecksilberoxyds und die Oberflächenspannung fester Körper. *Z. Phys. Chem.* **1900**, *34U*, 495–503.
- [127] Lee, D.; Park, S.; Lee, J.; Hwang, N. A theoretical model for digestive ripening. *Acta Materialia* **2007**, *55*, 5281–5288.
- [128] Peng, X.; Manna, L.; Yang, W.; Wickham, J.; Scher, E.; Kadavanich, A.; Alivisatos, A. P. Shape control of CdSe nanocrystals. *Nature* **2000**, *404*, 59–61.
- [129] Li, D.; Nielsen, M. H.; Lee, J. R. I.; Frandsen, C.; Banfield, J. F.; Yoreo, J. J. de. Direction-specific interactions control crystal growth by oriented attachment. *Science* **2012**, *336*, 1014–1018.
- [130] Li, J.; Chen, J.; Wang, H.; Chen, N.; Wang, Z.; Guo, L.; Deepak, F. L. In Situ Atomic-Scale Study of Particle-Mediated Nucleation and Growth in Amorphous Bismuth to Nanocrystal Phase Transformation. *Adv. Sci. (Weinh.)* **2018**, *5*, 1700992.
- [131] Niederberger, M.; Cölfen, H. Oriented attachment and mesocrystals: non-classical crystallization mechanisms based on nanoparticle assembly. *Phys. Chem. Chem. Phys.* **2006**, *8*, 3271–3287.
- [132] Zheng, H.; Smith, R. K.; Jun, Y.-W.; Kisielowski, C.; Dahmen, U.; Alivisatos, A. P. Observation of single colloidal platinum nanocrystal growth trajectories. *Science* **2009**, *324*, 1309–1312.
- [133] Li, Q.; Yin, D.; Li, J.; Deepak, F. L. Atomic-Scale Understanding of Gold Cluster Growth on Different Substrates and Adsorption-Induced Structural Change. *J. Phys. Chem. C* **2018**, *122*, 1753–1760.

- [134] Smets, M. M. H.; Brugman, S. J. T.; van Eck, E. R. H.; van den Ende, J. A.; Meekes, H.; Cuppen, H. M. Understanding the Solid-State Phase Transitions of dl -Norleucine: An in Situ DSC, Microscopy, and Solid-State NMR Study. *Cryst. Growth Des.* **2015**, *15*, 5157–5167.
- [135] Vaksler, Y.; Idrissi, A.; Shishkina, S. V. High-Pressure Influence on Piracetam Crystals: Studying by Quantum Chemical Methods. *Cryst. Growth Des.* **2021**, *21*, 5697–5711.
- [136] Konovalova, I. S.; Shaposhnyk, A. M.; Baumer, V. N.; Chalyk, B. A.; Shishkina, S. V. Polymorphic transition due to grinding: the case of 3-1-(tert-butoxycarbonyl)azetid-3-yl-1,2-oxazole-4-carboxylic acid. *Acta Crystallogr. B Struct. Sci. Cryst. Eng. Mater.* **2022**, *78*, 510–519.
- [137] Potter, C. B.; Kollamaram, G.; Zeglinski, J.; Whitaker, D. A.; Croker, D. M.; Walker, G. M. Investigation of polymorphic transitions of piracetam induced during wet granulation. *Eur. J. Pharm. Biopharm.* **2017**, *119*, 36–46.
- [138] Krishnan, B. P.; Sureshan, K. M. A spontaneous single-crystal-to-single-crystal polymorphic transition involving major packing changes. *J. Am. Chem. Soc.* **2015**, *137*, 1692–1696.
- [139] Guo, J.; Ziegler, G. R.; Kong, L. Polymorphic transitions of V-type amylose upon hydration and dehydration. *Food Hydrocoll.* **2022**, *125*, 107372.
- [140] Matsuo, K.; Matsuoka, M. Solid-State Polymorphic Transition of Theophylline Anhydrate and Humidity Effect. *Cryst. Growth Des.* **2007**, *7*, 411–415.
- [141] Sarcevic, I.; Orola, L.; Belyakov, S.; Veidis, M. V. Spontaneous cocrystal hydrate formation in the solid state: crystal structure aspects and kinetics. *New J. Chem.* **2013**, *37*, 2978.
- [142] Yoshinari, T.; Forbes, R. T.; York, P.; Kawashima, Y. Moisture induced polymorphic transition of mannitol and its morphological transformation. *Int. J. Pharm.* **2002**, *247*, 69–77.
- [143] Park, H.; Kim, J.-S.; Hong, S.; Ha, E.-S.; Nie, H.; Zhou, Q. T.; Kim, M.-S. Tableting process-induced solid-state polymorphic transition. *J. Pharm. Investig.* **2022**, *52*, 175–194.
- [144] Woo, M. W.; Lee, M. G.; Shakiba, S.; Mansouri, S. Controlling in situ crystallization of pharmaceutical particles within the spray dryer. *Expert Opin. Drug Deliv.* **2017**, *14*, 1315–1324.
- [145] Wang, H.; Wang, Z.; Liu, L.; Gong, X.; Wang, M. Alumina Hydrate Polymorphism Control in Al–Water Reaction Crystallization by Seeding to Change the Metastable Zone Width. *Cryst. Growth Des.* **2016**, *16*, 1056–1062.
- [146] Nagy, Z. K.; Braatz, R. D. Advances and new directions in crystallization control. *Annu. Rev. Chem. Biomol. Eng.* **2012**, *3*, 55–75.

- [147] Liu, F.; Bagi, S. D.; Su, Q.; Chakrabarti, R.; Barral, R.; Gamekkanda, J. C.; Hu, C.; Mascia, S. Targeting Particle Size Specification in Pharmaceutical Crystallization: A Review on Recent Process Design and Development Strategies and Particle Size Measurements. *Org. Process Res. Dev.* **2022**, *26*, 3190–3203.
- [148] Kulkarni, S. A.; Meekes, H.; Horst, J. H. ter. Polymorphism Control through a Single Nucleation Event. *Cryst. Growth Des.* **2014**, *14*, 1493–1499.
- [149] Griffin, D. J.; Kawajiri, Y.; Grover, M. A.; Rousseau, R. W. Feedback Control of Multicomponent Salt Crystallization. *Cryst. Growth Des.* **2015**, *15*, 305–317.
- [150] Garg, R. K.; Sarkar, D. Polymorphism control of p-aminobenzoic acid by isothermal anti-solvent crystallization. *J. Cryst. Growth* **2016**, *454*, 180–185.
- [151] Comerci, C. J.; Herrmann, J.; Yoon, J.; Jabbarpour, F.; Zhou, X.; Nomellini, J. F.; Smit, J.; Shapiro, L.; Wakatsuki, S.; Moerner, W. E. Topologically-guided continuous protein crystallization controls bacterial surface layer self-assembly. *Nat. Commun.* **2019**, *10*, 2731.
- [152] Bhattacharya, B.; Das, S.; Lal, G.; Soni, S. R.; Ghosh, A.; Reddy, C. M.; Ghosh, S. Screening, crystal structures and solubility studies of a series of multidrug salt hydrates and cocrystals of fenamic acids with trimethoprim and sulfamethazine. *J. Mol. Struct.* **2020**, *1199*, 127028.
- [153] Deng, Y.; Zhang, Y.; Huang, Y.; Zhang, M.; Lou, B. Preparation, Crystal Structures, and Oral Bioavailability of Two Cocrystals of Emodin with Berberine Chloride. *Cryst. Growth Des.* **2018**, *18*, 7481–7488.
- [154] Izatulina, A. R.; Gurzhiy, V. V.; Krzhizhanovskaya, M. G.; Kuz'mina, M. A.; Leoni, M.; Frank-Kamenetskaya, O. V. Hydrated Calcium Oxalates: Crystal Structures, Thermal Stability, and Phase Evolution. *Cryst. Growth Des.* **2018**, *18*, 5465–5478.
- [155] Singaraju, A. B.; Nguyen, K.; Jain, A.; Haware, R. V.; Stevens, L. L. Aggregate Elasticity, Crystal Structure, and Tableting Performance for p-Aminobenzoic Acid and a Series of Its Benzoate Esters. *Mol. Pharm.* **2016**, *13*, 3794–3806.
- [156] Wang, C.; Paul, S.; Wang, K.; Hu, S.; Sun, C. C. Relationships among Crystal Structures, Mechanical Properties, and Tableting Performance Probed Using Four Salts of Diphenhydramine. *Cryst. Growth Des.* **2017**, *17*, 6030–6040.
- [157] Wang, J.; Dai, X.-L.; Lu, T.-B.; Chen, J.-M. Temozolomide–Hesperetin Drug–Drug Cocrystal with Optimized Performance in Stability, Dissolution, and Tableability. *Cryst. Growth Des.* **2021**, *21*, 838–846.
- [158] Zheng, K.; Xie, C.; Li, X.; Wu, W.; Li, A.; Qian, S.; Pang, Q. Crystal structures, thermal stabilities, and dissolution behaviours of tinidazole and the tinidazole–vanillic acid cocrystal: insights from energy frameworks. *Acta Crystallogr. C Struct. Chem.* **2020**, *76*, 389–397.

- [159] Duggirala, N. K.; Perry, M. L.; Almarsson, Ö.; Zaworotko, M. J. Pharmaceutical cocrystals: along the path to improved medicines. *Chem. Commun.* **2016**, 52, 640–655.
- [160] Aitipamula, S.; Banerjee, R.; Bansal, A. K.; Biradha, K.; Cheney, M. L.; Choudhury, A. R.; Desiraju, G. R.; Dikundwar, A. G.; Dubey, R.; Duggirala, N.; Ghogale, P. P.; Ghosh, S.; Goswami, P. K.; Goud, N. R.; Jetti, R. R. K. R.; Karpinski, P.; Kaushik, P.; Kumar, D.; Kumar, V.; Moulton, B.; Mukherjee, A.; Mukherjee, G.; Myerson, A. S.; Puri, V.; Ramanan, A.; Rajamannar, T.; Reddy, C. M.; Rodriguez-Hornedo, N.; Rogers, R. D.; Row, T. N. G.; Sanphui, P.; Shan, N.; Shete, G.; Singh, A.; Sun, C. C.; Swift, J. A.; Thaimattam, R.; Thakur, T. S.; Kumar Thaper, R.; Thomas, S. P.; Tothadi, S.; Vangala, V. R.; Variankaval, N.; Vishweshwar, P.; Weyna, D. R.; Zaworotko, M. J. Polymorphs, Salts, and Cocrystals: What's in a Name? *Cryst. Growth Des.* **2012**, 12, 2147–2152.
- [161] Berry, D. J.; Steed, J. W. Pharmaceutical cocrystals, salts and multicomponent systems; intermolecular interactions and property based design. *Adv. Drug Deliv. Rev.* **2017**, 117, 3–24.
- [162] Gryl, M.; Koziel, M.; Stadnicka, K. M. A proposal for coherent nomenclature of multicomponent crystals. *Acta Crystallogr. B Struct. Sci. Cryst. Eng. Mater.* **2019**, 75, 53–58.
- [163] Grothe, E.; Meekes, H.; Vlieg, E.; Horst, J. H. ter; Gelder, R. de. Solvates, Salts, and Cocrystals: A Proposal for a Feasible Classification System. *Cryst. Growth Des.* **2016**, 16, 3237–3243.
- [164] d'Agostino, S.; Fornasari, L.; Braga, D. Binary and Ternary Solid Solutions of Ionic Plastic Crystals, and Modulation of Plastic Phase Transitions. *Cryst. Growth Des.* **2019**, 19, 6266–6273.
- [165] Lusi, M. Engineering Crystal Properties through Solid Solutions. *Cryst. Growth Des.* **2018**, 18, 3704–3712.
- [166] Lusi, M.; Vitorica-Yrezabal, I. J.; Zaworotko, M. J. Expanding the Scope of Molecular Mixed Crystals Enabled by Three Component Solid Solutions. *Cryst. Growth Des.* **2015**, 15, 4098–4103.
- [167] Riaz, U.; Shabib, I.; Haider, W. The current trends of Mg alloys in biomedical applications-A review. *J Biomed Mater Res B Appl Biomater* **2019**, 107, 1970–1996.
- [168] George, E. P.; Raabe, D.; Ritchie, R. O. High-entropy alloys. *Nat. Rev. Mater.* **2019**, 4, 515–534.
- [169] Zhou, M.; Li, C.; Fang, J. Noble-Metal Based Random Alloy and Intermetallic Nanocrystals: Syntheses and Applications. *Chem. Rev.* **2021**, 121, 736–795.
- [170] Wu, Z.; Bei, H.; Otto, F.; Pharr, G. M.; George, E. P. Recovery, recrystallization, grain growth and phase stability of a family of FCC-structured multi-component equiatomic solid solution alloys. *Intermetallics* **2014**, 46, 131–140.

- [171] Laurent-Brocq, M.; Perrière, L.; Pirès, R.; Champion, Y. From high entropy alloys to diluted multi-component alloys: Range of existence of a solid-solution. *Mater. Des.* **2016**, *103*, 84–89.
- [172] LaRosa, C. R.; Shih, M.; Varvenne, C.; Ghazisaeidi, M. Solid solution strengthening theories of high-entropy alloys. *Mater. Charact.* **2019**, *151*, 310–317.
- [173] Koshima, H.; Wang, Y.; Matsuura, T.; Mibuka, N.; Imahashi, S. Two-Component Mixed Crystals Consisting of Nitroanilines and Nitrophenols and Their Nonlinear Optical Property. *Mol. Cryst. Mol. Cryst. Liq. Cryst. Sci. Technol., Sect. A* **1996**, *275*, 233–239.
- [174] Fiala, T.; Ludvíková, L.; Heger, D.; Švec, J.; Slanina, T.; Vetráková, L.; Babiak, M.; Nečas, M.; Kulhánek, P.; Klán, P.; Sindelar, V. Bambusuril as a One-Electron Donor for Photoinduced Electron Transfer to Methyl Viologen in Mixed Crystals. *J. Am. Chem. Soc.* **2017**, *139*, 2597–2603.
- [175] Alkhidir, T.; Saeed, Z. M.; Shunnar, A. F.; Abujami, E.; Nyadzayo, R. M.; Dhokale, B.; Mohamed, S. Expanding the Supramolecular Toolkit: Computed Molecular and Crystal Properties for Supporting the Crystal Engineering of Higher-Order Molecular Ionic Cocrystals. *Cryst. Growth Des.* **2022**, *22*, 485–496.
- [176] Braga, D.; Grepioni, F.; Maini, L.; Prospero, S.; Gobetto, R.; Chierotti, M. R. From unexpected reactions to a new family of ionic co-crystals: the case of barbituric acid with alkali bromides and caesium iodide. *Chem. Commun.* **2010**, *46*, 7715–7717.
- [177] Braga, D.; Grepioni, F.; Shemchuk, O. Organic–inorganic ionic co-crystals: a new class of multipurpose compounds. *CrystEngComm* **2018**, *20*, 2212–2220.
- [178] Dyker, G.; Mastalerz, M.; Müller, I. M.; Merz, K.; Koppe, K. Solvent-Dependent Pseudopolymorphism of Tripyridoxycalix[4]arene:cone versus partial-cone Conformation. *Eur. J. Org. Chem.* **2005**, *2005*, 4963–4966.
- [179] Lipkowski, J.; Bielejewska, A.; Presly, O. Pseudo-polymorphism of a camphor α -cyclodextrin complex. *Carbohydr. Res.* **2022**, *520*, 108601.
- [180] Mukherjee, A.; Desiraju, G. R. Synthron polymorphism and pseudopolymorphism in co-crystals. The 4,4'-bipyridine-4-hydroxybenzoic acid structural landscape. *Chem. Commun.* **2011**, *47*, 4090–4092.
- [181] Bernstein, J. ...And Another Comment on Pseudo polymorphism. *Cryst. Growth Des.* **2005**, *5*, 1661–1662.
- [182] Farias, M. A. D. S.; Soares, F. L. F.; Carneiro, R. L. Crystalline phase transition of ezetimibe in final product, after packing, promoted by the humidity of excipients: Monitoring and quantification by Raman spectroscopy. *J. Pharm. Biomed. Anal.* **2016**, *121*, 209–214.
- [183] Feth, M. P.; Nagel, N.; Baumgartner, B.; Bröckelmann, M.; Rigal, D.; Otto, B.; Spitzenberg, M.; Schulz, M.; Becker, B.; Fischer, F.; Petzoldt, C. Challenges in the

- development of hydrate phases as active pharmaceutical ingredients—an example. *Eur. J. Pharm. Sci.* **2011**, 42, 116–129.
- [184] Vogt, F. G.; Brum, J.; Katrincic, L. M.; Flach, A.; Socha, J. M.; Goodman, R. M.; Haltiwanger, R. C. Physical, Crystallographic, and Spectroscopic Characterization of a Crystalline Pharmaceutical Hydrate: Understanding the Role of Water. *Cryst. Growth Des.* **2006**, 6, 2333–2354.
- [185] Healy, A. M.; Worku, Z. A.; Kumar, D.; Madi, A. M. Pharmaceutical solvates, hydrates and amorphous forms: A special emphasis on cocrystals. *Adv. Drug Deliv. Rev.* **2017**, 117, 25–46.
- [186] Pettersen, A.; Putra, O. D.; Light, M. E.; Namatame, Y. A peculiar dehydration and solid–solid phase transition of the active pharmaceutical ingredient AZD9898 based on in situ single crystal-to-single crystal transformations. *CrystEngComm* **2020**, 22, 7280–7289.
- [187] Reutzel-Edens, S. M.; Braun, D. E.; Newman, A. W. Hygroscopicity and Hydrates in Pharmaceutical Solids. In *Polymorphism in the pharmaceutical industry: Solid form and drug development*, Second edition; Hilfiker, R., Raumer, M. von, Eds.; Wiley-VCH Verlag GmbH & Co, **2019**; pp 159–188.
- [188] Tong, H. H. Y.; Chow, A. S. F.; Chan, H. M.; Chow, A. H. L.; Wan, Y. K. Y.; Williams, I. D.; Shek, F. L. Y.; Chan, C. K. Process-induced phase transformation of berberine chloride hydrates. *J. Pharm. Sci.* **2010**, 99, 1942–1954.
- [189] Nyman, J.; Day, G. M. Static and lattice vibrational energy differences between polymorphs. *CrystEngComm* **2015**, 17, 5154–5165.
- [190] Gelbrich, T.; Braun, D. E.; Ellern, A.; Griesser, U. J. Four Polymorphs of Methyl Paraben: Structural Relationships and Relative Energy Differences. *Cryst. Growth Des.* **2013**, 13, 1206–1217.
- [191] Rivera, S. A.; Allis, D. G.; Hudson, B. S. Importance of Vibrational Zero-Point Energy Contribution to the Relative Polymorph Energies of Hydrogen-Bonded Species. *Cryst. Growth Des.* **2008**, 8, 3905–3907.
- [192] Boothroyd, S.; Kerridge, A.; Broo, A.; Buttar, D.; Anwar, J. Why Do Some Molecules Form Hydrates or Solvates? *Cryst. Growth Des.* **2018**, 18, 1903–1908.
- [193] Braun, D. E.; Griesser, U. J. Why do Hydrates (Solvates) Form in Small Neutral Organic Molecules? Exploring the Crystal Form Landscapes of the Alkaloids Brucine and Strychnine. *Cryst. Growth Des.* **2016**, 16, 6405–6418.
- [194] Takieddin, K.; Khimiyak, Y. Z.; Fábíán, L. Prediction of Hydrate and Solvate Formation Using Statistical Models. *Cryst. Growth Des.* **2016**, 16, 70–81.
- [195] Almarsson, O.; Zaworotko, M. J. Crystal engineering of the composition of pharmaceutical phases. Do pharmaceutical co-crystals represent a new path to improved medicines? *Chem. Commun.* **2004**, 1889–1896.

- [196] Berge, S. M.; Bighley, L. D.; Monkhouse, D. C. Pharmaceutical salts. *J. Pharm. Sci.* **1977**, 66, 1–19.
- [197] dos Santos, J. A. B.; Chaves Júnior, J. V.; Araújo Batista, R. S. de; Sousa, D. P. de; Ferreira, G. L. R.; Lima Neto, S. A. de; Santana Oliveira, A. de; Souza, F. S. de; Aragão, C. F. S. Preparation, physicochemical characterization and solubility evaluation of pharmaceutical cocrystals of cinnamic acid. *J. Therm. Anal. Calorim.* **2021**, 145, 379–390.
- [198] Joshi, M.; Roy Choudhury, A. Salts of Amoxapine with Improved Solubility for Enhanced Pharmaceutical Applicability. *ACS Omega* **2018**, 3, 2406–2416.
- [199] Nikam, V. J.; Patil, S. B. Pharmaceutical cocrystals of nebivolol hydrochloride with enhanced solubility. *J. Cryst. Growth* **2020**, 534, 125488.
- [200] Zhang, Y.; Zhang, Y.; Chang, L.; Ji, Y.; Liu, L.; Feng, Y.; Wu, L.; Zhang, L.; Zhang, Y.; Zou, D.; Liu, Y.; Su, X. Crystalline palmatine saccharinate pharmaceutical salt without reducing solubility and improving its hygroscopic stability with regard to palmatine chloride. *J. Mol. Struct.* **2021**, 1230, 129631.
- [201] Deka, P.; Gogoi, D.; Althubeiti, K.; Rao, D. R.; Thakuria, R. Mechanochemistry, Characterization, and Physicochemical Property Investigation of a Favipiravir Cocrystal with Theophylline and GRAS Coformers. *Cryst. Growth Des.* **2021**, 21, 4417–4425.
- [202] Kruger, C. The relevance of international assessments to GRAS determinations. *Regul. Toxicol. Pharmacol.* **2016**, 79 Suppl. 2, S119-23.
- [203] Zheng, Q.; Unruh, D. K.; Hutchins, K. M. Cocrystallization of Trimethoprim and Solubility Enhancement via Salt Formation. *Cryst. Growth Des.* **2021**, 21, 1507–1517.
- [204] Haskins, M. M.; Lusi, M.; Zaworotko, M. J. Supramolecular Synthons Promiscuity in Phosphoric Acid-Dihydrogen Phosphate Ionic Cocrystals. *Cryst. Growth Des.* **2022**, 22, 3333–3342.
- [205] Guerin, S.; Khorasani, S.; Gleeson, M.; O'Donnell, J.; Sani, R.; Zwane, R.; Reilly, A. M.; Silien, C.; Tofail, S. A. M.; Liu, N.; Zaworotko, M.; Thompson, D. A Piezoelectric Ionic Cocrystal of Glycine and Sulfamic Acid. *Cryst. Growth Des.* **2021**, 21, 5818–5827.
- [206] Duggirala, N. K.; Smith, A. J.; Wojtas, Ł.; Shytle, R. D.; Zaworotko, M. J. Physical Stability Enhancement and Pharmacokinetics of a Lithium Ionic Cocrystal with Glucose. *Cryst. Growth Des.* **2014**, 14, 6135–6142.
- [207] Kavanagh, O. N.; Walker, G.; Lusi, M. Graph-Set Analysis Helps To Understand Charge Transfer in a Novel Ionic Cocrystal When the $\Delta p K_a$ Rule Fails. *Cryst. Growth Des.* **2019**, 19, 5308–5313.
- [208] Song, L.; Shemchuk, O.; Robeyns, K.; Braga, D.; Grepioni, F.; Leyssens, T. Ionic Cocrystals of Etiracetam and Levetiracetam: The Importance of Chirality for Ionic Cocrystals. *Cryst. Growth Des.* **2019**, 19, 2446–2454.

- [209] Wang, T.; Stevens, J. S.; Vetter, T.; Whitehead, G. F. S.; Vitorica-Yrezabal, I. J.; Hao, H.; Cruz-Cabeza, A. J. Salts, Cocrystals, and Ionic Cocrystals of a “Simple” Tautomeric Compound. *Cryst. Growth Des.* **2018**, *18*, 6973–6983.
- [210] Childs, S. L.; Stahly, G. P.; Park, A. The salt-cocrystal continuum: the influence of crystal structure on ionization state. *Mol. Pharm.* **2007**, *4*, 323–338.
- [211] Edwards, P. T.; Saunders, L. K.; Pallipurath, A. R.; Britton, A. J.; Willneff, E. A.; Shotton, E. J.; Schroeder, S. L. M. Proton Transfer on the Edge of the Salt/Cocrystal Continuum: X-Ray Photoelectron Spectroscopy of Three Isonicotinamide Salts. *Cryst. Growth Des.* **2021**, *21*, 6332–6340.
- [212] Hathwar, V. R.; Pal, R.; Guru Row, T. N. Charge Density Analysis of Crystals of Nicotinamide with Salicylic Acid and Oxalic Acid: An Insight into the Salt to Cocrystal Continuum. *Cryst. Growth Des.* **2010**, *10*, 3306–3310.
- [213] Rajput, L.; Banik, M.; Yarava, J. R.; Joseph, S.; Pandey, M. K.; Nishiyama, Y.; Desiraju, G. R. Exploring the salt-cocrystal continuum with solid-state NMR using natural-abundance samples: implications for crystal engineering. *IUCrJ* **2017**, *4*, 466–475.
- [214] Surov, A. O.; Vasilev, N. A.; Churakov, A. V.; Stroh, J.; Emmerling, F.; Perlovich, G. L. Solid Forms of Ciprofloxacin Salicylate: Polymorphism, Formation Pathways, and Thermodynamic Stability. *Cryst. Growth Des.* **2019**, *19*, 2979–2990.
- [215] Stainton, P.; Nauha, E.; Grecu, T.; McCabe, J. F.; Munshi, T.; Scowen, I.; Chan, H. C. S.; Nilsson, S.; Blagden, N. Chameleon Behavior of a New Salt of 3-(Aminocarbonyl) Pyridinium Malonate and Implications for Polymorphism on the Salt/Cocrystal Continuum. *Cryst. Growth Des.* **2022**, *22*, 1665–1679.
- [216] Perumalla, S. R.; Wang, C.; Guo, Y.; Shi, L.; Sun, C. C. Robust bulk preparation and characterization of sulfamethazine and saccharine salt and cocrystal polymorphs. *CrystEngComm* **2019**, *21*, 2089–2096.
- [217] Salajee, A.; Morrison, C.; Erasmus, R.; Lemmerer, A. Polymorphism and photoluminescence seen in (2-amino-5-chloropyridine)·(9-anthracenecarboxylic acid)·(trinitrobenzene): a further example of the salt-cocrystal continuum observed by virtue of isolating multiple crystal forms. *CrystEngComm* **2022**, *24*, 6297–6301.
- [218] Jones, C. L.; Skelton, J. M.; Parker, S. C.; Raithby, P. R.; Walsh, A.; Wilson, C. C.; Thomas, L. H. Living in the salt-cocrystal continuum: indecisive organic complexes with thermochromic behaviour. *CrystEngComm* **2019**, *21*, 1626–1634.
- [219] Good, D. J.; Rodríguez-Hornedo, N. Solubility Advantage of Pharmaceutical Cocrystals. *Cryst. Growth Des.* **2009**, *9*, 2252–2264.
- [220] Batisai, E.; Ayamane, A.; Kilinkissa, O. E. Y.; Báthori, N. B. Melting point–solubility–structure correlations in multicomponent crystals containing fumaric or adipic acid. *CrystEngComm* **2014**, *16*, 9992–9998.

- [221] Chu, K. A.; Yalkowsky, S. H. An interesting relationship between drug absorption and melting point. *Int. J. Pharm.* **2009**, 373, 24–40.
- [222] Kilinkissa, O. E. Y.; Govender, K. K.; Báthori, N. B. Melting point–solubility–structure correlations in chiral and racemic model cocrystals. *CrystEngComm* **2020**, 22, 2766–2771.
- [223] Wyttenbach, N.; Niederquell, A.; Kuentz, M. Machine Estimation of Drug Melting Properties and Influence on Solubility Prediction. *Mol. Pharm.* **2020**, 17, 2660–2671.
- [224] Kelley, S. P.; Narita, A.; Holbrey, J. D.; Green, K. D.; Reichert, W. M.; Rogers, R. D. Understanding the Effects of Ionicity in Salts, Solvates, Co-Crystals, Ionic Co-Crystals, and Ionic Liquids, Rather than Nomenclature, Is Critical to Understanding Their Behavior. *Cryst. Growth Des.* **2013**, 13, 965–975.
- [225] Alhameedi, K.; Karton, A.; Jayatilaka, D.; Thomas, S. P. Bond orders for intermolecular interactions in crystals: charge transfer, ionicity and the effect on intramolecular bonds. *IUCrJ* **2018**, 5, 635–646.
- [226] Koumpouras, K.; Larsson, J. A. Distinguishing between chemical bonding and physical binding using electron localization function (ELF). *J. Phys. Condens. Matter.* **2020**, 32, 315502.
- [227] Lu, T.; Chen, Q. Interaction Region Indicator: A Simple Real Space Function Clearly Revealing Both Chemical Bonds and Weak Interactions**. *Chem. Methods* **2021**, 1, 231–239.
- [228] Ray, U.; Pang, Z.; Li, T. Programming material properties by tuning intermolecular bonding. *J. Appl. Phys.* **2022**, 132, 210703.
- [229] Shaik, S.; Danovich, D.; Hiberty, P. C. On the nature of the chemical bond in valence bond theory. *J. Chem. Phys.* **2022**, 157, 90901.
- [230] Chen, X.; Jin, S.; Zhang, H.; Xiao, X.; Liu, B.; Wang, D. Structure of five molecular salts assembled from noncovalent associations between organic acids, imidazole, benzimidazole, and 1-(2-(1H-benzimidazol-1-yl)ethyl)-1H-benzimidazole. *J. Mol. Struct.* **2017**, 1144, 514–528.
- [231] Bickelhaupt, F. M.; Solà, M.; Guerra, C. F. Table salt and other alkali metal chloride oligomers: structure, stability, and bonding. *Inorg. Chem.* **2007**, 46, 5411–5418.
- [232] Du Chen, H.; Pan, R.; Dong, X.; Huan, W. Theoretical Study on the Compounds of Chlorine Fluoride (ClF₃, ClOF₃) and Superhalogens (BeF₂, MgF₂): Preferred Structures and Significant Nonlinear Optical Properties. *Russ. J. Phys. Chem. B* **2020**, 14, 905–909.
- [233] Li, Y.; Di Wu; Li, Z. Compounds of superatom clusters: preferred structures and significant nonlinear optical properties of the BLi₆-X (X = F, LiF₂, BeF₃, BF₄) motifs. *Inorg. Chem.* **2008**, 47, 9773–9778.

- [234] Spruijt, E.; van den Berg, S. A.; Cohen Stuart, M. A.; van der Gucht, J. Direct measurement of the strength of single ionic bonds between hydrated charges. *ACS Nano* **2012**, 6, 5297–5303.
- [235] Yang, H.; Li, Y.; Di Wu; Li, Z. Structural properties and nonlinear optical responses of superatom compounds BF₄⁻M (M = Li, FLi₂, OLi₃, NLi₄). *Int. J. Quantum Chem.* **2012**, 112, 770–778.
- [236] Salikolimi, K.; Sudhakar, A. A.; Ishida, Y. Functional Ionic Liquid Crystals. *Langmuir* **2020**, 36, 11702–11731.
- [237] Kapernaum, N.; Lange, A.; Ebert, M.; Grunwald, M. A.; Haege, C.; Marino, S.; Zens, A.; Taubert, A.; Giesselmann, F.; Laschat, S. Current Topics in Ionic Liquid Crystals. *Chempluschem* **2021**, 87, e202100397.
- [238] Goossens, K.; Lava, K.; Bielawski, C. W.; Binnemans, K. Ionic Liquid Crystals: Versatile Materials. *Chem. Rev.* **2016**, 116, 4643–4807.
- [239] Steiner, T. The Hydrogen Bond in the Solid State. *Angew. Chem. Int. Ed.* **2002**, 41, 48–76.
- [240] Bolla, G.; Sarma, B.; Nangia, A. K. Crystal Engineering of Pharmaceutical Cocrystals in the Discovery and Development of Improved Drugs. *Chem. Rev.* **2022**, 122, 11514–11603.
- [241] Buckingham, A. D.; Del Bene, J. E.; McDowell, S. The hydrogen bond. *Chem. Phys. Lett.* **2008**, 463, 1–10.
- [242] Emamian, S.; Lu, T.; Kruse, H.; Emamian, H. Exploring Nature and Predicting Strength of Hydrogen Bonds: A Correlation Analysis Between Atoms-in-Molecules Descriptors, Binding Energies, and Energy Components of Symmetry-Adapted Perturbation Theory. *J. Comput. Chem.* **2019**, 40, 2868–2881.
- [243] Meot-Ner, M. The ionic hydrogen bond. *Chem. Rev.* **2005**, 105, 213–284.
- [244] Kenny, P. W. Hydrogen-Bond Donors in Drug Design. *J. Med. Chem.* **2022**, 65, 14261–14275.
- [245] Lin, X.; Jiang, X.; Wu, W.; Mo, Y. Induction, Resonance, and Secondary Electrostatic Interaction on Hydrogen Bonding in the Association of Amides and Imides. *J. Org. Chem.* **2018**, 83, 13446–13453.
- [246] Sinnokrot, M. O.; Sherrill, C. D. Substituent effects in pi-pi interactions: sandwich and T-shaped configurations. *J. Am. Chem. Soc.* **2004**, 126, 7690–7697.
- [247] Thakuria, R.; Nath, N. K.; Saha, B. K. The Nature and Applications of π - π Interactions: A Perspective. *Cryst. Growth Des.* **2019**, 19, 523–528.
- [248] Yao, Z.-F.; Wang, J.-Y.; Pei, J. Control of π - π Stacking via Crystal Engineering in Organic Conjugated Small Molecule Crystals. *Cryst. Growth Des.* **2018**, 18, 7–15.

- [249] Zhuang, W.-R.; Wang, Y.; Cui, P.-F.; Xing, L.; Lee, J.; Kim, D.; Jiang, H.-L.; Oh, Y.-K. Applications of π - π stacking interactions in the design of drug-delivery systems. *J. Control. Release* **2019**, 294, 311–326.
- [250] Sherrill, C. D. Energy component analysis of π interactions. *Acc. Chem. Res.* **2013**, 46, 1020–1028.
- [251] Salini, P. S.; Rajagopal, S. K.; Hariharan, M. Haloacetylation-Driven Transformation of Sandwich Herringbone to Lamellar/Columnar Packing in Pyrene. *Cryst. Growth Des.* **2016**, 16, 5822–5830.
- [252] Wang, D.-X.; Wang, M.-X. Exploring Anion- π Interactions and Their Applications in Supramolecular Chemistry. *Acc. Chem. Res.* **2020**, 53, 1364–1380.
- [253] Chifotides, H. T.; Dunbar, K. R. Anion- π interactions in supramolecular architectures. *Acc. Chem. Res.* **2013**, 46, 894–906.
- [254] Tkatchenko, A. Current Understanding of Van der Waals Effects in Realistic Materials. *Adv. Funct. Mater.* **2015**, 25, 2054–2061.
- [255] Geim, A. K.; Grigorieva, I. V. Van der Waals heterostructures. *Nature* **2013**, 499, 419–425.
- [256] Cavallo, G.; Metrangolo, P.; Milani, R.; Pilati, T.; Priimagi, A.; Resnati, G.; Terraneo, G. The Halogen Bond. *Chem. Rev.* **2016**, 116, 2478–2601.
- [257] Kellett, C. W.; Kennepohl, P.; Berlinguette, C. P. π covalency in the halogen bond. *Nat. Commun.* **2020**, 11, 3310.
- [258] Lee, L. M.; Tsemperouli, M.; Poblador-Bahamonde, A. I.; Benz, S.; Sakai, N.; Sugihara, K.; Matile, S. Anion Transport with Pnictogen Bonds in Direct Comparison with Chalcogen and Halogen Bonds. *J. Am. Chem. Soc.* **2019**, 141, 810–814.
- [259] Scilabra, P.; Terraneo, G.; Resnati, G. The Chalcogen Bond in Crystalline Solids: A World Parallel to Halogen Bond. *Acc. Chem. Res.* **2019**, 52, 1313–1324.
- [260] Varadwaj, A.; Varadwaj, P. R.; Marques, H. M.; Yamashita, K. The Pnictogen Bond: The Covalently Bound Arsenic Atom in Molecular Entities in Crystals as a Pnictogen Bond Donor. *Molecules* **2022**, 27.
- [261] Wang, W.; Ji, B.; Zhang, Y. Chalcogen bond: a sister noncovalent bond to halogen bond. *J. Phys. Chem. A* **2009**, 113, 8132–8135.
- [262] Liu, Y.; Wang, Y.; Huang, X.; Li, X.; Zong, S.; Wang, N.; Hao, H. Conformational Selectivity and Evolution Affected by the Desolvation Process. *Cryst. Growth Des.* **2022**, 22, 1283–1291.
- [263] Choong, K. L.; Smith, R. Optimization of batch cooling crystallization. *Chem. Eng. Sci.* **2004**, 59, 313–327.

- [264] Gregson, F. K. A.; Robinson, J. F.; Miles, R. E. H.; Royall, C. P.; Reid, J. P. Drying Kinetics of Salt Solution Droplets: Water Evaporation Rates and Crystallization. *J. Phys. Chem. B* **2019**, 123, 266–276.
- [265] Izutsu, K.-I.; Koide, T.; Takata, N.; Ikeda, Y.; Ono, M.; Inoue, M.; Fukami, T.; Yonemochi, E. Characterization and Quality Control of Pharmaceutical Cocrystals. *Chem. Pharm. Bull.* **2016**, 64, 1421–1430.
- [266] He, G.; Bhamidi, V.; Wilson, S. R.; Tan, R. B. H.; Kenis, P. J. A.; Zukoski, C. F. Direct Growth of γ -Glycine from Neutral Aqueous Solutions by Slow, Evaporation-Driven Crystallization. *Cryst. Growth Des.* **2006**, 6, 1746–1749.
- [267] Liang, S.; Duan, X.; Zhang, X.; Qian, G.; Zhou, X. Supersaturation-dependent polymorphic outcome and transformation rate of L-glutamic acid. *RSC Adv.* **2016**, 6, 74700–74703.
- [268] Sudha, C.; Srinivasan, K. Nucleation control and separation of paracetamol polymorphs through swift cooling crystallization process. *J. Cryst. Growth* **2014**, 401, 248–251.
- [269] Bai, C.; Zheng, T.; Wang, C. Glycine polymorphs screening by antisolvent crystallization in a surface acoustic wave microfluidic device. *Inorg. Chem. Commun.* **2022**, 143, 109816.
- [270] Kumar, R.; Thakur, A. K.; Banerjee, N.; Kumar, A.; Gaurav, G. K.; Arya, R. K. Liquid antisolvent crystallization of pharmaceutical compounds: current status and future perspectives. *Drug Deliv. Transl. Res.* **2023**, 13, 400–418.
- [271] Lonare, A. A.; Patel, S. R. Antisolvent Crystallization of Poorly Water Soluble Drugs. *IJCEA* **2013**, 337–341.
- [272] Park, M.-W.; Yeo, S.-D. Antisolvent crystallization of carbamazepine from organic solutions. *Chem. Eng. Res. Des.* **2012**, 90, 2202–2208.
- [273] Beckmann, W. Seeding the Desired Polymorph: Background, Possibilities, Limitations, and Case Studies. *Org. Process Res. Dev.* **2000**, 4, 372–383.
- [274] He, Y.; Gao, Z.; Zhang, T.; Sun, J.; Ma, Y.; Tian, N.; Gong, J. Seeding Techniques and Optimization of Solution Crystallization Processes. *Org. Process Res. Dev.* **2020**, 24, 1839–1849.
- [275] Svanberg, L.; Ahrné, L.; Lorén, N.; Windhab, E. Effect of sugar, cocoa particles and lecithin on cocoa butter crystallisation in seeded and non-seeded chocolate model systems. *J. Food Eng.* **2011**, 104, 70–80.
- [276] Dowling, R.; Davey, R. J.; Curtis, R. A.; Han, G.; Poornachary, S. K.; Chow, P. S.; Tan, R. B. H. Acceleration of crystal growth rates: an unexpected effect of tailor-made additives. *Chem. Commun.* **2010**, 46, 5924–5926.

- [277] Lee, S.-H.; Lee, G.-H.; Lee, K.-H.; Jazbinsek, M.; Kang, B. J.; Rotermund, F.; Kwon, O.-P. In Situ Tailor-Made Additives for Molecular Crystals: A Simple Route to Morphological Crystal Engineering. *Cryst. Growth Des.* **2016**, *16*, 3555–3561.
- [278] Surov, A. O.; Solanko, K. A.; Bond, A. D.; Perlovich, G. L.; Bauer-Brandl, A. Crystallization and Polymorphism of Felodipine. *Cryst. Growth Des.* **2012**, *12*, 4022–4030.
- [279] Thomas, L. H.; Wales, C.; Wilson, C. C. Selective preparation of elusive and alternative single component polymorphic solid forms through multi-component crystallisation routes. *Chem. Commun.* **2016**, *52*, 7372–7375.
- [280] Zhang, K.; Xu, S.; Liu, S.; Tang, W.; Fu, X.; Gong, J. Novel Strategy to Control Polymorph Nucleation of Gamma Pyrazinamide by Preferred Intermolecular Interactions during Heterogeneous Nucleation. *Cryst. Growth Des.* **2018**, *18*, 4874–4879.
- [281] Barret, P.; Smith, B.; Worlitschek, J.; Bracken, V.; O’Sullivan, B.; O’Grady, D. A Review of the Use of Process Analytical Technology for the Understanding and Optimization of Production Batch Crystallization Processes. *Org. Process Res. Dev.* **2005**, *9*, 348–355
- [282] Darmali, C.; Mansouri, S.; Yazdanpanah, N.; Woo, M. W. Mechanisms and Control of Impurities in Continuous Crystallization: A Review. *Ind. Eng. Chem. Res.* **2019**, *58*, 1463–1479.
- [283] Ma, Y.; Wu, S.; Macaringue, E. G. J.; Zhang, T.; Gong, J.; Wang, J. Recent Progress in Continuous Crystallization of Pharmaceutical Products: Precise Preparation and Control. *Org. Process Res. Dev.* **2020**, *24*, 1785–1801.
- [284] Wieckhusen, D. Development of Batch Crystallizations. In *Crystallization: Basic concepts and industrial applications*; Beckmann, W., Ed.; Wiley-VCH, **2013**; pp 187–202.
- [285] Yano, Y.; Kasai, H.; Zheng, Y.; Nishibori, E.; Hisaeda, Y.; Ono, T. Multicomponent Crystals with Competing Intermolecular Interactions: In Situ X-ray Diffraction and Luminescent Features Reveal Multimolecular Assembly under Mechanochemical Conditions. *Angew. Chem. Int. Ed. Engl.* **2022**, *61*, e202203853.
- [286] Saikia, B.; Seidel-Morgenstern, A.; Lorenz, H. Role of Mechanochemistry in Solid Form Selection and Identification of the Drug Praziquantel. *Cryst. Growth Des.* **2021**, *21*, 5854–5861.
- [287] Parakatawella, S.; Gogoi, D.; Deka, P.; Xu, Y.; Sandaruwan, C.; Jayasundera, A. C. A.; Arhangel'skis, M.; Thakuria, R.; Adassooriya, N. M. Mechanochemical Synthesis of Polymorphic Urea · Adipic Acid Cocrystal as a Sustained-Release Nitrogen Source. *ChemSusChem* **2022**, *15*, e202102445.
- [288] Orehek, J.; Teslić, D.; Likozar, B. Continuous Crystallization Processes in Pharmaceutical Manufacturing: A Review. *Org. Process Res. Dev.* **2021**, *25*, 16–42.
- [289] Douroumis, D.; Ross, S. A.; Nokhodchi, A. Advanced methodologies for cocrystal synthesis. *Adv. Drug Deliv. Rev.* **2017**, *117*, 178–195.

- [290] Kumar, S.; Prakash, O.; Gupta, A.; Singh, S. Solvent-free Methods for Co-crystal Synthesis: A Review. *Curr. Org. Synth.* **2019**, *16*, 385–397.
- [291] Muresan-Pop, M.; Vulpoi, A.; Simon, V.; Todea, M.; Magyari, K.; Pap, Z.; Simion, A.; Filip, C.; Simon, S. Co-Crystals of Etravirine by Mechanochemical Activation. *J. Pharm. Sci.* **2022**, *111*, 1178–1186.
- [292] Kulla, H.; Haferkamp, S.; Akhmetova, I.; Röllig, M.; Maierhofer, C.; Rademann, K.; Emmerling, F. In Situ Investigations of Mechanochemical One-Pot Syntheses. *Angew. Chem. Int. Ed. Engl.* **2018**, *57*, 5930–5933.
- [293] Beyer, M. K.; Clausen-Schaumann, H. Mechanochemistry: the mechanical activation of covalent bonds. *Chem. Rev.* **2005**, *105*, 2921–2948.
- [294] Beamish-Cook, J.; Shankland, K.; Murray, C. A.; Vaqueiro, P. Insights into the Mechanochemical Synthesis of MOF-74. *Cryst. Growth Des.* **2021**, *21*, 3047–3055.
- [295] Haskins, M. M.; Zaworotko, M. J. Screening and Preparation of Cocrystals: A Comparative Study of Mechanochemistry vs Slurry Methods. *Cryst. Growth Des.* **2021**, *21*, 4141–4150.
- [296] Koskela, J.; Sutton, J. J.; Lipiäinen, T.; Gordon, K. C.; Strachan, C. J.; Fraser-Miller, S. J. Low- versus Mid-frequency Raman Spectroscopy for in Situ Analysis of Crystallization in Slurries. *Mol. Pharm.* **2022**, *19*, 2316–2326.
- [297] Qu, H.; Jin, S.; Gong, J.; Du, S.; Jia, L.; Wu, S. Enhancing Stability and Formulation Capability of Fungicides by Cocrystallization through a Novel Multistep Slurry Conversion Process. *Cryst. Growth Des.* **2020**, *20*, 7356–7367.
- [298] Feng, H.; Wang, N.; Huang, X.; Wang, T.; Zhou, L.; Hao, H. Recent progress in melt crystallization. *Chem. Eng. Res. Des.* **2023**, *190*, 268–281.
- [299] Shtukenberg, A. G.; Tan, M.; Vogt-Maranto, L.; Chan, E. J.; Xu, W.; Yang, J.; Tuckerman, M. E.; Hu, C. T.; Kahr, B. Melt Crystallization for Paracetamol Polymorphism. *Cryst. Growth Des.* **2019**, *19*, 4070–4080.
- [300] Yao, X.; Henry, R. F.; Zhang, G. G. Z. Ritonavir Form III: A New Polymorph After 24 Years. *J. Pharm. Sci.* **2023**, *112*, 237–242.
- [301] Bunaciu, A. A.; Udriștioiu, E. G.; Aboul-Enein, H. Y. X-ray diffraction: instrumentation and applications. *Crit. Rev. Anal. Chem.* **2015**, *45*, 289–299.
- [302] von Dreele, R. B.; Toby, B. H. X-Ray Powder Diffraction. In *Characterization of Materials 2 Volume Set*; Kaufmann, E. N., Ed.; Wiley Interscience Imprint, **2003**.
- [303] Fucke, K.; Steed, J. W. X-ray and Neutron Diffraction in the Study of Organic Crystalline Hydrates. *Water* **2010**, *2*, 333–350.
- [304] Pope, C. G. X-Ray Diffraction and the Bragg Equation. *J. Chem. Educ.* **1997**, *74*, 129
- [305] Lavina, B.; Dera, P.; Downs, R. T. Modern X-ray Diffraction Methods in Mineralogy and Geosciences. *Rev. Mineral Geochem.* **2014**, *78*, 1–31.

- [306] Meisburger, S. P.; Thomas, W. C.; Watkins, M. B.; Ando, N. X-ray Scattering Studies of Protein Structural Dynamics. *Chem. Rev.* **2017**, 117, 7615–7672.
- [307] Jamrógiewicz, M. Application of the near-infrared spectroscopy in the pharmaceutical technology. *J. Pharm. Biomed. Anal.* **2012**, 66, 1–10.
- [308] Czarnecki, M. A.; Morisawa, Y.; Futami, Y.; Ozaki, Y. Advances in Molecular Structure and Interaction Studies Using Near-Infrared Spectroscopy. *Chem. Rev.* **2015**, 115, 9707–9744.
- [309] van Eerdenbrugh, B.; Taylor, L. S. Application of mid-IR spectroscopy for the characterization of pharmaceutical systems. *Int. J. Pharm.* **2011**, 417, 3–16.
- [310] Tolstorozhev, G. B.; Bel'kov, M. V.; Skornyakov, I. V.; Bazyl, O. K.; Artyukhov, V. Y.; Mayer, G. V.; Shadyro, O. I.; Kuzovkov, P. V.; Brinkevich, S. D.; Samovich, S. N. Infrared Spectroscopy of Hydrogen Bonds in Benzoic Acid Derivatives. *J. Appl. Spectrosc.* **2014**, 81, 109–117.
- [311] Flakus, H. T.; Michta, A.; Nowak, M.; Kusz, J. Effects of dynamical couplings in IR spectra of the hydrogen bond in N-phenylacrylamide crystals. *J. Phys. Chem. A* **2011**, 115, 4202–4213.
- [312] Liao, X.; Zhou, N. Dehydration Study of Piracetam Co-Crystal Hydrates. *J. Pharm. Sci.* **2018**, 107, 2804–2809.
- [313] Suzuki, T.; Araki, T.; Kitaoka, H.; Terada, K. Studies on mechanism of thermal crystal transformation of sitafloxacin hydrates through melting and recrystallization, yielding different anhydrates depending on initial crystalline forms. *Int. J. Pharm.* **2010**, 402, 110–116.
- [314] da Silva, C. C.; Guimarães, F. F.; Ribeiro, L.; Martins, F. T. Salt or cocrystal of salt? Probing the nature of multicomponent crystal forms with infrared spectroscopy. *Spectrochim. Acta A Mol. Biomol. Spectrosc.* **2016**, 167, 89–95.
- [315] Ali, H. R. H.; Alhalaweh, A.; Mendes, N. F.; Ribeiro-Claro, P.; Velaga, S. P. Solid-state vibrational spectroscopic investigation of cocrystals and salt of indomethacin. *CrystEngComm* **2012**, 14, 6665.
- [316] Luan, Y.; Li, J.; Kaliwanda, M.; Wang, N.; Chen, K.; Li, X.; Su, W.; Hao, H. Solution Thermodynamics of Benzotriazole in Different Pure Solvents. *J. Chem. Eng. Data* **2018**, 63, 1546–1555.
- [317] Jouyban-Gharamaleki, V.; Jouyban, A.; Acree, W. E.; Rahimpour, E. Smart systems for determination of drug's solubility. *Drug Dev. Ind. Pharm.* **2019**, 45, 177–187.
- [318] Sou, T.; Bergström, C. A. S. Automated assays for thermodynamic (equilibrium) solubility determination. *Drug Discov. Today Technol.* **2018**, 27, 11–19.
- [319] Bharti, S. K.; Roy, R. Quantitative ¹H NMR spectroscopy. *TrAC, Trends Anal. Chem.* **2012**, 35, 5–26.

- [320] Dikmen, G. Determination of the solubility of 2-Methyl-1,3-benzothiazol-5-amine molecule with aqueous ethanol by NMR spectroscopy. *J. Mol. Liq.* **2018**, 272, 851–856.
- [321] Lin, M.; Tesconi, M.; Tischler, M. Use of (1)H NMR to facilitate solubility measurement for drug discovery compounds. *Int. J. Pharm.* **2009**, 369, 47–52.
- [322] Zloh, M. NMR spectroscopy in drug discovery and development: Evaluation of physico-chemical properties. *ADMET DMPK* **2019**, 7, 242–251.
- [323] Zheng, Q.; Zhang, Y.; Montazerian, M.; Gulbiten, O.; Mauro, J. C.; Zanutto, E. D.; Yue, Y. Understanding Glass through Differential Scanning Calorimetry. *Chem. Rev.* **2019**, 119, 7848–7939.
- [324] Knopp, M. M.; Löbmann, K.; Elder, D. P.; Rades, T.; Holm, R. Recent advances and potential applications of modulated differential scanning calorimetry (mDSC) in drug development. *Eur. J. Pharm. Sci.* **2016**, 87, 164–173.
- [325] Clas, S. D.; Dalton, C. R.; Hancock, B. C. Differential scanning calorimetry: applications in drug development. *Pharm. Sci. Technol. Today* **1999**, 2, 311–320.
- [326] Saadatkhah, N.; Carillo Garcia, A.; Ackermann, S.; Leclerc, P.; Latifi, M.; Samih, S.; Patience, G. S.; Chaouki, J. Experimental methods in chemical engineering: Thermogravimetric analysis—TGA. *Can. J. Chem. Eng.* **2020**, 98, 34–43.
- [327] Fang, T.; Li, W.; Gu, F.; Li, S. Accurate prediction of lattice energies and structures of molecular crystals with molecular quantum chemistry methods. *J. Chem. Theory Comput.* **2015**, 11, 91–98.
- [328] Greenwell, C.; McKinley, J. L.; Zhang, P.; Zeng, Q.; Sun, G.; Li, B.; Wen, S.; Beran, G. J. O. Overcoming the difficulties of predicting conformational polymorph energetics in molecular crystals via correlated wavefunction methods. *Chem. Sci.* **2020**, 11, 2200–2214.
- [329] Price, S. L.; Braun, D. E.; Reutzel-Edens, S. M. Can computed crystal energy landscapes help understand pharmaceutical solids? *Chem. Commun.* **2016**, 52, 7065–7077.
- [330] Surov, A. O.; Solanko, K. A.; Bond, A. D.; Bauer-Brandl, A.; Perlovich, G. L. Cocrystals of the antiandrogenic drug bicalutamide: screening, crystal structures, formation thermodynamics and lattice energies. *CrystEngComm* **2016**, 18, 4818–4829.
- [331] Yuan, S.; Chan, H. S.; Hu, Z. Using PyMOL as a platform for computational drug design. *WIREs Comput. Mol. Sci.* **2017**, 7.
- [332] van Mourik, T.; Bühl, M.; Gaigeot, M.-P. Density functional theory across chemistry, physics and biology. *Philos. Trans. A Math. Phys. Eng. Sci.* **2014**, 372, 20120488.
- [333] Baseden, K. A.; Tye, J. W. Introduction to Density Functional Theory: Calculations by Hand on the Helium Atom. *J. Chem. Educ.* **2014**, 91, 2116–2123.
- [334] Paier, J.; Hirschl, R.; Marsman, M.; Kresse, G. The Perdew-Burke-Ernzerhof exchange-correlation functional applied to the G2-1 test set using a plane-wave basis set. *J. Chem. Phys.* **2005**, 122, 234102.

- [335] Stephens, P. J.; Devlin, F. J.; Chabalowski, C. F.; Frisch, M. J. Ab Initio Calculation of Vibrational Absorption and Circular Dichroism Spectra Using Density Functional Force Fields. *J. Phys. Chem.* **1994**, 98, 11623–11627.
- [336] Bursch, M.; Mewes, J.-M.; Hansen, A.; Grimme, S. Best-Practice DFT Protocols for Basic Molecular Computational Chemistry. *Angew. Chem. Int. Ed. Engl.* **2022**, 61, e202205735.
- [337] Beran, G. J. O. Modeling Polymorphic Molecular Crystals with Electronic Structure Theory. *Chem. Rev.* **2016**, 116, 5567–5613.
- [338] Kronik, L.; Tkatchenko, A. Understanding molecular crystals with dispersion-inclusive density functional theory: pairwise corrections and beyond. *Acc. Chem. Res.* **2014**, 47, 3208–3216.
- [339] Marchese Robinson, R. L.; Geatches, D.; Morris, C.; Mackenzie, R.; Maloney, A. G. P.; Roberts, K. J.; Moldovan, A.; Chow, E.; Pencheva, K.; Vatvani, D. R. M. Evaluation of Force-Field Calculations of Lattice Energies on a Large Public Dataset, Assessment of Pharmaceutical Relevance, and Comparison to Density Functional Theory. *J. Chem. Inf. Model.* **2019**, 59, 4778–4792.
- [340] Bader, R. F. W. A quantum theory of molecular structure and its applications. *Chem. Rev.* **1991**, 91, 893–928.
- [341] Popelier, P. L. A.; Aicken, F. M.; O'Brien, S. E. Atoms in molecules. In *Chemical Modelling: Applications and Theory Volume 1*; Hinchliffe, A., Ed.; Royal Society of Chemistry, **2000**, pp. 143–198.
- [342] Bartlett, R. J. Coupled-cluster approach to molecular structure and spectra: a step toward predictive quantum chemistry. *J. Phys. Chem.* **1989**, 93, 1697–1708.
- [343] Blom, M. N.; Compagnon, I.; Polfer, N. C.; Helden, G. von; Meijer, G.; Suhai, S.; Paizs, B.; Oomens, J. Stepwise solvation of an amino acid: the appearance of zwitterionic structures. *J. Phys. Chem. A* **2007**, 111, 7309–7316.
- [344] Nugrahani, I.; Jessica, M. A. Amino Acids as the Potential Co-Former for Co-Crystal Development: A Review. *Molecules* **2021**, 26.
- [345] Price, W. D.; Jockusch, R. A.; Williams, E. R. Is arginine a zwitterion in the gas phase? *J. Am. Chem. Soc.* **1997**, 119, 11988–11989.
- [346] Wyttenbach, T.; Witt, M.; Bowers, M. T. On the Stability of Amino Acid Zwitterions in the Gas Phase: The Influence of Derivatization, Proton Affinity, and Alkali Ion Addition. *J. Am. Chem. Soc.* **2000**, 122, 3458–3464.
- [347] Bormann, J. The 'ABC' of GABA receptors. *Trends Pharmacol. Sci.* **2000**, 21, 16–19.
- [348] Luo, Y.; Balle, T. GABAA receptors as targets for anaesthetics and analgesics and promising candidates to help treat coronavirus infections: A mini-review. *Basic Clin. Pharmacol. Toxicol.* **2022**, 131, 443–451.

- [349] Naffaa, M. M.; Hung, S.; Chebib, M.; Johnston, G. A. R.; Hanrahan, J. R. GABA- ρ receptors: distinctive functions and molecular pharmacology. *Br. J. Pharmacol.* **2017**, 174, 1881–1894.
- [350] Decavel, C.; van den Pol, A. N. GABA: a dominant neurotransmitter in the hypothalamus. *J. Comp. Neurol.* **1990**, 302, 1019–1037.
- [351] Gottesmann, C. GABA mechanisms and sleep. *Neuroscience* **2002**, 111, 231–239.
- [352] Jasmin, L.; Wu, M. V.; Ohara, P. T. GABA puts a stop to pain. *Curr. Drug Targets CNS Neurol. Disord.* **2004**, 3, 487–505.
- [353] Kalueff, A. V.; Nutt, D. J. Role of GABA in anxiety and depression. *Depress. Anxiety* **2007**, 24, 495–517.
- [354] Dobson, A. J.; Gerkin, R. E. gamma-Aminobutyric acid: a novel tetragonal phase. *Acta Crystallogr. C Cryst. Struct. Commun.* **1996**, 52 (Pt 12), 3075–3078.
- (355) Lamkowski, L.; Komisarek, D.; Merz, K. GABA-Controlled Synthesis of the Metastable Polymorphic Form and Crystallization Behavior with a Chiral Malic Acid. *Cryst. Growth Des.* **2022**, 22, 356–362.
- [356] Tomita, K.; Higashi, H.; Fujiwara, T. Crystal and Molecular Structure of ω -Amino Acids, ω -Amino Sulfonic Acids and Their Derivatives. IV. The Crystal and Molecular Structure of γ -Aminobutyric Acid (GABA), a Nervous Inhibitory Transmitter. *BCSJ* **1973**, 46, 2199–2204.
- [357] Wang, L.; Sun, G.; Zhang, K.; Yao, M.; Jin, Y.; Zhang, P.; Wu, S.; Gong, J. Green Mechanochemical Strategy for the Discovery and Selective Preparation of Polymorphs of Active Pharmaceutical Ingredient γ -Aminobutyric Acid (GABA). *ACS Sustain. Chem. Eng.* **2020**, 8, 16781–16790.
- [358] Dai, L.; Feng, W.-X.; Zheng, S.-P.; Jiang, J.-J.; Wang, D.; van der Lee, A.; Dumitrescu, D.; Barboiu, M. Progressive Folding and Adaptive Multivalent Recognition of Alkyl Amines and Amino Acids in p-Sulfonatocalix4arene Hosts: Solid-State and Solution Studies. *Chempluschem* **2020**, 85, 1623–1631.
- [359] Fabbiani, F. P. A.; Buth, G.; Levendis, D. C.; Cruz-Cabeza, A. J. Pharmaceutical hydrates under ambient conditions from high-pressure seeds: a case study of GABA monohydrate. *Chem. Commun.* **2014**, 50, 1817–1819.
- [360] Vries, E. J. C. de; Levendis, D. C.; Reece, H. A. A hexagonal solvate of the neurotransmitter γ -aminobutyric acid. *CrystEngComm* **2011**, 13, 3334.
- [361] Losev, E. A.; Boldyreva, E. V. A salt or a co-crystal – when crystallization protocol matters. *CrystEngComm* **2018**, 20, 2299–2305.
- [362] Losev, E. A.; Pishchur, D. P.; Boldyreva, E. V. A new monohydrated molecular salt of GABA with l-tartaric acid: the structure-forming role of water. *CrystEngComm* **2021**, 23, 6086–6092.

- [363] Bockbrader, H. N.; Wesche, D.; Miller, R.; Chapel, S.; Janiczek, N.; Burger, P. A comparison of the pharmacokinetics and pharmacodynamics of pregabalin and gabapentin. *Clin. Pharmacokinet.* **2010**, 49, 661–669.
- [364] Evoy, K. E.; Morrison, M. D.; Saklad, S. R. Abuse and Misuse of Pregabalin and Gabapentin. *Drugs* **2017**, 77, 403–426.
- [365] Kukkar, A.; Bali, A.; Singh, N.; Jaggi, A. S. Implications and mechanism of action of gabapentin in neuropathic pain. *Arch. Pharm. Res.* **2013**, 36, 237–251.
- [366] Mao, J.; Chen, L. L. Gabapentin in Pain Management. *Anesth. Analg.* **2000**, 91, 680–687.
- [367] Rose, M. A.; Kam, P. C. A. Gabapentin: pharmacology and its use in pain management. *Anaesthesia* **2002**, 57, 451–462.
- [368] Sills, G. J. The mechanisms of action of gabapentin and pregabalin. *Curr. Opin. Pharmacol.* **2006**, 6, 108–113.
- [369] Delaney, S. P.; Smith, T. M.; Korter, T. M. Conformation versus cohesion in the relative stabilities of gabapentin polymorphs. *RSC Adv.* **2014**, 4, 855–864.
- [370] Hsu, C.-H.; Ke, W.-T.; Lin, S.-Y. Progressive steps of polymorphic transformation of gabapentin polymorphs studied by hot-stage FTIR microspectroscopy. *J. Pharm. Pharm. Sci.* **2010**, 13, 67–77.
- [371] Lin, S.-Y.; Hsu, C.-H.; Ke, W.-T. Solid-state transformation of different gabapentin polymorphs upon milling and co-milling. *Int. J. Pharm.* **2010**, 396, 83–90.
- [372] Reece, H. A.; Levendis, D. C. Polymorphs of gabapentin. *Acta Crystallogr. C* **2008**, 64, o105-8.
- [373] Kumar, Y.; Khanduri, C. H.; Ganagakhedkar, K. K.; Chakraborty, R.; Dorwal, H. N.; Rohtagi, A.; Panda, A. K. Crystallization of gabapentin polymorph IV and its applications in treatment of cerebral disorders WO2004106281. **2004**.
- [374] Patel, D. J.; Patel, A. M.; Patel, H. P.; Hublikar, M.; Agarwal, V. K.; Pandita, K.; Patel, P. R. A novel process for preparing gabapentin polymorph II IN2003MU00454. **2003**.
- [375] Satyanarayana, C.; Ramanjaneyulu, G. S.; Kumar, I. V. S. Novel polymorph of gabapentin and its conversion to gabapentin form-II WO2004110342. **2004**.
- [376] André, V.; Fernandes, A.; Santos, P. P.; Duarte, M. T. On the Track of New Multicomponent Gabapentin Crystal Forms: Synthon Competition and pH Stability. *Cryst. Growth Des.* **2011**, 11, 2325–2334.
- [377] Fowler, D. A.; Tian, J.; Barnes, C.; Teat, S. J.; Atwood, J. L. Cocrystallization of C-butyl pyrogallol[4]arene and C-propan-3-ol pyrogallol[4]arene with gabapentin. *CrystEngComm* **2011**, 13, 1446–1449.
- [378] Kumari, H.; Zhang, J.; Erra, L.; Barbour, L. J.; Deakyne, C. A.; Atwood, J. L. Cocrystals of gabapentin with C-alkylresorcin[4]arenes. *CrystEngComm* **2013**, 15, 4045.

- [379] Martins, I. C. B.; Sardo, M.; Čendak, T.; Gomes, J. R. B.; Rocha, J.; Duarte, M. T.; Mafra, L. Hydrogen bonding networks in gabapentin protic pharmaceutical salts: NMR and in silico studies. *Magn. Reson. Chem.* **2019**, *57*, 243–255.
- [380] Reddy, L. S.; Bethune, S. J.; Kampf, J. W.; Rodríguez-Hornedo, N. Cocrystals and Salts of Gabapentin: pH Dependent Cocrystal Stability and Solubility. *Cryst. Growth Des.* **2009**, *9*, 378–385.
- [381] Shaikjee, A.; Levendis, D. C.; Marques, H. M.; Mampa, R. A gold(III) complex and a tetrachloroaurate salt of the neuroepileptic drug gabapentin. *Inorg. Chem. Commun.* **2011**, *14*, 534–538.
- [382] Wenger, M.; Bernstein, J. An Alternate Crystal Form of Gabapentin: A Cocrystal with Oxalic Acid. *Cryst. Growth Des.* **2008**, *8*, 1595–1598.
- [383] Zhao, C.; Su, X.; Fang, L.; Shang, Z.; Li, Z.; Gong, J.; Wu, S. Multivariate Analysis of a Highly Effective Drug Combination Tablet Containing the Antiepileptic Drug Gabapentin to Enhance Pharmaceutical Properties with a Multicomponent Crystal Strategy. *Cryst. Growth Des.* **2022**, *22*, 7234–7247.
- [384] Soliman, I. I.; Kandil, S. M.; Abdou, E. M. Gabapentin-saccharin co-crystals with enhanced physicochemical properties and in vivo absorption formulated as oro-dispersible tablets. *Pharm. Dev. Technol.* **2020**, *25*, 227–236.
- [385] Aramini, A.; Allegretti, M.; Bianchini, G.; Lillini, S.; Tomassetti, M. “CO-CRYSTAL OF KETOPROFEN, LYSINE AND GABAPENTIN, PHARMACEUTICAL COMPOSITIONS AND THEIR MEDICAL USE” WO2021224217. **2021**.
- [386] Vittal, Tangirala Venkata Subramanya Krishna; Taj, S. A.; Kodimuthali, A.; Maddali, K. Preparation of new mineral acid addition salts of gabapentin WO2003070683. **2002**.
- [387] Samineni, R.; Chimakurthy, J.; P., G.; Muneer, S.; Kolakaluri, C. S.; Tirumala, C. S. K. A formulation for improved drug release characteristic of gabapentin with benzoic acid as co-former IN202241039465. **2022**.
- [388] Zhang, J.; Ho, K.-Y.; Wang, Y. Efficacy of pregabalin in acute postoperative pain: a meta-analysis. *Br. J. Anaesth.* **2011**, *106*, 454–462.
- [389] Verma, V.; Singh, N.; Singh Jaggi, A. Pregabalin in neuropathic pain: evidences and possible mechanisms. *Curr. Neuropharmacol.* **2014**, *12*, 44–56.
- [390] Lauria-Horner, B. A.; Pohl, R. B. Pregabalin: a new anxiolytic. *Expert Opin. Investig. Drugs* **2003**, *12*, 663–672.
- [391] Federico, C. A.; Mogil, J. S.; Ramsay, T.; Fergusson, D. A.; Kimmelman, J. A systematic review and meta-analysis of pregabalin preclinical studies. *Pain* **2020**, *161*, 684–693.
- [392] Bonnet, U.; Scherbaum, N. How addictive are gabapentin and pregabalin? A systematic review. *Eur. Neuropsychopharmacol.* **2017**, *27*, 1185–1215.

- [393] Marras, G. Polymorphic crystalline form alpha of (S)-pregabalin and process for its preparation EP1977744. **2007**.
- [394] Plata Salaman, C. R.; Tesson, N.; Trilla Castano, M.; Cardenas Romana, L. Crystalline forms of pregabalin and co-formers in the treatment of pain EP2527319. **2012**.
- [395] Khandavilli, U. B. R.; Lusi, M.; Frawley, P. J. Plasticity in zwitterionic drugs: the bending properties of Pregabalin and Gabapentin and their hydrates. *IUCrJ* **2019**, 6, 630–634.
- [396] Khandavilli, U. B. R.; Yousuf, M.; Schaller, B. E.; Steendam, R. R. E.; Keshavarz, L.; McArdle, P.; Frawley, P. J. Plastically bendable pregabalin multi-component systems with improved tableability and compressibility. *CrystEngComm* **2020**, 22, 412–415.
- [397] Li, M.; Sun, J.; Kuang, W.; Zhou, L.; Han, D.; Gong, J. Drug–Drug Multicomponent Crystals of Epalrestat: A Novel Form of the Drug Combination and Improved Solubility and Photostability of Epalrestat. *Cryst Growth Des* **2022**, 22, 5027–5035.
- [398] Venu, N.; Vishweshwar, P.; Ram, T.; Surya, D.; Apurba, B. (S)-3-(Ammoniomethyl)-5-methylhexanoate (pregabalin). *Acta Crystallogr C Cryst Struct Commun* **2007**, 63, o306-8.
- [399] Samas, B.; Wang, W.; Godrej, D. B. *CCDC 663673: Experimental Crystal Structure Determination*, Cambridge Crystallographic Data Centre, **2007**.
- [400] Thaper, R. K.; Prabhavat, M. D.; Arora, S. K.; Pawar, Y. D.; Varma, D. K. P.; Kamble, V. S.; Shinde, V. S. Resolution of pregabalin using chiral salts IN2008KO00929. **2008**.
- [401] Gore, V.; Datta, D.; Gadakar, M.; Pokharkar, K.; Mankar, V.; Wavhal, S. Resolution of pregabalin WO2009122215. **2009**.
- [402] Gore, V.; Datta, D.; Gadakar, M.; Pokharkar, K.; Mankar, V.; Wavhal, S. Novel process US20110124909. **2011**.
- [403] Khaja, A.; Potla, V. S. R.; Rawat, G. S.; Konudula, B. R.; Chauhan, Y. K.; Datta, D. Process for preparing (S)-3-(aminomethyl)-5-methylhexanoic acid WO2009125427. **2009**.
- [404] Mafatlal, K. B.; Keshavlal, K. N.; Sivaprasad, K.; Rajendra, P. C.; Bhikhalal, V. P.; Rajaram, B. U.; Ambalal, M. I. Improved process for the preparation of pregabalin using a mixture of two acids for the resolution of its racemic IN2009MU01587. **2009**.
- [405] Pradhan, B. S. A process for resolution of (\pm)-3-(aminomethyl)-5-methylhexanoic acid IN2010CH01584. **2010**.
- [406] Reddy, S. R. D.; Velivela, S. R.; Reddy, R. R. V. An improved process for the preparation of enantiomerically pure pregabalin IN2010CH00299. **2010**.
- [407] Zvejniece, L.; Vavers, E.; Svalbe, B.; Veinberg, G.; Rizhanova, K.; Liepins, V.; Kalvinsh, I.; Dambrova, M. R-phenibut binds to the $\alpha 2$ - δ subunit of voltage-dependent calcium channels and exerts gabapentin-like anti-nociceptive effects. *Pharmacol. Biochem. Behav.* **2015**, 137, 23–29.

- [408] Owen, D. R.; Wood, D. M.; Archer, J. R. H.; Dargan, P. I. Phenibut (4-amino-3-phenyl-butyric acid): Availability, prevalence of use, desired effects and acute toxicity. *Drug Alcohol Rev.* **2016**, 35, 591–596.
- [409] Lapin, I. Phenibut (beta-phenyl-GABA): a tranquilizer and nootropic drug. *CNS Drug Rev.* **2001**, 7, 471–481.
- [410] Kupats, E.; Vrublevska, J.; Zvejniece, B.; Vavers, E.; Stelfa, G.; Zvejniece, L.; Dambrova, M. Safety and Tolerability of the Anxiolytic and Nootropic Drug Phenibut: A Systematic Review of Clinical Trials and Case Reports. *Pharmacopsychiatry* **2020**, 53, 201–208.
- [411] Jouney, E. A. Phenibut (β -Phenyl- γ -Aminobutyric Acid): an Easily Obtainable “Dietary Supplement” With Propensities for Physical Dependence and Addiction. *Curr. Psychiatry Rep.* **2019**, 21, 23.
- [412] Dambrova, M.; Zvejniece, L.; Liepinsh, E.; Cirule, H.; Zharkova, O.; Veinberg, G.; Kalvinsh, I. Comparative pharmacological activity of optical isomers of phenibut. *Eur. J. Pharmacol.* **2008**, 583, 128–134.
- [413] Y. Mao, P. Y. Zavalij, *CCDC 1821706: Experimental Crystal Structure Determination*, Cambridge Crystallographic Data Centre, **2018**.
- [414] Senior, T.; Botha, M. J.; Kennedy, A. R.; Calvo-Castro, J. Understanding the Contribution of Individual Amino Acid Residues in the Binding of Psychoactive Substances to Monoamine Transporters. *ACS Omega* **2020**, 5, 17223–17231.
- [415] Addolorato, G.; Leggio, L. Safety and efficacy of baclofen in the treatment of alcohol-dependent patients. *Curr. Pharm. Des.* **2010**, 16, 2113–2117.
- [416] Brennan, J. L.; Leung, J. G.; Gagliardi, J. P.; Rivelli, S. K.; Muzyk, A. J. Clinical effectiveness of baclofen for the treatment of alcohol dependence: a review. *Clin. Pharmacol.* **2013**, 5, 99–107.
- [417] Bowery, N. G. Baclofen: 10 years on. *Trends Pharmacol. Sci.* **1982**, 3, 400–403.
- [418] Dario, A.; Tomei, G. A benefit-risk assessment of baclofen in severe spinal spasticity. *Drug Saf.* **2004**, 27, 799–818.
- [419] Kent, C. N.; Park, C.; Lindsley, C. W. Classics in Chemical Neuroscience: Baclofen. *ACS Chem. Neurosci.* **2020**, 11, 1740–1755.
- [420] Leggio, L.; Garbutt, J. C.; Addolorato, G. Effectiveness and safety of baclofen in the treatment of alcohol dependent patients. *CNS Neurol. Disord. Drug Targets* **2010**, 9, 33–44.
- [421] Leo, R. J.; Baer, D. Delirium associated with baclofen withdrawal: a review of common presentations and management strategies. *Psychosomatics* **2005**, 46, 503–507.
- [422] Couvrat, N.; Sanselme, M.; Poupard, M.; Bensakoun, C.; Drouin, S. H.; Schneider, J.-M.; Coquerel, G. Solid-State Overview of R-Baclofen: Relative Stability of Forms A, B and C and Characterization of a New Heterosolvate. *J. Pharm. Sci.* **2021**, 110, 3457–3463.

- [423] Maniukiewicz, W.; Oracz, M.; Sieroń, L. Structural characterization and Hirshfeld surface analysis of racemic baclofen. *J. Mol. Struct.* **2016**, 1123, 271–275.
- [424] Mirza, S.; Miroshnyk, I.; Rantanen, J.; Aaltonen, J.; Harjula, P.; Kiljunen, E.; Heinämäki, J.; Yliruusi, J. Solid-state properties and relationship between anhydrate and monohydrate of baclofen. *J. Pharm. Sci.* **2007**, 96, 2399–2408.
- [425] Báthori, N. B.; Kilinkissa, O. E. Y. Are gamma amino acids promising tools of crystal engineering? – Multicomponent crystals of baclofen. *CrystEngComm* **2015**, 17, 8264–8272.
- [426] Kavuru, P.; Aboarayas, D.; Arora, K. K.; Clarke, H. D.; Kennedy, A.; Marshall, L.; Ong, T. T.; Perman, J.; Pujari, T.; Wojtas, Ł.; Zaworotko, M. J. Hierarchy of Supramolecular Synthons: Persistent Hydrogen Bonds Between Carboxylates and Weakly Acidic Hydroxyl Moieties in Cocrystals of Zwitterions. *Cryst. Growth Des.* **2010**, 10, 3568–3584.
- [427] Malapile, R. J.; Nyamayaro, K.; Nassimbeni, L. R.; Báthori, N. B. Multicomponent crystals of baclofen with acids and bases—conformational flexibility and synthon versatility. *CrystEngComm* **2021**, 23, 91–99.
- [428] Córdova-Villanueva, E. N.; Rodríguez-Ruiz, C.; Sánchez-Guadarrama, O.; Rivera-Islas, J.; Herrera-Ruiz, D.; Morales-Rojas, H.; Höpfl, H. Diastereomeric Salt Formation by the γ -Amino Acid RS -Baclofen and L -Malic Acid: Stabilization by Strong Heterosynthons Based on Hydrogen Bonds between RNH³⁺ and COOH/COO⁻ Groups. *Cryst. Growth Des.* **2018**, 18, 7356–7367.
- [429] Songsermsawad, S.; Nalaoh, P.; Promarak, V.; Flood, A. E. Chiral Resolution of RS -Baclofen via a Novel Chiral Cocrystal of R -Baclofen and L -Mandelic Acid. *Cryst. Growth Des.* **2022**, 22, 2441–2451.
- [430] Zaworotko, M.; Clarke, H.; Kapildev, A.; Kavuru, P.; Shytle, R. D.; Pujari, T.; Marshall, L.; Ong, T. T. Nutraceutical co-crystal compositions WO2008153945. **2008**.
- [431] Coquerel, G.; Mahieux, J.; Gendron, F.-X. Method for the resolution of baclofen salts WO2018015677. **2017**.
- [432] Peterson, M.; Oliveira, M. Preparation of organic acid salts of gabapentin WO2004091278. **2004**.